Journal of
Optoelectronics and
Advanced Materials

Journal of Optoelectronics and Advanced Materials

REPORT DOCUMENTATION PAGE

Form Approved OMB No. 0704-0188

1. AGENCY USE ONLY (Leave blank)	2. REPORT DATE 2001	3. REPORT TYPE AND DATES COVERED June 25-28, 2001 Conference Proceedings - Final Report

4. TITLE AND SUBTITLE
International Workshop on Amorphous and Nanostructured Chalcogenides (1st) – Fundamentals and Applications held in Bucharest, Romania. June 25-28,2001. Proceedings, Part 1.

5. FUNDING NUMBERS

6. AUTHOR(S)
Mihai A. Popescu, Editor

7. PERFORMING ORGANIZATION NAME(S) AND ADDRESS(ES)

National Institute of Materials Physics
Bucharest, Romania

8. PERFORMING ORGANIZATION REPORT NUMBER

ISSN 1454-4164

9. SPONSORING/MONITORING AGENCY NAME(S) AND ADDRESS(ES)

Office of Naval Research,
European Office
PSC 802 Box 39
FPO AE 09499-0039

10. SPONSORING/MONITORING AGENCY REPORT NUMBER

11. SUPPLEMENTARY NOTES
Published in the Journal of Optoelectronics and Advanced Materials, Vol. 3 No.2, June 2001. Published by the Journal of Optoelectronics and Advanced Materials, 1 Atomistilor St., PO Box MG.5, 76900 Bucharest-Magurele, Romania. This work relates to Department of the Navy Grant issued by the Office of Naval Research International Field Office. The United States has a royalty free license throughout the world in all copyrightable material contained herein.

12a. DISTRIBUTION/AVAILABILITY STATEMENT

12b. DISTRIBUTION CODE

A

12. ABSTRACT (Maximum 200 words)
Includes papers presented at the First International Workshop on Amorphous and Nanostructured Chalcogenides – Fundamentals and Applications held in Bucharest, Romania. June 25-28,2001

13. SUBJECT TERMS
ONRIFO, Foreign reports, Conference Proceedings, Chalcogenide alloys, Electronic structure, Nanostructures

15. NUMBER OF PAGES

16. PRICE CODE

17. SECURITY CLASSIFICATION OF REPORT UNCLASSIFIED	18. SECURITY CLASSIFICATION OF THIS PAGE UNCLASSIFIED	19, SECURITY CLASSIFICATION OF ABSTRACT UNCLASSIFIED	20. LIMITATION OF ABSTRACT UL

NSN 7540-01-280-5500

Standard Form 298 (Rev. 2-89)
Prescribed by ANSI Std. 239-18
298-102
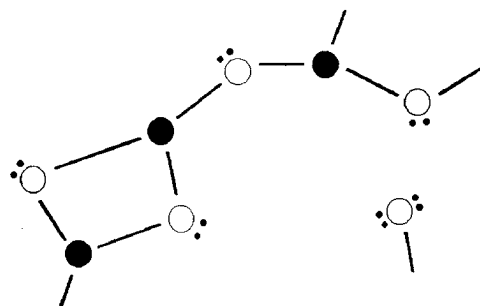
First International Workshop on

AMORPHOUS AND NANOSTRUCTURED CHALCOGENIDES

-Fundamentals and Applications-

Bucharest, Romania, June 25-28, 2001

Proceedings, Part I

dedicated to
Acad. Prof. Dr. Doc. **Radu Grigorovici**
with the occasion of his 90th anniversary

20011130 017

Editor: Prof. Dr. Mihai A. Popescu

AO F02-02-0293

Sponsors of the Workshop:
- Romanian Ministry of Education and Research
- Office of Naval Research, International Field Office, U.S.A.
- Rom Tech S.R.L./Bruker aXS, Romania
- TRANSGAZ S.A., Medias, Romania
- S.C. Rulmentul SA – Brasov, Romania

Organizers:
- National Institute of Materials Physics, Bucharest
- National Institute of Optoelectronics, Bucharest
- Romanian Academy
- University of Bucharest
- Romanian Materials Science-Crystal Growth Society
- University "Polytechnica", Bucharest
- National Institute of Glass, Bucharest

Honorary Director: Radu Grigorovici,
                    Romanian Academy
Director: Mihai A. Popescu, NIMP, Bucharest

CONTENT

ELECTRONIC STRUCTURE, AMORPHOUS MORPHOLOGY AND THERMAL STABILITY OF TRANSITION METAL OXIDE AND CHALCOGENIDE ALLOYS

G. Lucovsky

Departments of Physics, Electrical and Computer Engineering, and Materials Science and Engineering, North Carolina State Univ., Raleigh, NC 27695, USA

This paper is presented to honor Professor Radu Grigorovici at his 90th birthday celebration for his outstanding contributions to the chemical bonding and atomic structure of amorphous semiconductors, including the chalcogenides that are highlighted at this conference. A chemical bonding approach is applied in this paper to non-crystalline transition metal oxides and their silicate and aluminate alloys. Transition metal oxides and alloys are considerably more ionic than SiO_2, and this increased ionicity, along with the localized electronic structure associated with transition metal atom d-states is the basis for the significant differences in their optical and electrical properties. This paper also provides new insights into the electronic structure of transition metal chalgogenide alloys.

1. Introduction

Interest in the electronic structure of amorphous semiconductors was stimulated by two advances in technology that occurred more than 25 years ago: i) the discovery of reversible and irreversible electronic and optical switching in chalcogenide alloys by Ovshinsky and his coworkers at Energy Conversion Devices, ECD [1,2], and ii) the fabrication of photovolatic devices in hydrogenated amorphous silicon by Carlson and Wronski at RCA [3]. These advances in technology resulted in a world-wide interest in the properties of amorphous semiconductors, including Si and Ge, the elemental and compound chalcogenides, as well as *more complex* chalcogenide alloys. Whilst the primary dedication of this paper is to Professor Radu Grigorovici for his pioneering work in chemical bonding, atomic structure, and transport and optical properties of chalcogenides and other elemental amorphous semiconductors, three other pioneers in this field warrant recognition as well. This are i) Sir Neville Mott for the role he and his coworkers at University of Cambridge and elsewhere played in the development of a microscopic understanding of the electronic properties of amorphous semiconductors [4], iii) Josef Stuke for his pioneering studies of crystalline Se and Te, and transport properties of amorphous Si and Ge [5.6], and finally, iii) Stan Ovshinsky for having the courage, determination and remarkable insight to seek, and to find new and *unanticipated* properties in complex chalcogenide alloys that were well outside of the *comfortable envelope of the prevailing conventional wisdom* [1,2].

The primary motivation for the research presented in this paper has been the search for new dielectric materials for advanced Si devices. Non-crystalline alloys of group IIIB and IVB transition metal oxides and rare earth oxides, e.g., $Y(La)_2O_3$ and $Zr(Hf)O_2$. and $Gd(Dy)_2O_3$, respectively. alloyed with SiO_2 and Al_2O_3, have been proposed as alternative high-k gate dielectrics for these advanced Si devices with decreased dimensions and increased levels of integration [7]. Increases in k relative to SiO_2 permit the use of physically thicker films to obtain the same effective capacitance as devices with physically thinner SiO_2 gate dielectrics, providing potential for significantly decreased direct tunneling. However, decreases in direct tunneling associated with this increased physical thickness are negated in part by reductions in the conduction band offset energies that define the tunneling barrier between the Si substrate and the dielectric. This paper develops a classification scheme for non-crystalline oxide-based dielectrics [8], and uses this as the basis for molecular orbital, MO, calculations that have established an inherent correlation between the energy difference of transition metal atomic n+1 s- and n d-states and the conduction band offset energies between transition metal oxides and oxide alloys and Si [9,10]. These offset energies determine i) the barrier for direct tunneling between the Si substrate and the transition metal dielectric, and ii) the activation energy for

injection into localized transition metal anti-bonding states in the silicate and aluminate alloys. The paper then extends the new insights obtained for this new understanding of the fundamental electronic of transition metal and rare earth oxide non-crystalline alloys to transition metal chalcogenide non-crystalline alloys. For example, it establishes a theoretical approach for electronic structure of amorphous semiconductors in which the coordination of the constituent atoms is outside the confines of the 8-N rule description that applies to amorphous Se, and $As_2S(Se)_3$, $GeS(Se)_2$, etc [6].

As applied to the transition metal and rare earth oxides and their alloys, the empirical model of Ref. 10 has shown that the lowest lying conduction bands in crystalline transition metal elemental and binary oxides are derived from atomic d-states of the transition metals. The ab initio MO model of this paper demonstrates this assignment is not restricted to elemental and binary crystalline oxides, but applies more generally to non-crystalline transition metal oxides and their alloys as well [11-13]. This approach and the qualitative electronic structure results are directly transferable to transition metal chacogenides in which sulfur or selenium atoms replace oxygen, and the p-state derived valence bands of S and Se do not overlap the d-state derived conduction bands of the transition metal atoms. However, there are qualitatively different electronic and optical properties in transition metal telluride alloys that result from the overlap of Te 5p valence bands with anti-bonding transition metal d-states.

2. Classification of non-crystallne oxides

Zallen [14] has identified and discussed three different atomic scale amorphous morphologies for non-crystalline solids i) continuous random networks, crn's, as exemplified by SiO_2 with predominantly covalent bonding between the constituent atoms, ii) modified continuous random networks, mcrn's, as exemplified by silicate alloys in which metal atom ionic bonds *disrupt* and *modify* the covalently bonded crn structure, and iii) random close packed, rcp, non-periodic solids comprised entirely of negative and positive ions. A classification scheme based on bond ionicity is used to distinguish three different groups of non-crystalline dielectrics with these three distinct amorphous morphologies [8].

There are several different ways to define bond ionicity. The most rigorous way is through calculations of the electronic structure with the application of an *atomic scale metric* such as an atomic radius that is defined in a self-consistent manner and preserves overall charge neutrality. However, there is an intimate relationship between electronegativity [15], X, and the fundamental atomic electronic structure that is reflected in the variation of X across the periodic table. This means that X provides an appropriate metric for defining a bond ionicity that is correlated directly with the electronic structure of the constituent atoms. A definition of bond ionicity, I_b, as originally introduced by Pauling, is the basis for a classification scheme of this paper [15].

For example, if X(O) is the *Pauling electronegativity* of oxygen, 3.44, and X(Si) is the corresponding electronegativity of silicon, 1.90, then the electronegativity difference between these two atoms, $\Delta X = X(O) - X(Si)$, is 1.54. Applying Pauling's empirical definition of bond ionicity, I_b,

$$I_b = 1 - \exp(-0.25(\Delta X)^2), \tag{1}$$

gives a value of I_b for Si-O bonds of $\sim 45\%$. The range of ΔX values for the oxides of interest in this paper ranges from about from 1.5 to 2.4. For this range of ΔX, I_b is approximately a linear function of ΔX, so that ΔX and I_b are functionally *equivalent* scaling variables. It is important to understand that charge localization on the silicon and oxygen atoms, i.e., effective ionic charges, cannot be determined directly from these values of bond ionicity. In SiO_2, there are π-bonding interactions between silicon atom states with d-like symmetries that are the acceptor states for a back donation of charge from oxygen 2p π states that make the definition of an effective ionic charge a more subtle, and inherently complex issue [16,17].

The non-crystalline oxides, and As and Ge chalcogenides as well, with ΔX up to about 1.5 form covalently-bonded continuous random networks, crn's, in which the constituent atoms have a coordination that reflects its primary chemical valence; e.g., two for O, S and Se, three for N and As, and four for Si and Ge [14]. The bonding in these crn materials obeys the 8-N rule independent of any π-bonding contributions that arise from back donation into d-like polarization states of the P, As, Si or Ge atoms [4]. The glass forming character of these materials, as well as their low defect densities in thin films and bulk glasses, is correlated with the number of bonding constraints per atom and has been discussed in detail in a series of seminal papers by Phillips and his coworkers [18-21].

The second class of non-crystalline dielectrics form modified crn's, mcrn's, which include

ionic bonding arrangements of metal atoms that *modify and disrupt* the network structure. This class of dielectrics is characterized by values of ΔX between about 1.6 and 2.0, or equivalently bond ionicities between about 47 and 67%. The most extensively studied and characterized oxides in this group in are the metal atom silicate alloys, for example SiO_2 that has been alloyed with Na_2O, CaO, TiO_2, ZrO_2, etc., and quenched from the melt [14]. This class also includes deposited thin film Al_2O_3, TiO_2 and Ta_2O_5, and transition metal atom silicate alloys such as $(Zr(Hf)O_2)_x(SiO_2)_{1-x}$ in the composition range up to about x~0.5 [8]. The non-crystalline range of alloy formation in deposited thin films is increased significantly with respect to what it is in bulk glasses quenched from the melt. The coordination of oxygen atoms in crn's is typically two, and increases to approximately three in the mcrn's (see Table 1). As examples, the average coordination of oxygen is 2.8 in thin film Ta_2O_5 and 3.0 in Al_2O_3, and increases from 2 to 3 in the group IVB silicate alloys as the ZrO_2 or HfO_2 fraction, x, is increased from doping levels less 0.01 up to alloy levels of 0.5.

Table 1. Electronegativity difference, ΔX, average bond ionicity, I_b, and metal and oxygen coordination for SiO_2 and high-k alternative dielectrics. The $(La_2O_3)_2(SiO_2)_1$ alloy contains both O ions and silicate groups, and as such the O atoms have more local coordinations of 4 and 3, respectively.

DIELECTRIC	ΔX	I_b	COORDINATION M, M or Si	COORDINATION O
CONTINUOUS RANDOM NETWORKS			metal / silicon	oxygen
SiO_2	1.54	0.45	4	2.0
CRN'S WITH NETWORK MODIFIERS				
Al_2O_3	1.84	0.57	4 and 6 (3:1)	3.0
Ta_2O_5	1.94	0.61	6 and 8 (1:1)	2.8
TiO_2	1.90	0.59	6	3.0
$(ZrO_2)_{0.1}(SiO_2)_{0.9}$	1.61	0.48	8 and 4	2.2
$(ZrO_2)_{0.23}(SiO_2)_{0.77}$	1.70	0.51	8 and 4	2.46
$(ZrO_2)_{0.5}(SiO_2)_{0.5}$	1.88	0.59	8 and 4	3.0
$(TiO_2)_{0.5}(SiO_2)_{0.5}$	1.72	052	6 and 4	2.5
$(Y_2O_3)_1(SiO_2)_2$	1.88	0.59	6 and 4	2.86
$(Y_2O_3)_2(SiO_2)_3$	1.93	0.61	6 and 4	3.0
$(Y_2O_3)_1(SiO_2)_1$	1.99	0.63	6 and 4	3.11
$(Al_2O_3)_4(ZrO_2)_1$	2.02	0.64	4 and 8	3.0
$(Al_2O_3)_3(Y_2O_3)_1$	1.97	0.62	4 and 6	3.0
RANDOM CLOSE PACKED IONS				
HfO_2	2.14	0.68	8	4.0
ZrO_2	2.22	0.71	8	4.0
$(La_2O_3)_2(SiO_2)_1$	2.18	0.70	6 and 4	3.5
Y_2O_3	2.22	0.71	6	4.0
La_2O_3	2.34	0.75	6	4.0

The third group of non-crystalline oxides has a random close packed ionic amorphous morphology [14]. This class of oxides is correlated with $\Delta X > 2$, and a Pauling bond ionicity of greater than ~67%. This group includes transition metal oxides that are deposited by low temperature techniques including plasma deposition, and sputtering with post-deposition oxidation [7]. The coordination of the oxygen atoms in these rcp structures is typically four.

Table 1 includes i) a list of representative elemental and binary oxide alloys, as well as values of ii) ΔX, iii) I_b, and iii) the average O-atom and cation bonding coordinations. In summary, values of ΔX of ~1.6 and ~2.0 separate these elemental and binary into three different groups: i) crns for ΔX up to 1.6, ii) mcrn's for ΔX between ~1.6 and 2.0, and iii) rcp ionic structures for $\Delta X > 2$. As

The average coordination of O-atoms is 2 for the crn's, between 2 and 3 for the mcrn's and greater than 3, and typically four for the rcp oxides. The values of I_b, calculated from Eqn. [2], that separate these three groups, are approximately 47% and 67%.

Fig. 1 contains a plot of the average oxygen atom coordination as a function of the average bond ionicity, I_b. The values of oxygen atom coordination are either i) inferred from measurements or measured directly [22], or ii) determined from crystalline compounds [16]. Since I_b is a linear function of ΔX for the oxides, and silicate and aluminate alloys of interest, the average oxygen atom coordination also scales linearly with ΔX. The approximately linear variation suggests a fundamental relationship between charge localization of the oxygen atom and bonding coordination. A classification scheme for chalcogenides can be formulated in terms of electronegativity; however, the scale is severely compressed due to the decreased electronegativities of S, Se and Te with respect to O. However, a classification scheme based on the bonding coordination of the chalcogen atoms is more useful. For example, it separates chalcogenides into groups with inherently different amorphous morphologies, the most important of which are crn's and mcrn's.
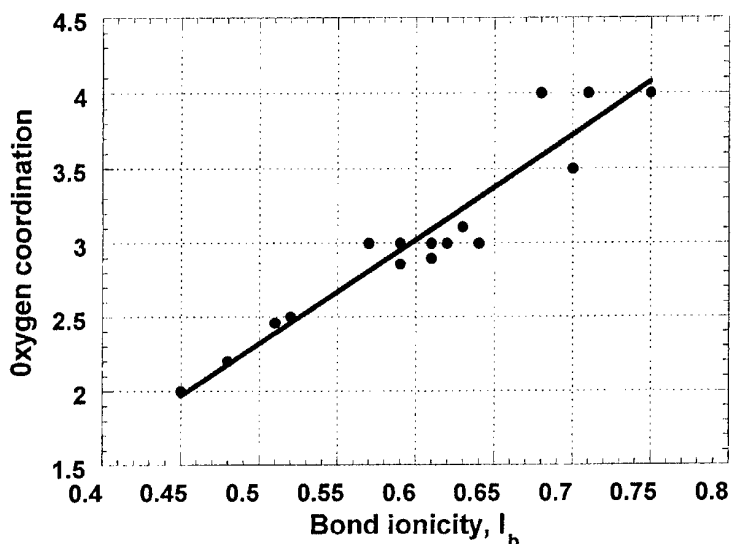
Fig. 1. Average oxygen atom coordination as a function of the average bond ionicity, I_b for SiO_2 and elemental and binary oxides that have been considered as alternative high – k gate dielectrics.

Returning to the oxides, the emphasis of the next few sections of the paper will be on transition metal silicate and aluminate, pseudo-binary alloys of group IIIB and IVB transition metals and rare earth lanthanides, with either SiO_2 or Al_2O_3, respectively. These pseudo-binary alloys have modified continuous random network structures in which the transition metals atoms either disrupt the work crn structure of SiO_2, or substitute for the six-fold coordinated Al^{3+} ions of the non-crystalline Al_2O_3 structure [22]. The coordination of group IVB transition metals such as Zr and Hf has been shown to be a function of the Zr(Hf)O_2 fraction in the low concentration silicate alloys [23], so that both tetrahedral and higher coordinations up to eight oxygen neighbors must be addressed. In order to evaluate the potential of these alloys for applications as high-k gate dielectrics for advanced semiconductor devices, it is necessary to understand their electronic structure. Conversely, a quantitative understanding of electronic structure, particularly the atomic parentage of the valence band states, and the lowest conduction band or anti-bonding states provides a basis for interpretation of many important optical and electrical experimental results.

3. Molecular orbital calculations

Fig. 2 is a molecular orbital energy level diagram for a group IV transition metal, e.g., Ti, in an octahedral bonding arrangement with six oxygen neighbors [11-13]. Each oxygen atom is assumed to provide one σ and two π 2p-electrons for potential bonding with the neutral group IV atoms, each of which contributes four additional electrons. The symmetries and π or σ character of the resulting orbitals are determined by symmetries of the group IVB and oxygen atomic states. Of the twenty-two available electrons, fourteen are involved σ and π bonding, and the remaining four are in oxygen atom

non-bonding orbitals with π character. The calculations show that the spatial localization of the transition metal atomic d-states gives a solid state broadening significantly less than their energy separation relative to transition metal s-states. The top of the valence band is associated with non-bonding π orbitals of oxygen atom p-states, and the first two conduction bands are associated with transition metal d-states. In order of increasing energy these conduction bands have the following symmetries $t_{2g}(\pi^*)$, and $e_g(\sigma^*)$. The next conduction band is derived from transition metal s-states with $a_{1g}(\sigma^*)$ character. The energy separation between the top of the valence band and the $a_{1g}(\sigma^*)$ band edge defines an effective *ionic band gap* with essentially the same energy as that of non-transition metal insulating oxide; i.e., $\sim$ 8-9 eV [13]. Higher lying conduction bands are derived from transition metal p-states with both σ and π character, t_{1u} (σ^*,π^*). The ordering of the first three conduction bands in crystalline TiO_2 has been verified by electron energy loss and X-ray spectroscopies, which confirm the relative sharpness of the $t_{2g}(\pi^*)$, and $e_g(\sigma^*)$ bands, the increased width of the $a_{1g}(\sigma^*)$ band, as well as an ionic band energy > 8 eV [24].
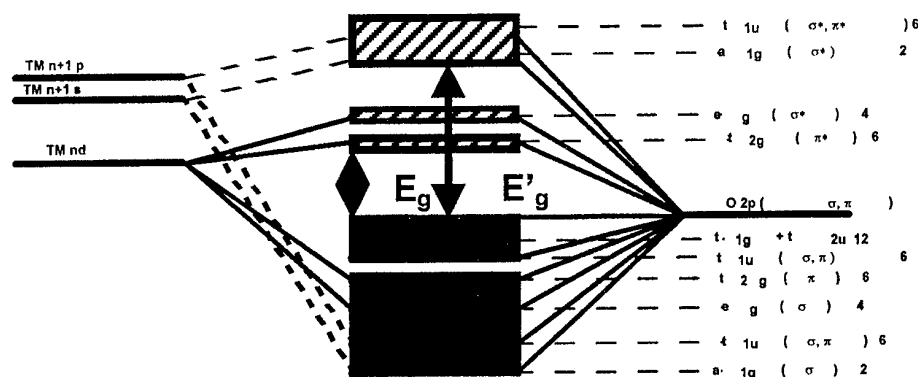
Fig. 2. Relative orbital energies for a group IVB transition metal in an octahedral bonding geometry with six oxygen atom neighbors.

A group theoretical analyses of the relative energies and symmetries of valence and conduction band orbitals for four- and six-fold coordinated transition metal atoms in tetrahedral and octahedral bonding environments [13,16] reveals a different ordering and σ and π assignment of the transition metal d-states (see Table 2). The lowest lying anti-bonding or conduction band states are derived from the triply degenerate transition metal d-states for the octahedral bonding, and the doubly degenerate d-states for the tetrahedral bonding. The symmetry of these anti-bonding states can be correlated directly with the spatial orientation between the d-orbitals and the oxygen neighbors. If the orbitals of one of the d-states groups, t_g or e_g, can be directed toward the nearest neighbors, then these orbitals are involved in s bonding interactions, whilst the other set is involved in p bonds. This establishes the ordering in relative energy of the bonding and anti-bonding derived from these d-states. This type of analysis can be readily extended to other coordinations; e.g., eight-fold, and other bonding symmetries, e.g., cubic and trigonal prism. The reader is referred to Refs 13 and 16 for details, including the group theory symmetry designations of the bonding, non-bonding and anti-bonding states.

Table 2. Comparison of bonding, non-bonding and anti-bonding states for octahedral and tetrahedral coordination of transition metal atoms.

Symmetry Designation*	Octahedral Coordination	Tetrahedral Coordination
Bonding States, (^{b})	$a_{1g}(\sigma^b)$ [2], $t_{1u}(\sigma^b, \pi^b)$ [6], $e_g(\sigma^b)$ [4], $t_{2g}(\pi^b)$ [6]	$a_1(\sigma^b)$ [2], $t_2(\sigma^b, \pi^b)$ [6], $e(\pi^b)$ [4], $t_1(\pi^b)$ [6]
Non-bonding States (1 σ and 2 π electrons/O)	$t_{1u}(\sigma,\pi)$ [6], $t_{1g} + t_{2u}$ [12]	$t_1(\pi)$ [12]
Anti-bonding States, (*)	$t_{2g}(\pi^*)$ [6], $e_g(\sigma^*)$ [4], $a_{1g}(\sigma^*)$ [2], $t_{1u}(\sigma^*, \pi^*)$ [6]	$e(\pi^*)$ [4], $t_2(\sigma^*,\pi^*)$ [12], $a_1(\sigma^*)$ [2], $t_2(\sigma^b)$ [6]

* The numbers in brackets are the number so states available in each orbital. The occupancy depends on the number of electrons available from the transition metal (i.e., its formal ionization state), and coordination of the oxygen atom ligands.

The calculations further demonstrate that the energy difference between the lowest conduction band with $t_{2g}(\pi^*)$ symmetry, and the bottom of the $a_{1g}(\sigma^*)$ band scales with the difference in energy between the n+1 s- and n d-states of the transition metal atoms [25]. The argument for this proceeds as follows: since the ionic band gaps, defined in terms of transitions between the p-derived valence band states of the oxygen and the s-derived conductions band states of the transition metals, are at about the same energy, ~ 8-9 eV, the larger the energy difference between the transition metal atomic s- and d-states, and the closer the d-state bands are to the top of valence band. This means that the smallest band gaps of transition metal oxides and silicate and aluminate alloys will scale approximately with the difference in energy between the transition metal s- and d-states. Since the transition metal s-states are all at approximately the same energy with respect to vacuum, this means additionally that the lowest band-gaps are expected to scale with the energy difference between oxygen or chalcogen atom p-states and the transition metal d-states (see Fig. 3).
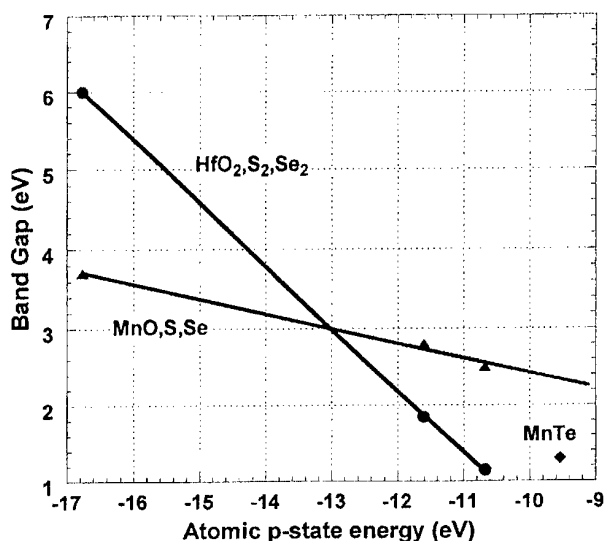
Fig. 3. Optical band gap versus the energy of the atomic p-states of oxygen, sulfur and selenium for i) HfO_2, HfS_2 and $HfSe_2$, and ii) MnO, MnS, and MnSe.

The scaling in Figs. 3 and the results in Table 3 show that energy level schemes similar to Fig. 2 apply to transition metal chalcogenides in which oxygen is replaced by sulfur and selenium [19,20]. Fig. 3 is a plot i) optical band gap versus the energy of the atomic p-states of oxygen, sulfur and selenium for (a) HfO_2, HfS_2 and $HfSe_2$ [4,19], and (b) MnO, MnS, and MnSe [20], and Table 3 compares the optical band gap versus atomic n d-state energy of the transition metal atom for group IVB oxides, sulfides and selenides [4,19]. The plot in Fig. 3 shows that for a given transition metal, the band gap scales with the p-state energy of the chalcogen, whereas the results in Table 3 show that for a fixed negative ion, O or S, the band gap scales with the energy of the transition metal atom d-state. The results in Table 3 show that for a given cation, O, S or Se, the optical band gap scales as the energy of the atomic d-state of the transition metal.

Table 3 . Comparison between band gaps of group IV B oxides, sulfides, and selenides, and d-state energy of group IVB transition metals, Ti, Zr and Hf.

group IVB atom	d-state (eV)	band gap (eV)		
		oxide	sulfide	selenide
Ti	-11.1	3.05 6.0	<0.5	<0.5
Zr	-8.5	6.0	1.9	1.1
Hf	-8.8	6.0	1.9	1.15

4. Band offset energy

The band offset energy between the conduction band of Si and the empty anti-bonding or conduction band states of a high-k dielectric is important in metal-oxide-semiconductor, MOS, device performance. It defines the barrier for direct tunneling, and/or thermal emission of electrons from an n^+ Si substrate into the dielectric. In alloys such as Al_2O_3-Ta_2O_5, or SiO_2-ZrO_2, it defines the energy of localized Ta and Zr transition metal electron trapping states, respectively, relative to the Si conduction band minimum [28].

The energies with respect to vacuum of the atomic n+1 s-states of the group IIIB, IVB and VB are approximately constant, ~ -7 eV. The band gaps of the transition metal oxides have been shown in Table 3 to scale with the energies of the n d-atomic states of the transition metal atoms. Based on the molecular orbital model of Fig. 2, it is reasonable to assume that the difference in energy between the lowest anti-bonding d-states and s-states scales with the difference in the energies of the atomic n+1 s- and n d-states. If this is the case, then the band offset energy between the conduction band of Si and the lowest conduction band of the transition metal oxides must also scale with the absolute value of the difference between the energies of the atomic n+1 s- and n d-states (see Fig. 2). Fig. 4 displays the band offset energies of transition metal oxides from Refs. 9 and 10 as a function of the atomic s- state to d-state energy difference. The data points in Fig. 4 display an approximately linear dependence, supporting the assumptions made on the basis of the molecular orbital model description of the electronic structure of the transition metal oxide derived conduction band states.
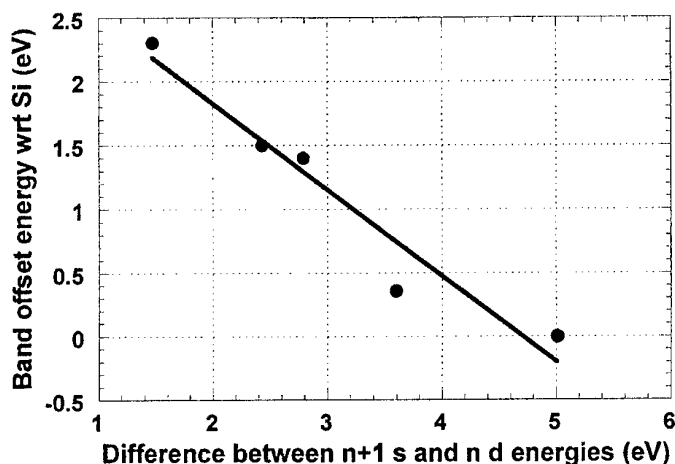
Fig. 4. Band offset energies from versus the absolute value of the n+1 s - n d energy difference for transition metal elemental oxides and silicates.

5. Recent experimental results

5.1. Trapping at Transition Metal Sites in Al_2O_3-Ta_2O_5 Alloys

Alloys of Al_2O_3 and Ta_2O_5 with different concentrations of Ta_2O_5 have been prepared by remote plasma assisted deposition onto hydrogen terminated Si(100) substrates and incorporated into MOS capacitors. These alloys are pseudo-binary in character with Ta-O and Al-O bonds, but no spectroscopic evidence for Al-Ta bonds; the details are discussed in Ref. 21. In addition as shown in Ref. 9, there is a large anisotropy between the conduction and valence band offset energies of Ta_2O_5, ~ 0.3 eV and 3.0 eV, whilst the corresponding offset energies for Al_2O_3 show a smaller anisotropy, 2.1 eV as compared with 3.7 eV. Fig. 5 indicates the leakage current from an n^+ Si substrate as a function of temperature. Flat band voltage shifts, and hysteresis in for capacitance-voltage C-V, data in the low temperature regime, are consistent with electron trapping, whereas the C-V data in the high temperature regime are consistent with emission out of trapping states. Combining these C-V data with the energy band scheme of Fig. 2, the activation energy in the low temperature regime, ~0.3 eV, for electron trapping is assigned to the difference in energy between the Si conduction band and the lowest lying $t_{2g}(\pi^*)$ state of a six fold coordinated Ta atom, and the activation energy at higher temperatures, ~1.5 eV, is assigned to emission out of these Ta traps into the conduction band of the Al_2O_3 matrix. These two energies are consistent with the measured band offset energy of Ta_2O_5 with

respect to Si, ~0.36 eV, as determined from X-ray photoelectron spectroscopy, XPS [9], and the energy difference between the measured band offset energies for Al_2O_3 and Ta_2O_5 with respect to Si, ~1.7 eV, also measured by XPS.
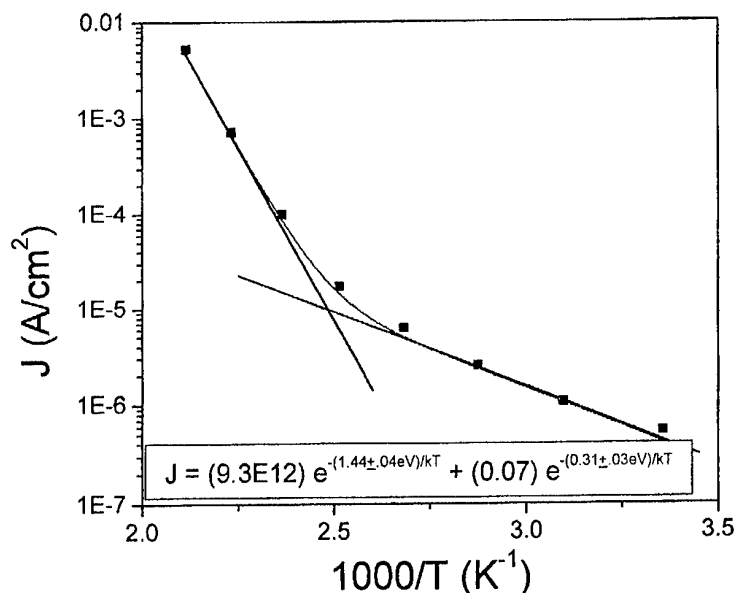
Fig. 5. Current versus 1/T for a capacitor with a Ta_2O_5-Al_2O_3 alloy dielectric, x ~ 0.4.

5.2. Coordination dependent dynamic infrared effective charges

A comparative study of the infrared reflectivity of group IVB and VIB crystalline dichalcogenides, $Zr(Hf)S(Se)_2$ and $Mo(W)S(Se)_2$, respectively, has yielded significantly different dynamic transverse infrared, ir, effective charges, e^*_T, for vibrational modes with atomic displacements perpendicular to the crystalline c-axis (for details see Ref. 29). The group IVB transition metals are in an octahedral bonding geometry, whilst the group VIB transition metals are in trigonal prism geometry. The values of e^*_T, for the group IVB dichalcogenides are about 8 to 9 times larger than for the group VIB dichalcogenides. e^*_T is typically ~ 4-5e for the group IV chalcogenides, and ~ 0.25e for the group VI chalcogenides. These differences in e^*_T can not be explained on the basis of an ionic bonding model; e.g., the bond ionicity for Zr-S is ~0.3, so that the ionic charge would be no more than about 1.2e. However, in the context of the MO model, the charges are dynamic character, and the large difference derives an increased dynamic contribution due to the more symmetric bonding orbital geometry at the octahedral bonding sites of the group IVB chalcogenides.

A similar effect has been identified for the Zr and Hf silicates, where there is a significant enhancement of the dielectric constant for low concentration silicate alloys [23]. In this instance, the increase has been correlated with a change in bonding coordination. In the low concentration regime, analysis of extended X-ray absorption fine structure spectra, EXAFS, has indicated a Zr atom coordination of about four, whilst for the stoichiometric silicates, e.g., $ZrSiO_4$, the coordination is eight. The bonding geometry at the four-fold site is presumed to be tetrahedral, whereas, at the higher concentrations it is assumed to the same as in the crystalline zircon phase, i.e., a cubic prism [30]. An empirical model indicates a decrease in e^*_T by at least a factor of two between these two geometries, with the effective charge being larger in the more symmetric tetrahedral geometry. A linear combination of the transition metal e_g d-states can be directed along the tetrahedral directions when there is mixing with the transition metal s-states. These four orbitals are equivalent in character, hence the high symmetry of this coordination. However, expansion to eight fold coordination does not provide eight equivalent orbitals, hence a distortion from a perfect cubic bonding arrangement, a reduction in symmetry, and a decreased dynamic effective charge. This is underlying region for the bond order reduction of two between the four and eight fold bonding coordinations of Ref. 23.

5.3. Localized anti-bonding d-state derived levels in Zr silicate alloys

Fig. 6 displays X-ray absorption spectroscopy, XAS, spectra for series of Zr silicate alloys, $(ZrO_2)_x(SiO_2)_{1-x}$, x ~0.05, 0.2, 0.5 and 1.0 as obtained at Brookhaven National Laboratory; details of these measurements [31] and the alloy preparation are described elsewhere as well. The spectral features are assigned to dipole-allowed transitions between $M_{2,3}$ p-core states of the Zr atoms, and conduction band states derived from the 4d (a and b, and a' and b') and 5s (c and c') atomic states of Zr. The bonding arrangements of Zr and Si atoms in these alloys have been addressed in Refs. 22 and 23. As-deposited alloys prepared by plasma deposition are non-crystalline and pseudo-binary with Si-O and Zr-O bonds, but no detectable Zr-Si bonds. After annealing at 900 to 1000°C the x = 0.5 alloys phase separates in SiO_2 and crystalline ZrO_2, and x = 1.0 is also crystallizes. The energies of the highlighted features in the $M_{2,3}$ XAS spectra in Fig. 6 are independent, up to an experimental uncertainty of ± 0.1 eV, of the alloy composition and state of crystallinity. The independence of these spectral features on alloy composition, and the relatively small changes that take place on crystallization of a ZrO_2 phase after annealing are consistent with a molecular orbital description. The MO calculations indicate localization of d-states on the TM atoms with energies determined predominantly by coordination and symmetry of their oxygen neighbors, and are not influenced by either their second neighbors or the absence or presence of long range order.

$(ZrO_2)_x(SiO_2)_{(1-x)}$ Zr 3p edge
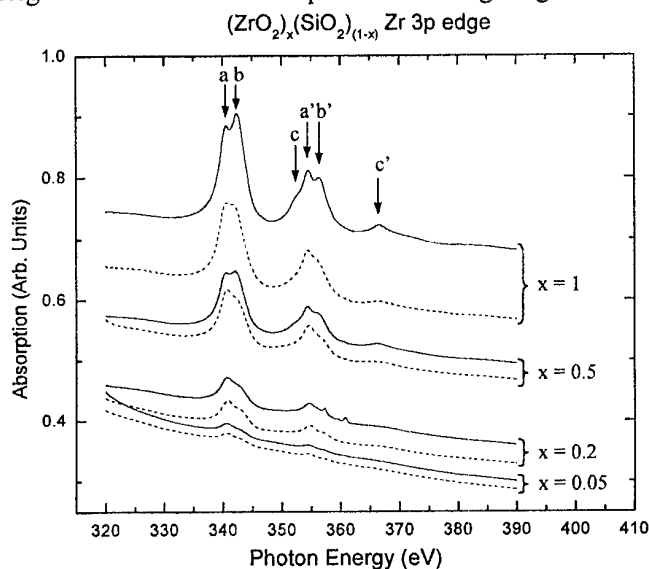
Fig. 6. X-ray absorption spectra as a function of photon energy for excitation from Zr $M_{2,3}$ p-states in empty Zr 4d and 5s states of Zr silicate alloys. Before and after a rapid thermal anneal at 1000 C. The letters a, b and c and a', b' and c' designate the energy differences between the M_2 and M_3 p-states, respectively, and the anti-bonding Zr states.

6. Non-crystalline chalcogenides

Calculations based on the Pauling bond-ionicity approach have also been applied to amorphous morphology and properties of transition metal chalcogenide alloys, e.g., Ni in As_2Se_3 based alloys. Since the electronegativities of S and Se are significantly smaller than that of oxygen, scaling based on bond ionicity is compressed, and neither X nor I_b is an appropriate scaling variable. On the other hand bond coordination is more significant, in particular the breakdown of the 8-N rule in which chalcogen atoms are assumed to have a coordination of two. As indicated in Fig. 1 and Table 1, the 8-N rule breaks down whenever SiO_2 is alloyed with a transition metal oxide. A similar situation prevails for alloys of chalcogen compounds such as As_2Se_3, and transition metal chalcogenides that are alloys of As_2Se^3 and Cu_2Se or NiSe. For example, the bonding coordination of Se increases from two to four in the alloy system: As_2Se_3-Cu_2Se, and this increase in Se coordination also occurs in disordered alloys with compositions along the pseudo-binary join line from As_2Se_3 to $CuAsSe_2$ [32] In addition, the energies of the transition metal electronic states relative to the conduction and valence bands of a chalcogenide alloy host, the occupancy of these states and the

transition metal concentration are the important factors in promoting a transition from insulating to metallic conductivity as a function of increasing metal atom content.

This section of the paper addresses two different types of chalcogenide materials that do not conform to the 8-N rule [4], alloys containing: i) tellurium, such as the Te, As, Ge glass used by the IBM group for laser writing [33] the memory materials initially studied by ECD, Ge, Te, Sb or As and S alloys [1,34], and ii) transition metals such as Ni [35-37]. Consider first the changes in bonding and structure that take place when Te is substituted for either S or Se in chalcogenide compounds and alloys.

Building on the comparisons made between transition metal oxides, sulfides, and selenides earlier in this paper there are two issues to consider that are different for the corresponding tellurides; i) band overlap between the valence band states of Te and the d-states of the transition metals, and ii) changes in crystalline structure associated with the Te substitutions. Consider first MnO and the Mn chalcogenides. The results presented in Fig. 3 and in Ref. 27, indicate: i) scaling between optical band gaps for the oxide, sulfide and selenide, and the atomic energy of the valence band p-state of the anion, and ii) a breakdown of this scaling relationship for MnTe as indicated by the point for MnTe that is below the linear fit. The discussion in Ref. 27 has attributed the departure from linear scaling to a qualitatively and quantitatively different electronic structure of MnTe in which the d-states of Mn overlap the p-states of Te. This overlap also promotes a change in the crystal structure from rock salt, NaCl, to the nickel arsenide, NiAs. In this example MnTe is still a semiconductor, whereas in the transition metal dichalcogenides that involve a smaller number of d-electrons, a similar overlap of anti-bonding d-bands of the transition metal with the p-states of Te that comprise the valence band, results in metallic behavior [26]. The Te doped alloys used in optical and electronic switching [1,34] generally have significantly reduced band gaps with respect to their Se and S analogs, and in addition display transitions to metallic conductivity with, and without crystallization.

Differences in the properties between Te containing non-crystalline chalcogenides and those containing S and Se are also correlated with increased coordination of the Te atoms [35]; i.e., a breakdown of the 8-N rule. This increase in coordination requires the use of d-orbitals of the Te changing the basic electronic structure and the resulting properties. The large differences in the band gap and optic mode vibrational frequencies between crystalline and amorphous Te are consistent with these changes in the effective coordination and the resulting valence band structure [38].

The second example of a transition metal induced change in conducting properties occurs in chalcogenides that have been alloyed with Ni. Two different effects have been reported: i) crystallization resulting in metallic conductivity [37], and ii) metallic conductivity in the non-crystalline state that occurs above a threshold concentration of Ni [35,36]. The second of these effects is attributed to local bonding arrangements comprised of i) Ni with six Se neighbors, and ii) an increase in the coordination of Se as well. This arrangement has an odd number of electrons available for bonding resulting in a partially filled valence band and the potential for metallic conductivity. Based on the atomic 3d-state energy of Ni and the valence p-state energy of Te, the Ni d-band overlaps the Te valence states, so that at a sufficiently high concentration of Ni, electrons can be transported between localized Ni bonding sites resulting in the observed metallic conductivity.

7. Discussion

This paper has presented a classification scheme for high-k dielectrics that separates SiO_2 and the alternative non-crystalline dielectrics into three groups with qualitatively different amorphous bonding morphologies. This paper has emphasized group IIIB and IVB silicate and aluminate alloys that have a modified continuous random network structure. In the silicate alloys, the transition metal atoms disrupt the covalent bonding of the host SiO_2 network with the transition metal atoms displaying a higher bond ionicity with respect to their oxygen neighbors. The classification scheme is integrated into a molecular orbital model that is used to establish energy level diagrams for insulating transition metal oxides and their silicate and aluminate alloys. The ordering of the conduction band or anti-bonding states is determined by the symmetry and coordination at the transition metal atom, and their energy level separations are correlated with differences between σ and π overlap integrals [11-13], One test of the model is the scaling of the optical band gap with anion atomic p-state energy for a given transition metal; e.g., HfO_2, HfS_2 and $HfSe_2$. The results in Fig. 3 show that as the anion becomes less electronegative from oxygen, to sulfur and selenium, the bandg gap between the lowest lying transition metal d-states and valence band derived from anion p-states, decreases in direct

proportion to changes in the anion atomic p-state energies. This establishes that the transition metals d-states are not significantly shifted in energy with respect to changes in the anion electronegativity. In a complementary manner, the data in Table 3 establish that the energy difference between the valence band derived from chalcogen or oxygen atom p-states, and the first conduction associated with $t_{2g}(\pi^*)$ d-states scales with the atomic d-state energy of the transition metal. The results in Fig. 4 show that conduction band offset energies with respect to Si display a linear scaling in which the energy of the bottom of the lowest conduction band is correlated with the energy difference between the transition metal n+1 s- and n d-atomic states. The results displayed in Fig. 5 indicate that the energies of transition metal d-states associated with the lowest unoccupied orbitals have approximately the same energy relative to the Si conduction in an elemental oxide, Ta_2O_5, that they do in a binary alloy, Al_2O_3-Ta_2O_5. The results in Fig. 6 indicate the energies of the Zr d-states that define the lowest conduction bands are independent of the ZrO_2 concentration in Zr silicate alloys, and independent of crystallization as well. The results presented above support the validity of the local molecular orbital description of the electronic structure of transition metal oxides and their silicate and aluminate alloys. The model is being refined to include additional solid state effects associated with renormalization of orbitals and orbital energies that includes interactions with more distant neighbors. Based on the results in Figs. 5 and 6, these interaction are not expected to significantly shift the average energies of anti-bonding states derived from transition metal atomic d-states, but are expected to yield a measure of their width which can be studied experimentally with X-ray absorption and electron energy loss spectroscopies.

The results displayed in Fig. 4 are of particular importance to advanced Si devices. First, they demonstrate that the band offset energies that define the tunneling barrier, scale with atomic properties, i.e., the energy separation between n+1 s and n d states of transition metal and rare earth atoms. Second, they demonstrate that the energies of intrinsic localized states present in transition metal alloys also scale with the energy difference between the Si conduction band and the transition metal d-state energy. Finally, they provide an important atomic scale metric for identification of potential high-k gate dielectrics. The larger the energy separation between the energies of the n+1 s- and n d-states of transition metal atoms of an elemental oxide, or transitional metal silicate or aluminate alloy, the higher the conduction band offset energy between Si and that dielectric, and the lower the direct tunneling and/or interfacial and bulk electron trapping. The model raises additional issues with respect to tunneling in transition metal silicate and aluminate alloys. For alloys that are transition metal oxide rich, the effective barrier for tunneling will be determined primarily by the lowest anti-bonding or conduction band states derived from the transition metal d-states, either the $t_{2g}(\pi^*)$ or $e_g(\sigma^*)$ band depending on the coordination of the particular transition metal. However, localized transition metal derived $t_{2g}(\pi^*)$ or $e_g(\sigma^*)$ states in SiO_2 or Al_2O_3 rich alloys will act more like traps than conduction band states, and their effect on tunnel transport is yet to be determined. For example, they clearly provide a pathway for increased tunneling, but will not necessarily define an effective barrier for direct tunneling.

There are other factors that contribute to the performance of advanced Si devices. Paramount among them are interfacial defects that can trap electrons and/or holes, and/or be a source of fixed charge that shifts threshold voltages and reduces channel mobilities in field effect transistors. This paper has addressed one class of interface trapping states that are present in silicate and aluminate alloys. It has not addressed fixed charge in the interfacial bonding region that is associated with the increased ionic bonding character of alternative transition metal high-k dielectrics, and for a discussion of these effects the reader is referred to Ref. 39.

The structural model for transition metal alloys that has emerged from the classification scheme, combined with the molecular orbital calculations provide insights into contributions to the transverse dynamic infrared effective charge. Contributions of vibrational modes scale as the square of these charges, so that changes in atomic coordination with concentration, or between different transition or rare earth metals, can change their effective charges, and therefore their dielectric constants as well. The two-fold bonding coordination of S and Se in chalcogenide alloys obeying the 8-N rule as in $As_2Se(S)_3$, is increased upon alloying with transition metal selenides in which the coordination of Ni and Se atoms is six. The coordination of Se in As_2Se_3-NiSe alloys will increase monotonically between two and six as the NiSe concentration is increased. Finally, the properties of non-crystalline chalcogenides containing Te are qualitatively different their S and Se analogs. This is attributed to two factors: i) reduced band gaps due to differences in the energies of the atomic p-states that comprise the valence, and ii) increases in atomic coordination which require d-state participation in the valence band electronic structure.

Acknowledgement

References

[1] S. R. Ovshinsky, Phys. Rev. Lett. **21**, 1450 (1968).
[2] S. R. Ovshinsky, J. Non-Cryst. Solids **8-10**, 892 (1972); J. Feinleib, S. Iwasa, S. C. Moss, J. P DeNeuville, S. R. Ovshinsky, J. Non-Cryst. Solids **8-10**, 909 (1972).
[3] D. E. Carlson, C. R. Wronski, Appl. Phys. Lett. **28**, 671 (1976).
[4] N. F. Mott, AIP Conf. Proc. **32**, 1 (1976); N. F. Mott, E. A. Davis, Electronic Processes in Non-Crystalline Solids (Clarendon Press, Oxford, 1972).
[5] J. Stuke, Festkorperprobleme **IX**, 46 (1969).
[6] W. Beyer, J. Stuke, J. Non-Cryst. Solids **8-10**, 321 (1072).
[7] G. Wilk, R. W. Wallace, J. M. Anthony, J. Appl. Physics (2001), in press.
[8] G. Lucovsky, J. Vac. Sci. Technol. **A 19** (2001), in press.
[9] S. Miyazaki, J. Vac. Sci. Technol. **B 19** (2001), in press.
[10] J. Robertson, C. W. Chen, Appl. Phys. Lett. **74**, 1164 (1999) and J. Robertson, J. Vac. Sci. Technol. **B 18**, 1785 (2000).
[11] H. B. Gray, "Electrons and Chemical Bonding" (W.A. Benjamin, New York, 1962), Chapter. 9.
[12] C. J. Ballhausen and H. B. Gray, "Molecular Orbital Theory" (W. A. Benjamin, New York, 1964), Chapter. 8.
[13] P. A. Cox. "Transition Metal Oxides" (Oxford Science Publications, Oxford, 1992), Chapter 2.
[14] R. Zallen, "The Physics of Amorphous Solids" (John Wiley and Sons, New York, 1983), Chapter 2.
[15] L. Pauling, "The Nature of the Chemical Bond", Third Edition, (Cornell University Press, Ithaca, NY, 1948), Chapter 2.
[16] F. A. Cotton, G. Wilkinson, "Inorganic Chemistry, Third Edition", (Interscience, New York, 1972), Chapter 4.
[17] L. Pauling, American Mineralogist **65**, 321 (1960).
[18] J. C. Phillips, J. Non-Cryst. Solids **34**, 153 (1979).
[19] J. C. Phillips, J. Non-Cryst. Solids **43**, 37 (1981).
[20] G. Lucovsky. J. C. Phillips, J. Non-Cryst. Solids **227**, 1221 (1998).
[21] J. C. Phillips, X. Kerner, Solid State Commun. **117**, 47 (2001).
[22] B. Rayner, H. Niimi, R. Johnson, R. Therrien, G. Lucovsky, F. L. Galeener, in "Proc. of Characterization and Metrology for USLI Technology", AIP Conf. Proc. **550**, 149 (2001).
[23] G. Lucovsky, G. B. Rayner, Appl. Phys. Lett. **77**, 2912 (2000).
[24] L. A. Grunes, R. D. Leapman, C. D. Walker, R. Hoffman, A. B. Kunz, Phys. Rev. **B 25**, 7157 (1982).
[25] W. A. Harrison, "Elemntary Electronic Structure", (World Scientific, Singapore, 1999).
[26] J. A. Wilson, A. D. Yoffe, Advances in Physics, **18**, 193 (1969).
[27] J. A. Allen, G. Lucovsky, J. C. Mikkelsen, Jr., Solid State. Commun. **24**, 367 (1977).
[28] R. S. Johnson, G. Lucovsky, J. Hong, Appl. Surf. Sci., these proceedings.
[29] G. Lucovsky, R. M. White, J. A. Benda, J. F. Revelli, Phys. Rev. **B 7**, 3859 (1973).
[30] K. Robinson, G. V. Gibbs, P. H. Ribbe, The American Mineralogist **56**, 782 (1971).
[31] G. Lucovsky, et al. submitted to Appl. Phys. Lett. (2001).
[32] S. H. Hunter, A. Bienenstock, T. M. Hayes, in Amorphous and Liquid Semiconductors, ed. by W. E. Spear (University of Edinbourgh, 1977), p. 78.
[33] P. Chaudhari, S. R. Herd, D. Ast, M. H. Brodsky, R. J. Von Gutfield, J. Non-Cryst. Solids, **8-10**, 900 (1972).
[34] F. Betts, A. Bienenstock, C.W. Bates, J. Non-Cryst. Solids **8-10**, 364 (1972).
[35] S. R. Ovshinsky, in Ref. 32, p. 519.
[36] R. Flasck, M. Izu, K. Sapru, T. Anderson, S. R. Ovshinsky, H, Fritzsche, in Ref. 31, p. 524.
[37] Y. Sawan, F. Wakim, M. Abu-Zeid, M. El_Gabaly, Proc. 15th Int. Conf. Physics of Semiconductors, Kyoto, 1980, J. Phys. Soc. Japan **49** (Suppl. A), 1163 (1980).
[38] G. Lucovsky, Phys. Stat. Sol. **(b) 49**, 633 (1972).
[39] G. Lucovsky, J. C. Phillips, M. F. Thorpe, in Ref. 22, p. 154.

CURRENT UNDERSTANDING OF PHOTOINDUCED VOLUME AND BANDGAP CHANGES IN AMORPHOUS CHALCOGENIDES

K. Shimakawa, A. Ganjoo

Department of Electrical and Electronic Engineering, Gifu University,
Gifu 501-1193, Japan

The terms "photodarkening (PD)" and "photostructural changes (PSC)" have been used equivalently in the study of photoinduced changes in amorphous chalcogenides. A recent observation, e.g. the rate of PVC is higher than that of PD under bandgap illumination, demonstrates that there is no one-to-one correlation between the two phenomena. Furthermore, recent results on the dynamics of PSC (in-situ measurements) have shed new light on our understanding of D and PVC and the current understanding should be modified. A review is given on these topics through the recently obtained interesting results on the reversible PD and PVC for As-based chalcogenides. We pay attention in particular to the time evolution of these changes (*in situ* measurements etc).

1. Introduction

Photostructural change (PSC) and the related photodarkening (PD) are phenomena unique to glassy or amorphous chalcogenides and are not observed in amorphous group IV and V semiconductors (a-Si, a-As etc.), or in crystalline chalcogenides [1-5]. It is noted also that the PD disappears in some metal-doped chalcogenide glasses (e.g. by doping with Cu, Mn etc.) [6,7]. For a long time, PD was believed to be the result of PSC and hence one believed that there is one-to-one correlation between PD and PSC. An element of uncertainty has existed in the literature in establishing a relation between PD and volume expansion (VE). Recent experimental results by Ke.Tanaka [8] indicated that the rate of VE is greater than that of PD for bandgap illumination. Under subgap illumination, however, VE increases more gradually than PD. This seems to indicate that no direct correspondence exists between PD and VE. These results, however, were obtained for metastable PD and PVC, the mechanisms during illumination (dynamics) are still unclear.

It is believed that a change in the interaction of chalcogen lone-pair (LP) electrons is responsible for PD. The increase in LP-LP interactions yields a broadening of the valence band, causing a reduction in the bandgap (PD). The models, which have been put forward in support of the above mechanism, can be placed into the following categories: 1) a change in the atomic (chalcogen) positions [2], 2) bond breaking and/or alternations between the atoms [5, 9, 10], and 3) repulsion and slip motion of structural layers (RS model) [11]. Any model should be able to explain the observed behaviors of PD and PSC (VE for As-based chalcogenides). The study of PD and PSC has therefore received renewed interest, and new attempts, e.g. through an in-situ measument of PD or PSC etc., have been made to understand these changes [10, 12, 13]. In the present article, we try to review the recently obtained interesting results on the reversible PD and VE for As-based chalcogenides. We pay attention in particular to the time evolution of these changes (*in situ* measurements etc.), which is useful in understanding deeply the dynamics of PD and VE.

2. Principal experimental data

As we expect that most of readers engaged in amorphous chalcogenides know what PD is, only the principal results for these reversible changes are summarized here (for the readers who are

also interested in the historical background of PD, see the review papers [1-5]): 1) a decrease in the optical gap, e.g. $\Delta E_g/E_g \approx$ -2 % in As_2S_3 (PD); 2) a volume expansion (VE), e.g. $\Delta V/V \approx$ 0.5 % for As_2S_3; 3) a change in the first sharp diffraction peak (FSDP) in X-ray measurements for As_2S_3. All these changes can be reversed by annealing near the glass transition temperature.

First, we start from the metastable changes in PD and VE. Recent systematic experimental data of PD and VE for amorphous chalcogenides are informative and one of examples for the obliquely deposited a-As_2Se_3 is shown in Fig.1. It is found that giant reversible changes are induced in obliquely deposited films [14]. The relative change $\Delta d/d$ in thickness and relative change $\Delta E_g/E_g$ in optical bandgap are shown for various treatments: A, as deposited; B after pre-illumination annealing; C, after illumination; D, after post-illumination annealing. The full circle represents the thickness estimated by mechanical measurement [14]. The film thickness decreases (thermal contraction) and the bandgap increases (thermal bleaching) by annealing. On illumination, the thickness increases (VE) and the bandgap decreases (PD). Post-illumination annealing decreases the thickness and increases the bandgap. The above observations seem to indicate that there exist some correlation between PD and PVC.
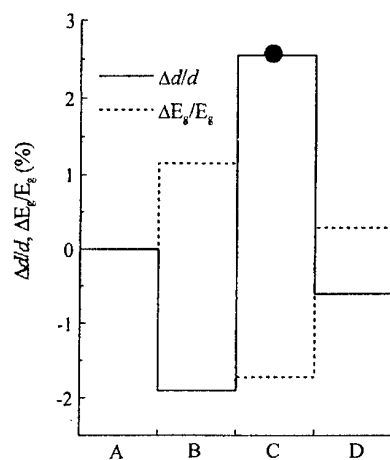
Fig. 1. Variation in relative changes in thickness d and optical bandgap E_g of a-As_2Se_3
(after [14]). Measurement conditions are described in the text.

It was believed for a long time that PD and VE were two different sides of the same phenomenon and hence one-to-one correlation should exist between PD and VE. Recently, however, Ke.Tanaka [8] has experimentally shown that the time constants of the PD and the VE in As_2S_3 are different. That is, the VE saturates earlier than the PD for bandgap illumination as shown in Fig.2 (a). In contrast, under subgap illumination PD saturates earlier than the VE as shown in Fig. 2(b). These experimental observations, on the other hand, suggest that these two phenomena (PD and VE) are not directly related to each other.

The composition dependence of PD in the As-Se system is of interest and this is shown in Fig. 3 which is plotted from the Table in ref. [15]. The magnitude of PD increases linearly with the As-content in this composition region. From this result, we expect that arsenic atoms may play an important role in inducing PD. Note, however, that PD is not found in pure amorphous arsenic (a-As) [16], whereas PD occurs in pure Se [2]. The fact that PD disappears in metal-doped chalcogenides is of interest, where it is reported that by the incorporation of Cu, Ag, Zn [6], and of Mn and rare earths [7], PD vanishes.
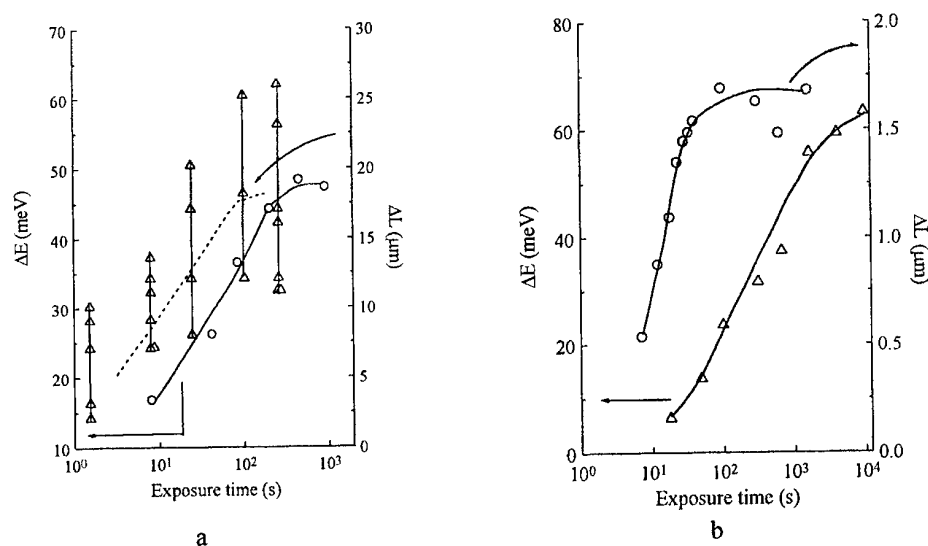
Fig. 2. Photoexpansion ΔL and photodarkening ΔE as a function of exposure time in a-As$_2$S$_3$ for (a) bandgap and (b) subgap illumination (after [8]).
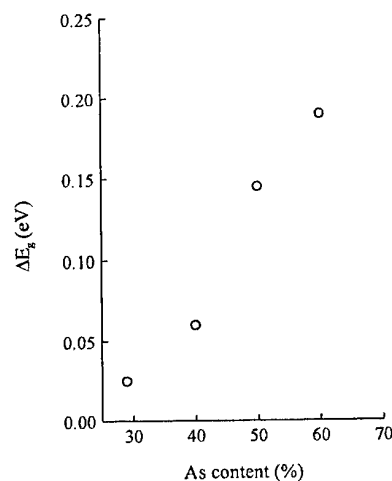
Fig. 3. The dependence of As-content on the magnitude of photodarkening ΔE_g in As-Se system.

Most of the above measurements on PD have been made after, rather than during, illumination and the various conclusions have been drawn for metastable PD. To clear the dynamics of PD during illumination, the time evolution of changes in the optical absorption coefficient with illumination has been studied for As$_2$S$_3$ in detail (*in situ* measurement) [13]. The variation of the changes in absorption coefficient ($\Delta \alpha$) with the number of absorbed photons (n_p), at different temperatures, is shown in Fig.4. Note that $\Delta \alpha$ is calculated as $\Delta \alpha = (-1/d) \; ln(\Delta T)$, where d is the film thickness and ΔT the change in optical transmission which is defined here as $\Delta T = T/T_0$ (T_0 is the transmission when the illumination is put on and T is the transmission at any time t). The details of experimental conditions are described in the figure caption. Initially, $\Delta \alpha$ increases slowly with n_p, followed by a large increase and then almost saturation. The magnitude of the changes decreases with increasing temperature with $\Delta \alpha$ being a maximum at 50 K (in spite of a slow initial variation with

time or n_p) and smallest at 300 K. At 50 and 100 K, the changes are very slow to start with and increase rapidly as n_p increases, while at 200 and 300 K, there is a more continuous growth of $\Delta\alpha$. The slow initialization at low temperatures is attributed to a smaller number of absorbed photons, as the initial absorption coefficient is small at lower temperatures (α_0=150 cm^{-1} at 50 K). With increasing time of illumination, the number of absorbed photons rises owing to an increase in the absorption coefficient resulting in a large PD at low temperatures. Taking into account the initial absorption coefficient α_0, Fig.4 is replotted as Fig.5, where the variation of the total absorption coefficient ($\alpha=\alpha_0 + \Delta\alpha$) with total absorbed photons (n_p). The solid lines are the fitting to a model, which will be discussed in section 3.
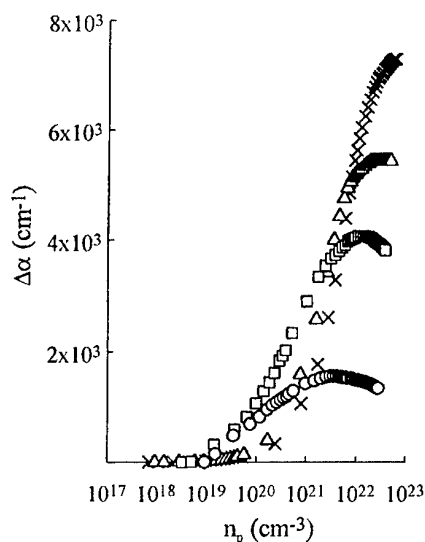
Fig. 4. *In situ* variation of changes in absorption coefficient $\Delta\alpha$ as a function of absorbed photons n_p at various temperatures. ×, Δ, $\square$, and O show the changes at 50, 100, 200, and 300 K, respectively. Illumination is by Ar$^+$ laser (20mW/cm^2) (after [13]).
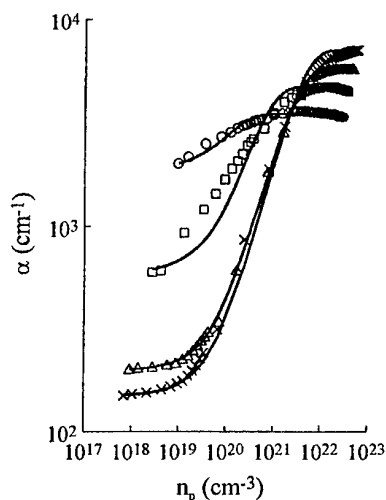
Fig. 5. Variation of absorption coefficient ($\alpha=\alpha_0+\Delta\alpha$) as a function of number of absorbed photons n_p at various temperatures. Description of symbols is the same as in Fig.4. Solid line is the fitting obtained using Eq.(3) in the text (after [13]).

In situ measurements of photoexpansion have also been made for As_2S_3 [12]. Fig. 6 shows the relative changes of thickness, $\Delta d/d$, with time during and after illumination. As soon as the light (mercury lamp) is switched on, the thickness increases rather rapidly, reaches a maximum after approximately 30 s, and then decreases slowly with time. This decrease continues during the rest of the illumination. This behavior of decrease in thickness change *during* illumination is similar to that of the degradation of photocurrent [4, 17] in amorphous chalcogenides. By turning off the illumination, the thickness decreases slightly. With the passage of time it decays slowly, due to relaxation of the structure, and reaches a metastable state which can be observed as usual VE [2], i.e. VE observed *after* illumination. This decay behavior of VE after the illumination is switched off is found to be very similar to that of the decay of photocurrent [12].

To understand the behavior of the initial rapid increase of thickness in more detail, the changes of thickness with time for short time illumination (before showing the maximum change in Fig. 6) have been studied. The light was put on and off for 5 and 10 s, respectively. The results for the relative changes in thickness are shown in Fig. 7. The thickness decreases rapidly as it is switched off, but does not return to the original value. This indicates that the total increase of VE is a combination of transient and metastable VE, the latter remaining as the observed VE *after* switching off the illumination. This behavior shows that the metastable VE occurs even for short time illumination, and accumulates with successive illuminations. It is suggested that the observed VE is purely due to photoelectronic effects and not due to thermal effects [12]. Note, however, that the in situ measurements of PVC have been done by white light and thus the change in PVC was not given as a function of n_p. The correlation between the rate of PVC and PD during illumination has not been established, and hence difficult to comment upon.
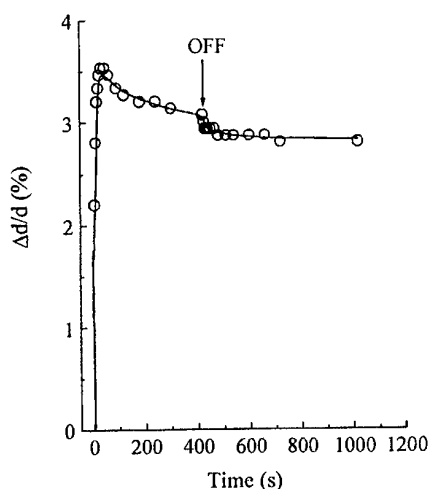
Fig. 6. Relative changes in thickness $\Delta d/d$ with time for a-As_2S_3 (after [12]).
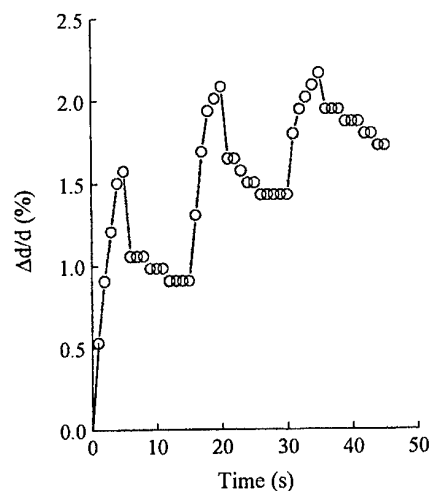
Fig. 7. Relative changes in thickness $\Delta d/d$ with time for short duration of illumination for a-As_2S_3. Light ON and OFF states is 5 and 10 s, respectively (after [12]).

3. Discussion

As already stated, a change in the interaction of chalcogen lone-pair (LP) electrons should be responsible for PD to occur. Any model, classified into three categories (see Introduction), should basically explain the observed behaviors, microscopically and macroscopically.

To understand an elemental process of PD, pure a-Se (not compounds) should be taken into consideration. An important step in the understanding of the mechanism of the photostructural changes was the suggestion that changes in positions of atoms (bond-twisting of Se or S) without

bond breaking can be possible, as illustrated in Fig. 8 (a) [2]. In this figure, A and A' are alternative sites for a-Se atom within the chain. B depicts a Se atom belonging to a neighboring chain. A photon should be absorbed by a particular LP orbital (atom A), which thus becomes *positively* charged. This particular positively charged atom moves closer to another nearest-neighbor chalcogen atom by bond twisting, which can be induced by an attractive Coulomb interaction between the two atoms. A stronger LP-LP interaction can yield a broadening of the VB, and thus resulting in PD. Recently, this original bond-twisting model has been slightly modified as follows [18]: As electrons are more localized than holes in nature, *negatively* ionized chalcogen atoms by trapping photoexcited electrons are responsible for VE (and PD) through some unspecified processes. The similar spectral dependence between the photoconductivity and VE may indicate the importance of free-carrier generation (not excitonic or geminate pair generation). This may suggest that optical excitation of electron and hole itself is not responsible for structural changes. This point will be discussed latter again in the model of repulsive and slip motion.
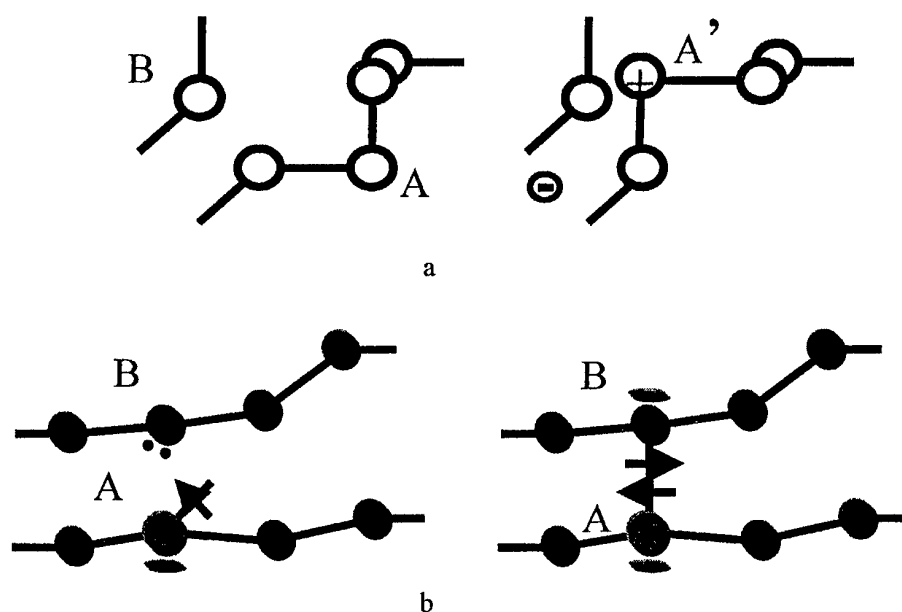
Fig. 8. (a) Bond-twisting model (after [2]) and (b) bond-breaking model (after [10]) which are applied to a-Se.

To get information about the excited states of photostructural changes under illumination, *in situ* measurements of EXAFS have been performed for a-Se [5, 10]. A reversible increase in the coordination number by about 5 % in the excited state is observed. Associated with the change in coordination, the disorder (mean-square relative displacement) also increases under illumination. After illumination, the local change of coordination disappears whereas the light-induced structural disorder remains [10]. Thus the change in coordination number is *transient* phenomenon (not metastable change), which has been observed in VE (see Fig. 7). The observed increase in the coordination number suggests the formation of 3-fold coordination of Se. If an excited Se atom finds itself close to another Se atom belonging to a nearest-neighbor chain, its unpaired electron in the former LP orbital may interact with LP electrons of the neighboring chain, creating an inter-chain bond. A pair of 3-fold neutral sites Se_3^0-Se_3^0 will be formed as shown in Fig. 8 (b) [10]. The formation of inter-chain bonds may induce a local distortion, resulting in an increase in the mean-square relative displacement of the EXAFS spectrum. The formation of triply coordinated pairs in the photoexcited state (during illumination) is also supported by the Raman scattering data [5, 19]. This bond alternation model is somewhat similar to the model proposed by Elliott [9]: Excitation of an electron into the conduction band (anti-bonding state) changes the balance between the attractive and repulsive interactions in the system. This results in a change of intermolecular bonds (covalent bonds) and weaker intramolecular bonds, inducing PD and VE for compounds materials (i.e. As_2S_3 etc.).
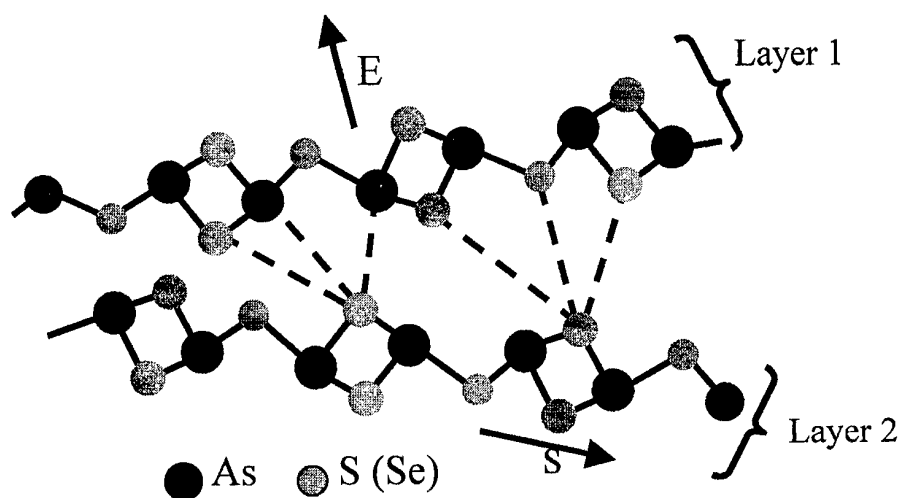
Fig. 9. The repulsion and slip motion of layered cluster model (after [11]). The arrows E and S indicate the expansion (due to repulsion) and the slip motions, respectively. The difference in local enviroments (and hence LP interactions) between chalcogen atoms is indicated by the broken lines.

The microscopic models proposed for elemental Se [2, 5, 10, 18], however cannot account the occurrence of VE (see Fig. 8). For example, a distortion around 3-fold coordination pair itself suggests "contraction" around the network. Probably, overall network changes, which are initiated by bond-twisting or bond alternation, should be taken into consideration in VE [20]. Some other shortcoming for these models can be difficulty of unification, i.e. how to explain the PD in compound materials? Answer to the above questions should be required in particular for the case of compound chalcogenides.

Both these basic models consider only *particular atoms* which are excited by photoirradiation. It is difficult to understand, however, that how and why particular atoms can be excited in a solid. The top of the VB is formed by LP *bands*, and hence there is no reason why particular atoms should be excited selectively. In fact, the bandgap illumination is known to be more effective in inducing PD (localized states are not selectively excited). It is therefore suggested that the "mesoscopic or macroscopic" interaction is dominant for both PD and VE to occur, because LP electrons have equal probabilities of being excited. Therefore, electrons or holes in the extended states (or band-tail states) can be regarded as being responsible for PD or VE, but not individual atoms [11].

Now, let us briefly review the model of repulsion and slip motion of structural layers (RS model) [11]. As a typical example, PD and VE for a-As$_2$Se(S)$_3$ which is known to have basically layered structures, should be discussed. During illumination, the photocreated electrons should reside mostly in the CB tails, while the photocreated holes diffuse away to the unilluminated region through VB and VB tails, since the mobility of electrons is much lower than that of holes in amorphous chalcogenides. Thus the layers which absorb photons become negatively charged, giving rise to a repulsive Coulomb interaction between layers which produces a weakening of the van der Waals forces, and hence the interlayer distance increases (VE).

This process is indicated by the arrow E (process E) in Fig. 9. The experimentally observed widening of the valence angle subtended at sulphur atoms within a layer and hence subsequent increase in the distance between two arsenic atoms bridged by a chalcogen atom on illumination [21] can be explained by the repulsive force involved in the process E (dashed arrow); the reaction of repulsive force between layers acts as a compressive force for each layer. Note, however, that the third coordination sphere (As-S-As-S) remains unchanged, which suggests that the dihedral angle between the two adjacent AsS$_3$ pyramids changes simultaneously with the increase in the valence angle at the bridging chalcogen atom. It is expected, however, that no change in the LP-LP interaction occurs in this process and hence the PD is not induced at this stage. A slip motion along the layers should also take place with the occurrence of the E process between neighboring clusters. This slip motion is shown by the arrow S (process S). As the energy required for a slip motion along layers is expected to be greater than that for expansion normal to layers, the rate of S may be lower than process E. This can be supported by the fact that cleaving is very easy for layered materials, for example graphite.
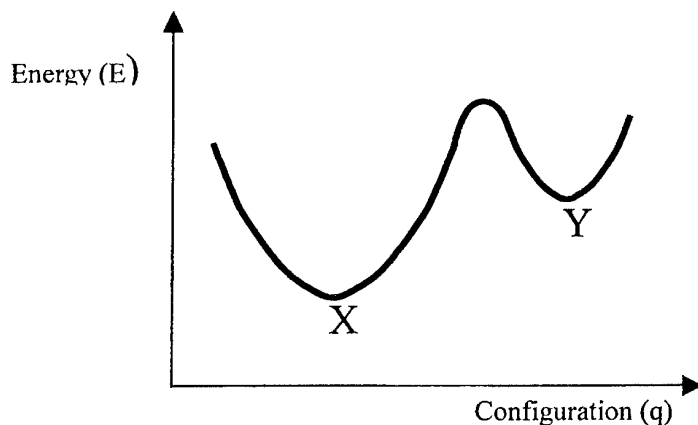
Fig. 10. Configurational-coordinate potential-energy diagram illustrating schematically the
relative energies of the ground-state (X) and the photo-excited state (Y).

Both the process E and S occur owing to the same repulsion force between the layers, but only
process S is expected to be directly related to PD. Refer to corresponding crystalline form, as shown in Fig.
9, Sulphur atom B is more closely surrounded by sulphur atoms from the neighboring layer, while sulphur
atom A has a different configuration. If the neighboring layer slips away from the equilibrium position, an
increase in the energy of the highest occupied states (VB) is expected owing to an increase in the total LP-
LP interactions. This leads to a widening of the VB, but the CB remains almost unchanged [22], resulting
in PD. The total free energy of the system in well annealed samples should be minimized and hence the
atomic or molecular configurations can be taken to be at the minimum LP-LP interactions. Thus
quasistable states (higher energy states) can be induced by illumination, owing to both E and S processes.
The potential energy stored in a layer (the disc-shaped layers of radius of 1 nm placed at a separation of 0.5
nm for a simple assumption) during illumination conditions is estimated to be 6-60 meV [11]. This
repulsive energy can induce VE by reducing the attractive van der Waals energy which is estimated to be
about 750 meV for each layer [23]. The energy introduced into the layers is about 1-10 % of the van der
Waals energy, which seems to be reasonable for inducing VE about 0.5 %.

The above models deal mainly with the metastable PD and let us now consider the mechanism to
understand the dynamics of changes *during* illumination. The dynamics of PD and VE can be described
well in terms of configurational-coordinate (CC) diagram for all three models mentioned above, since a
quasi-thermal equiliblium between the ground and photoinduced states can be established. A double-well
potential with a barrier separating these states (i.e. two-level systems) can be simply assumed. A CC
configuration as shown in Fig. 10 is used to study the time evolution of changes in PD for the repulsion
and slip motion model. To explain the behavior of the variation of the total absorption coefficient ($\alpha = \alpha_0 +
\Delta\alpha$) with total absorbed photons (n_p), we consider the films to contain clusters that act as potential sites for
PD. On illumination, these clusters undergo *photon-assisted site switching* (PASS) forming photodarkened
sites (PDS), which are associated with higher energy (Y) than the original state (X).

Let us consider that, before illumination, there exist N_T clusters in the ground state. "Clusters"
may be considered as equivalent to the "layers" in the RS model. The rate of the growth of the number (N)
of the PDS with the number of absorbed photons (n_p) can be expressed as

$$\frac{dN}{dn_p} = k_p\left(N_T - N\right) - k_r N, \tag{1}$$

where k_p is the promotion rate and k_r the recovery rate. Assuming a time-dispersive reaction for
the PASS, the forward and backward reactions can be expressed as $k_p = An_p^{\beta-1}$ and $k_r = Bn_p^{\beta-1}$, respectively,
where A and B are constants that depend on temperature and illumination intensity, and β is a dispersion
parameter ($0 < \beta < 1$). The dispersive nature in the reaction rates, k_p and k_r, should originate from cooperative
motions of layerd clusters. N is then given as

$$N = N_s\left[1 - \exp\left\{-\left(\frac{n_p}{N_p}\right)^\beta\right\}\right], \tag{2}$$

where $N_s=AN_T/(A+B)$ and $N_p=[\beta/(A+B)]^{1/\beta}$ are the saturated number of photodarkened sites and the effective number of photons, respectively. The fraction of PD occurrence $C(n_p)$ at any n_p is defined as $C(n_p)=N/N_s$. $C(n_p)$ lies between 0 and 1 (0 for the intial state, i.e., before illumination when no sites are converted, and 1 when all the potentially available sites are converted to photodarkened sites). The effective medium approximation (EMA) can be used to calculate the optical absorption coefficient of a random medium [13, 24]. Note that originally the EMA was used to calculate the dc conductivity of a random mixture of particles under the assumption that the inhomogeneous surroundings of a particle can be replaced by an effective medium [25]. The total network conductivity σ_m in D dimension is given as

$$\left\langle \frac{\sigma - \sigma_m}{\sigma + (D-1)\sigma_m} \right\rangle_\sigma = 0, \tag{3}$$

where σ is a random value of conductivity. Springett [26] extended the idea of EMA for the evaluation of the ac behavior of a random system by replacing the conductivity by a complex admittance ($\sigma^*=\sigma_1+i\sigma_2$). As the optical constants are closely related to σ^*, i.e. the complex dielectric constants, $\varepsilon^*=\varepsilon_1-i\varepsilon_2=\sigma_2/\omega-i\sigma_1/\omega$, the optical absorption coefficient $\alpha(\omega)$ can be also calculated through the relation of $\alpha(\omega)=\sigma (\omega)/cn\varepsilon_0$, where c is the light velocity and n the refractive index.

Using the derived $C(n_p)$ (from Eq.(2)) along with Eq.(3), we can evaluate α as a function of n_p. The fitting to α as derived from Eq.(3) is reasonably good at all temperatures. The description of the symbols is given in the figure caption. Details of the fitting parameters, N_p and β, are given elsewhere [13]. It is expected that a percolative growth of photon-assisted site switching of "cluster" to PD sites takes place. The RS model may further be supported by the following experimental results. As already stated, the PD effect disappears in metal-doped chalcogenides [6.7]. This can be explained as follows: atoms of an introduced metals, such as copper, may act as bridging atoms between the layers and hence reduce the flexibility of the layer network. Such bridging will then reduce the ability of both VE as well as the slip motion. Furthermore, the introduction of such a strong constraint also induces dangling bonds which act as recombination centers [27] and which reduce the number of photoexcited free carriers considerably. We now know that constraint of structural network reduces PD. A pressure dependence of PD confirms the importance of constraint. The magnitude of PD in As_2S_3 reaches maximum at ~5 kbar and decreases gradually, vanishing at ~57 kbar [28]. Under high pressure, the motion of the layers is suppressed and VE cannot occur and hence no slip motion leads to no PD. On the other hand, the fact that the magnitude of PD increases with the As-content in As-Se system (see Fig. 3) can be explained as follows: It is known that a-Se is formed mostly by linear chains. Introduction of As atoms bridge these Se chains and partially layered structure can be produced. This in turn increases the magnitude of PD, since the number of layered clusters can be increased in higher As-content in As-Se system. The reason why PD occurs in pure Se can be due primary the repulsion force between linear chains. Repulsive force due to electronic charges between layers is expected to be more stronger than that between chains. It is noted, however, that As-rich system (more than 40 % of As-content) may have different structural unit, e.g. As_4Se_4 molecule. A linear increase of PD with As-content cannot simply be explained in terms of the present model. This point is unclear [4]. As already suggested, one more important factor for structural changes to occur is the *charge separation* during illumination [11, 18]. The RS model predicts also that no VE and PD can occur in very thin films, because then the photoexcited holes cannot diffuse away from the illuminated region and hence the layer surface area will remain electrically neutral. It was reported, in fact, that no PD can be induced in As_2S_3 films thinner than 50 nm [29]. Application of electric field may assist charge separation if the field is properly applied and may enhance PD. It is of interest to examine whether this kind of field effect is found or not.

From the similar spectral dependence between the PD and the photoconductivity in As_2S_3 [18], and the similar behaviors between VE and photoconductivity during and after stopping the illumination [12], free-carrier generation but not geminate (excitonic) pairs is suggested to be responsible for the structural changes, which seems to be consistent with the RS model. However, this model has been criticized in a view of hole diffusion length: The major difficulty in the RS model suggested by Ke. Tanaka [18] may be the temperature dependence of VE. The VE becomes greater at lower temperatures, while the hole diffusion length will be shorter at low temperatures. To our view, however, the ability of *charging negatively* in illuminated region should not only be dominated by "diffusion length (or mobility) of holes". The number of free- and or tail-electrons in layers increases at low temperatures, since recombination time increases with decreasing temperature ($G\tau$ product), while the number of holes also increases with decreasing temperature. Complete diffuse-away of holes in illuminated region, e.g. longer than micrometers [18], however, is not required for VE and PD to occur in the RS model. Large difference of

diffusion coefficient between electron and hole may still produce excess electrons in layers, yielding large VE and PD at lower temperatures. Thus we prefer the RS model to account the VE and PD in amorphous chalcogenides.

Finally, we should argue the transient effect of PD. As the transient VE has been found experimentally [12], similar transient PD should be observed and these should be related to photocurrent. The detail of these will be presented elsewhere [30].

4. Conclusions

A review was given on the topics through the recently obtained interesting results on the reversible photinduced volume changes (PVC) and photodarkening (PD) for amorphous chalcogenides, in particular for As-based chalcogenides. We paid attention for the time evolution of these changes (*in situ* measurements etc) and discussed the origin of PVC and PD in terms of the model of repulsion and slip motion of clustered layers.

Acknowledgements

References

[1] K. Tanaka, J. Non-Cryst. Solids, **35&36**, 1023 (1980).
[2] Ke. Tanaka, Rev. Solid St. Sci., **4**, 641 (1990).
[3] G. Pfeiffer, M. A. Paesler, S. C. Agarwal, J. Non-Cryst. Solids, **130**, 111 (1991).
[4] K. Shimakawa, A. V. Kolobov, S. R. Elliott, Adv. Phys., **44**, 475 (1995).
[5] A. V. Kolobov, K. Tanaka, Handbook of Advanced Electronic and Photonic Materials and Devices Vol. 5, edited by H. S. Nalwa (Academic Press, San Diego) p.47, 2001.
[6] J. Z. Liu, P. C. Taylor, Phys. Rev. Lett., **59**, 1938 (1987); Phys. Rev., **B41**, 3163 (1990).
[7] M. Iovu, S. Shutov, S. Rebeja, E. Colomeyco, M. Popescu, J. Optoelectronics and Advanced Materials, **2**, 53 (2000).
[8] Ke. Tanaka, Phys. Rev., **B57**, 5163 (1998).
[9] S. R. Elliott, J. Non-Cryst. Solids, **81**, 71 (1986).
[10] A. V. Kolobov, H. Oyanagi, K. Tanaka, Ke. Tanaka, Phys. Rev., **B 55**, 726 (1997).
[11] K. Shimakawa, N. Yoshida, A. Ganjoo, A. Kuzukawa, J. Singh, Philos. Mag. Lett., **77**, 153 (1998).
[12] Ashtosh Ganjoo, Y. Ikeda, K. Shimakawa, Appl. Phys. Lett., **74**, 2119 (1999).
[13] Ashtosh Ganjoo, K. Shimakawa, H. Kamiya, E.A. Davis, Jai Singh, Phys. Rev., **B62**, R14601 (2000).
[14] Y. Kuzukawa, Ashtosh Ganjoo, K. Shimakawa, Y. Ikeda, Philos. Mag., **B79**, 249 (1999).
[15] S. B. Gurevich, N. N. Ilyashenko, B. T. Kolomiets, V.M. Lyuvin, Proc. 6th Int. Conf. on Amorphous and Liquid Semiconductors, ed. By B. T. Kolomiets (Nauka, Moscow) p.451, 1975.
[16] E. Mytilineou, P. C. Taylor, E.A. Davis, Solid State Commun., **35**, 497 (1980).
[17] K. Shimakawa, S. Inami, S. R. Elliott, Phys. Rev., **B42**, 11857 (1990).
[18] Ke. Tanaka, Philos. Mag. Lett., **79**, 25 (1999).
[19] A. V. Kolobov, H. Oyanagi, A. Roy, K. Tanaka, J. Non-Cryst. Solids, **232-234**, 80 (1998).
[20] A. V. Kolobov, private commun.
[21] C. Y. Yang, M. A. Paesler, D. E. Sayers, Phys. Rev., **B36**, 9160 (1987).
[22] T. Watanabe, H. Kawazoe, M. Yamane, Phys. Rev., **B38**, 5677 (1988).
[23] Ke. Tanaka, Solid St. Commun., **54**, 867 (1985).
[24] K. Shimakawa, J. Non-Cryst. Solids, **266-269**, 233 (2000).
[25] S. Kirkpatrik, Rev. Mod. Phys., **45**, 574 (1973).
[26] B.E. Springett, Phys. Rev. Lett., **31**, 1463 (1973).
[27] J. Hautala, S. Yamasaki, P. C. Taylor, J. Non-Cryst. Solids, **114**, 85 (1989).
[28] G. Pfeiffer, M. A. Paesler, J. Non-Cryst. Solids, **114**, 130 (1989).
[29] Ke. Tanaka, S. Kyoya, A. Odajima, Thin Solid Films, **111**, 195 (1984).
[30] Astosh Ganjoo, K. Shimakawa, this conference.

PHOTOINDUCED CHANGES OF STRUCTURE AND PROPERTIES OF AMORPHOUS BINARY AND TERNARY CHALCOGENIDES

M. Frumar, Z. Cernosek, J. Jedelsky, B. Frumarova[a], T. Wagner

Research Center and Dep. General and Inorg. Chemistry, University of Pardubice,
53210 Pardubice, Caech Republic
[a]Joint Lab. of Solid State Chemistry of Acad. Sci. of Czech Rep. and University of Pardubice,
53210 Pardubice, Czech Republic

New results obtained recently in the study of isotropic photoinduced effects are described and discussed. The isotropic effects in binary systems such as As-S, Sb-S and in some ternary systems (As-Ga-S, As-Sb-S, Ge-Sb-S, Ge-Ga-S) are connected with the changes of bond statistics and short range order not only in the case of irreversible changes but also in the case of reversible ones. Similar changes of optical properties and the structure that are produced by photodarkening can be obtained by change of stoichiometry of a film. It supports the idea that the exposure of such systems creates bonds among like atoms by photolytic reactions. The exposure influences also index of refraction. The present or potential applications of isotropic photoinduced effects for production of optical and optoelectronics elements and optical storage are also described and discussed.

1. Introduction

Photoinduced changes of structure and properties of amorphous chalcogenides have been the focus of many laboratories for many years because of their present and potential applications in optoelectronics (photoresists, optical storage, optical waveguides, optical gratings and other elements, optical circuits etc. (see, e.g. recent papers [1-6] and papers cited in)). Photoinduced effects have been studied intensively also in order to describe and understand these interesting phenomena [7-20].

Photoinduced changes of optical transmittivity and reflectivity, of index of refraction, changes of reactivity, of rates of diffusion and inter-diffusion, of viscosity and of the state (phase) have been observed in many materials, e.g. in a-Se [17, 19], in the systems of As-S, As-Se, As-Te, As-S-Te, Ge-S, Ge-Sb-S, Ge-Ga-S, Ge-Se, Ge-Sb-Se, Ge-Sb-Te, Ge-In-Te etc. [1-16, 18, 20-32]. In spite of the fact that large effort was given to this subject and several models for the description of individual photoinduced changes has been proposed, the mechanism of many photoinduced processes is still unclear [8,11,13-17, 20-22, 25-30]. Such a situation is partly caused by the fact that the photoinduced phenomena are apparently numerous and this term covers several effects with different mechanisms (changes of short-range-, medium-range- and long-range- orders, photolysis, photosynthesis, photoinduced oxidation, photoenhanced dissolution, diffusion and inter-diffusion, changes of reactivity, viscosity, polarization and anisotropy, vectoral effects, see e.g. [8, 18-20, 28-32]). In our view, the microscopic mechanism of all these effects cannot be the same. Even more, some of the photoinduced changes are relatively small (e.g. changes of medium-range order, some vectoral effects etc.), and their unambiguous determination and explanation is difficult.

In this paper, we will confine ourselves to scalar photostructural changes. New results will be presented and the papers published on this subject in recently will be discussed. Broader group of materials (e.g. As_2S_3, As-S and Sb-S systems, As-Sb-S, As-Ga-S, Ge-S, Ge-Sb-S and Ge-Se) will be discussed in order to support the elucidation of a model of these phenomena and to contribute to find new (or better) systems, properties or larger effects. At the end, present or possible applications of these phenomena will be mentioned.

2. Photoinduced effects

The interaction of amorphous chalcogenides with light is generally complex. The first step in all effects is the electronic excitation by exposure. In the second step, the excited state can relax to the original one, or to an electronic and atomic structure, which is different from the original. In the first case, the changes are temporary, in the second case the new state can be stable for a longer time. In evaporated films, the light can promote changes of electron densities, but also induce chemical reactions among fragments [29, 30]. It can also induce other photochemical reactions such as polymerization or depolymerization, photolysis, changes of local structure, changes of long-range order (crystallization - amorphization) [11, 19, 28-33]. These processes can proceed separately or simultaneously and in amorphous solids are enabled by two factors:

a) The first one is the large free volume of glasses [11, 31] (and no free volume in the crystals). The free volume of amorphous thin films is even larger than that of glasses due to the larger disorder. The free volume can be inversely proportional to the ω [11, 31]

$$\omega = [M - S]\delta = [M - S]\left[\rho \frac{\sum(A_i x_i / \rho_i) - \sum(A_i x_i / \rho)}{\sum A_i x_i}\right], \tag{1}$$

where [M − S] represents the density of M-S bonds, δ reflects the compactness of the structure. The A_i, x_i, ρ_i stand for atomic weights, atomic fraction and densities of the i-th element of the glass, respectively. The quantity ρ is the experimentally found density of the glass. In many amorphous systems, the largest photoinduced changes were found for compositions with the largest "free volume" (Fig. 1, [11, 29-31]).

b) The second positive factor for the evolution of photoinduced changes of structure in a-chalcogenides is generally a low coordination number (N_c) of chalcogens (mostly $N_c \cong 2$), and of pnictogens, (e.g. $N_c(As) \cong 3$), which makes the structure flexible. The largest photoinduced effects were found in our experiments in the As-S system for $As_{42}S_{58}$ films ($N_c = 2.42$), and in Ge-As-S films for $N_c = 2.67$ [11, 31].

2.1. Irreversible photoinduced changes

In several recent papers [7-11, 18, 21-23, 29-31], the irreversible and reversible photoinduced scalar phenomena in the model As-S system but also in Sb-S, As-Sb-S, Ge-Sb-S, Ge-Ga-S and other systems have been studied. The mechanisms of irreversible photoinduced changes in such systems are relatively well understood (see, e.g. [7, 8, 18, 25, 29, 30, 32]). During the high temperature vacuum evaporation of compounds or alloys or during their sputtering, which are the most common ways of preparation of their thin films, the starting materials are often thermally dissociated to fragments of original material. When the vapors are condensed on a cold substrate, the backward synthetic chemical reactions among the fragments to the original compounds (alloys) are not quick enough and the high-temperature state is then partly or fully frozen in and preserved. A micro-heterogeneous film, which is far from thermodynamic equilibrium, is then obtained.

For example, in as-evaporated films of the As-S system large amounts of As_4S_4 and S_n molecules are present (Figs. 2-4, bands between 120-260 cm^{-1} and bands with maxims near 345, 352, 361 cm^{-1} for As_4S_4 vibrations, and a band near 495 cm^{-1} for S-S vibrations (Figs. 2, 3) [8, 9, 29]). Exposure of such films can promote (or increase the rates of) chemical reactions among individual fragments of the film. This process accompanied by decrease of amplitudes of bands with maximum near 137, 148, 170, 193, 215, 223, 361, 495 cm^{-1}. The film is then homogenized and also polymerized. Its state becomes closer to the target glass and to thermodynamic equilibrium. (Figs. 2-4). This process of homogenization on atomic level goes even further when the films are annealed. The Raman bands corresponding to vibrations of As-As and S-S- bonds and vibration modes of As_4S_4 structural units (see above) are according to their composition ceasing or lowering their amplitudes. After thermal annealing of as-evaporated films, their structure approaches the structure of the original bulk glass (Figs. 2-4).
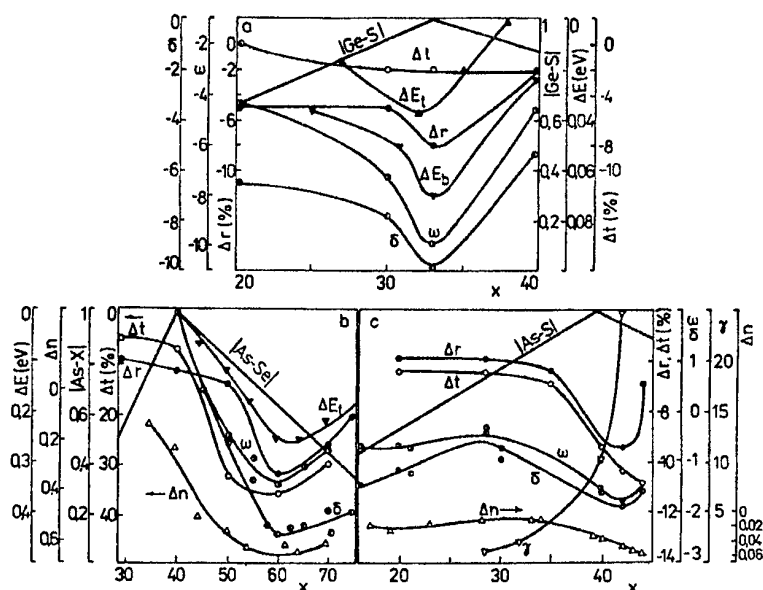
Fig. 1. Compositional dependence of optically induced changes of transmittivity, Δt, of thin films (d = 1 μm) and reflectivity, Δr, of powdered glasses of Ge_xS_{100-x} (a), As_xSe_{100-x} (b), and As_xS_{100-x} (c) systems [32]. The ΔE stands for photoinduced changes of absorption edge position of annealed bulk samples (ΔE_b) and thin films (ΔE_t), Δn stands for photoinduced changes of index of refraction. The quantity γ stands for the ratio of dissolution rates of exposed and unexposed films. The $|M-X|$ are the densities of heteropolar bonds which might be changed by incident light (M = Ge, As; X = S, Se). The ω and δ are given by Eq. 1.

The difference between Raman spectra of the as-evaporated film after their annealing or after their exposure is mainly in amplitude of the band of As-As vibrations (235 cm^{-1} [20, 29, 30]), which is increased relatively to other bands after exposure (Figs. 2-4) due to photochemical reactions that will be discussed later. The exposure produces also photolysis.

Raman shift (cm^{-1})
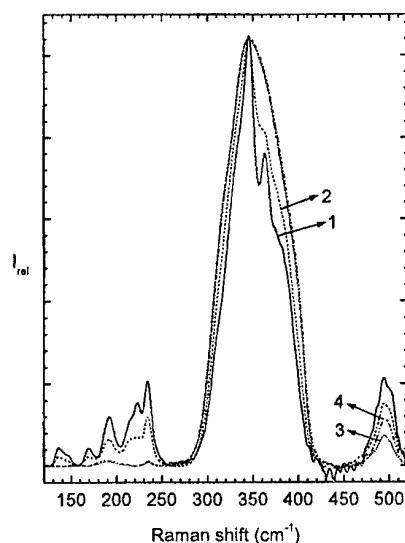
Fig. 2. Reduced Raman spectra of $As_{38}S_{62}$ thin films and bulk glass. 1: as-evaporated film, 2: exposed film, 3: annealed film, 4: bulk glass. The curves 3 and 4 are overlapping in the spectral region up to 270 cm^{-1}. Some narrow bands of the spectrum (130-250 cm^{-1}, 361 cm^{-1}) can be assigned to As_4S_4 molecules (see Fig. 5), the band 235 cm^{-1} can be assigned to As-As bonds vibrations [20], the band 495 cm^{-1} to S-S bonds vibrations [20, 24].
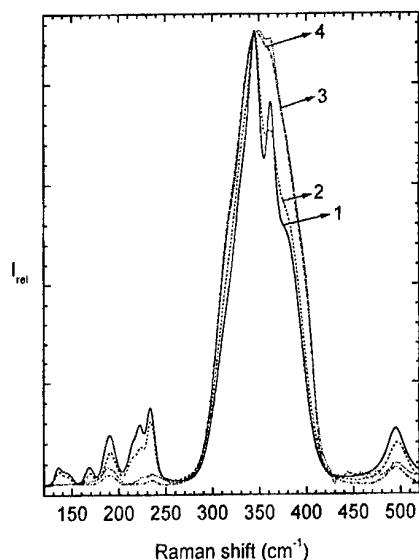
Fig. 3. Reduced Raman spectra of $As_{40}S_{60}$ thin films and bulk glass. 1: as-evaporated film, 2: exposed film, 3: annealed film, 4: bulk glass. For assignment see Fig. 2. The amplitudes of 495 cm^{-1} band (S-S vibrations) are lower than in S-rich films of $As_{38}S_{62}$ in Fig. 2.
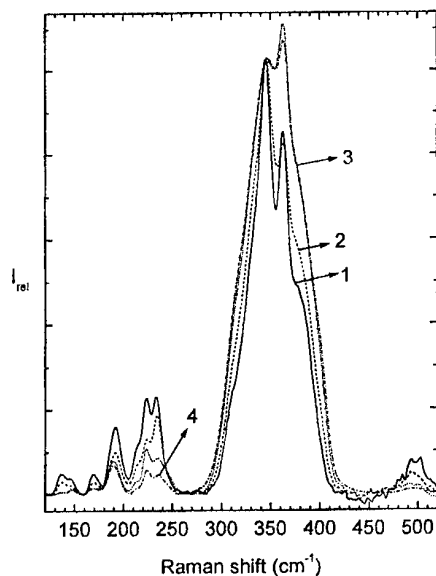
Fig. 4. Reduced Raman spectra of $As_{42}S_{58}$ thin films and bulk glass. 1: as-evaporated film, 2: exposed film, 3: annealed film, 4: bulk glass. The amplitudes of the curves 1-4 were normalized to the same value for the band 345 cm^{-1} (AsS_3 pyramids vibrations). For assignment see Fig. 2.

The process of photoinduced or thermally induced interaction of fragments can be described, e.g. in As-S films by a reaction

$$As_4S_4 + S_2 \rightarrow 2As_2S_3 \tag{2}$$

Such process was simulated in [8] considering that the as-evaporated chalcogenide film of As-S system is a solid solution (or molecular mixture) of As_4S_4, S_n and $(As_2S_3)_n$. The Raman spectra of such mixtures are similar to the spectra of as-evaporated films (Figs. 5-7, see also [8]). Comparing the intensities of individual bands, we were able to evaluate approximately the content of As_4S_4 in as-evaporated films of $As_{42}S_{58}$. This value is $\geq$ 20 mol.% [8]. Exposure, and even more annealing,

decreased the content of As_4S_4 molecules in films. In exposed films of $As_{42}S_{58}$, the content of As_4S_4 was decreased to $c(As_4S_4) \sim 10$-15 mol.%. In $As_{40}S_{60}$ and $As_{38}S_{62}$ films the amount of As_4S_4 is lower. It is interesting to note that according to Raman spectroscopy, the As_4S_4 molecules were found also in $As_{42}S_{58}$ bulk glasses (Figs. 5, 7) [8]. It does mean that the excess As in these As-rich glasses is partly in the form of As_4S_4 molecules.

Photoinduced effects were observed also in thin films of the Sb-S system (Figs. 8-10). The optical transmittance of as-evaporated films of Sb_2S_3 decreases after exposure (photodarkening). The exposure of as-evaporated Sb_2S_3 films is accompanied by a decrease of amplitude of the 165 cm^{-1} Raman band. This band (Fig. 10) can be assigned to Sb-Sb vibrations of S_3Sb-SbS_3 structural units [11]. As-evaporated films of Sb_2S_3 were evidently also dissociated during evaporation, and the films after evaporation are microheterogeneous, analogously to As_2S_3 films. The exposure accelerates the reactions between Sb-rich and S-rich parts of the film and the film becomes more homogeneous. The index of refraction of exposed (more homogeneous) films increases (Fig. 9), partly because of densification.
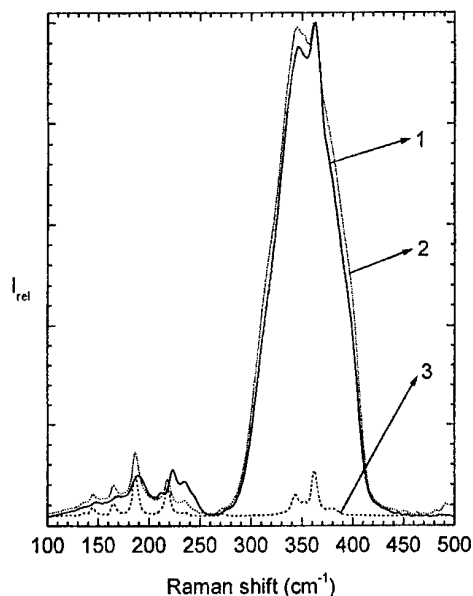
Fig. 5. Reduced Raman spectra. 1: $As_{42}S_{58}$ bulk glass, 2: powdered mixture of 0.85 $As_{40}S_{60}$ glass + 0.15 As_4S_4 crystals, 3: As_4S_4 crystals. The amplitudes of curves 1 and 2 were normalized to the same value for the band ~ 361 cm^{-1}. Amplitudes of As_4S_4 (curve 3) were reduced to be comparable with curves 1 and 2.

The analogous model, which was proposed for description of irreversible photoinduced effects in As-S systems ([8, 20, 29, 30], Eq. 3), can be probably applied for Sb-S system as well.

2. 2. Reversible photoinduced changes

In well-annealed films, the photoinduced changes of structure and optical properties due to exposure are often reversible. Annealing of exposed films can shift the film to the state before exposure. Annealed films of the As-S system, with a structure similar to glasses do not contain larger amounts of "fragments", e.g. of S_n and As_4S_4 (Figs. 2-4). They are evidently closer to thermodynamic equilibrium. The optically induced reactions among fragments (e.g. of the type of Eq. 2) do not play a role. Under exposure, the photolytic reactions in As-S films are more important, at least at room and lower temperatures [8]. At higher temperatures (close to the glass transition temperature, T_g, or above it), atoms or polyatomic fragments of structure are more mobile and they can react together to

eliminate the presence of photolytic products or lower their density. The system approaches the equilibrium by annealing.

The mechanism of *reversible* photoinduced changes still remains not fully clear in spite of the fact that strong evidence for structural atomic changes has been given [8,20,24,25]. Many authors (see e. g. [28]) generally accept that the photoinduced phenomena are connected with changes of local bonding configuration.
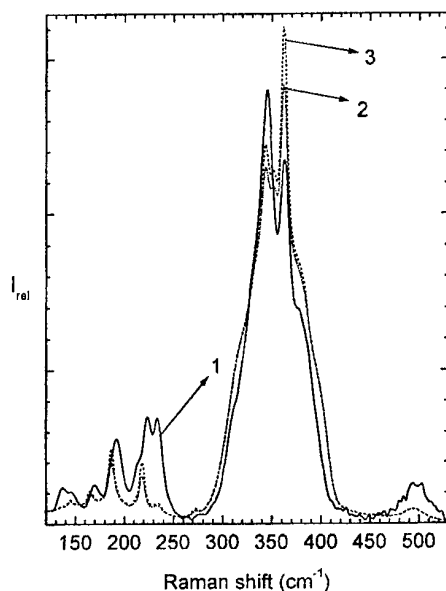
Fig. 6. Reduced Raman spectra. *1:* $As_{42}S_{58}$ as-evaporated film, *2:* mixture of powdered 0.85 $As_{40}S_{60}$ glass + 0.15 As_4S_4 crystals, *3:* mixture of powdered 0.8 $As_{40}S_{60}$ glass + 0.2 As_4S_4 crystals [8].
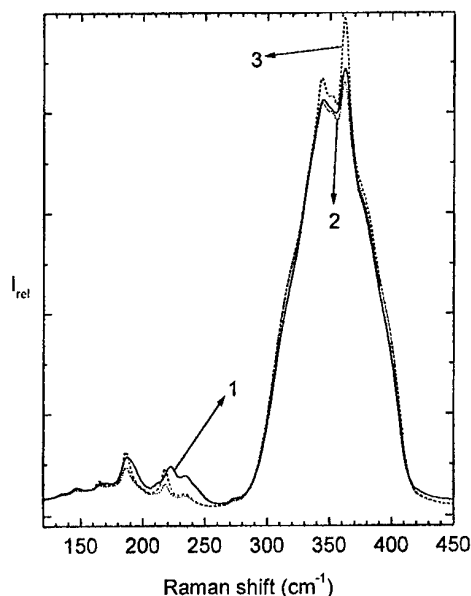
Fig. 7. Reduced Raman spectra. *1:* $As_{42}S_{58}$ bulk glass, *2:* mixture of powdered 0.95 $As_{40}S_{60}$ glass and 0.05 As_4S_4 crystals, *3:* powdered mixture of 0.9 $As_{40}S_{62}$ glass and 0.1 As_4S_4 crystals.

The chemically simplest system, in which photoinduced effects were observed, is amorphous selenium. Kolobov found that, within the errors of experiment, there are nearly no photoinduced changes in coordination number of Se, but an increase in this number during photoexcitation was observed [19]. This increase means that the structure is changed during photoexcitation but without an invariable change of the coordination number after the light is off. The changes can proceed via changes of Se_8 rings to Se_n chains and vice versa (see, e.g. [17, 19]). In fact, in other systems, such as in the As-S system, the photoinduced phenomena are not connected with the changes of mean coordination number [20] but with changes of bond statistics, too.
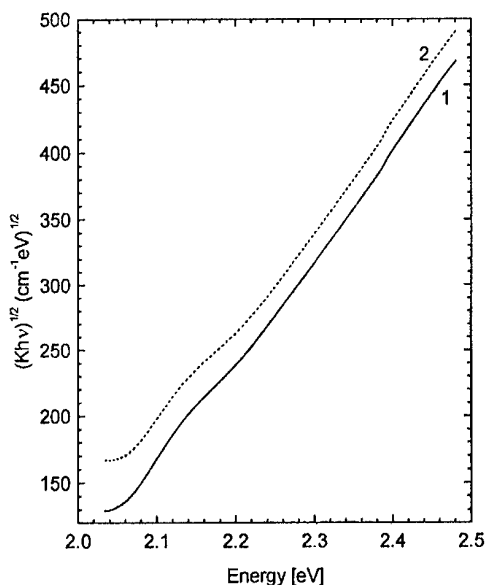
Fig.8. Absorption edge of thin film of Sb_2S_3.
1: as-evaporated film, *2:* exposed film.
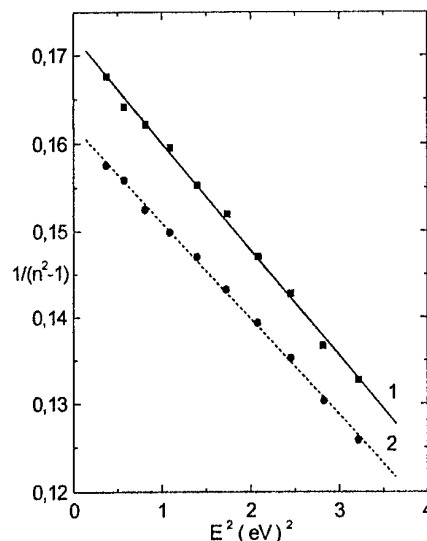
Fig. 9. Spectral dependence of $(n^2-1)^{-1}$ for thin films of Sb_2S_3. Then is index of refraction.
1: as-evaporated film, *2:* exposed film.

Photoinduced changes of structure and of optical properties were found also in thin films of the As-Ga-S [7], in Ge-Sb-S [11, 31], and As-Sb-S system (Figs. 11, 12). The reversible part of changes of index of refraction is much stronger in $(As_2S_3)_{95}(Sb_2S_3)_5$ thin films than in pure As_2S_3 films of the same composition (Fig. 11). The reason is not clear up to now. Large irreversible changes of index of refraction were found also after exposure or after annealing of as evaporated films of $(As_2S_3)_{95}(Sb_2S_3)_5$ (irreversible changes).

Photoinduced changes in As_2S_3 containing Ga [7] are again accompanied by changes of intensities of Raman bands, which can be assigned to the vibrations of As-As bonds (235 cm^{-1}, Fig. 12). The amplitude of this band is enhanced after the exposure of annealed films. It is reduced after annealing. It does mean that not only the irreversible part of photoinduced effects, but also the reversible part is accompanied by changes of bond statistics and of structure in these amorphous systems, analogously as it was shown in pure As-S system [8, 20, 29-32].

For a description of reversible changes in As-S, As-Ga-S, As-Sb-S, and Sb_2S_3 films and bulk glasses, a model based on our earlier results of the study of a-As_2S_3 [20] is proposed. The exposure to light can shift the equilibrium of reaction (3) to the left- or right-hand side, depending on the composition and state of the sample, wavelength and intensity (Wcm^{-2}) of the light. Generally, a lower wavelength and larger intensity of light supports the photolysis (right-hand side direction), a lower energy and/or intensity can shift the reaction (3) to the left-hand side direction.

$$2\left|A-B\right| \xrightarrow{h\nu_i, I_i} \left|A-A\right| + \left|B-B\right|. \qquad (3)$$
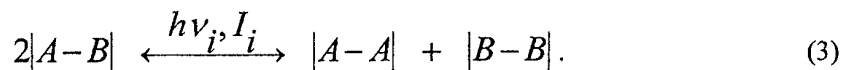
The $|A\text{-}B|$ in Eq. 3 is a chemical bond between atoms A and B, v_i and I_i are frequencies and intensities of incident light. Increasing frequency and/or intensity shifts the equilibrium of the reaction (3) to the right hand side, lowering of energy or intensity of incident light or annealing of sample shifts the equilibrium of Eq. 3 to the left hand side.

Reaction (3) proceeds not only in thin films, but also in bulk samples and glassy powders, both stoichiometric and non-stoichiometric as confirmed by Raman spectroscopy [8]. The formation of As-As bonds due to exposure of As_2S_3 was confirmed recently by Uchino et al. [34], based on ab-initio molecular orbital calculations.

It was found earlier that the mechanisms described by Eq. (3) could be applied also for Ge-Sb-S glasses and films [11, 31].
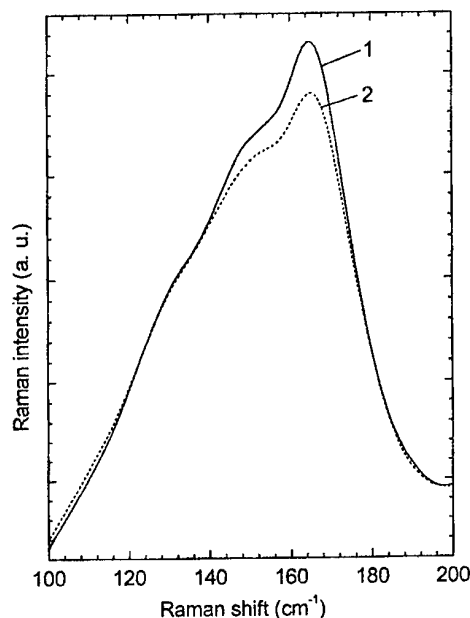
Fig. 10. Reduced Raman spectra of Sb_2S_3 film. *1:* as-evaporated film, *2:* exposed film. The band near 165 cm^{-1} corresponds to $S_3Sb\text{-}SbS_3$ vibration modes. The spectra were normalized to the equal amplitude of the band near 303 cm^{-1} which corresponds to the SbS_3 pyramids vibrations. The density of such structural units is prevailing in the structure of evaporated Sb_2S_3 films and it is considered that their density is constant during the exposure.

It is now generally accepted that both irreversible and reversible photoinduced changes are connected with structural changes of amorphous films and glasses. We have shown without any doubt, that in many above mentioned systems an important role is played by photochemical reactions among fragments of amorphous films (irreversible changes) or by photolytic reactions mainly in annealed films and bulk glasses (reversible changes). The other possibilities e.g. over-coordinated or under-coordinated structural entities (atoms, defects) can also play a role (see, e.g. [34] and papers cited), but there were found only small changes of the mean coordination numbers [19] of different atoms in amorphous films. The photoinduced changes of structure (excluding crystallization and amorphization) are generally small, only a small part of all atoms changes probably their positions and chemical partners. As a result, the experimental evidence of structural changes is often non-persuading (see, e. g. [20]) and several (partly speculative) models can be applied. We believe, that many under-coordinated and over-coordinated defects are only intermediate ones and the system becomes stabilized by change of chemical bonds statistics to approach chemical equilibrium.
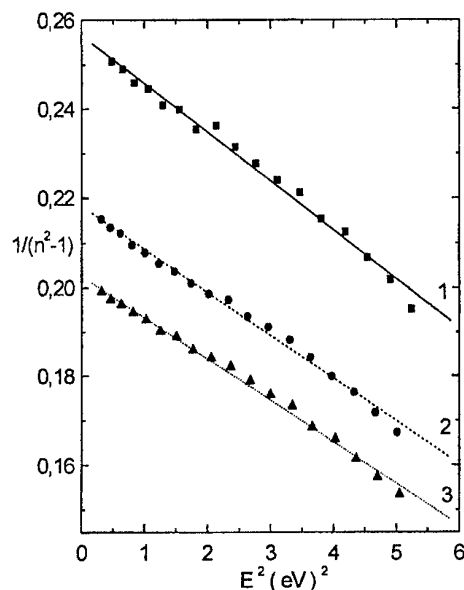
Fig.11. Spectral dependence of $(n^2-1)^{-1}$ for $95As_2S_3.5Sb_2S_3$. The n is index of refraction.
1: as-evaporated film, *2:* exposed film, *3:* annealed film.
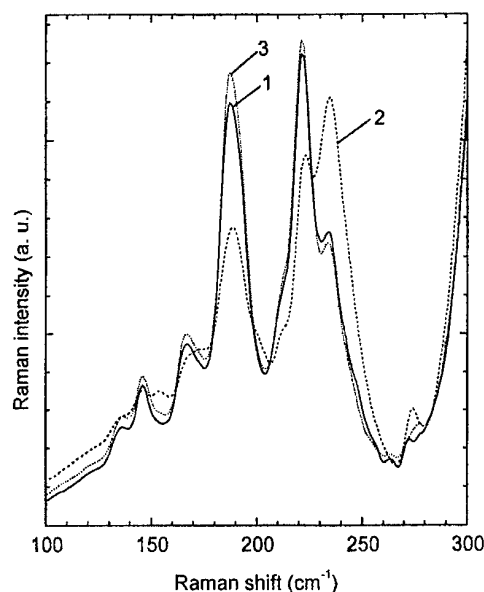
Fig. 12. Reduced Raman spectra of thin films (d = 1000 nm) of $95As_2S_3.5GaS$. *1:* annealed film, *2:* film exposed after annealing, *3:* film was annealed after exposure. The change of amplitude corresponds to reversible structural changes, the band (235 cm^{-1}) with increased amplitude corresponds to As-As vibrations [7, 20].

All changes of local structure or state of samples are accompanied by changes of physico-chemical properties, such as optical transmittivity and reflectivity, index of refraction, and chemical reactivity (see, e.g. Figs. 1, 8, 9, 11, and [7-12, 20, 29-32]. The changes of physicochemical properties, e.g. the "photodarkening" can be modeled. A similar shift of absorption edge can be received by change of composition in mixtures of supposed components of the glass or of the amorphous film. Similar shift can be received in mixtures of supposed photochemical products [8]. All photoinduced changes are dependent on the composition, state of the samples, temperature, intensity and wavelength of the exciting light [8, 20, 29-32]. Some of these changes are large enough to be applied (presently or potentially) in optics, electronics and optoelectronics.

3. Applications

Chalcogenide films are contrary to oxide films, transparent in the near- or mid-infrared region of the spectrum (~ 0.8 – 12 μm), and they can be used for applications in this region. The refractive index of chalcogenides is larger in the near- and mid- infrared region (typically from 2.2-2.9) then in silica and silicates; chalcogenides can match with high refractive index materials, such as Si, GaAs, ZnSe, InSb and others.

Photoresists of large size (areas) can be prepared by vacuum evaporation and very high resolution of 5000-10000 lines/mm can be obtained after their exposure [29, 30, 35]. The resolution capability of chalcogenide films can be further increased to sub-wavelengths region by near – field optical technique [35, 36]. Nano-writing is then possible (e.g. 125 nm lines were obtained [35]). In this case and in similar ones, the sensitivity can be increased by several orders when short pulses are used (see e. g. Ref. [37] and papers cited in) instead of continuous-light exposure. This effect is not fully understood; some local heating, which enables changes of atomic positions and possibly also non-linear effects, or two-photon excitation, could produce such effects.

For some pattern production, e.g. for IR gratings production, deep etching is necessary. Sharp edges with height up to 5-10 μm were obtained (see, e.g. [38, 39]). The etching solutions for As chalcogenides are based on alkylamines or on other alkaline solutions; pure, or such solutions containing surface-active additives, are applied [33, 39]. Solutions containing H_2O_2 are used for Ge-chalcogenide based photoresists [40]. The contrast obtained after etching can be very high (with sharp edges). It can be also very gentle or low, and gray tones or gray scale can be achieved by variation of exposure and etching conditions [37].
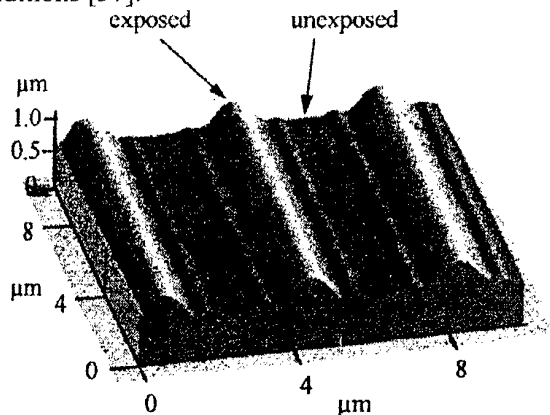
Fig. 13. Grating produced by exposure through a mask by cw-light of wavelength 364 nm [33].

The exposure can change also the volume and surface profile – the exposed parts often have larger volume and gratings and micro-lenses were prepared (Fig. 13, [10, 40]). Micro-lenses or micro-lens arrays can be fabricated from photoresists of As-Se and As-S systems [36, 41] by exposure through a mask with microhole(s). Lenses with focal length several tens of μm and diameter of several microns can be produced [19]. Spherical microlenses can be also prepared. The optical image of the patterns is often directly visible after exposure. Such microlenses can be applied in CCD cameras, imaging machines, optical communication and in IR technology.

Part of the changes of index of refraction due to exposure, e.g. of As chalcogenides, can be ascribed to changes of the volume (photoinduced expansion, density change). The atomic model is analogous [37] to that given in papers [20, 31] for As-S and Ge-Sb-S systems.

It was already mentioned that sub-band gap writing is also possible. In this case, the absorption of light in band tails in the optical gap plays a role. Such tails in films and glasses are formed mainly by fluctuations in bond angles and lengths. The exposure can change the local structure (including bond angles and lengths), the optical transmittivity and the index of refraction. As a result, the sub-band -gap exposure can be applied for holographic recording (e.g. in amorphous As_2S_3 films at room temperature [42]). The photoinduced effect under these conditions has some different features: the changes are not permanent and the thickness of the films is not changed. Sub-band-gap illumination strongly decreases also the viscosity of As_2S_3 glass, which is apparently caused by excitation of weaker or Van der Waals bonds connecting some blocs in the glass structure [40, 41].

A very promising application of photoinduced effects in chalcogenide amorphous films is connected with optical storage. Some of these effects in ternary tellurides are already applied for optical discs (the change from amorphous to crystalline state and vice versa) with a capacity of several Gb per disk [44, 45]. The optically induced crystallization or amorphization can be observed in many binary systems such as As-Se, As_2S_3, Sb_2S_3, Sb_2Se_3, Sb_2Te_3 [36, 43] and in many ternary tellurides [44-51] and selenides [52]. Both thermal and photoinduced effects, or their combination, are apparently behind such effects. When compared with the hole-burning methods that usually use thin metal films, the crystallization – amorphization process needs lower laser power and can be in principle reversible. The threshold power necessary for such a transition (crystallization) is from 100 - 200 W/cm^2 for Sb_2S_3, Sb_2Se_3 and Sb_2Te_3 films. The lowest threshold power was found for Sb_2S_3 [45]. The photoinduced changes of optical properties can have also a deteriorating effect on optical elements and such changes are undesirable. They can lower the performance of fibers or of optical elements as noticed in many materials, e.g. in Ge-Ga-S glass [41], which are used as hosts for rare-earth ions with a relatively intense luminescence in the near – infrared region and can be applied for light generation and amplification. Exposure by UV light causes a red shift of the absorption edge and lowers the transmission of the material. The crystallization can also lower the transmittance of optical elements. In such cases, lower light intensities, longer wavelengths of light, or materials with negligible photoinduced effects have to be used.

4. Conclusion

Photoinduced effects in chalcogenide amorphous systems are still not fully clear in spite of the fact that many of them are already applied or can be applied in the future. It was shown that an important part of photoinduced changes of structure is accompanied by changes of chemical bond statistics and by changes of atomic structure. Further materials and effects are studied in order to elucidate the photoinduced effects.

For application of these effects we are at the beginning and many new materials are studied in order to find systems with new or better properties for current or future applications, which are at present evidently far from the optimal state.

Acknowledgments

References

[1] G. Beadie, W. S. Rabinovich, J. Sanghera, I. Aggarwal, Optics Communications, 152, 215 (1998).
[2] C. Meneghini, A. Villeneuve, J. Opt. Soc. Am. B, Optical Physics, 15 2946 (1998).
[3] O. Nordman, A. Ozols, N. Nordman, J. Opt. Soc. Am. B, Optical Physics, 16, 631 (1999).
[4] V. Palyok, A. Mishak, I. Szabo, D. L. Beke, A. Kikineshi, Appl. Phys. A, Mat. Sci. and Processing, 68, 489 (1999).
[5] S. Ramachandran, S. G. Bishop, Appl., Phys. Lett., 74, 13 (1999).
[6] G. Rosenblum, B. G. Sfez, Z. Kotler, V. Lyubin, M. Klebanov, Appl. Phys. Lett., 75, 3249 (1999).
[7] M. Frumar, J. Jedelsky, Z. Polak, Z. Cernosek, Thin Solid Films, 344, 488 (1999).
[8] M. Frumar, Z. Polak, Z. Cernosek, J. Non-Cryst. Solids, 257, 105 (1999).
[9] Z. Polak, M. Frumar, B. Frumarova, Thin Solid Films, 343-344, 484 (1999).
[10] M. Vlcek, K. Nejezchleb, T. Wagner, M. Frumar, M. Vlcek, A. Vidourek, P. J. S. Ewen, Thin Solid Films, 317, 228 (1998).
[11] I. P. Kotsalas, D. Papadimitriou, C. Raptis, M. Vlcek, M. Frumar, J. Non-Cryst. Solids, 226, 85 (1998).
[12] R. Prieto-Alcon, E. Marquez, J. M. Gonzales-Leal, R. Jimenez-Garay, A. V. Kolobov, M. Frumar, Appl. Phys., A68, 653 (1999).

[13] A. Ganjoo, I. Ikeda, K. Shimakawa, Appl. Phys. Lett., **74**, 267 (1999).
[14] A. V. Kolobov, H. Oyanagi, M. Kondo, A. Matsuda, A. Roy, K. Tanaka, J. Luminesc., **83-84**, 205 (1999).
[15] A. V. Kolobov, H Oyanagi, A. Roy, K. Tanaka, J. Non-Cryst. Solids, **234**, 80 (1998).
[16] A. V Kolobov, H. Oyanagi, A. Roy, K. Tanaka, J. Non-Cryst. Solids, **230**, 710 (1998).
[17] A. Roy, A. Kolobov, H. Oynagi, Ka. Tanaka, Phil. Mag., **B 78**, 87 (1998).
[18] M. Popescu, A. Lörinzi and F. Sava, J. Phys. IV France, **8**, Pr5-9 (1998).
[19] A. V. Kolobov, K. Tanaka, Fiz. Tekh. Poluprovodnikov (Phys. Tech. Semiconductors), **32**, 899 (1998).
[20] M. Frumar, A. P. Firth, A. E. Owen, Phil. Mag., **B 50**, 463 (1984).
[21] Ke. Tanaka, Phil. Mag. Letters, **79**, 25 (1999).
[22] K. Shimakawa, N. Yoshida, A. Ganjoo, Y. Kuzukawa, J. Singh, Phil. Mag. Letters, **77**, 153 (1998).
[23] P. Hari, T. Su, P.C. Tylor, P.L. Kuhns, W.G. Moulton, N.S. Sulivan, J. Non-Cryst. Solids, **266-269**, 929 (2000).
[24] A. Ganjoo, Y. Ikeda, K. Shimakawa, J. Non-Cryst. Solids, **266-269**, 919 (2000).
[25] H. Jain, S. Krishnaswami, A.C. Miller, P. Krecmer, S.R. Elliott, M. Vlček, J. Non-Cryst. Solids, **274**, 115 (2000).
[26] H. Ogura, K. Matsiushi, S. Onari, J. Non-Cryst. Solids, **270**, 147 (2000).
[27] C.R. Schardt, J.H. Simmons, P. Lucas, L. Le Neindre, J. Lucas, J. Non-Cryst. Solids, **274**, 23 (2000).
[28] H. Fritzsche, Fiz. Tekh. poluprovodnikov, **32**, 952 (1998).
[29] M. Frumar, Z. Polak, M. Vlcek, B. Frumarova, in: A. Andriesh and M. Bertolotti (eds.), Physics and Applications of Non-Crystalline semiconductors in Optoelectronics, pp. 123-139, Kluwer Acad. Publ., 1997.
[30] M. Frumar, Z. Polak, Z. Cernosek, B. Frumarova, T. Wagner, Chem. Papers, **51**, 310-327 (1997).
[31] M. Vlcek, M. Frumar, A. Vidourek, J. Non-Cryst. Solids, **97-98**, 1223 (1987).

[32] M. Frumar, Z. Polak, J. Jedelsky, Z. Cernosek, B. Frumarova, in: M.F. Thorpe, L. Tichy (eds.), Properties and Applications of Amorphous Materials, pp. 321-328. Kluwer Acad. Publ. Netherlands 2001.
[33] K. Sakai, T. Uemoto, H. Yokoyama, A. Fukuyama, K. Yoshino, T. Ikari, K. Maeda, J. Non-Cryst. Solids, **266-269**, 933 (2000).
[34] T. Uchino, D.C. Clary, S.R. Elliott, Physical Review Letters, **85**, 3305 (2000).
[35] Y. Isbi, S. Sternklar, E. Granot, V. Lyubin, M. Klebanov, A. Lewis, Optics Commun., **171**, 219-223 (1999).
[36] T. Tsujioka, M. Irie, J. Opt. Soc. Am., **B15**, 1140-1146 (1998).
[37] V. Lyubin, M. Klebanov, I. Bar, S. Rosenwaks, N. P. Eisenberg, M.Manevich, J. Vac. Sci. Tech., **B15**, 823 (1997).
[38] M. Vlcek, P. J. S. Ewen , T. Wágner, J. Non-Cryst. Solids, **227-230**, 743-747 (1998).
[39] S. Noach, M.Manevich, M. Klebanov, V. Lyubin, N. P. Eisenberg, SPIE, **3778**, 158 (1999).
[40] R. Loeffler, T. Schwarz, H. Sautter and D. Lezal, J. Non-Cryst. Solids, **232-234**, 526 (1998).
[41] H. Hisakumi, Ke. Tanaka, Optics Lett,. **20**, 958 (1995).
[42] A. Ozols, N. Nordman, O. Nordman, P. Riihola, Phys. Rev., Condens. Matter, **B55**, 14216 (1997).
[43] P. Arun, A. C. Vedesgwar, N. C. Mehra, J. Phys. D Appl. Phys., **32**, 183 (1999).
[44] L. P. Shi, T. C. Chong, P. K. Tan, X. S. Miao, Y. M. Huang, R. Thao, Jpn. J. Appl. Phys., **38**, 1645 (1999).
[45] Guo-Fu Zhou, Bernardus A. J. Jacobs, Jpn. J. Appl. Phys., **38**, 1625 (1999).
[46] J. Park, M. R. Kim, W. S. Choi, H. Seo, Ch. Yeon, Jpn. J. Appl. Phys., **38**, 4775 (1999).
[47] S. Y. Kim, S. J. Kim, H. Seo, M. R. Kim, Jpn. J. Appl. Phys., **38**, 1713 (1999).
[48] P. K. Khulbe, X. Xun, M. Mansuripur, Applied Optics, **39**, 2359 (2000).
[49] Ch. M Lee, T. S. Chin, Y. Y. Huang, I. Ch. Tung, T. R Jeng, D. Y. Chiang, D. R. Huang, Jpn. J. Appl. Phys., **38**, 6369 (1999).
[50] K. Hirota, G. Ohbayashi, Jpn. J. Appl. Phys., **37**, 1847 (1998).
[51] J. Tominaga, H. Fuji, A. Sato, T. Nakano, T. Fukaya, N. Atoda, Jpn. J. Appl. Phys., **37**, L1323 (1998).
[52] T. Nagase, S. Ashida, K. Ichihara, Jpn. J. Appl. Phys., Part 1, **38**, (3B) 1665 (1999).

THE CHARGED DEFECT EXISTS?

Ke. Tanaka

Department of Applied Physics, Faculty of Engineering, Hokkaido University,
Sapporo 060-8628, Japan

The origin of gap states in chalcogenide glasses has been studied on the basis of optical spectra obtained for As_2S_3 using photoluminescence, photothermal deflection, and (resonant) Raman scattering. These results combined with other observations suggest that the weak-absorption tail arises from gap states below the conduction band, which are produced by As-As wrong bonds. The bond density is estimated at ~1 at.%, which is much greater than that of the charged defect proposed by Mott et al. These insights imply that, not the charged defect, but the wrong bond governs electronic properties in covalent chalcogenide glasses.

1. Introduction

Pioneering work upon chalcogenide glasses started in the middle of 20 century, and now at the beginning of 21 century, we have obtained a fair amount of experimental data, several hypotheses, and a few basic ideas [1-3]. Among the hypotheses, one of the most frequently employed for covalent chalcogenide glasses such as As_2S_3 is the charged-defect and valence-alternation pair models proposed by Street and Mott [4] and Kastner et al. [5]. Using these charged-defect concepts, they and successive researchers have asserted that unique electronic properties can be understood in coherent ways [1,3]. For instance, the photoluminescence (PL) with large Stokes shifts has been interpreted as creation of D^0 from D^+ and/or D^- (in Motts' notation). However, since D^+ and D^- are inherently ESR-*in*active and the density is estimated to be ppm levels [1,3-5], direct evidence of the existence has not been obtained. On the other hand, other possibilities for gap states have been suggested by several researchers [6-10].

I have studied the origin of optical absorption spectra in covalent chalcogenide glasses with two motives. One is to understand the mechanism of subgap photoinduced phenomena, which are in some cases more prominent than those induced by bandgap light [11]. Since the subgap phenomena are induced by light with photon energies in Urbach-edge regions, which are expressed as $\alpha \propto \exp(\hbar\omega/E_U)$, where $E_U \approx 50$ meV in As_2S_3 [1,3], structural origins of the Urbach edge should be understood. The other is to grasp the origin of weak-absorption tails (WATs), which extend below the Urbach edge as $\alpha \propto \exp(\hbar\omega/E_W)$, where $E_W \approx 300$ meV in As_2S_3 [1,3]. Tauc et al. have demonstrated that Fe impurities enhance the WAT [12]. However, even in highly-purified ingots the tails still remain, which becomes to be a serious problem in applications to IR-transmitting optical fibers [13]. Therefore, the origin should be examined in more details.

To understand optical absorption mechanisms, it is necessary to resolve the spectra into densities-of-states. That is, the optical absorption spectrum $\alpha(\hbar\omega)$ in amorphous semiconductors is governed by the densities of occupied and unoccupied states, $D_V(E)$ and $D_C(E)$, as [1,3]

$$\alpha(\hbar\omega) \propto \int D_C(E + \hbar\omega) D_V(E)\, dE, \tag{1}$$

and accordingly, $D_V(E)$ and $D_C(E)$ must be known. We may expect that these densities can directly be obtained through photoemission studies, while nevertheless, the sensitivity of photoemission measurements seems to be insufficient at present for evaluation of gap states [1,3]. Then, another way to know the gap states responsible for $D_V(E)$ and $D_C(E)$ is to employ a variety of experiments, and to construct a model from the results. If several observations can be understood coherently by a simple model, we can assume it to be plausible.

Previously, it has been suggested that the Urbach edge arises from tail states above the valence band [7,14,15]. Circumstantial evidence for this suggestion is that the so-called Urbach

energy E_U is similar to the characteristic energy of the valence-band tail [15], which is obtained from pulsed photoconduction measurements through some assumptions.

In the present work, I will show that the WAT in As_2S_3 arises from unoccupied gap states below the conduction band and that the states are produced by As-As wrong bonds. Its density is estimated at percent levels, which are much greater than that of the charged defects. Actually, the existence of many homopolar bonds seems to be inherent to covalent glasses, and accordingly, I believe that the charged defects cannot govern electronic properties in chalcogenide glasses.

2. Experiments

Samples employed were As_2S_3 glasses of two purity levels. One was those prepared previously [16]. Here, an ingot was synthesized from As and S chunks with 6-nine purity through the conventional melt-quenching procedure. Then, splinters obtained from the ingot were sealed again into quartz ampoules, heated to 1000 °C, and then rapidly-quenched (10^2 K/s) or slowly-cooled (10^{-1} K/s) to room temperature. The other was a high-purity ingot, which was prepared for optical fibers, the details of purification and synthesis procedures being unknown [17]. Sliced samples were polished to small disks, and then annealed at 180 °C before optical measurements. In addition, As_xS_{100-x} glasses with x = 17 − 43, which were prepared through the conventional melt-quenching procedure, were also investigated.

Sample compositions were inspected using an X-ray fluorescence system (MESA-500, HORIBA). Comparison of As_2S_3 glasses with crystalline As_2S_3 (orpiment) demonstrated that the compositional ratio between As and S was held at 40/60 within ± 1 at. % accuracy. For impurities, the conventional ingot might contain Fe by ~10 ppm, which was a detection limit of the X-ray system, while the high-purity ingot did not show any traces except As and S. The 10 ppm impurity level is similar to those of Taucs' samples [12].

Three kinds of optical measurements were performed. These were PL, photothermal deflection spectroscopy, and (resonant) Raman-scattering spectroscopy.

PL was excited at 5 - 300 K using several lasers and a Xe lamp filtered by a monochromator. PL spectra were monitored by a polychromator attached with a linear InGaAs detector. For PL-excitation spectra, i.e. dependence of PL intensities on excitation photon-energies, PL total intensities at a photon-energy region of 0.7 - 1.3 eV were measured using an InGaAs detector fitted with wavelength filters.

Small absorption in thin As_2S_3 samples was evaluated using the photothermal deflection spectroscopy [18]. The spectra were obtained at room temperature using a system described by Nonomura et al. [19]. In brief, the absorption of monochromatic light, the wavelength being varied, in a sample was monitored as a deflecting signal (mirage effect) of probe light which propagated nearby the sample surface. The deflecting signals were converted to absorption coefficients by following the conventional procedure [18,19]. Then, the absolute values were determined by fitting the spectra at α ≈ 10^2 cm^{-1} to absorption spectra obtained from subsidiary optical transmission measurements. Among several kinds of photothermal methods, the deflection spectroscopy appears to possess the highest sensitivity at room temperature [18,19].

Raman-scattering spectra were obtained at room temperature using a triple dispersing system fitted with a cooled charge-coupled-device (T64000, Jobin Yvon). Several laser sources were employed to monitor resonant Raman-scattering spectra. The laser light could provide photoinduced changes in some cases [11], and accordingly, samples were moved during spectral measurements. Polarization of scattered light was unanalyzed.

3. Results and discussion

A. Electronic state

Fig. 1 shows a PL-excitation spectrum for a high-purity sample with a thickness of ~1 mm. For comparison, two spectra are also plotted; one being a spectrum obtained by the constant-photocurrent method for a sample obtained from the same ingot [15] and the other being an optical absorption curve, in which small absorption is evaluated using high-purity As_2S_3 optical fibers [13]. These photocurrent and absorption spectra are obtained at room temperature, and the PL-excitation

spectrum has been measured at 5 K. Accordingly, the PL-excitation spectrum is redshifted, taking the temperature dependence [20] of the absorption edge into account. The vertical position of the PL-excitation spectrum is tentatively fixed by fitting it to the absorption spectrum at $\alpha \approx 10$ cm^{-1}.
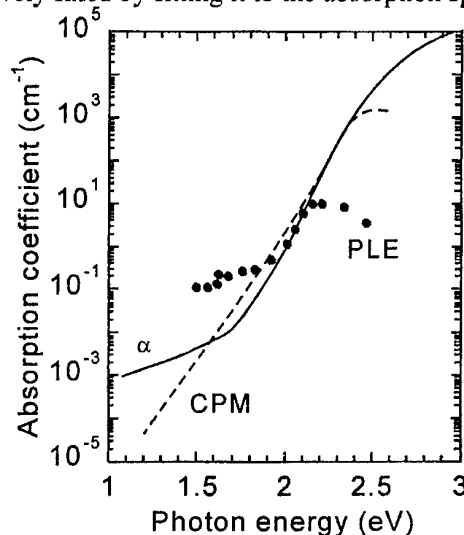
Fig. 1. Dependence of PL intensities on the excitation photon energy (PLE) in high-purity As$_2$S$_3$. Also shown are a photoconductive spectrum (CPM) [15] and an absorption spectrum α [13] at room temperature.

We see in the figure that the PL-excitation spectrum also shows a WAT-like exponential response at $\hbar\omega \leq 2$ eV. This feature is the same as those previously reported for conventional-purity samples [21]. A characteristic energy of the exponential tail is ~ 300 meV, which is similar to E_W of the WAT [1,3]. It is mentioned here that, although the WAT level of the PL-excitation spectrum appears to be higher than the real WAT, the PL level depends on the PL spectral region detected (described later) and also on other experimental conditions such as sample thickness [21]. In addition, the difference may partly be due to different ingots. Accordingly, we neglect the quantitative difference of the WAT levels between the PL-excitation spectrum and the optical absorption spectrum.

What should be underlined here is that only the photocurrent spectrum does not manifest the WAT. The non-existence of the photoconductive WAT suggests that the WAT arises from optical absorption processes which cannot produce mobile carriers, i.e. holes in As$_2$S$_3$. (Also in Se and As$_2$Se$_3$, WATs are not detected by the constant-photocurrent method [15].) Then, what electronic density causes the WAT?
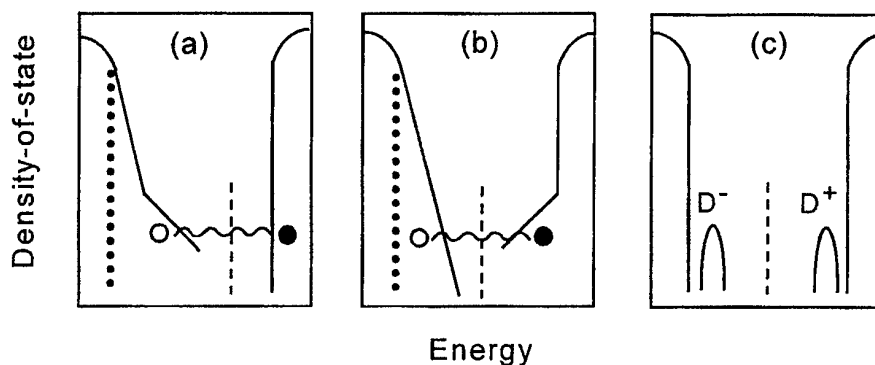
Fig. 2. Proposed densities-of-states and related sub-gap electron-hole generation processes (a,b) and the charged-defect model (c). In (a), both the Urbach edge and the WAT belong to the valence band. In (b), the Urbach edge and the WAT arise from the valence and the conduction band, respectively. Dotted and dashed lines show the mobility edge in the valence band and the Fermi level.

Here, since the WAT shows a broad exponential curve, as the simplest cases, we can assume two possibilities for the energy location of the density-of-states responsible for the WAT. That is, as illustrated in Fig. 2, the WAT may arise from the valence-band (occupied) tail (a) or from the conduction-band (unoccupied) tail (b) [15]. In these illustrations, following the previous idea [7,10,14,15], we have located the density-of-states giving rise to the Urbach edge at the valence-band edge. The mobility edge is indicated there [22].

The following three reasons support the model in which the WAT states exist below the conduction band, Fig. 2(b). First, it is demonstrated that the chalcogenide glass behaves as an intrinsic semiconductor [1,3], i.e. the Fermi energy being pinned near the center of the bandgap. This feature is inconsistent with the model (a), in which the Fermi level tends to approach the conduction band, and as a result, n-type behaviors may emerge. Second, it is also demonstrated that holes are more mobile than electrons in conventional chalcogenide glasses [1,3,15], which suggests the existence of deep trapping states for electrons. The tail states below the conduction band in (b) can work as such traps. Third, a simple calculation shows that if tail states existed at above the valence band, as in (a), these could give photocurrent signals [23]. But, no such signals can be detected as shown in Fig. 1. This disagreement is negative for the model (a). For the case of (b), electron-hole pairs in the conduction-band tail (WAT) and the valence-band tail (Urbach edge) may geminately recombine, and accordingly photocurrents cannot appear, in consistent with the observations. With these three reasons, we can assume that the gap states, which govern the WAT, are located at the conduction-band tail, as illustrated in Fig. 2(b). It is mentioned here that in amorphous hydrogenated Si the density-of-states has the (a) form, which is consistent with n-type conduction behaviors [1,3]

B. Structural origin

Fig. 3 shows optical absorption spectra obtained using the photothermal deflection spectroscopy for rapidly-quenched and slowly-cooled. As mentioned in 2, these samples were made from one original ingot, and accordingly, the purity levels of these samples are assumed to be comparable. Hence, we may neglect impurity effects upon the WATs [12]. For each samples, two specimens with thicknesses of 0.2 - 0.4 mm have been examined, and the two data show satisfactory agreements. The dips at 1.4 eV are artificial noises arising from filter exchange. Note that, since quenched glasses are necessarily cracked into small pieces with mm scales, it is difficult to evaluate low optical absorption without using such sensitive methods as the photothermal deflection spectroscopy [18,19].

In this result, the most remarkable difference between the two kinds of samples is the level of the WATs. The quenched samples exhibit the WAT which is higher by one order than that in the slowly-cooled samples.

With regard to structural differences between the rapidly-quenched and slowly-cooled samples, the most noticeable one appears to be the density of wrong bonds. The previous [16] and the present (Fig. 4) Raman-scattering spectra indicate that the concentration of As-As bonds, which can be estimated from the intensity of 230 cm^{-1} peak [24], in the quenched samples is greater than that in the slowly-cooled samples. Although the S-S peak at 490 cm^{-1} [24] is weak, the present Raman spectra in Fig. 4 show that it is stronger also in the quenched samples. That is, these observations demonstrate that the wrong-bond density is higher in the quenched samples. Here, although quantitative evaluation of the concentration difference is not straightforward, a plausible difference is typically 5 times [25].

These optical and structural correspondences imply that the wrong bonds (As-As and/or S-S) are responsible for the WAT. The higher concentration of the wrong bonds in the quenched samples appears to cause the greater WAT. Then, does the WAT arise from As-As or from S-S?
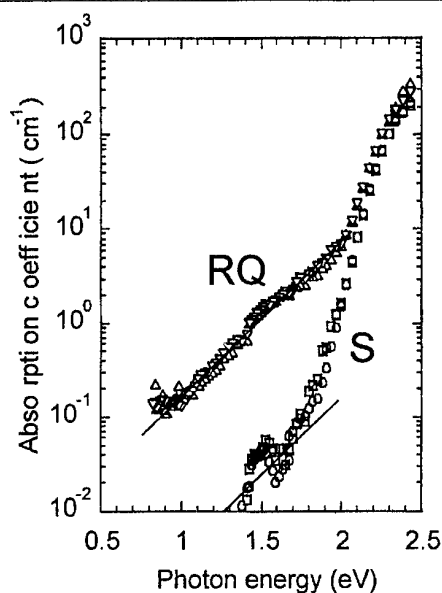
Fig. 3. (left) Optical absorption spectra obtained using the photothermal deflection spectroscopy for As_2S_3 glasses prepared through rapidly-quenching (triangles) and slowly-cooling (circles and squares) processes. The lines represent WATs.
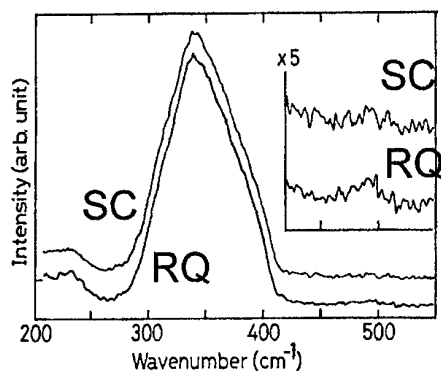
Fig. 4. (right) Raman spectra of slowly-cooled (upper) and rapidly-quenched (lower) samples obtained using probe light of $\hbar\omega$ = 2.0 eV. The inset shows magnified views for the 490 cm^{-1} peak.

Fig. 5 displays a series of Raman-scattering spectra with the photon energy of probe light. Here, the intensity is normalized with a peak at 340 cm^{-1}, which is identified to As-S vibrations [24]. We see that the As-As peak (230 cm^{-1}) increases with an increase in the photon energy, while the S-S peak (490 cm^{-1}) does not show appreciable changes. The details are shown in the inset, in which the As-As peak exponentially increases with the photon energy in the spectral range of 1.5 - 2.4 eV, which covers the WAT. In contrast, the S-S peak remains at a small level. It should be underlined that the results obtained for the conventional and the high-purity samples, which are plotted by different symbols, show no meaningful difference.
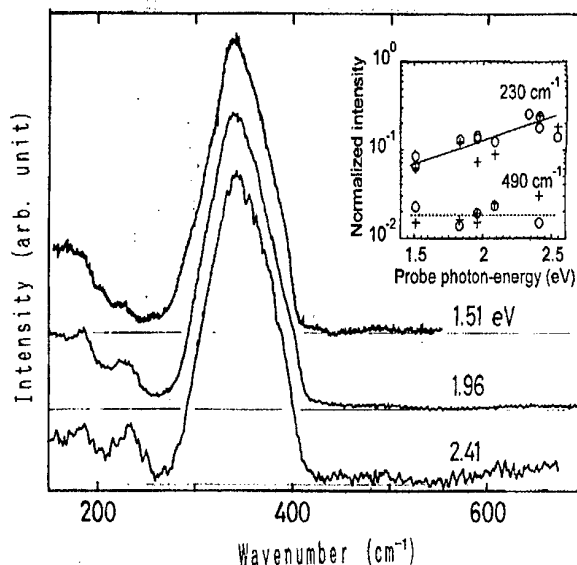
Fig. 5. A series of Raman scattering spectra obtained for a high-purity As_2S_3 as a function of the photon energy of probe light. The inset shows the intensities of 230 and 490 cm^{-1} Raman peaks as a function of the photon energy of probe light. The intensity is normalized with that of the main peak at 340 cm^{-1}. The two symbols show the two kinds of samples; high – purity samples (+) and conventional - purity samples (O).

That is, these photon-energy dependences are intrinsic to As_2S_3 glass. The present result may be consistent with that reported for 1.96 - 2.61 eV probe light by Kawazoe et al. [26].

The exponential dependence of the As-As peak intensity on the photon energy implies a resonant Raman-scattering process [27]. Conventional analyses of resonant Raman scattering show that, when the photon energy of probe light coincides with an electronic excitation energy E_i, Raman scattering processes associated with the electronic transition enhance dramatically, resulting in the strengthening of related Raman peaks [27]. The resonance curve may be written as $R(\hbar\omega - E_i)$, which has a prominent peak at $\hbar\omega = E_i$. Here, in a disordered system, E_i is probably distributed, and we may intuitively assume that the resonant Raman scattering measures $\Sigma_i R(\hbar\omega - E_i)$. This represents the electronic density-of-states of the resonant sites, provided that R is replaced by the δ-function, which we take here as a rough approximation.

Then, we can assume that As-As bonds cause the WAT. Actually, the characteristic energy representing the exponential increase in the As-As Raman peak (the inset in Fig. 5) is ~ 700 meV, which is comparable to E_W (≈ 300 meV) in the WAT [28].

On the other hand, the photon-energy independence of the S-S peak implies that its resonance feature is similar to that of As-S bonds. Since the bandgap in As_2S_3 is constructed between lone-pair electron states of S and anti-bonding states of As-S [1,3], these similar resonance behaviors are plausible. In other words, it is inferred that S-S wrong bonds are not responsible for the WAT.

To obtain some more insight into the atomic structure responsible for the WAT, I have also investigated the dependence of PL spectra upon excitation photon-energy, which is varied at 1.5 - 2.6 eV. Then, a similar result to that reported by Tada et al. [29] has been obtained; i.e. when the excitation photon-energy is higher (Urbach edge) and lower (WAT region) than ~ 2 eV, a broad PL peak appears at around $\hbar\omega \approx 1.1$ eV and 0.9 eV. Tada et al. interpret on the basis of their compositional study that the 0.9 eV PL originates from As-As bonds. This interpretation is consistent with the present idea, which assumes the correspondence between the WAT and As-As bonds. However, Tadas' interpretation may be inconsistent with a result obtained using optically induced electron-spin resonance [30]. In addition, I have also observed that other samples such as crystalline As_2S_3 (orpiment), which nominally has no As-As bonds, give rise to broad peaks at $\hbar\omega \approx 0.9$ eV. Therefore, it is fair to conclude that, although Tadas' assertion is consistent with the present idea, the 0.9 eV PL peak cannot be a firm evidence indicating the existence of As-As bonds.

C. Energy level and atomic structure

We have obtained two ideas, and the connection of the two is the next subject. That is, in A, it has been inferred that the WAT arises from tail states below the conduction band. In B, some observations suggest that the WAT is produced by As-As wrong bonds. Then, can the tail states below the conduction band be produced by As-As bonds ? Fig. 6 shows several levels of interest in As_2S_3. In this illustration, the energy difference between the outermost p levels of As and S atoms is estimated at ~ 2.5 eV [31]. The lone-pair p-electron level of S broadens to form the top of the valence band (LP), the width of which is demonstrated to be 2 - 3 eV [1,3]. On the other hand, the conduction band is produced by the anti-bonding state σ^* of As-S bonds, and the gap giving rise to the so-called Tauc optical gap of ~ 2.4 eV appears [1,3].

We now consider the energy levels of wrong bonds. As-As bonds existing in As_2S_3 glass must also produce the bonding and anti-bonding states, and the energy split can be estimated at 3 - 4 eV from experimental studies on solid As [32]. Then, we can predict that the As-As σ^* states are located at just below (or at around the bottom of) the conduction band [33]. Since As-As bonds are weaker than As-S bonds [6,34], which form disordered environments, the As-As bond distance (R' in Fig. 7) probably fluctuates at around a typical value 2.5 Å [32]. Related dihedral angles may also fluctuate. Then, it is plausible that such fluctuation causes a broad energy distribution of As-As σ^* states, which appears as the WAT. (However, why the distribution has the exponential form remains to be studied.) On the other hand, it is known that S dimers possess excitation energy of ~ 10 eV [35], and accordingly the antibonding states are probably included in the conduction band, i.e. these cannot provide any contribution to gap states. (In As_2Se_3, Se-Se σ^* bonds may contribute to the WAT, since the energy difference between the p-electron levels of As and Se is ~ 2.0 eV [31], and the excitation

energy of Se dimers seems to be comparable to that of As dimers.)

Fig. 7 gives an image of atomic structures in As_2S_3 glass. As suggested previously [7,14,15], we here assume that the Urbach edge arises from an exponential density-of-states at the top of the valence band. Such an exponential edge may appear, since the valence band is formed by lone-pair electron states of S atoms [1,3] and the interaction between the lone-pair electrons is governed by disordered interlayer distances (R in the figure). In addition, the covalent atomic structures are in favor of production of homopolar bonds, As-As and S-S, and the exponential edge may also be influenced by intralayer S-S interaction. On the other hand, As-As bonds are assumed to be responsible for the WAT as described above.
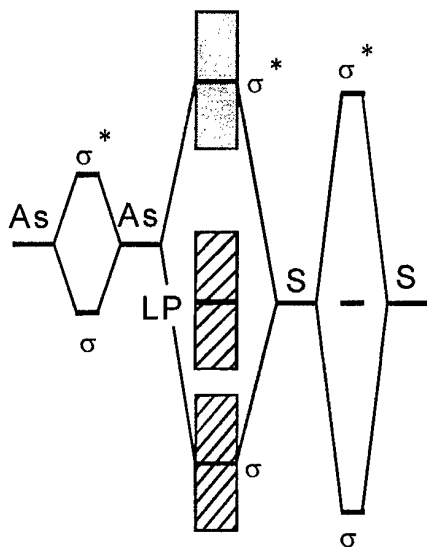
Fig. 6. (left) Electronic structures in As_2S_3 containing As-As and S-S wrong bonds. LP denotes the lone-pair electron state.
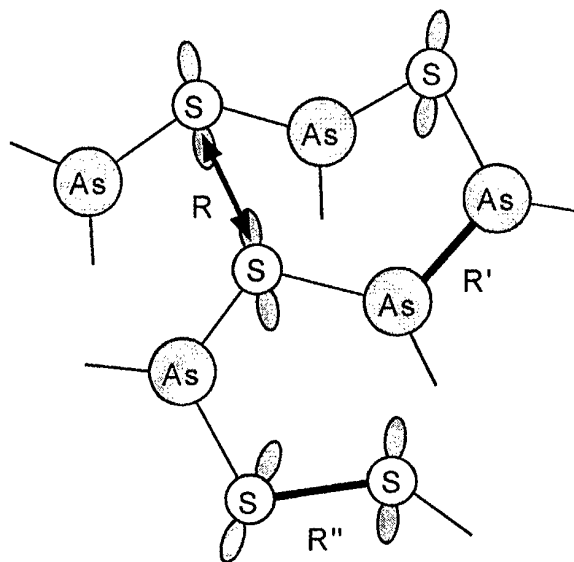
Fig. 7. (right) A schematic structure of As_2S_3 glass. R, R', and R'' denote, respectively, the interlayer distance, intralayer As - As distance, and intralayer S-S distance.

D. Other related features

The present model seems to be consistent with temperature dependence of WATs. Tauc et al. have demonstrated for As_2S_3 that, with an increase in temperature from 100 to 600 K, the Urbach edge substantially redshifts while the WAT changes little [36]. This temperature independence of the WAT is consistent with the present model, since the wrong-bond density cannot change at temperatures below the melting temperature, 580 K [2,16]. On the other hand, thermal disordering may govern the Urbach-edge behavior [37].

The present model is also in harmony with the fact that, in crystalline $As_2S(Se)_3$, electrons are more mobile than holes [38]. In these crystals, As-As wrong bonds do not exist under ideal situations, and accordingly, in the present view, no traps for electrons exist.

The present model predicts that elemental chalcogenide glasses, in which no wrong bonds exist, do not show WATs, while reported results appear to be inconclusive. Among many optical spectra reported for amorphous Se, the smallest attenuation may be 10^{-2} cm^{-1} at $\hbar\omega \approx 1$ eV with WAT-like spectral features [39]. The photo-acoustic spectroscopy [40] and the present photothermal deflection spectroscopy for Se layers (unpublished) also demonstrate absorption levels of 10^{-1} cm^{-1} at 1 eV with WAT-like features. These attenuation or absorption levels appear to be comparatively smaller than those in compound glasses such as As_2Se_3 ($\alpha \approx 10^{-1}$ cm^{-1}) [1], while WAT-like features still remain. However, we cannot identify the origin of these attenuations, which may be governed by surface and/or bulk scattering. Alternatively, it may be due to absorption caused by impurities and/or defects. Liquid S also shows absorption of $\sim 10^{-1}$ cm^{-1} with WAT-like features [41].

The present model also predicts that, in the As-S glass system, the WAT becomes smaller

with an increase in the S content, since As-As bonds become fewer. Fig. 8 shows related absorption spectra for As_xS_{100-x} (x = 17 ~ 43), which were obtained using the photothermal deflection spectroscopy. The inset shows composition dependence of the absorption coefficients evaluated at, tentatively, $\hbar\omega$ = 1.5 eV. We see that, with an increase in S content, the level of WAT decreases, which is consistent with the prediction. We also see, however, that the level becomes smaller in $As_{43}S_{57}$. This result may indicate that many As-As bonds form extended states. It is mentioned here that subsidiary X-ray fluorescence measurements did not show marked impurity difference in these glasses.
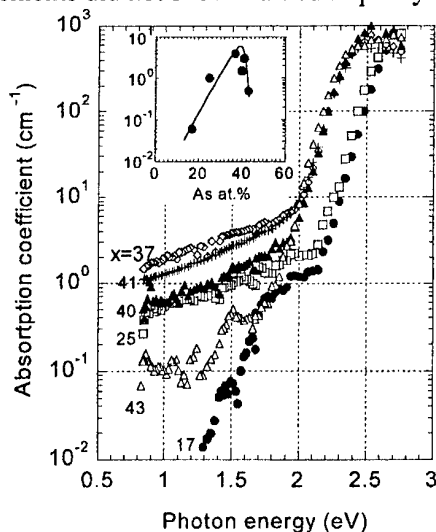
Fig. 8. Absorption spectra of As_xS_{100-x} glasses. The inset shows the composition dependence of absorption coefficients evaluated at a photon energy of 1.5 eV.

In contrast to chalcogenide glasses, it has been repeatedly demonstrated that SiO_2 glass possesses no WAT [42]. Alternatively, optical attenuation below the Urbach edge is governed by light scattering arising from density fluctuation. This ultimate transparency can be understood coherently with the present model, since Si-O bonds are fairly ionic [31], and accordingly the wrong bonds (Si-Si and O-O) are few. Similar situations may be expected for ionic chalcogenide glasses such as Ga_2S_3-Na_2S, while the glass is hygroscopic and residual absorption still remains [43].

E. Comment on the charged-defect model

It seems valuable to consider a consequence of the present model upon the charged-defect models proposed by Street and Mott [4] and Kastner et al.[5]. The charged-defect models assert [1,3] that, in chalcogenide glasses, D^- and D^+ (in Motts' notation) become to be intrinsic gap states, and their electronic states are located, respectively, at above the valence band and below the conduction band (see, Fig. 2c). The density is estimated at ppm levels, $\sim 10^{18}$ cm^{-3}.

These models should be re-considered, at least, in two respects. One is that the models presume that the chalcogenide glass is completely transparent [4,5], i.e. no midgap states. However, we have seen that there is residual absorption in highly-pure As_2S_3 glasses, in which no impurities are detected, i.e. less than 10 ppm. The other is that recent studies suggest that the PL with large Stokes shifts, which was interpreted as creation of D^0 from D^+ and/or D^- [1,3], has been demonstrated using optically-detected ESR to be caused by self-trapped excitons [44]. That is, no charged defects are needed.

The present model assumes the electronic density-of-states with the form of Fig. 2(b). Here, the conduction-band tail is composed with the As-As bonds of 0.1 - 1 at.% [25], which govern the WAT. On the other hand, it has been inferred that the valence-band tail is governed by the disordered interaction between lone-pair electrons of S atoms [7,10,14,15]. No unpaired electrons exist in the present model, which is consistent with observations [1,3].

The two models may be incompatible. Since the existence of a large number of As-As bonds has been firmly demonstrated by several experiments [25], and since the bonds appear to produce gap states as discussed in 3C, it is difficult to envisage that the charged defects govern macroscopic

electronic properties, at least, in real $As_2S(Se)_3$ glasses. It seems that *most of electronic properties in covalent chalcogenide glasses can be understood with homopolar bonds and interlayer interaction.* For instance, the photoinduced ESR [1,3] can be understood by assuming creation of D^0 states through photoinduced bond scission of homo- and hetero-polar bonds, which is predicted theoretically [45].

4. Summary

The existence of WATs appears to be inherent to chalcogenide glasses, and understanding of its origin has been desired. The understanding has also been required from a viewpoint of applications to IR-transparent optical fibers.

We have studied the WAT using As_2S_3 glass as a sample, and have presented some observations, which give the following two ideas:
i) The WAT originates from tail states below the conduction band.
ii) As-As wrong bonds (0.1 - 1 at.%) are responsible for the WAT.
These two ideas have been understood coherently with an electronic-level diagram, in which the antibonding states of As-As are located below the conduction band. Finally, it has been asserted that the wrong bonds behave as more dominant gap states than the charged defects.

Acknowledgements

References

[1] N. F. Mott, E. A. Davis, Electronic Processes in Non-Crystalline Materials, (Clarendon, Oxford, 1979).
[2] Z. U. Borisova, Glassy Semiconductors, (Plenum, New York, 1981).
[3] K. Morigaki, Physics of Amorphous Semiconductors , (Imperial College Press, London, 1999).
[4] R. A. Street, N. F. Mott, Phys. Rev. Lett , **35**, 1293 (1975).
[5] M. Kastner, D. Adler, H. Fritzsche, Phys. Rev. Lett., **37**, 1504 (1976).
[6] V. Halpern, Philos. Mag., **34**, 331 (1976).
[7] S. R. Ovshinsky, D. Adler, Contemp. Phys., **19**, 109 (1978).
[8] J. C. Phillips, J. Non-Cryst. Solids, **43**, 37 (1981).
[9] D. Vanderbilt, J. D. Joannopoulos, Phys. Rev., B **23**, 2596 (1981).
[10] Y. Watanabe, H. Kawazoe, M. Yamane, J. Non-Cryst. Solids, **95&96**, 365 (1987).
[11] K. Shimakawa, A. Kolobov, S. R. Elliott, Adv. Phys., **44**, 475 (1995).
[12] J. Tauc, F. J. Di Salvo, G. E. Peterson, D. L. Wood, Amorphous Magnetism, edited by H.O. Hooper and A. M. de Graaf (Plenum, NY, 1973) p. 119: J. Tauc, Optical Properties of Highly Transparent Solids, edited by S.S. Mitra and B. Bendow (Plenum, NY, 1975) p. 245.
[13] J. Nishii, T. Yamashita, Infrared Fiber Optics, edited by J. S. Sanghera, I. D. Aggarwal (CRC Press, Boca Raton, 1998) p. 143.
[14] G. J. Adriaenssens, A. Eliat, edited by A. Andriesh and M. Bertolotti, Physics and Applications of Non-Crystalline Semiconductors in Optoelectronics, (Kluwer Academic Publishes, Dordrecht, 1997) p.77.
[15] K. Tanaka, S. Nakayama, Jpn. J. Appl. Phys., **38**, 3986 (1999).
[16] K. Tanaka, S. Gohda, A. Odajima, Solid State Commun., **56**, 899 (1985): K. Tanaka, Phys. Rev., B **36**, 9746 (1987).
[17] In the present study, I have focussed upon As_2S_3 with some reasons. First, high-purity samples are available. For instance, no such pure samples are available for Se and As_2Se_3, at least, to me. $GeS(Se)_2$ glasses are difficult to prepare in reproducible ways, which may be related to the average coordination of 2.67 and/or the existence of several crystalline polymorphs. In addition, these Ge-chalcogenide glasses are exceptional in a sense that the glasses exhibit ESR signals in the dark. Second, considerable data (including photoinduced changes) are presented for As_2S_3, and the bandgap energy of about 2.4 eV is appropriate for optical investigations.
[18] A. Mandelis, Photoacoustic and Thermal Wave Phenomena in Semiconductors, (North-Holland,

New York, 1987).

[19] S. Nonomura, T. Nishiwaki, S. Nitta, Philos. Mag., B **69**, 335 (1994).

[20] J. R. Zakis, H. Fritzsche, Phys. Stat. Sol. (b), **64**, 123 (1974): R. A. Street, T. M. Searle, I. G. Austin, and R. S. Sussmann, J. Phys. C: Solid State Phys., **7**, 1582 (1974).

[21] R. A. Street, Adv. Phys., **25**, 397 (1976).

[22] K. Tanaka, S. Nakayama, J. Opt. Adv. Mater., **2**, 5 (2000).

[23] It is assumed that carriers trapped in gap states with an energy depth of E_B can be thermally activated into extended states with a relaxation time τ, which is given by $\Omega^{-1} \exp(E_B/k_BT)$ [1]. Suppose $\Omega = 10^{12}$ Hz, a typical phonon frequency, we have $\tau = 1$ s when $T = 300$ K and $E_B = 0.7$ eV. The photocurrent measurement was performed with a time constant of ~ 5 s [15], and accordingly, it could possibly detect a trace arising from the WAT in As_2S_3 if the WAT belongs to the valence band. In smaller gap materials such as Se and As_2Se_3, the possibility is higher, since the trap depth becomes smaller than 0.7 eV, but no such traces appear.

[24] P. J. S. Ewen, M. J. Sik, A. E. Owen, The Structure of Non-Crystalline Materials, (Taylor and Francis, London, 1977) p. 231: R. J. Nemanich, G. A. N. Connell, T. M. Hayes, R. A. Street, Phys. Rev., B **18**, 6900 (1978).

[25] Previous studies using chemical analyses (F. Kosek, J. Chlebny, Z. Cimpl, J. Masek, Philos. Mag., B **47**, 627 (1983)), EXAFS (C.Y. Yang, M.A. Paesler, and D.E. Sayers, Phys. Rev., B **36**, 9160 (1987)), Mössbauer spectroscopy (I. Zitkovsky and P. Boolchand, Diffusion and Defect Data, **53**, 167 (1987) and Raman scattering [16] estimate the wrong-bond (As-As and S-S) density in As_2S_3 at 0.1 - 1 at.%. Here, the large error is inevitable due to the uncertainty (~ ±1 at.%) of the absolute compositional ratio between As and S in As_2S_3 glasses.

[26] H. Kawazoe, H. Yanagita, Y. Watanabe, M. Yamane, Phys. Rev., B **38**, 5661 (1988).

[27] M. Cardona, Light Scattering in Solids II, edited by M. Cardona and G. Günterodt (Springer-Verlag, Berlin, 1982) p. 19: P.Y. Yu and M. Cardona, Fundamentals of Semiconductors (2nd Edition), (Springer-Verlag, Berlin, 1999) Chap. 7.

[28] Since the peak intensity in Fig. 4 is normalized, it is not necessarily required that the two characteristic energies are identical. Rather, the comparable magnitudes support the present idea, i.e. As-As bonds produce the WAT.

[29] T. Tada, T. Ninomiya, J. Non-Cryst. Solids, **137&138**, 997 (1991).

[30] J. A. Freitas, Jr., U. Strom, and S.G. Bishop, Phys. Rev., B **35**, 7780 (1987).

[31] W. A. Harrison, Electronic Structure and the Properties of Solids (Freeman, San Francisco, 1980) Chap. 2.

[32] G. N. Greaves, S. R. Elliott, E. A. Davis, Adv. Phys., **28**, 49 (1979).

[33] This positioning of As-As σ^* bonds is different from those proposed previously [6,9]. The reason may be due to unreliable energy values. Instead, we have employed empirical data here.

[34] S. Tsuchihashi, Y. Kawamoto, J. Non-Cryst. Solids, **5**, 286 (1971).

[35] B. Meyer, M. Gouterman, D. Jensen, T. V. Oommen, K. Spitzer, T. Stroyer-Hansen, Sulfur Research Trends, (American Chemical Society, Washington, D.C., 1972), p. 53.

[36] J. Tauc, A. Menth, D. L. Wood, Phys. Rev. Lett., **25**, 749 (1970).

[37] J. Ihm, J. Phys. C: Solid State Phys.,**18**, 4741 (1985).

[38] R. Zallen, D. Blossey, Physics and Chemistry of Materials with Layered Structures, edited by E. Mooser (D. Reidel Publishing Company, Dordrecht, 1976) p. 231: G. Brunst and G. Weiser, Philos. Mag., B **51**, 67 (1985).

[39] J. Stuke, J. Non-Cryst. Solids, **4**, 1 (1970): A. Vasko, D. Lezal, and I. Srb, J. Non-Cryst. Solids, **4**, 311 (1970).

[40] G. P. Ceasar, M. Abkowitz, J. W-P. Lin, Phys. Rev., B **29**, 2353 (1984).

[41] M. Zanini, J. Tauc, J. Non-Cryst. Solids, **23**, 349 (1977): S. Hosokawa, T. Matsuoka, and K. Tamura, J.Phys.: Condens. Matter, **6**, 5273 (1994).

[42] G. A. Thomas, B. I. Shraiman, P. F. Glodis, M. J. Stephen, Nature, **404**, 262 (2000).

[43] H. Tawarayama, E. Ishikawa, K. Yamanaka, K. Itoh, K. Okada, H. Aoki, H. Yanagida, Y. Matsuoka, H. Toratani, J. Am. Ceram. Soc., **83**, 792 (2000).

[44] L. H. Robins, M. A. Kastner, Phys. Rev., B **35**, 2867 (1987): J. Risten, P. C. Taylor, W. D. Ohlsen, G. Weiser, Phys. Rev., B **42**, 11845 (1990): D. Mao, W. D. Ohlsen, P. C. Taylor, Phys. Rev., B **48**, 4428 (1993).

[45] K. Hoshino, F. Shimojo, T. Nishida, J. Phys. Soc. Jpn., **68**, 1907 (1999): J. Li and D. A. Drabold, Phys. Rev. Lett. **85**, 2785 (2000): T. Uchino, D. C. Clary, and S. R. Elliott, Phys. Rev. Lett., **85**, 3305 (2000).

ATOMIC AND ELECTRONIC STRUCTURES OF GLASSY Ge$_x$Se$_{1-x}$ AROUND THE STIFFNESS THRESHOLD COMPOSITION

S. Hosokawa

Institut für Physikalische-, Kern-, und Makromolekulare Chemie, Philipps Universität Marburg, D-35032 Marburg, Germany

Anomalous x-ray scattering experiments on glassy Ge$_x$Se$_{1-x}$ have been carried out at energies close to the Ge and Se K edges at concentrations close to the onset and completion of the rigidity percolation threshold ($x = 0.195$ and 0.23). The total structure factors $S(Q)$ show rapid changes in both the position and intensity of the prepeak around 10 nm^{-1}, while remaining almost unchanged in the other Q ranges. The differential structure factors $\Delta_i S(Q)$ obtained have characteristic features of their own. A detailed comparison among them suggests that the prepeak originates from only the Ge-Ge correlation. On the basis of the concentration dependence of the spectra and the existing partial structure factors of glassy GeSe$_2$ obtained by Petri et al., the origin of the prepeak is discussed. Valence- and conduction-band electronic density of states of glassy Ge$_x$Se$_{1-x}$ ($0 \leq x \leq 0.33$) were also investigated by measuring the ultraviolet photoemission and inverse-photoemission spectra. They exhibit a remarkable change in their spectral features near $x = 0.20$. These observations in both the atomic and electronic structures are consistent with the occurrence of a percolation threshold in non-crystalline covalent network systems as predicted by Phillips and Thorpe. The threshold is characterized by the percolation of a specific Ge(Se$_{1/2}$)$_4$ molecular unit spread over the network.

1. Introduction

There is a general agreement that in glassy (*g-*) Ge$_x$Se$_{1-x}$ systems, the coordination numbers of Ge and Se are 4 and 2, respectively, in the concentration range $0.00 \leq x \leq 0.33$. This chemically-ordered continuous-random-network model was originally proposed by Zachariasen [1], and experimentally supported by electron diffraction- [2,3], x-ray diffraction- [4], and Raman scattering [5] measurements.

Mean-field constraint theory [6,7] for network glasses provides a powerful tool to explain the experimentally observed numerous anomalies around the critical composition of rigidity percolation threshold at an average coordination number, $\langle r \rangle = 2.4$, where the number of constraints per atom is equal to the degree of freedom. In case of *g*-Ge$_x$Se$_{1-x}$ systems, this corresponds to $x = 0.20$. The character of the network glass undergoes a steep "first-order-like" transition from easily deformable at $\langle r \rangle < 2.4$ (*floppy*) to rigid at $\langle r \rangle > 2.4$. Katamigahara et al. [8] reported a dynamic density of states around 5 meV to prove the existence of the *floppy* mode (*zero-frequency* mode in the *floppy* glass) by measuring inelastic neutron scattering spectra. Recently, Boolchand and co-workers [9] demonstrated that results from Raman scattering, modulated scanning calorimetry, molar volume, and Mössbauer spectroscopy provide evidence for a multiplicity of stiffness transitions; an onset point near $\langle r \rangle = 2.40$ ($x = 0.20$) and a completion point near $\langle r \rangle = 2.46$ ($x = 0.23$). Of particular interest are the Raman scattering results of the concentration variation of corner-sharing mode frequency of Ge(Se$_{1/2}$)$_4$ units, which show an abrupt jump at $x = 0.23$. These Raman results led to the suggestion that they correlate rather well with the atomic and electronic structures of *g*-Ge$_x$Se$_{1-x}$ around this stiffness threshold composition.

X-ray absorption fine structure (XAFS) results provide excellent information on first-shell local structure, or the so-called short-range order (SRO), around each constituent element even in non-crystalline materials. For this reason, precise studies of the concentration dependence of the atomic structure of *g*-Ge$_x$Se$_{1-x}$ in the range $0.00 \leq x \leq 0.33$ were performed using XAFS technique

[10,11,12]. They confirmed the predicted coordination numbers (8–N rule) with the bond length similar to that in the crystal. Only ref. [12] suggests minor deviations of the coordination numbers from the 8–N rule. The higher shell information was, however, very limited due to a short lifetime of photoexcited electrons during the XAFS process.

An x-ray diffraction study was performed at compositions $x = 0.00$, 0.04, 0.10, 0.15, 0.20, and 0.25 [13], which demonstrated that besides the well-established SRO information, a prepeak appears in the total structure factors $S(Q)$ at a scattering vector Q of about 10 nm^{-1}. The prepeak, which is clear evidence for the existence of intermediate-range order (IRO), shows a systematic decrease in the intensity and shifts towards higher Q with decreasing Ge concentration. The earlier x-ray scattering experiment [4], as well as a recent neutron diffraction measurement [14], indicated the same concentration variation of the prepeak in $S(Q)$.

An anomalous x-ray scattering (AXS) experiment was carried out by Armand et al. [15] at $x = 0.167$ and 0.25. From the differential structure factors $\Delta_i S(Q)$ obtained, they concluded that the structure at $x = 0.25$ is based on that of the crystalline GeSe$_2$ with the presence of edge- and corner-sharing Ge(Se$_{1/2}$)$_4$ tetrahedra, and that at $x = 0.167$, the structure is built up from isolated Ge(Se$_{1/2}$)$_4$ tetrahedra interconnected by short Se chains. Moreover, they suggested that the prepeak seems to be due to the Ge-Ge correlations. However, due to the rough concentration steps at which the diffraction experiments were performed, it is still difficult to discuss how the IRO in g-Ge$_x$Se$_{1-x}$ changes when crossing the stiffness threshold composition $x = 0.20$.

We have carried out AXS experiments on g-Ge$_x$Se$_{1-x}$ [16] to obtain detailed structural information, i.e., to clarify the role of each element on the SRO and IRO. The experiments were performed at the Ge concentrations of 0.195 and 0.23, which are respectively very close to the onset and completion concentration points of the Boolchand's criterion [9]. Additionally an $S(Q)$ measurement was performed at $x = 0.185$.

As mentioned above, the Raman scattering results of the corner-sharing mode frequency of Ge(Se$_{1/2}$)$_4$ units show a sudden jump at $x = 0.23$ [9]. The origin of the covalent bond is, of course, a distribution of electron clouds between atoms. Valence-band electronic density of states can be investigated by means of photoemission spectroscopy (PES). Some decades ago, PES spectra of g-GeSe$_2$ [17,18,19] and g-Se [20] were obtained using this technique. The results confirmed simple band models for each glass.

On the other hand, information on the conduction bands or the empty states has been limited so far. Measurements of optical reflectance [19,21,22] is one of the indirect methods to estimate the conduction bands. The imaginary part of dielectric function, ε_2, can be calculated by a Kramers-Kronig analysis of the reflectance spectra. The ε_2 spectrum was for a long time believed to be the simple convolution of the valence and conduction bands, which is the so-called constant-transition-matrix-element assumption for disordered materials. However, our recent PES-IPES works on g-Se and As$_2$Se$_3$ [23] and amorphous Ge [24] provide the first clear-cut evidence that this historic assumption is not generally valid. Core-absorption spectroscopy [18,25,26,27] was also widely used to obtain information on the empty states. However, it was very difficult to obtain the conduction-band DOS from the reflectance and core-absorption measurements, because the role of the exciton effects as well as the matrix elements on these optical transitions were not sufficiently understood for analysing them further.

It is well known that inverse-photoemission spectroscopy (IPES) is a powerful method to directly obtain conduction-band DOS. We have measured PES and IPES spectra of g-Ge$_x$Se$_{1-x}$ in the concentration range $0 \le x \le 0.33$, especially near $x = 0.20$ in detail, and found a dramatic change in the spectral features near $x = 0.20$ [28].

In this paper, I review our recent investigations on the atomic and electronic structures of g-Ge$_x$Se$_{1-x}$ near the stiffness threshold composition $x = 0.20$ by means of the AXS and PES/IPES measurements. Following this section, principles of these noble techniques and actual experimental procedures are given in Sec. II and III, respectively, with separated subsections for each technique. Then, the experimental results are presented in Sec. IV. In Sec. V, I discuss the critical behaviours of the atomic and electronic structures in g-Ge$_x$Se$_{1-x}$ mixtures in terms of the Phillips-Thorpe rigidity percolation theory [6,7]. I conclude in the last section.

2. Principles of experimental techniques

A. Anomalous x-ray scattering

The scattered x-ray intensity varies with energy E of the incident x-ray beam due to the energy dependence of the atomic form factor,

$$f(Q,E) = f_0(Q) + f'(E) + if''(E),\tag{1}$$

where f_0 is the energy-independent form factor, f' and f'' the real and imaginary parts of anomalous term, respectively. When the incident x-ray energy is tuned near an absorption edge of an element in a multicomponent material, the variation of $f(Q,E)$ is significant, which can produce a substantial contrast among the scattering patterns, i.e., $S(Q)$, recorded at different energies. As an example, f' and f'' of Ge and Se are shown in Fig. 1 as a function of energy E, which were calculated by Sasaki [29]. As is clearly seen in the figure, each f' exhibits a considerable decrease at energies near its K absorption edge.
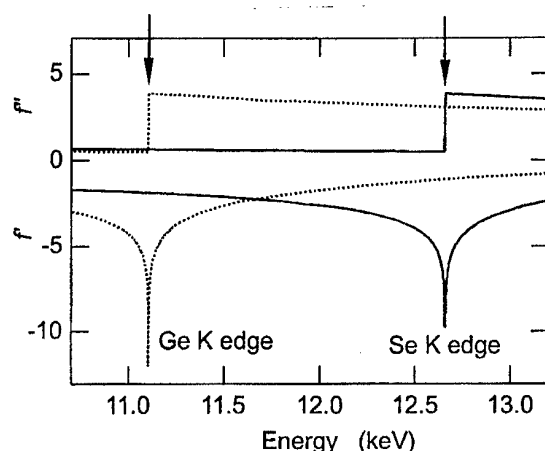
Fig. 1. f' and f'' of Ge (dashed lines) and Se (solid lines) as a function of energy E
calculated by Sasaki [29]. Arrows indicate energies at K absorption edges.

This contrast can be used to obtain $\Delta_i S(Q)$ by taking the difference of two scattering spectra measured typically at about 10 eV and some hundred eV below the absorption edge. The $\Delta_i S(Q)$ mainly results from pair correlations of the element near whose absorption edge the experiments are carried out. For example, for a binary alloy AB, if the measurements are performed close to an absorption edge of A element, the $\Delta_A S(Q)$ usually contains only A-A and A-B correlations, because $f(Q,E)$ of B element does not change significantly over the energy range used, and thus the B-B correlation is eliminated by taking the difference. Like XAFS, AXS provides selective information on the structural environment around a specific element. A distinct advantage of AXS compared to XAFS is that it provides a sensitive IRO information as already mentioned in the introductory section.

The pair distribution function $g(r)$ of an average atom is expressed as

$$4\pi r \rho_0 [g(r) - 1] = \frac{2}{\pi} \int Q[S(Q) - 1]\sin Qr dQ\tag{2}$$

where ρ_0 is the averaged number density. $S(Q)$ is related to the elastically scattered x-ray intensity $I(Q,E)$ by

$$\alpha I(Q,E) = \langle f(Q,E)^2 \rangle - \langle f(Q,E) \rangle^2 + \langle f(Q,E) \rangle^2 S(Q)\tag{3}$$

where α is a normalization constant, and $\langle \rangle$ represents the chemical average of the atomic form factors, i.e., for a binary alloy,

$$\left\langle f(Q,E)^2 \right\rangle = \sum_{i=1}^{2} c_i \left| f_i(Q,E) \right|^2 \tag{4}$$

and

$$\left\langle f(Q,E) \right\rangle^2 = \left[\sum_{i=1}^{2} c_i f_i(Q,E) \right]^2 . \tag{5}$$

Here c_i is the atomic fraction of element i. Then, $S(Q)$ can be written as a linear combination of three partial structure factors, $S_{ij}(Q)$, weighted by weighting factors $W_{ij}(Q,E)$,

$$S(Q,E) = \sum_{i=1}^{2} \sum_{j=1}^{2} W_{ij}(Q,E) S_{ij}(Q), \tag{6}$$

where

$$W_{ij}(Q,E) = c_i c_j \frac{f_i(Q,E) f_j(Q,E)}{\left\langle f(Q,E) \right\rangle^2}, \tag{7}$$

The imaginary part of anomalous terms $f''(E)$ in the atomic form factors can be experimentally obtained from XAFS experiments, and $f'(E)$ can be calculated from $f''(E)$ using the Krammers-Kronig relation [30,31,32]. However, the difference between the theory and their experimental results are small in the energy range more than 15 eV below the absorption edge. Therefore, theoretical data calculated by Sasaki [29] were used for the present analyses. Theoretical value of the energy-independent form factor f_0 was also taken from a literature [33]. The energies and corresponding theoretical values of $f'(E)$ and $f''(E)$ used for our experiments and analyses are given in Table 1.

Table 1. f' and f'' values (electron units) of Ge and Se elements at energies measured.

Energy (eV)	f'_{Ge}	f''_{Ge}	f'_{Se}	f''_{Se}
10903	−3.647	0.510	−1.750	0.656
11088	−6.292	0.494	−1.844	0.635
12454	−1.254	3.157	−3.725	0.515
12639	−1.113	3.084	−6.141	0.500

Fig. 2(a) shows the weighting factors W_{ij} of Ge-Ge, Ge-Se, and Se-Se atomic correlations for g-Ge$_{0.23}$Se$_{0.77}$ at the incident energy of 10903 eV (−200 eV from the Ge K edge) as a function of Q. Due to the dominant concentration of Se in g-Ge$_{0.23}$Se$_{0.77}$, the largest contribution is W_{SeSe} of about 65%, the second W_{GeSe} of about 30%, and the smallest W_{GeGe} of about 5%. They slightly change with Q.

As mentioned above, for analysing the local structures, one can use the difference of the scattering intensities,

$$\Delta I(Q) = \Delta \left[\left\langle f^2 \right\rangle - \left\langle f \right\rangle^2 \right] + \Delta \left[\left\langle f \right\rangle^2 \right] \Delta S(Q), \tag{8}$$

where Δ indicates the difference between energies E_1 and E_2 of the following quantity. If the energies are chosen so that mainly i element's $f(Q,E)$ changes, i.e., E_1 is relatively far (some hundred eV) from the i element's absorption edge, and E_2 very close (about 10 eV) to it, Eq. (8) is very sensitive to correlations comprising i element. $\Delta S(Q)$ is also defined as a linear combination of $S_{ij}(Q)$,

$$\Delta S(Q) = \sum_{i=1}^{2} \sum_{j=1}^{2} W_{ij}(Q,E_1,E_2) S_{ij}(Q), \tag{9}$$

where the weighting factors are

$$W_{ij}(Q,E_1,E_2) = c_i c_j \frac{\Delta \left[f_i f_j \right]}{\Delta \left[\left\langle f \right\rangle^2 \right]} . \tag{10}$$
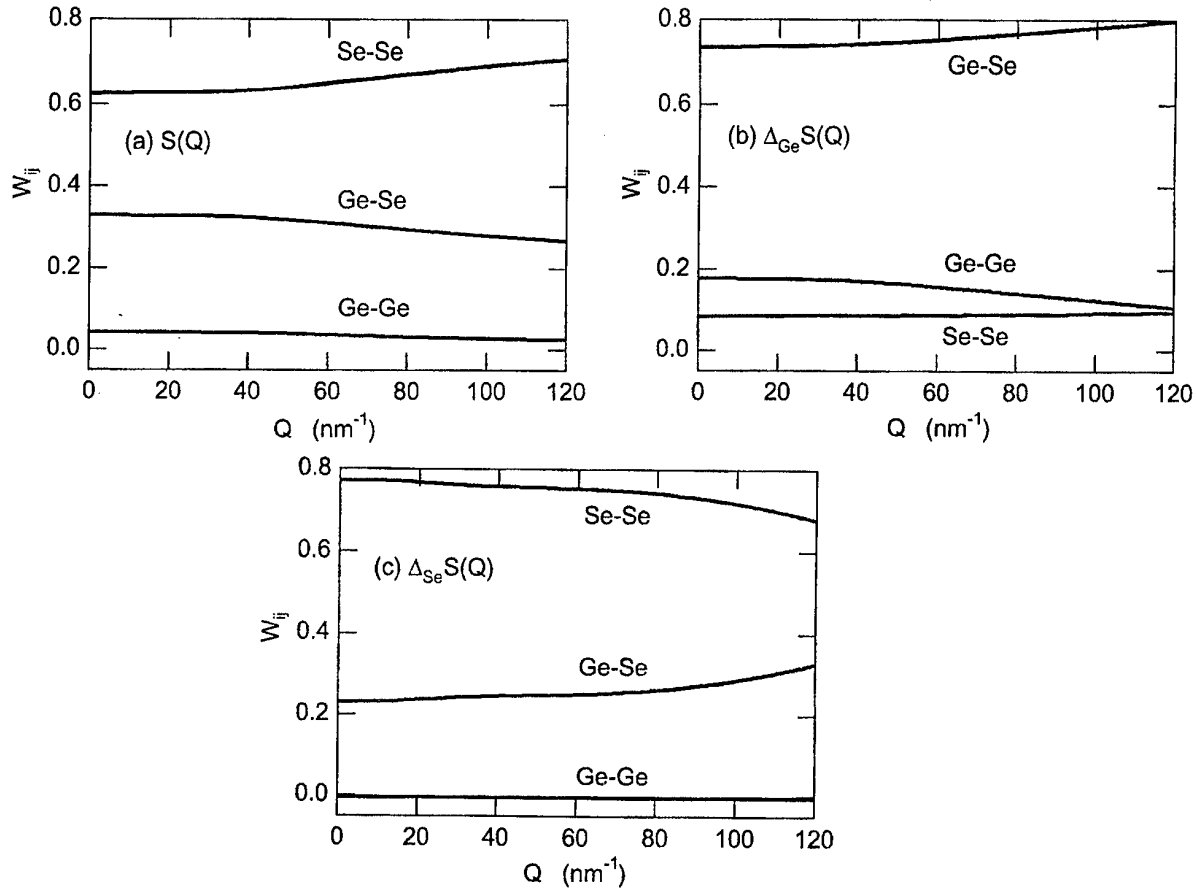
Fig. 2. W_{ij} of Ge-Ge, Ge-Se, and Se-Se atomic correlations in (a) $S(Q)$ for g-Ge$_{0.23}$Se$_{0.77}$ at the incident energy of 10903 eV (200 eV below the Ge K edge), in (b) $\Delta_{Ge}S(Q)$, and in (c) $\Delta_{Se}S(Q)$ as a function of Q.

For g-Ge$_{0.23}$Se$_{0.77}$, W_{ij}s obtained from two different energies close to the Ge and Se K edges, *i.e.*, those in $\Delta_{Ge}S(Q)$ and $\Delta_{Se}S(Q)$, in the present experiments are shown in Figs. 2(b) and 2(c), respectively. As seen in Fig. 2(b), the Se-Se correlation is highly suppressed in comparison to W_{SeSe} for $S(Q)$ shown in Fig. 2(a). However, the Ge-related weighting factors (Ge-Ge and Ge-Se) are considerably larger in $\Delta_{Ge}S(Q)$ than in $S(Q)$. On the other hand, the Ge-Ge correlation in $\Delta_{Se}S(Q)$ shown in Fig. 2(c) is negligibly small, whereas the Se-related correlations are highly enhanced. They slightly change with Q.

B. Photoemission and inverse-photoemission spectroscopies

Photoelectron or photoemission spectroscopy (PES) is well known as a technique to evaluate valence-band electron density of states (DOS) using the photoelectron effect. Fig. 3(a) shows a schematic band scheme to explain how one can obtain the occupied-state DOS by means of the PES measurement. When a light photon irradiates a material, an electron is excited with the corresponding energy of the photon, $h\nu$, when the final state is empty for excitation.

Inverse-photoemission spectroscopy (IPES) or Bremsstrahlung Isochromat spectroscopy (BIS) is a relatively new technique to investigate conduction-band DOS. The word 'inverse-' means phenomenologically inverse to the PES procedure, but the process of the IPES is not inversely. Figure 3(b) shows a schematic band scheme to explain how one can obtain the conduction-band or empty-state DOS by means of IPES measurement. When a material is irradiated by an electron with a kinetic energy of E_K, the electron enters an empty (conduction-band) state of the material with the corresponding energy. This electron can radiatively loose its energy by releasing to a conduction-band state with a lower energy level, and emits a photon with the corresponding energy $h\nu$. Hence, one can estimate the conduction-band DOS by measuring the energy and intensity of the photons coming from the surface of material.

(a) Photoemission Spectroscopy   (b) Inverse-Photoemission Spectroscopy
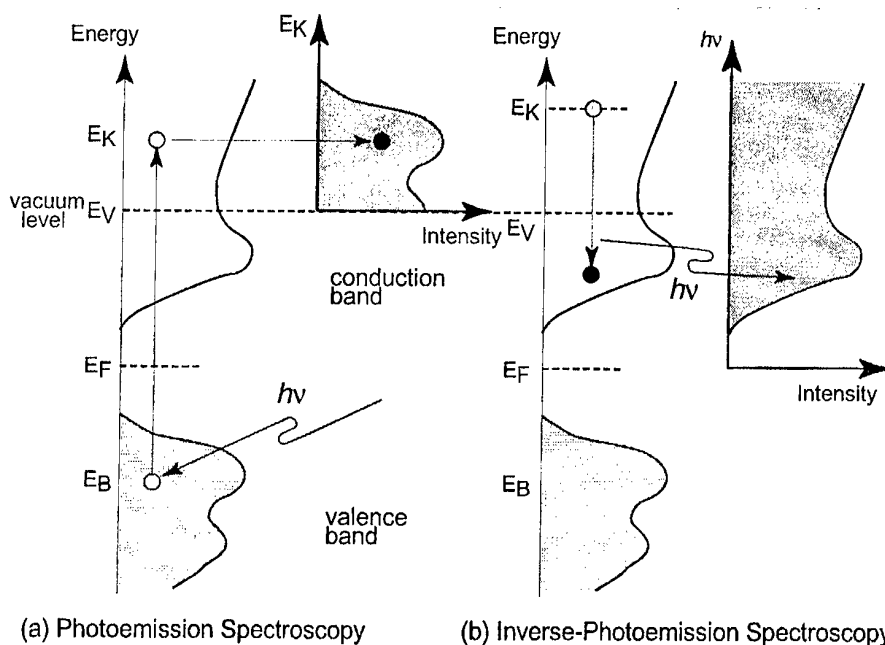
Fig. 3. Schematic band scheme to explain how one can obtain (a) valence-band and (b) conduction - band DOSs by means of the PES and IPES measurements, respectively.

Technically, the PES and IPES measurements must be performed under ultrahigh vacuum conditions of better than 10^{-9}-10^{-10} Torr (or mbar). This is because the PES and IPES processes occur near the surface of material (1-10 nm) and a contamination by oxygen *etc.* causes fatal effects to the PES and IPES spectra. The sample surface must be clean on the atomic level. Additionally, if the sample is not metallic, such as the present semiconducting Ge-Se system, an electrostatic charging of the sample must carefully be avoided in the IPES process. The injected electron can smoothly be escaped from the sample surface to the ground by preparing the nonmetallic sample with a thickness of 1-10 nm.

3. Experimental procedure

A. Anomalous x-ray scattering

The Ge_xSe_{1-x} bulk samples were prepared by quenching the melts after rocking the quartz ampoule of the mixed compound for at least 48 hours. The purity of each starting element was 99.999%. The concentration and homogeneity of the samples were examined by measuring Raman scattering spectra at several parts of the quenched samples.

The AXS measurements were carried out using an ω-2θ diffractometer installed at the beamline BM02 of the European Synchrotron Radiation Facility (ESRF) in Grenoble, France. X-rays produced by a bending magnet were monochromatized using an Si(111) double-crystal monochromator with a sagittal focusing shape, which was located between two cylindrically bent mirrors. This x-ray optics provided a small size of incident x-ray beam with 0.2 mm height and 0.5 mm width, and an energy resolution of about 1 eV. Energy was calibrated using the L_{III} absorption edge of an Au foil (11918 eV) before the experiments, and additionally *in situ* by using the Ge and Se K edges of the sample during the experiments.

The diffraction experiments were performed at two energies (−15 and −200 eV) below the K edge of each element (Ge: 11103 eV, Se: 12654 eV). In order to obtain $\Delta_i S(Q)$s, or partial structure factors $S_{ij}(Q)$, of good statistical quality, there are two requirements which need to be fulfilled: 1) A sufficient energy resolution of the detector to discriminate the elastic signal from the fluorescence and Compton contributions, and 2) a sufficient number of scattered x-ray photons in a reasonable data acquisition time. In case of the present samples near $Ge_{0.2}Se_{0.8}$ concentration, provided that 30,000 counts at the Q position of the first $S(Q)$ maximum give enough statistical quality, 600,000 counts at

the same Q position are necessary to obtain $\Delta_{Ge}S(Q)$ of identical quality. This is because the contrast in the vicinity of the Ge K absorption edge is only about 5%. At least three times more counts would even be needed to obtain $S_{ij}(Q)$s. For these reasons, we chose a pyro-graphite crystal analyzer, which provides a good Bragg reflection efficiency. The scattered x-ray photons were energy-analysed with this crystal, and counted using a photomultiplier with NaI crystal scintillators. To satisfy the first requirement mentioned above, the detector was placed on a long arm of 40 cm.

Fig. 4 shows rocking curves obtained from this detector system measured close to the Se K edge (–15 and –200 eV) at Q = 60 nm^{-1}, where the nonelastic contributions to the elastic signal are large. The energy resolution of this detector system was about 90 eV in these energy ranges. The dotted curves are ten times enlarged in comparison to the solid curves to clearly show the Se K$_\beta$ fluorescence and Compton scattering intensities. As seen in the figure, both the Se K$_\beta$ and Compton contributions can be estimated to be less than 0.3% at energies where the elastic spectra were measured (arrows in Fig. 4). Nevertheless, we measured such rocking curves for each scan at Q = 12, 22, 40, 60, and 90 nm^{-1} to estimate these contributions in order to use them for the data correction. Similar rocking curves were also obtained close to the Ge K absorption edge.
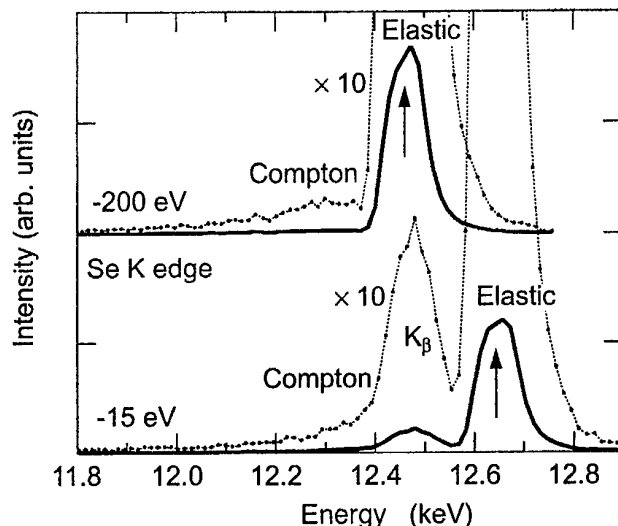
Fig. 4. Rocking curves of the detector system measured at energies close to the Se K
absorption edge at Q = 60 nm^{-1}.

The diffraction measurements were performed in steps of 0.5 nm^{-1} in the Q range from 4 nm^{-1} up to 94 and 109 nm^{-1} at energies close to the Ge and Se K edges, respectively. More than 600,000 counts at the Q position of the first $S(Q)$ maximum could be acquired at the incident energies close to the Ge edge, and 180,000-250,000 counts close to the Se K edge. The data collection durations were about 4 and 6 hours for each scan around the Ge and Se K edges, respectively. The incident beam intensity was monitored by counting the scattering signal from a thin Kapton foil in front of the sample using a photomultiplier with NaI crystal scintillators, and used for the normalization of the spectra.

B. Ultraviolet photoemission and inverse-photoemission spectroscopies

Fig. 5 shows a schematic diagram of the experimental apparatus used for recording the ultraviolet PES (UPS) and IPES spectra. It is mainly composed of four ultrahigh-vacuum chambers: two chambers for the sample preparation, an IPES analyser chamber and an UPS analyser chamber, operating under base pressures of 4.0 $\times$ 10^{-10}, 7.0 $\times$ 10^{-11}, and 4.0 $\times$ 10^{-10} Torr, respectively.
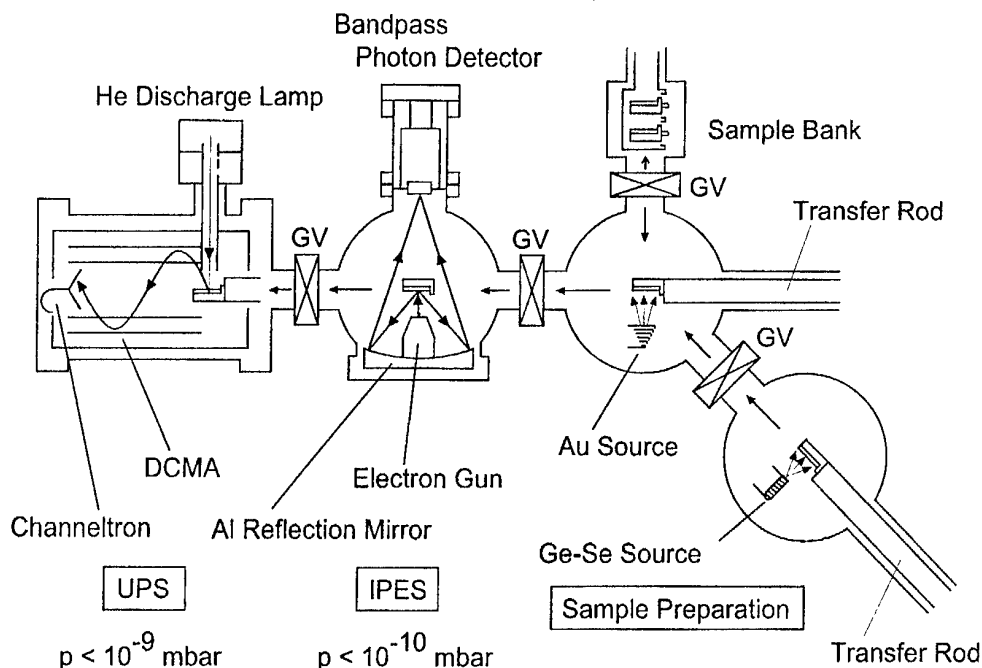
Fig. 5. Schematic diagram of the apparatus composed of the UPS and IPES spectrometers, and two sample preparation chambers. The *in situ* measurements of the UPS and IPES spectra enable us to connect the both spectra at the Fermi level.

In the IPES chamber, a monoenergic electron beam from an electron gun of Erdman-Zipf type with a BaO cathode, which can deliver a high beam current down to low kinetic energy (1-10 μA at 10 eV) with an energy spread of 0.25 eV, was focused onto the sample. Light emitted from the sample was focused by an Al reflection mirror coated with an MgF_2 film and detected using a bandpass photon detector of our own design [34]. The detector consists basically of a simple combination of a pure SrF_2 entrance window and a commercial Cu-BeO photomultiplier. Evaporation of KCl onto the first dynode of the photomultiplier improved the bandpass characteristics and the sensitivity. The full-width at half-maximum of the detector was 0.47 eV centred at 9.43 eV. The sensitivity was increased by about one order of magnitude in comparison to the original one. The overall energy resolution of the spectrometer was 0.56 eV [35].

The UPS spectrometer was composed of a He discharge lamp ($h\nu = 21.2$ eV) as an excitation light and a double-stage cylindrical-mirror analyser (DCMA) as an electron energy analyser for recording angle-integrated spectra. The energy resolution of the UPS spectrometer was set to be 0.2 eV. The energy calibrations of the IPES and UPS spectra were experimentally performed using the spectra measured for the same surface of a fresh polycrystalline Au film, and the energy scale were connected at the Fermi level.

The source alloys for the sample preparation were prepared by a standard melt quenching method using mixed alloys from commercial samples of $GeSe_2$ and Se with purity of 99.999% each, in quartz ampoules. Each g-Ge_xSe_{1-x} film sample was prepared *in situ* by evaporating the source alloy onto a fresh Au film, which was evaporated onto a metal substrate. The Au film is inactive against the sample. The evaporation was performed in one of the preparation chambers using a quartz furnace under a vacuum of about 1.5×10^{-9} Torr during the evaporation. The composition of films with a thickness of ~3 μm was carefully determined by electron-probe microanalysis. They were in all cases close to the starting composition within 2-3%.

For the UPS an IPES measurements, the thickness of films was reduced to 5-10 nm to avoid an electrostatic charging effect in the IPES measurements as mentioned in Sec II(B). After the UPS and IPES measurements, the UPS spectra for these thin films were checked to be fully consistent with those of the thick films in order to determine the concentrations. The deposition rate was controlled by means of a quartz thickness monitor placed close to the sample substrate. The typical deposition rate was 20-30 pm/sec. We also checked carefully the contamination of the samples during the measurements by observing the change of the UPS spectra repeatedly, because the typical effect of the contaminants appears in the valence-band DOS.

4. Results

Fig. 6(a) and (b) show elastic scattering intensities $\alpha I(Q,E)$ for g-$Ge_{0.23}Se_{0.77}$ at energies close to the Ge and Se K edges, respectively, as a function of Q, together with $<f>^2$. The intensities are normalized to the electron unit using the method proposed by Krogh-Moe [36] and Norman [37]. As clearly seen in the figures, distinct contrast appears with a small energy change of the incident x-rays around the absorption edges. Especially in Fig. 6(a), the intensity increases at the Q value of the first maximum around 20 nm^{-1} when the incident x-ray energy approaches to the Ge K edge, although $<f>^2$ decreases. Such an anomaly is also seen in Fig. 6(b) at the prepeak position around 10 nm^{-1} when the energy approaches to the Se K edge. The same trend is also seen in g-$Ge_{0.195}Se_{0.805}$.
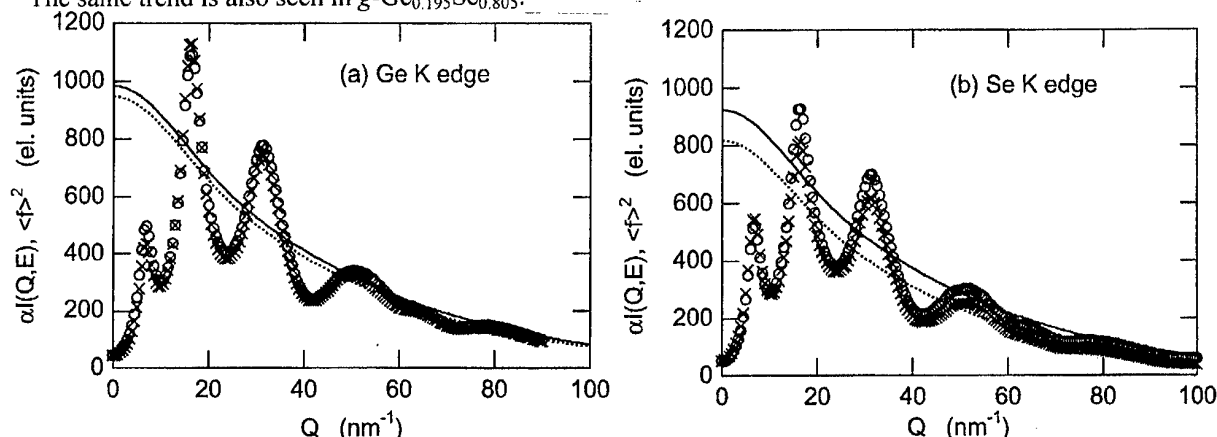
Fig. 6. Normalized elastic scattering intensities $\alpha I(Q,E)$ (marks) for g-$Ge_{0.23}Se_{0.77}$ at energies close to the (a) Ge and (b) Se K edges as a function of Q, together with $<f>^2$ (lines). Circles and solid lines indicate the values at-200eV below the absorption edge, and crosses and dashed lines at-15eV.

The $S(Q)$ spectra can be calculated by using Eq. (3). Fig. 7(a) shows the concentration dependence of $S(Q)$ measured at the incident x-ray energy of 10903 eV (200eV below the Ge K edge) at $x = 0.23$ (crosses), 0.195 (triangles), and 0.185 (circles). For clarity, the spectra are shifted against one another by 0.2. In the large Q range beyond 40 nm^{-1}, they are extremely similer. On the other hand, the magnitudes of the first and second peaks at $Q = 20.5$ and 35.2 nm^{-1}, respectively, slightly decrease with decreasing x, while their Q positions remain unchanged. The prepeaks in the $S(Q)$s are shown in Fig. 7(b) on an enlarged scale, along with the previous results at $x = 0.25$ (dashed line) and 0.167 (solid line) [15]. It can be clearly seen in the figure that a decrease in the Ge concentration x leads to a rapid decrease of the intensity of prepeak, and its position considerably shifts to higher Q values.
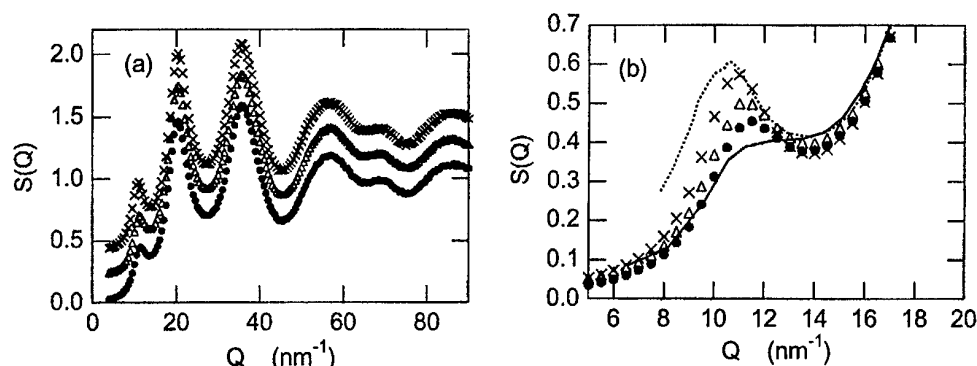
Fig. 7. (a) Concentration dependence of $S(Q)$ measured at E = 10903 eV (200 eV below the Ge K edge) and at x = 0.23 (crosses), 0.195 (triangles), and 0.185 (circles). For clarify, the spectra are shifted against one another by 0.2. (b) $S(Q)$s around the prepeak position on an enlarged scale, along with the previous results [15] at x = 0.25 (dashed line) and 0.167 (solid line).

Fig. 8 shows $\Delta_i S(Q)$s for g-$Ge_{0.195}Se_{0.805}$ close to the Ge (crosses) and Se (circles) K edges. For comparison, $S(Q)$ measured at 10903 eV is also displayed as a solid line. The shape of $\Delta_{Ge} S(Q)$ is very different from that of $S(Q)$, i.e., it has a much larger prepeak at $Q = 11$ nm^{-1} in comparison to $S(Q)$. It shows a large minimum with negative sign at the first peak position in $S(Q)$ at $Q = 20.5$ nm^{-1}. The second

peak in $S(Q)$ at $Q = 35.2$ nm^{-1} disappears in $\Delta_{Ge}S(Q)$. On the other hand, $\Delta_{Se}S(Q)$ has almost no signal at the prepeak position, while it is very similar to $S(Q)$ beyond the Q position of the first peak ($Q > 20$ nm^{-1}). Closely similar results were obtained for g-Ge$_{0.23}$Se$_{0.77}$ as seen in Fig. 9.
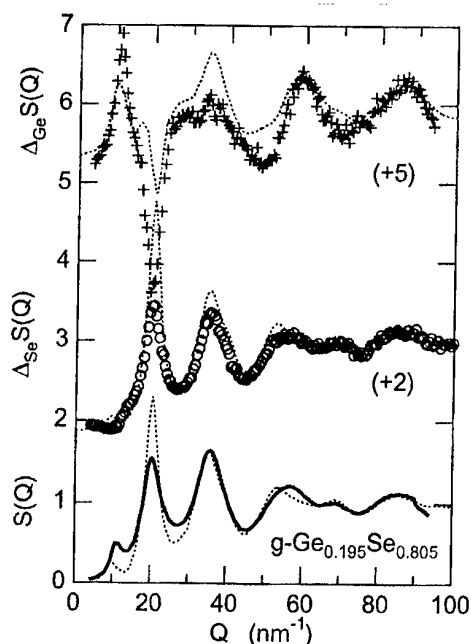
Fig. 8. $\Delta_i S(Q)$s for g-Ge$_{0.195}$Se$_{0.805}$ close to the Ge (crosses) and Se (circles) K edges together with $S(Q)$ (solid line) measured at $E = 10903$ eV (200 eV below the Ge K edge). Dotted lines indicate spectra calculated from $S_{ij}(Q)$s for g-GeSe$_2$ measured by Petri et al. [39]. See text for detail.
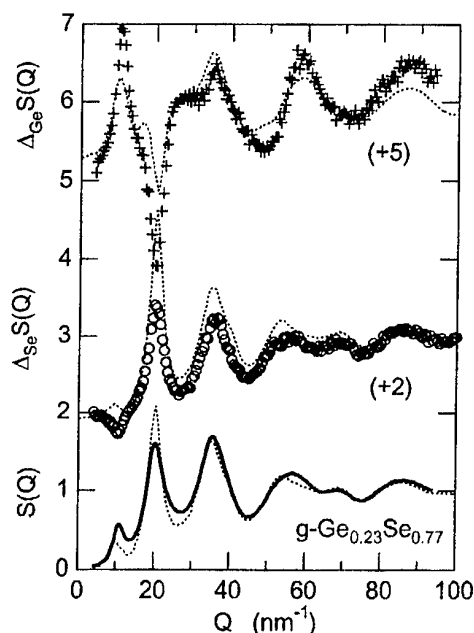
Fig. 9. $\Delta_i S(Q)$s and $S(Q)$ for g-Ge$_{0.23}$Se$_{0.77}$. Explanations are the same as in Fig. 8.

Fig. 10 shows a series of valence-band UPS and conduction-band IPES spectra on g-Ge$_x$Se$_{1-x}$ with x from 0 to 0.33. Intensities of the UPS spectra are normalized at -2.7 eV, and those of the IPES spectra at 3.1 eV ($x = 0$, 0.10, 0.15, and 0.18) and 2.4 eV ($x = 0.20$, 0.25, and 0.33). Vertical bars indicate the positions of the peaks. Energies are referred to the Fermi level.
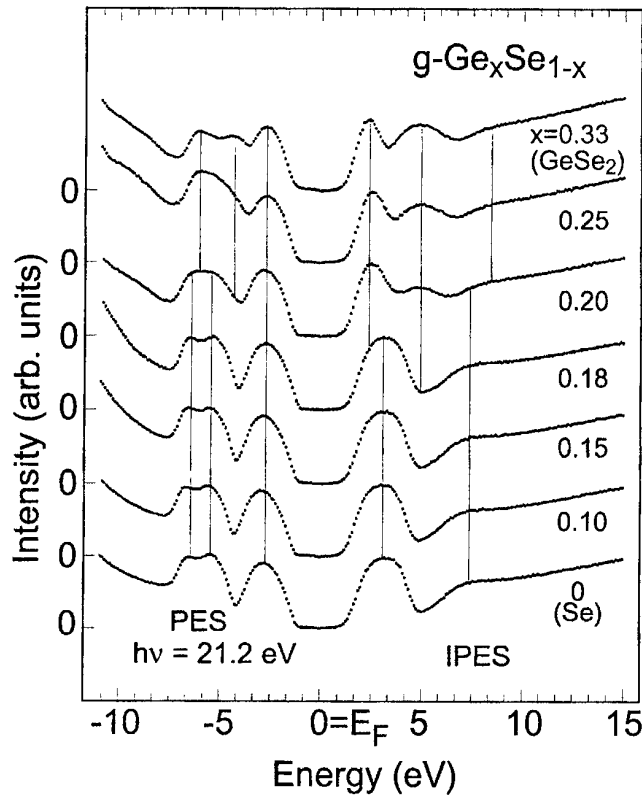
Fig. 10. A series of valence-band UPS and conduction-band IPES spectra on g-Ge_xSe_{1-x} with x from 0 to 0.33. Intensities of the UPS spectra are normalized at –2.7 eV, and those of the IPES spectra at 3.1 eV (x = 0, 0.10, 0.15, and 0.18) and 2.4 eV (x = 0.20, 0.25, and 0.33). Vertical bars indicate the positions of the peaks. Energies are referred to the Fermi level.

The UPS spectra for g-Se (x = 0) show distinct structures at –2.7, –5.4, and –6.4 eV, which are in good agreement with previous data [20] although in this case the samples were much thicker. The IPES spectra have also clear structures at 3.1 and 7.4 eV in good agreement with our previous measurements [23]. With increasing the Ge concentration from x = 0 to 0.18, the UPS and IPES spectra do not show any noticeable change in the spectral shape and the energy positions of peaks. With a further increase of the Ge concentration x by only 2%, however, the IPES spectra drastically change to another shape with mainly three peaks; a sharp peak at 2.4 eV, a relatively broad peak at 4.9 eV, and a highly damped peak at 8.4 eV. In addition in the UPS spectrum at x = 0.20, a slight blurring of the peaks at –6.4 and –5.4 eV occurs, and at the same time new peaks around –6.0 and –4.3 eV can be recognized. For the further increase of x, features of the UPS and IPES spectra reach those of g-$GeSe_2$. The UPS spectrum for g-$GeSe_2$ is in good agreement with previous data [17,18,19], and the IPES spectrum coincides well with our previous measurement [38].

5. Discussion

As mentioned before, it can be seen in Fig. 7(b) that a decrease of the Ge concentration x leads to a rapid decrease of the prepeak intensity in $S(Q)$, and its position considerable shifts to higher Q values. Fig. 11 shows the Q position of the prepeak, Q_p, and the intensity, $S(Q_p)$, as a function of x. Since the $S(Q)$ at x = 0.167 shows no longer a peak but a shoulder in the range of interest, a two-Gaussian fit was applied to obtain the Q_p and $S(Q_p)$. With decreasing x from x = 0.25 to 0.195, Q_p increases linearly. With the further decrease of x, Q_p increases much more rapidly (or shows a jump) between x = 0.195 and 0.185. At the same time, there is a noticable decrease of $S(Q_p)$ in this concentration range. For the further discussion of the prepeak or the IRO in this concentration range, it is essential to clarify the origin of the prepeak.
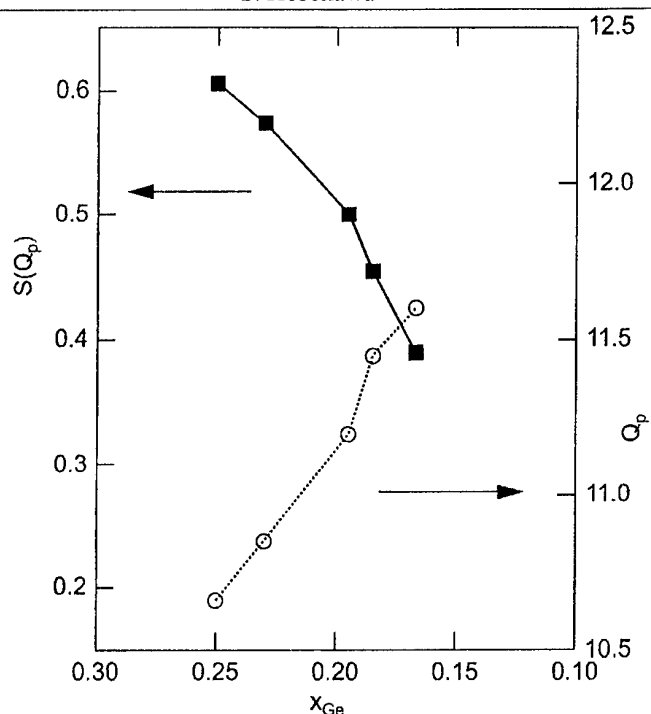
Fig. 11. The Q position of the prepeak, Q_p, and the intensity, $S(Q_p)$, as a function of the Ge concentration x.

It can be seen at a glance from Figs. 8 and 9 that the height of the prepeak is much larger in $\Delta_{Ge}S(Q)$ than in $S(Q)$, whereas there is no characteristic feature seen in $\Delta_{Se}S(Q)$. As already pointed out in Sec III (see Fig. 2), the Ge-related W_{ij}s in $\Delta_{Ge}S(Q)$ are much larger than those in $S(Q)$, while W_{GeGe} in $\Delta_{Se}S(Q)$ is negligibly small. Thus it appears highly plausible to speculate that the prepeak originates from the Ge-Ge correlation in g-Ge_xSe_{1-x} in the concentration range near $x = 0.20$.

The same conclusion was recently reached by Petri et al. [39] for g-$GeSe_2$ from an analysis of neutron scattering experiments with isotope enriched samples. They observed a prepeak in the experimentally determined $S_{GeGe}(Q)$, which has almost the same height as of the first peak. On the other hand, almost no characteristic features were visible in $S_{GeSe}(Q)$ and $S_{SeSe}(Q)$ at the prepeak position. In addition, they observed a large minimum in $S_{GeSe}(Q)$ with negative sign at the first peak position in $S(Q)$.

For comparison, we calculated "modeled" spectra from the $S_{ij}(Q)$ data of Petri et al. [39] employing the W_{ij}s for g-$Ge_{0.195}Se_{0.805}$ and $Ge_{0.23}Se_{0.77}$. The dotted lines in Figs. 8 and 9 indicate the calculated spectra for g-$Ge_{0.195}Se_{0.805}$ and $Ge_{0.23}Se_{0.77}$, respectively. Surprisingly, the obtained spectra show features similar to our experimental $\Delta_iS(Q)$ and $S(Q)$ data. However, quantitatively there are large deviations from our experimental data in the Q ranges of the prepeak and the first peak. The height of the prepeak in each of our $\Delta_{Ge}S(Q)$ spectrum is much larger than that in the "model" spectrum (see dotted line). The same is also true for $S(Q)$. This is consistent with the speculation that the prepeak in $S_{GeGe}(Q)$ in this concentration region is much larger in height than that for $GeSe_2$.

For obtaining the local structural information (not only for confirming the above speculation) requested in this concentration range, it is, needless to say, crucial to directly obtain $S_{ij}(Q)$s from our AXS data. As seen in Figs 8 and 9, however, the obtained $\Delta_iS(Q)$s slightly lean to the left, although the $S(Q)$ data do not. Such slight slopes unfortunately produce a considerable error in $S_{ij}(Q)$s. This trend was also found in the previous AXS results by Armand et al. [15]. It prevents us from reaching the final goal of structural studies using the AXS technique. It can be pointed out that f' and/or f'' seem to have small Q-dependencies.

For this reason, the analysis of the prepeak was performed under a very rough assumption that near the prepeak position the Se related $S_{ij}(Q)$s, i.e., $S_{GeSe}(Q)$ and $S_{SeSe}(Q)$, in our concentration range are identical to those of g-$GeSe_2$ obtained by Petri et al. [39], and that only $S_{GeGe}(Q)$ can vary with x. The analysis was carried out using the $S(Q)$ data at $x = 0.185$, 0.195, and 0.23. Fig. 12 shows the estimated $S_{GeGe}(Q)$s (solid lines) near the prepeak position along with that of g-$GeSe_2$ (dashed line) obtained by Petri et al. [39]. As mentioned above, the prepeaks at $x = 0.23$ and 0.195 (almost the same

as each other) are more than twice larger in height than that at x = 0.333. One can also see a rapid decrease of the prepeak height at x = 0.185 by only 1% further decrease of x. Based on these structural results on the prepeak or the IRO around the stiffness threshold composition, a further discussion is given later in combination with the results of the electronic structures.
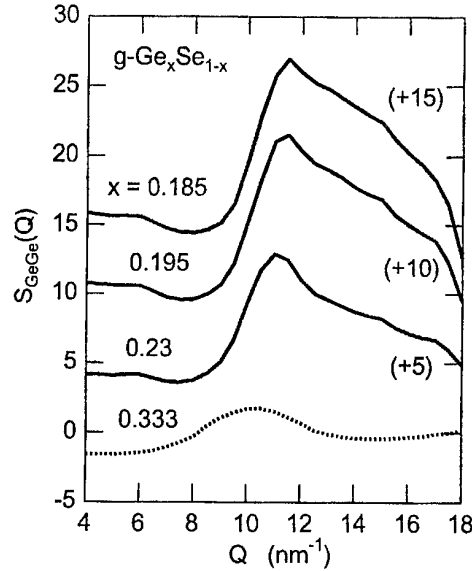
Fig. 12. Estimated $S_{GeGe}(Q)$s (solid lines) near the prepeak position along with that of g-GeSe$_2$ (dashed line) obtained by Petri *et al.* [39]. See text for details.

In Figs. 8 and 9, the heights of the first peaks in our $A_{Se}S(Q)$ and $S(Q)$ spectra are much smaller than that of the calculated spectra (dotted lines), and the dips found in $A_{Ge}S(Q)$ of the present work are much deeper. Since $S_{GeSe}(Q)$ dominates $A_{Ge}S(Q)$, and the heights of the first peaks in $A_{Se}S(Q)$ and $S(Q)$ are determined by compensating a large maximum in $S_{SeSe}(Q)$ for a large minimum in $S_{GeSe}(Q)$, one expects that $S_{GeSe}(Q)$s for x = 0.195 and 0.23 have much deeper minima at the first peak position than that for g-GeSe$_2$. Although $A_iS(Q)$s could only be measured along limited Q ranges, it is instructive to perform Fourier transformations to obtain differential pair distribution functions $A_ig(r)$ in order to examine the SRO around each constituent element. Fig. 13(a) and (b) show $A_ig(r)$s of g-Ge$_{0.195}$Se$_{0.805}$ and Ge$_{0.23}$Se$_{0.77}$, respectively. Dashed and solid lines indicate $A_ig(r)$s near the Ge and Se K edges, respectively. The first nearest neighbour distances around both Ge and Se are found to be 0.236 ± 0.002 nm in each concentration, which coincides with the previous scattering- [4,13,14] and XAFS [10-12] results within the experimental error.
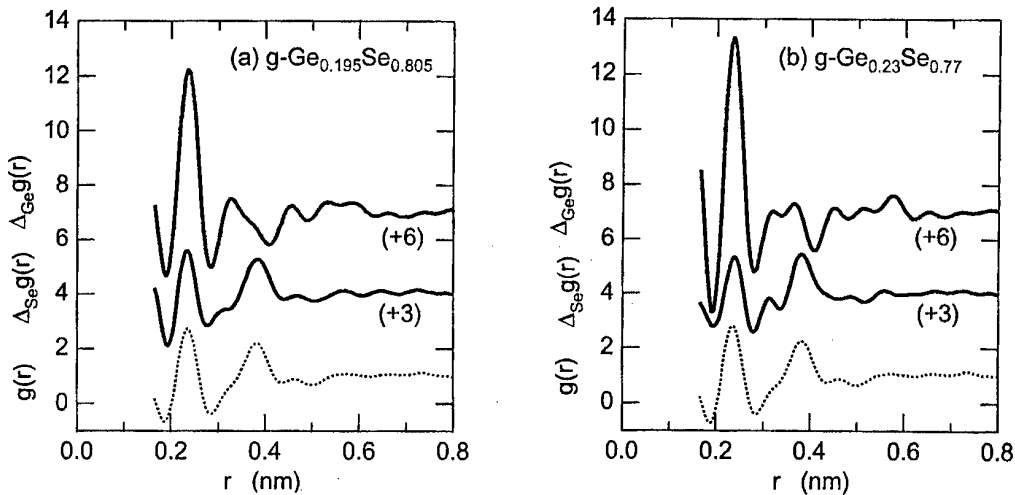
Fig. 13. $A_ig(r)$s of (a) g-Ge$_{0.195}$Se$_{0.805}$ and (b) Ge$_{0.23}$Se$_{0.77}$ together with $g(r)$. Solid lines indicate $A_ig(r)$s, and dashed lines $g(r)$s.

This result supports the model that the glasses in this concentration range have an SRO similar to the GeSe$_2$ crystal. As mentioned in the last section (see Fig. 10), the spectral shapes of both the valence-band UPS and the conduction-band IPES spectra remarkably change around the stiffness threshold composition $x = 0.20$ from g-GeSe$_2$-like to g-Se-like. They have characteristic peaks of their own in the spectra.

The character of peaks in the UPS spectra can be assigned using PES data with different energies of incident light, because the excitation cross-section is depend on the quantum number of the orbital angular momentum. The peak positions of the UPS spectra and their electronic states for g-GeSe$_2$ and g-Se are tabulated in Table 2. In g-GeSe$_2$, the top of the valence bands at -2.7 eV is formed by a lone-pair (LP) band of the Se 4p states. It is followed by two Ge 4p–Se 4p bonding (σ) states at -4.3 and -6.0 eV. When using a higher energy of incident light, one can also observe a Ge 4s–Se 4p bonding (σ) band around -9 eV and an Se 4s state around -14 eV [19]. In g-Se, the top of the valence bands is also formed by the Se LP state at -2.7 eV. Beneath it, two Se 4p bonding (σ) states are located at -5.4 and -6.4 eV. The Se 4s states are located around $-12\sim-15$ eV [20].

Table 2. Energy positions of peak structures in the UPS and IPES spectra on g-GeSe$_2$ and g- Se. These peaks are assigned to electronic states contributed predominantly.

	Energy (eV)	Electronic states
g-GeSe$_2$	-6.0	⎫
		⎬ σ [Ge sp^3 (4p-rich) – Se 4p]
	-5.4	⎭
	-2.7	lone pair [Se 4p]
	2.4	σ^* [Ge sp^3 (4s-rich) – Se 4p]
	4.9	σ^* [Ge sp^3 (4p-rich) – Se 4p]
	8.4	Ge 4d and/or 5s, Se 4d and/or 5s
g-Se	-6.4	⎫
		⎬ σ [Se 4p]
	-5.4	⎭
	-2.7	lone pair [Se 4p]
	3.1	σ^* [Se 4p]
	7.4	Se 4d and/or 5s

The electronic state assignment can also be carried out for peaks in IPES spectra by comparing them with core-absorption spectra, which are affected by the selection rule of excitations from the core-level (s, p, or d) to the conduction band. The peak positions of the IPES spectra and their electronic character for g-GeSe$_2$ and g-Se are also tabulated in Table 2. In g-GeSe$_2$ [38], the bottom of conduction bands at 2.4 eV is formed by an antibonding (σ^*) band with the Ge sp^3 (4s-rich) – Se 4p hybridized states. It is followed by an antibonding (σ^*) band with the Ge sp^3 (4p-rich) – Se 4p hybridized states at 4.9 eV, and the 4d and /or 5s states of both Ge and Se at 8.4 eV. In g-Se [23], the bottom of the conduction bands at 3.1 eV is formed by an antibonding (σ^*) band with the Se 4p states. It is followed by the Se 4d and /or 5s states at 7.4 eV.

Noteworthy questions are why the electronic structure of g-Ge$_x$Se$_{1-x}$ does not vary gradually from g-GeSe$_2$-like to g-Se-like with x, but shows a sudden (transition-like) change around the stiffness threshold composition $x = 0.20$, and why the prepeak in $S_{GeGe}(Q)$ or the IRO of the Ge-Ge correlation enhances at this composition. In order to solve these questions, it seems worthwhile to recall an old idea by Feltz $et\ al.$ [40]. They examined the concentration dependence of several physical properties of g-Ge$_x$Se$_{1-x}$, such as dielectric constant, molar volume, glass transition temperature, and thermal expansion coefficient. As a result, they came to the conclusion that GeSe$_4$ ($x = 0.20$) is a new non-

crystalline compound which exists in the liquid or glassy state, and there, $Ge(Se_{1/2})_4$ units should be predominantly linked by Se-Se bridges.

Based on this concept, one can try to explain our experimental results. At $x = 0.33$, $Ge(Se_{1/2})_4$ tetrahedra are linked to each other by their edge- or corner-sharing, $i.e.$, the Ge-Ge correlation is always $(Se_{1/2})_3Ge-Se-Ge(Se_{1/2})_3$. With decreasing x from 0.33 to 0.20, successive structural changes occur from the direct connection at $x = 0.33$ to two-Se-linked tetrahedra at $x = 0.20$, $i.e.$, $(Se_{1/2})_3Ge-Se-Se-Ge(Se_{1/2})_3$ all over the material. The Ge-Ge correlation in g-$Ge_{0.20}Se_{0.80}$ still exists by forming these connections because the correlation-length of this new connection is well defined. The correlation is even stronger than in g-$GeSe_2$ due to the relaxed formation of the connections. The gradual movements of the prepeak would be caused by these reconnections of the $Ge(Se_{1/2})_4$ tetrahedra. With further decrease of x, the tetrahedra become isolated and are connected by short chains, $i.e.$, $(Se_{1/2})_3Ge-Se-Se-Se-Ge(Se_{1/2})_3$ as the shortest case. Due to the flexible conformation of this connection, the Ge-Ge correlation length of this connection is no longer well defined, and the prepeak starts to disappear with x. It seems to be much more difficult to explain the concentration change of the electronic structure using this simple atomic structure model. This is because this requires the additional constraints that the electronic structure of the $(Se_{1/2})_3Ge-Se-Se-Ge(Se_{1/2})_3$ conformation at $x = 0.20$ should be very similar to that of $(Se_{1/2})_3Ge-Se-Ge(Se_{1/2})_3$ in g-$GeSe_2$, and that of $(Se_{1/2})_3Ge-Se-Se-Se-Ge(Se_{1/2})_3$ at $x < 0.20$ should be identical to that of Se chains. Molecular orbital band calculation would be useful to estimate the energy positions of the corresponding bonding-, lone-pair-, and antibonding states in the above small fragments. For this, however, precise structural determinations for several concentrations near the stiffness threshold composition, $i.e.$, the information of $S_{ij}(Q)$s, is essential. Further AXS investigations are now in progress.

6. Conclusion

Anomalous x-ray scattering experiments on glassy Ge_xSe_{1-x} were carried out at energies close to the Ge and Se K edges at both the onset and completion concentrations of the rigidity percolation threshold. The total structure factors $S(Q)$ show rapid changes in both the position and intensity of the prepeak around 10 nm^{-1}, while remain almost unchanged in the other Q ranges. The differential structure factors $\Delta_i S(Q)$ obtained have characteristic features of their own, which suggest that the prepeak originates from only the Ge-Ge concentration. The origin of the prepeak was discussed in the sight of the concentration dependence of the spectra and a comparison with the partial structure factors on glassy $GeSe_2$ obtained by Petri $et\ al.$ [39].

Valence- and conduction-band electronic density of states were investigated on glassy Ge_xSe_{1-x} ($0 \leq x \leq 0.33$) by measuring ultraviolet photoemission and inverse-photoemission spectra. They exhibit a distinct change in their spectral features near $x = 0.20$.

These observations in both the atomic and electronic structures are consistent with an occurrence of percolation threshold in non-crystalline covalent network systems predicted by Phillips and Thorpe. The threshold is characterized by the percolation of a specific $Ge(Se_{1/2})_4$ molecular unit spread over the network.

References

[1] W. H. Zachariasen, J. Am. Chem. Soc. **54**, 3841 (1932).

[2] R. W. Fawcett, C. N. J. Wagner, G. S. Cargill III, J. Non-Cryst. Solids **8-10**, 369 (1972).

[3] O. Uemura, Y. Sagara, T. Satow, Phys. Stat. Sol. (a) **26**, 99 (1974).

[4] T. Satow, O. Uemura, Y. Sagara, J. Jpn. Inst. Met. **37**, 1348 (1973) (in Japanese).

[5] P. Tronc, M. Bensoussan, A. Brenac, C. Sebenne, Phys. Rev. B **8**, 5947 (1973).

[6] J. C. Phillips, J. Non-Cryst. Solids **34**, 153 (1979).

[7] M. F. Thorpe, J. Non-Cryst. Solids **57**, 355 (1983).

[8] W. A. Katamigahara, R. L. Cappelletti, P. Boolchand, B. Halfpap, F. Gompf, D. A. Neumann, H. Mutka, Phys. Rev. B **44**, 94 (1991).

[9] X. Feng, W. J. Bresser, P. Boolchand, Phys. Rev. Lett. **78**, 4422 (1997).

[10] C. Peyroutou, S. Peytavin, M. Ribes, J. Solid State Chem. **82**, 78 (1989).

[11] W. Zhou, M. Paesler, D. E. Sayers, Phys. Rev. B **43**, 2315 (1991).

[12] E. Gulbrandsen, H. B. Johnsen, M. Endregaard, T. Grande, S. Stølen, J. Solid State Chem. **145**, 253 (1999).

[13] J. C. Malaurent, J. Dixmier, J. Non-Cryst. Solids **35&36**, 1227 (1980).

[14] N. R. Rao, P. S. R. Krishna, S. Basu, B. A. Dasannacharya, K. S. Sangunni, E. S. R. Gopal, J. Non-Cryst. Solids **240**, 221 (1998).

[15] P. Armand, A. Ibanez, Q. Ma, D. Raoux, E. Philippot, J. Non-Cryst. Solids **167**, 37 (1993).

[16] S. Hosokawa, Y.Wang, J.-F. Bérar, J. Greif, W.-C. Pilgrim, D. Raoux, K. Murase, Phys. Chem. Chem. Phys, to be submitted.

[17] S. Hino, T. Takahashi, Y. Harada, Solid State Commun. **35**, 379 (1980).

[18] T. Ueno, A. Odajima, Jpn. J. Appl. Phys. **21**, 1382 (1982).

[19] K. Inoue, T. Katayama, K. Kawamoto, and K. Murase, Phys. Rev. B **35**, 7496 (1987).

[20] N. J. Shevchik, M. Cardona, J. Tejeda, Phys Rev. B **8**, 2833 (1973).

[21] D. E. Aspnes, J. C. Philipps, K. L. Tai, P. M. Bridenbaugh, Phys. Rev. B **23**, 816 (1981).

[22] J. Stuke, J. Non-Cryst. Solids **4**, 1 (1970).

[23] S. Hosokawa, Y. Hari, K. Nishihara, M. Tamura, M. Taniguchi, J. Non-Cryst. Solids **164-166**, 1199 (1993)..

[24] S. Hosokawa, H. Sato, K. Nishihara, Y. Hari, M. Taniguchi, J. Non-Cryst. Solids **250-252**, 415 (1999).

[25] J. Bordas, J. B. West, Philos. Mag. **34**, 501 (1976).

[26] E. Belin, C. C. Sememaud, S. Guita, Philos. Mag. B **63**, 1159 (1991).

[27] S. Hosokawa, T. Kouchi, I. Ono, M. Taniguchi, Y. Takata, N. Kosugi, J. Phys.: Condens. Matter **8**, 1607 (1996).

[28] M. Taniguchi, T. Kouchi, I. Ono, S. Hosokawa, M. Nakatake, H. Namatame, K. Murase, J. Electron Spectrosc. Relat. Phenom. **78**, 507 (1996).

[29] S. Sasaki, KEK Report 1989 (Nat. Lab. High Energy Phys., Tsukuba, Japan), p. 1.

[30] T. Kawamura, T. Fukamachi, Jpn. J. Appl. Phys. Suppl. **17-2**, 228 (1978); T. Fukamachi, S. Hosoya, T. Kawamura, M. Okunuki, Acta Cryst. A **35**, 104 (1979).

[31] P. H. Fuoss, W. K. Warburton, A. Bienenstock, J. Non-Cryst. Solids **35&36**, 1233 (1980).

[32] U. Bonse, I. Hartmann-Lotsch, H. Lotsch, K. Olthoff-Mienter, Z. Phys. B **47**, 297 (1982).

[33] C. H. MacGillavry, G. D. Rieck (ed.), International Tables for X-ray Crystallographie, 2nd ed., (Kynoch, Birmingham, 1968), Vol. III.

[34] K. Yokoyama, K. Nishihara, K. Mimura, Y. Hari, M. Taniguchi, Y. Ueda, M. Fujisawa, Rev. Sci. Instrum. **64**, 87 (1993).

[35] Y. Ueda, K. Nishihara, K. Mimura, Y. Hari, M. Taniguchi, M. Fujisawa, Nucl. Instrum. Methods A **330**, 140 (1993).

[36] J. Krogh-Moe, Acta Cryst. **9**, 951 (1956).

[37] N. Norman, Acta Cryst. **10**, 370 (1957).

[38] S. Hosokawa, K. Nishihara, Y. Hari, M. Taniguchi, O. Matsuda, K. Murase, Phys. Rev. B **47**, 15509 (1993).

[39] I. Petri, P. S. Salmon, H. E. Fischer, Phys. Rev. Lett. **84**, 2413 (2000).

[40] A. Feltz, H. Aust, A. Blayer, J. Non-Cryst. Solids **55**, 179 (1983

PHYSICAL PROPERTIES OF DOPED CHALCOGENIDE GLASSY SEMICONDUCTORS WHICH ARE GOVERNED BY THE INTERACTION OF NEGATIVE-U DEFECTS AND IMPURITY STATES.

K. D. Tsendin

A. F. Ioffe Physico-Technical Institute, 194021 St.Petersburg, Russia

It is shown that negative-U centres in doped chalcogenide glasses control the electrical properties of the materials. Possible superconductivity is discussed theoretically.

1. Introduction

Previous investigations have been revealed that electrical and optical properties of doped chalcogenide glassy semiconductors (CGS) may be interpreted in the frame of model which considers a doped CGS as a medium consists of small clusters which are constructed from atoms with a first coordination mean number z more than this one (z_0) in the low-coordinated CGS [1-3]. In As_2Se_3 films doped with Bi and prepared by thermal sputtering technique the clusters have been observed in optical microscope. They have Bi_2Se_3 composition and size L which is equal or less than 100 nm [3]. In As_2Se_3 films prepared and doped with Ni by modification technique the clusters have not been observed by direct methods but all electrical and optical data evidenced that its L is equal or less than 5 nm. The real composition of clusters in this case is unknown. The clusters of the same size $L \approx 5$ nm in synthesized samples of Ge-(S, Se) systems doped with Bi have been observed in electronic microscope [4].

According to the paper [1] the appearance of clusters with $z > z_0$ very important for effective doping process. It is known that CGS have soft, labile atomic structure with a great number lone-pair (LP) electrons of chalcogenide atoms, which do not take part in a net of CGS covalent bonds. These facts together with a disorder provide a fulfillment of famous 8-N rule and inefficiency of CGS doping. More rigid atomic structure of clusters prevents a fulfillment of 8-N rule and allows to exist donor- and acceptor-like electronic impurity states inside the clusters. Then "official" doping elements (Bi and Ni in our cases) together with CGS atoms (As and Se) play role of the main constituent atoms of clusters. Therefore the real chemical nature of donor- or acceptor-like electronic impurity states must be determined in each individual case and may not coincides with the "official" doping elements.

This approach allows us to consider these doped CGS as nanostructured chalcogenides in which an efficiency of doping process depends on appearance of nano-clusters.

The second result of doping treatment is creation of intrinsic defects of CGS (negative-U centers). Experimental facts have evidenced, that concentrations of intrinsic defects D and electronic impurity states N are very close to each other [2,3,5]. This phenomenon may be considered as self-compensation process. Then one can see that a strong interaction of negative-U centers and impurity centers takes place. This interaction has both statistical (or thermodynamically) and direct quantum-mechanical character. The main result of the statistical interaction is so-called self-compensation processes, which happen in time of doping treatment. Due to self-compensation processes a concentration of negative-U centers D is approximately equal to concentration of electrically active impurity centers N. The direct quantum-mechanical interaction has a result in a correlation between energies of negative-U centers and impurity states.

The first part of the present paper is devoted to consideration of physical properties of doped chalcogenide glassy semiconductors which are governed by different relationship between D and N ($D \geq N$ or $N \geq D$).

First of all it will be discussed how relationship between D and N manifests in theoretical temperature dependence of direct current conductivity. Then we will discuss the experimental temperature dependence of direct current conductivity in CGS doped with transitional metals and temperature dependence of drift mobility in CGS doped with halogens.

The last part of the paper concerns with the case when concentration of negative-U centers is enough to create band-like states. Possible superconductivity of this system is considered theoretically. The experimental data on mixture of doped selenium with micro-crystalline particles of high temperature superconductors is discussed.

2. The self-compensation processes

2.1 Direct current measurement data

In the our paper [5] a compensation coefficient $k = D/N$ has been estimated for As_2Se_3 doped with Ni using direct current measurement data. We were surprised by values of k which were very close to unity: $1-k=10^{-5}-10^{-3}$. The similar results may be obtained for As_2Se_3 doped with Bi from data [3]: $1-k=10^{-2}-10^{-1}$. From our point of view this means that there is a strong correlation between localization of impurity and defect states.
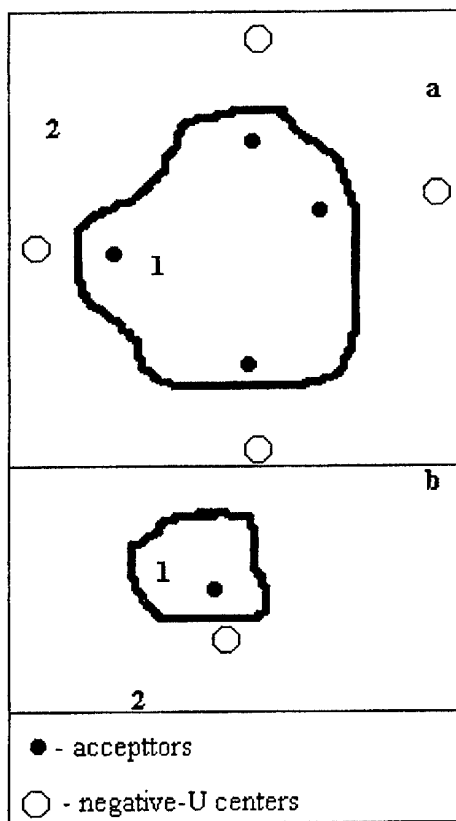
Fig. 1. Schematically representation of doped As_2Se_3 with Bi (a) and Ni (b) in the microgeterogenity doping model [1]. Area 1 – Bi_2Se_3 on figure (a) and area enriched with Ni on figure (b). Area 2 - As_2Se_3 with a little amount of doped impurities.

For example one can imagines the correlated situation which is depicted in the Fig 1. The cases 1a and 1b schematically present the $As_2Se_3(Bi)$ and $As_2Se_3(Ni)$ correspondingly. In the first case

L is great enough to allow appearance several acceptors inside the clusters. According to [3] energy level of acceptor E_a, which exists in Bi_2Se_3 clusters is approximately equal 0.25 eV. Then radius of electronic state "a" equals ~ 5-10 A for effective mass $m^*=(1-0.25)m$. We do not know the real microscopic reason of simultaneously appearance of impurity and defect states but one can suppose that vacancy of Se or extra Se atom in Bi_2Se_3 clusters may be introduced from CGS matrix. The process of atoms exchanging may be more effective in the nearest vicinity of nano-cluster boundary. In the $As_2Se_3(Ni)$ case, if we suppose, that "a" equals ~ 5-10 A also, then approximately only one electronic impurity state may be put into the cluster.

Data for $As_2Se_3(Bi)$ have evidenced that fresh films correspond to case $N \approx D$. For this case according the paper [6] direct current conductivity may be written as

$$\sigma = \sigma_0 exp(-(\varepsilon_1 + \varepsilon_2 + E_a)/3kT) \tag{1}$$

where ε_1 and ε_2 are ionization energies of first and second holes from negative-U center. The formulae (1) means that Fermi energy (E_F) lies at the $(\varepsilon_1 + \varepsilon_2 + E_a)/3$ distance from valence band edge E_v. This value is a mean energy of thermal ionization of each of three holes involved in the processes, which have determined the E_F position. After thermal annealing of $As_2Se_3(Bi)$ films temperature dependence of conductivity became

$$\sigma = \sigma_0 exp(-E_a/kT) \tag{2}$$

which takes place for N>D case.
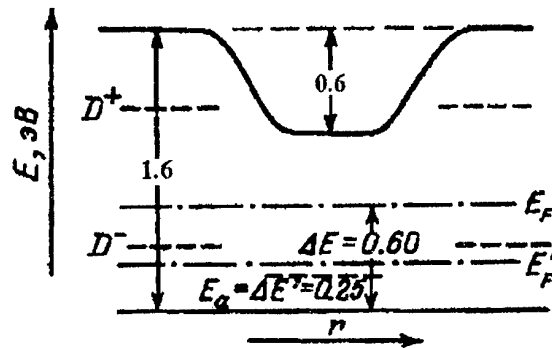
Fig. 2. Energy band diagram of $As_2Se_3Bi_{0.1}$ near Bi_2Se_3 cluster. All energies in eV. E_F and E_F' are Fermi energies before and after annealing.

For the estimations we take the case of $As_2Se_3(Bi)_{0.1}$ [3]. Energy of optical gap E_g and energy activation of conductivity ΔE in glassy Bi_2Se_3 films is equal to 1.0 eV and 0.25 eV correspondingly. The latter coincides with energy activation of conductivity for thermal annealed films. This is the reason, why we consider, that E_F in the both cases coincides with $E_a=0.25$ eV, put this value in the (2) and reconstruct the band energy diagram depicted on Fig. 2. Before annealing the energy activation of conductivity is equal to 0.6 eV, i.e. initial position of Fermi level (E_F) is situated as it is shown in Fig. 2. Then one can obtain from relation $0.6 = (\varepsilon_1 + \varepsilon_2 + 0.25)/3$ that mean energy ionization of negative-U centers per one hole $\varepsilon = (\varepsilon_1 + \varepsilon_2)/2 = 0.78$ eV. This value is very close to half of the energy of optical gap $E_g/2=0.80$ eV measured for $As_2Se_3(Bi)_{0.1}$ and so one can conclude that negative-U centers belong to matrix outside the clusters. In the paper [3] it has been shown that at the annealing temperature 130 C the changing of acceptor concentration N occurs in $a-Bi_2Se_3$ films. So far as at the same annealing temperature the changing from dependence (1) to dependence (2) occurs, we consider that changing of acceptor concentration N is the reason of this. Thus the present estimation corroborates the model depicted on Fig. 1a. One has not any correlation between the position of acceptor level E_a and ionization energies of negative-U centers and it may be concluded that space distance between impurity and negative-U centers is more than several tens of angstrom and overlapping between its wave functions is absent.

Another situation takes place for $As_2Se_3(Ni)$ films. Detail analysis, which has been undertaken, in the papers [7,8] shows, that different temperature dependencies of σ, obtained by different groups of scientists, for approximately the same doping level, correspond to N>D (results of papers [9,10]) and to N<D (results of paper [11]) cases. Comparison of these two sets of experimental results has allowed us to determine the position of the acceptor level E_a and ionization energies of negative-U centers. A strong correlation has been revealed, namely $\varepsilon = (\varepsilon_1 + \varepsilon_2)/2 = E_a$ for all doping level. Then it may be concluded that space distance between impurity and negative-U centers is close to sum of its radii, which may be estimated as 15-25 angstrom and there is overlapping between its wave functions, which is the reason for correlation of positions of acceptor level E_a and mean ionization energy of negative-U centers. This conclusion agrees with L value for $As_2Se_3(Ni)$ case, because one can not separate acceptor more far from nanocluster boundary than radii of nanocluster.

2.2 Drift mobility data

The method of drift mobility measurement is a very informative for evaluating of defect and impurity states concentrations, because an electron and hole drift mobility (μ_e and μ_h) can be expressed as

$$\mu_{e,h} = (\mu_0)_{c,v}(N_{c,v}/D_{e,h})\exp(-\Delta E_{e,h}/kT) \tag{3}$$

where $(\mu_0)_{c,v}$ are the free electrons and holes mobility in the conduction and valence bands. $N_{c,v}$ are the effective concentrations of band states at the conduction E_c and valence E_v band edges. $D_{e,h}$ are the concentrations of localized traps which control the electron and hole drift mobility and $\Delta E_{e,h}$ are the absolute values of energy distance between traps energy $E_{e,h}$ and $E_{c,v}$ for electrons and holes correspondingly. It is known that in CGS mobility has been controlled by the charged states D^+ and D^- of negative-U centers, i.e. one can consider that $D_{e,h} = D^+, D^-$. Fig. 3 shows the values of D^+ and D^- which we evaluate using (3) and experimental data on values of the drift mobility are taken from paper [12].
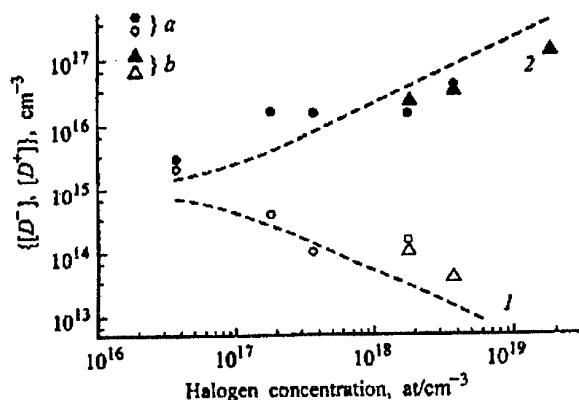
Fig. 3.Dependence of the concentration of negatively (1) and positively (2) charged intrinsic defects in $Se_{95}As_5$ doped with Br (a) and Cl (b). Data on values of the drift mobility for concentration of Br and Cl impurities in the range 10^{17} to 10^{19} are taken from [12]. The dashed lines are theoretical dependencies.

In this paper mobility has been measured in $Se_{95}As_5$ films, doped with Br and Cl. There are strong dependencies of D^+ and D^- on impurity concentration and therefore one can see the strong pronounced self-compensation process. Electrically active atoms of halogens Br and Cl has negative charge, then according to electro-neutrality equation its promote increasing of the D^+ and suppress the appearance of D^-. We have not any investigations of sample homogeneity and can not conclude would the electrically active impurity centers belong to clusters or not.

3. The possible superconductivity in the negative-U centers system.

The pairs of electrons or holes which are localized at the D^- and D^+ states of negative-U are bosons. If the concentration D of negative-U centers small, all pairs (bosons) are localized.

But in previous sections it has been demonstrated, that due to self-compensation processes doping treatment increases the D and, if the D becomes large enough and disorder is not large one can suppose that band-like non-localized boson states may appear. The Bose condensation of non-localized pairs may provides the superconductivity property of negative-U centers set in principle.

In the paper [13] we applied the theory [14] to the system of negative-U centers in CGS and named model as "negative-U centers model of superconductivity" (NUCS-model). Bose condensation or superconductivity transition temperature T_c may be expressed as

$$T_c = W(1-2v)/\ln(v^{-1} - 1) \qquad (4)$$

Where $v=n/2D$ is relative concentration of pairs, n is electron concentration. $W=2zt^2/U$ is width of pairs band for simple cubic lattice of negative-U centers with $z=6$. Absolute value of effective negative correlation energy of electrons is U; t is tunneling integral

$$t = t_0\exp(-2r/a) \qquad (5)$$

for electron transferred from one negative-U centers to another, which are separated by distance r. The expression (4) has been obtained for $t<<U$. In this case we have two narrow bands (Fig. 4, for example we consider a-Se with a large value of D) for electron D^- and hole D^+ pairs, which are separated by large distance U .
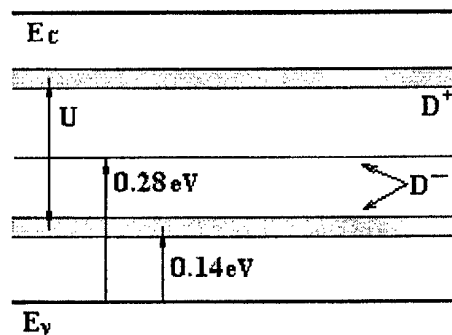
Fig. 4. Band energy diagram of a- Se. The vertical arrows show the thermal and optical transitions of holes to the D^- states of the negative-U center. Dark bands represent the bands of non - localized electron and hole pairs (D^- and D^+ bands), whose Bose condensation is responsible for the superconductivity.

For $v<1/2$ and $v>1/2$ the electron and hole pairs superconductivity takes place for $T< T_c$. It has been shown in [13] that, if electron (hole) wave function radius "a" is equal 10 A, the T_c of order several hundred degrees may be obtained for concentration D of order 10^{19} cm^{-3}. But this estimation is valid for ordered cubic lattice of negative-U centers only. For disorder lattice of negative-U centers the distance r between negative-U centers, which form band-like pairs states, may be more than mean distance (which is of order $D^{-1/3}$) consequently t and T_c may be less.

This model has been applied in [13] to channels, which arise during an switching effect in thin layer of CGS. Typical radii of channel or current filament R equals to ~ 1 micron. It has been supposed that in this channels reversible appearance of large concentration of negative-U centers takes place. The appearance of D^+ (or C_3^+ according to [15]) occurs due to response of active region of channel on pressure which arises during the switching event. The large number of C_3^+ centers with $z = 3$, which exceeds the $z_0 = 2$ for chalcogenide atoms removes stress inside the channel. Ordinarily the concentration D of negative-U centers in CGS is equal 10^{16}-10^{18} cm^{-3}. We have to suppose the increasing of D up to 10^{19}-5 10^{19} cm^{-3} in order to explain the temperature of order 300 K and higher. We also suppose that negative-U centers model of superconductivity can explain the states with a resistance which was not greater than instrumental error observed in low-coordinated organic polymers [16].

It is known that classic BCS theory encounters serious difficulties in explanation of high- T_c superconductivity in metal oxides. In our paper [17] it has been shown that negative-U centers model

of superconductivity explains both the high transition temperature T_c and specific – with a maximum – dependence of T_c on chemical composition of samples, observed in many metal oxides. In the contrast to the classic superconductors, high temperature metal oxides superconductors (HTSC) have a very small correlation length $\xi \sim$ 10-15 A. It means, that superconductivity current may be observed if the distance between micro-crystals of superconductors does not exceed the value of order ξ. In this connection our attention has been attracted by the results of the paper [18]. These results have been discussed in details in the [19] at the present conference and here I would like to emphasize only crucial facts.

The mixture of glassy Se with micro-crystalline pieces of HTSC compound $Y_1Ba_2Cu_3O_7$ with $T_c \approx 90$ K has been investigated in [18]. Micro-crystalline pieces of $Y_1Ba_2Cu_3O_7$ have linear size about several micrometers, occupy approximately 14% of whole volume then all of them have been separated by a-Se. At the high temperature $T > T_c$ the conductivity of samples was of order 10^{-6} Ω^{-1} cm^{-1}. This value strong differs from conductivity $\sim 10^3$ Ω^{-1} cm^{-1} of $Y_1Ba_2Cu_3O_7$ and shows that at the high temperature the conductivity is governed by doped a-Se. It is known that pure a-Se has conductivity of order 10^{-12} Ω^{-1} cm^{-1}, which may be increased by many of orders by doping with oxygen.

The transition temperature T_c of the mixture was the same as for $Y_1Ba_2Cu_3O_7$, i.e. $T_c \approx 90$ K and superconductivity current existences at this temperature through the whole sample. But the mean distance between micro-crystalline pieces of $Y_1Ba_2Cu_3O_7$ was very large. It was equal to several micrometers, i.e. more than 10^3 times exceeded the correlation length ξ. In the [19] we suppose that micro-crystals of HTSC are connected by channels which are similar to those appeared during the switching effect in CGS. A large number of negative-U centers may exist in the channel due to self-compensation processes induced by doping with oxygen. Additional concentration of negative-U centers may be generated during the switching effect in the internal electric field or in the weak external electric field which is used for current observation. The superconductivity in the system of negative-U centers in the channel may be induced by superconductivity phase transition in micro-crystalline pieces of $Y_1Ba_2Cu_3O_7$ which occupy two ends of each channel.

References

[1] T. F. Mazets, K. D. Tsendin, Sov. Phys. Semiconduct. **24**, 1214 (1990).

[2] Electronic Phenomena in chalcogenide glassy semiconductors, edited by K.D. Tsendin, Science, Moscow (1996).

[3] N. P. Kalmikova, T. F. Mazets, E. A. Smorgonskaya, K. D. Tsendin, Fiz. Tekh. Polupr., **23**, 297 (1989).

[4] S. P. Vihrov, G. A. Yushka, V. N. Ampilogov, Fiz. Tekh. Polupr., **18**, 348 (1984).

[5] B. L. Gelmont, K. D. Tsendin, Fiz. Tekh. Polupr., **17**, 1040 (1983).

[6] K. D. Tsendin, Fiz. Tekh. Polupr., **24**, 1019 (1990).

[7] K. D. Tsendin, J. Non-Cryst. Solids, **114**, 118 (1989).

[8] K. D. Tsendin, Fiz. Tekh. Polupr., **25**, 617 (1991).

[9] V. L. Aver'anov, B. T. Kolomiets, V. M. Lyubin, O. Yu. Prihod'ko, Pis'ma Zh. Tekh. Fiz., **6**, 577 (1980).

[10] O. Yu. Prihod'ko, Ph. D. Thesis, Leningrad (1982).

[11] R. P. Barclay, J. M. Marshall, C. Main, J. Non-Cryst. Solids, **77-78**, 1269 (1985).

[12] L. P. Kazakova, E. A. Lebedev, A. I. Isayev, S. I. Mehtieva, N. B. Zakharova, I. I. Yatlinko, Sov. Phys. Semicond., **27**, 520 (1993).

[13] B. P. Popov, K. D. Tsendin, Tech. Phys. Lett., **24**, 265 (1998).

[14] I.O. Kulik, A.G.Pedan, Sov. Phys.- JETP, **79**, 1469 (1980).

[15] M. Kastner, D. Adler, H. Fritzsche, Phys. Rev. Lett., **37**, 1504 (1976).

[16] V. M. Arkhangorodskii, A. N. Ionov, M. V. Tuchkevich, I. S. Shlimak, JETP Lett., **51**, 67 (1990).

[17] K. D. Tsendin, B. P. Popov, Supercond. Sci. Technol., **12**, 255 (1999).

[18] A. V. Prihod'ko, S. V. Kozirev, V. F. Masterov, Superconductivity: physics chemistry engineering, **3**, 1130 (1990).

[19] K. D. Tsendin, A. V. Prihod'ko, B. P. Popov, J. Optoel. Adv. Mat. 3 (2), this issue.

TRANSIENT AND METASTABLE PHOTODARKENING IN AMORPHOUS CHALCOGENIDES

A. Ganjoo, K. Shimakawa

Department of Electrical and Electronic Engineering, Gifu University,
Gifu 501-1193, Japan.

Transient photodarkening (PD), which is only observed during illumination, has been discovered in some amorphous chalcogenides. During illumination, total changes in absorption coefficient are a combination of transient and metastable part of PD. The transient PD decays as the illumination is switched off to give the usually observed metastable PD. The decay of the transient part, is similar to the decay of photocurrent in a-As$_2$Se$_3$ suggesting the importance of photocarriers in inducing PD. Although no metastable PD is observed for a-Se at 300 K, there exists transient PD.

1. Introduction

Amorphous chalcogenides exhibit remarkable photo-induced changes in their physical properties upon optical excitations [1-3]. Two types of metastabilities, the defect-related and structure-related, are introduced and are evident from many studies. Presently amorphous chalcogenides are attracting added attentions, basically due to these metastabilities. Amorphous chalcogenides are finding uses in fabrication of imaging devices [2] and more recently as fascinating opto-mechanical devices for nano-technologies [3]. The study of photodarkening (PD), one of the main structure-related metastability, in amorphous chalcogenides has received renewed interest recently and efforts have been made to have a better understanding of these changes (see, for example, Refs. [1, 3] and [4]). Recently some theoretical calculations, based on ab-inito calculations and molecular dynamics, have been performed to understand these light-induced structural changes in a microscopic way [5, 6].

Experimentally, however, most of the changes in optical transmission have been studied *after* the illumination is switched off. The behavior and nature of the changes taking place *during* illumination have been less well investigated. Recently, we have studied the PD kinetics during illumination of a-As$_2$S$_3$ films, where a laser beam was used to illuminate the sample and the changes in its transmission simultaneously recorded [7]. These measurements gave us new insights into the time evolution of changes in the absorption coefficient, namely the percolative growth of the photo-darkened sites explains the time evolution of PD.

In the present paper, we report direct measurements of *transient* changes in the absorption coefficient at 50 and 300 K for a-As$_2$Se$_3$, 100, 200 and 300 K for a-As$_2$S$_3$ and at 300 K for a-Se films. We have found a significant transient change in the PD observed during illumination for a-As$_2$Se$_3$ and a-As$_2$S$_3$. The transient part decays after the illumination is turned off leaving only the usually observed metastable change. This decay behavior is similar to the decay of photocurrent in a-As$_2$Se$_3$. For a-Se a significant transient PD is observed at room temperature that vanishes as soon as the illumination is switched off and no metastable PD is observed.

2. Experimental

Thin films of amorphous As$_2$Se$_3$ (a-As$_2$Se$_3$), amorphous As$_2$S$_3$ (a-As$_2$S$_3$) and amorphous Se (a-Se) thickness, d~500 nm, were deposited onto glass (Corning 7059) substrates by thermal evaporation in a vacuum of ~1x10^{-6} Torr. The films were annealed below the respective glass transition temperature (T$_g$) for 2 h for the case of a-As$_2$Se$_3$ and a-As$_2$S$_3$ and kept in vacuum for 24 h at

room temperature for a-Se before being placed in an evacuated cryostat for the measurement of optical transmission. Two laser beams were used: an Ar ion laser (hv = 2.41 eV, power = 80 mW/cm² and linear spot size ≈ 5mm) was used as the illuminating light and a He-Ne laser (hv = 1.95 eV, power < 0.1 mW/cm² and linear spot size ≈ 0.5 mm) was used as the probe light. The beams were directed such that they crossed each other at the sample. The transmitted signal of the He-Ne probe laser beam was detected with a photo-diode and the changes in the transmitted light were measured as a function of time. Suitable filters were used so as not to allow the photo-diode to be subjected to any interference from the illumination provided by the Ar ion laser. The schematic diagram of this two-beam experimental set up is shown in Fig. 1.
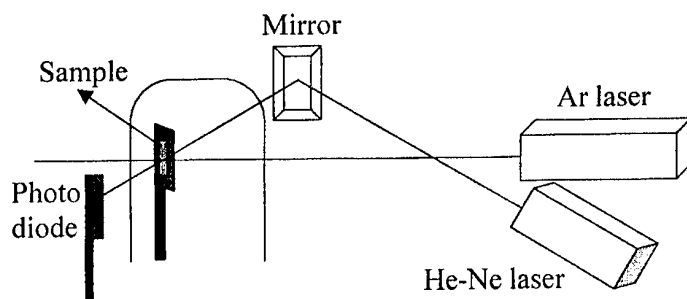
Fig. 1. Schematic illustration of the two beam experimental set up to study transient and metastable PD.

The changes in the absorption coefficient, $\Delta\alpha$, are calculated from $\Delta\alpha = \left(-\frac{1}{d}\right)\ln\left(\frac{T}{T_0}\right)$,

where d is the film thickness and T/T_0 is the ratio of the measured transmission signals of the He-Ne laser during and on putting on the illumination.

3. Results

Fig.s 2 and 3 show the time evolution of the changes in the absorption coefficient, $\Delta\alpha$, at 1.95 eV during various cycles of Ar laser illumination at 50 and 300 K for a-As$_2$Se$_3$ and at 300 K for a-Se, respectively. A similar type of behavior, as for a-As$_2$Se$_3$, is also observed for a-As$_2$S$_3$ but we will discuss the results of a-As$_2$Se$_3$ considering it to be a representative material. First we give the results of changes in $\Delta\alpha$ in a-As$_2$Se$_3$ films. For a-As$_2$Se$_3$ films, $\Delta\alpha$ increases rapidly at first at both temperatures before reaching close to saturation after some time. The magnitude of changes is larger at 50 K as compared to 300 K, which is consistent with the earlier results on amorphous chalcogenides (a-As$_2$S$_3$) [9]. When the Ar-laser illumination is switched off, a decrease in $\Delta\alpha$ is observed which reaches a constant value quite quickly. This portion of the total change is the *transient* part induced by illumination and the portion remaining after the illumination is switched off is the usually observed metastable PD. Thus the total increase in $\Delta\alpha$ for a-As$_2$Se$_3$ films, during illumination, is the sum of the transient and the metastable PD. The transient parts of the changes are found to be nearly 60% and 30 % of the total changes induced during illumination at 300 and 50 K, respectively. It should be noted that illumination is known to cause an increase in the thickness d of the films [8], but here d is assumed to be constant. The changes in d are around 5% at 300 K which is very small compared to the changes in $\Delta\alpha$ observed. It is also clear that an increase in d will result in a decrease in $\Delta\alpha$, which is opposite to that observed in PD.

Successive cycles of illumination with the Ar laser (laser on and off), after the metastable PD is reached (see Fig. 2), result in increase and decrease in $\Delta\alpha$ equal to the transient part observed after the first cessation of illumination. The cycling was repeated many times after the metastable state was reached, and every illumination confirmed the occurrence of only the transient PD.
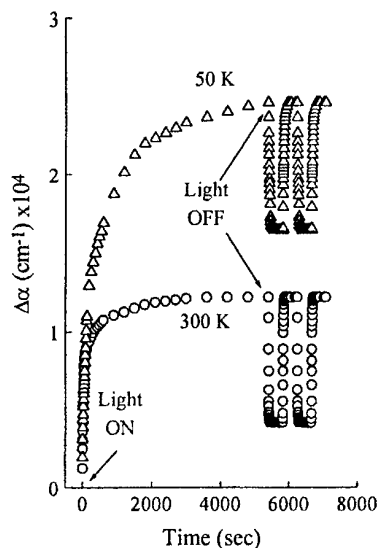
Fig. 2. Time evolution of changes in absorption
coefficient, $\Delta\alpha$, for a-As$_2$Se$_3$ films at 50 (D) and
300 K (O). ON and OFF stages of the Ar laser
are indicated by the arrows.
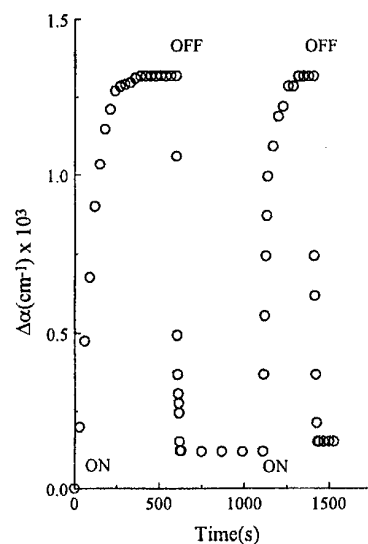
Fig. 3. Time evolution of changes in absorption
coefficient, $\Delta\alpha$, for a-Se films at 300 K. ON and
OFF stages of the Ar laser are indicated
by the arrows.

To understand the transient and metastable changes during the initial rapid increase of $\Delta\alpha$ in more detail, we have studied the changes in $\Delta\alpha$ for short-time illumination at 50 and 300 K, i.e., before reaching the saturated state shown in Fig. 2. The light was switched on and off for 20 s each at 50 K and 10 and 20 s, respectively at 300 K. The light was switched on for 20 s at 50 K instead of the 10 s used at 300 K, because $\Delta\alpha$ is still increasing rapidly even after 10 s at 50 K. The resulting changes in the absorption coefficient, $\Delta\alpha$, at 50 and 300 K are shown in Fig. 4. At both temperatures, $\Delta\alpha$ increases and decreases very rapidly when the illumination is switched on and off, but in neither case does it return to the original values. The total increase in $\Delta\alpha$ is larger at 50 K as compared to 300 K. The cycle of increase and decrease is repeated with each illumination cycle. This shows that the transient as well as the metastable changes occur for short illumination times and that the metastable part accumulates with each successive illumination. The accumulation of the metastable changes is slightly faster at 50 K as compared to 300 K.

In a-Se (Fig. 3), $\Delta\alpha$ increases as the Ar laser is made incident on the films and after some time reaches saturation. As soon as the illumination is switched off, the changes in absorption coefficient quickly revert back to the level before illumination. On switching on the illumination again, a similar behavior as the initial illumination is observed and any changes induced reverts back to the original state when the Ar laser is switched off. This indicates that only transient part is induced by illumination that vanishes as the illumination is switched off. Even on repeating the on/off cycle several times, a similar behavior is observed and no metastable PD is observed.

4. Discussion

First we discuss the changes in $\Delta\alpha$ for a-As$_2$Se$_3$ as shown in Fig. 2. The results clearly show that during illumination there exists a transient part and the metastable part of PD. The transient part decays when the illumination is switched off and the changes in $\Delta\alpha$ reach the usually observed metastable PD. Thus, during illumination, the total changes are a combination of the transient and metastable part. Even for short time illuminations (Fig. 4) transient and metastable parts of PD are observed. The observation of transient and metastable PD, during illumination, both for short and long times of illumination, parallels the changes observed in thickness on illumination [10]. This seems to confirm the correlation which is suggested to exist between the metastable changes in thickness and band gap observed in amorphous chalcogenides, experimentally [9] as well as phenomenologically [10]. Observations of the transient part of PD and the thickness changes in amorphous semiconductors

suggest that there may exist a correlation between these changes during illumination as well. However, as the changes in thickness were observed with white light [10], no further comments about the rate can be made at this stage.
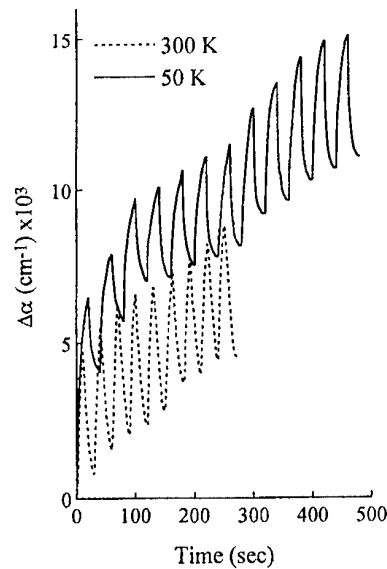
Fig. 4. Variation of changes in absorption coefficient, $\Delta\alpha$, with time for short duration of illumination for a - As_2Se_3 films at 50 (solid line) and 300 K (dashed line). Ar laser ON and OFF stages is 20 s each at 50 K and 10 and 20 s respectively at 300 K.

Next we discuss the decay of the transient changes in absorption coefficient, $\Delta\alpha$, for a-As_2Se_3 after turning off the illumination. As discussed earlier, the transient change in $\Delta\alpha$ decays as the illumination is switched off and the changes finally reach the metastable state. The decays of the transient part at 50 and 300 K are shown in Fig. 5. Here, the decrease of the transient part is plotted as a function of time on a logarithmic scale. The scale is adjusted to show the starting time as the time when the Ar-laser illumination is switched off. The decay is faster at 300 K as compared to 50 K. The decay can be best explained by a stretched exponential function:

$$\Delta\alpha = C \exp\left[-\left(\frac{t}{\tau}\right)^{\beta}\right] + \Delta\alpha_s, \tag{1}$$

where t is time after the illumination is switched off, τ is the effective decay time, β is a dispersion parameter ($0 \leq \beta \leq 1$) and $\Delta\alpha_s$ is the saturated value of $\Delta\alpha$ (i.e. the metastable part of the changes). C is a temperature-dependent quantity (the absolute amount of transient PD) and its value is obtained by fitting to experimental data. The solid line in Fig. 5 shows the fitting of Eq. (1) to the experimental results. The fitting seems to be reasonable and it gives values of β and τ as 0.7 and 20 s at 50 K and 0.85 and 5 s at 300 K, respectively. The effective decay time τ decreases and the dispersion parameter β increases with increasing temperature.

Next, the role of photocarriers on PD will be discussed. In Fig.6, both the decays of transient PD and photocurrent for a-As_2Se_3 induced by Ar-laser illumination at 300 K, which are nomalized to the intial value, are plotted as a function of time. Note that the transient PD is subtracted from the metastable PD. It is evident from the figure that the photocurrent decays mostly within 3 seconds and is followed by residual photocurrent [11]. The transient PD (TPD), on the other hand, the decay looks slower than that of photocurrent. However, as stated before, the effective decay time for TPD is 5 seconds that is comparable to the decay of the photocurrent (~3 sec), suggesting that there may be a correlation between photocurrent and TPD. A slightly slower decay of TPD as compared to the decay of photocurrent is expected and can be considered as follows: The decay of transient PD is the motion of the layers to a new equilibrium position (structural relaxation) in slip and repulsion model and some delay time is necessary for the movement of clustered layers in mesoscopic scale to occur. Similarity between the photocurrent and TPD suggests that photocarriers play an important role in inducing PD as well.
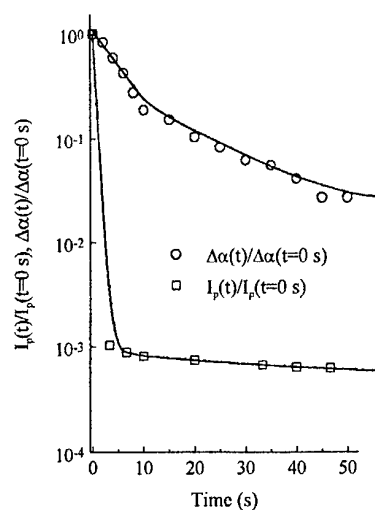
Fig. 5. The dacay of the transient part of PD after switching off the Ar laser for a-As₂Se₃ films
at 50 and 300 K. The symbols have the same meaning as in Fig. 2. The solid line is the fitting
using Eq. 1.

Next we take a look at the results of a-Se. It is reported (see for example [1]) that no PD is observed in a-Se at 300 K but it is observed at low temperatures. However, on measuring changes in absorption coefficient, $\Delta\alpha$, during illumination (see fig. 3), transient changes can be easily seen in a-Se at 300 K, which revert back to the original state as soon as the illumination is switched off. This shows that although there is no metastable PD in a-Se at 300 K, transient PD exists. The results presented till now dealt with the changes in $\Delta\alpha$ after the illumination was switched off, i.e., the metastable changes in PD. The reason for the observation of TPD and no metastable PD can be summarized as follows: It is well understood that PD is a reversible process, i.e., annealing near T_g in amorphous chalcogenides can reverse the changes. As the glass transition temperature of a-Se is just near room temperature [12] any changes induced in absorption coefficient at 300 K, during illumination are annealed out automatically as soon as the illumination is switched off leaving no metastable PD. This means that there exists only the transient part of PD at 300 K for a-Se.
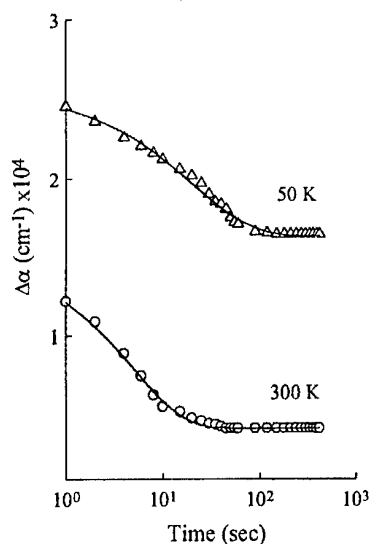
Fig. 6. Decay of transient part of PD and the decay
of photocurrent in a-As₂Se₃ films at 300 K.
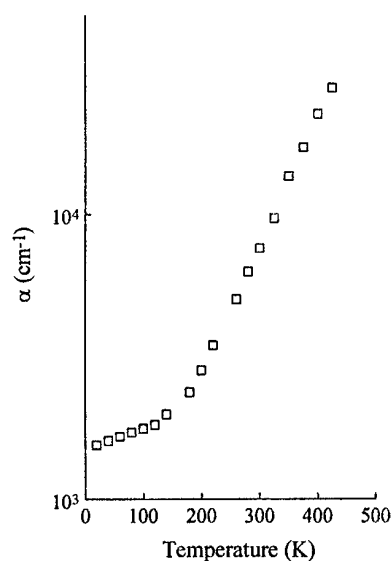
Fig. 7. Temperature dependence of absorption
coefficient, α, for a-As₂Se₃ films.

In order to clarify whether the transient changes in absorption coefficient are caused by photoelectronic or thermal mechanisms, we determined the temperature dependence of the absorption coefficient, α, for a-As₂Se₃ (as a representative of amorphous chalcogenides) that is shown in Fig. 7. $\Delta\alpha$

was estimated at different temperatures from the transmission intensity of the He-Ne laser light, as explained earlier. The room-temperature value of α at 1.95 eV for the films used in the present work is estimated from direct measurements and was found to be 7.8×10^3 cm^{-1}. This was then used to convert $\Delta\alpha$ to α. The transient part of $\Delta\alpha$ is approximately 8000 cm^{-1} at 50 and 300 K for a-As$_2$Se$_3$, as is evident from Fig. 1. To obtain such a large change in $\Delta\alpha$ purely by a thermal mechanism, a temperature increase of nearly 275 K at 50 K and nearly 100 K at 300 K would be required. This is unreasonably higher than expected from the Ar laser illumination in the present experimental conditions. It can thus be concluded that the transient changes are not thermally induced.

Note the present decrease in the transmission (increase in absorption coefficient) at 1.95eV (He-Ne laser) can not be considered as similar to the "optical stopping" effect as observed in As-S films, where the He-Ne laser light is stopped by switching on a He-Cd laser in the path of the He-Ne laser light [13]. The optical stopping effect may be considered as an opto-electronic property while the present PD appears to be pure photo-structural property. It is considered that the He-Ne laser light (the guided light) uses its energy to excite the trapped electrons that are introduced by the light of the He-Cd laser. This leads to the stopping of He-Ne laser light. Note the He-Ne laser (1.95 eV) is sub-gap illumination for the case of As-S samples (band gap $\sim$ 2.5 eV) studied in the optical stopping experiments. In the present experiment, the probe and the action lasers are He-Ne laser and Ar-laser, respectively, which are the band gap illumination and above band gap illuminations, respectively. Thus, the situation is very different from the above mechanism. Thus, we rule out optical stopping in the present experimental conditions.

5. Conclusions

We have made a direct observation of the transient changes of absorption coefficient, $\Delta\alpha$, in a-As$_2$Se$_3$ films at 50 and 300 K. During illumination, the total changes constitute transient and metastable PD, with the transient changes decaying when the illumination is switched off to give the usually observed metastable PD. The transient changes are nearly 60 % and 30 % of the total changes, observed during illumination, at 300 and 50 K, respectively. These transient changes are purely due to photoelectronic mechanisms. The decay of transient part after stopping the illumination is explained by a stretched exponential function. The decay of transient part is similar to the decay of photocurrent and thus suggesting the importance of number of photo-carriers. These photo-carriers assist site switching resulting in PD. Further illumination, after the metastable state is reached, induces only transient changes in $\Delta\alpha$. For a-Se, we have observed a significant transient PD at 300 K that vanishes and the changes revert back to the original state as soon as the illumination is switched off.

Acknowledgements

References

[1] A.V. Kolobov, K. Tanaka, Handbook of Advanced Electronic and Photonic Materials and devices: Chalcogenide Glasses and Sol-Gel Materials, ed. by H.S. Nalwa, 5, 47 (Academic Press) 2001.
[2] J. Rowlands, S. Kasap, Physics Today, November 24 (1997).
[3] P. Krecmer, A. M. Moulin, R.J. Stephenson, T. Rayment, M.E. Welland, S.R. Elliott, Science, 277, 1799 (1997).
[4] Ke. Tanaka, Phys. Rev. B 57, 5163 (1998).
[5] Jun Li, D. A. Drabold, Phys. Rev. Lett., 85, 2785 (2000).
[6] T. Uchino, D.C. Clary, S. R. Elliott, Phys. Rev. Lett., 85, 3305 (2000).
[7] A. Ganjoo, K. Shimakawa, H. Kamiya, E.A. Davis, J. Singh, Phys. Rev. B62, R14601 (2000).
[8] Ashtosh Ganjoo, Y. Ikeda, K. Shimakawa, Appl. Phys. Lett., 74, 2119 (1999).
[9] Y. Kuzukawa, A. Ganjoo, K. Shimakawa, Y. Ikeda, Philos. Mag. B79, 249 (1999).
[10] K. Shimakawa, N. Yoshida, A. Ganjoo, Y. Kuzukawa, J. Singh, Philos. Mag. Lett., 77, 153 (1998).
[11] K. Shimakawa, Phys. Rev. B34, 8703 (1986).
[12] Z.U. Borrisava, Glassy Semiconductors, Plenum, New York, 1981.
[14] A. Matsuda, H. Misuno, T. Kakayama, M. Saito, M. Kikuchi, Appl. Phys. Lett. 24, 314 (1974).

NEW Ag-CONTAINING AMORPHOUS CHALCOGENIDE THIN FILMS - PROSPECTIVE MATERIALS FOR REWRITEABLE OPTICAL MEMORIES

T. Wágner, M. Frumar, S. O. Kasap[a], Mir. Vlcek, Mil. Vlcek[b]

University of Pardubice, Department of General and Inorganic Chemistry, Pardubice, 53210, Czech Republic.
[a] University of Saskatchewan, Department of Electrical Engineering, Campus Dr. 57, Saskatoon S7N 5A9, Canada.
[b] Joint Laboratory of Solid State Chemistry of Czech Academy of Sciences and University of Pardubice, Studentská 84, 53210 Pardubice, Czech Republic

The technique of step-by-step optically-induced diffusion and dissolution (OIDD) of Ag with $As_{33}S_{67}$ amorphous films has allowed to design films with exact silver concentration. The photodoped films with a silver concentration of 25 at.%, i.e. with composition of the stoichiometric $AgAsS_2$ compound were prepared. The host $As_{33}S_{67}$ films were photodoped by consecutive dissolving thin (~ 10 nm) layer of silver, which resulted in a single-phase optically homogeneous films. We have analyzed affect of the silver doping in the host material on optical, thermal properties, and its structure by means of optical spectroscopy, temperature-modulated differental scanning calorimetry and Raman spectroscopy respectively. Application of such films can be foreseen for rewritable high resolution optical memories (reversible phase change "amorphous-crystalline" or film optical surface nanoshaping in dependence on intensity and silver concentration). The surface structure of optically shaped films were studied by atomic force microscopy.

1. Introduction

Products manufactured by the consumer electronics, communications and computer industries are beginning to converge into a single multiple-purpose digital devices with entertainment, communications and computing functions. Rewritable DVD disks, with their very high storage capacity, are the ideal removable storage media for these new generations of products [1].

Phase change memories are based on thin-film alloys typically incorporating one or more elements from Column 16 of the Periodic Table.These chalcogenide materials can exist in two or more distinct atomic states. Structural state can be changed by overcoming energy barrier between those stable states. Energy can be supplied to the material by exposure to laser beam. Optical memories are recorded, rewrittten or erased by laser exposure or other light sources. The memory material is excited to a state of high atomic mobility, in which it becomes possible for chemical bonding rearrangements by slight movement of individual atoms. Chalcogenide containing materials are very appropriate materials for optical memories because amorphous or crystalline state is reachable due to high structural flexibility employing weakly bonding "lone pair" *p*-electrons [2, 3]. Stechiometric compounds, which are able to be transformed between the amorhous and crystalline structural states using laser pulses of extremely short duration, are used [4]. Other important condition of those compounds is their stability at room temperature. Optical memory media using binary stoichiometric compounds show the necessary crystallization speeds, but a slight deviation of the stoichiometric composition could lead to dramatic crystallization speeds loss [4]. Adding third element, e. g. Sb, to GeTe binary system improves the rapid crystallization speed over the broad compositional range [3].

Optically-induced diffusion and dissolution (OIDD) of metals in amorphous chalcogenides has been widely studied [e.g. 5-8] and could be used to synthesis of stoichiometric amorphous solid solutions, which could be optically crystallized. The technique of the step-by-step OIDD between Ag and $As_{33}S_{67}$ amorphous films was studied in [9] by which the films with the thicknesses 0.5 μm were

prepared. The amourphous films with compostion of $As_{33}S_{67}$ are favourable for optically-induced solid state reaction with silver, because they yield optically homogeneous photodoped reaction products. The compositional tie-line between $As_{33}S_{67}$ and Ag in Ag-As-S ternary diagram also intersects the region where the solid solution with the composition of the stoichiometric $AgAsS_2$ compound is formed.Such technique is very promising to be applied for preparation of films used for the rewritable high resolution optical memories.

In this work we have studied synthesis of $AgAsS_2$ glass, OIDD preparation of $AgAsS_2$ films and their physical and chemical properties.

2. Experimental techniques

The $As_{33}S_{67}$ host films were prepared by using well-established vacuum evaporation technique. The bulk chalcogenide glass used as an evaporation source was prepared from the constituent elements. Arsenic and sulphur or silver of 5N purity were weighed and placed in cleaned and outgassed (by heating under vacuum to 900 °C) quartz ampoules. The ampoules were evacuated to a pressure of $1 \times 10^-$ ^{3} Pa for 30 minutes and then sealed. The synthesis was performed in a rocking furnace with ampoules exposed to a temperature of 650 °C for 24 hours. The fragments of the bulk material were evaporated from quartz crucible to reduce any contamination of the prepared layers. The layers were evaporated on glass substrates in a 1×10^{-4} Pa vacuum, at a rate of 1 nm.s^{-1}. Constant thickness of the films was guaranteed by rotating substrate holders in planetary system. Thickness was monitored during evaporation with a quartz crystal monitor. The thickness of the $As_{33}S_{67}$ films were 2000 nm, which is the appropriate thickness for the accurate evaluation of the optical parameters. Constant thickness silver films (~10 nm) were evaporated subsequently on the top of the chalcogenide film. The host $As_{33}S_{67}$ films were photodoped by means of OIDD i.e. by consecutive photodissolution of Ag films (~10 nm) up to the saturation, i.e. 320 nm of overall silver thickness. The photodoping was carried out by illuminating samples by 500W tungsten lamp accomodated in a lamp house eguipped with large Fresnel lens and IR-cut filter. The thickness of the photo-doped layers ranged between 2000 and 2700 nm. The silver concentration of the prepared samples ranged between 1 and 41 at.%. The values of silver concentration quoted were calculated from measured silver and photodoped layer thicknesses. The compositions of chalcogenide films (both doped and undoped) were also measured by electron microprobe (using a Kevex 8000 instrument) with an accuracy of 0.5 at. %. The concentrations of silver in films established by both techniques were in agreement within an error 1 at. %.

Further, we have analyzed the affect of the silver doping in the host material on optical, thermal and mechanical properties, and its structure.

The optical transmission spectra of the films were recorded with ultra-violet, visible and near infrared (UV/VIS/NIR) spectrophotometer (JASCO). According to Kosa [9] the homogeneity of our doped thin-film samples was clearly confirmed by the corresponding spectral dependence of transmission, where no shrinkage of the interference fringes was observed. In order to calculate the thickness, d, the refractive index, n, and absorption coefficient, α, from the thin film transmission spectra, an evaluation method described by Swanepoel [10] was used. Maximum possible error varies in $n = +/- 0.005$; in $d = +/- 5$ nm.

The recent temperature-modulated differental scanning calorimetry (TMDSC, TA instruments 2920) technique has been applied to the measurement of the thermal properties of chalcogenide glasses [11] and at present work also of the silver doped $As_{33}S_{67}$ films and bulk glasses. All samples in this work were exposed to the same temperature-modulated heating schedules with the average heating rate of 1 °C/min, temperature modulation amplitude $+/-2$ °C and period of 60s. The total heat flow, modulated heat flow, reversing heat flow and parameters, glass transition temperature, T_g, specific heat capacity C_p, crystallization temperature, T_c, which characterize the thermal events in the glass transition and crystallization regions were also determined, respectively. The photodoped films (Ag-$As_{33}S_{67}$) were mechanically peeled from the substrates, or bulk glass samples crushed, and immediately weighed into aluminium crimped pans and then properly sealed. A typical film sample weight was approximately 18 mg. The experimental errors of the T_g, values are within a range $+/-0,1$ °C. Also DSC scan in non-modulated regime at different heating rates were performed in the temperature range from 100 to 500 °C.

Raman spectroscopy has been used to study the structure of the bulk $AgAsS_2$ glass and the films of $As_{33}S_{67}$ as silver was photo-doped into them. The Raman spectroscopy study was performed on a Fourier Transformation (FT) Raman spectrometer (model IFS/FRA 106, Bruker). Raman spectra were excited using a laser beam with $\lambda = 1064$ nm having an output power 50 mW. The wavelength of the laser beam was critical to avoid any photostructural changes in the chalcogenide glasses within the time scale of 100 scans. The resolution of the Raman spectrometer was 1 cm^{-1}. The photodoped films ($Ag-As_{33}S_{67}$) were both mechanically peeled from the substrates crushed, and immediately pressed into aluminium targets, which are used as a powdered material holder during the Raman measurements.

Surface dimension of the optically exposed dots on films were measured by atomic force microscopy (AFM).

3. Results

It was proved that by the means of OIDD can be prepared the optically homogeneous films with a $AgAsS_2$ composition which are not possible to prepare by other methods, e.g. direct thermal evaporation due to thermal decomposition or bulk glass synthesis because of restricted glass forming ability of Ag-As-S system [12].

The typical optical transmission curve of the $AgAsS_2$ amorphous films prepared by OIDD as well as calculated values of the spectral dependence of refractive index, n, are shown in Fig. 1. Compositional dependence of refractive indeces, n, proves an increase in refractive indeces values up to 25 at.% of silver, as can be seen in Fig. 2.
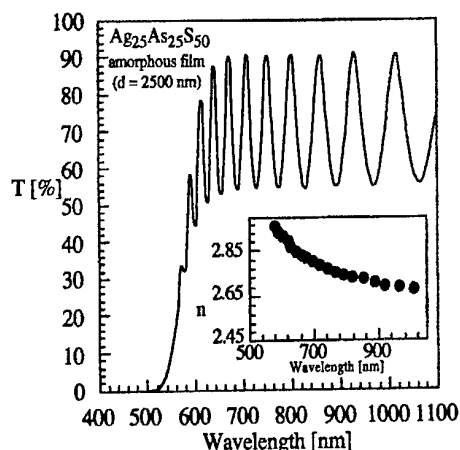
Fig. 1. Optical transmissivity and refractive index spectral dependence of the $AgAsS_2$ amorphous film.

The dependence of the glass transition temperature, T_g (taken at three important points of the sigmoidal curve C_p versus T [13], i.e. $T_{g,onset}$; $T_{g,inflex}$ and $T_{g,end}$), on composition of the Ag-As-S films is apparent from Fig. 2. The glass transition temperature in all three sets of data decreases with increasing Ag concentration down to a local minimum at around 10 at.%, then T_g increases up to a local maximum at 25 at. %. T_g again decreases with Ag content beyond 25 at.% Ag.

Thermal properties of the silver optically doped films were also measured non-reversing heat flow (NHF) [11] in crystallization regions using modulated regime (parameters described in experimental part) of DSC apparatus, which allowed to establish crystallization temperatures (T_c on, T_c) and crystallization enthalpies (ΔH). The typical NHF vs. Temperature curve and silver content dependence of crystallization parameters (T_c, ΔH) is presented in Fig. 3. There is noticable maximum of ΔH when composition of film reaches x = 25 at.% Ag.
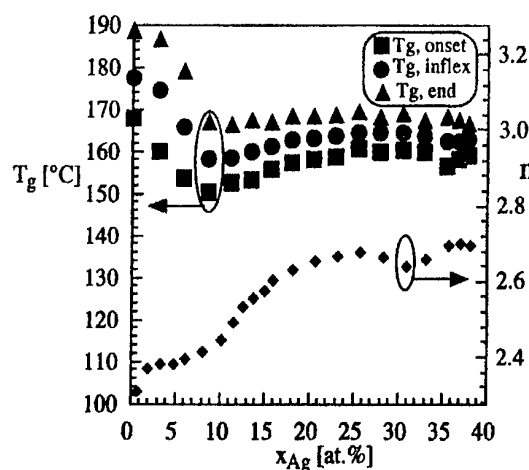
Fig. 2. Glass transition temperature T_g and the refractive index, n, dependence (at wavelength equal to 1000 nm) on silver content in the prepared Ag-As-S films.
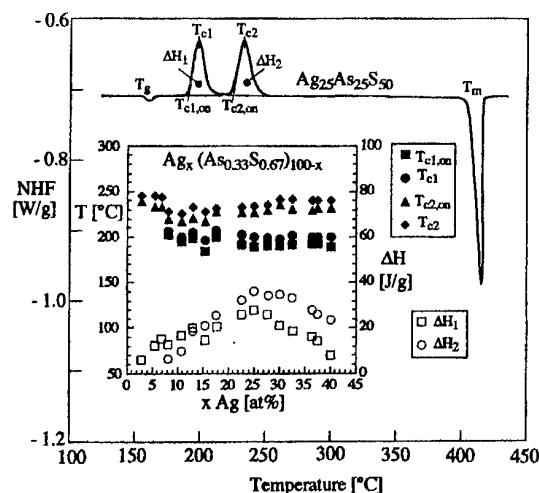
Fig. 3. Typical non-reversing heat flow DSC signal obtained from OIDD prepared Ag-As-S films. Inserted figure shows dependence of T_c and ΔH on silver content in Ag-As-S films.

The heat flow dependence on temperature was measured in temperature non-modulated DSC regime in heating scans for the $AgAsS_2$ amorphous film prepared by OIDD and for the $AgAsS_2$ melt-quenched glass. Both heat flow curves are shown in Fig. 4. There is a clear evidence that the glass transition, crystallization and melting regions which are very similar for both samples. Small discrepancies can explained by different particles size (crushed pieces of bulk glass and pealed thin film particles).
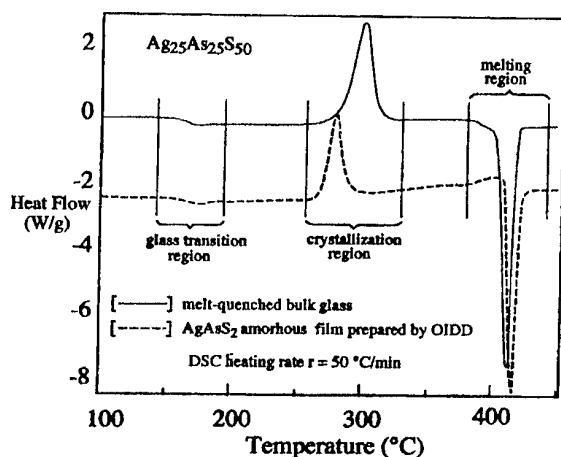
Fig. 4. Typical heating scan in non-modulated DSC experiments at a rate of 50 °C/min[-1] for the samples of $AgAsS_2$ glass prepared by melt-quenching and $AgAsS_2$ amorphous film prepared by optically-induced diffusion and dissolution (OIDD), respectively.
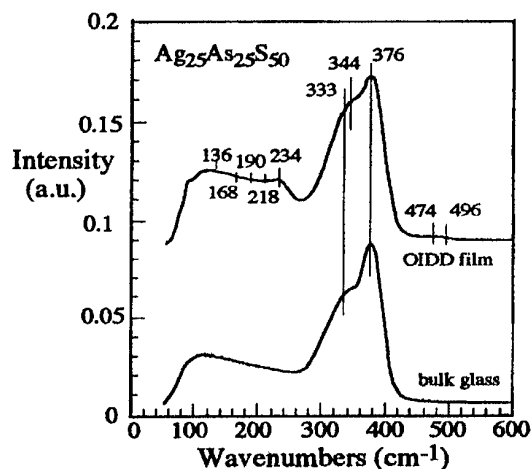
Fig. 5. Raman spectra of the samples of $AgAsS_2$ glass prepared by melt-quenching and $AgAsS_2$ amorphous film prepared by optically-induced diffusion and dissolution (OIDD), respectively.

The Raman spectra measured in $AgAsS_2$ amorphous films and bulk glass are shown in Fig. 5. Spectra were interpreted using references [14 - 16]. The Raman spectra of the film contains strong bands at 333, 344 cm^{-1} (units $AsS_{2/3}$) also weak bands at 474 and 496 cm^{-1} (S_8 rings and S rings fragments, respectively). The OIDD of silver (explained in experimental section) leads to an appearance of a new strong band at 376 cm^{-1} (AsS_3 pyramids joined by S-Ag-S linkage), and to a decrease of intensities of the weak multiple weak bands in spectral region 100-300 cm^{-1} (As-As bonds). Film with the content of silver, x = 25 at.% Ag, possess the same vibration bands as glassy bulk sample of the composition $AgAsS_2$.

4. Discussion

All analitycal techniques used in this work show common and supporting results for the fact that it is possible to prepare by means of OIDD the new Ag-As-S films with desired stoichiometric composition of $AgAsS_2$ glass.

Optical parameters T, n, show a strong evidence that silver is incorporated into a host matrix, with a distinct features close to content of 25 at. % of Ag, i.e. where stoichiometric compound $AgAsS_2$ exists.

Measured thermal properties support the idea of optically-induced solid state reaction of silver with $As_{33}S_{67}$ films, as T_g, T_c and ΔH are structuraly sensitive parameters [9, 11], show maxima in their compositional dependences at 25 at. % Ag. The point when silver reaches in Ag-As-S films the composition of $AgAsS_2$ (25 at. % Ag) can be interpret that silver has a role of glass-former. The turning point at 10 at. % Ag on T_g vs. x_{Ag} curves is not fully understand. It could be phenomelogicaly described as a transition from the role of silver as glass structure modifier to glass former.

As it is evident from Raman spectra silver can create either one bond at the chain end or can brake S-S chain and rings. The S-S units disapearance is clearly seen from evolution of the Raman spectra. Raman spectrum of Ag As-S films at $x = 25$ at. % Ag shows the homogenous reaction products and the spectrum of film at this composition represents almost identical structure of OIDD films as that of bulk glass of composition $AgAsS_2$ (Fig. 5). It proves that OIDD process between silver and $As_{33}S_{67}$ could reach the same reaction products as it is during high temperature syntesis from elements in a melt. This conclusion is also supported by DSC curves in Fig. 4.

MDSC curves of $AgAsS_2$ films and DSC curves of $AgAsS_2$ (Fig. 6) bulk glass show two peaks in crystallization regions. This two peaks could be attributed to the cold crystalization and following recrystallization of the two crystallografic modifications of $AgAsS_2$ stoichiometric compound, i.e. lower temperature modification is monoclinic smithite and higher temperature modification is hexagonal trechmanite. Heating rate and final temperature during heating (light-exposure) of an amorphous $AgAsS_2$ influences which of the crystalline modification of the compound will grow during cold crystallization. Application of such films can be foreseen for rewritable high resolution optical memories (reversible phase change "amorphous-crystalline" or film optical surface nanoshaping in dependence on intensity and silver concentration). The surface structure of optically shaped films were studied by atomic force microscopy as it is documented in Fig. 7.
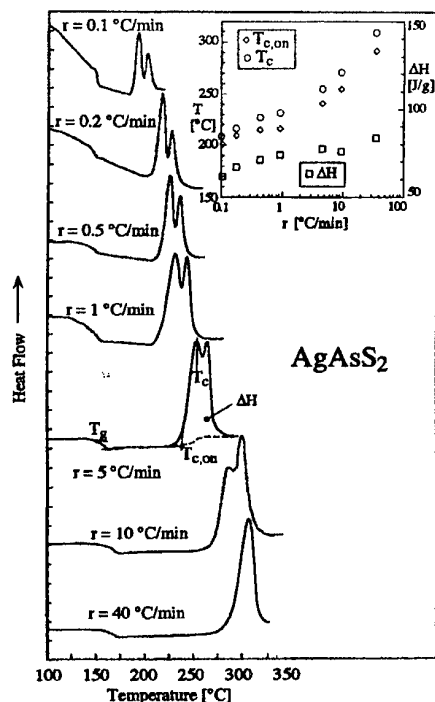
Fig. 6. Typical heating scan in non-modulated DSC experiments at different heating rates. Inserted figure shows dependence of T_c and ΔH on silver content in Ag-As-S films.
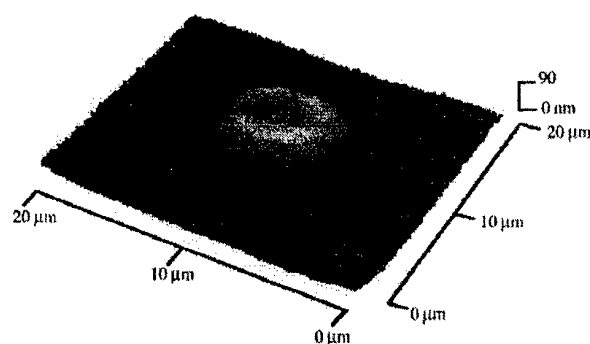
Fig. 7. AFM scan of $AgAsS_2$ film surface after exposure by light of 200 W Hg lamp through mask.

5. Conclusion

The OIDD of Ag in $As_{33}S_{67}$ films was used to tailor desired silver content in the final reaction product, i.e. $AgAsS_2$. The $Ag_x(As_{0.33}S_{0.67})_{100-x}$ films were prepared as a single-phase optically homogeneous material in the compositional range from $x = 1$ to $x= 41$ at.%. The structure of the films containing 25 at. % of Ag have the structure close to the $AgAsS_2$ bulk glass. The photodoped films with a silver concentration equal to 25 at.%, i.e. with composition of the stoichiometric compound $AgAsS_2$, showed characteristic features in their optical, thermal and stuctural properties. Such OIDD film techniques preparation could be potencially used for application in phase change optical memories.

Acknowledgements

References

[1] S. R. Ovshinsky, in: Insulating and Semiconducting Glasses, Series on Directions in Condensed Matter Physics, vol. 17,, (ed. P. Boolchand), World Scientific, London, , p. 729, 2000.
[2] D. Strand, J. Gonzalez-Hernandez, B. S. Chao, S. R. Ovshinsky, P. Gasiorowki, D. Pawlik, Spring Meeting Mat. Res. Soc. Symp., Anaheim, California, 1991.
[3] J. Gonzalez-Hernandez, B. S. Chao, D. Strand, S. R. Ovshinsky, D. Pawlik, P. Gasiorowki, Appl. Phys. Commun., 11, 557, (1992).
[4] Chen M., Rubin K. A., Barton R. W., Appl. Phys. Lett. 49, 502 (1986).
[5] M. T. Kostyshin, E. V. Mikhailovskaya and P. F. Romanenko, Sov. Phys. Solid State 8, 451 (1966).
[6] T. Wagner, M. Frumar, V. Suskova, J. Non-Cryst. Solids 128, 197 (1991).
[7] A. V. Kolobov, S. R. Elliott, Advances in Physics, 40, 625 (1991).
[8] T. Wagner, E. Marquez, J. Fernandez-Pena, J. M. Gonzalez-Leal, P.J. S. Ewen, S. O. Kasap, Phil. Mag., B79, 223 (1999).
[9] T. I. Kosa, T. Wagner, P.J. S. Ewen and A. E. Owen, Phil. Mag., B71, 311 (1995).
[10] R. Swanepoel, J. Phys. E.: Sci. Instrum., 16, 1214 (1983).
[11] T. Wagner, S. O. Kasap, Phil. Mag,. B74, 667 (1996).
[12] Y. Miyamoto, M. Itoh, Ke. Tanaka, Sol. State Commun. 92, 895 (1994).
[13] T. Wagner, S. O. Kasap, M. Vlcek, A. Sklenar, A. Stronski, J. Mat. Sci., 33, 5581 (1998).
[14] A. P. Firth, A. E. Owen, P.J. S. Ewen, in: The Structure of Non-Crystalline Materials, Taylor and Francis, London, p. 231, 1983.
[15] G. Lukovski, F. L. Geils, R. C. Keezer, The Structure of Non-Crystalline Materials, Taylor and Francis, London, p. 127, 1977.

POLYMORPHOUS-CRYSTALLOID STRUCTURE AND RELAXATION PROCESSES IN SOME CHALCOGENIDE GLASS-FORMING SUBSTANCES

V. S. Minaev

Research Institute of Material Science and Technology, Elma Corp., Moscow, 103460, Russia

The processes related to the modification of glass and glass - forming liquid structure have been explained by the concept of polymeric polymorphous - crystaloid structure.

1. Introduction

1.1. General remarks on relaxation of structure of substance in condensed state

The nature of vitreous state can not be perceived deeply without analysis of crystal and liquid states, without analysis of structure in these states, without understanding of ways and means of mutual transformations of these three states, as well as transformations inside them that take place under influence of such external influences as temperature, pressure, electromagnetic radiation, etc. As a matter of fact such transformations of various states (phase transformations) and transformations inside each of them (phase transformations – in crystal state, structural transformations – in liquid and vitreous states) represent relaxation* of substance, i.e. the process of establishment of thermodynamic equilibrium (complete or partial) in a physical system consisting of a large number of particles [1].

In this work phenomenological aspects of relaxation processes taking place, mainly, in individual chemical substances based on chalcogenides of IV and V main subgroups of the Periodic Table as well as in chalcogene Se are considered. Special attention is given to the most deeply investigated germanium diselenide $GeSe_2$.

Our consideration is confined only structural relaxation above substances in crystalline, vitreous and, partially, liquid states, information on which is quite limited.

The largest experimental material in the field of chalcogenides is collected for the case of influence of temperature on substance, so in this work the relaxation of substance will be considered mainly as establishment of equilibrium in substance as a result of temperature influence, i.e. as a result of "placement" of substance from one temperature conditions to others. At that, as it will be shown later, for understanding of the nature of glass-formation the processes connected with relaxation of substance at placing it in higher temperature conditions (heating) are no less important than processes of cooling of substance to which a lion's share of experimental materials is devoted that is evidenced, for example, such notions as "relaxation of glass-forming liquid" and "glass relaxation in region T_g".

Considering relaxation processes, it must be kept in mind that very frequently a substance does not achieve the equilibrium state due to not sufficient duration of conditions in which the system is kept. In the case conditions continuously change, the potential equilibrium state, to which the system aims at, changes as well.

Any alteration of state of a system leads to alteration of its properties. Substance properties in accordance with the main formula of physics-chemical analysis, the formula of Kurnakov-Tananaev [2], are functionally dependent on composition, structure and dispersion (the ratio of substance surface to its volume). At constant chemical composition and absence of significant dispersion, alteration of substance properties is directly related with alteration of its structure.

---

* In this work we do not consider the vapors state of substance, analysis of transformation of which in condensed non-crystalline state, in particular in ultra-dispersed and vitreous, is very important in obtaining non-crystalline films of chalcogenides.

Knowledge of substance structure is the most important condition of understanding of relaxation processes in it. As for individual chemical substances and, in particular, chalcogenides, there is a lack of data on structure of even "the most simple" crystal state, for example, crystallographic parameters of one of two polymorphous modifications (PM) as for $GeSe_2$ and AsSe. There is no confidence that all PM of individual chemical substances and chalcogenides, in particular, are discovered.

The situation is more complicated with structure of vitreous substances, and glass-forming liquids in particular.

For description of structure of liquid (melt) Tool, who founded the kinetic theory of glass-formation [3], introduced the notion of "the fictitious temperature" T_f that is frequently called "the structural temperature". T_f (according to Tool) is the temperature of melt which structure coincides with the structure fixed in this glass. But although structures of glass and liquid at certain temperature in accordance with the kinetic theory of glass-formation are similar, it says nothing about their peculiar concrete stereometry of atom arrangement in glass or liquid.

1.2. Main concepts of glass structure

Analyzing and interpreting diffractometry and spectrometry data which evidence on structure and structure changes in glass and glass-forming liquid, investigators, consciously or unconsciously, are relied on a certain concept of glass structure or guided by some model of structure.

The most famous concepts of glass structure are the crystallite concept of Frankengeim (1835) – Lebedev (1921) [4, 5] in which for the first time a guess was given about connection of glass-formation and polymorphism, the concept of polymeric structure (Mendeleev – 1864 [6], Sosman – 1927 [7] and others), the concept of a continuous random network of Zachariasen – 1932 [8], the polymeric-crystallite concept of Poray-Koshits – 1959 [9] which relatively successfully combined three previous conceptions, the concept of clusters of structural-independent polyforms of Goodman [10] (actually developing ideas of Frankelgeim-Lebedev).

Each of above mentioned concepts reflects to certain extent an objective glass structure, but is distinctive either in excessive generality (the concept of polymeric structure and, to the certain extent, the Zachariasen's concept) or contents theses contradicting to experimental data – modern diffractometric investigations show that in well synthesized glass there are no even smallest crystal inclusions.

We establish our interpretation of all processes related with alteration of glass and glass-forming liquid structure on the concept of polymeric polymorphous-crystalloid structure of glass and glass-forming liquid (CPPCSGL) produced from individual chemical substances [11-15] that we have been developing since the second half of eighties.

1.3. Main theses of the concept of polymeric polymorphous-crystalloid structure of glass

Basing on critical analysis of existing concepts of glass structure, a number of theses related with the structure of glass-forming liquid and glass expressed by Brukner (1970), Landa (1977), Balmakov, Blinov (1985), Gerber (1988) and others, Golubkov (1992), as well as on other data analyzed in [11-15], the following main theses of CPPCSGL have been established:

1. The process of formation of vitreous substance is the process of generation, mutual transformation and co-polymerization of structural fragments of various polymorphous modifications of a crystal substance without long-range order (crystalloids) in disordered polymeric polymorphous-crystalloid structure (network, tangle of chains, ribbons, etc.) of glass.

The term "crystalloid" was in the first time introduced by Graham and it meant particles of substance in the state of molecular fragmentation which are able to crystallize from solution [16]. It is evident that in our case this definition must be transformed to some extent and that has been done in [12].

2. The crystalloid is a fragment of the crystal structure consisting of a group of atoms connected by chemical bonds according to stereometric ordering rules inherent to one of crystal PMs of the substance and having no translational symmetry of the crystal. There is no even minimum long-

range order (LRO) in the crystalloid, i.e. two neighboring elementary cells of crystal structure which are able to intertranslate.

3. The notion "crystalloid" is directly connected with notions "short-range order" and "intermediate-range (medium) order" (SRO and IRO, MRO), "short-range ordering" and "medium-range ordering", applied both to non-crystalline and crystalline substances.

The short-range order is topologically determined composition of atoms including the atom taken as the origin point and surrounding atoms of the first coordination sphere. The SRO is characterized by the coordination number, by types (kinds) constituent atoms, by distances between atoms and interbond angles.

The intermediate (medium) order – is a stereometrically determined composition (topology) of short-range orders in the limits of a crystalloid characterized by parameters of all SROs (coordination numbers, distances between atoms, interbond angles) and dihedral angles.

The intermediate-range order, at least along one of crystallographic axes, has dimensions less than two periods of the crystal lattice. Otherwise, the crystalloid transforms in a crystallite.

The short-range ordering is a combination of various short-range orders (in crystalline and non-crystalline substances).

The intermediate-range ordering is a combination of various intermediate orders in a non-crystalline substance. In a crystalline substance the term "intermediate-range ordering" coincides with the term "intermediate-range order".

4. In every non-crystalline substance there are two or more SROs, two or more IROs (plurality of SRO and IRO), and there is no LRO. The number of IRO types is equal to the number of polymorphous modifications taking part in formation of the non-crystalline substance. In a crystalline substance there may be one, two or more SROs and only one type of IRO and LRO.

5. Stereometrically ordered crystalloids of different PMs join together (polymorphous polymerization) also according to ordering rules of one of PMs (except for rules of translational symmetry, but because of statistical alternation of inherent to them IROs they form disordered polymeric polymorphous-crystalloid structure of vitreous substance in which the order (microlevel) and the disorder (macrolevel) organically co-exist.

6. Glass structure is not absolutely continuous, there are separate broken chemical bonds and other structural defects.

In accordance with above notions of the CPPCSGL glass structure and properties are determined by the concentration ratio of crystalloids of different PMs inherent to the given glass and depending on origin substance state, conditions of formation and treatment of the vitreous material.

In glas-forming liquid and glass substantial changes of structure and properties take place depending on concrete realization of the process of intertransformations of crystalloids of different PMs.

$$A_k + B_l + C_m + ... + Z_x \quad \overset{(T,P,Ph,E,H)}{?} \quad A_p + B_q + C_r + ... + Z_y \qquad (1)$$

where A, B, C .... Z – crystalloids of different PMs of substances which concentrations k, l, m ...p, q, n ... x, y are changed depending on conditions (temperature T, pressure P, irradiation Ph, electrical field E, magnetic field H, etc.) in the range from 0 to 100% [12, 17].

Actually, the expression (1) reflects physical-chemical essence of relaxation processes in crystal, vitreous and liquid states of substance.

2. Germanium diselenide GeSe₂

2.1. Crystalline polymorphous modifications and phase transitions

Germanium diselenide $GeSe_2$ exists at normal pressure in two polymorphous modifications – high-temperature (HTPM, β-modification) and low-temperature (LTPM, α-modification) [18, 19]. The HTPM has two-dimensional layered structure in which $GeSe_{4/2}$ tetrahedrons, connected in vertexes (corner-shared tetrahedrons - CST), form chains connected by bridges from pairs of tetrahedrons, connected in edges (edge-shared tetrahedrons - EST). In HTPM there are equal numbers of CSTs and ESTs. The HTPM has yellow [20] (orange [21]) color and the melt temperature of

740 ^{0}C [20]. The LTPM is constructed of tetrahedron chains arranged along directions [001] and [101] and connected by only CST in the three-dimensional network [22]. LTPM can be obtained by photo-irradiation of thin vitreous samples by the He-Ne laser [23], by annealing at 325 ^{0}C of an amorphous film deposited by vacuum evaporation [22]. A comprehensive X-ray determination of LTPM structure is absent.

Azoulay in 1975 [21], heating glasses of Ge-Se system with 15-30 at.% Ge content up to temperatures of 280-300 ^{0}C, discovered in all cases inclusions of the same phase consisting of small crystals of red-brown color with approximate composition $Ge_{30}Se_{70}$. With further heating the orange phase $GeSe_2$ appears which co-exists with the red-brown phase. At heating to 400 ^{0}C and higher, the latter disappears while the orange phase $GeSe_2$ remains.

In accordance with the eutectic type of the phase diagram Ge-Se,in the range $Se-GeSe_2$, at partial crystallization in the range of15-30 at.% Ge only $GeSe_2$ phase can be formed. Therefore, Azoulay appears to be the first who discovered LTPM $GeSe_2$ and observed the phase transition LTPM $\rightarrow$ HTPM which can be interpreted as the process of relaxation of crystalline $GeSe_2$ at temperature increase. The confirmation of the fact that Azoulay dealt with the phase transition in $GeSe_2$ is the Inoue's experiment [22] who at thermal annealing of amorphous film obtained LTPM at 325 ^{0}C and HTPM at 425 ^{0}C. The phase transition in the opposite direction HTPM $\rightarrow$ LTPM is registered in the work [19] at increasing pressure to 7 GPa. The transition is realized via intermediate, completely disordered at 6.2 GPa, phase.

For $GeSe_2$, two PMs obtained at high pressures are also known [24].

As it's seen from presented data the information on the crystal state of $GeSe_2$ is far from comprehensive. But the fact of existing of stable HTPM and LTPM at normal pressure in certain temperature intervals [18, 19, 23] says itself that $GeSe_2$ has the enantiotrope phase transition HTPM$\rightarrow$LTPM which is characterized by certain temperature of polymorphous transformation T_{tr}. Temperature of the enantiotrope transition T_{tr} is unknown. It is clear only that this transition is in the temperature range of 300-400 ^{0}C according to data [21] or 325-425 ^{0}C according to [22]. We didn't come across any facts of existing of HTPM $\rightarrow$ LTPM transition at normal pressure. It appears that it is difficult to take place because of not sufficiently high temperatures. It is possible that it does take place, although slowly, at temperatures slightly less than the real T_{tr}. The transition HTPM $\rightarrow$ LTPM can be activated by high pressure [19] that can be interpreted as a process of relaxation of crystalline $GeSe_2$ as a result of pressure increase or as a result of presence of structural fragments (crystalloids) LTPM which takes place in amorphous $GeSe_2$ film consisting, in accordance with CPPCSGL as well as [22, 23] data, from fragments of structure of both PMs. But in any case, one should not already say about the pure enantiotropic transition because, on definition, the enantiotropic transition must take place at normal pressure and in crystalline, but not in non-crystalline, substance. Nevertheless, the presented facts give evidence that LTPM is significantly more stable at temperatures below T_{tr} than HTPM that allows to state that the discussed phase polymorphous transformation is enantiotropic one. Some results of presented discussion are shown in Fig.1.

2.2. Structure of vitreous GeSe₂

Several structural models of vitreous $GeSe_2$ are known.

The model of a continuous random network (1973) of Poltavtsev and Pozdniakova [25] is practically not distinctive from Zachariazen's model – all $GeSe_{4/2}$ tetrahedrons are connected in vertexes through Se atoms.

In 1979 Bridenbaugh, Phillips, Griffits and others [26] proposed a layered structure for v-$GeSe_2$ constructed from large ribbon-like structural units (clusters) called by the authors "outrigger-raft". These structural units are obtained by extraction from the layer of HTPM. Along edges of ribbons the Se atoms are joined in pairs by Se-Se bonds.

In the beginning of eighties works of Lucovsky and others [27] and Nemanih and others [28] were published where authors proposed models of structure containing both tetrahedrons, connected along edges, and tetrahedrons, connected in vertexes that is the model of chemically ordered continuous random network.
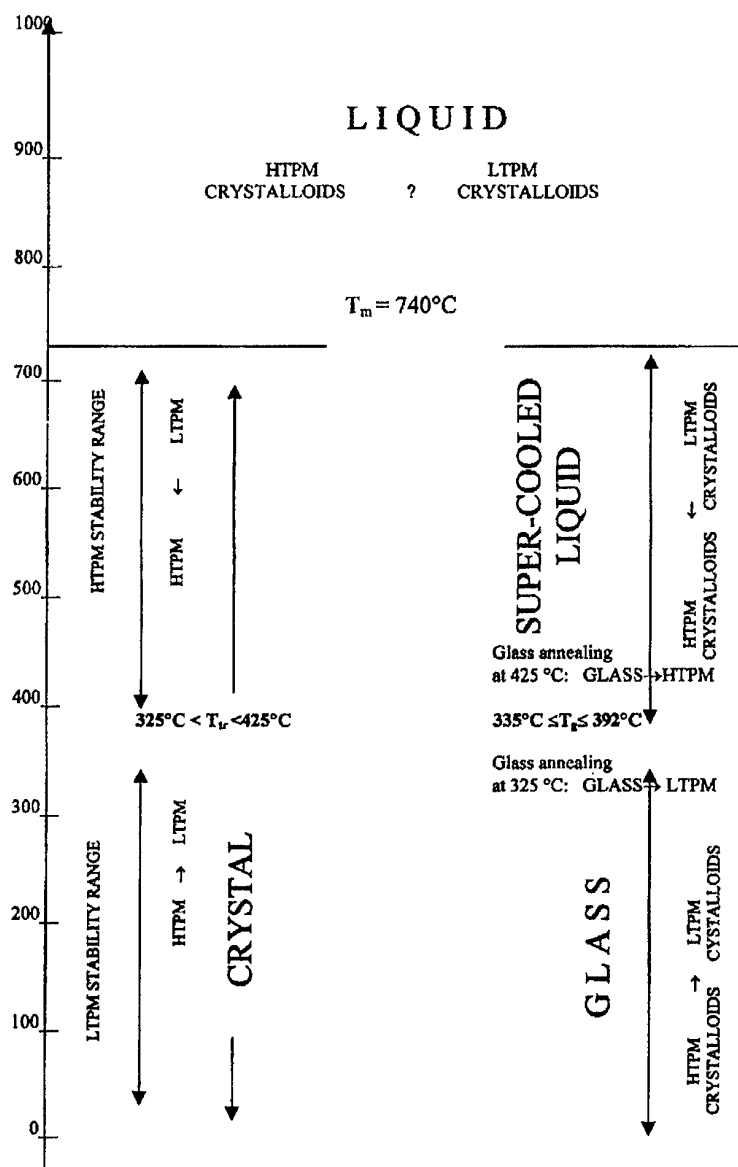
Fig. 1. Varieties of condensed state of $GeSe_2$.

In 1986-87 Sugai [23, 29] proposed a new stochastic random network model of germanium and silicon chalcogenides. The model is based on author's experiments who discovered existence of two different microcrystalline states (phases) – HTPM and LTPM obtained by photo-irradiation of vitreous $GeSe_2$ samples (and also obtained by vacuum deposition of amorphous films) by the beam of He-Ne laser (6328 A) of various intensity – higher and lower than the threshold (≈ 0.7 kW/cm^2). The stochastic random network model is characterized by one parameter P representing the probability of the ratio of chemical bonds of edge-shared tetrahedrons and chemical bonds of corner-shared tetrahedrons. P can be changed: it decreases at irradiation with intensity lower than the threshold and increases at irradiation with intensity higher than the threshold. The stochastic model gives, in the author's opinion, equal possibilities for photo-induced crystallization in two different crystalline phases while the "outrigger-raft" model – only one possibility.

Change of the ratio of chemical bonds of edge-shared tetrahedrons and corner-shared tetrahedrons (P) that was concluded basing on comparison of intensities of corresponding modes of Raman scattering A_1^c (219 cm^{-1}) and A_1 (202 cm^{-1}) was confirmed by other investigators as well. It is known [22-23] that Raman-spectra of HTPM are characterized by intensive bands 211 and 216 cm^{-1}, and LTPM is characterized by 201 cm^{-1} band. The works [22, 30-32] expand and make deeper investigations of problems studied by Sugai, confirming in the first place, presence of corner-shared

and edge-shared tetrahedrons in glass and glass-forming liquids, and, in the second place, fixing their different quantitative ratio.

2.3. Outdated ideas - the deadlock for solving problems of glass structure

Sugai has constructed his model from stochastically joined in three-dimensional network two types of "molecules": tetrahedrons $GeSe_{4/2}$ and edge-shared tetrahedrons $Se_{2/2}GeSe_2GeSe_{2/2}$ [26] leaving aside the problem of short-range and intermediate-range ordering.

In works [22, 27, 28, 31, 32] the problem of the short-range and intermediate-range ordering has been mentioned directly or indirectly, but only the question of similarity of the intermediate-range order of glass and liquid to HTPM structure has been discussed. For example, in the work [32] it has been stated that at lesser liquid's cooling rates the medium-range structure is topologically more similar to a crystal structure. At that, a layered crystal, i.e. HTPM, is meant. The short-range ordering, if mentioned, has been considered in passing, without any detailed analysis.

As we can see, one of the most important aspects in all considered models of structure of non-crystalline germanium diselenide is the aspect concerning conservation of similarity of its structure to the structure of crystalline germanium diselenide. Such approach is also typical for another non-crystalline substances (for example, for v-SiO_2) beginning from Lebedev [5] and Zachariasen [8]. For example, since Zachariasen's times it is considered that the short-range order (SRO) in glass and crystal is the same. In this seemingly natural thesis a deadlock for solving the problem of glass structure has been made long ago.

During about 20 last years most investigators of non-crystalline substance structure have been already saying about the intermediate-range order in non-crystalline substance outside limits of the short-range order. The progress is evident. The situation has been lead out to the higher level of understanding. But the deadlock has not been broken yet. There is no a generally accepted definition of the IRO. There is no understanding of insufficiency, and moreover – falseness, of the concept of presence in an individual non-crystalline substance of a single short-range order and a single intermediate-range order.

The exit of the deadlock has been proposed in the CPPCSGL concept [11-15]. In the framework of this concept the definition of IRO has been formulated, the notion of multiplicity short- and intermediate-range orders in an individual non-crystalline substance has been introduced corresponding multiplicity of different polymorphous modifications taking part in formation of its structure. Therefore, the described deadlock situation has been liquidated and the way for further development of understanding of an individual non-crystalline, and particularly vitreous, substance structure has been opened.

According to the CPPCSGL concept, the feature of the short-range ordering in vitreous $GeSe_2$ is presence, mainly, of two types of SRO, with two different atoms taken as a reference point. In the first case it is a germanium atom surrounded by four selenium atoms $GeSe_{4/2}$, and, in the second case, it is a selenium atom surrounded by two germanium atoms $SeGe_{2/4}$. As we can see, both SROs are in agreement with the principle of the chemically ordered network [27, 28]. It must be noted straight away that each of these SROs has its own variations: differences in bond lengths Ge-Se and interbond angles Ge-Se-Ge and Se-Ge-Se in corner-shared and edge-shared $GeSe_{4/2}$ [28], i.e. SROs around Ge atoms and SROs around Se atoms in LTPM and HTPM are different.

The intermediate-range ordering in v-$GeSe_2$ is characterized mainly by two alternating intermediate-range orders: IRO inherent to HTPM (two-dimensional layered structure) and IRO adopted from LTPM (three-dimensional network structure). Each of these IROs includes variations of the short-range order corresponding to one or another PM.

On the base of mentioned works [22, 23, 27-29, 31, 32], from positions of the concept of polymeric polymorphous-crystalloid structure, the conclusion has been made [13, 15, 33] that the structure of vitreous $GeSe_2$ (and glass-forming liquid) is formed by co-polymerized (de-polymerized) crystalloids (structural fragments without a long-range order) of layered (two-dimensional) HTPM and three-dimensional LTPM which are joined in glass in a single three-dimensional network characterized by alternation of mainly two intermediate orders inherent to HTPM and LTPM.

2.4. Structure of GeSe$_2$ amorphous films and liquid

According to Sugai's data [29] Raman spectra of amorphous GeSe$_2$ films obtained by vacuum deposition show the structure similar to that of glass obtained by quenching from melt shows.

Data on viscosity of Ge-Se liquid [37] show that GeSe$_2$ in the liquid state starting from melt temperature ~740 ^{0}C to ~1000 ^{0}C behaves as a chemical compound, i.e. its short-range ordering is similar to that of the crystal substance. The structure of the glass-forming liquid is, according to the Tool's kinetic theory of glass-formation [3], a "precursor", and, taking into account fictitious, or structural temperature T$_f$, an analogue of glass structure.

Investigations of GaSe$_2$ melt at 771 ^{0}C by the neutron diffraction method have shown that its structure is mainly analogous to glass structure [30].

Authors of the work [31] assumed that similarity of liquid and glass structures is confirmed by similarity of Raman spectra of vitreous samples at 420 ^{0}C and melt at 730 ^{0}C.

Thus, there is no principal difference between structures of glass, deposited films and glass-forming liquid. So, the conclusion can be made about similarity of structures of glass, obtained by quenching from melt, films, obtained by vacuum deposition, and liquid. Difference of their structures, one can think, is concluded in the extent of co-polymerization of crystalloids which is the most in solid glass, some lesser in deposited films, and even lesser in liquid. As for structures of solid glass, obtained in different conditions, or liquids at different temperatures, they differ, in accordance with the CPPCSGL, in ratio of crystalloids of different PMs, and, seemingly, in their dimensions – the higher the temperature of tempering the lesser the dimensions.

2.5. Relaxation processes in vitreous GeSe$_2$ at heating. Physical-chemical essence of glass transition temperature T$_g$

In the temperature range of 250-350 ^{0}C which directly precedes the glass-transition temperature (T$_g$ according to several authors lays in the range of 335-392 ^{0}C [20, 31, 38]) smooth exothermal rise is observed on the thermogram of differential scanning calorimetry (DSC) obtained at 10 K/min heating rate [38]. Raman-spectra at temperatures 250, 300 and 350 ^{0}C show some increase of relative intensity of A$_1$ band inherent to LTPM (201 cm^{-1}) and decrease of intensity of HTPM band (216 cm^{-1}) [31].

It is known that for individual substances the transition from HTPM to LTPM is followed by exothermal effect [39]. Therefore, data of DSC and Raman-spectra evidence that at heating of GeSe$_2$ glass in the temperature interval that precedes Tg a partial transformation of HTPM crystalloids in LTPM crystalloids takes place with concentration increase of the latter that is confirmed by annealing of non-crystalline GeSe$_2$ films at 325 ^{0}C leading to LTPM crystallization [22]. DSC and Raman-spectra in described experiments show transformation of a part of containing in glass HTPM crystalloids in LTPM crystalloids in the range "~250 ^{0}C – Tg" – the process that can be identified as the latent period preceding LTPM crystallization.

Higher T$_g$ temperature on DSC thermogram [38] the endothermal effect is observed. The Raman-spectrum [31] shows decrease of A$_I$ band intensity that characterizes vibrations of corner-shared tetrahedrons, and increase of A$_I^c$ band intensity that characterizes edge-shared tetrahedrons (HTPM). The ratio of band intensities I(A$_I^c$):I(A$_I$) changes from 1:3 (below T$_g$) to 1:1 in the range T$_g$-T$_c$ (T$_c$ – the crystallization temperature). The 1:1 ratio characterizes overcooled liquid just before the beginning of HTPM crystallization that coincides with the ratio of corner-shared and edge-shared tetrahedrons, also equal 1:1, for crystallized HTPM. This fact allows to evaluate quantity of corner-shared and edge-shared tetrahedrons from the ratio of band intensities of Raman-spectra, and this way a share of structural fragments (crystalloids) of HTPM and LTPM in glass and glass-forming liquid. In the interval "T$_g$-T$_c$" the Raman-spectra, therefore, show disintegration of LTPM and growth of HTPM crystalloids concentration.

The polymorphous transition of LTPM in HTPM is followed, as it is known, by endothermal effect [39] that is just observed in DSC thermogram at temperatures higher T$_g$. The endothermal effect related with softening temperature of glass, formed from individual chemical substance with enantiotropic transformation in crystal state, represents energy (heat) absorbed by glass at structural transformation of LTPM crystalloids in HTPM crystalloids that is a part of polymorphous

transformation heat at enantiotropic transition LTPM → HTPM in crystal substance. If the latter is known, it is possible, having measured energy absorbed at glass softening, to evaluate concentration of HTPM and LTPM crystalloids ratio in glass. It would be rather useful to compare such evaluation with evaluation of concentration ratio HTPM → LTPM based on ratio of intensities of Raman-spectra bands. Thus, both DSC and Raman-spectra evidence that in the temperature range of T_g instability of LTPM structure fragments is observed that is also confirmed by annealing of non-crystalline $GeSe_2$ films at 425 ^{0}C (some lower than T_c in DSC thermograms) leading to HTPM crystallization [22].

If at crystallization of non-crystalline $GeSe_2$ films at 325 ^{0}C LTPM is formed and at 425 ^{0}C HTPM is formed, it means that in the interval of 325-425 ^{0}C the equilibrium temperature between these crystal modifications is located, i.e. the temperature of their enantiotropic transformation T_{tr}.

Therefore, at heating of glass in the range which directly precedes Tg, transformation of HTPM structure fragments (crystalloids) in LTPM crystalloids takes place. Higher Tg, in the Tg-Tc interval, a transformation process goes (and significantly more intensive due to higher temperature) in reverse direction. Tg expresses itself as a temperature point where inversion of inter-transformation of structural fragments of HTPM and LTPM takes place, as a temperature point separating stability regions of LTPM and HTPM crystalloids of $GeSe_2$, regions in which latent processes in glass take place preceding LTPM crystallization (lower T_g) and HTPM crystallization (higher T_g), and processes of glass softening, its de-polymerization and transformation in super-cooled liquid followed by increase of HTPM crystalloids concentration and their consequent crystallization. T_g is genetically related with temperature of enantiotropic transformation T_{tr} in crystal substance; T_g in glass is analogous to T_{tr} in crystal substance.

If glass is heated with the rate at which HTPM:LTPM crystalloids ratio do not reach a critical level for the beginning of crystallization during the time of passing the T_g-T_m interval (T_m − the melting temperature), the substance will pass the temperature interval of super-cooled liquid existence without crystallization and come to liquid state at T_m. At lesser heating rates, the substance crystallizes and then this crystalline HTPM phase melts.

2.6. Relaxation of glass-forming liquid

In the work [37] it is shown that just after melting (higher than 712 ^{0}C) of HTPM $GeSe_2$ films the intensity of A_1^c band (HTPM) decreases and intensity of A_1 band (LTPM) increases that evidences, in our opinion, on generation in liquid, along with HTPM structural fragments, of LTPM structural fragments. At increasing liquid temperature to 720-730 ^{0}C, as it was noted before, the band intensity ratio shifts to increase of LTPM crystalloid concentration.

The fact of generation of both HTPM and LTPM in melt along with mentioned data on polymorphous-crystalline structure of liquid is very important: cooling such melt below Tg will lead to co-polymerization of structural fragments (crystalloids) of different PMs that obstructs melt crystallization, increase viscosity of melt and promotes glass formation.

Liquid state at certain temperature is characterized by a certain concentration ratio of crystalloids of different PMs. At temperature changes the inverse reaction of crystalloids inter-transformation takes place: HTPM →LTPM.

During cooling of liquid below the melting temperature there are two main processes take place. The first one is the process of co-polymerization of crystalloids of different PMs leading to viscosity increase and obstructing melt crystallization.

The second process is conditioned by the fact of passing of liquid of the HTPM stability range and LTPM instability range in the interval T_m-T_{tr}. It is naturally to expect that in these conditions crystalloids inter-transformation will be shifted in direction of HTPM fragments concentration increase and LTPM fragments disintegration is becoming apparent as the process of de-polymerization of super-cooled liquid going along with the main process of its polymerization.

At high cooling rate the first process (co-polymerization) prevails, overcooled liquid passes the LTPM instability range, having conserved, along with increasing HTPM crystalloids concentration which is sufficient for glass formation, LTPM crystalloids concentration. Then the substance is cooled being in glass state.

If the cooling rates is less than critical one, all LTPM crystalloids have enough time to transform in HTPM crystalloids before reaching the temperature range (T< T_{tr}) where LTPM is stable and HTPM is unstable. In this case super-cooled liquid crystallizes as HTPM.

Long aging of cooled substance at temperature directly under T_g in the high-temperature part of the LTPM stability range can lead to glass crystallization as LTPM, as it was shown for amorphous $GeSe_2$ films annealed at 325 ^{0}C [22].

Thus, relaxation of $GeSe_2$ glass-forming liquid at cooling, depending on change of the temperature factor, can results in formation of glass, HTPM or LTPM.

2.7. Relaxation processes in vitreous $GeSe_2$ caused by photo-irradiation

Let us consider now relaxation processes taking place in the result of the other type of external influence – photo-irradiation, in particular He-Ne laser irradiation (λ=6328 A).

In fresh vacuum deposited non-crystalline $GeSe_2$ films at He-Ne laser irradiation a shift of optical absorption edge is observed in the direction of shorter (the yellow region) wave lengths (photo-enlightenment) at 300 K and in the direction of longer (the red region) wave lengths (photo-darkening) at 77 K [40].

In the Sugai's experiment [23] the luminous flux of the He-Ne laser (less than 0.7 kW/cm^2) changed the intensities ratio $I(A_1^c):I(A_1)$ bands from 0.43 to 0.33 (the shift in the direction of LPTM concentration increase). At the flux more than 0.7 kW/cm^2 the intensities ratio $I(A_1^c):I(A_1)$ changed from 0.43 to 1.0. (the shift in the direction of HTPM, to the yellow region of the spectrum). In this experiment it was possible either to crystallize LTPM of red color (in the first case) or to crystallize HTPM of yellow color (in the second case).

The shift of the adsorption edge in the process of photo-irradiation (with corresponding change of the band intensities ratio responsible for LTPM and HTPM) visually, in color (yellow-red), demonstrates the physical-chemical nature of relaxation processes - mutual transformation of structural fragments of different PMs preceding photoinduced crystallization.

Photo(thermo)-darkening and photo(thermo)-enlightenment are photo(thermo)-indication of the latent pre-crystallization processes – the processes of transformation of HTPM crystalloids in LTPM crystalloids at darkening and LTPM crystalloids in HTPM crystalloids at enlightenment taking place during the latent periods which directly precede crystallization of LTPM and HTPM.

2.8. High pressure and relaxation processes in $GeSe_2$

The relaxation process of crystalline HTPM of $GeSe_2$ under influence of high pressure with phase identification by Raman-spectroscopy goes as follows [19]. Single crystal HTPM at pressure increase to 6,2 GPa loses its crystal structure completely and trnsforms in disordered non-crystalline substance, the color of the sample being changed from yellow to red. At further pressure increase to 7 GPa the transition from the disordered phase to the crystalline low-temperature polymorphous modification of $GeSe_2$ is observed. Further pressure increase (8-12.5 GPa) leads to transformation of LTPM in the disordered phase that becomes dark and nontransparent. If pressure was not higher than 10 GPa, the process turned out to be reversible: pressure removal caused $GeSe_2$ relaxation leading to recovering of HTPM. Correspondingly, the color reverse takes place to yellow color.

The character of Raman-spectra change, given in [19], as well as change of the sample color both at increase and removal of pressure, allow on the base of CPPCSGL to make the conclusion that relaxation of $GeSe_2$ at pressure increase present gradual transformation of HTPM in LTPM with formation of an intermediate phase cocnsisting of cristalloids of both PMs which concentration ratio changes with pressure change: at its increase to 7 GPa LTPM crystalloids concentration increases and HTPM crystalloids concentration decreases. The reverse process takes place at pressure decrease (from 7 GPa).

Pressure increase higher 8 GPa leads to LTPM destruction and formation of crystalloids of some new, in our opinion, polymorphous modification and, as a result of that, the intermediate disordered phase is formed again. At further pressure increase higher 12.5 GPa the crystalloids concentration of the new PM can, finally, reach 100% and then a new crystalline phase of high

pressure will appear, possibly one of that mentioned in the beginning of this paper. We suggest this prognosis basing on main theses of CPPCSGG [11-15].

3. Chalcogenides GeS₂, SiSe₂, SiS₂. Relaxation processes in glass under influence of photo-irradiation

GeS_2, like $GeSe_2$, exists at normal pressure as high-temperature and low-temperature polymorphous modifications (HTPM and LTPM). The former forms a layered structure from tetrahedrons $GeSe_{4/2}$, one half of which are corner-shared and the other - edge-shared. The latter presents a three-dimensional network of corner-shared tetrahedrons. GeS_2 glass, according to interpretation of Raman-spectra and diffractometry data, built of corner-shared and edge-shared tetrahedrons, the average distance between atoms Ge-S corresponds with good approximation to bond lengths of both crystal PMs [20] that evidences in favor of the concept of polymorphous-crystalloid structure of glass according to which glass consists of co-polymerized fragments of structure of different PMs without a long-range order (crystalloids) [18]. T_g of v-GeS_2 is equal to 495 ^{0}C that practically coincides with the phase equilibrium temperature of HTPM and LTPM (with S excess) in the Ge-S phase diagram [20], i.e. here also, like the case of $GeSe_2$, a genetic relation is observed between T_g and the temperature of enantiotropic polymorphous transformation [33-36].

Photoinduced crystallization of vitreous GeS_2 according to Sugai's data [29] causes, depending on radiation intensity, crystallization of LTPM or HTPM that shows complete analogy of relaxation processes taking place in GeS_2 and $GeSe_2$ at photo irradiation.

Unlike germanium chalcogenides, SiS_2 and $SiSe_2$ have HTPM where all tetrahedrons are edge-shared.

Glass structures SiS_2, $SiSe_2$, GeS_2, $GeSe_2$, according to Sugai [29], can be characterized by one parameter P representing a ratio of probabilities of existence of edge-shared and corner-shared bonds between tetrahedrons. Value of P can be changed by photo-irradiation. P decreases after irradiation with intensity lesser than the threshold and increases if intensity is higher than the threshold. For example, at irradiation of $SiSe_2$ glass by Ar-ion laser (4579 A) with 15 mW power during 310 min the intensity ratio $I(A_1^c)$: $I(A_1)$ decreases from 2.3 (P=1.05) to 1.8 (P=0.8) while irradiation with 30 mW power during just 10 min increases $I(A_1^c)$: $I(A_1)$ to 3.0 (P=1.41). Sugai's experiments are in complete compliance with our polymorhous-crystalloid concept of structure of these glasses and show that physical-chemical essence of processes taking place in vitreous disulfides and diselenides of germanium and silicon effected by photo-irradiation is mutual transformation of structural fragments of edge-shared and corner-shared tetrahedrons $AX_{4/2}$, i.e. mutual transformation of HTPM and LTPM crystalloids: HTPM → LTPM. If intensity of the external impact changes and exceeds a threshold, the direction of crystalloids transformation changes to the opposite direction that reflects ability of given substances to undergo enantiotropic polymorphous transformation in crystal state.

4. Arsenic selenide As₅₀Se₅₀. Relaxation processes.

Crystalline arsenic selenide $As_{50}Se_{50}$ exists in two polymorphous modifications. LTPM is isomorphic to molecular modification As_4Se_4. HTPM is not identified comprehensively by X-ray analysis. In works [41, 42] diffractograms of both PM are presented.

Annealing of amorphous films $As_{50}Se_{50}$ obtained by vacuum deposition at temperatures less than T_g (~180 ^{0}C) leads to crystallization of LTPM, and at temperatures higher than T_g - to crystallization of HTPM [42]. This situation is similar to situation with $GeSe_2$ films behavior described earlier and evidences that amorphous $As_{50}Se_{50}$ is apparently formed by crystalloids of both PMs. At $T<T_g$ the process of transformation of crystalloids HTPM→LTPM and crystallization of the latter take place. At $T>T_g$ the relaxation takes place in direction of HTPM concentration increase. Like the case of v-$GeSe_2$ the softening temperature is in this case a point where the reverse of mutual transformation direction HTPM→LTPM takes place that is the analog of the enantiotropic transformation in crystalline substance. Thus, the relaxation of amorphous $As_{50}Se_{50}$ also goes by two ways determined by heating temperature of films and results in two-variant crystallization depending on annealing temperature: as LTPM or as HTPM. The additional confirmation of this relaxation

model are data of differential scanning calorimetry of $As_{50}Se_{50}$ films [42] that show two exothermal peaks one of which is lower T_g and another is higher T_g. This model is well blended with the experiment on photo-amorphization of crystallized as LTPM $As_{50}Se_{50}$ films [42, 43]. From the CPPCSGL point of view the process of transformation of LTPM in HTPM is taking place (but not finishing) here. The result is the formation of a structure containing crystalloids of both PMs with the concentration ratio depending on time and intensity of radiation. Increase of duration or intensity of these two factors must lead to crystallization of amorphous films as HTPM. Authors [42] have interpreted described relaxation processes differently in some respects, although they are close enough to our point of view. They consider that $As_{50}Se_{50}$ glass has two structural modifications related correspondingly to low- and high temperature forms of crystal. Irradiation and annealing can move glass from one modification to another.

Assumptions of existence of different modifications of non-crystalline, including vitreous, substance have been proposed during more than 20 last years. Some data on that are presented in [11, page 50]. It has been also shown there, based on the concept of polymorphous-crystalloid structure of non-crystalline substance making first steps that time and being a general case of CPPCSGL, that "poly-amorphism" does not exist in the nature, and "polyforms" of non-crystalline substance represent a composition of structural fragments of different PMs without long-range order, having different concentration ratios which are able to change from 0 to 1 depending on time and intensity of external influence. During the last 20 years, neither proofs of existence of amorphous polyforms nor a strict definition of this notion have appeared. The "relationship" sign [42] is evidently not enough for such definition.

5. Selenium

5.1. Structure of crystalline and vitreous selenium

Selenium forms three types (α-, β- and γ-) of monoclinic PM [20] which structures are constructed from molecules Se_8. For Se_8 molecules the cis-configuration in arrangement of four consecutive linked atoms is inherent. α-monoclinic Se melts at 144 ^0C and spontaneously transforms in hexagonal Se; β-modification behaves similarly but at temperatures higher than 100 ^0C [20] (Fig.2).

Rhombohedral selenium constructed from Se_6 molecules is also known [44]. The thermodynamically stable Se modification is hexagonal PM consisting of spiral chains of atoms [20] with trans-configuration atom arrangement in four-fold fragments of the chain.

Analysis of IR- and Raman-spectroscopy, X-ray diffractometry, UV-photoelectron spectroscopy data as well as structural models proposed by Lukovsky [45] and other authors [20] allows to make the conclusion based on CPPCSGL [11-15] that vitreous selenium is constructed from a tangle of chains consisting of fragments of 8-fold rings of monoclinic PM, fragments of 6-fold rings of rhombohedral PM (in smaller amount) and fragments of chains of hexagonal selenium [46].

5.2. Structural relaxation in crystalline and vitreous selenium under temperature influence

Relaxation processes in metastable PMs (MSPM) at temperature influence manifest themselves on phenomenological level as polymorphous transformations "monoclinic PM → hexagonal PM" (in single crystal samples the beginning of transformation is fixed after heating during 630 min at 70 ^0C [47] and "rhombohedral PM → hexagonal PM" at temperature higher 105 ^0C [44]. Both transformations are characterized by irreversibility that shows monotropic character of the performing phase transition.

Investigations of viscosity-elastic properties and strain relaxation in vitreous selenium, carried out by Bomer and Angel [47], have shown that at heating of glass in the temperature range of 27-42 ^0C the fraction of ring-like conformations sharply decreases and the fraction of chain-like conformations sharply increases in softening glass structure ($Tg \approx 37\pm10$ ^0C). Such change of "ring-chain" ratio is identified by authors as a phase transition between ring and chain structures. From CPPCSGL positions the presented facts are considered as structural transformation in glass Se phase of crystalloids of monoclinic MSPM in crystalloids of stable hexagonal PM (SPM), as the latent pre-

crystallization period preceding crystallization of hexagonal SPM. The beginning of this crystallization is fixed at 50 ^{0}C [48].
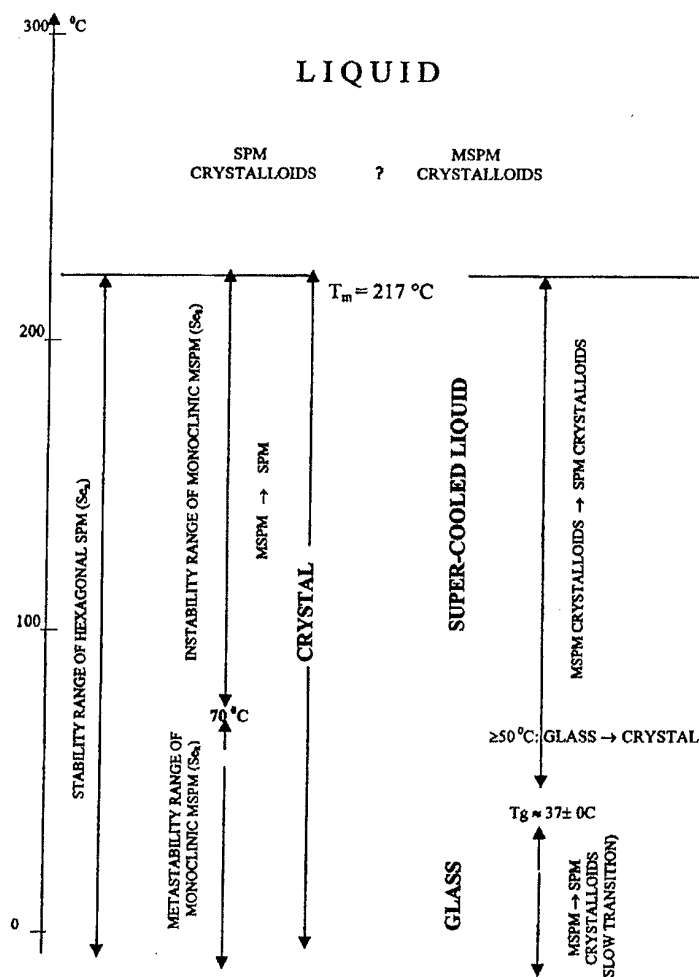
Fig. 2. Varieties of condensed state of Se.

As it can be seen from presented data, relaxation processes in vitreous selenium taking place at heating are similar to that in crystal substance (transformation of MSPM crystalloids in SPM crystalloids – "MSPM→ SPM"), but they begin at lower temperatures that is related, in our opinion, with greater energy of the disordered glass network, with heterogeneity of glass structure and the activation role of presented structural fragments of hexagonal SPM.

5.3. Phenomenological aspects of liquid selenium relaxation at cooling

Heating of crystallized hexagonal PM leads to its melting at 217 ^{0}C. Diffractometry data, as well as data on the viscosity temperature dependence [20, 48], give evidence that the melt structure is very similar to glass structure and there is also a statistical distribution of cis- and trans- configuration of selenium that is characteristic for ring and chain structures. Formation in melt of fragments of SPM and MSPM, change their ratio with temperature change [48] evidences that the main physical-chemical feature of liquid selenium relaxation is mutual transformation of SPM and MSPM crystalloids "MSPM → SPM", unlike to the one-directional transformation "MSPM→ SPM",- in crystal and glass states.

Mutual transformation of crystalloids "SPM → MSPM" and their growing polymorphous co-polymerization at melt cooling is the main cause hindering melt crystallization and increasing its viscosity right up to solid glass state. However, if the melt cooling rate is less than the critical cooling

rate (CCR), equal to 20 K/min [20], all crystalloids of MSPM will have enough time during cooling to transform in crystalloids of stable hexagonal PM and super-cooled liquid will crystallize. This observed fact evidences that CCR is a function of concentration and crystalloids transformation rate MSPM→ SPM.

5.4. Photo-irradiation and relaxation processes in vitreous selenium

Sugai [29] investigated the process of photo-crystallization in vitreous selenium at irradiation by the He-Ne laser (λ=6328 A) of different effective incident power (4 W/cm^2, 8 W/cm^2 and 8kW/cm^2). Raman spectra of monoclinic selenium is characterized by the peak at 251.5 cm^{-1} attributed to the A_1 mode of Se rings, hexagonal selenium chains are characterized by the 234 cm^{-1} peak. In glass spectra bands corresponding to modes of both PM are observed. At irradiation by the laser beam with increasing effective power the intensity of 251.5 cm^{-1} band decreases to almost complete disappearance at 0.8 kW/cm^2 power and the intensity of 234 cm^{-1} band increases that evidences on transformation of monoclinic modification crystalloids (cis-configuration of atom arrangement) in hexagonal modification crystalloids (trans-configuration). The same structural changes are observed at thermal annealing.

As these facts show, relaxation processes in vitreous Se and v-GeSe$_2$ under temperature influence and He-Ne laser irradiation are principally different. The relaxation in GeSe$_2$ follows two-variant LTPM- and HTPM-crystallization that is characteristic for substances with enantiotropic polymorphous transformation.

For selenium with its monotropic polymorphous transformations in crystal state, influence of temperature and photo-irradiation leads to the single way of structural relaxation in glass - increase of concentration of crystalloids of thermodynamically stable hexagonal PM at the expense of decrease of concentration of structural fragments of metastable monoclinic and, possibly, rhombohedral modifications. As the result, only single-variant crystallization is characteristic for v-Se.

6. Nanoheteromorphism and Ge-Se glass-forming system

The main cause and physical-chemical essence of glass formation is co-polymerization of different fragments of structure without long-range order. Difference in fragment's structures do not allow co-polymerizing substance to organize translational symmetry (a long-range order), i.e. to be crystallized.

Nanoheteromorphism in non-crystalline substance is co-existence of different structural fragments (structural inhomogeneities) having no long-range order. Nanoheteromorphism and nanoheteromorphous co-polymerization are the necessary and sufficient conditions for glass-formation.

In the case of individual chemical substances which are able to exist in non-crystalline, vitreous in particular, state, such structural fragments are crystalloids of different polymorphous modifications. If glass contains more than one component, i.e. it is formed of two and more individual chemical substances (ICS), presence of structural fragments of these ICS is sufficient for glass formation irrespective of existence or non-existence of their different PMs.

An intermediate variant is possible: presence in glass of crystalloids of different PMs modifications of one of ICS and structural fragments of the other (others) ICS irrespective of its (theirs) ability to form polymorphous modifications.

Let us consider from this point of view the glass-forming system Ge-Se. The glass-formation region in this system ranges from 100 at.% to ~ 45 at.% Se [20]. As it has been shown before, glass-formation in individual chemical substances GeSe$_2$ and Se is caused by co-polymerization of crystalloids of different PMs of GeSe$_2$ and Se. At adding Se to GeSe$_2$, Se atoms are built in between GeSe$_{4/2}$ tetrahedrons forming at first two- and then three-, four-fold chains, etc. When reaching Se content of 80%, all tetrahedrons turn to be isolated from each other by chemical bonds Se-Se and, as a result, all crystalloids belonging to HTPM and LTPM of GeSe$_2$ turn to be destructed. (The smallest crystalloid of GeSe$_2$ - the carrier of the intermediate-range order of this or that PM - contains two united tetrahedrons having common Se atom (atoms). It means that in the composition Ge$_{20}$Se$_{80}$ the

intermediate-range order (IRO), which is characteristic for both GeSe$_2$ PMs, vanishes away. All Ge atoms in this composition are connected to each other by selenium's two-fold chains which are also not characteristic for any of selenium PMs because they cannot form an intermediate-range order for any of selenium PMs. The minimum quantity of atoms necessary for formation of selenium IRO, with cis- or trans-configuration of atom arrangement, is four. The first chain of 4 selenium atoms appears (theoretically) in the composition where Se:Ge ratio is more than 6:1 (Ge$_{14.886}$Se$_{85.714}$).

Thus, glass-formation in ICS GeSe$_2$ and Se is ensured by nanoheteromorphism based on crystalloids inherent to different PMs. For the range of compositions where 80.0> Se >66.6(6) at.%, nanoheteromorphism is based on presence of crystalloids of different PMs of GeSe$_2$ and structural fragments of Se composed of two- and three-fold chains and not being IRO carriers of any PM. In the range of compositions where 80.0 < Se < 85.714 at.%, there are no structural fragments with IRO of GeSe$_2$ or Se. Here, nanoheteromorphisn is presented by structural fragments with three types of the short-range order: SRO, which is typical for GeSe$_4$, SRO, which is characteristic for three-fold Se chains, and SRO, which is typical for structural fragments consisting from a selenium atom connected by one bond (Ge-Se) with a germanium atom and by one bond (Se-Se) with a selenium atom. For the range of compositions 85.714< Se < 100 at.%, IROs of both selenium PMs, SRO of GeSe$_{4/2}$,and SRO, where selenium atom is connected with germanium atom and other selenium atom, are typical. From above, the conclusion can be made that in Ge-Se system the glass-formation region, which is characterized by concentration change of each elements of more than 40 at.%, only in the range of ~5.7% nanoheteromorphism is not related with structural fragments of different polymorphous modifications.

Thus, in pure GeSe$_2$ and Se the basis of relaxation processes is the transformation of crystalloids of one PM to crystalloids of another PM, being reversible in GeSe$_2$ and irreversible in Se. In the rest compositions relaxation processes are related with structural polymorphous transformations either partially, or (in compositions 80.0 < Se < 85.714 at.%) not related completely and follow to the classical relaxation theory [49].

7. Conclusion

1. Chalcogenides of Ge-Se system, individual chalcogenides GeS$_2$, SiSe$_2$, SiS$_2$, AsSe and chalcogen Se being as examples, it has been shown that glass represents a co-polymer of structurally different nanoheteromorphous fragments of crystal lattices without a long-range order. Nanoheteromorphism and co-polymerization of fragments with different structures is the main cause hindering crystallization of substance when liquid is cooled. In the case of individual chemical substance, nanoheteromorphous fragments are exclusively structural fragments of different PMs of given substance without a long-range order (crystalloids), having medium-range order inherent to one or another PM. A combination of different medium-range orders is the main feature of structure of individual chemical substances in vitreous state.

2. Glass-forming melt of individual chemical substances is also built of HTPM and LTPM crystalloids in the case of substances with enantiotropic polymorphous transformation in crystal state (GeSe$_2$, GeS$_2$, SiSe$_2$, SiS$_2$, AsSe), or it is built of SPM and MSPM crystalloids in the case of substances with monotropic transformation (Se). One in two physical-chemical essence of relaxation of cooled glass-forming liquid is as follows:

a)   the process of co-polymerization of crystalloids of HTPM and LTPM (or SPM and MSPM), and

b)   the process of disintegration of LTPM (or MSPM) crystallods in the range of their instability lower T$_m$ followed by partial de-polymerization and transformation in HTPM (SPM) crystalloids which are stable in this temperature region.

At cooling rates less than critical one, the latter process prevails, and glass crystallization in the form of HTPM (or SPM) takes place. At cooling rates higher than critical one, the former process prevails, and glass - co-polymer of HTPM and LTPM (or SPM and MSPM) crystalloids - is formed.

3. Relaxation of individual vitreous substance at heating is determined by relaxation behavior of its crystal analog which, at heating, undergoes: a) enantiotropic or b) monotropic polymorphous transformation.

In the a) case, at slow heating or annealing lower $T_g \approx T_{tr}$ glass crystallizes in the form of LTPM, and at slow heating or annealing in the T_g - T_m interval glass crystallizes in the form of HTPM (two-variant crystallization). T_g represents the temperature separating stability temperature regions of LTPM and HTPM crystalloids, the temperature where inversion of mutual transformation direction of LTPM and HTPM structural fragments takes place, the temperature which is the analog of the enantiotropic transformation temperature T_{tr} of crystal substance.

In the b) case at slow heating or annealing, glass crystallizes exclusively in the form of SPM (one-variant crystallization). T_g is the temperature of the beginning of the active stage of transformation of MSPM crystalloids in SPM crystalloids.

4. The main physical-chemical essence of relaxation processes in glass at photo-irradiation is mutual transformation of LTPM and HTPM crystalloids or transformation of MSPM crystalloids in SPM crystalloids.

Aknowledgement

References

[1] Soviet Encyclopedic Dictionary. "Soviet Encyclopedia" Publishers, Moscow (1962).
[2] I. V. Tananaev, Bulletin of Academy of Sciences of the USSR, **2**, 21-29 (1972).
[3] A. Q. Tool, J.Amer. Ceram.Soc., , **29**, 240 (1946).
[4] M. L. Frankenheim, J.Prakt.Chem., **54**, 430-476 (1851).
[5] A. A. Lebedev, GOI Proc., **2**, No.10, pp.1-20 (1921).
[6] D. I. Mendeleev, Glass Production, S.-Peterburg (1864).
[7] R. B. Sosman, The properties of Silica, N.Y. (1927).
[8] W. N. Zachariasen, J.Amer.Chem.Soc., **54**, 3841 (1932)
[9] M. A. Bezborodov, N. N. Bobkova, E. A. Porai-Koshitz et al., Diagrams of Vitreous
    Systems, Minsk: Belorussian Polytechnical Institute, 314 pp. (1959).
[10] C. H. L. Goodman, Nature, **257**, No.5525, p.370 (1975).
[11] V. S. Minaev, Vitreous Semiconductor Alloys, Moscow, "Metallurgia" Publishers (1991).
[12] V. S. Minaev, Glass Physics and Chemistry, **22**, 235 (1996).
[13] V. S. Minaev, Glass Physics and Chemistry, **24**, 597 (1998).
[14] V. S. Minaev, Glastech. Ber. Glass Sci. Technol., **71C**, 416 (1998).
[15] V. S. Minaev, Proceedings of ICG Annual Meeting 2000, May 15-17, Amsterdam (2000).
[16] Encyclopedic Dictionary of Physics. **7**, Oxford, London: Pergamon Press, (1962).
[17] V. S. Minaev, Proc.Intern.Conference "Non-Crystalline Semiconductors-89", **1**, 190, Uzhgorod,
    USSR (1989).
[18] G. Dittmar, H. Schafer, Acta Crystallogr., **B32**, 2726 (1976).
[19] Z. Popovic, Y. S. Raptis, E. Anastassakis, Z. Jakis, J.Non-Cristalline Solids, **227-230**,
    794 (1998).
[20] A. Frltz, Amorphous and Vitreous Non-Organic Solids. "Mir" Publishing House, Moscow,
    558 (1986).
[21] R. Azoulay, H. Thibierge, A. Brenac, J.Non-Crystalline Solids, **18**, 33 (1975).
[22] K. Inoue, Matsuda, K. Murase, Solid State Commun., **79**,905 (1991).
[23] S. Sugai, Phys.Rev.Lett., **57**, 456 (1986).
[24] M. Shimada, F. Dachille, Inorg.Chem., **16**, 2094 (1977).
[25] Y. G. Poltavtsev, V. M. Pozdniakova, USSR Academy of Sciences Proceedings. Non-Organic
    Materials, **9**, 853 (1973).
[26] P. M. Bridenbaugh, G. P. Espinosa, Y. E. Griffits, Y. C. Phillips, J. P. Remeika, Phys. Rev. B.,
    20,4140 (1979).
[27] G. Lucovsky, C. K. Wong, W. B. Pollard, J.Non-Crystalline Solids, **59-60**, 839 (1983).
[28] R. J. Nemanich, F. L. Galeener, J. C. Mikkelsen Jr., G. A. N. Connel, G. Etherington,
    A. C. Wright, B. N. Sinclair, Physica, **117B & 118B**, 959 (1983).

[29] S. Sugai, Phys.Rev.B, **35**, 1345 (1987).

[30] O. Uemura, Y. Sagara, D. Muro, T. Satow, J.Non-Crystalline Solids, **30**, 155 (1978).

[31] Y. Wang, M. Nakamura, O. Matsuda, I. Inoue, K. Murase, J.Non-Cryst.Solids., **198-200**, 753 (1996).

[32] Y. Wang, O. Matsuda, K. Inoue, K. Murase, J.Non-Crystalline Solids, **227-230**, 728 (1998).

[33] V. S. Minaev, Proceedings of ICG Annual Meeting 2000. May 15-17, Amsterdam. CD (2000).

[34] V. S. Minaev, Reports of Scientific Seminar "Tarasov Lattice and New Problems of Glass-Forming State. Mendeleev's University of Chemical Technology of Russia, p.73 (1999).

[35] V. S. Minaev, Bulletin of V.Tarasov Center of Chemitronics of Glass. Mendeleev Chemical Society of Russia. Mendeleev's University of Chemical Technology of Russia. Moscow, Russia, **1**, 55 (2000).

[36] V. S. Minaev, Glastech.Ber.Glass Sci.Technol., **73 C1**, 186 (2000).

[37] V. M. Glazov, O. V. Situlina, Proceedings of Academy of Sciences of the USSR. Ser.: Chemistry, **187**, 799 (1969).

[38] M. Afifi, Phys.Rev. B, **48**, 16304 (1993).

[39] V. I. Lihtman, Brief Chemical Encyclopedia. Moscow. "Soviet Encyclopedia" Publishing House, **4**, 194 (1965).

[40] A. V. Kolobov, B. T. Kolomiets, V. M. Lubin, N. Sebastian, M.A. Tagirjanov, Solid State Physics (Russian), **24**, 4, 1062 (1982).

[41] M. F. Kotkata, A. M. Shamah, M. B. El-Den, M. K. El-Mously Acta Physica Hungarica., **54**, 49 (1983).

[42] A. V. Kolobov, K. Shimakava, Electronic phenomena in chalcogenide glassy semiconductors, Editor K.D. Tsendin. S-Peterburg, "Nauka" Publishing House, 365 (1996).

[43] A. V. Kolobov, S. R. Elliott, Phylos. Mag. B., **71**, 1 (1995).

[44] Y. Miymoto, Japan J.Applied Physics, **19**, 1813 (1980).

[45] G. Lucovsky, The physics of selenium and tellurium. Eds. E. Gerlach, P. Grosse. Springer Vorlag. Berlin-Heidelberg-New-York, 178 (1979).

[46] V. S. Minaev, Proceed. 18th Intern. Congress on Glass. July 5-10, 1998. San Francisco, California. The American Ceramic Society. CD ROM. (1998)

[47] R. Bohmer, C. A. Angell, Physical Review B, **48**, 857 (1993).

[48] H. Rawson, Inorganic glass-forming systems. Academic Press, London & New York (1967).

[49] G. M. Bartenev, D. S. Sanditov, Relaxation Properties in Vitreous Systems. Novosibirsk (USSR): "Nauka" Publishing House (1986).

MICROPARACRYSTALLINE MODEL FOR MEDIUM-RANGE ORDER IN NON-CRYSTALLINE CHALCOGENIDES

M. Popescu, H. Bradaczek[a]

National Institute of Materials Physics, 76900 Bucharest-Magurele,
P.O.Box MG-7, Romania
[a]Research Center of EFG International, Dueppelstrasse 13, 14163 – Berlin, Germany

The medium range order in disordered chalcogenides has been explained by the existence of reminiscent crystal-like configurations with distorted arrangement of the atoms. Using the paracrystalline theory, two parameters have been defined for the characterization of the MRO in glass: paracrystallite thickness and paracrystallite distortion.

1. Introduction

One of the most important problems in the physics of amorphous materials in general and non-crystalline chalcogenides in particular is the structure at the atomic scale. The extent of the order in a disordered material is still a subject of controversy [1].

The short-range order (SRO) in a given solid is related to the chemical bonding. Therefore, a profound similarity does exist between the SRO in crystalline and non-crystalline state of the same compound.

The medium-range order (MRO) or intermediate-range order (IRO) is defined by the correlation between the positions of the atoms in the range 0.5 – 1 nm, in excess of those expected for an ideal Zachariasen-type continuous random network characterized by a random dihedral angle distribution [2].

It is very unlikely that a detailed physical theory will be developed to relate all macroscopic properties of glass with atomic processes without providing practical means of defining atomic geometry.

The "signature" of MRO in covalently bonded glasses is the first sharp diffraction peak (FSDP) or pre-peak in the X-ray diffraction pattern, I(Q). The intensity, half-width and position of this peak on the scale of the scattering vector, Q, are characteristic for every material. The FSDP of an amorphous solid exhibits high sensitivity against temperature, pressure, aggregation state, etc. [3-5].

The FSDP is situated at low Q values (1.0 – 1.5 Å^{-1}) and arises probably from correlation at distances of 4.5 – 6.0 Å rather than from simple nearest or next nearest neighbours.

In this paper we discuss the X-ray diffraction features of several amorphous solids exhibiting FSDP, with special emphasis on non-crystalline chalcogenides, in the frame of a new model based on the paracrystalline theory of Hosemann [6], proposed for disordered materials.

2. Structural models for medium-range order

Careful analysis of the X-ray diffraction patterns in many amorphous and glassy materials has shown that FSDP is a widely observed feature (e.g. in a-As [7], a-SiO_2 [8], a-As_2Se_3 [9]) but not universal (e.g. FSDP is lacking in a-Si [10]). This particular feature of many non-crystalline solids aroused much speculation as to its origin in real space.

Four main models for the atomic scale configuration, that determine the special aspects of MRO in amorphous solids, were developed up to day.

a) Microcrystalline model

The model was applied firstly to amorphous As_2S_3. Leadbetter and Apling [11] have calculated the correlation functions in real and wave vector space for small randomly oriented fragments of crystal structure. The agreement between the model and experiment was found to be poor. The strongest discrepancy in the radial distribution curves is related to the strong peak at about 4.5 Å, due to cross ring correlations in the crystal, which are absent in the experimental functions.

b) Layered model

As an alternative, the experimental results on the same $a-As_2Se_3$ were interpreted in the frame of a structure with disordered layers [3,12].

The fundamental evidence for layers in $a-As_2S_3$ was the presence of the FSDP and its near coincidence with the (020) reflection of the crystal. A layer is defined as two or more sheets or roughly parallel and planar atom groupings, which are bound mainly by non-bonded forces. In this model, the non-bonded interactions, i.e. interlayer correlations, give rise to the FSDP. The definition of the layer does not exclude single sheets of atoms wrapped over each other. Because the layers can be appreciably cross-linked by chemical bonds the structure approaches that of a cluster and, therefore, an ambiguous interpretation of FSDP cannot be avoided.

c) Clustered model

A cluster is defined as a group of atoms (in general greater than six) constrained to a particular internal geometry by chemical bonds. Clusters can be either chemically bonded within the main structure or packed randomly and held together by non-bonded forces. The first clustered model was developed by Phillips [13] and is represented by condensation of the so-called "outrigger rafts".

In the clustered model the MRO is expressed as intra-cluster correlations and from this order appears FSDP.

Nevertheless, the major difficulty with clusters (especially big cluster $\sim$ 20 atoms, as e.g. "outrigger rafts") is that they introduce too much medium-range order. To overcome this difficulty the clusters must be distorted but this implies a serious problem of stability.

d) Void correlation model

Fowler and Elliott [14] gave arguments to support the conclusion that FSDP is due to contributions of Fourier components from a broad region of the real space (including e.g. a density deficit at about 4.5 Å in the case of $a-As_2S_3$), rather than a distinct structural feature. They speculated that the presence of lone pairs in the amorphous solid, rather than clusters could cause such a density deficit. After Fowler and Elliott [14] lone pairs strongly repel each other and, therefore, force a structure to become more open, especially if the structure is disordered. The presence of lone pairs (absent in a-Si) forces an expansion of the average ring size, with the concomitant deficit in inter-atomic correlations near 4.5 Å, necessary for the observation of FSDP.

According to the void correlation model [15] FSDP is a chemical order pre-peak due to interstitial volume around cation centered structural units. The calculated positions of FSDP for some covalent glasses (SiO_2, GeO_2, $ZnCl_2$, $GeSe_2$) agree well with the experiment and the temperature and pressure dependencies of the FSDP can be, thus, explained in terms of density effects.

Although successful in many instances, the model cannot explain satisfactorily the difference in behaviour of the FSDP when the glass is subjected to uniaxial compression and when hydrostatic compression is applied. In both cases the peak intensity decreases [16].

All the above-described models fail to account for all details of I(Q) function. In general only FSDP or FSDP + main diffraction peak are examined in order to establish the validity of a model.

3. Paracrystallinity and the microparacrystalline model

The paracrystalline theory developed by Hosemann [6] and formerly applied to fibers, stems from the idea that the non-crystalline solid consists from crystalline, distorted configurations, that are preserved during crystal-amorphous or crystal-melt transition. These configurations are quasi-aligned in the disordered matrix. The general structure based on paracrystallites gives rise to an X-ray

diffraction pattern similar to that corresponding to a multilayer structure. First order intense peak is followed by higher diffraction order peaks with rapidly decreasing intensity.

Hindeleh and Hosemann [17] found a very important relation between the peak width and the diffraction order. There exists a linear dependence between the width of the diffraction halos, δb, and the square of the quadratic sum of the Miller indices for the basical paracrystalline plane, (00h):

$$\delta b = 1/D + [(pgh)^2/d] \tag{1}$$

In the case of layered structures, the basical layer plane can be assimilated to a (001) plane. The linear dependence $\delta b \sim f(h^2)$, where h is the diffraction order, is a strong argument for the existence of microparacrystallites as constituent elements of a given glass [18].

From the Hindeleh-Hosemann plot one can extract two important parameters. The intercept of the line with the ordinate gives the value 1/D, where D is the mean paracrystallite thickness normal to the paracrystalline base plane. From the slope of the right line one gets the paracrystalline distortion, g, as defined in the theory as the relative paracrystalline distance fluctuation:

$$g^2 = (d^2/\bar{d}^2 - 1)^{1/2} \tag{2}$$

where d is the net plane spacing, d^2 is the mean of d^2 and $\bar{d}$ is the averaged d, that is the quasi-periodicity.

For the ideal crystalline structure g = 0 and for the complete disappearance of crystal-like structural features g = 1.

The application of the theory of paracrystallinity to catalysts, bio-polymers, fibbers, synthetic polymers, glasses and melts [19,20] led to an empirical relation of a new kind of equilibrium state:

$$N^{1/2} g = \alpha^* \tag{3}$$

with $\alpha^* = 0.15 \pm 0.05$. N is the mean number of net-plane layers in a paracrystallite.

The equation 3 implies that there is a limit to the growth of paracrystal layers, N, depending on the magnitude of the paracrystalline distortion, g.

We must finally remark that, based on a wide range of data, Phillips [21] suggested that in vitreous SiO_2 there are clusters, which have the internal topology of cristobalite, a cubic structure of SiO_2 with density 5 % greater than vitreous SiO_2 and with the Si atoms arranged on a diamond lattice. The dominant surface structure of the cristobalite paracrystallites is expressed by (001) planes and the clusters are about 60 Å in diameter.

Taking into account the above discussed data, we developed a paracrystallite model for medium-range order, which was applied to vitreous SiO_2 and to a number of glassy chalcogenides.

In the case of chalcogenides, which are characterized by mean atomic coordinations between 2 and 3, the basical layers in crystals lose their intrinsic order by amorphization, but preserve the layer stacking along the distances of the order of paracrystallite thickness parameter. The type of structural element preserved in the glassy state seems to depend on the chemical composition of the material. The most stable structural planes of the corresponding crystalline phases are maintained in the disordered materials with ill-defined packing and they give rise to MRO structural effects. The existence of long-lived crystal-like clusters in melt, before quenching, leads to a lower free energy for gas-like + crystal-like configurations than for homogeneous gas-like atomic configuration [22].

Supposing the formation of paracrystallites in bulk chalcogenide glasses it is possible to treat the problem of medium-range order in the frame of the Hindeleh-Hosemann theory. Thus, after careful processing of the X-ray diffraction data, it is possible to get two parameters, which characterize the paracrystallites in the glass and, therefore, the atomic correlations: the paracrystallite thickness and the paracrystalline distortion.

4. Documented cases

We have applied the microparacrystalline model for medium-range order, firstly to vitreous SiO_2 and then to several representative glassy chalcogenides: $GeSe_2$, $AsS_{1.66}$ and As_2Se_3. Figure 1

shows the Hindeleh-Hosemann plot for vitreous SiO_2. From this plot the two MRO parameters were obtained: $D = 18.5$ Å and $g = 0.056$.
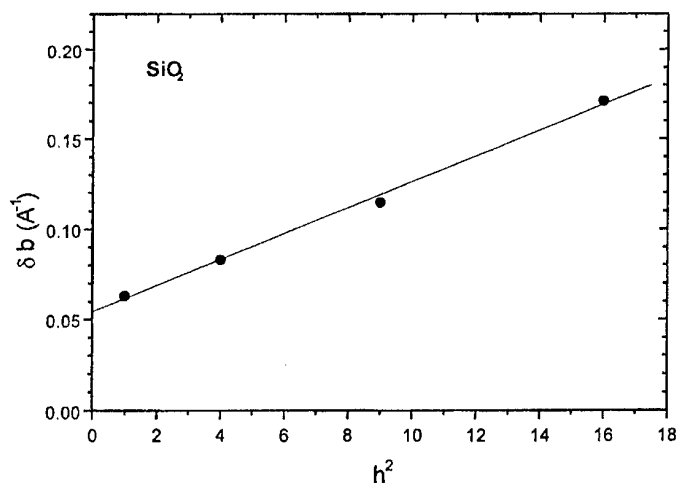
Fig. 1. Hindeleh-Hosemann plot for the determination of the paracrystallite parameters D and g in vitreous SiO_2.

The paracrystalline clusters in glassy SiO_2, after Phillips [24], are extended over a distance of at least 25 Å. Cristobalite domains with size ~60 Å were observed from TEM by Zarzycki [21]. Meade et al. [25] reported a mean size of quasi-ordered configurations of ~20 Å. The distortion of the paracrystallite is enough low, if one compares our result with the value reported by Hosemann et al. [26]: $g = 0.15$.

The peaks in the X-ray diffraction diagrams of $GeSe_2$ and $AsS_{1.66}$ [27] have been carefully measured, in order to draw the Hindeleh-Hosemann plots (see Fig. 2 and 3). The results show for glassy $GeSe_2$: $D = 69.6$ Å and $g = 0.071$, and for $AsS_{1.66}$: $D = 26.6$ A and $g = 0.068$. While the paracrystalline distortion is nearly identical in both cases, the paracrystalline thickness differs considerably, and this is an interesting result. The values of D extracted from the width of FSDP and reported in the literature are 60 Å for $GeSe_2$ and 30 Å for As_2S_3 [28].

a   b
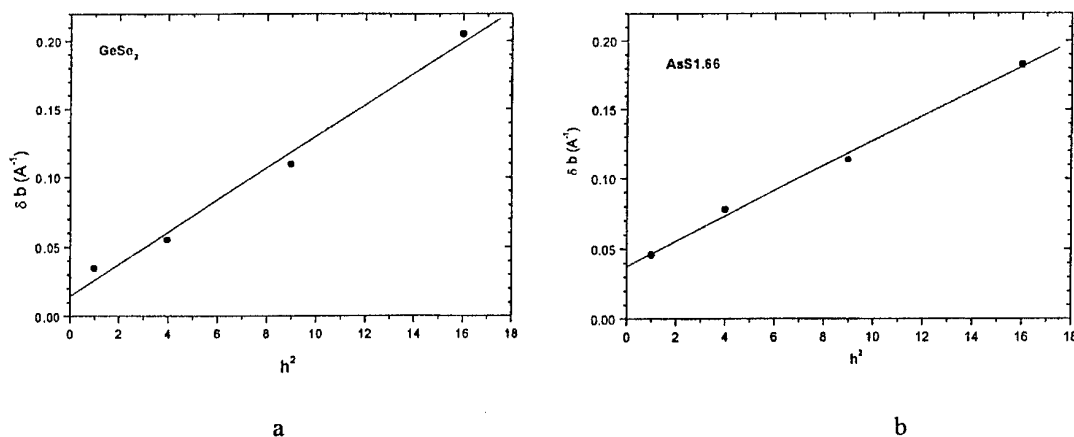
Fig. 2. The Hindeleh-Hosemann plot for the determination of the paracrystallite parameters in glassy $GeSe_2$ (a) and $AsS_{1.66}$ (b).

Finally we analyzed the cases of As_2Se_3 chalcogenide when heated above the softening temperature ($T_g = 215$ °C) at 400 °C and at 630 °C [29]. It is well known that, during heating, and even in the molten state, the MRO tends to develop itself, as evidenced by the amplification of the FSDP intensity. Figure 4 shows the results.
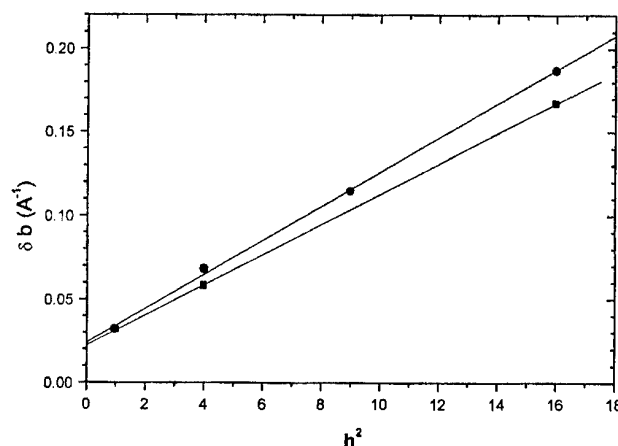
Fig. 3. The Hindeleh-Hosemann plot for an As_2Se_3 sample in the molten state at 400 °C (■)
and at 600 °C (●).

When the sample temperature is raised from 400 to 630 °C the paracrystallite thickness decreases from 45.1 to 42.1 Å and the paracrystalline distortion increases from 0.067 to 0.072. At the room temperature As_2Se_3 exhibit a D value of 30.4 Å [18] while g is 0.067. This discrepancy can be explained as follows. In the molten state few constraints are exerted on the disordered paracrystalline layers and, therefore, more relaxation is produced with the consequence of a better alignment of the layers. In the amorphous solid state the stacking of the disordered layers is more difficult to appear on a longer scale, because the constraint from the surrounding matrix is higher, and, therefore, the thickness of the paracrystallite is smaller.

5. Conclusions

A new model for medium-range order in non-crystalline chalcogenides has been introduced. The model is based on the old paracrystalline theory of Hosemann with one major amendment: the paracrystallites consist of the backbones of the original stable crystal corresponding to the chemical composition of the material (or crystal of the most approached composition), including as entities the planes of closest packed arrangement of the atoms. These planes represent the ultimate reminiscence of a crystal in the melt. For many chalcogenides these planes are not composed of ordered configuration of atoms as in the crystal, but are characterized by a disordered arrangement of atoms, reflected in the ring configuration with various number of atoms.

References

[1] S. R. Elliott, J. Non-Cryst Solids **97-98**, 159 (1987).
[2] W. H. Zachariasen, J. Amer. Chem. Soc. **54**, 4381 (1932).
[3] L. E. Busse, Phys. Rev. **B 29**, 3639, 5060 (1984).
[4] K. Tanaka, J. Non-Cryst. Solids **90**, 363 (1987).
[5] O. Uemura, Y. Sagara, D. Muno, T. Satow, J. Non-Cryst. Solids **30**, 155 (1978).
[6] R. Hosemann, Z.fur Physik **128**, 1 (1950); **128**, 465 (1950).
[7] B. Singh, S. Rajagopalan, K. L. Chopra, J. Appl. Phys. **51**, 1768 (1980).
[8] K. L. Chopra, K. S. Harshvardhan, S. Rajagopalan, L. K. Malhotra, Solid State
    Comm. **40**, 387 (1981).
[9] S. R. Elliott, J. Non-Cryst. Solids **81**, 71 (1986).
[10] Y. Montiel, H. Vincent, Z. Inorg. Nucl. Chem. **37**, 2053 (1975).
[11] A. I. Leadbetter, A.I. Apling, J. Non-Cryst. Solids **15**, 250 (1974).

[12] M. Popescu, in Physics and Applications of Non-Crystalline Semiconductors in Optoelectronics, Ed. A. Andriesh and M. Bertolotti, Kluwer Academic Publishers, NATO ASI Series, 3- High Technology, vol.36, Dordrecht (Boston) London, p. 215, 1996.
[13] J. C. Phillips, J. Non-Cryst. Solids **43**, 37(1981).
[14] T. G. Fowler, S. R. Elliott, J. Non-Cryst. Solids **92**, 31 (1987).
[15] S. R. Elliott, Phys. Rev. Lett. **67**(6), 711 (1991).
[16] K. Tanaka, J. Non Crystal. Solids **119**, 243 (1990).
[17] A. M. Hindeleh, R. Hosemann, J. Mat. Sci. Mat. **26**(19), 5127 (1991).
[18] H. Bradaczek, M. Popescu, J. Optoel. Adv. Mat. **2**(2), 153 (2000).
[19] W. Vogel, R. Hosemann, Acta Cryst. **A26**, 272 (1970).
[20] R. Hosemann, Physica Scripta **1**, 141 (1982).
[21] J. C. Phillips, Solid State Phys. **37**, 93 (1982).
[22] V. V. Brazhkin, J. Non-Cryst. Solids **124**, 34 (1990).
[23] A. R. Regel, V. M. Glazov, Fiz. Tehn. Poluprov. (russ.) **17**, 1729 (1983).
[24] J. C. Phillips, J. Non-Cryst. Solids **63**, 347 (1984).
[25] C. Meade, R. J. Hemley, H. K. Mao, Phys. Rev. Lett. **69**, 1387 (1992).
[26] R. Hosemann, M. P. Hentschel, U. Schmeisser, R. Bruckner, J. Non-Cryst. Solids **83**, 223 (1986).
[27] S. R. Elliott, Natutre **354**, 445, 12 Dec. 1991.
[28] Ke. Tanaka, Jpn. J. Appl. Phys. **37**, 1747 (1998).

INFLUENCE OF THE INTEGRATION LIMITS ON THE SHAPE OF PAIR CORRELATION FUNCTIONS OF NON-CRYSTALLINE MATERIALS

W. Hoyer, I. Kaban, Th. Halm

Institute of Physics, TU - Chemnitz, D-09107, Chemnitz, Germany

Influence of the termination effect on the shape of pair correlation functions and values of structural parameters of liquid and amorphous materials has been investigated. It is shown that termination of the diffraction curve at $Q_{min} > 0$ rather strongly affects the region around the first peak of $g(r)$ especially its left flank. On the other hand, presence or absence of a prepeak at low Q-values of the structure factor does not bring any difference to the pair correlation functions. Decreasing of the upper limit of the diffraction vector causes shift, decrease and broadening of the first peak of the pair correlation function. Besides, this yields spurious oscillations in the vicinity of the first and the second maximum of $g(r)$ of the liquid and amorphous materials. Therefore straightforward interpretation of the experimental data may be misleading. Some procedures to solve the problem are considered.

1. Introduction

Studies of non-crystalline structure are mainly based on the experimental determination of the X-ray or neutron diffraction curve as a function of the scattering vector Q ($Q = (4\pi/\lambda)\sin\theta$, where λ is the used wavelength and θ is half the scattering angle). Transformation of the scattering intensity $I=I(Q)$ to the pair correlation function $g(r)$ and (or) to the radial distribution function $4\pi r^2 \rho(r)$ yields such structural characteristics as the nearest neighbour distance r^J and the coordination number of the first coordination sphere as well as corresponding values for the higher coordination spheres which are important parameters of the short- and medium-range order.

The pair distribution function $g(r)$ can be calculated by Fourier transformation of the $S(Q)$ spectrum using the standard transformation technique:

$$g(r) = \frac{\rho(r)}{\rho_0} = 1 + \frac{1}{2\pi^2 r \rho_0} \int_0^\infty Q[S(Q)-1]\sin(Q \cdot r)dQ \qquad (1)$$

Here $\rho(r)$ and ρ_0 are the local and average number densities, respectively, and $S(Q)$ is the Faber-Ziman total structure factor [1] obtained from the coherent scattering intensity:

$$S(Q) = \frac{I_{e.u.}^{coh}(Q) - \left\{ \langle f^2(Q) \rangle - \langle f(Q) \rangle^2 \right\}}{\langle f(Q) \rangle^2} \qquad (2)$$

with

$$\langle f^2(Q) \rangle = \sum_j c_j f_j^2(Q), \qquad \langle f(Q) \rangle = \sum_j c_j f_j(Q), \qquad (3)$$

where c_j is the mole fraction and $f_j(Q)$ the total atomic scattering factor of the j-th component in the alloy.

The position of the first maximum of $g(r)$ is the mean nearest neighbour distance r^1. The coordination number

$$N = \int_{r_1}^{r_2} 4\pi r^2 \rho(r) dr \tag{4}$$

is the mean number of atoms within the coordination sphere limited by r_1 and r_2. The first coordination number can be estimated by several methods. Most commonly used ones are: i) symmetrical (the coordination shell is considered as symmetrical about a first maximum in the $g(r)$ curve, i.e. the right-hand side of the peak is made symmetrical with that on the left) and ii) integration from the left-hand edge of the first peak to the first minimum in the radial distribution function.

The transform in Eq.(1) requires data from $Q = 0$ to $Q = \infty$. In principle, the scattering intensity can be measured down to $Q = 0$. However, experimental limitations and in some cases additional small angle scattering lead to a lower limit $Q_{min} > 0$ for each diffraction experiment. On the other hand, the diffraction vector is terminated by a certain value Q_{max} which is determined by the wavelength used: $Q_{max} = 4\pi/\lambda$. As a result, the integrand in Eq.(1) is limited by Q_{min} and Q_{max}, that is:

$$g^{exp}(r) = 1 + \frac{1}{2\pi^2 r \rho_0} \int_{Q_{min}}^{Q_{max}} Q[S(Q) - 1]\sin(Q \cdot r) dQ \tag{5}$$

Due to such limitation of the diffraction vector, the resulting pair distribution function $g^{exp}(r)$ differs from the ideal $g(r)$. So-called termination or truncation effect yields spurious details on the pair correlation functions. This deforms the radial distribution functions, changes the position and profile of the maxima and minima and introduces errors in the calculated coordination numbers [2 – 5].

In this paper we examine influence of the termination effect on the shape of the pair correlation functions of the non-crystalline materials with low-coordinated (open) structure. Liquid Te and amorphous Ge-telluride have been chosen for the investigation.

2. Experimental

Neutron scattering experiment on liquid Te has been carried out on the double-axis spectrometer of the research reactor at Rossendorf. The neutron wavelength was $\lambda = 0.91$ Å and the accessible Q-values range – from 1.0 Å^{-1} to 9.35 Å^{-1}. The sample was contained in a sealed quartz tube (internal diameter 15 mm, wall thickness 1 mm). The overall uncertainty in the sample temperature was smaller than 5 K. The data correction procedure has been described in [6].

The X-ray diffraction experiments were performed with a θ -θ diffractometer using MoK$_\alpha$– radiation which has been selected by a focusing graphite monochromator placed in the diffracted beam. The X-ray intensity scattered at the free surface was measured by a scintillation detector with a pulse height analyser. The liquid Te temperature was constant within an error of about 1 K. The scattering intensity has been measured from 1.0 to 11.85 Å^{-1} of Q in the case of liquid Te.

The amorphous Ge$_{25}$Te$_{75}$ alloy was prepared by the melt-spinning technique. The X-ray intensity diffracted by the amorphous sample at room temperature was counted over the range of Q between 0.5 and 12.5 Å^{-1}. The correction and normalization of the experimental data were done as described in [7 –9].

3. Results and discussion

3.1. Liquid Tellurium

The experimental structure factors of liquid Te at 550 °C (neutron diffraction) and 500 °C (X-ray diffraction) are shown in Fig. 1. The differences between the results of X-ray and neutron scattering are mainly caused by the rather sensitive absorption correction of the neutron experiment. In both cases scattered intensity has been measured down to $Q_{min} = 1.0$ Å^{-1}. For smaller Q-values we have employed a parabolic extrapolation of $S(Q)$:

$$S(Q) = S(0) + AQ^2. \tag{6}$$

The value of $S(0) = 0.062$ has been taken from Ref. [10] and the coefficient A was determined by fitting the extrapolation function to the experimental $S(Q)$ at $Q = Q_{min}$.
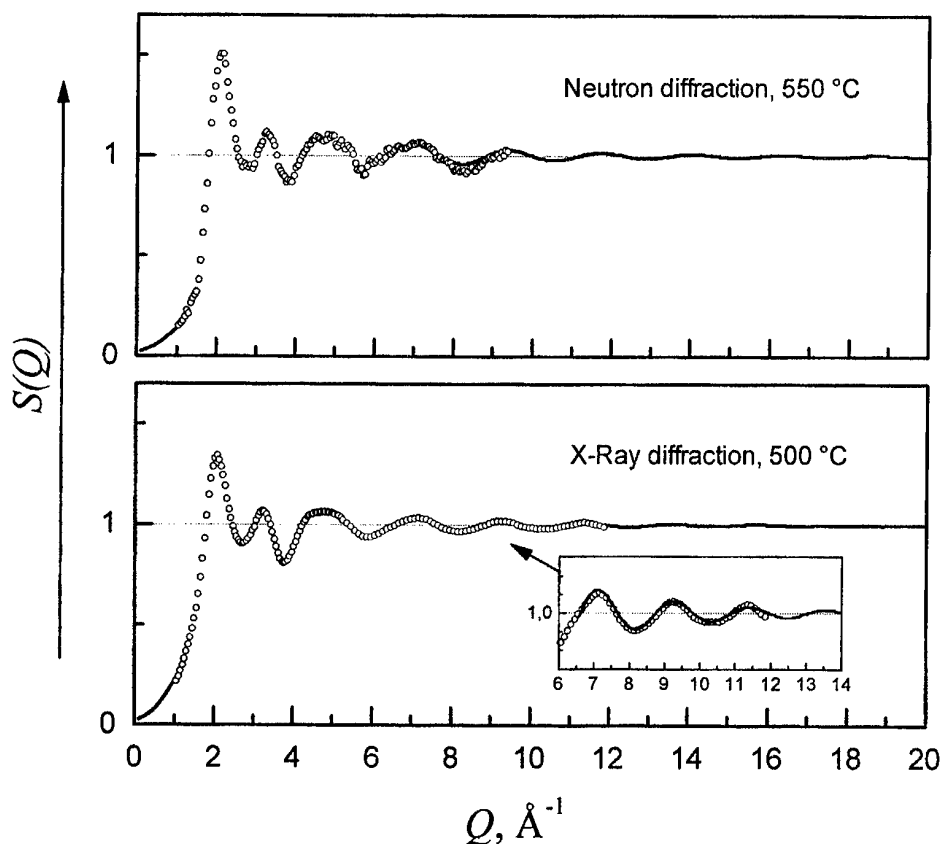
Fig. 1. Structure factors of the liquid Te: *circles* – experimental results; *lines* – extrapolation.

Fig. 2 shows the pair correlation and radial distribution functions calculated with Eq. (5) using lower integration limits of $Q_{min} = 0$ Å^{-1} and $Q_{min} = 1.0$ Å^{-1}. The upper integration limit was $Q_{max} = 9.35$ Å^{-1} for neutrons and $Q_{max} = 11.85$ Å^{-1} for X-rays. It is very good seen that the region around the first coordination shell, especially its left flank, is rather strongly affected. Termination of the structure factor at $Q_{min} > 0$ substantially increases the pair correlation and radial distribution function in the region of the first maximum that yields overestimated coordination number.
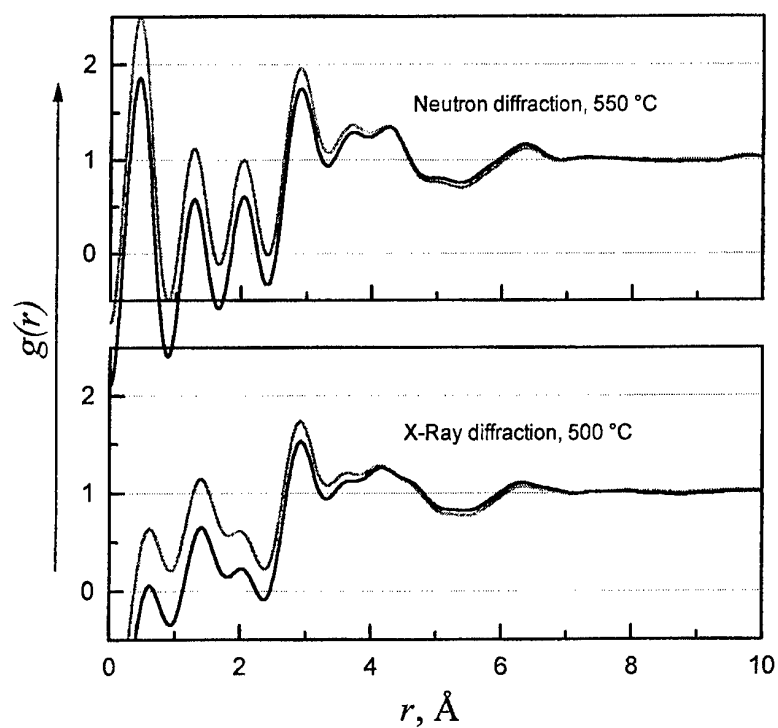
a)
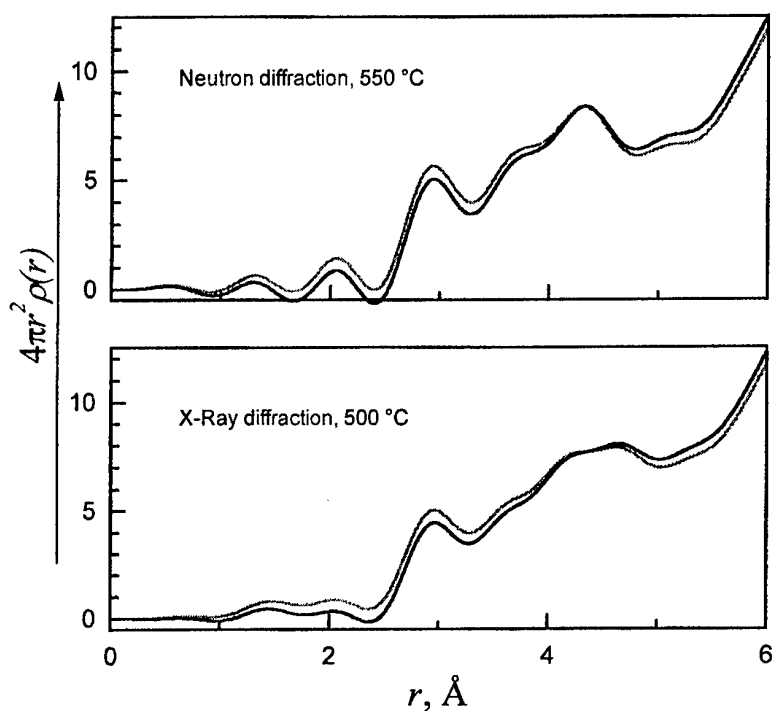
b)

Fig. 2. Pair correlation (a) and radial distribution (b) functions of liquid Te calculated with different integration limits Q_{min}: *black lines* - $Q_{min} = 0$ Å^{-1}; *gray lines* - $Q_{min} = 1.0$ Å^{-1}.
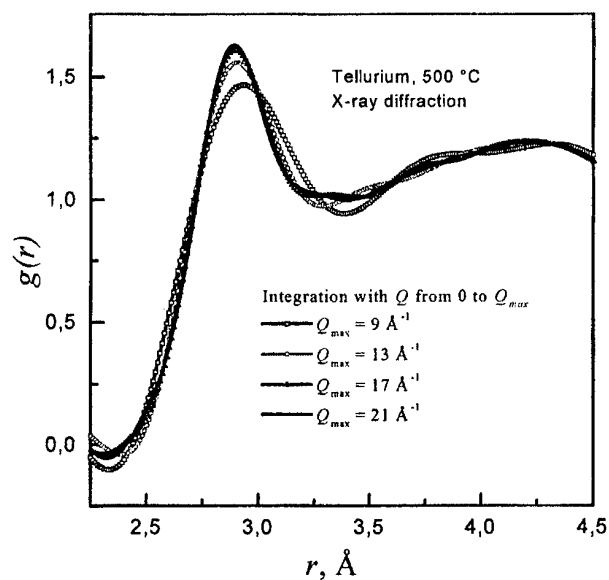
Fig. 3. Pair correlation function of liquid Te calculated with different integration limits Q_{max}.
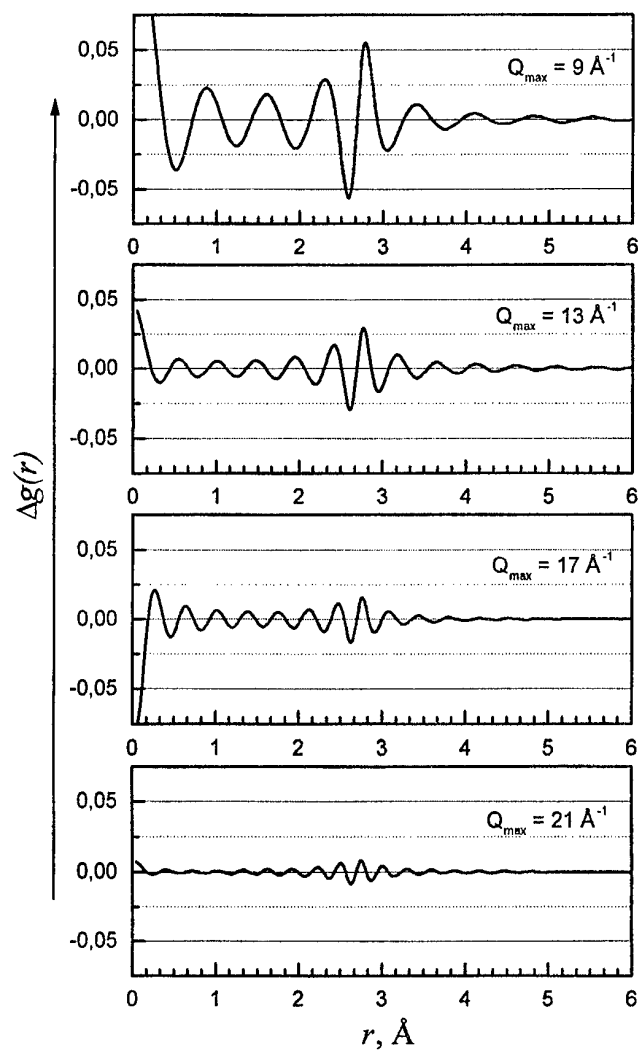
Fig. 4. Residual pair correlation function $\Delta g(r)$ calculated with $S(Q)$ from Q_{max} to ∞.

The next step was to examine the effect of the structure factor termination at high Q-values. For this purpose we have extrapolated the experimental structure factor for $Q > Q_{max}$ using the function

$$S(Q) = 1 + c_1 \cos(c_2 Q - c_3) \exp(-c_4 Q)/Q \tag{7}$$

which enables one to obtain an analytical expression for $g(r)$ up to infinity. The parameters $c_1...c_4$ have been determined by a least squares fit of the high Q-region of the experimental $S(Q)$. The extrapolated parts of the liquid Te structure factors are given in Fig. 1.

In Fig. 3 the region of the first and the second maximum of the pair correlation function of liquid Te at 500 °C calculated with different upper Q-limit is shown. It is seen that with increasing Q_{max} the height of the first peak increases while its width decreases. Besides, the position of the first maximum is shifted to the smaller r-values and "false" oscillations disappear.

Fig. 4 illustrates the termination error in $g(r)$ by limiting the structure factor to $Q_{max} = 9$, 13, 17 and 21 Å^{-1}. It is seen that the high-angle contribution to the pair correlation function

$$\Delta g(r) = 1 + \frac{1}{2\pi^2 r \rho_0} \int_{Q_{max}}^{\infty} Q[S(Q) - 1] \sin(Q \cdot r) dQ \tag{8}$$

is the most essential in the vicinity of the first and the second peak.

The pair correlation functions of the liquid Te calculated with different lower and upper integration limits in Eq. (5) are presented in Fig. 5. It is seen that both limitations significantly affect the resulting curve, especially in the range of the first and the second coordination spheres. Therefore a straightforward interpretation of the "experimental" pair correlation functions may be misleading.
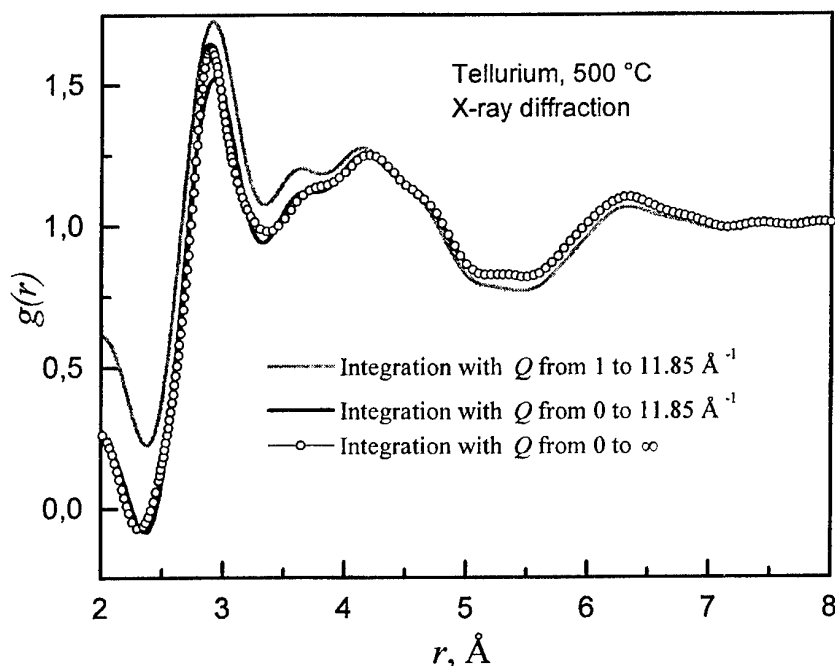
Fig. 5. Pair correlation functions of the liquid Te calculated with different integration limits Q_{min} and Q_{max}.

In Fig. 6 we show some structural parameters of liquid Te in dependence on the upper integration limit Q_{max}. The nearest neighbour distance r^I and coordination number N^I continuously decrease with increasing Q_{max} up to 19 – 20 Å^{-1} while the value of $g(r^I)$ increases. Beginning with

$Q_{max} \sim 20$ Å^{-1} all parameters remain practically unchanged. This is in good correspondence with the result shown in Fig. 4. Indeed, the residual pair correlation function $\Delta g(r)$ becomes very small when Q_{max} achieves ~ 21 Å^{-1} or more.
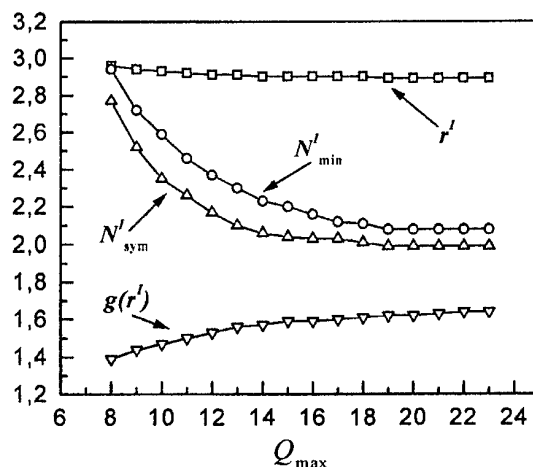
Fig. 6. Nearest neighbour distance r^I, coordination number N^I_{min}, N^I_{sym} and $g(r^I)$ as a function of Q_{max} ($Q_{min} = 0$).

3.2. Amorphous Ge$_{25}$Te$_{75}$

The experimental structure factor of the amorphous Ge$_{25}$Te$_{75}$ alloy measured at room temperature is shown in Fig. 7. It is seen that the modulations of the $S(Q)$ of the amorphous Ge-telluride are much more pronounced than those of liquid objects (e. g. liquid Te). Besides the shape of the maxima and minima in the $S(Q)$ of the a-Ge$_{25}$Te$_{75}$ alloy are much more complex than that in the hard-sphere structure factor. This means that one can not analytically extrapolate the experimental structure factor in the same or similar manner as we did it for the liquid Te. In such cases it is better to use experimental data up to the limited value of the diffraction vector Q_{max} than to introduce additional errors employing a theoretical function for $Q > Q_{max}$.
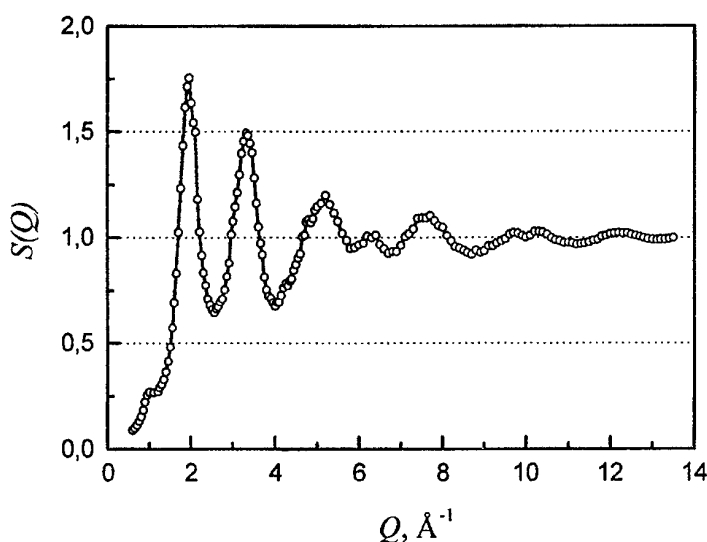
Fig. 7. Experimental structure factor of the amorphous Ge$_{25}$Te$_{75}$ alloy.

As we have seen above, the termination of the structure factor at $Q = Q_{max}$ yields ghost oscillations in the vicinity of the first peak of the pair correlation function. It is very interesting and

important to know whether these false modulations depend on the value of Q_{max} with regard to the shape of the structure factor. In order to test it, we have calculated the residual pair correlation function using Eq. (8) with different limit Q_{max}. As a structure factor we employed the analytical function given by Eq. (7) with parameters $c_1 = 0.9239$, $c_2 = 2.8576$, $c_3 = 20.2316$, $c_4 = 0.2012$. Figs. 8 and 9 show the high-angle contribution to the pair correlation function $\Delta g(r)$ in dependence on Q_{max}. The oscillations of the residual pair correlation function are the greatest when the structure factor is terminated at the position where the $S(Q)$ equals unity and shows maximum slope (e.g. at 13.1 Å^{-1} and 14.2 Å^{-1}). On the other hand, oscillations of the $\Delta g(r)$ are minimal when Q_{max} falls at the position of a minimum or a maximum (e.g. at 13.7 Å^{-1}) at the end of the structure factor where the slope of $S(Q)$ is zero.
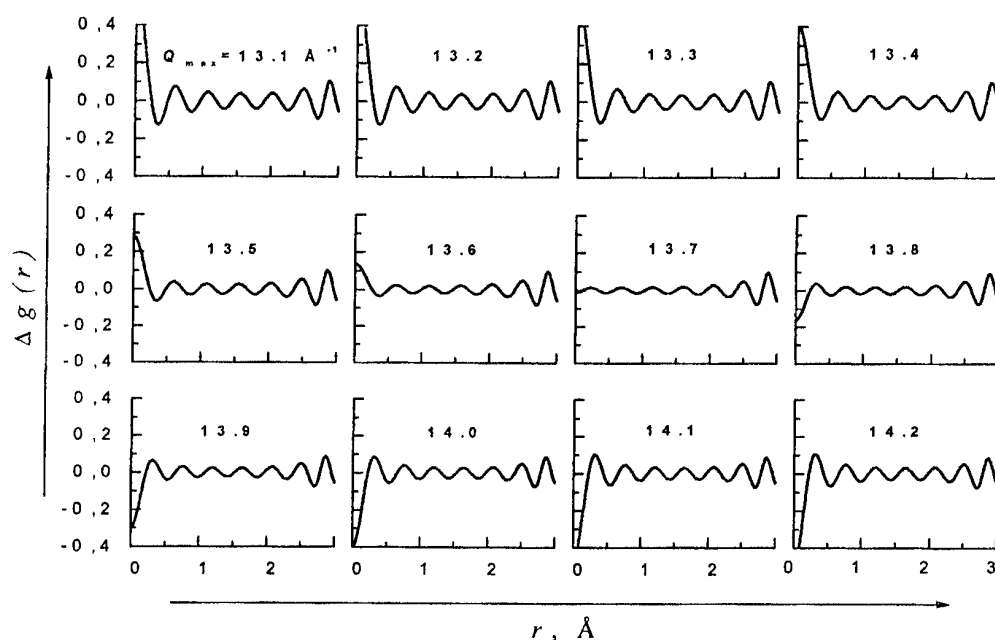
Fig. 8. Residual pair correlation function $\Delta g(r)$ calculated with $S(Q)$ from Q_{max} to ∞.
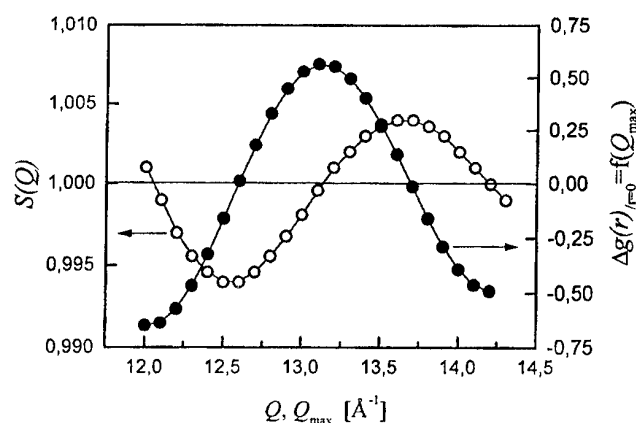
Fig. 9. $\Delta g(r)|_{r=0}$ as a function of Q_{max} in Eq.(8). $S(Q)$ – part of the structure factor of liquid Te at 500 °C (as in Fig. 1).

Taking into account the result mentioned above we have truncated the experimental structure factor of the a-Ge$_{25}$Te$_{75}$ alloy at Q_{max} of 11.2 and 13.5 Å^{-1} that respects to the position of the minimum at the end of curve. Fig. 10 illustrates that decrease of the upper integration limit in Eq. (5) causes

decrease, shift and broadening of the first peak and yields spurious oscillations in the pair correlation functions of the amorphous material in the same manner as in the case of liquids.
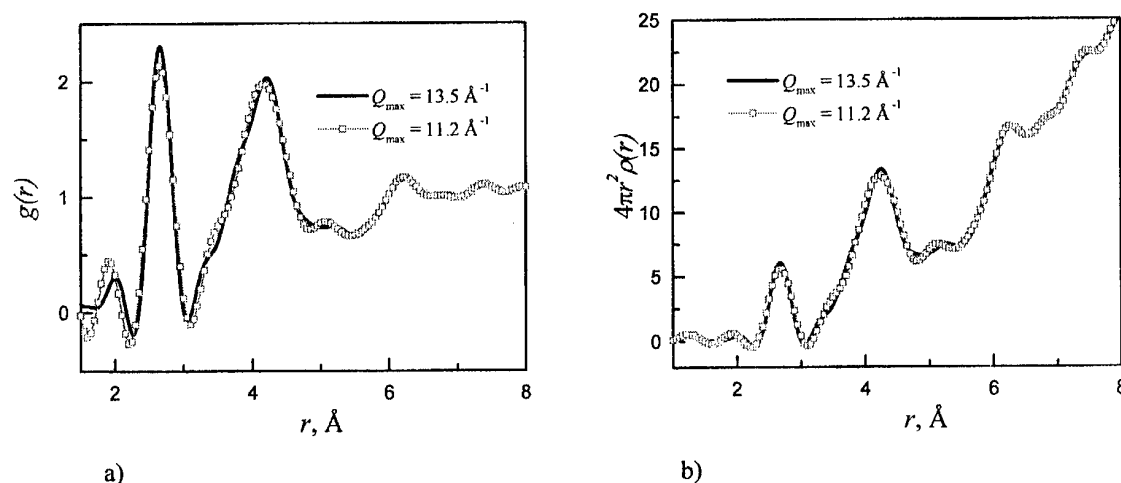
Fig. 10. Pair correlation (a) and radial distribution (b) functions of amorphous $Ge_{25}Te_{75}$ alloy calculated with different integration limits Q_{max}.
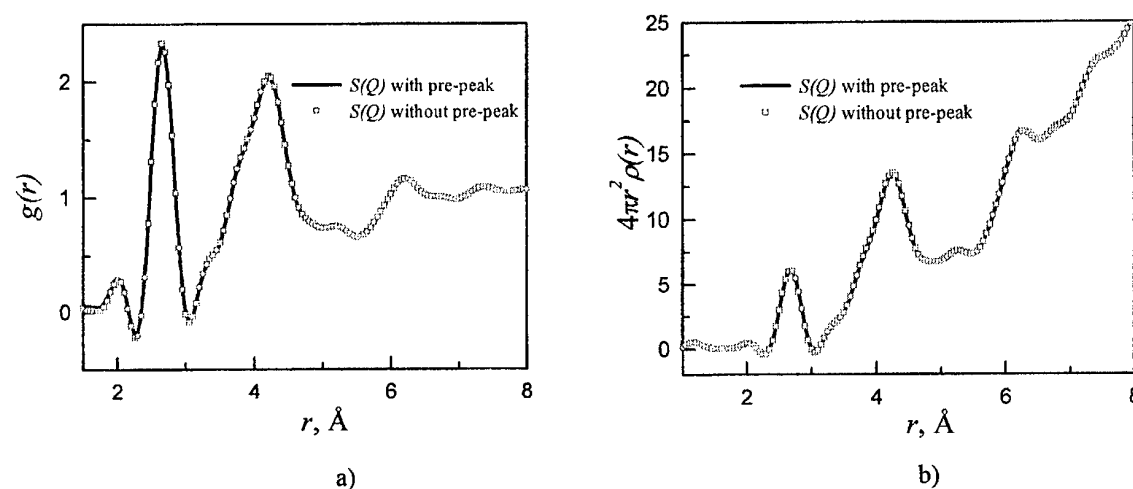
Fig. 11. Pair correlation (a) and radial distribution (b) functions of amorphous $Ge_{25}Te_{75}$ alloy.

In the experimental structure factor of the a-$Ge_{25}Te_{75}$ alloy (Fig. 7) one can see a small prepeak at $Q = 1.1$ Å^{-1}. It is generally assumed that i) this feature of the diffraction pattern is associated with medium-range order (MRO) and (or) ii) prepeak reflects strong bonding of unlike atoms. As regards the amorphous $Ge_{25}Te_{75}$ alloy we believe that the prepeak in the structure factor arises due to connection of Ge and Te atoms. However in the present paper we would like to examine whether and how the shape of the pair correlation function depends on the prepeak. Therefore we calculated pair correlation function using experimental structure factor i) from $Q_{min} = 0.5$ Å^{-1} to $Q_{max} = 13.5$ Å^{-1}; and ii) from $Q_{min} = 1.5$ Å^{-1} to $Q_{max} = 13.5$ Å^{-1}. In both cases $S(Q)$ was extrapolated from $S(Q_{min})$ to $S(0)$ as described above for the liquid Te. As one can see from Fig. 11 there is practically no difference between pair correlation functions calculated with structure factor containing prepeak and without that.

4. Conclusions

Limitation of the experimental scattering intensity at certain values of the diffraction vector Q_{min} and Q_{max} that differ from zero and infinity, respectively, yields spurious details on the pair correlation functions and introduces errors in the calculated structural parameters of the liquid and amorphous materials.

Termination of the diffraction curve at $Q_{min} > 0$ significantly increases the pair correlation and radial distribution functions in the region of the first maximum that yields overestimated coordination number.

Termination of the structure factor at high Q-values of the diffraction vector causes shift, decreasing and broadening of the first peak of the pair correlation functions. In addition, this results in spurious oscillations in the vicinity of the first and the second maximum of $g(r)$.

Termination effect in the pair correlation functions can be eliminated or significantly reduced by extrapolation of the experimental scattering intensity or structure factor to zero and to infinity using analytical functions. In cases when this cannot be done the termination at high Q-values should be made at the position of minimum or maximum of the structure factor.

References

[1] T. E. Faber, J. M. Ziman, Phil. Mag. **11**, 153 (1965).
[2] R. Hosemann, K. Lemm, H. Krebs, Z. Phys. Chem. **41**, 121 (1964).
[3] R. Kaplow, S. L. Strong, R. L. Averbach, Phys. Rev. **138(5A)** 1336 (1965).
[4] W. Hoyer, H. Neumann, M. Wobst, Rostocker Physikalische Manuskripte **14**, 75 (1990).
[5] W. Hoyer, H. Neumann, M. Wobst, Z. Naturforsch. **47a**, 833 (1992).
[6] H. Neumann, W. Matz, W. Hoyer, Experimentelle Technik der Physik **36**, 105 (1988).
[7] J. Krogh-Moe, Acta Cryst. **9**, 951 (1956).
[8] N. Norman, Acta Cryst. **10**, 370 (1957).
[9] D. T. Cromer and J.B. Mann, J. Chem. Phys. **47**, 1892 (1967).
[10] S. Blairs, U. Joasoo, J. Inorg. Nucl. Chem. **42**, 1555 (1980).

INTERACTION OF POLARIZED LIGHT WITH CHALCOGENIDE GLASSES

V. Lyubin, M. Klebanov

Physical Department, Ben-Gurion University, Beer-Sheva 84105, Israel

In the first part of the paper we summarize the results of our study of photoinduced optical anisotropy in thin film and bulk samples of different chalcogenide glasses. We distinguish three ranges of exciting photons energy: above-band-gap excitation, sub-band-gap excitation and super-band-gap excitation. We claim that in each of these excitation ranges, different mechanisms are responsible for appearance of photoinduced anisotropy, namely, creation and next orientation of photoinduced defects, creation of anisotropically scattering defects and orientation of main covalent bonds of the glass (in addition to creation and orientation of defects) are the main reasons of observed anisotropy in the mentioned spectral ranges. We consider also some interesting results obtained recently in different research groups. Among them: polarization-dependent photocrystallization of some amorphous films, polarization-dependent photodoping of chalcogenide films by metals, photoinduced anisotropy of photoconductivity, polarization-dependent optomechanical effect and photoinduced anisotropy in the ion-conducting amorphous chalcogenide films.

1. Introduction

Investigation of interaction of polarized light with chalcogenide glasses continues already more than twenty years, after discovery of the linearly polarized light induced anisotropy in several chalcogenide glassy films made by Zhdanov, Kolomiets, Lyubin and Malinovskii [1,2]. Many research groups studied photoinduced anisotropy (linear dichroism, linear birefringence) and also photoinduced gyrotropy (circular dichroism, circular birefringence, optical activity) excited by linearly polarized light or circularly polarized light in thin films and in bulk chalcogenide glasses. Main results of these studies can be found in [3-10]. Later, some new effects were discovered at studying of interaction of polarized light with chalcogenide glasses: polarization-dependent photodoping of chalcogenide films by silver [12], polarization-dependent photocrystallization of some amorphous chalcogenide films [13-15], polarization-dependent optomechanical effect [16] etc.

In first publications, the photoinduced anisotropy (PA) in chalcogenide films was explained by interaction of polarized light with some optically anisotropic structural elements whose optical axes are oriented randomly [1,2]. Later, more detailed models of PA in thin chalcogenide films were proposed that are based on consideration of interaction of the inducing light with native quasiatomic defects [17], with quasimolecular defects [18], with bistable centers having a wide distribution of relaxation times [19] or with valence-alteration pairs (VAP's) [20]. An electronic model, in which PA is attributed to photogeneration and trapping of oriented geminate electron-hole pairs in chalcogenide glass, was also proposed recently [21].

In this paper we try to summarize and discuss the recent results of PA study performed mainly in the laboratory of amorphous semiconductors in the Ben-Gurion University (Beer-Sheva, Israel) either independently or in close cooperation with colleagues from other research centers. It is convenient for us to consider and discuss successively the data on PA obtained at excitation by above-band-gap light, sub-band-gap light and super-band-gap light. Additionally we will consider the other effects of polarized light studied recently, including the case of observation of photoinduced photoelectrical anisotropy.

2. Experimental

Two groups of samples were investigated in this research. Thin-film glassy samples of As_2Se_3, $As_{50}Se_{50}$, As_2S_3, $GeS_{2.2}$, Se, $Se_{80}Te_{20}$ and $Ge_xAs_{40-x}S_{60}$ were produced by thermal evaporation of starting glassy materials from usual quartz crusibles onto suitably cleaned Corning glass substrates in vacuum (p~10^{-6} Torr). The $Se_{70}Ag_{15}I_{15}$ films were prepared by evaporation from a vaporiser with a small opening [22]. The film thickness was 0.3-4.0 mm. Bulk samples of As_2S_3, As_2Se_3, $Ge_{20}As_{20}S_{60}$ and $As_{34}S_{52}I_{14}$ were prepared by polishing of melt-quenched chalcogenide glasses and had typical thickness of several millimeters.
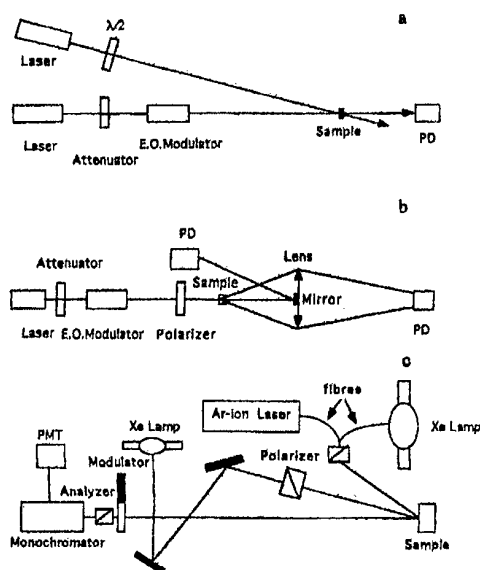
Fig. 1. Experimental installations for investigation of photoinduced anisotropy of absorbtion (a) scattering (b) and reflection (c) of laser light.

Optical setups used in our experiments are shown schematically in Fig.1. The set-up of Fig. 1a was used for investigation of linear dichroism and linear birefringence in the thin film samples at excitation by above-band-gap light. Two beams of gas lasers illuminate simultaneously the same area of the studied film. The wavelength of one laser is selected so that it is the above-band-gap light. It is an inducing laser beam. The linear polarization state of this beam could be changed to the orthogonal one with a half wave plate. The attenuated light beam from the other laser (probing laser beam) passed through an electrooptical modulator, which modulated the polarization discontinuously between two orthogonal states at a frequency of 1kHz. Then this laser beam was passed through the sample and was incident on the Si photodiode, permitting to measure the photoinduced transmission anisotropy $T_y - T_x = 2 (I_y - I_x) / (I_y + I_x)$, where I_y and I_x are the intensities of the beams with two orthogonal electric vectors. To measure the difference signal $I_y - I_x$ we used the method of synchronous detection. If the wavelength of second laser is selected so that it is also the above-band-gap light, we can measure the photoinduced dichroism. In order to study the photoinduced birefringence, the wavelength of second laser must be selected in the range of transparency of the studied film. Usually we used the He-Ne lasers, working at λ = 633 nm and the Ar^+ lasers, working at λ= 515 nm. This set-up permitted us to study very initial periods of PA kinetics and relaxation. For study of PA of transmission in the bulk chalcogenide samples excited by sub-band-gap light, we also used the installation of Fig. 1a. Additionally for simultaneous measurement of the laser radiation transmitted through the bulk sample and radiation scattered by the sample to various angles up to 230 mrad. We used the set-up shown in Fig. 1b. Collecting lens, arranged behind the sample, focused the scattered light to a photodiode, and a small mirror, fixed in the central part of the lens, reflected the transmitted light beam to a second photodiode. He-Ne laser radiation (λ = 633 nm) which was sub-band-gap radiation for the studied bulk glass samples (As_2S_3 glass) played in this installation, by turns, a role of inducing or probing light. This installation

allowed us to study both anisotropy and gyrotropy of transmission and scattering of linearly and circularly polarized light in bulk samples.

The experimental set-up for reflectance difference measurements is shown in Fig. 1c. It is again the two-beams installation. The anisotropy in this case was induced using the light of either a 1000 W Xenon lamp which generated radiation in a wide energy range, including sub-band-gap and super-band-gap light, or an Ar^+ ion laser ($\lambda = 488$ nm) generating above-band-gap light for the studied samples. The inducing light passed through a Glan-prism polarizer and besides the light intensity on the surface of the sample was around 100 mW/cm^2. The intensity of the measuring linearly polarized light, generated by small Xenon lamp, was much smaller (about 5 mW/cm^2). Application of a monochromator allowed to investigate the spectra of PA of light reflection. For a detailed acquaintance with the reflection-difference spectroscopy see Ref.23.

3. Results and discussion

3.1. Above-band-gap light excitation

Most of early experiments on the PA were performed in the regime of above-band-gap light excitation of thin film chalcogenide glassy samples. Both photoinduced linear dichroism and photoinduced linear birefringence generation and multiple reorientation were revealed under action of linearly polarized light. PA could be decreased to zero at the next irradiation by non-polarized or circularly polarized light.

The best from the different models of PA generation at above-band-gap light excitation is, in our opinion, the model of Tikhomirov and Elliott [20], which is based on the photoinduced orientation of VAP's, the charged defects with negative correlation energy, characteristic for chalcogenide glasses. It is known that there are natural VAP's and photoinduced VAP's in chalcogenide glasses. Our experiments show that photoinduced VAP's play especially important role in generation of PA at above-band-gap light excitation [24].
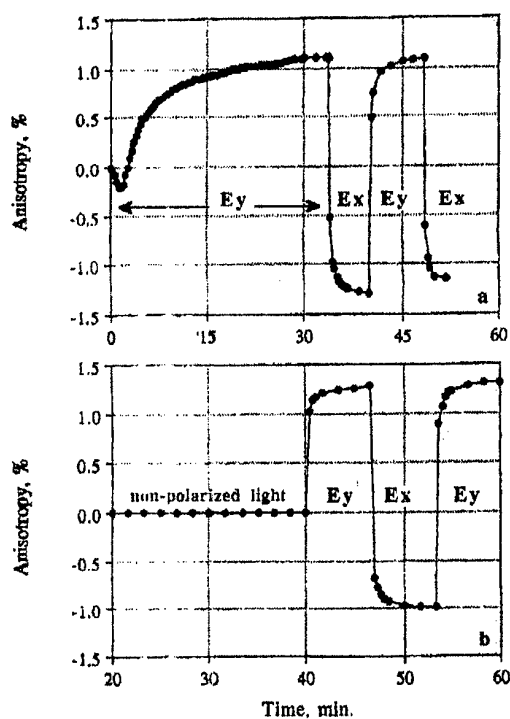
Fig. 2. Kinetics of dichroism generation and reorientation in $As_{50}Se_{50}$ film under action of linearly polarized laser light with two orthogonal directions of electrical vector (y and x), when reorientation starts after dichroism saturation (a) or when polarized light irradiation starts after long illumination with unpolarized light (b).

The process of photoinduced dichroism generation and reorientation is illustrated in Fig. 2 for the case of the AsSe film of 1.2 μm thickness. It is seen from Fig. 2a that the initial dichroism generation is rather prolonged (10-20 min), while the dichroism reorientation happens much quicker (< 1min). In the case of long film irradiation with the unpolarized light, the following irradiation with linearly polarized light results in the rapid appearance of dichroism as it is shown in Fig.2b. Similar peculiarities in the kinetics of dichroism generation and reorientation were observed also in amorphous As $_{45}$Se$_{55}$, As$_2$S$_3$ and Ge$_2$PbS$_4$ films.

These data and other results described in [24] show that irradiation with both polarized and non-polarized above-band-gap light creates in the non-irradiated film some centers that can be oriented quickly by the subsequent irradiation by linearly polarized light (in case of initial irradiation with the polarized light, these centers are oriented quickly during irradiation). Such centers can be born in the form of VAP's (photoinduced VAP's) in the reaction [25]:

$$2C_2^0 + h\nu ... C_1^- + C_3^+ \tag{1}$$

In all previous experiments the authors investigated PA in chalcogenide films that are characterized by the scalar photoinduced effect, photodarkening, when transparency of the sample decreases under light irradiation. At the same time, in some Ge containing chalcogenide glassy films, initial light irradiation induces photobleaching instead of photodarkening. Subsequent light irradiation carried out after annealing of photobleached films results in photodarkening. Photobleaching was investigated in detail in the three-component chalcogenide Ge-As-S films [26,27].

We investigated PA in photobleached Ge$_{25}$As$_{15}$S$_{60}$, Ge$_{32}$As$_8$S$_{60}$ and Ge$_{36}$As$_4$S$_{60}$ films in which large photoinduced changes were observed and studied previously [26]. The results were qualitatively identical for all three studied films and we will illustrate them for the case of Ge$_{32}$As$_8$S$_{60}$ films. Fig. 3 shows the typical kinetics of dichroism generation and reorientation in both as-prepared and annealed films. A 2.5 W/cm^2 linearly polarized Ar$^+$ laser beam at 488 nm with two orthogonal directions of electrical vector was used in these experiments. A 0.5 mW/cm^2 linearly polarized 515 nm Ar$^+$ laser beam was applied as a probe beam.
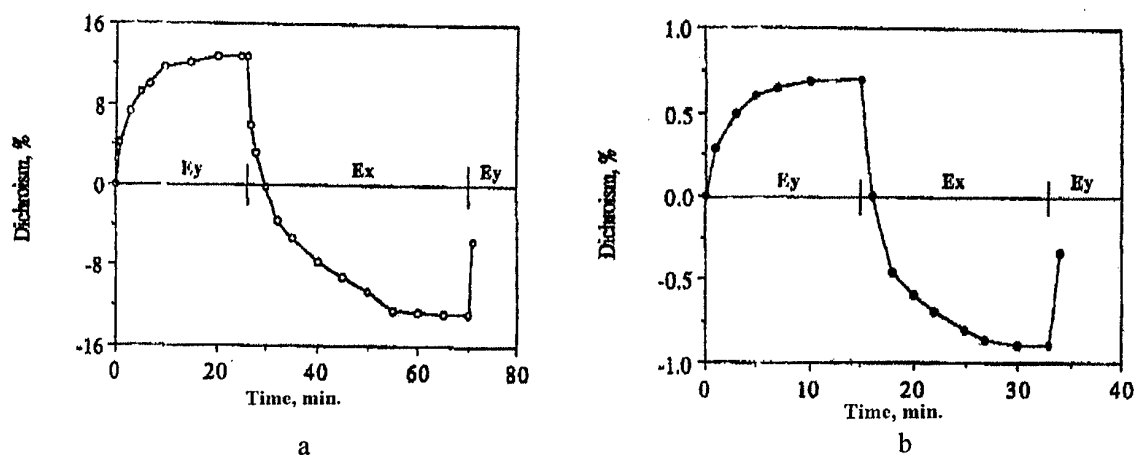
Fig. 3. Kinetics of dichroism generation and reorientation in as-prepared (a) and annealed at 210 °C (b) Ge$_{32}$As$_8$S$_{60}$ glassy film, measured by 515 nm probing laser beam.

Quantitative results of photoinduced dichroism study are summarized in Table 1. It is seen that the values of PA in Ge$_{25}$As$_{15}$S$_{60}$ and Ge$_{32}$As$_8$S$_{60}$ are approximately the same but for Ge$_{36}$As$_4$S$_{60}$ films smaller PA values are observed. We can say that the value of the photoinduced dichroism in as-prepared photobleached films (10-15%) is substantially larger than that in most of the previously studied elementary or binary chalcogenide glassy films. Annealing of such films does not result in change of the sign of dichroism. However, the value of dichroism is considerably smaller in annealed films. In this respect, the studied films differ essentially from the binary films where dichroism decreases after annealing very weakly. Generation and reorientation of birefringence was also observed and studied in these photobleached films.

Table 1. The photoinduced dichroism values (in %) for $GeAs_{(40-x)}S_{60}$.

	$Ge_{36}As_4S_{60}$	$Ge_{32}As_8S_{60}$	$Ge_{25}As_{15}S_{60}$
As - prepared	3 - 4	12 - 15	8 - 15
Annealed	1 - 2	0.6 - 0.8	-

Summarizing the obtained results, we conclude that characteristics of PA do not depend on photodarkening or photobleaching observed in the as-prepared chalcogenide glassy films. More details about the study of the photobleached films could be found in [28].

3.2. Sub-band-gap light excitation

In early experiments on interaction of linearly polarized and circularly polarized sub-band-gap light with bulk chalcogenide glassy samples about 1 cm thick, several photoinduced phenomena: anisotropy, gyrotropy and light-scattering were discovered and studied [4 and literature cited there]. It was shown also that the polarization state of the light changed essentially as it passed through bulk samplees: both rotation of the plane of polarization (optical activity) and ellipticity were seen to occur [4]. Photoinduced liner and circular dichroism and birefringence were shown to be comparable in magnitude and to be responsible for the occurence of elliptical dichroism and birefringence. These effects were observed and studied later in direct experiments when the bulk samples were irradiated by the elliptically polarized laser light with different ellipticity [29,30].

In the next series of investigations, we measured the linearly polarized or circularly polarized laser radiation transmitted through the bulk sample and radiation scattered by the sample to various angles up to 230 mrad [31,32]. In these experiments we used the set-up shown in Fig.1b.

We studied the kinetics of change of scattered light intensity induced by strong linearly polarized or circularly polarized radiation with two orthogonal directions of electrical vector (E_y - radiation and E_x - radiation, E_r - radiation and E_l - radiation). It was shown that the E_y-radiation, for example, induces an increase of scattering of the corresponding (I_y) light. Simultaneously, the intensity of I_x light usually decreases. On the contrary, the E_x - radiation induces a decrease of I_y light and a growth of I_x light. The analogous results were recorded in the case of circularly polarized light.

Fig. 4 and 5 show a typical kinetics of photoinduced changes of the scattered and transmitted light anisotropy and also of the scattered and transmitted light gyrotropy. It is seen from the figures that scattering anisotropy (gyrotropy) and transmittance anisotropy (gyrotropy) always change in opposite directions: an increase of one of them is accompanied by the decrease of the other one and vice versa. The anisotropy (gyrotropy) of scattering and transmittance were shown to remain practically invariant during at least 3 - 5 hours.

In some experiments the sample was first excited by non-polarized light and only then was irradiated by linearly or circularly polarized radiation. Non-polarized radiation induced additional isotropic light scattering, while the subsequent linearly or circularly polarized radiation resulted in appearance of scattering anisotropy or gyrotropy which could be reoriented. This peculiarity is demonstrated in Fig. 5 for the case of photoinduced gyrotropy.

Obtained quantitative data about the photo-induced light scattering anisotropy and gyrotropy permit us to draw some interesting conclusions. The oppositely directed changes of photoinduced anisotropy (gyrotropy) of transmittance and scattering allow us to assume that the creation of anisotropically or gyrotropically scattering centers is the basis of the whole group of photoinduced vectorial phenomena in bulk chalcogenide glasses excited by the sub-band-gap light. The energy of corresponding light quanta is not sufficient for breaking the interatomic covalent bond, but sufficient to produce some changes in the system of weaker bonds, for example, intermolecular Van der Waals bonds or the so-called three-center bonds [18]. These changes can result in the appearance of scattering centers in the glass. Such centers will scatter the light isotropically, anisotropically or gyrotropically depending on the polarization state of the inducing radiation. The anisotropy (gyrotropy) of such centers can be reoriented when the polarization state of the inducing radiation is changed.
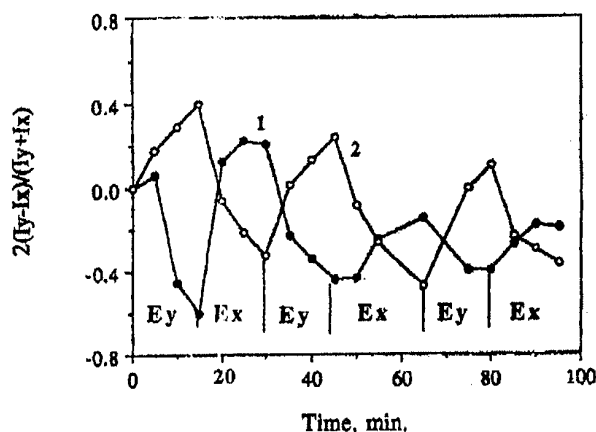
Fig. 4. Kinetics of transmittance anisotropy (1) and scattering anisotropy (2) changes in an As₂S₃ bulk glass sample induced by Ey and Ex laser radiation.
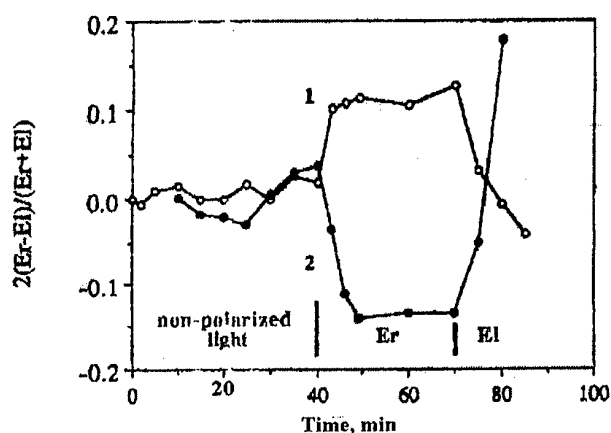
Fig. 5. Kinetics of scattered gyrotropy (1) and transmittance gyrotropy (2) changes in an As₂S₃ bulk glass sample induced by Er and El laser radiation.

3.3. Super-band-gap light excitation

Interaction of super-band-gap photons with chalcogenide glass could not be studied using the transmittance measurements because of strong light absorption. In this case we applied the reflectance-difference spectroscopy which allowed us to investigate the photoinduced anisotropy in glassy samples both thin films and bulks in a broad spectral range [33]. In these experiments we used the set-up shown in Fig.1c. The measured value is defined as $Dr/r = 2 \ (r_y - r_x)/(r_y + r_x)$, where r_y and r_x are the reflectance values for the polarization of the probing beam in the direction parallel or perpendicular to the polarization of the inducing beam.

Main new results, obtained in this research, were the observation of anisotropy excited by photons with energy substantially exceeding the band-gap of the chalcogenide glass and observation of PA at energies much higher than the energy of exciting photons.

Fig. 6 shows the PA of light reflection in the bulk As₂S₃ induced by the linearly polarized light of Xe lamp or Ar⁺ laser. It is seen that the PA is appeared in the whole 1.5-5.0 eV range. Interesting that for the glass excited by Xe-lamp light the trend in the reflectance change was the same (increase or decrease depending on the polarization) throughout the whole studied spectral range. At the same time, in case of the Ar⁺ laser excitation, sign variation of the effect is clearly recorded. The increase in Dr/r is observed for larger photon energies (above 4.0 eV) similar to the previous case of polychromatic light excitation, but for smaller photon energies an opposite change (decrease) is detected. It is seen also that a change of the light polarization to the orthogonal one results in a reversal of the PA with the same crossover energy of 4.0 eV. All peculiarities of PA of reflection were shown to be characteristic not only for As₂S₃ glass but also for all chalcogenide glasses studied.
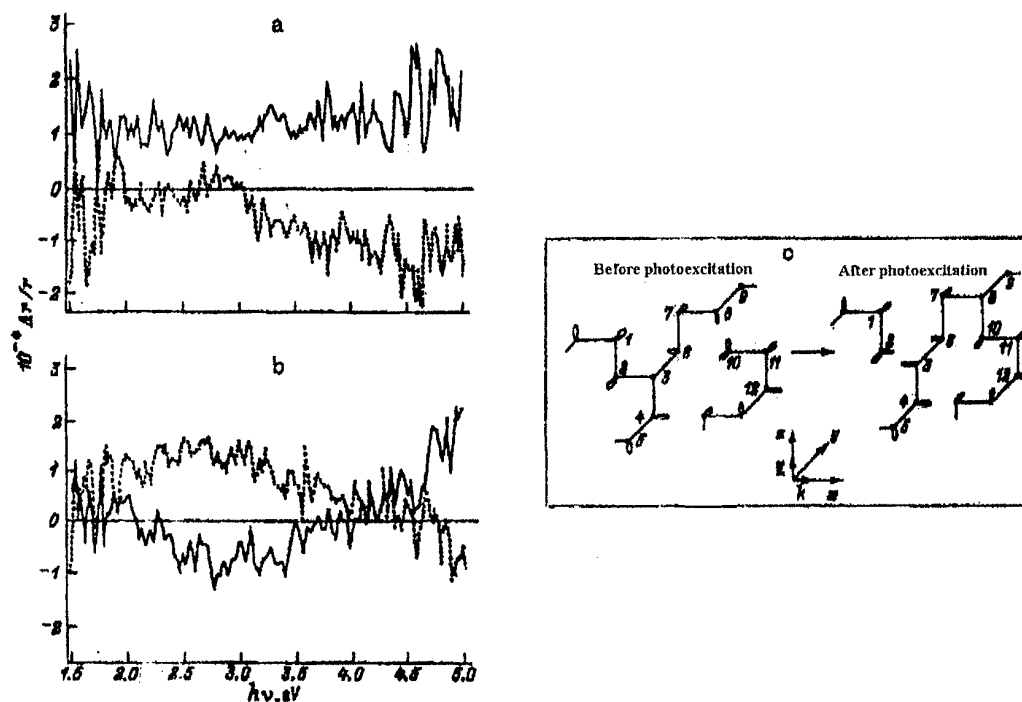
Fig. 6. Photoinduced reflectance anisotropy (solid lines) and its reorientation (dotted lines) in an As_2S_3 bulk glass sample irradiated by the light of 1000 W Xe lamp (a) or Ar^+ ion laser (b) and schematic representation of photostrucrural changes induced by the above-band-gap light (c).

The possibility to observe PA at energies much larger than the exciting photon energy indicates that by irradiation with linearly polarized light not only defects or the scattering centers in the glass can be oriented and reoriented by light but that the main interatomic covalent bonds can be also oriented and reoriented.

The most interesting result which must be explained is the essential difference of reflection spectra for the cases of Xe lamp and Ar^+ laser light excitation (Figs. 6a and 6b). One of the posibilities to understand this difference is demonstrated in Fig.6c for the simplest case of elemental amorphous selenium. In the initial state, atom 3 is threefold coordinated and atom 10 is onefold coordinated. Following the photoexcitation by the Ar^+ laser light (above-band-gap light) with polarization shown in the figure, lone-pair (LP) electrons oriented parallel to this orientation will predominantly be excited. As a result, atom 10 may form a covalent bond with a neighbouring atom 8, making the latter threefold coordinated. To keep the defect concentration and charge balance, initial threefold coordinated atom 3 decays into a singly coordinated defect and a twofold coordinated "regular" atom. We see here a redistribution of LP and bonding orbitals. Before photoexcitation, the bond between atoms 2 and 3 was covalent (parallel to the x axis), while atoms 8 and 10 had LP orbitals parallel to the z axis. After the photoexcitation, atoms 8 and 10 became bonded by a covalent bond in the z direction, while the bond between atoms 2 and 3 is broken, and two LP orbitals parallel to the x axis are created. As a result, the total number of bonding electrons along the z axis decreases, while the number of non-bonding electrons along the x axis increases, which explains the opposite change in the anisotropy probed at lower and higher energies. In other words, conversion between bonding and non-bonding electrons proceeds.

In the case of broad-spectrum light (Xe lamp), the above-considered process still exists but, additionally, the direct excitation of bonding electrons by the high-energy light quanta becomes possible, resulting in the decrease in the number of bonding electrons in the direction of the light polarization. Since the density of states is larger for bonding electrons than for LP electrons, this latter process will overcompensate a decrease in the number of covalent bonds caused by the excitation with the above-band-gap light, leading to the same change in the sign of anisotropy for both lower and higher energies.

Concluding this part of the paper, we can repeat that, in our opinion, the mechanisms of PA (and of photoinduced gyrotropy) are different for the cases of excitation in different spectral ranges. In case of the above-band-gap excitation, the polarized light orients the natural VAP's existing in the film and creates the photoinduced VAP's that can be quickly oriented. At the sub-band-gap excitation, light creates scattering centers in the glass. Such centers will scatter the light isotropically, anisotropically or gyrotropically depending on the polarization state of the inducing radiation. This process is displayed also in isotropy, anisotropy or gyrotropy of the light transmitted trough the sample. At last, in the case of the super-band-gap light, excited radiation is able to orient and reorient the main interatomic covalent bonds of the glass.

3.4. Polarization-dependent photocrystallization

Application of the polarized light resulted in revealing of new peculiarites in the phenomenon of photocrystallization which was studied already during about 30 years [35]. It was shown that the polarization state of excited light influences on the photocrystalization process and on the properties of crystallized samples [13-15,36]. Irradiation of glassy $Se_{70}Ag_{15}I_{15}$, Se and $Se_{80}Te_{20}$ films with linearly-polarized He-Ne- and Ar^+ - laser light was shown to result in formation of polycrystalline films with strong optical anisotropy (dichroism), the sign of which is determined by the direction of the electrical vector of light.

Some peculiarities were observed in the processes of reorientation of PA. Reorientation of dichroism in the films studied was characterized by a change of reorientation kinetics and the dichroism sign. At the beginning of the experiment, when the film was amorphous, the vertical polarization vector stimulated increase of positive dichroism while the horizontal polarization vector diminished positive dichroism and led to negative dichroism. In the following stages, the reverse processes were observed as it is demonstrated for the $Se_{80}Te_{20}$ films in Fig. 7. Final dichroism was stable, it did not relax in the darkness and could not be erased in the process of annealing at the glass transition temperature.
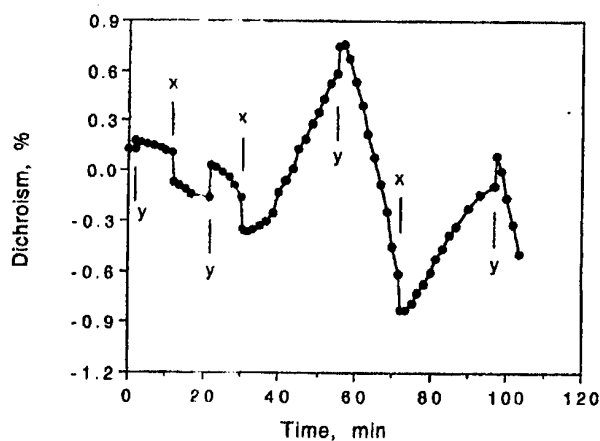
Fig. 7. Kinetics of dichroism generation and reorientation in a thermally treated $Se_{80}Te_{20}$ film induced by a linearly polarized He-Ne laser beam with horizontal (x) and vertical (y) directions of electrical vector.

In [37] the phenomenon of laser-induced suppression of the rate of photocrystallization, induced by another laser beam, was observed in glassy Se films. A decisive role of the polarization state of the two laser beams was demonstrated, namely, the suppression effect was observed only when the linear polarization of both beams were parallel to each other. If the polarizations were orthogonal, enhancement of the photocrystallization was observed.

In the $Se_{80}Te_{20}$ films, which are characterized by much smaller electrical resistance than the other studied films, we succeeded to observe the photoinduced anisotropy of photoconductivity. The results of study of the $Se_{80}Te_{20}$ samples, having special electrodes and working in the bridge-type scheme (which will be shown in Fig. 10 and discussed later) are demonstrated in Fig.8. It is seen that irradiation of the sample by strong linearly polarized light leads to appearance and growth of photocurrent in the circuit that was preliminary balanced. The change of the exciting light polarization to the orthogonal one was always accompanied by the reversible jumps of the current. Such kinetics of photocurrent is very analogous to the kinetics of the optical dichroism changes that proceed at the polarization-dependent laser crystallization. The early stages can be related towards the kinetics of polarization-dependent laser-induced crystallization and the next stages indicate to the anisotropy of photoconductivity in the photocrystallized $Se_{80}Te_{20}$ films.
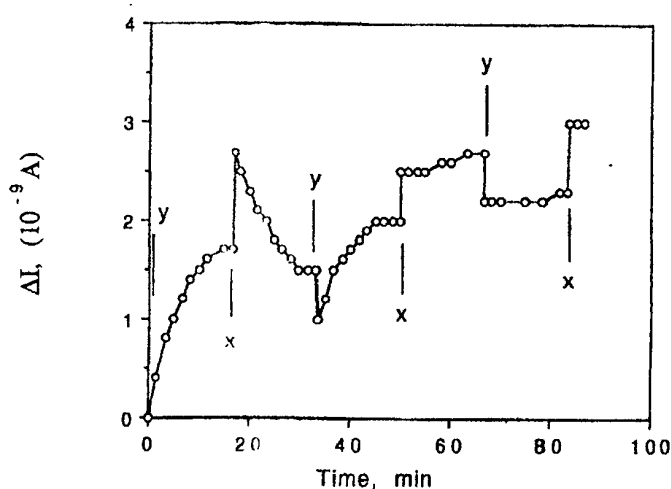
Fig. 8. Kinetics of photocurrent ΔI in a thermally treated $Se_{80}Te_{20}$ film induced by a linearly polarized He-Ne laser beam with horizontal (x) and vertical (y) directions of electrical vector.

3.5. Polarization-dependent photodoping

It was shown previously that the Ag-photodoping of As_2S_3 glassy films by linearly polarized light is accompanied by generation of strong dichroism with sign opposite to that generated in Ag-free films [34]. This phenomenon was called by "polarized photodoping". Recently we demonstrated that polarized photodoping by silver is characteristic not only for As_2S_3 films but also for many different chalcogenide glassy films (As_2Se_3, $As_{50}Se_{50}$ and $GeS_{2.2}$). Some peculiarities were observed in the kinetics of photoinduced dichroism generation. These peculiarities are demonstrated in Fig. 9 for the case of polarized photodoping of $As_{50}Se_{50}$ film. When the structure Ag - $As_{50}Se_{50}$ is irradiated by linearly polarized He-Ne laser beam of certain polarization, for example, with horizontal direction of the electrical vector, the positive dichroism appeared and increased quickly. Then, after passing through some maximum value, dichroism started to decrease (Fig.9a). Very unusual was the kinetics of dichroism reorientation. In the first cycles of dichroism reorientation, the horizontal polarization vector stimulated increase of positive dichroism, while the vertical polarization vector decreased the dichroism value, in the following stages the reverse picture was recorded as it is shown in Fig. 9b. This situation remined us the picture that we observed in case of above-considered photoinduced polarized crystallization and we assumed existence of photocrystallization also in this case. Some experimental confirmations of this assumption were obtained but this fact needs in further investigation. At last we can say that some interesting results were also obtained at the Zn-photodoping of chalcogenide glassy films.
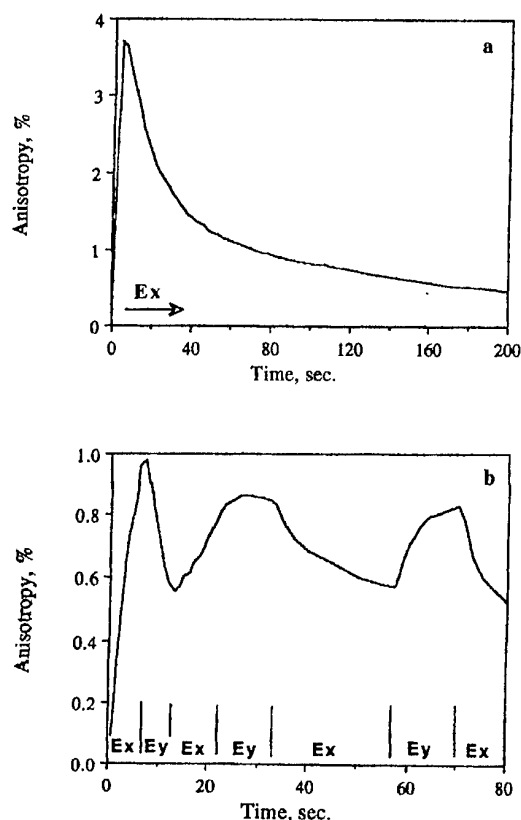
Fig. 9. Kinetics of dichroism generation and reorientation in Ag-photodoped $As_{50}Se_{50}$ film under action of linearly polarized laser light with two orthogonal directions of electrical vector (x and y).

3.6. Photoinduced anisotropy of photoconductivity

In our recent research we demonstrated that the photoinduced optical anisotropy in amorphous $As_{50}Se_{50}$ chalcogenide films is accompanied by the photoinduced anisotropy of photoconductivity and that this effect is optically reversible. 0.3-2.0 μm thick amorphous $As_{50}Se_{50}$ films were prepared by conventional vacuum evaporation technique. A set-up for study of photoconductivity employed one linearly polarized beam of either a He-Ne laser (P=2.75 W/ cm^2, λ=633 nm) or an Ar^+ laser (P=0.3 W/cm^2, λ=488 nm) which was used for creating of anisotropy and at the same time for generation of photocarriers. Anisotropy of photoconductivity was measured using films with evaporated golden electrodes, as it is shown in Fig. 10. The space between parallel electrodes 1-2 and 2-3 was 50 μm. The electric circuit was equilibrated by moving the non-polarized beam (shown as a circle 4 in Fig.10) until the nanoampermeter G read a zero current. Irradiation with a linearly polarized beam with an electric vector parallel either to 1-2 or to 2-3 electrodes resulted in a differential current detected by a nanoampermeter.

Fig. 11 shows the data on anisotropic photoconductivity. Irradiation of sample by the intense linearly polarized beam with an electric vector parallel either to 1-2 or to 2-3 electrodes resulted in a current in the circuit of Fig. 10, which was a differential current between 1-2 and 2-3 electrodes. A change in the polarization state of the inducing light resulted in the respective change of the sign of the resultant current. Kinetics of the change of resultant current was similar to the kinetics of reorientation of the optical dichroism. Qualitatively similar results were obtained when using the intense linearly polarized Ar^+ laser beam.
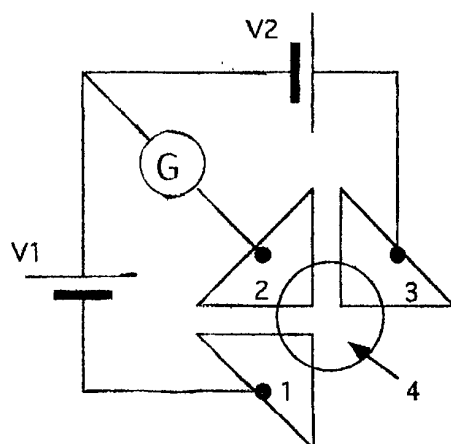
Fig. 10. Layout of electrodes and electrical circuit for measurement of anisotropy of photocurrent. 1,2,3 are the golden electrodes, 4 is a laser beam, G is a nanoampermeter, V1 and V2 are the voltage sources.
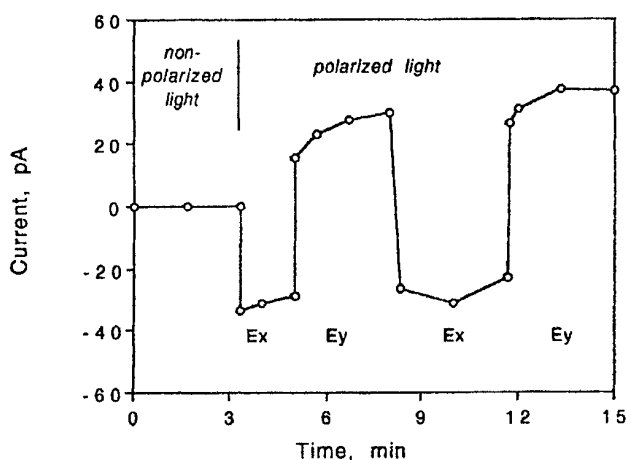
Fig. 11. Kinetics of photocurrent ΔI in $As_{50}Se_{50}$ film induced by Ex and Ey linearly polarized He-Ne laser beam with electrical vector directed parallel or orthogonal to 1-2 electrodes of the sample shown in Fig.10.

One would doubt that the observed change of photocurrent in Fig. 11 is due to photoinduced anisotropy of photoconductivity because the current might appear also due to a subtle shift (drift) of the laser beam relative to electrodes. In order to reject this possibility, we carried out experiment with films CdSe, where photoinduced optical anisotropy was not observed. Large photoconductivity is a property of these films. Irradiation by the non-polarized He-Ne laser beam resulted in gradual increase of the photocurrent up to 400 times. However, irradiation of CdSe film with a linearly polarized He-Ne laser beam with either Ex or Ey polarization did not result in any change of optical absorption or in appearance of anisotropy of photocurrent. This result rules out an effect of laser beam instability (drift) on the data presented in Fig. 11 regarding anisotropy of photoconductivity in $As_{50}Se_{50}$ films. To the best of our knowledge, we report a first observation of photoinduced anisotropy of electrical properties and its optical reversibility in chalcogenide films.

3.6. Some other results of interaction of polarized light with calcogenide glasses

We want to mention shortly two recently discovered and studied effects of polarized light interaction with chalcogenide glassy films. First effect, anisotropic optomechanical effect, consists in appearance of optically controllable, reversible nanocontraction and nanodilatation induced in chalcogenide glassy film ($As_{50}Se_{50}$ film) by the linearly polarized light [38]. Very good correlation of this effect with photoinduced dichroism was observed. Mechanism of this effect (also as the mechanism of other photoinduced vectorial effects in chalcogenide glases) needs in farther study but even now it is clear that it can form the base of a number of mechanical applications driven by polarized light.

Other interesting phenomena were discovered recently in the ion-conducting chalcogenide glasses [39,40]. Studying the Ag-As-S films excited by linearly polarized light, Tanaka, Gotoh and Hayakawa revealed large reversible positive birefringence and anisotropic surface deformations. The anisotropic shape reflected the polarization direction and moreover, the shape changed from a crater-like to anticrater-like form, following change from illumination on the free surface of the film to illumination through a substrate [40]. The authors connnected the formation mechanism of such patterns with photoinduced migration of Ag^+ ions in the film.

Concluding this short review paper, we can say that investigation of interaction of polarized light with chalcogenide glasses is in the initial stage. It was demonstrated that irradiation with polarized light can result in many unusual and interesting phenomena in chalcogenide glasses. Examples of such phenomena are polarization-dependent photocrystallization, polarization-dependent metal photodoping, photoinduced anisotropy of photoconductivity, anisotropic optomechanical effect and anisotropic surface deformations which were shortly considered in this paper. Now we are able to give only some speculative explanation to all these phenomena but hope to obtain more detailed understanding in the process of future research. We hope also that some of these phenomena will find interesting application in modern electrooptics and photonics.

Acknowledgments

References

[1] V. G. Zhdanov, V. K. Malinovskii, Sov.Tech.Phys.Lett., 3, 387 (1977).
[2] V. G. Zhdanov, B. T. Kolomiets, V. M. Lyubin, V. K. Malinovskii, phys.stat.sol.,
    A52, 621 (1979).
[3] J. M. Lee, M. A. Paesler, D. E. Sayers, A. Fontaine, J.Non-Cryst.Sol., 123, 295 (1990).
[4] V. M. Lyubin, V. K. Tikhomirov, J.Non-Cryst.Sol. 135, 37 (1991).
[5] V. M. Lyubin, V. K. Tikhomirov, Avtometrija No. 4, 14 (1991).
[6] H. Fritzsche, Phys.Rev., B52, 15854 (1995).
[7] K. Tanaka, M. Notani, H. Hisakuni, Solid State Commun., 95, 461 (1995).
[8] S. R. Elliott, V. K. Tikhomirov, J. Non-Cryst. Sol., 198-200, 669 (1996).
[9] V. K. Tikhomirov, G. J. Adriaenssens, S. R. Elliott, Phys. Rev., B55, R660 (1997).
[10] V. M. Lyubin, M. L. Klebanov, Semiconductors, 32, 817 (1998).
[11] P. Hertogen, G. J. Adriaenssens, J. Non-Cryst.Sol., 266-269, 948 (2000).
[12] A. V. Kolobov, V. M. Lyubin, V. K. Tikhomirov, Phil. Mag. Lett., 65, 67 (1992).
[13] V. Lyubin, M. Klebanov, M. Mitkova, T. Petkova, Appl. Phys.Lett., 71, 2118 (1997).
[14] K. Ishida, K. Tanaka, Phys.Rev., B56, 206 (1997).
[15] V. K. Tikhomirov, P. Hertogen, C. Glorieux, G. I. Adriaenssens, phys.stat.sol., A162,
     R1 (1997).

[16] P. Krecmer, A. M. Moulin, R. J. Stephenson, T. Rayment, M. E. Welland, S. R. Elliott, Science **277**, 1799 (1997).

[17] V. M. Lyubin, V. K. Tikhomirov, J. Non-Cryst. Sol. **114**, 133 (1989).

[18] S. A. Dembovsky, Sol. St. Commun. **83**, 761 (1992).

[19] T. Kosa, I. Janossy, Phil. Mag., **B64**, 355 (1991).

[20] V. K. Tikhomirov, S. R. Elliott, Phys.Rev., **B51**, 5538 (1995).

[21] E. V. Emelianova, P. Hertogen, V. I. Arkhipov, G. J. Adriaenssens, J. Non-Cryst. Sol., **266-269**, 954 (2000).

[22] T. Petkova, M. Mitkova, Thin Solid Films, **205**, 25 (1991).

[23] D. E. Aspnes, J. P. Harbison, A. A. Studna, L. F. Florez, J. Vac. Sci. Technol., **A6**, 1327 (1988).

[24] V. Lyubin, M. Klebanov, Phys. Rev., **B53**, R 11924 (1996).

[25] M. Kastner, H. Fritzsche, Philos. Mag., **B37**, 199 (1978).

[26] E. Vateva, E. Skordeva, D. Arsova, Philos. Mag., **B67**, 225 (1993).

[27] K. Petkov, B. Dinev, J. Mater. Sci., **29**, 468 (1994).

[28] M. Klebanov, V. Lyubin, D. Arsova, E. Vateva, V. Pamukchieva, Physica B (2001), in press.

[29] V. M. Lyubin, V. K. Tikhomirov, J. Non-Cryst. Sol., **137-138**, 993 (1991).

[30] V. K. Tikhomirov, Fizika i Tekhnika Poluprovodnikov, **26**, 1415 (1992).

[31] V. Lyubin, M. Klebanov, S. Rosenwaks, V. Volterra, J. Non-Cryst. Sol., **164-166**, 1165 (1993).

[32] M. Klebanov, V. Lyubin. Physica, **B245**, 206 (1998).

[33] A. V. Kolobov, V. Lyubin, T. Yasuda, M. Klebanov, K. Tanaka, Phys. Rev., **B55**, 8788 (1997).

[34] A. V. Kolobov, V. M. Lyubin, V. K. Tikhomirov, Phil. Mag. Lett. **65**, 67 (1992).

[35] J. Dresner, G. B. Stringfellow, J. Phys. Chem. Sol., **29**, 303 (1968).

[36] V. Lyubin, M. Klebanov, M. Mitkova, Appl. Surf. Sc., **154-155**, 135 (2000).

[37] A. Roy, A. V. Kolobov, K. Tanaka, J. Appl. Phys., **83**, 4951 (1998).

[38] P. Krecmer, A. M. Moulin, R. J. Stephenson, T. Rayment, M. E. Welland, S. R. Elliott, Science, **277**, 1799 (1997).

[39] K. Tanaka, T. Gotoh, H. Hayakawa, Appl. Phys. Lett., **75**, 226 (1999).

[40] T. Gotoh, K. Tanaka, J. Appl. Phys, **89**, 4703 (2001).

MODELLING OF THE STRUCTURE AND STRUCTURAL TRANSFORMATIONS IN AMORPHOUS CHALCOGENIDES

M. Popescu

National Institute of Materials Physics, 76900-Bucharest-Magurele, P. O. Box MG. 7, Romania

Computer relaxed structural models of arsenic based chalcogenide glasses allowed to demonstrate that the atomic configurations in these materials are anisotropic with a strong tendency to extend as disordered layers. In the frame of these models the photostructural transformations and photoinduced anisotropy find a straightforward explanation.

1. Introduction

The atomic scale structure of non-crystalline chalcogenides is still a challenging problem. With the advent of surprising discoveries in the field of chalcogenide glasses, as e.g. the photoinduced anisotropy [1] and photoinduced fluidity [2] the problems related to the atomic scale structure and to structural modifications induced by light become more and more important.

In this paper are presented the main results obtained in the modelling of the structure of some arsenic based chalcogenides and of structural transformations in these glasses.

2. Modelling

The modelling of the non-crystalline arrangements of the atoms was carried out starting from simulated assemblies of atoms constructed by hand, with special building units. The coordinates of the atoms were measured by a cathetometer method and the tables of coordinates and atom bonding topology were introduced into computer. By using appropriate force constants for the covalent bonds between the atoms, after [3], and a Monte Carlo-Metropolis procedure for the minimization of the free energy of every model, we got a physically realistic structure. A FORTRAN computer program in Lynux system was run on a Pentium PC, in order to perform the energy relaxation of the atomic models.

3. Results

3.1. Is there amorphous arsenic made of anisotropic layer-like configurations?

As stated by Krebs and Steffen [4] and by Breitling and Richter [5] the amorphous arsenic can be obtained in two forms: β-As and γ-As. Bulk samples and precipitated amorphous arsenic exhibit a β-type structure while evaporated films are of γ-type. The differences in the X-ray scattered intensities and the corresponding RFD's are evident in Fig. 1a,b.

The first sharp diffraction peak (FSDP) plays an essential role when the two forms are identified. Moss and Price [6] have shown that during annealing this peak increases and becomes narrow, thus suggesting a transition from γ to β form.

In order to explain the amorphous structure of arsenic, firstly microcrystalline models were tried. Two types of As-crystal do exist: a rhombohedral phase (Rh-As) and an orthorhombic (Or-As) one. The first one has a "chair-like" configuration of the atoms and the second one exhibits a "layered" structure. Smith et al.[7] have shown that only for the orthorhombic crystal the special

deformation of the lattice gives rise to FSDP. They concluded that a-As is related to the orthorhombic crystal.
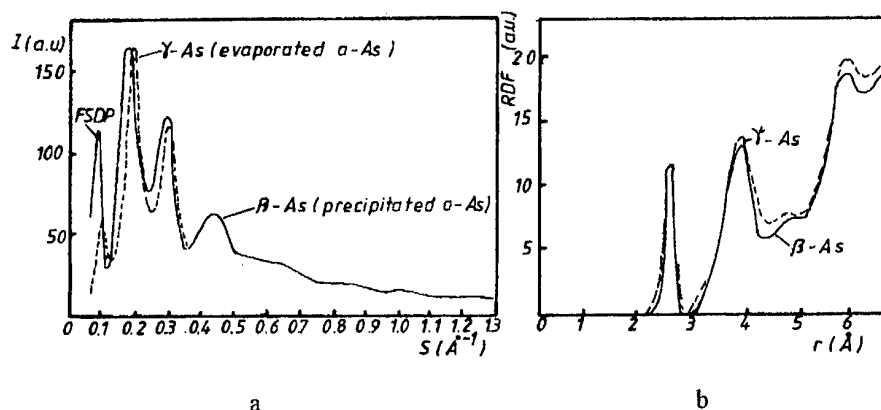
Fig. 1. The structure factor (a) and the radial distribution function (b) for the two forms of amorphous arsenic: β and γ arsenic.

Davis et al.[8] have built an amorphous arsenic (a-As) model with 533 atoms and computed its minimum free energy configuration. The authors concluded that the model reproduces quite well the experimental RDF. Nevertheless, two unresolved problems still remain: a). the explanation of the differences between β-As and γ-As in the frame of the CRN model and b). the aptitude of the model to reproduce FSDP. In order to explain the FSDP some authors assume the existence of definite molecular species in the material (e.g. As_4 molecules found, also, in the vapour phase).

In modeling the structure of disordered three-fold coordinated arsenic we started from the assumption that disordered folded layers are the main constituents of the non-crystalline phases. This idea seems to have the chance to explain the increase of the internal distance deduced from the position of the FDSP, d FDSP, when one passes from crystal to amorphous phase. In the same time the way seems to be opened to explain the structural differences between β-As and γ-As: in γ-As the disordered layers are highly interconnected and kept together by occasional bonds which, during annealing break and a new equilibrium distance between layers is established. Thus, the new relaxed form β-As is obtained. The distance d FDSP is larger for the relaxed case, as observed.

With the aim to shed more light on the structure of a-As we carried out structural simulations using atomic scale models. The free energy of a hand built model as a disordered layer with 146 atoms was minimized by computer using a Monte Carlo procedure. Bond stretching, f_1 and bond bending, f_2 force constants with $f_2/f_1=1$ were used. An equilibrium distance $r_1=2.51$ Å and a bond angle $\alpha=98°$ were used.

The main characteristics of the disordered layer with minimum free energy are:

-number of 5,6,7,8 –fold rings are 22,16,11,3, respectively.

-r.m.s. of r_1 is 0.11 Å and r.m.s. of α is 7.87°.

Now we shall try to prove the validity of the hypothesis regarding the structure with disordered layers for a-As. An important experimental finding in a-As and other glasses with arsenic[9] is that, as a general feature, the distance corresponding to the angular position of FSDP is significantly higher than the interlayer distance in the parent crystals. For a-As the interlayer distance is 5.85 Å, appreciably exceeding that of 5.50 Å for the interlayer distance in orthorhombic arsenic. No reasonable explanation for this difference was given up to day. It is quite improbable that the Van der Waals equilibrium distances between layers in amorphous and crystalline materials would be essentially different. Nevertheless, if one supposes that the effective thickness of the layers are different in the amorphous and crystalline phase, the apparent increase of the interlayer distance can be understood.

In order to determine accurately the thickness of the simulated irregular layer we computed the statistics of the height of the individual As-pyramids. We have obtained the mean value of the heights: 1.63 Å. If one takes into account that the layer thickness in As crystal d=1.25 Å, then the increase in the layer thickness (from c-As to a-As) is 0.38 Å. This increase of the layer thickness

correspond to the increase of the interlayer distance and is in excellent agreement with the best experimental value: d= 5.85 – 5.50 = 0.35 Å.

Thus, on the basis of the above calculation, we can furnish a sound argument for the origin of FSDP in a-As, but the problem is now to stack layers in order to obtain a correct three-dimensional structure.

Three identical layers, shifted along the Oz axis by 5.85 Å give rise to a spatial model, which is unsatisfactory as concerning the details of the RDF. To avoid the exact periodicity of the layers which constitute the model, each of them was differently oriented (rotated by $\pi/2$, reflected in the XOY plane). The resulting RDFs (especially for the model with reflection) after correction for their finite size, is in quite good agreement with the experimental RDF for a-As (Fig. 2)
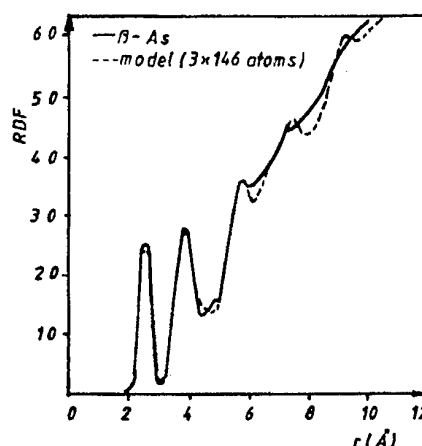
Fig. 2. The radial distribution function of the Popescu's model with disordered layers
(3 × 146 atoms) compared to the experimental function.

The agreement of the experimental and model RDFs seems to be as good as the agreement of the experimental RDF and the RDF for the CRN model devised by Davis et al. A decisive test for the validity is however the aptitude of the model to reproduce the FSDP.

We performed a detailed analysis of several typical models for a-As:
the Greaves-Elliott-Davis model [10], the Beeman's model (private communication of the coordinates) and our layered model (Popescu's model). Firstly, we calculated the structure factor in the region of the FSDP for the above models. Secondly, we calculated the hole radius distribution (in the models).

In order to determine the radius distribution of the holes in a given computer model we used a Monte-Carlo procedure. Starting from a given position inside the model, the distance d to the nearest atom was calculated. Afterwards, small random movements were given to this arbitrary position and were retained only those moves which led to higher radius of the hole. Finally the maximum radius was obtained. By repeating the procedure at different starting positions inside the model, the complete distribution of the holes was obtained.

While FSDP reflects the degree of layering of the model, hole radius distribution (HRD) accounts for the layer packing characteristics. Fig. 3 shows the structure factor in the FSDP range for various models of a-As and for crystalline As (c-As).

A significant correlation is evidenced between the height of the FSDP and the width of the HRD. If no layers are developed in the model, the FSDP is lacking (see the GED model). The Beeman's model exhibits a bimodal distribution of hole radii and this feature is correlated with the splitting of the FSDP. The Popescu's model with well-correlated layers shows a very strong FSDP. The peak developed by the crystal in the region of FSDP has low intensity. The r.m.s. of HRD in the GED model is large (not yet computed from the data given in Fig. 3 !) while for the Popescu's model is narrow. We must point out that the careful investigation of the Beeman's model (633 atoms) has evidenced some compressed regions with the tendency to raise the first coordination sphere and

regions with lower density (normal coordination sphere: N=3). This inhomogeneity seems to be responsible for the split FSDP.
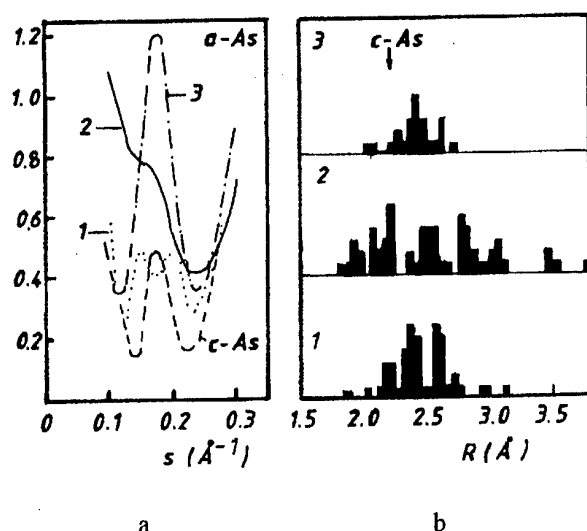
Fig. 3. The FSDP region (a) and the hole radius distribution (b) in three models for a-As: 1. Beeman's model; 2. GED's model; 3. Popescu's model.

As a conclusion it seems plausible to have layered configurations in amorphous arsenic.

One important result of this modelling is the discovery of the relation between the quasi-periodicity obtained from the position of the FSDP, d_{FSDP}, and the inter-layer distance, as introduced in the models. Fig. 4 shows the results.
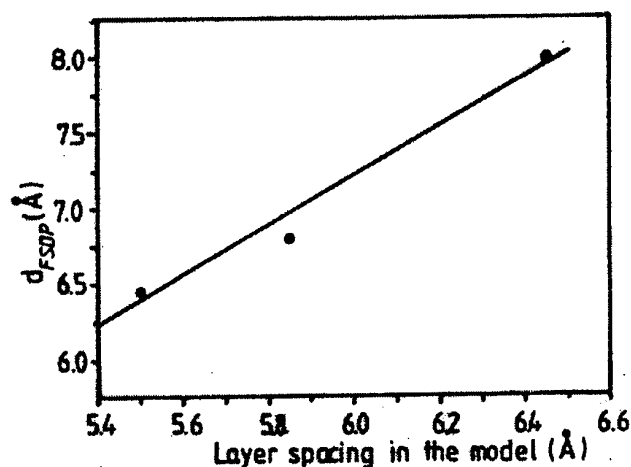
Fig. 4. The relation between the quasi-periodicity distance characteristic to FSDP position, calculated from arsenic models, and the inter - layer distance, d_{model}, in the same physical models.

The following correlation holds:

$$d_{FSDP} = 1.23 \ d_{model} \qquad (1)$$

A simple explanation of this relation is related to the waved character of the disordered layers. The mean interlayer distance for a waved atomic configuration is, obviously, larger than that of a

"planar" configuration. Thus, the modelling results bring a firm proof for the waved layer structure of amorphous arsenic, which can be extended to other layered chalcogenide alloys.

It is remarkable that Apling et al. [11] found a relation between the quasi-periodicity, d_{FSDP}, calculated from the FSDP position in As_2S_3 films, and the diameter, d_{mol}, of the molecular As_4S_6 (~6.5 Å), as $d_{FSDP} = 0.83\ d_{mol}$.

3.2. Amorphous As₂Se₃

The intensity patterns of the X-ray diffraction in binary chalcogenide glasses of composition As_2S_3, As_2Se_3, As_2Te_3 and of their alloys show obvious similarities. The most striking one is the presence of the FSDP around s~0.1 $Å^{-1}$.

The structure of some As-Se glasses was modelled by Rechtin and Averbach [12]. In the framework of their computer model, the free energy minimization was avoided: a quasi-random assembly of As and Se atoms was arranged using a Monte-Carlo method so as to obtain a best fit to the radial distribution function (RDF) of the glass. For a-As_2Se_3 the authors claim a very good agreement of of the experimental and model RDFs. Nevertheless, if one computes the structure factor I(s) of the model, a discrepancy does appear in the region of the FSDP. The I(s) curve calculated by us on the basis of published data in [13] does not exhibit any FSDP.

A continuous random model (CRN) for a-As_2Se_3 (a cluster with 146 simulated atoms) of minimum free energy was devised by Prof. Grigorovici and me. Although the RDF of our model seemed to be quite satisfactory (Fig. 5b), the calculated s.I(s) again did not reproduce the FSDP (Fig. 5a). We are forced to conclude that a true random model for this glass is inadequate.

a   b
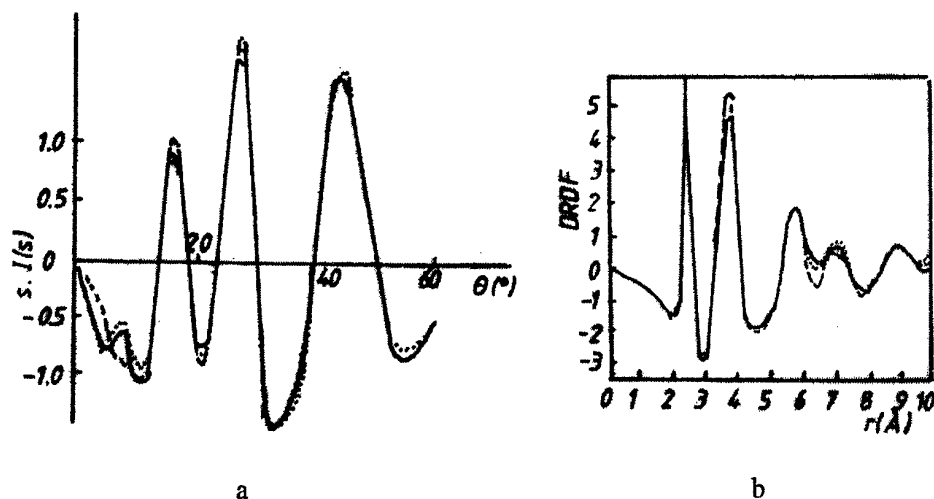
Fig. 5. Modelling results for As_2Se_3. (--- CRN model; ····LCRN model;—— experiment).

A new model with 146 atoms, with a bias towards a layered structure (LCRN) was obtained by changing the bonding pattern in the initial CRN model of a-As_2Se_3. Its atoms were partitioned into three superposed layers. Bonds were established chiefly among the atoms of each layer. Only four selenium atoms formed bridges between layers, two for each pair. The RDF of this layer-biased model differs only slightly from that of the CRN model, but its reduced structure factor s.I(s) displays the previously lacking FSDP (Fig. 5). This is a strong argument in favour of the structure with anisotropic, layer-like configurations in arsenic chalcogenides.

3.3. Amorphous As₂S₃.Geₓ

In the series of ternary chalcogenides, based on As_2S_3 and allied with various content of germanium, the main feature in the structure factor is the appearance of a well-developed FSDP. Fig. 6 shows the X-ray diffraction pattern for several compositions in the system.
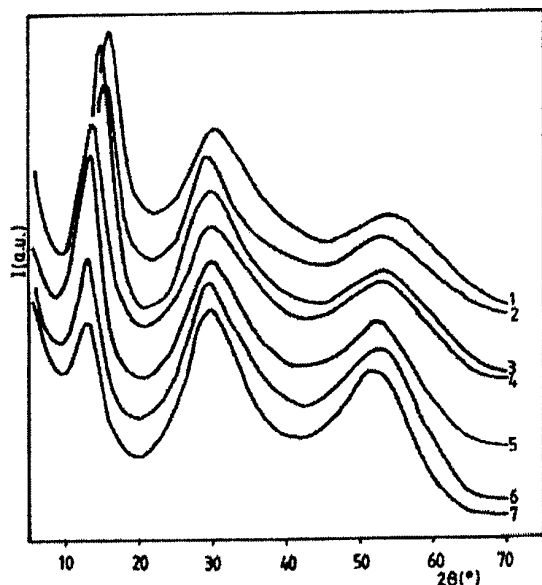
Fig. 6. X-ray diffraction pattern of $As_2S_3.Ge_x$ (x =0.26; 0.68; 0.88; 1.67; 2.14; 2.70; 3.33).
Cu K_α radiation. 1) x = 0.26; 2) x = 0.68; 3) x = 0.88; 4) x = 1.67; 5) x = 2.14; 6) x = 2.70;
7) x = 3.33.

Firstly, we must observe that the intensity of the FSDP firstly increases with x and, after reaching a maximum intensity around the composition x = 0.88 decreases and becomes broader. A gradual shift of the FSDP position towards larger quasi-periodicity, when more and more germanium is added, is supposed to be correlated to the layer configurations in the material. We have used the detailed structural unit distribution deduced by Andreichin, Grigorovici et al. [14], for every composition x and have calculated the average thickness of the layers (it was assumed that the layer thickness is given by the mean value of the height of different structural units weighted by the compositional coefficients). We found the theoretical values of the interlayer distance, d_{model}. A comparison with the experimental values is shown in Fig. 7.
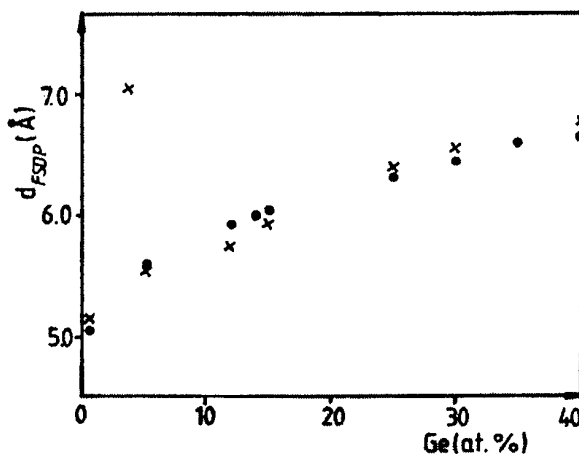
Fig. 7. The quasi-periodicity, d_{FSDP}, in the $As_2S_3Ge_x$ system, as a function of the germanium content, x. (× – experimental points; • - theoretical, based on structural units).

The excellent agreement is a new argument in favour of the anisotropic configurations in glass. On the other hand we must stress that the strong intensity developed around the topological threshold Z= 2.67 seems to indicate a maximum extension and alignment of the anisotropic configurations in this system.

3.4. The anisotropic configurations and the photo-anisotropy effect

The mechanism of the photoinduced anisotropy in chalcogenide glasses is still speculative. Nevertheless, several models have been developed. Grigorovici et al. [15] proposed the first model for the vectorial (anisotropic) reversible transformations in two stages, based on biphotonic processes, where VAP dipolar state is the same with that in the case of the scalar (isotropic) transformations, i.e. of the photodarkening (PD). The vectorial and scalar transformations differ only by the second stage of the induced modifications. In the scalar processes the polymerization has not a directional character. The two types of processes are necessarily limited to the materials where are possible the light induced transitions towards a metastable excited state with a different degree of structural connectivity. In the vectorial transformations, the second stage leads to a preferential orientation of the covalent bonds due to the directional character of the interaction between the VAP dipole and the electric field of the incident light wave.

Lyubin and Klebanov [16] discussed the various possible mechanisms for the photoanisotropic transformations and concluded that the mechanisms are different for the cases of excitation in different spectral ranges. At the sub-band-gap excitation, light creates scattering centers in the glass. Such centers will scatter the light isotropically, anisotropically or gyrotropically depending on the polarization state of the inducing radiation. In the case of the super-band-gap light, the excited radiation is able to orient and reorient the main interatomic covalent bonds of the glass.

In the framework of our models with anisotropic disordered configurations of atoms, it is possible to explain the anisotropy induced by polarized light. The system of anisotropic, layer-like configurations, looks are an assembly of domains which can be partially oriented by elementary bond breaking and rebonding processes, which fact induces a macro-anisotropy observed in many cases. An example case of bond switching can be followed in Fig. 8.

a   b
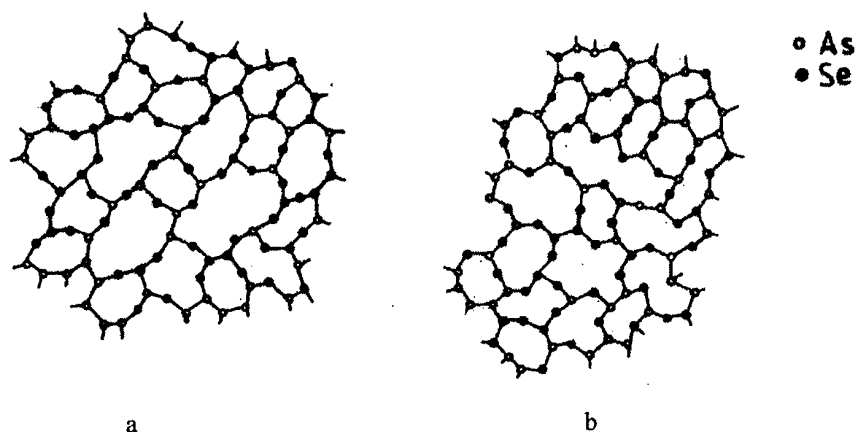
Fig. 8. The relaxed layer configuration in As_3Se_2 (a) and the stressed configuration (b) obtained by bond switching within the atomic configuration.

If one supposes that a quantum of polarized light is acting on the configuration, then the orbitals situated in the direction of oscillation of the electrical vector, that takes part into the covalent bond, are excited, the bond breaks and the energy in excess allows for a new bonding within the configuration. This effect is facilitated for the atoms with more distorted bonds. In our case when two bonds are broken by a two photon process, then new bonds can be formed, and, as a consequence, other two breaking are committed in order to compete with the loss of distortion energy. A new metastable configuration correlated with the orientation of the neighbouring configurations (this is somewhat similar to the case of cooperative orientation of the magnetic domains) account for new directional properties: photoinduced macro-anisotropy. Energetical relaxation of the models with 110 atoms (Fig. 8) shows that the difference between the free energy of the two configurations is enough low to account for a possible photo-induced effect when the material is illuminated by laser light, as observed in the experiment.

4. Conclusions

The ball and stick modelling combined with the computer relaxation of the models provide important informations on the structure of non-crystalline chalcogenides. The anisotropic configurations of atoms demonstrated in the structure of arsenic based chalcogenides, proved to be useful in the explanation of the photoinduced anisotropy in glassy chalcogenides. The anisotropic domains switch their bonding according to the direction of the polarization vector of the exciting light and determine new bonding and orientation of the anisotropic cluster, within a cooperative effect shared by the neighbouring configurations, that gives rise to the macroscopic anisotropy observed in these materials.

References

[1] V. G. Zhdanov, V. K. Malinovskii, Sov. Tech. Phys. Lett., **3**, 387 (1977).
[2] H. Hisakuni, Ke. Tanaka, Science, 270, 974 (1995).
[3] G. Pfeiffer, C. J. Brabec, S. R. Jeffreys, M. A. Paessler, Phys. Rev. **B**, **39**(17), 12861 (1989).
[4] H. Krebs, R. Steffen, Z. anorg. Allg. Chem. **327**, 224 (1964).
[5] G. Breitling and H. Richter, Mat. Res. Bull. **4**, 19(1969).
[6] S. C. Moss, D. L. Price in Physics of Disordered Materials, Ed. D. Adler, H. Fritzsche,
     S. R. Ovshinsky, Plenum Press, 1985, p. 77.
[7] P. M. Smith, A. J. Leadbetter, A. J. Apling, Phil. Mag. **31**, 57 (1975).
[8] E. A. Davis, S. R. Elliott, G. N. Greaves, D. P. Jones, Proc. Intern. Conf. on the Structure of
     Non-Cryst. Mater., Cambridge, 1976, pag. 205.
[9] S. Tsuchihashi and Y. Kawamoto, J. Non-Cryst. Solids, **5**, 286 (1971).
[10] G. N. Greaves, S. R. Elliott, E. A. Davis, Adv. Phys., **28**, 49 (1979).
[11] A. S. Apling, A. J. Leadbetter, A. C. Wright, J. Non-Cryst. Solids, **23**, 369 (1977).
[12] M. D. Rechtin, A. L. Renninger, B. L. Averbach, J. Non-Cryst. Solids, **15**, 74 (1974).
[13] A. L. Renninger, M. D. Rechtin. B. L. Averbach, J. Non-Cryst. Solids, **16**, 1 (1974).
[14] A. Andreichin, M. Nikiforova, E. Skordeva, L. Yurukova, R. Grigorovici, R. Manaila,
     M. Popescu, A. Vancu, J. Non-Cryst. Solids, **20**, 101 (1976).
[15] R. Grigorovici, A. Vancu, L. Ghita, J. Non-Cryst. Solids, **58&60**, 909 (1983).
[16] V. Lyubin, M. Klebanov, J. Optoel. Adv. Mat., 3 (2), 265 (2001).

ON THE CHANGES IN THE STRUCTURAL AND OPTICAL PROPERTIES ACCOMPANYING THE ATHERMAL PHOTOVITRIFICATION PHENOMENON IN As$_{50}$Se$_{50}$ THIN FILMS

R. Prieto-Alcón, J. M. González-Leal, R. Jiménez-Garay, E. Márquez

Departamento de Física de la Materia Condensada. Facultad de Ciencias
Universidad de Cádiz. 11510 – Puerto Real (Cádiz) Spain

The effect of successive annealing-illumination cycles on the structural and optical properties of wedge-shaped As$_{50}$Se$_{50}$ amorphous chalcogenide thin films, has been studied. It is observed that illumination increases the thickness and shrinks the bandgap. Annealing of the chalcogenide films, before or after illumination, decreases the thickness. However, although annealing after illumination increases the bandgap, when this treatment is carried out upon the as-evaporated films, the bandgap decreases. The photostructural changes have been explained in terms of two different mechanisms, which can coexist. One of them involving the repulsion and slip motion of the 2D structural layers comprising the 'pyramidal' network, as a consequence of the negative charging of these structural layers, by electron accumulation in conduction-band tails, and the other, involving the As$_4$Se$_4$ molecules, typical of thermally-evaporated As-rich chalcogenides films, and forming particularly the crystalline form of medium-thickness (1÷2 µm) As$_{50}$Se$_{50}$ films.

1. Introduction

Amorphous chalcogenides exhibit a wide variety of photoinduced structural transformations [1]. A flexible structure due to the presence of lone-pair electrons, on the one hand, and localization of carriers because of the disorder, on the other hand, are both responsible for this light-induced structure-related metastability. As a consequence of such photoinduced changes, optical absorption and many other properties of these amorphous materials including refractive index, density, elastic constants, photoconductivity and chemical solubility, are altered drastically.

Let us consider a process for producing amorphous state, namely the athermal light-induced vitrification of crystalline As$_{50}$Se$_{50}$ thin films. The essence of this process is as follows: Amorphous As$_{50}$Se$_{50}$ films deposited onto either glass or silicon wafer substrates can crystallize by thermal annealing, and subsequent irradiation will cause the vitrification of the films. It has been shown that these amorphous films, when evaporated onto glass substrates, crystallized into different structures, depending on the annealing temperature [2]. On the other hand, the photovitrification phenomenon depends on the film thickness [2], which underlines the influence of the interaction between the film and the substrate. In fact, we have analyzed in a previous work [3], the role played by the silicon substrate in this particular light-induced process. The photoamorphization, which is also dependent on the spectral irradiance of the light source employed [3], is reversible and we will study the results corresponding to the first two crystallization-amorphization cycles. In the present work we will focus our attention on the changes in the structural and optical properties, which accompany the athermal photovitrification phenomenon in As$_{50}$Se$_{50}$ thin films.

2. Experimental details

The bulk starting material was prepared by direct synthesis from 5N purity elements, heated together in an evacuated quartz ampoule at a temperature of 950 °C, for about 24 h. After the

synthesis, the melt was air-quenched, resulting in a bulk glass of the required chemical composition. X-ray diffraction measurements (Philips, model PW 1710), using Cu Kα radiation (1.54 Å), proved that the ingot was amorphous. The studied amorphous thin films were prepared by thermal evaporation of the $As_{50}Se_{50}$ bulk glass onto room-temperature glass substrates, in a vacuum of $\approx 10^{-6}$ Torr, using for this purpose a conventional coating unit (Edwards, model E306A). During evaporation, the substrates were rotated (45 rpm) in order to improve the degree of film thickness uniformity, and the deposition rate was ≈ 1 nm s^{-1}, this quantity having been continuously measured by a quartz-crystal monitor (Edwards, model FTM-5). Electron microprobe analysis of the as-deposited $As_{50}Se_{50}$ thin films showed that the film stoichiometry is correct to $\pm$ 0.5 at.%. The samples were annealed at 150 °C ($T_g = 164$ °C) for periods of time of, typically, 72 h in a $\approx 10^{-3}$ Torr vacuum. Illumination of the glass films was carried out using a 500 W high-pressure mercury lamp (Oriel, model 6285), through an IR-cut filter, providing broadband white light (with a very high UV output), using a light intensity of ≈ 50 mW cm^{-2}. X-ray diffraction analysis was also used in order to examine the glassy or crystalline nature of the films.

The optical transmission spectra used in this study were obtained over the 300÷2000 nm spectral region by a double-beam UV/Vis/NIR spectrophotometer (Perkin-Elmer, model Lambda-19). The spectrophotometer was set with a slit width of 1 nm. It was therefore unnecessary to make slit width corrections, since that value of the slit width was much smaller than the different linewidths. The area of illumination, over which a single optical transmission spectrum was obtained, was approximately 1 mm × 10 mm. A surface-profiling stylus (Sloan, model Dektak 3030) was used to determine the thickness of the films, for the sake of comparison with the results derived from the optical transmission spectra. Typical thicknesses of the as-deposited films studied were around 1 μm, and, thus, according to Kolobov and Elliott [2], our samples can be considered as medium-thickness (1÷2 μm) films.

Table 1. Values of the average thickness, $\bar{d}$, thickness variation, Δd, dispersion parameters, E_o and E_d (single-oscillator analysis), and optical bandgap, E_g^{opt} (Tauc's extrapolation), for the $As_{50}Se_{50}$ chalcogenide thin films under study.

State	$\bar{d}$ (nm)	Δd (nm)	E_o (eV)	E_d (eV)	E_g^{opt} (eV)
As-evaporated	1119 ± 10 (0.9 %)	18 ± 1	4.07 ± 0.02	24.08 ± 0.1	1.87 ± 0.01
First annealing	1066 ± 11 (1.1 %)	28 ± 1	3.92 ± 0.03	25.86 ± 0.2	1.81 ± 0.01
First illumination	1109 ± 19 (1.7 %)	34 ± 2	3.64 ± 0.03	19.56 ± 0.2	1.78 ± 0.01
Second annealing	930 ± 35 (3.8 %)	—	3.83 ± 0.04	24.68 ± 0.2	1.81 ± 0.02
Second illumination	1030 ± 39 (3.8 %)	—	3.68 ± 0.04	20.59 ± 0.3	1.73 ± 0.02

3. Results and discussion

The athermal photovitrification phenomenon in $As_{50}Se_{50}$ films, has been studied from the optical point of view by means of two different methods, enabling the determination of the average thickness and the refractive index of the as-deposited, annealed and exposed $As_{50}Se_{50}$ non-uniform films (see Table 1). The first one, which is based on creating the upper and lower envelope curves of the optical transmission spectrum, at normal incidence, assumes the film thickness, d, to vary linearly over the illuminated area, i.e., $d = \bar{d} + \eta\Delta d$, where $-1 \leq \eta \leq 1$. Δd refers to the variation in thickness from the average thickness $\bar{d}$, as shown in Fig. 1. The applicability of this method is limited by the condition, $0 < \Delta d < \lambda/4n$. Details about this first optical characterization procedure can be found in [4-6].

Due to the larger degree of morphological alteration shown by the $As_{50}Se_{50}$ thin films submitted to a second annealing-illumination cycle, the above-mentioned condition is no longer satisfied. Therefore, a second optical characterization method, based only on wavelengths measurements, was used to determine the average thickness and the refractive index of the samples. Such a procedure takes into consideration the shift of the transmission spectrum at oblique (30°) incidence towards shorter wavelengths, with respect to the transmission spectrum taken at normal incidence. For details of this second characterization procedure see our previous works [7,8].

Fig. 1 shows the optical transmission spectra at normal incidence, in the short-wavelength region, for the as-deposited, crystallized and photoamorphized $As_{50}Se_{50}$ thin films, corresponding to the first annealing-illumination cycle. An irreversible shift of the optical transmission spectrum towards longer wavelengths is observed in the interference-free region of this transmission spectrum when the as-evaporated film is annealed (i.e., thermal darkening). Subsequent illumination of the film induces again a shift of the optical transmission spectrum towards longer wavelengths (i.e., photodarkening), but it is reversible, in the sense that post-illumination annealing returns partly the interference-free region to its initial annealed state.
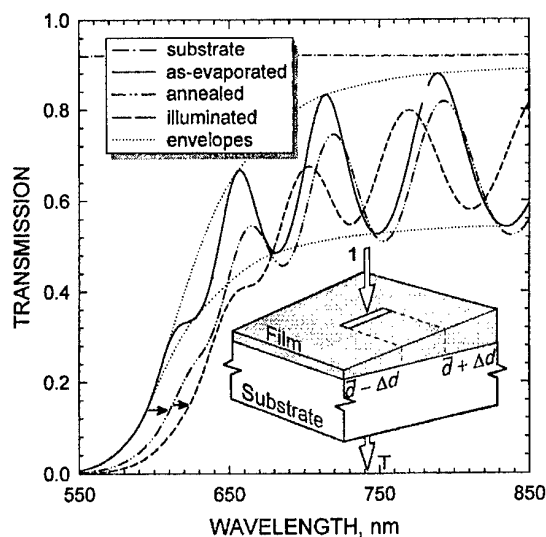
Fig. 1. Typical optical transmission spectra, in the short-wavelength region, for the as-evaporated, annealed (crystallized) and illuminated (photovitrified) $As_{50}Se_{50}$ thin layers. The envelopes corresponding to the as-evaporated layer are also drawn as a representative example. Additionally, a diagram representing a weakly-absorbing thin layer, with a linear variation in thickness on a thick transparent substrate, is also displayed.

It has been found that the refractive index increases with annealing and decreases upon illumination, under the initial value (see Fig. 2). The spectral dependence of the refractive index has been fitted to the Wemple-DiDomenico single-oscillator model [10]:

$$\varepsilon_1(\hbar\omega) = n(\hbar\omega)^2 = 1 + \frac{E_o E_d}{E_o^2 - (\hbar\omega)^2} \tag{1}$$

where E_o is the single-oscillator energy (typically near the main peak of the $\varepsilon_2(\hbar\omega)$-spectrum) and E_d is the dispersion energy. By plotting $(n^2 - 1)^{-1}$ against $(\hbar\omega)^2$ and fitting a straight line, as shown in the
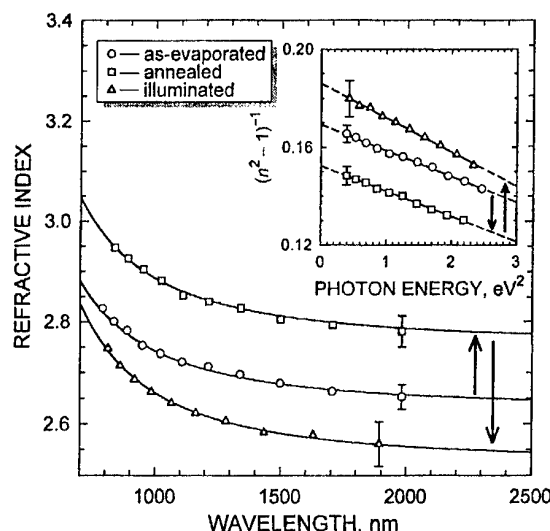
Fig. 2. Refractive index versus wavelength. Also, it is shown in the inset, a plot of the refractive-index factor $(n^2 - 1)^{-1}$ versus $(\hbar\omega)^2$, for the as - evaporated, crystallized and photoamorphized layers.

inset of Fig. 2, E_o and E_d are determined directly from the slope, $(E_o E_d)^{-1}$, and the intercept, E_o/E_d, on the vertical axis. The values of the dispersion parameters for the as-evaporated, crystallized and photovitrified films are listed in Table 1 (two annealing-illumination cycles). The trend of E_o is such that it is verified that $E_o \approx 2 \times E_g^{opt}$, E_g^{opt} being the so-called Tauc gap, which is a widely accepted measure of the bandgap and will be formally introduced below, whereas E_d obeys the following empirical relationship [10,11]:

$$E_d = \beta \, N_c \, Z_a \, N_e \quad (\text{eV}) \tag{2}$$

where N_c is the coordination number of the cation nearest-neighbour to the anion, Z_a is the formal chemical valency of the anion, N_e is the effective number of valence electrons per anion and $\beta = 0.37 \pm 0.04$ eV, for covalent crystalline and amorphous materials.

In addition, the following relationship was proposed by Wemple [11]:

$$E_d^a / E_d^x = (\rho^a / \rho^x)(N_c^a / N_c^x) \tag{3}$$

where ρ represents the mass density (the film thickness could be used instead, because changes in the mass of the films were not measured), and 'a' and 'x' refer to the amorphous and crystalline forms, respectively. The thermal densification process, as well as the photoinduced volume expansion, which have been observed, respectively, upon annealing of the as-deposited $As_{50}Se_{50}$ film, and illumination of the crystallized film (see the thicknesses listed in Table 1), have to be considered to explain the variation of the oscillator strength. Although this analysis is also qualitatively valid for the second annealing-illumination cycle, we will point our discussion to the first annealing-illumination cycle. An increase of ≈ 7 % is observed in the E_d-value as a consequence of the annealing process. By means of Eq. (3), we find that the difference between N_c's, before and after annealing, is less than 2 %; therefore, the small change in N_c indicates a rather insignificant change in the average coordination number in the short-range region. Moreover, E_d calculated from Eq. (2) (considering $N_c = 3$, $Z_a = 2$, N_e

$= (50 \times 5 + 50 \times 6)/50 = 11$ [11]) was found to be 24.42 ± 2.6 eV; that is, allowing the corresponding scatter in β, E_d is certainly close to the experimental values of the as-deposited and annealed films. Going one step further, the comparison of the E_d-values corresponding to the annealed and illuminated films shows a large decrease of ≈ 24 %, accompanied by a decrease of the mass density of ≈ 4 %. The extra 20 % reduction in the E_d-value, as a consequence of the photovitrification of the crystallized film, could be due to a decrease in the effective As coordination number.

On the other hand, following Swanepoel's ideas [4,12], in the strong-absorption region, the values of the optical absorption coefficient, α, have been directly derived from the transmittance measurements, using Eq. (22) from [12]. Fig. 3 shows the optical absorption spectra, $\alpha(\hbar\omega)$, for the as-deposited, crystallized and photoamorphized $As_{50}Se_{50}$ films. It can be seen a shift of the absorption edge to lower photon energies as a consequence of the annealing, as well as the illumination treatment. According to Tauc [13], the spectral dependence of the absorption coefficient in the strong-absorption region ($\alpha \tau 10^4$ cm^{-1}), is given by the following quadratic equation:

$$\alpha(\hbar\omega) = B \frac{(\hbar\omega - E_g^{opt})^2}{\hbar\omega} \qquad (4)$$

where B is an energy-independent constant. Formally, the Tauc gap, E_g^{opt}, is obtained as the intercept of the plot of $(\alpha\hbar\omega)^{1/2}$ against $\hbar\omega$. This graph is shown in the inset of Fig. 3 for the as-evaporated, annealed and illuminated $As_{50}Se_{50}$ films. The values of E_g^{opt}, thus determined, lead us to the conclusion that a clear reversible photodarkening process accompanies the present photoinduced phenomenon.
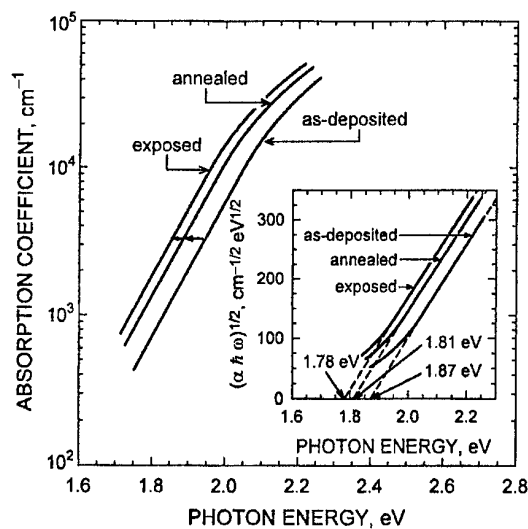
Fig. 3. Optical absorption spectra for the as-deposited, annealed and exposed $As_{50}Se_{50}$ films. In the inset, the determination of the optical bandgap based on the Tauc law.

The relative changes in the average thickness and in the Tauc gap, after two annealing-illumination cycles, are displayed in Fig. 4. These results clearly indicate that, illumination always expands the films and decreases E_g^{opt}, while annealing, before or after illumination, is found to contract the $As_{50}Se_{50}$ films. However, although annealing after illumination increases the bandgap, when the thermal treatment is carried out upon the as-evaporated films, the bandgap decreases, instead. These results suggest a certain correlation between these two types of changes.

We have observed 'giant' changes in $\overline{d}$ and E_g^{opt}. Increases in the average thickness of up to ≈ 4 %, in the case of the illumination after the first annealing, and of up to ≈ 11 %, in the case of the
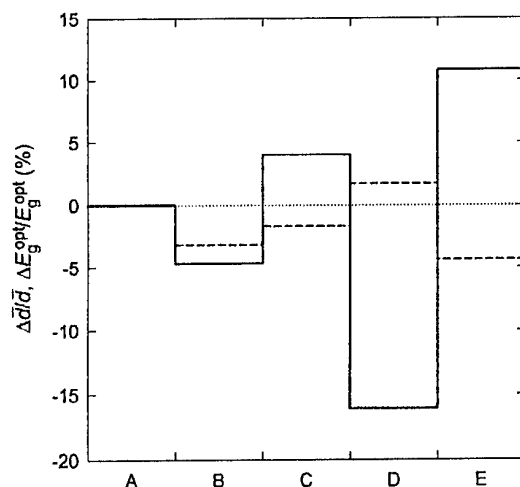
Fig. 4. Variation in relative changes in the average thickness $\overline{d}$ (solid line), and Tauc gap E_g^{opt} (dashed line), of the $As_{50}Se_{50}$ thin layers. Measurement conditions are represented by: A, as-evaporated; B, first annealing; C, first illumination; D, second annealing; E, second illumination.

illumination after the second annealing, have been found. In which the bandgap is concerned, a decrease larger than 4 % has been obtained with the illumination after the second annealing. Other authors [14-18] have also observed large changes in the thickness and the optical bandgap of As-based and Ge-based obliquely-deposited chalcogenide thin films. Furthermore, it was found in [18] that post-illumination annealing causes the changes to revert to nearly the initial conditions. However, the morphological changes undergone by our wedge-shaped $As_{50}Se_{50}$ chalcogenide films, because the successive thermal and optical treatments, make somehow the results obtained by means of the two different optical characterization methods, to be only comparable up to a certain degree.

It is believed that a change in the interaction of chalcogen lone-pair electrons is responsible for the photodarkening phenomenon. The increase in lone-pair–lone-pair interactions causes a broadening of the valence band, giving rise to a reduction in the optical bandgap. Various models have been proposed to explain this mechanism [19-21]. In particular, the expansion and slip motion model was proposed by Shimikawa et al. [19] to explain the photoinduced changes in volume observed in normally-deposited films. Recently, Kuzukawa et al. [17] have justified the 'giant' changes observed in the thickness and the bandgap of As_2Se_3 and As_2S_3 thin films, as a consequence of illumination, on the basis of the same model. The essence of this model is schematically illustrated in Fig. 5 and it can be summarized as follows: It is assumed that amorphous chalcogenides contain disordered structural layers as a constituent element of their structure, and considered that during illumination there is an accumulation of electrons in these layered clusters, which causes Coulomb repulsion between them and therefore it gives rise to volume expansion. Unlike these electrons, which reside in the conduction-band tails, photocreated holes diffuse away to a non-illuminated area through the valence band or their tail states. Since it has been shown that the rate of volume expansion is greater than photodarkening [22], it is expected that photodarkening is not induced at this stage. Instead, it is believed that in conjunction with the occurrence of the interaction between adjacent clusters, a slip motion along the structural layer is generated, which causes an increase in the energy of the highest occupied states in the valence band, due to an increase in the lone-pair–lone-pair interactions. Thus, although the conduction band remains practically unchanged, the valence band gets wider [23].

On the other hand, since thermally-evaporated arsenic-rich amorphous films, such as $As_{50}Se_{50}$, can be regarded as a mixture of As_2Se_3 and As_4Se_4 molecules, whose structure can be represented as As_4Se_4 molecules dissolved in a matrix formed by $AsSe_3$ pyramids, it could be suggested that two mechanisms could coexist. One of them would involve the 'pyramidal' network (repulsion and slip motion of the structural layers), whereas the other would deal with As_4Se_4
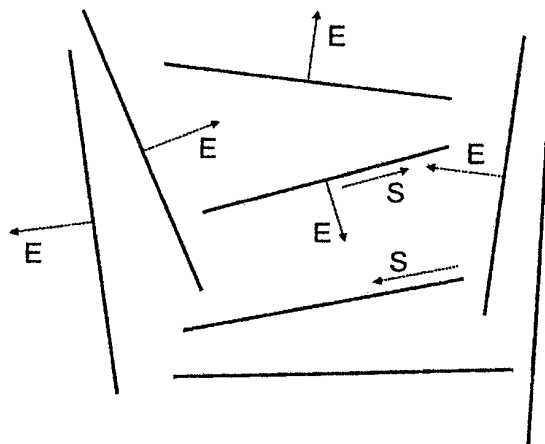
Fig. 5. Schematic illustration of the layered clusters in amorphous chalcogenides. The expansion and slip motions are indicated by arrows E and S, respectively.

molecules. These molecules have a cage-like structure, in which a square of Se atoms bisects a distorted tetrahedron of As atoms. The average As-As bond length in As_4Se_4 is 2.57 Å, and the As-As-Se bond angle subtended at either one of the As atoms comprising the As-As bonds, is 101.2°. If one compare those values with the corresponding bond distance and bond angle in a-As, 2.49 Å and 98°, respectively, it is found that they are larger in the case of the As_4Se_4 molecule. The intermolecular distances, less than 3.70 Å, are shorter than the predicted van der Waals distance of 4.0 Å, which could be associated with relatively strong intermolecular interactions. As-As bonds play an important, although not predominant, role in reversible photodarkening in well-annealed As-rich thin-film samples [24]. An increase in the As-As bond concentration, as a consequence of illumination, leads to a decrease of the bandgap, owing to formation of electronic states associated with such bonds at the top of the valence band. Similarly, the subsequent annealing of the sample will lead to a decrease in the As-As bond concentration. Therefore, the bandgap will increase because breaking of As-As bonds will replace the electronic states in the gap, associated with these homopolar bonds, by non-bonding As states located near the conduction band edge.

4. Conclusions

We have studied the changes in the structural and optical properties, which take place in $As_{50}Se_{50}$ amorphous thin films, as a consequence of two successive annealing-illumination cycles. It was found that on annealing the film thickness decreases (i.e., thermal contraction), and the bandgap also decreases (i.e, thermal darkening). On subsequent illumination of the crystallized films, the thickness is found to increase (i.e., volume expansion), while the bandgap decreases (i.e., photodarkening). Post-illumination annealing decreases notably the thickness and, at the same time, increases the bandgap. Finally, the second illumination treatment gives rise to an increase of the film thickness accompanied, as before, by a decrease in the optical bandgap. We have observed 'giant' changes in both thickness and bandgap with illumination, especially after the second illumination treatment. It has also been found that the conditions of the samples after both annealing-illumination cycles, are not close to the initial conditions, although the morphological changes undergone by the wedge-shaped $As_{50}Se_{50}$ films, prevented us from obtaining results which could be easily compared.

It is suggested that in order to be able to explain all these changes, it is necessary to consider two different mechanisms. The first one would involve the expansion and slip motion of the structural

layers comprising the 'pyramidal' network, and the second one operative with the As_4Se_4 molecules, typical of thermally-evaporated As-rich chalcogenides films, and forming particularly the crystalline form of medium-thickness ($1 \div 2$ µm) $As_{50}Se_{50}$ films.

Acknowledgements

References

[1] A. V. Kolobov, Ka. Tanaka, J. Opt. Adv. Mater., **4**, 3 (1999).
[2] A. V. Kolobov, S. R. Elliott, Philos. Mag. B, **71**, 1 (1995).
[3] R. Prieto-Alcón, E. Márquez, J. M. González-Leal, J. Opt. Adv. Mater., **2**, 139 (2000).
[4] R. Swanepoel, J. Phys. E: Sci. Instrum., **17**, 896 (1984).
[5] E. Márquez, J. B. Ramírez-Malo, P. Villares, R. Jiménez-Garay, R. Swanepoel, Thin Solid Films, **254**, 83 (1995).
[6] E. Márquez, J. M. González, R. Jiménez-Garay, S. R. Lukic, D. M. Petrovic, J. Phys. D: Appl. Phys., **30**, 690 (1997).
[7] C. Corrales, J. B. Ramírez-Malo, J. Fernández-Peña, P. Villares, R. Swanepoel, E. Márquez, Appl. Opt., **34**, 7907 (1995).
[8] C. Corrales, J. B. Ramírez-Malo, E. Márquez, R. Jiménez-Garay, Mat. Sci. Eng. B–Solid, **47** 119 (1997).
[9] S. R. Elliott, J. Non-Cryst. Solids, **81**, 71 (1986).
[10] S. H. Wemple, W. DiDomenico, Phys. Rev. B, **3**, 1338 (1971).
[11] S. H. Wemple, Phys. Rev. B, **7**, 3767 (1973).
[12] R. Swanepoel, J. Phys. E: Sci. Instrum., **16**, 1214 (1983).
[13] J. Tauc, J. Non-Cryst. Solids, **8**, 569 (1972).
[14] B. Singh, S. Rajagopalan, P. K. Bhat, D. K. Pandaya, K. L. Chopra, Solid State Commum., **29** 167 (1979).
[15] S. Rajagopalan, K. S. Harshvardhan, K. S. Malhotra, K. L. Chopra, J. Non-Cryst. Solids, **50** 29 (1982).
[16] C. A. Spence, S. R. Elliott, Phys. Rev. B, **39**, 5452 (1989).
[17] Y. Kuzukawa, A. Ganjoo, K. Shimikawa, J. Non-Cryst. Solids, **227**, 715 (1998).
[18] Y. Kuzukawa, A. Ganjoo, K. Shimikawa, Philos. Mag. B, **79**, 249 (1999).
[19] Ka. Tanaka, J. Non-Cryst. Solids, **35**, 1023 (1980).
[20] A. V. Kolobov, H. Oyanagi, Ka. Tanaka, Ke. Tanaka, Phys. Rev. B, **55**, 726 (1997).
[21] K. Shimakawa, N. Yoshida, A. Ganjoo, Y. Kuzukawa, J. Singh, Philos. Mag. Lett., **77**, 153 (1988).
[22] Ke. Tanaka, Phys. Rev. B, **57**, 5163 (1998).
[23] T. Watanabe, H. Kawazoe, M. Yamane, Phys. Rev. B, **38**, 5677 (1988).
[24] G. Pfeiffer, M. A. Paesler, S. C. Agarwal, J. Non-Cryst. Solids, **130**, 111 (1991).

RAMAN INVESTIGATION OF STRUCTURAL PHOTOINDUCED IRREVERSIBLE CHANGES OF $Ga_{10}Ge_{25}S_{65}$ CHALCOGENIDE GLASSES

S. H. Messaddeq, M. Siu Li, D. Lezal[a], Y. Messaddeq[b], S. J. L. Ribeiro[b], L. F. C. Oliveira[c], J. M. D. A. Rollo[d]

Instituto de Física de São Carlos – Universidade de São Paulo, C.P. 369 , CEP: 13560-970, São Carlos, SP - Brazil
[a]Laboratory of Inorganic Materials IIC ASCR and ICT, Pelleova 24, Prague 6, Czech Republic
[b]Instituto de Química – UNESP– C.P. 355, CEP: 14801-970, Araraquara, SP- Brazil
[c]Depto de Química- Universidade Federal de Juiz de Fora, Juiz de Fora, MG- Brazil
[d]Escola de Engenharia de São Carlos- – Universidade de São Paulo, C.P. 369 , CEP: 13560-970, São Carlos, SP – Brazil

The influence of time exposure, when exposed to above band gap light (3,52 eV) and annealing, on $Ga_{10}Ge_{25}S_{65}$ glasses has been studied through their effects on the structure and optical properties. To evaluate the photostructural change infrared and Raman spectra for bulk $Ga_{10}Ge_{25}S_{65}$ glasses have been measured before and after exposure. The Raman spectra are interpreted in terms of models in which the Ge atoms are fourfold coordinated and the S atoms are two fold coordinated. The observed changes in the spectral region of (S-S) stretching vibration (470-490 cm $^{-1}$) is a direct evidence for the occurrence of important structural changes in local bonding configuration caused by optical irradiation. It is shown that the dominant photostrucural changes are chain formation tendency of the chalcogenide atoms under the laser irradiation rather than rings.

1. Introduction

Photoinduced changes of amorphous chalcogenide glasses have been the subject of extensive study from the point of view of both technological applications and also understanding of the nature of the phenomena [1-3]. These glasses, when illuminated by band-gap light, usually exhibit a blue or a red shift of the optical gap, namely photobleaching or photodarkening, respectively. Furthermore, such photoinduced changes can be in general irreversible, i.e., the changes are permanent after irradiation, or reversible in which case the changes can be removed by annealing to the glass transition temperature, T_g.

A number of different phenomenological models have been suggested to explain these experimental results as part of efforts to determine and understand the structures of chalcogenide glass networks [4-6]. In stoichiometric As_2S_3 glasses for example, where one expects just As-S bonds [7], it was concluded from Raman scattering studies that a number of the so-called "wrong" As-As bonds was created with light exposure. In our previous investigation of photoinduced changes in GaGeS glass [8] we have reported a UV induced photobleaching effect associated with a positive volume change (photoexpansion). Nevertheless, many photoinduced effects are still not understood and new photoinduced phenomena, such as photoinduced anisotropy, gyrotropy, etc. have emerged [9-12]. Behind all this effort is the need to describe and understand the physical and chemical properties of amorphous chalcogenides and their interaction with light.

As a part of the efforts to understand the structure of chalcogenide glasses network as well the structural change which can occur after illumination, Raman scattering continues to provide useful insights into the local structures of the vitreous state. The Raman spectra of GeS glasses have been

discussed in terms of structural model in which the element of local order is a tetrahedral arrangement of S atoms about a central Ge atom, i.e., a GeS$_4$ tetrahedron. We used Raman scattering to determine as far as possible the structural change which can occur in this glass after illumination. We have observed diffusion of S atoms towards the illuminated area [8] and in this work we present more results on the characterization of the species so formed.

2. Experimental

Polycrystalline germanium, gallium and sulfur were weighted, mixed together and transferred to a silica ampoule. After vacuum sealing, a heat process with a heating rate 0.33 K/min up to 950° C was started. At 950° C the liquid was homogenized for 6 hours through a continuous horizontal rotation. Then the ampoule was withdrawn from the furnace and air-cooled. Annealing at 400° C for several hours followed.

These samples were illuminated at different exposure times (1 to 6 hours) with light from a cw Kr$^+$ ion laser (351 nm). The output power density of the laser was 5 W/cm^2.

The optical absorption edge was determined using a spectrophotometer (Cary 5). For this experiment, samples of 1 mm in thickness were measured in transmission in the wavelength range from 200 to 700 nm.

The morphology and composition were measured before and after exposure to U.V. light. Exposed and non-exposed surface areas were analyzed using a scanning electron microscope (SEM) (Zeiss 960) to which an Energy Dispersive X-Ray (EDX) analyzer (QX2000) is coupled. Compositional contrast of the exposed and non-exposed areas was determined by backscattered electrons (BSE).

The Raman scattering measurements were preformed with the normal back scattering configuration in the wavenumber region from 200 to 800 cm^{-1}. The 488 nm line of an Ar$^+$ ion laser was used as a light source.

3. Results

Fig. 1 shows a plot of absorption coefficient (α) against photon energy (hν) which illustrate the shift of the edges for Ge$_{25}$Ga$_{10}$S$_{65}$ exposed at to the UV light for different times. The optical absorption measurements reveal that the absorption edge of the glass sample shifted to shorter wavelengths after irradiation indicating a photobleaching effect. Nevertheless there is a significant difference between the shift of the edge for samples exposed and annealed at glass transition temperature (T$_g$). A photodarkening effect is observed in the last case. Unlike to exposure, it is observed that the annealing leads to darkening. We observed that E$_g$ increases from E$_g$= 2.63 eV for non-exposed glass, to E$_g$ =2.64 eV for exposure during 10 hours and E$_g$ decreases to E$_g$= 2.55 eV for annealing at T$_g$.
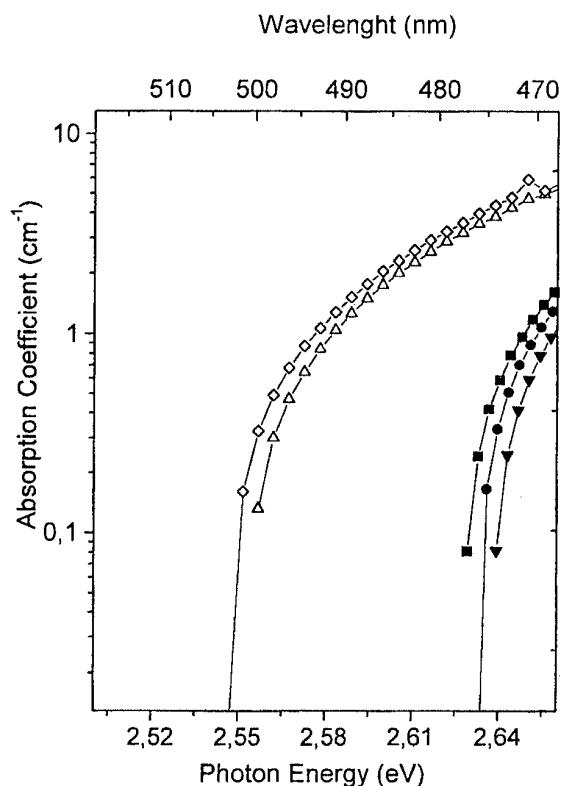
Fig. 1. Optical absorption spectra for $Ga_{10}Ge_{25}S_{65}$ exposed at different time: (■) non-exposed,
(●) exposed 5 hours, (▲) exposed 10 hours, (□) exposed 5 hours and annealing at Tg, (◇)
exposed 10 hours and annealing at Tg. Lines are drawn as guides for the eyes.

Fig. 2 shows morphological analyses of the exposed area by backscattering electrons (BSE).
Local analysis of the glass surface area by backscattering electrons (BSE) images distinguishes two
regions: a brighter area (non–exposed to UV light) and a darker area corresponding to the S-rich
element (photoexpanded and photobleached).
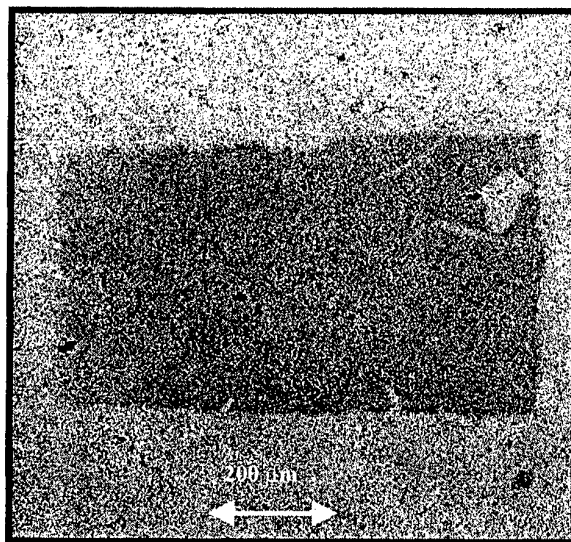
Fig. 2. Back scattering electron (BSE) of the irradiated surface area of the $Ga_{10}Ge_{25}S_{65}$, reveals
a change in the glass composition, the brighter region representing non-exposed and the darker
region is the photoexpanded and photobleached area.

As the image of (BSE) is built in contrast caused by element difference, the higher the atomic number, the more likely it is that backscattering will occur. Thus, as the electron beam passes to region of larger Z (atomic number), the signal due to backscattering, and consequently the image brightness increases. The gray levels, observed in Fig. 2, can be interpreted as regions of different composition with decreasing average atomic number corresponding to the decreasing brightness.

Irradiated samples (exposure time 2 hours, power density 5 W/cm^2) with 800 nm on thickness of the expanded area, have been treated at different temperature from room temperature to the glass crystallization temperature (T_g=470 °C). Fig. 3 shows a set of photographs of the samples at different temperatures.

non-exposed   exposed
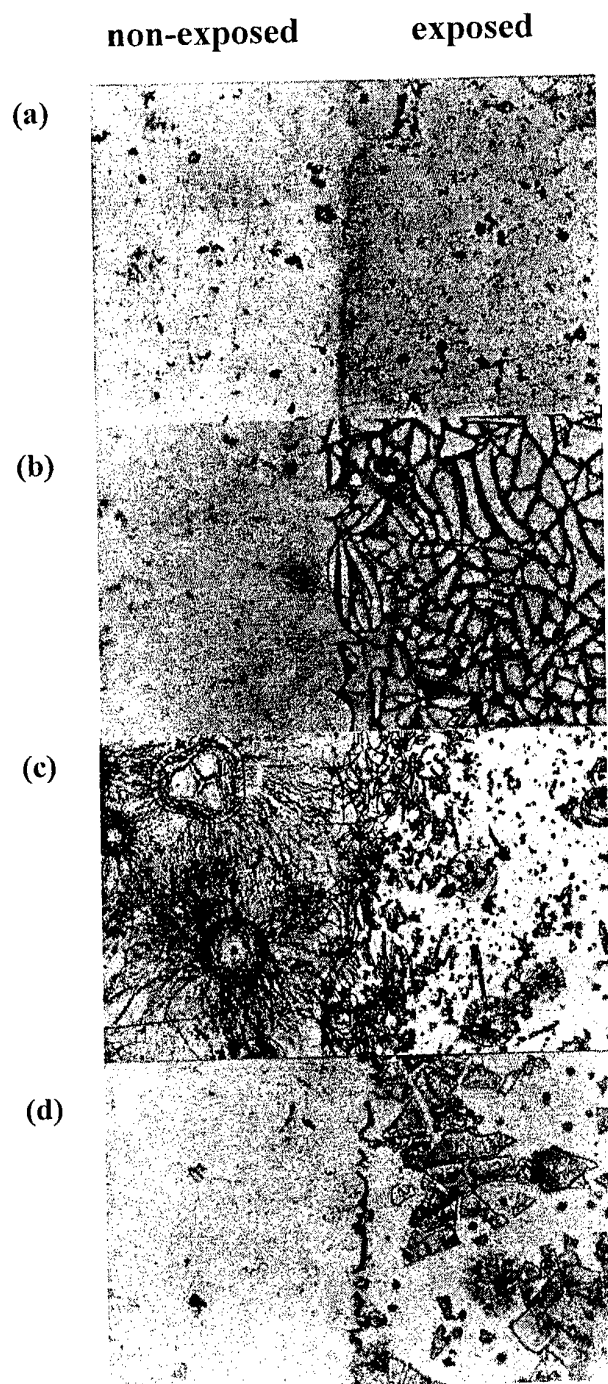
Fig. 3. Photographs of a evolution of the glass surface exposed at 5 W/cm^2 during 2 hours (right side) and non - exposed (left side) heat treated at different temperatures: (a) room temperature, (b) 420 °C, (c) 450 °C and (d) 470 °C.

When temperature reaches 420°C cracking of the glass surface is observed. Initial crystallization at the glass surface is noted at temperature around 450 °C and completed at 470 °C.

Fig. 4 presents Raman spectra performed in the spectrum 200-800 cm^{-1} range for the glass $Ga_{10}Ge_{25}S_{65}$ (a-GaGeS). Four bands at 273, 340, 430 and 475 cm^{-1} are observed. The Raman spectra obtained for crystalline sulfur (c-S) and GeS_2 (c-GeS_2) are also shown for comparison. Good agreement with spectra of GeS_2 crystal reported earlier by other research groups [13,14].
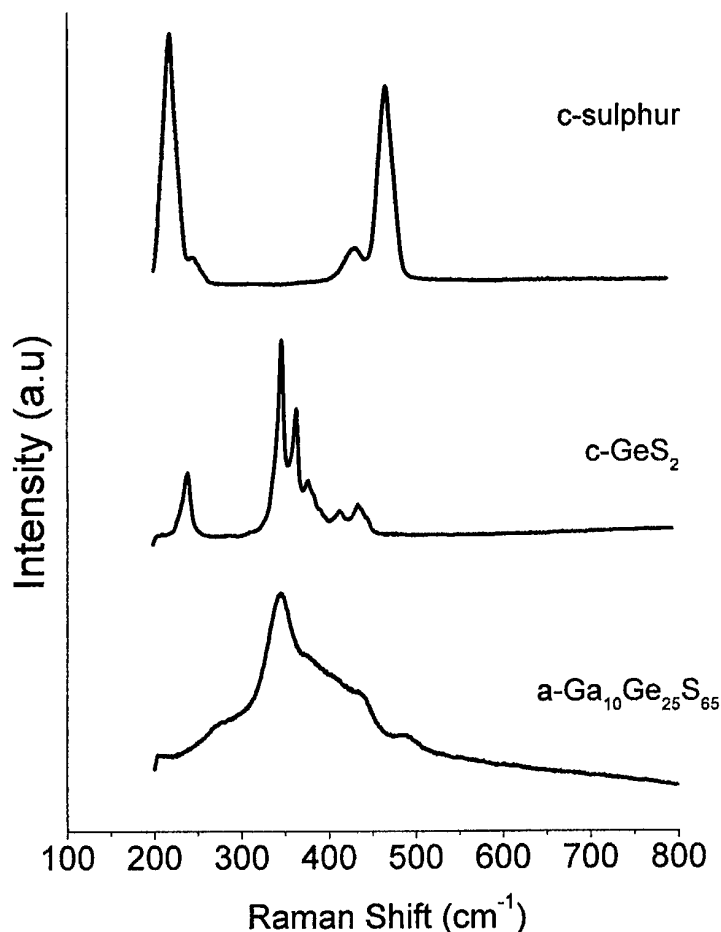
Fig. 4. Raman scattering spectra for Ga $_{10}Ge_{25}S_{65}$, c-GeS_2 and c-S taken with a 633 nm excitation energy at room temperature.

The first band at 273 cm^{-1} may be assigned to sulfur rings. The strong band at 340 cm^{-1} is due to a heteropolar bond, in this alloy system a Ge-S vibration assigned to bond-bending modes and the A_1-type bond-stretching mode of $GeS_{4/2}$ tetrahedra [13,14,15]. The band at 430 cm^{-1} is currently regarded following two ideas: one is to assign the band to vibrational modes of edge-sharing bi-tetrahedra, $Ge_2S_{2+4/2}$. This structure is known to exist in c-GeS_2, and its existence has also been demonstrated in a glassy phase [13] . On the other hand, some researchers have assigned the 430 cm^{-1} band to the S-S stretching mode, coming from cluster edges dimmers [16]. The band at 475 cm^{-1} is assigned to S_8 molecules [17].

Raman spectra of the samples irradiated for different times are presented in Fig. 5.
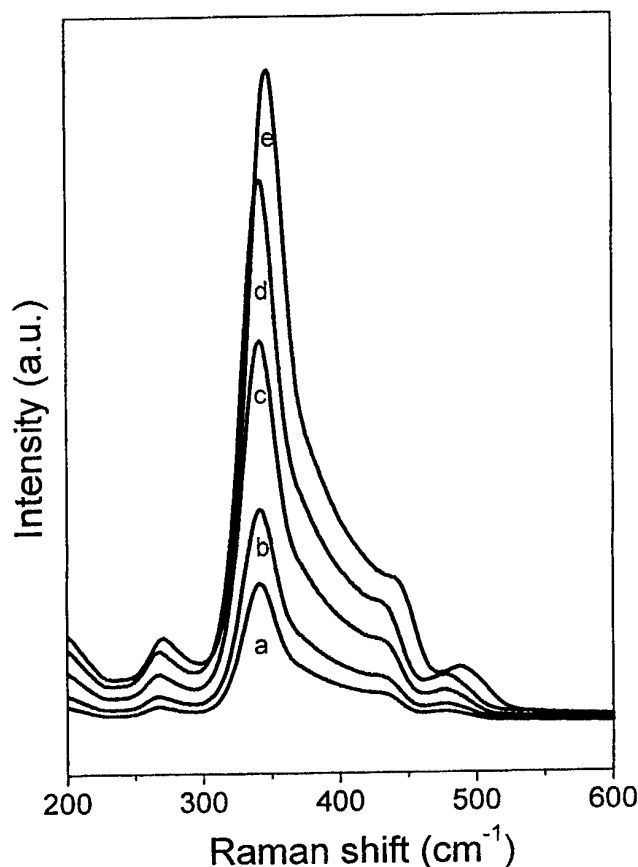
Fig. 5. Raman scattering spectra for $Ga_{10}Ge_{25}S_{65}$ illuminates at 5 W/cm^2 for different time exposure at room temperature. (a) non-exposed, (b) 1 hours, (c) 2 hours, (d) 4 hours and (e) 6 hours.

Finally the irreversible photobleaching of amorphous GaGeS glasses can be associated with a (i) an increase of the density of heteropolar bonds and (ii) increase of sulfur into the illuminated area of the Ge-S matrix surface.

5. Discussion

A large photobleaching effect is observed on samples exposed at different time using lower power density ($I=5$ W/cm^2). From Fig. 1, we may note the increase of the photobeaching with increase of time exposure and this process is irreversible, in the sense that annealing does not restore the original E_g to the initial value for non-exposed glass. It is known [18] that the absorption edge of an amorphous semiconductors shifts to lower energy if it contains mores defects. We think that the annealing at T_g could induce some defects through the weakens bond.

The present photobleaching effect differs from the one observed for As_2S_3 [19]. The Fig. 2 indicate a diffusion of sulphur atom into irradiated area. Consequently, we may assume that this diffusion will result in the creation of new S-S bonds in the irradiated area. Such polimerization may explains the effect of photobleaching which acompanies a glass network expasion in GaGeS glass.

With regards to the Raman spectra of the samples irradiated for different times (Fig. 5) an increase in intensity is observed for the whole spectrum. Moreover a blue shift is observed as the exposure time increases from 1 to 6 hours indicating that through the absorption of high energy photons, intramolecular covalents bonds are broken. The most obvious difference compared with non-exposed glasse is the dramatic shift of the band at 475 to 490 cm^{-1}. It is known that in S-rich composition there are additional absorption lines at 475 and 273 cm^{-1} correlated these with two of the

three dominant absorption bands of S_8 molecules. According to the structural model of binary Ge-S glasses proposed by Lucovsky et al [17] glasses with S contents in excess of stoiciometry contain increasing number of S-S bond and ultimatly, at the largest level of S_8 rings. As a first assumption the photoexpansion of these glasses results from a microstructural transformation with the formation of new sulfide chains which may be confirmed by the shift bound from 470 to 490 cm^{-1}. G.J. Janz et al. have assigned the shift to higher frequency (from 400 to 490 cm^{-1}) to a diminution in the size of polysulfides anions from S_6 to S_3 [20]. At this stage, the dissociation of a S_8 ring molecule into smaller chains can be proposed from the spectroscopic observation. Messaddeq et al. [8] observed that following the absorption of light, the sulfur atoms difuses to the irradiated area from the non irradiated surrounding. This motion will result in the creation of new S-S bonds in the irradiated area. The same behaviour has been observed in cryobaric Raman scattering experiment on g-GeS_2 [21]. The appearence of 486 and 250 cm^{-1} modes are signature of S-rich (S_8 or S^n chains) and Ge- rich (GeS microphase). These results provide additional support for our identification of broken bonds after ilumination.

As we have observed from Fig. 1, the annealing leads to a darkening and cracking of the glass surface (Fig. 3). The tendency toward formation of crack verified for samples heat treat could result from the higher intensity of the internal stresses associated with photoexpansion. Due the stiffness of the glass surface, the shrinkage must occur only in the perpendicular direction of the surface and the photoexpanded area is constrained by the bulk glass. As a consequence, the average stress at photoexpanded area-bulk glass interface is proportional to the thickness of the expansion [22],i.e., the tendency to cracking increases with the thickness of the expanded area.

6. Conclusions

The pronounced changes observed in the Raman spectra obtained for UV illuminated $Ga_{10}Ge_{25}S_{65}$ glasses are related to structural changes in the local bonding configuration. The $Ga_{10}Ge_{25}S_{65}$ glass is essentially a solid solution consisting of a network of very short S chains cross linked by four-coordinated Ge atoms, and a monomer component of S_8 ring molecule. It has been shown that under laser irradiation, the bonding tendency of the chalcogenide atoms is to forms chains rather than rings. In addition it was demonstrated that in these glasses the photoexpansion and photobleaching are irreversible after heat treatment.

References

[1] K. Tanaka, Solid State Comm. **34**, 201 (1990).
[2] K. Tanaka, Solid State Comm. **34**, 1521 (1974).
[3] S. S. Fouad, H. M. Talaat, S. M. Youssef, A. El-Korashy, M. M. El-Oker, phys. status solidi (b) **187**, K51 (1995).
[4] A. C. Wright, A. J. Leadbetter, Phys. Chem. Glasses **17**, 122 (1976).
[5] R. W. Fawcett, C. N. J. Wagner, G. S. Cargill, J. Non-Cryst. Solids **8-10**, 369 (1972).
[6] O. Uemura, Y. Sagara, T. Satow, phys. status solidi (a) **26**, 99 (1974).
[7] M. Frumar, M. Vlcek, Z. Cernosek, Z. Polak and T. Wagner, J. Non-Cryst. Solids **213&214** 215-224 (1997).
[8] S. H. Messaddeq, Y. Messaddeq, D. Lezal, M. Siu Li, J. Non-Cryst. Solids, May 2001, in press.
[9] H. Fritzche, Phys. Rev. **B 52**, 15854 (1995).
[10] M. Klevanov, S. Shutina, Bar, V. Lyubin, S. Rosenwaks, V. Voltera, Proc. SPIE **2426**, 198 (1995).
[11] K. Tikhomirov, S. R. Elliot, Phys. Ver. **B5**, 5538 (1995).

[12] V. K. Tikhomirov, S. R. Elliot, J Phys. Condens. Matter. **7**, 1737 (1995).

[13] P. Boolchand, J. Grothaus, M. Tenhover, M. A. Hazle, R. K. Grasseli, Phys. Rev. **B33**, 5421 (1986).

[14] Y. Nagata, S. Kokai, O. Uemura, Y. Kameda, J. Non-Cryst. Solids **169**, 104 (1994).

[15] J. Sukmanowski, I. Petscherizin, M. Soltwisch, D. Quitmann, J. Phys. Condens. Matter **2**, 2303 (1990).

[16] M. Cobb, D. A. Drabold, R. L. Cappelletti, Phys. Rev. **B54**, 1216 (1996).

[17] G. Lucovsky, F. L. Galeener, R. C. Keezer, R. H. Geils, H. A. Six, Phys. Rev. **B10**, 5134 (1974).

[18] N. F. Mott, E. A. Davis, Electronic Process in Non-Crystalline Materials, Clarendon, Oxford, 375 (1979).

[19] S. Shtutina, M. Klebanov, V. Lyubin, S. Rosenwaks, V. Volterra, Thin Solid Films, **261**, Issue: 1-2, June 1, pp. 263-265, 1995.

[20] G. J. Janz, J. W. Coutts, J. R. Downey, E. Rouduner, Inorganic Chemistry, **15**,8, 1755 (1975).

[21] A. Weinstein, M. L. Slade, in Optical Effects in Amouphous Semiconductors (Snowbird, Utah, 1984), edited by P. C. Taylor, S. G. Bishop (AIP, N.Y., 1984), p. 457.

[22] A. Jagota, C. Y. Hui, Mechanics of Materials **9**, 107 (1990).

UV IRRADIATION EFFECTS IN PURE AND TIN-DOPED AMORPHOUS AsSe FILMS

M. Popescu, M. Iovu [a], W. Hoyer [b], O. Shpotyuk [c], F. Sava, A. Lőrinczi

National Institute of Materials Physics, P.O. Box MG7, RO-76900 Bucharest-Magurele
[a] Center of Optoelectronics, 1 Academiei Str., MD-2028 Chishinau, Moldova
[b] Institut für Physik, TU-Chemnitz, D-09107 Chemnitz, Germany
[c] Institute of Materials of Scientific Research Company "Carat", UA-79031 Lviv, Ukraine

Pure and tin-doped AsSe amorphous films were investigated. The changes in the MRO induced by Sn were analysed be accurate profiling the first sharp diffraction peak (FSDP) in the X-ray diffraction diagram. A shift of FSDP as a function of tin concentration was observed. The structural changes induced by ultraviolet rays (λ = 336 nm) for various time intervals of irradiation were revealed by small angle X-ray diffraction. It was revealed the formation of a special layer at the surface of the films, whose thickness increases during UV irradiation.

1. Introduction

Amorphous chalcogenide materials based on As-S and As-Se show significant changes when illuminated with band-gap light [1].

The high-energy quanta situated in the UV spectral range are expected to induce qualitatively new changes in the chalcogenide glasses because the quantum energy is equal or exceeds the chemical bond energy [2]. Berkes et al. [3] and Tagantsev and Nemilov [4] have observed modifications induced by UV radiation in amorphous chalcogenide films. A significant decrease of viscosity and a flowing effect have been revealed. As a consequence of irradiation a smooth topography of fresh films was obtained.

In other chalcogenides, as e.g. in antimony chalcogenide films, UV radiation induces a shift of the optical absorption edge and significant changes in the dissolution kinetics of the material and this effect suggested the use of the films as optical memory media and as photoresist. Lőrinczi [5] observed that Ge-Sb-Se films are sensitive for the UV radiation, and exhibit mechanical, optical and structural changes.

Tin-doped AsSe and As_2Se_3 films are important because the metal stabilizes the parameters of the recording media through the formation of a more rigid network [6]. This opens the way for applications in optoelectronics. In this paper is investigated the effect of UV radiation on amorphous AsSe and AsSe:Sn_x films.

2. Experimental

The starting materials for thin film deposition were prepared by a standard melting procedure: the elements (6 N purity for As and Se; 5N purity for Sn) were mixed in an evacuated ampoule and then heated at two temperature steps: 870-920 K and 1070-1120 K [7]. The films of thickness from 2 to 3 μm were deposited by the flash evaporation technique in vacuum onto silicon wafer substrates held at 100 °C. AsSe:Sn_x films with x=0; 1; 2; 3; 5 and 7.5 at. % were prepared. X-ray diffraction measurements were carried out in a TUR M-62 diffractometer, provided with a copper target tube.

UV-irradiation was performed with a UV-Rom medical lamp (λ_{max}=336 nm) at a power density of 116 μW/cm^2. The temperature reached by the films during irradiation did not exceed 40 °C.

3. Results

Pure and tin-doped AsSe films were investigated by X-ray diffraction. The X-ray diffraction patterns before and after ten hours of UV-irradiation for the film with 7.5 % Sn are shown in Fig. 1. While the virgin film is completely amorphous, after the UV irradiation a crystalline phase identified as As_2O_3 (arsenolite) does appear.
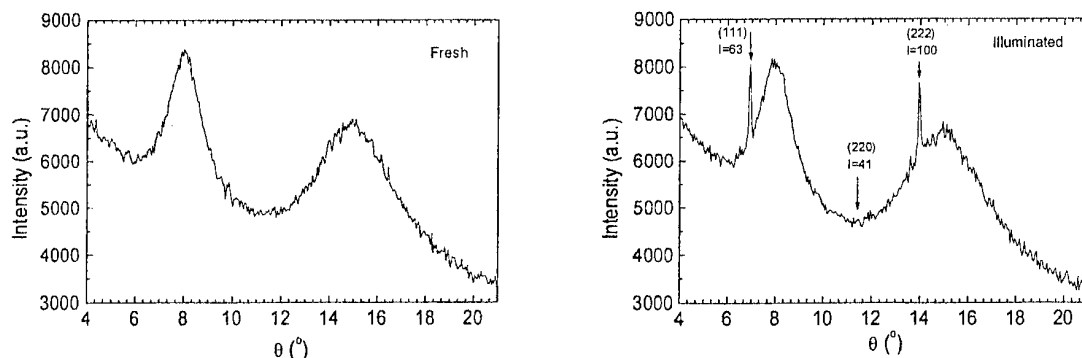
Fig. 1. X-ray diffraction patterns of fresh and UV-irradiated film of amorphous AsSe with 7.5 at.% Sn. The arrows indicate the positions of the arsenolite (As_2O_3) peaks.

The FSDP position for pure AsSe films corresponds to the quasi-periodicity, d, of 5.39 Å. A large peak width of 1.41 ° speaks in favour of a small correlation length in the film. After UV-irradiation the FSDP diminishes its intensity, shifts to lower quasi-periodicity (5.33 Å) and increases its width.

The changes induced by UV irradiation were studied by X-ray scattering at small diffraction angles. Significant interference peaks were observed (Fig. 2). From the periodicity of the peaks it was possible to calculate the thickness of the arsenolite layer formed at the surface of the film.
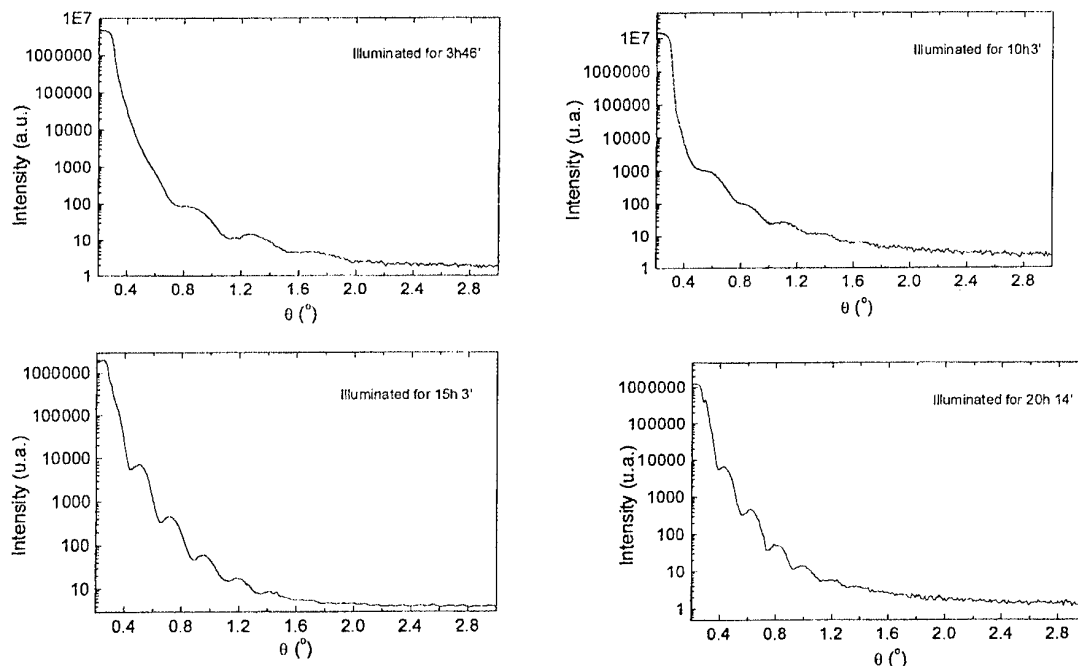
Fig. 2. Small angle X-ray scattering with the interference fringes due to the layer formed at the film surface, by UV irradiation (AsSe films doped by 7.5 at. % Sn).

For the case of the sample doped by 7.5 at.% Sn, long-time irradiation was carried out (~20 h) and after different time intervals the structure was investigated by X-ray diffraction. The thickness of the surface layer was calculated for each step of irradiation. Fig. 3 shows the results.
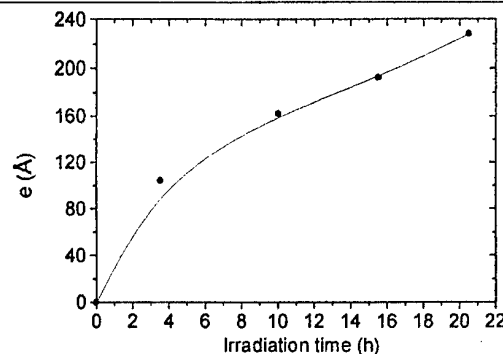
Fig. 3. The growth of the thickness of the As_2O_3 layer induced by UV-radiation for various exposure times in AsSe films doped by 7.5 at. % Sn.

The thickness, e, of the As_2O_3 layer raises rapidly in the first 3 hours of irradiation up to 105 Å. A linear relation e(t) holds for large irradiation times (Fig. 3). The rate of formation of the surface layer is 7 Å/h. For the tin-doped samples the quasi-periodicity of the amorphous network increases linearly. After UV-irradiation the increase of the quasi-periodicity with tin content maintains its linear character but the slope of the evolution line is larger. Fig. 4 shows the results.
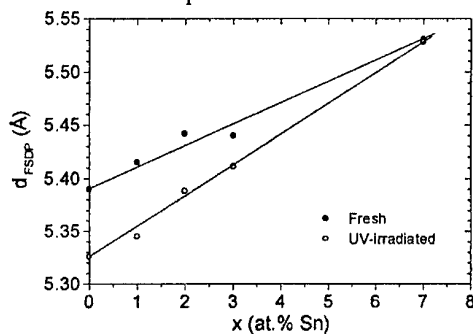
Fig. 4. The evolution of the quasi-periodicity distance, d, versus the tin content in AsSe before and after UV irradiation.
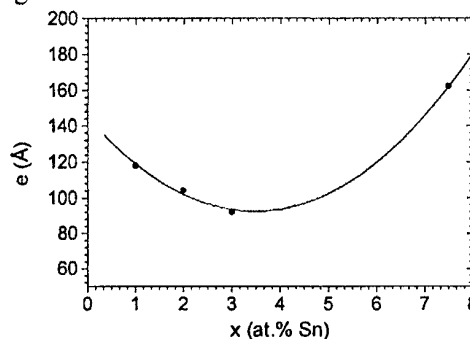
Fig. 5. The thickness of the As_2O_3 layer induced by UV radiation (10 h) versus tin content in amorphous AsSe films.

Fig. 5 shows the evolution of the thickness of the As_2O_3 layer as a function of tin content in the film for ~10 h of irradiation. The values for x=0 and x=5 were ommitted because the weakness of the interference fringes prevented the accurate determination. It is remarkable the fact that the thickness of the surface layer firstly decreases with the Sn content, then, after reaching a minimum at x = 3 at.% Sn, it increases. This effect speaks in favour of a better stability of the films induced by tin for small concentration of this metal.

4. Discussion

The role played by impurities in amorphous semiconductors is emphasizing for two structure-related problems: the nature of the defects and the medium-range ordering. The structure of the AsSe glass is usually treated on the base of a model built from structuro-chemical units: AsSe, $AsSe_2As$, $AsAs_3$ [8, 9]. The molecular units As_2Se_3 and As_4Se_4 prevail in AsSe [10], where each As site has one As-As homobond [11]. The homobonds significantly lower the mean bonding energy of the As-Se matrix in compositions with deviation from the stoichiometrical As_2Se_3. Under these conditions the formation of new structuro-chemical units like SnSe or $SnSe_2$ is probable. Such units were confirmed by a Mössbauer spectroscopic study [12] from which it was deduced that tin impurities in As-Se glasses interact only with Se atoms, and entered the glass matrix with a maximum valence (+4) and coordination number 6 (as in $SnSe_2$). The structuro-chemical units are joined together with various degree of polymerisation. The medium-range order in AsSe amorphous films can be understood as a system of corrugated layers similar to those in the crystalline As_2Se_3. Both in tin-doped As_2Se_3 [13] and in our tin-doped AsSe films it was found that the quasi-periodicity increases linearly when tin is added to the chalcogenide matrix. Tin, with its lower electronegativity in the case of Sn-Se bonding than in the case of Sn-As bonding acts as a network former by increasing

the effective thickness of the layers and, possibly, the correlation length. The photo-annealing process induced by UV irradiation determines a local rearrangement of the bonds. Part of the numerous bonds from AsSe is transformed into heteropolar bonds. The effect must be, therefore, higher for small amount of tin, and smaller for high tin content. This way the behaviour of the FSDP in both fresh and photo-annealed films can be explained. The quasi-periodicity distance is changed because UV light maximize the hetero-polar bonds, and, consequently, the disordered AsSe:Sn layers become thinner. As concerning the minimum in the thickness of the transformed layer at the surface of the film, we must compare this result with the result on photodarkening observed by Iovu et al. [7] on the same films. It was shown, that tin impurity reduces the photodarkening, and the degree of reduction becomes stronger as the impurity concentration is increased. Thermal treatment of the films at 100 °C and 170 °C, in vacuum, changes the photodarkening, as a function of Sn concentration: photodarkening is reduced for < 2 at.% Sn and is enhanced at higher concentrations. The effect of the tin additionon on the structure and photodarkening is in agreement with the model of Shimakawa et al. [14]. The metal atoms provide bridging between the layers and hence reduce the slip motion, thus hindering the photodarkening, while allowing a larger inter-layer distance. During exposure to light the layers becomes negatively charged due to capture of photoexcited electrons and repulsive forces are built between the layers. These forces cause the increase of the interlayer distance. In the same time the partial elimination of the wrong (homopolar) bonds causes a reverse process of interlayer decrease. Both effects are in competition. For high Sn content the two processes reach an equilibrium and no change of the quasi-periodicity distance takes place, as proved in figure 4 for the tin concentration of 7.5 at.% Sn. Shpotyuk et al. [15] have explained the photo- and thermo-induced transformation in simple amorphous chalcogenides (as e.g. As_2S_3) as a formation, and respectively annihilation of coordination defects. Up to now, we have no firm explanation of the minimum in the properties of AsSe:Sn_x films at ~3.5 at.% Sn, but the consideration of the effect of better dispersion of the Sn-Se units accompanied by the increase of the rigidity of the network, seems to be useful.

5. Conclusion

X-ray diffraction measurements allowed to reveal significant structural modifications induced in pure and tin-doped AsSe amorphous films by ultraviolet light. Long time UV irradiation in air induced the formation at the surface of the films of As_2O_3 (arsenolite) layer. Tin has a stabilizing effect against the transformations of the AsSe films with a maximum effect for ~3 at.%Sn. The structural modifications of the AsSe films as a function of tin doping and the resistance of the film against UV irradiation were explained in the frame of the Shimakawa's model.

References

[1] S. R. Elliott, J. Non-Cryst. Solids, **81**, 71 (1986).
[2] E. G. Barash, A. Iu. Kabin, V. M. Lyubin, R. P. Seysian, J. Techn. Phys. (russ.) **62** (3), 106 (1992).
[3] J. Berkes, S. W. Ing, W. J. Hillegas, J. Appl. Phys., **42**, 4908 (1971).
[4] D. K. Tagantsev, S. V. Nemilov, J. Stekl. Nauk (russ.) **11**, 352 (1986).
[5] A. Lőrinczi, J. Optoel. Adv. Mat. **1** (1), 37 (1999).
[6] M. Iovu, S. Shutov, S. Rebeja, E. Colomeyco, M. Popescu, J. Optoel. Adv. Mat., **2** (1), 53 (2000).
[7] M. S. Iovu, S. D. Shutov, S. Z. Rebeja, E. P. Colomeyco, M. Popescu, phys. stat. sol. (a) **181**, 529 (2000).
[8] G. A. N. Connel, G. Lucovsky, J. Non-Cryst. Solids, **31**, 123 (1987).
[9] O. Luksha, V. Ivanitsky, S. Kolinka, J. Non-Cryst. Solids, **136**, 43 (1991).
[10] T. Katahara, T. Arai, J. Phys. Soc. Japan, **49**, 1358 (1980).
[11] Z.M. Zaleh, G. A. Williams, P. C. Taylor, Phys. Rev. B **40**, 10557 (1990).
[12] P. P. Seregin, V. L. Sivcov, A. N. Vasilev, Fiz. The. Poluprov. (russ.) **8**, 2270 (1974).
[13] M. S. Iovu, N. N. Syrbu, S. D. Shutov, I. A. Vasiliev, S. Rebeja, E. Colomeyco, M. Popescu, F. Sava, phys. stat. sol. (a) **175**, 615 (1999).
[14] K. Shimakawa, N. Yoshida, A. Ganjoo, Y. Kuzakawa, J. Singh, Phil. Mag.-Lett. **77**, 153 (1998).
[15] O. I. Shpotyuk, Jkasperczyuk, I. V.Kityk, J. Non-Cryst. Solids, **215**, 218 (1997).

LASER PULSE EFFECTS IN Se-S GLASSY THICK FILMS

D. Savastru, R. Savastru, L. Ion[a], M. Popescu[b]

National Institute for Optoelectronics, INOE 2000, PO Box MG 5, RO-76900,
Bucharest-Magurele, Romania
[a]University of Bucharest, Dept. of Solid State Physics, PO Box MG 11, RO-76900,
Bucharest-Magurele, Romania
[b]National Institute of Materials Physics, PO Box MG 7, RO-76900,
Bucharest-Magurele, Romania

Amorphous thick films in the system Se-S have been prepared by splat-cooling. Local irradiation of the films with laser pulses of various intensities and wavelengths were carried out. The effects induced by laser pulses with special emphasis to the eutectic composition $Se_{42}S_{58}$ were investigated by optical microscopy and before and after annealing of the films. For low density of power incident on the film, a local photo-darkening effect is observed. For mean power density the photo-darkened region increases. For high power density a considerable destructive effect appears, which determine the appearance of clusters of bubbles after annealing the film at the softening temperature.

1. Introduction

Thick non-crystalline films in the system Se-S have been obtained by quenching the corresponding melts to room temperature. The photo-structural effects induced in the Se-S films are accompanied by modifications of the position of the absorption edge and of the refractive index [1]. For high incident power the accompanying thermal effect induces crystallization and local evaporation. The annealing effect after irradiation, with the formation of small bubbles, suggested using these films in designing a new type of optical memory device with $Se_{0.975}S_{0.025}$ [2].

In this paper we report the results of a study of the effect of laser pulses on the thick Se-S films, with special emphasis on the eutectic composition, prepared in non-crystalline state by splat cooling.

2. Experimental

Homogeneous composition in the system Se-S were prepared by encapsulating the mixture of selenium (99.999 Hoboken sulfur 99.9, Romanian Trade Mark) in evacuated Pyrex ampoules followed by heating at ~220 °C. The ampoules were maintained for 2 hours at this temperature and were shaked from time to time. Then the melts were quenched on a copper block covered by a tungsten foil. Glassy films of thickness ~ 0.1-0.2 mm were obtained. The following Se_xS_{1-x} compositions were prepared: (x= 0.25; 0.42, 0.5; 0.6; 0.8; 0.9). Red, dark-red and gray films were obtained, as a function of composition. All the films exhibited plasticity, related to the non-crystalline structure, as proved by optical inspection and x-ray diffraction.

Then the films were pressed between two ordinary glass plates when heated at 100° C, in order to get uniform thinner films to be used as targets for laser pulses. All the films are stable at temperatures of ~ −10 °C. At room temperature some compositions with high sulfur content are stable for ~ 2-4 weeks, then they crystallize.

Two pulsed lasers were used for the investigation of the photo-induced effects in glassy Se-S films:

- a ruby laser working in relaxed regime with the pulse length of τ = 500 μs, λ = 0.6943 μm.

- a YAG-Nd laser with $\tau = 10$ ns (working in the regimes: nanopulse (14 mJ/pulse) and double pulse (28 mJ/pulse) $\lambda = 1064$ nm.

The spot can be adjusted in the range: 10 μm - 1000 μm. The examinations of the laser pulse effects were performed in a Leitz-Orthoplan-pol microscope.

A considerable attention was paid to the sample with the eutectic composition in the system: $Se_{0.42}S_{0.58}$. This composition exhibits the lowest melting temperature ($T_t = 105$ °C) [3] and the highest stability in the glassy state.

3. Results

Under the action of light the glassy chalcogenides from the system changes the position of the fundamental absorption edge, and, therefore, of the transparency [4]. This is the so-called photo-darkening effect.

Laser pulses of variable total energy were applied on the Se-S films. As a consequence, the irradiated zone suffered transformations and a latent image of the spot was registered. In time, the image develops under the form of a darkened zone. The experimental data for the composition $Se_{0.42}S_{0.58}$ are given in Table 1.

Table 1. Ruby laser pulse effect on $Se_{0.42}S_{0.58}$ glassy film.

Pulse energy (mJ)	Spot diameter (μm)	Observed photo-darkening
< 100	-	Absent
200	23	after 24 h
330	80	after 24 h
580	300	after 3 h
750	350	after 1 h
980	400	immediately

The minimum energy of the pulse (200 mJ) corresponds to a threshold for the induced photo-structural effects. It is observed a strong correlation between the size of the photo-transformed region and the total energy of the laser pulse. This behavior can be explained by the thermal induced effect of photo-transformation around the zone of pulse impact. An induced crystallization seems to be responsible for the photodarkening of the sample.

In order to prove this transformation, a thin film was irradiated on a broad area and the transformation of the $Se_{0.42}S_{0.58}$ material was investigated by X-ray diffraction.

Fig. 1 shows the results.
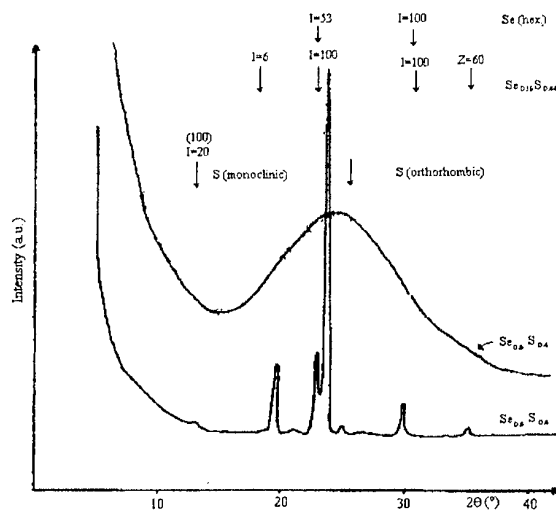
Fig. 1. X-ray diffraction before and after laser pulse irradiation and storage in dark for several days.

As a general observation, the photo-transformation of the glassy films advances in time and the advancing speed is increased by the macroscopic defects in the films (e.g. cracks, see Fig. 2c). The greatest stability against the advancement in time of the crystallization is manifested in the film of composition $Se_{42}S_{58}$. Low temperature storage determines a good stability of all the films.

Fig. 2 shows the general aspect of the photo-darkened regions in $Se_{42}S_{58}$ films.

                    a   b   c
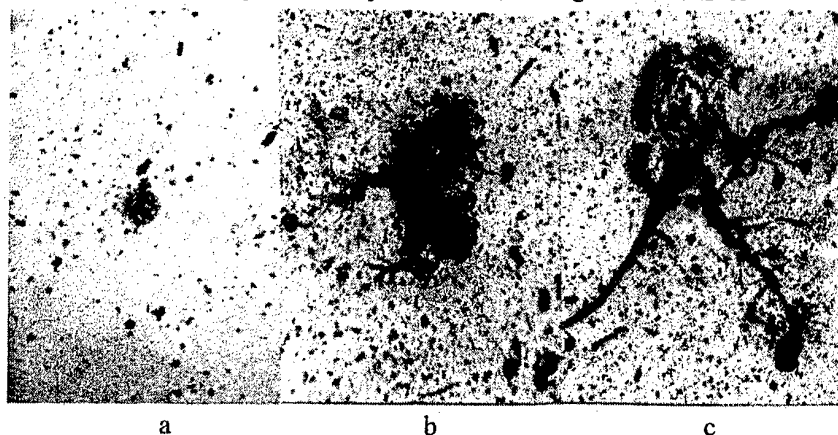
Fig. 2. Photograph of the darkened regions obtained by ruby laser pulse irradiation of a $Se_{42}S_{58}$ glassy film: a- 200 mJ (spot diameter:10 μm); b – 580 mJ; c – 750 mJ.

In the following stage of the research we have studied the effect of high-energy laser pulse on the Se-S films.

Fig. 3 shows the effect of the pulse with 980 mJ on a $Se_{42}S_{58}$ glassy film. The high power density changed considerably the region of the pulse impact (to a size of ~60-100 μm). A central crater is clearly seen. A diffusion of sulfur or even a release of this element outside the central crater is suggested. Some dark spots around the central crater are probable due to the strong thermal effects of the laser pulse.

Then, the film was subjected to thermal annealing at a temperature of ~ 100 ^{0}C. A strong transformation of the film takes place, while the central crater seems to preserve its feature: the dark spots around the crater transform in nearly perfect round bubbles, of size 10-40 μm (Fig. 4). The bubbles are very stable in time, and, due to the perfect transparency of every bubble, the cluster of bubbles defines a zone of transparency in the film.

The formation of transparent bubbles can be explained by a phase separation in the darkened zone. Some phases (e.g. sulfur) evaporates very easily during heating and, as a result of vapour pressure, it is formed in the film a disk filled with sulfur vapour. By cooling at room temperature, sulfur crystallizes at the margins of the disc, the inner part remaining empty.

Fig. 3. Images of the film $Se_{42}S_{58}$ in the region of impact of a simple laser pulse (ruby) of energy 980 mJ immediately after impact.
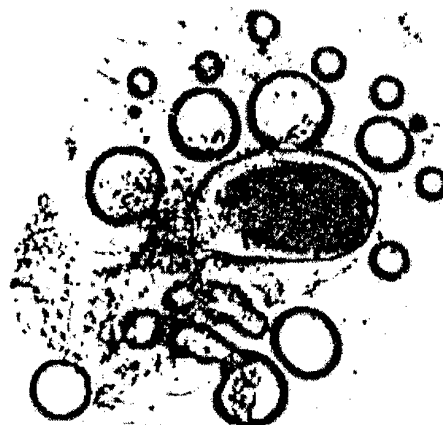
Fig. 4. The same region of the laser pulse impact, in $Se_{42}S_{58}$ film after heat treatment at ~100 ^{0}C.

The effect of the single pulse emitted by the YAG - Nd laser with the energy per pulse of 14 mJ and duration 10 ns (power per pulse : 1.4 MW; λ = 1064 nm) is shown in Fig. 5a.

a   b   c
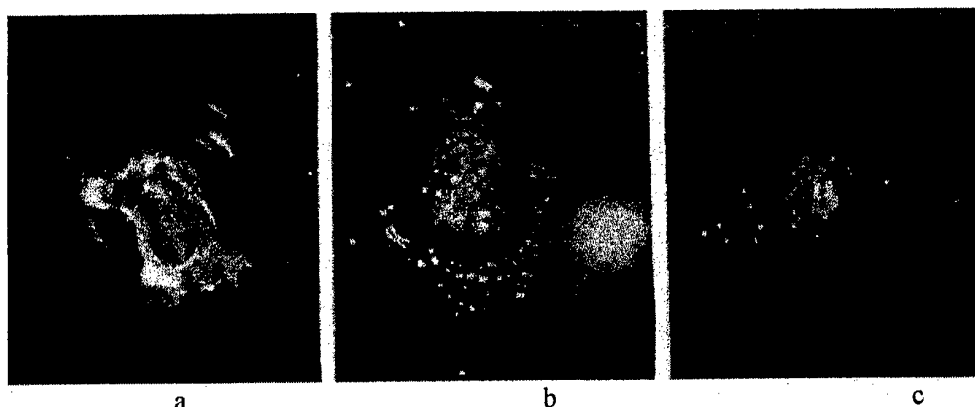
Fig. 5. The effect of a single laser pulse on the eutectic composition $Se_{42}S_{58}$. (YAG-Nd laser λ = 1064 nm : τ = 10 ns); a) E = 14 mJ; b) E = 6.7 mJ; c) E = 3.8 mJ. Magnitude: 1 cm $\rightarrow$ 50 μm

The chalcogenide film ($Se_{42}S_{58}$) is strongly damaged on a region of 70 × 120 μm. The pulse has a diameter of ~ 50μm. Fig. 5b and c shows the effect of the laser pulse whose intensity was reduced by 48% and 27%, respectively. The dimensions of the central irradiated zone are 50 × 80 μm and 30 × 50 μm, respectively. The irradiated zone changes the colour from the red to yellow due probably to the release of sulphur during irradiation. In the same time, around the laser pulse impact region, groups of micro - bubbles appears. These micro - bubbles transform into large, stable bubbles during thermal annealing as in the case of the experiments with ruby laser pulses.

The experiments with laser pulses of different wavelengths show that moderate energies produce significant modifications in Se-S materials. The main aspects are the release of sulphur and the formation of bubbles. An irreversible optical memory based on the diffusion of light on bubbles is under study.

4. Conclusions

The results obtained by irradiation of glassy Se-S films by laser pulses allowed to conclude that it is possible to get transparent bubbles, which can be suggested to be used for an optical memory. The most important composition for the formation of the bubbles seems to be $Se_{42}S_{58}$. The minimum of the bubble size obtained by us was 10 μm and the maximum 40 μm. A control of the bubble size and, especially, finding the conditions for getting of only one bubble for a laser shot can ensure an optical RAM memory of enough high density : 10^8 bit/cm^2.

References

[1] D. Jecu, J. Jaklovszky, A. Trutia, I. Apostol, M. Dinescu, I. N. Mihailescu, G. Aldica, M. Popescu, N. Vlahovici, S. Zamfira, E. Indrea, J. Non. Cryst. Solids, 90, 319 (1987).
[2] J. Feinleib, Information recording system employing amorphous materials, USA, Patent No. 3636526/1972.
[3] C. J. Smithells, Metal Reference Book, 5th Edition, Butterworths, 1978.
[4] D. Jecu, Ph. D. Thesis, Bucharest 1986.

LIGHT INDUCED CHANGES IN THE OPTICAL PROPERTIES OF THIN As - S - Ge(Bi, Tl) FILMS

R. Todorov, K. Petkov

Central Laboratory of Photoprocesses, Bulgarian Academy of Sciences, Acad. G. Bonchev Str., bl.109, 1113 Sofia, Bulgaria

In this paper we report results from studying changes in the optical properties of thin vacuum deposited films from the systems $As_{40-x}Ge_xS_{60}$ ($0 \leq x \leq 40$) and $(As_2S_3)_{100-x}Bi(Tl)_x$ ($0 \leq x \leq 15$) depending on the composition and conditions of evaporation and illumination to light. The optical transmission and reflection of thin layers deposited on BK-7 optical glass substrates have been measured in the spectral region of 350 - 1500 nm and the refractive indices and optical band gap E_g were calculated. It was found that the method of evaporation influences considerably the properties of thin chalcogenide films. The addition of Bi or Tl in As_2S_3 leads to an increase in the refractive index while Ge causes its decreasing. The illumination of as-deposited films leads to an effect of photodarkening and decreasing in the optical band gap for As-containing films and photobleaching for As - Ge - S layers. Using TRR_m methods (R_m is the reflection of 100 nm thick films deposited on Si substrate), the thickness of very thin layers from the systems As - S and As - S - Ge have been determined to an accuracy of ±2 nm. At the same time, the accuracy in the determination of the refractive index, n, was less than ±0.005. For the absorption coefficient, k, around the absorption edge, it was about ±0.01, using a combination of TTR_m and TR methods. A comparison between the results obtained from the spectrophotometric and ellipsometric measurements has been made.

1. Introduction

Chalcogenide glasses are one of the most widely known families of amorphous materials and have been extensively studied for several decades, partly because of their interesting fundamental properties and partly because of their many potential applications in optical imaging, optical recording, infrared optics, and more recently, optical communications [1-5]. The determination of the optical constants is of great importance for understanding the mechanism of the optical processing and for their utilisation in practice. Because glassy As_2S_3 is known as a stable stoichiometric binary compound, the systems As - S - Ge(Bi,Tl) have been chosen to continue our previous studies [6-9]. A number of works exist which trace the influence of composition and preparation conditions of thin films on the physico-chemical properties, and the changes in them induced by light. The structural changes in these materials are related to the change in their optical properties.

Various methods exist for determining the optical constants of thin films from the coefficients of transmission T and reflection R, or via their combination [10,11]. All these methods are based on the Swanepoel's method and different computer programs for calculation the optical constants and film thicknesses. As the film structure depends strongly on the conditions of evaporation there are some differences between the published data in the literature. The aim of the present work is to report results from a study of changes in the optical properties of thin As - S - Bi(Tl) films, depending on the composition and light illumination as well as to determine the optical constants of very thin As - S and As - Ge - S, using triple T, R, R_m methods [12, 13]. The major advantage of these is the simultaneous determination of d and the optical constants (n, k). The combination of triple and double TR methods results in a very accurate calculation of n and k [14, 15]. A comparison between the data, obtained by these methods and the ellipsometric measurements of the same films will be presented.

2. Experimental

The synthesis of the bulk samples as accomplished from starting substances (As, Ge, S, Tl and Bi) of 99.999 % purity, heated in a quartz ampoule at 970°C for 10 hours (As - Ge - S glasses) and at 870°C for 12 hours (As - S - Bi and As - S - Tl glasses). Thin films were deposited at room temperature onto optical glass substrates BK-7 and Si wafers in a high vacuum of 10^{-3} Pa by thermal evaporation of previously weighed quantities of glasses with a residual in the boat. The composition of the bulk materials as well as the thin films was determined in a Scanning electron microscope with a X-ray microanalyser (Jeol Superprobe 733, Japan).(For bulks it was generally $\approx$ 1 at.% of the expected compositions). The exposure was carried out in air with a halogen lamp (20 mW/cm^2), for saturation times experimentally established for each composition. The film transmission T was measured with a spectrophotometer (CARY 05E, USA) to an accuracy better than $\pm$ 0.1 %, and the absolute reflections R_f, R_b and R_m were measured with VW accessory to better than $\pm$ 0.5 % in the spectral range 350 to 1500 nm. The ellipsometric measurements were carried out at three angles of incidence of light (45, 48, 50 °), at λ = 632.8 nm, using MAI-ellipsometry.

3. Results

3.1. Optical properties of thin As - S and As - Ge - S films

The optical constants of thin As_xS_{100-x} (28 $\leq$ x $\leq$ 45) and $As_{40-x}Ge_xS_{60}$ (0 $\leq$ x $\leq$ 40) films deposited by thermal evaporation with a deposition rate 1.0-1.5 nm/s were calculated. The evaporation process was stopped when the film thickness was about 1000 nm with a residual in the boat. The refractive index and thickness were calculated from the transmission spectra using Swanepoel's method and a computer program developed by Konstantinov [13].
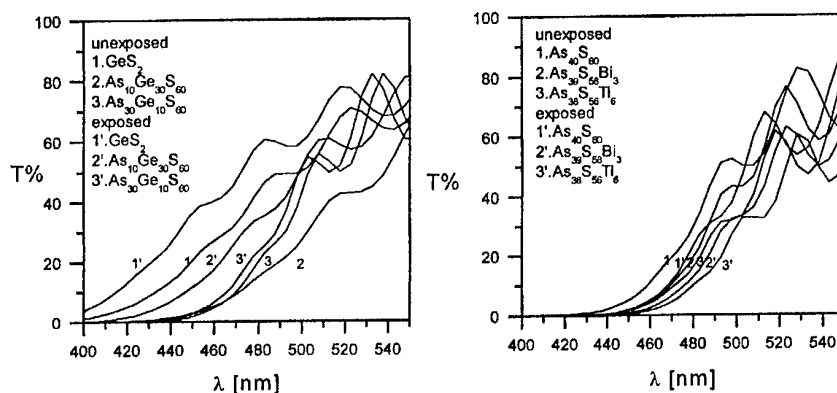
Fig. 1. Optical transmission of various chalcogenide thin films, T, vs. wavelength, λ, before and after illumination. This compositions are the ones exhibiting the largest light-induced changes in optical properties.

In Fig. 1 the plots of the optical transmission of various chalcogenie thin films versus wavelength, before and after exposure to light were presented. The compositions are the ones exhibiting the largest light-induced changes in the optical properties. It was found that after illumination the absorption edge for As - S - Bi(Tl) thin films shifts to the longer wavelengths (effect of photodarkening) while for the As - S - Ge system the effect was of photobleaching. In the system As - Ge - S the highest shift in the absorption edge ($\Delta\lambda$ = -30 % at T = 20%) and the refractive index (Δ n = - 0.07) were found for the composition $As_{10}Ge_{30}S_{60}$. When Ge content increases the changes in the optical properties decrease. The thickness to an accuracy of $\pm$ 1-3 nm and the optical constants of chalcogenide films (100 nm thick) were determined by two triple (T, R_f, R_m) and (T, R_b, R_m)

methods [12]. The subscripts f and b denote the light reflection from the film side and from the substrate (BK-7) side, respectively, while m represents the reflection of the same film deposited on a Si wafer. Table 1 shows the main data for the thickness of thin As - Ge - S films determined by UV-VIS-NIR spectrophotometry using T, R, R_m method and by ellipsometry. It seems that no difference in the thickness values of thin films from the investigated system.

Table 1. Data for the thickness of thin As-Ge-S films determined by UV-VIS-NIR spectrophotometry using a T, R, R_m method and by ellipsometry.

Composition	(T, R, Rm) method		Ellipsometric	
	d_{unexp} [nm]	d_{exp} [nm]	d_{unexp} [nm]	d_{exp} [nm]
As_2S_3	70 ± 1.0	68 ± 1.0	69.4 ± 0.1	69.5 ± 0.2
$As_{30}Ge_{10}S_{60}$	95 ± 1.5	91 ± 2.0	93.6 ± 0.2	91.5 ± 0.1
$As_{20}Ge_{20}S_{60}$	80 ± 1.0	85 ± .1.3	81.8 ± 0.2	86.2 ± 0.2
$As_{10}Ge_{30}S_{60}$	52 ± 1.0	57 ± 1.0	53.6 ± 0.2	57.7 ± 0.3
GeS_2	48 ± 1.5	50 ± 1.0	47.0 ± 0.2	49.7 ± 0.2

The most accurately calculated film thicknesses were used for the determination of the optical constants by double (T, R_f) and (T, R_b) methods, using the Newon-Raphson's interative method [14]. For each of the applied methods for determining the optical constants and thickness, the absolute maximum errors were evaluated [15]. From the relationship d = f(λ) = cons, obtained by the triple methods, the physically corrected solutions for d were isolated. The determined by UV-VIS-NIR spectrophotometry optical constants depending on the film composition were compared with the data obtained on the same samples by MAI-ellipsometry (Table 2). It was found that the refractive index, n, had a maximum value for the $As_{40}S_{60}$ films. After exposure to light to saturation n increases for all thin As_xS_{100-x} films while the thickness decreases. The highest change in n was observed for $As_{40}S_{60}$ layers (Δn = 0.12) (Fig. 2). The same dependence of n = f(λ) for unexposed and exposed thin As - S and As - Ge - S films was observed when (T, R_f) and (T, R_b) methods were used (Table 2).

Table 2. Data for the refractive index of thin As-Ge-S films with thickness of 1000 nm and below 100 nm at λ=632.8 nm obtained by UV-VIS-NIR spectrophotometry (1) and by ellipsometry (2).

Composition	Thin films 1000 nm thick				Thin films about 100 nm thick			
	Unexposed		Exposed		Unexposed		Exposed	
	1	2	1	2	1	2	1	2
As_2S_3	2.44	2.458	2.56	2.531	2.46	2.490	2.55	2.581
$As_{28}S_{72}$	2.33	2.428	2.40	2.417	2.33	2.414	2.42	2.456
$As_{33}S_{67}$	2.43	2.422	2.50	2.441	2.42	2.450	2.47	2.520
$As_{45}S_{55}$	2.43	2.456	2.52	2.553	2.45	2.454	2.54	2.553
$As_{10}Ge_{30}S_{60}$	2.32	2.336	2.23	2.258	2.34	2.327	2.12	2.201
$As_{20}Ge_{20}S_{60}$	2.35	2.369	2.30	2.280	2.34	2.388	2.23	2.281
$As_{30}Ge_{10}S_{60}$	2.45	2.431	2.44	2.415	2.46	2.556	2.46	2.552
GeS_2	2.15	2.131	2.11	2.096	2.12	2.131	2.02	2.027

The calculated values of the absorption coefficient, k , from the above mentioned methods were used for calculation of the absorption coefficient α (α = $4\pi k/\lambda$). Fig. 3 shows the plots of the $(\alpha h\nu)^{1/2}$ = f(hν) dependence. When Ge was added to As_2S_3 the optical band gap, E_g, increases for the unexposed layers. After exposure to light E_g increases and the biggest change ΔE_g = 0.21 ev was observed for thin film with composition $As_{20}Ge_{20}S_{60}$ (Table 3). The results for the composition dependence and the influence of the light obtained by refractive ellipsometry were in a good agreement with the data from the transmission spectrophotometry. It was found that k = 0 when the optical constants were detrmined at 3 different angles of incidence of light on the sample and the calculated values of n at 45, 48 and 50° show that both unexposed and exposed thin As - S and As - Ge - S films are homogeneous.
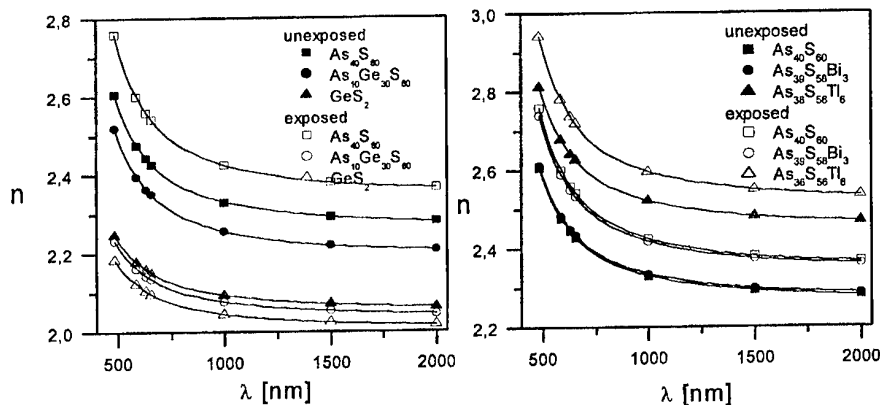
Fig. 2. Refractive index, n, vs. wavelength, λ, for various chalcogenide thin film samples before and after illumination. These compositions are the ones exhibiting the largest light-indused changes in optical properties.

Fig. 3. Optical absorption edge $(\alpha h\nu)^{1/2}$ vs. energy of photon $(h\nu)$ for unexposed and exposed thin As-Ge-S films

Table 3. Data for the optical band gap of unexposed and exposed thin As - Ge - S films.

Composition	$E_{g\,unexp.}$ [eV]	$E_{g\,exp.}$ [eV]	ΔE_g [eV]
As_2S_3	2.38	2.33	-0.05
$As_{30}Ge_{10}S_{60}$	2.42	2.49	+0.07
$As_{20}Ge_{20}S_{60}$	2.24	2.45	+0.21
$As_{10}Ge_{30}S_{60}$	2.27	2.39	+0.12
GeS_2	2.53		

3.2. Optical properties of thin As - S - Bi(Tl) films

Thin films (1000 nm thick) from the system As - S - Bi(Tl) were deposited by thermal evaporation of bulks with compositions $As_{39}S_{58}Bi_3$, $As_{38}S_{56}Bi_6$, $As_{36}S_{54}Bi_{10}$, $As_{39}S_{58}Tl_3$, $As_{38}S_{56}Tl_6$ and $As_{36}S_5Tl_{10}$. It was found that the absorption edge of unexposed thin layers was shifted to longer

wavelength increasing the Bi or T content in As_2S_3 (Fig.1). After exposure to light an effect of photobleching occured. The largest value of the shift of the absorption edge, $\Delta\lambda$, was observed for thin films with compositions $As_{39}S_{58}Bi_3$ ($\Delta\lambda$ = +15 nm at T = 20%) and $As_{38}S_{56}Tl_6$ ($\Delta\lambda$ = +26 nm at T = 20%). An increase in the Bi or Tl content leads to decreasing in the shift of the absorption edge.

From the transmission measurements we have calculated the refractive index of thin films from above systems. It was found that the values of n increases for the both systems (As - S - Bi and As - S - Tl) and the maximum changes in n was observed for thin layers with the same compositions - $As_{39}S_{58}Bi_3$ (Δn = 0.10) and $As_{38}S_{56}Tl_6$ (Δn = 0.16) (Fig.2). In the same time a decrease in the film thickness after exposure to light was found (for the composition $As_{38}S_{56}Tl_6$ Δd = -15 nm).

In Table 4 the ellipsometrically determined values of n and d of thin As - S - Bi(Tl) films are shown. The calculated optical constants considerably differ comparing them with those determined by UV-VIS-NIR spectrophotometry for both unexposed and exposed thin films but the composition and exposure dependence was the same.

Table 4. Data for n and d for unexposed and exposed thin As-S-Bi(Tl) films.

Composition	n_{unexp}	n_{exp}	d_{unexp} [nm]	d_{exp} [nm]
$As_{39}S_{58}Bi_3$	2.477	2.450	1014	978
$As_{38}S_{56}Bi_6$	2.367	2.353	1118	1117
$As_{39}S_{58}Tl_3$				
$As_{38}S_{56}Tl_6$	2.367	2.493	1036	1037
$As_{36}S_{54}Tl_{10}$	2.712	2.832	930	877
	2.599	2.632	1073	1044

3.3. Optical absorption of thin As - S - Bi(Tl) films

In the case of the amorphous chalcogenide semiconductors, the optical absorption coefficient, α, changes rapidly for the photon energies comparable to that of the band gap, E_g, giving rise to an absorption edge. Three regions can be distinguished: at the largest photon energies ($\alpha \geq 10^4$ cm^{-1}), in the region of the edge itself ($10 < \alpha < 10^4$ cm^{-1}) and at the lowest photon energies ($\alpha \leq 10$ cm^{-1}). The region with high absorption is characterised with interband transitions between valence and conduction bands, while in the last region transitions between (defect) states in the gap and the bands take place [16].

At the highest values of the absorption coefficient, α, when the condition $\alpha d > 1$ takes place, the absorption coefficient, α, should be calculated from the equation

$$T = (1 - R)^2 \exp(-\alpha d), \tag{1}$$

where T is the transmittance, R is the reflectance, α is the absorption coefficient and d is the film thickness.

Under certain conditions, the absorption coefficient in the region ($10^4 \leq \alpha \leq 10^5$ cm^{-1}) exhibits a power-law dependence on photon energy $h\nu$ if the densities of states in the valence and conduction bands also have a power-law energy dependence in the vicinity of the gap. In the special case, where both valence and conduction band edges have a parabolic shape. According to Mott and Davis the absorption coefficient is connected with the photon energy by the equation

$$(\alpha h\nu) = B(h\nu - E_g)^2, \tag{2}$$

where B is a substance parameter, h is Plank constant and ν is the frequency. Usually B depends on the width of the localised states in the band gap, which existing is due to the homeopolar bonds in the chalcogenide glasses. Thus Tauc plots of $(\alpha h\nu)^{1/2}$ versus $h\nu$ should be linear and extrapolate to values of the (optical) gap, E_g.
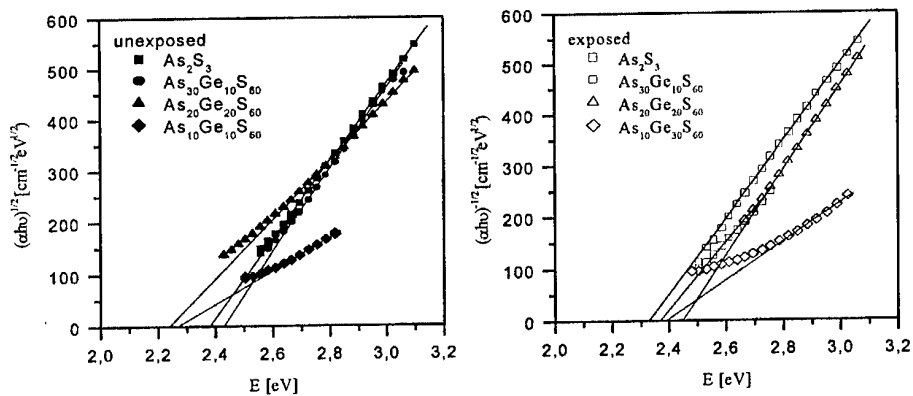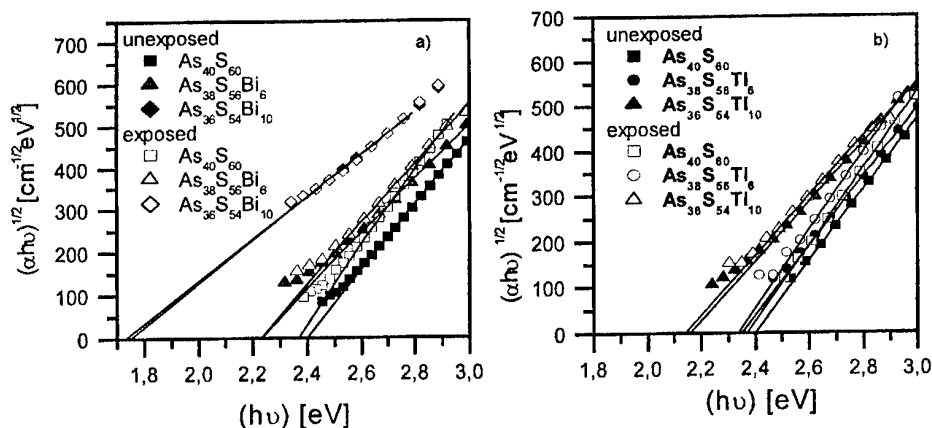
Fig. 4. Optical absorption edge $(\alpha h\nu)^{1/2}$ vs. energy of photon (hν) for unexposed and exposed thin As- S- Bi(Tl) films.

Figs. 3 and 4 represent plots of $(\alpha h\nu)^{1/2}$ vs. hν for various unexposed and exposed thin films from the systems As - Ge - S and As - S - Bi(Tl). It was found that the optical band gap decreases for as-deposited As-S thin films increasing the As content (E_g = 2.53 eV for $As_{28}S_{72}$ and E_g = 2.36 eV $As_{45}S_{55}$ (Fig.3). After exposure a decrease in Eg occurred and the highest change was for thin $As_{45}S_{55}$ films (ΔE_g = -0.05 eV). This decrease in the optical band gap could be connected with the increase in the constant B, which according to Mott and Davis is due to the increasing in the structural ordering.

The plots of $(\alpha h\nu)^{1/2}$ vs. hν for unexposed and exposed As - S - Bi films depending on Bi content are shown in Fig. 4a. In the range of high absorption the linear dependence retains and it is evident that the absorption edge shifts to lower photon energies as the Bi content increases. The band gap for the unexposed films decreases from E_g = 2.39 eV for As_{40069} to E_g = 2.06 eV for $As_{36}S_{54}Bi_{10}$). For as-deposited As - S - Tl films the optical band gap decreases to 2.16 eV for thin $As_{36}S_{54}Tl_{10}$ films (Fig. 4b) [9] In the same time the slope of the absorption coefficient decreases because of a decrease in disordering. The values of B decreases from 777 $cm^{-1/2}eV^{1/2}$for $As_{39}S_{58}Bi_3$ to 563 $cm^{-1/2}eV^{1/2}$ for the composition $As_{36}S_{54}Bi_{10}$. After exposure of thin As - S - Bi(Tl) films, the absorption edge is shifted to longer wavelengths - an effect of photodarkening is observed. The optical band gap decreases for both systems and the largest changes were found for composition $As_{39}S_{58}Bi_3$ - Eg = 0.04 eV) (Fig. 4a). The decrease in the band gap with an increased Bi or Tl content occurs because the latter creates localised states in the band gap.

4. Discussion

It should be noted that thin As-containing chalcogenide films represent inorganic polymers with specific branched polymer structure. According to some authors, the as-deposited As - S and As - S - Me layers are a heterogeneous mixture of structural units of the type As_2S_3, As_4S_3, As_4S_4, As_4, S_8, $TlAsS_2$, Tl_3AsS_3 or BiS_3. In As_2S_3 glasses the AsS_3 trigonal pyramidal units are linked by the sulphur atoms. It was suggested that the addition of Tl_2S to As_2S_3 glasses breaks some As - S - As bridges in order to form new bonds between electrically charged ions. On illumination, polymer-destrucive changes occur leading to the weakening of some bonds and to stregthening of others. The existence of structural changes in such chalcogenide films on illumination is supported by changes in their optical properties (the shift in the absorption edge, the refractive index and the optical band gap). The addition of Tl or Bi to thin As - S - Bi(Tl) films leads to the increase of the refractive index and decrease of E_g. Adding Tl to As_2S_3 the average bond strength of the compound decreases and

hence E_g will decrease. For better understanding the nature of the photostructural changes we need some IR and Raman investigations.

5. Conclusions

Bulk glasses from the systems As - S - Ge(Bi, 1) have been synthesized. The results of the X-ray microanalysis performed that the compositions of the bulks samples as well as thin As - S - Ge films are very close to the expected compositions. Some differences were observed in the compositions
As - S - Bi(Tl) films connected with the evaporation conditions. From the transmission and ellipsometic measurements the optical constants have been determined and the influence of the composition and light illumination has been demonstrated. For their precise calculation it is necessary to utilise both transmission and ellipsometric measurements. The results confirm for the first time the viability of the double and triple methods used for determining the optical constants of very thin vacuum deposited homogeneous As - S and As - Ge - S films to a very high accuracy. The great changes in the optical properties of some of the investigated chalcogenide films make possible their application as optical recording materials.

References

[1] S. R. Elliott, J. Non-Cryst.Solids, **81**, 71 (1986).
[2] K. Tanaka, Rev. Solid State Sci., **4**, 641 (1990).
[3] P. J. S. Ewen, A. E. Owen, High Performance Glasses, Eds. M. Cable and J.M. Parker, Blackie, London, 1992, p.287.
[4] K. Shimakawa, A. Kolobov, S. R. Elliott, Adv. Phys., **44**, 475 (1995).
[5] R. Andreichin, M. Nikiforova, E. Skordeva, L. Yurukova, R. Grigorovici, R. Manaila, M. Popescu, A. Vancu, J. Non-Cryst. Solids, **97-98**, 1135 (1987).
[6] K. Petkov, M. Sahatchieva, J. Dikova, J. Non-Cryst.Solids, **101**, 37 (1998).
[7] K. Petkov, B. Dinev, J. Mater. Sci., **29**, 468 (1994).
[8] K. Petkov, P. J. S. Ewen, J. Non-Cryst. Solids, **249**, 150 (1999).
[9] K. Petkov, Tz. Iliev, R. Todorov, D. Tzvetkov, Vacuum, **58**, 321 (2000).
[10] E. A. Davis, Electron and structural properties of amorphous semiconductors, Eds. P. G. Lecomber and J. Mort, Academic Press, London, New York, p. 425, 1973
[11] E. Marquez, J. m. Gonzalez-Leal, R. Prieto-alcom, M. Vlcek, A. Stronski, Appl. Phys. **A67**, 371 (1998).
[12] V. Panayotov, I. Konstantinov, Proc. SPIE, **2253**, 1070 (1994).
[13] R. Todorov, Tz. Babeva, K. Petkov, Proc. 11th ISCMP, 2000, in press.
[14] F. Abeles, M. Theye, Surf. Sci., **5**, 25 (196).
[15] I. Konstantinov, Tz. Babeva, S. Kitova, Appl. Opt., **37**, 4260 (1998).
[16] S. Elliott, Chalcogenide glasses, Chapter 7, Material Science and Technology, **9**, 376 (1991).

EFFECT OF OBLIQUE DEPOSITION ON OPTICAL AND ELECTRICAL PROPERTIES OF $As_2 S_3$ AND As_2Se_3

P. P. K. Shishodia, R. M. Mehra

Department of Electronic Science, University of Delhi South Campus,
New Delhi-110021, India

The effect of oblique deposition on the optical and electrical properties of As_2S_3 and As_2Se_3 thin films has been investigated. Amorphous films of As_2S_3 and As_2Se_3 were deposited on glass substrate by vacuum evaporation of source materials. The indirect- optical bandgap energy was obtained to be 2.40eV for As_2S_3 and 1.81 eV for As_2Se_3. The band gap was found to be independent of angle of deposition. DC conductivity of the films was very low. The refractive index and extinction coefficient have been calculated using the transmission spectra

1. Introduction

For the past four decades, devices based on amorphous and disordered materials have grown in importance. The atomic bond in these materials is covalent, while it can be modified to be metallic or ionic. It is this flexibility that enables tailoring of their properties over a wide range. The unique ability of amorphous materials to be engineered at molecular level and fabricated by vapour deposition processes in highly uniform large area structures has permitted them to be used in wide range of devices for sensing, encoding, switching, transmission and storage of information. It has also assisted the development of new, pollution free technology for the generation of electrical energy. Detailed studies have been reported on photoinduced structural transformations in amorphous chalcogenides[1-5]. These changes have been found to accompany different phenomena such as changes in refractive index, optical bandgap, film thickness and chemical activity.

In the present work, we report the effect of oblique deposition on optical and electrical properties of As_2S_3 and As_2Se_3 thin films. For optoelectronic devices, an accurate determination of the optical constants such as absorption coefficient, refractive index and dielectric costant of semiconductor thin films is important to precisely model their spectral response. To predict the photoelectronic behaviour of a device, it is important to know the variation of refractive index and absorption coefficient with wavelength. The DC conductivity has been determined to elucidate the conduction mechanism of the films.

2. Experimental details

The normal and oblique films of As_2S_3 and As_2Se_3 were prepared by vacuum evaporation technique. The oblique films were deposited at an angle of 80^0, this being the angle between the normal to the substrate and direction of incidence of the evaporated atoms. An optical glass slide with a thickness of about 1.5mm was used as the substrate for the films. Prior to evaporation, the substrate was cleaned with distilled water, acetone and ethanol respectively and then dried using a blower. The evaporation was conducted on the substrate at room temperature in a vacuum of about $1*10^{-6}$ Torr from a molybdenum boat heater. A surface profiler (Dektok 3) was used to measure the thickness of the films. The results presented here for typical film having thickness in the range 0.7-1.2µm.

The optical transmission measurements were performed on thin films using UV-VIS spectrophotometer (Hitachi 330). DC conductivity measurements were made on the films by evaporating aluminium contacts in a coplanar configuration.

3. Results and discussion

The amorphous nature of the samples was confirmed by the X-ray diffraction measurements. Refractive index and extinction coefficient have been calculated using the method suggested by Swanepoel [6-8]. The refractive index and absorption coefficient are obtained using the transmission spectra. The refractive index (n) has been obtained using the following expressions,

$$n = \left[M + \left(M^2 - s^2 \right)^{\frac{1}{2}} \right]^{\frac{1}{2}}$$

where $M = \dfrac{2s}{T_m} - \dfrac{\left(s^2 + 1 \right)}{2}$ for transparent region

and $= \dfrac{s^2 + 1}{2} + 2s \dfrac{T_M - T_m}{T_M T_m}$ for weak and medium absorption region

T_M and T_m are the values of maximum and minimum transmission at a particular wavelength. s is the refractive index of the substrate

The absorption coefficient was determined using the relation $\exp(-\alpha t) = T$ where t is the thickness of the film and T is the transmittance.

The bandgap, of the films has been estimated using Tauc's relation

$$\alpha = (B/h\nu)(h\nu - E_{opt})^n$$

where B is a constant, E_{opt} is the optical bandgap energy and $h\nu$ is the photon energy. n depends on electronic transitions in k-space and takes the values $\frac{1}{2}, 1, 2$ and 3.
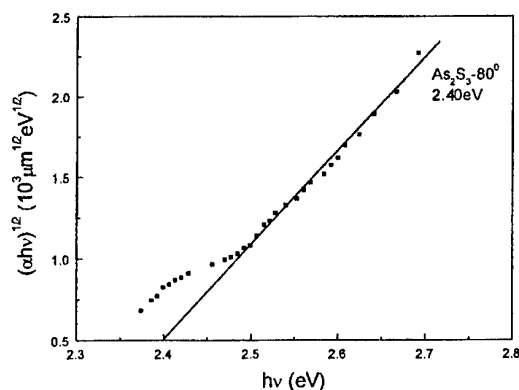
Fig.1. Variation of $(\alpha h\nu)^{1/2}$ Vs photon energy for As_2S_3.

The results are shown in Fig.(1) and Fig.(2) as a plot of $(\alpha h\nu)^{1/2}$ Vs photon energy $(h\nu)$. On extrapolating the linear portion of the curve to x-axis, E_{opt} is found to be 2.4eV for As_2S_3 and 1.81eV for As_2Se_3. The estimated value of the band gap is very close to the reported value of 2.4eV forAs_2S_3 and 1.8eV for As_2Se_3 [9].
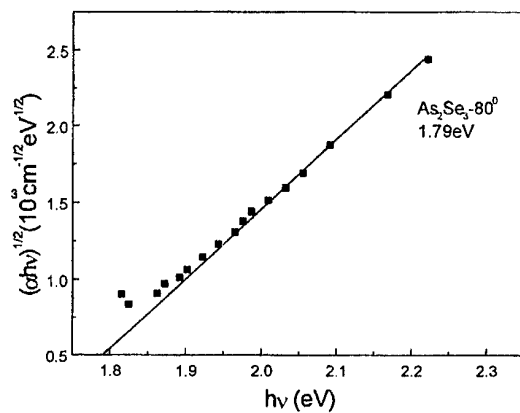
Fig. 2. Variation of $(\alpha h\nu)^{1/2}$ Vs photon energy for As_2Se_3.
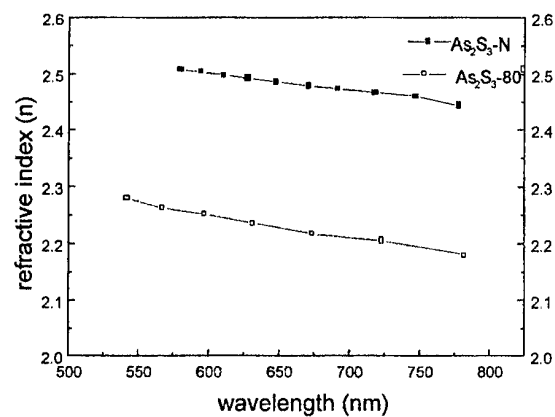
Fig. 3. Variation of refractive index with wavelength for As_2S_3.
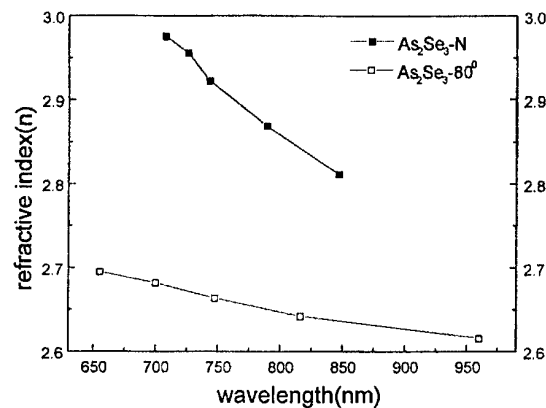
Fig. 4. Variation of refractive index with wavelength for As_2Se_3.

Fig. (3 and 4) show the refractive index(n) and Fig.(5 and 6) show extinction coefficient(κ) as a function of wavelength for the films deposited at normal and 80^0 oblique incidence of As_2S_3 and As_2Se_3 respectively.
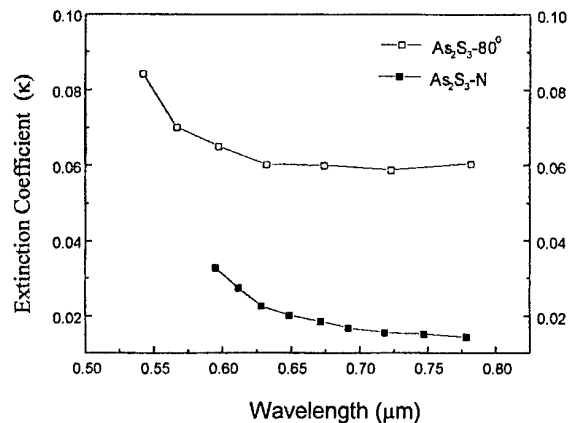
Fig. 5. Variation of extinction coefficient with wavelength for As_2S_3.
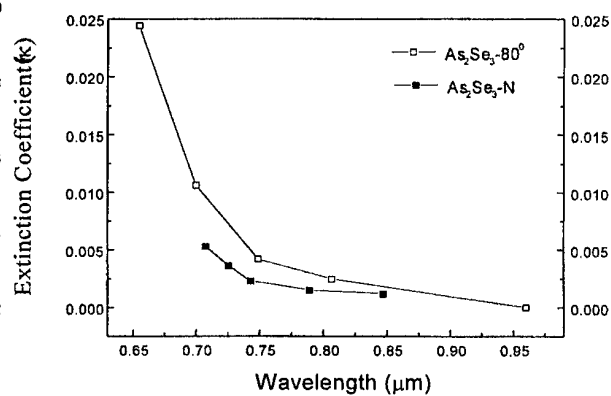
Fig. 6. Variation of extinction coefficient with wavelength for As_2Se_3.

The refractive indices of the films are found to obey the normal dispersive law. The typical values of refractive index 2.49 for As_2S_3 at 630nm wavelength and 2.95 at 730nm for As_2Se_3 are in close agreement with the reported data [10]. However the refractive index for obliquely deposited films were found to be low as compared to the normal deposited films. This change in refractive index could be attributed to the structural changes occurring in obliquely deposited films.
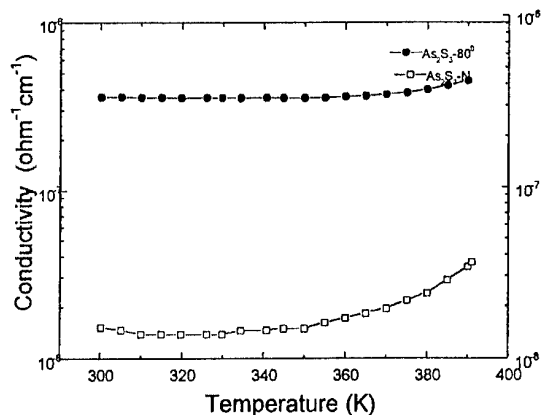
Fig. 7. Variation of dark conductivity with temperature for As_2S_3.
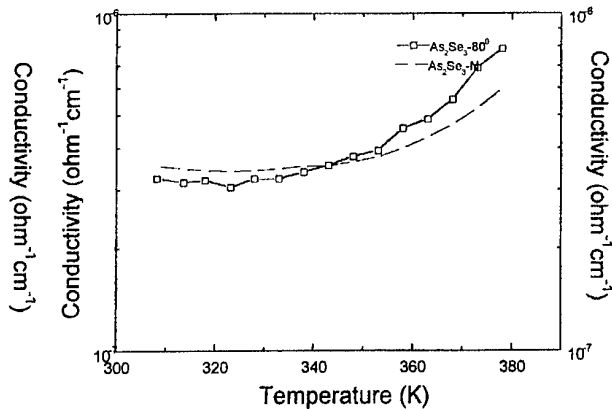
Fig. 8. Variation of dark conductivity with temperature for As_2Se_3.

Fig. (7 and 8) show the temperature dependence of the dark conductivity, for the samples of As_2S_3 and As_2Se_3 respectively. It has been observed that the conductivity increases with temperature, that can be attributed to thermal activation of carriers.

References

[1] K. Shimakawa, A. Kolobov, S. R. Elliot, Adv. Phys., **44**, 475, 1995.

[2] K. Tanaka, Phys. Rev., **B57**, 5163, 1998.

[3] K. Shimakawa, N. Yoshida, A. Ganjoo, Y. Kuzukawa, J. Singh, Philos. Mag. Lett. **77**, 153, 1998.

[4] Y. Kuzukawa, A. Ganjoo, K. Shimakawa, J. Non-Cryst. Solids, **227-230**, 715, 1998.

[5] Y. Kuzukawa, A. Ganjoo, K. Shimakawa, Y. Ikeda, Phil. Mag., **B227-230**, 715, 1998.

[6] J. C. Manifacier, J. Gassiot, J. P. Fillard, J. Phys. E **9**,1002 (1976).

[7] R. Swanepoel, J. Phys. E **16**,1214 (1983).

[8] R. Swanepoel, J. Phys. E **17**,896 (1984).

[9] N.F. Mott, Electronic Processes in Non-Crystalline Materials, Clarendon, Oxford, 1979.

[10] K. Tanaka, Y.Ohtsuka,"Measurements of Photoinduced Transformations in Amorphous.

[11] As_2S_3 Films by Optical Waveguiding,"J.Appl.Phys. **49**, 6132-6135 (1978).

PECULIARITIES OF γ-INDUCED OPTICAL EFFECTS IN TERNARY SYSTEMS OF AMORPHOUS CHALCOGENIDE SEMICONDUCTORS

A. Kovalskiy

National University "Lviv Polytechnics", Bandera str. 12, 79646 Lviv, Ukraine
Scientific Research Company "Carat", Stryjska str. 202, 79031 Lviv, Ukraine

Changes of optical transmittance induced by the influence of ^{60}Co γ-irradiation have been studied in ternary As-Ge-S, Sb-Ge-S, As-Ge-Se and As-Bi-Se systems. The characters of radiation-induced optical effects in all these systems have been compared It was shown that the compositional dependencies of such effects are almost linear for stoichiometric glasses and reveal some peculiarities connected with phase features, the "free volume" parameters and the specificity of radiation induced defects formation for non-stoichiometric families.

1. Introduction

Recent investigations of gamma-induced optical phenomena in various ternary systems of amorphous chalcogenide semiconductors (AChS) have shown that the value and character of these induced effects as well as their dynamic and static components essentially depends on the origin, concentration and valency of constituent atoms, the dimensionality, compactness and stoichiometry of structure as well as the concentration of homo- and heteropolar bonds [1-6]. The aim of this work is the comparative analysis of radiation-induced optical effects (RIOE) in different types of AChS systems.

2. Experimental

Traditional melt quenching method was used for the preparation of bulk AChS samples of As-Ge-S, Sb-Ge-S, As-Ge-Se and As-Bi-Se systems. 5N purity elements were chosen as precursors for synthesis. The cooled ampoules additionally heated at the temperatures just below the glass transition point T_g with the aim to avoid the postsynthesis residual stresses.

All samples were irradiated with 1.0-4.4 MGy doses in the conditions of stationary radiation field created in the closed cylindrical capacity by the concentrically placed ^{60}Co sources. The mean energy of γ–flow was 1.25 MeV; the power of exposure dose was 20 Gy/s. The value of absorbed dose was limited by the unwanted thermoradiation effects, which might suppress RIOE. In our case the temperature in the cavity of radiation sources did not exceed 320-330 K.

Optical transmittance spectra were measured before and after γ–irradiation for a wide range of chemical compositions inside of each system using "Specord M40" spectrophotometer with accuracy 0.5 %. Compositional dependencies of maximal radiation-induced changes of optical transmittance ($\Delta\tau_{max}$) at the region of fundamental absorption edge (Urbach tail) were chosen as controlled parameters for RIOE investigations.

Taking into account that the RIOE magnitude essentially increases with the sample thickness, obtained glasses were cut into the disks of 0.7-2 mm thickness in dependence on the sensitivity of AChS systems to the influence of γ-irradiation.

In order to analyse the interrelation between RIOE and structural parameters the compactness δ was calculated for each composition using known formula [7-12]:

$$\delta = \frac{\sum_i V_i - V_\text{э}}{V_\text{э}} = \frac{\sum_i \frac{A_i x_i}{\rho_i} - \sum_i \frac{A_i x_i}{\rho}}{\sum_i \frac{A_i x_i}{\rho}},$$ (1)

where V_i is the volume occupied by the atoms of i-th chemical element of glass; V_{exp} is the experimentally measured volume of glass; A_i, x_i and ρ_i are the atomic weight, the atomic fraction and the atomic density of i-th chemical element, respectively; ρ is the measured density of glass. The quantities δ can take the negative values, corresponding to larger "free" volume.

3. Results and discussion

3.1. As-Ge-S system

The compositional dependencies of maximum value of optical transmittance difference before and after γ-irradiation for stoichiometric As_2S_3-GeS_2 and non-stoichiometric As_2S_3-Ge_2S_3 sections of As-Ge-S system are presented in Figs. 1 and 2, respectively. Radiation-induced changes were measured 1 day after irradiation (total RIOE described by $\Delta\tau_{max}^{\Sigma}$) and 2 months later (static component of RIOE described by $\Delta\tau_{max}^{st}$). It is clear that dynamic component of RIOE is equal to the difference between the total effect and static component. The average coordination number Z (calculated as the number of covalent chemical bonds per atom of the formula unit [13,14]) was chosen as composition parameter. This parameter is appropriate for consideration only in the ternary glasses of A^{IV}-B^{V}-C^{VI} type when Z changes essentially with composition.

It must be mentioned that phenomenological model for RIOE in stoichiometric glass compositions can be built on the basis of radiation-induced redistribution of chemical bonds too. Moreover, such processes are confirmed by IR investigations in 400-100 cm^{-1} region.
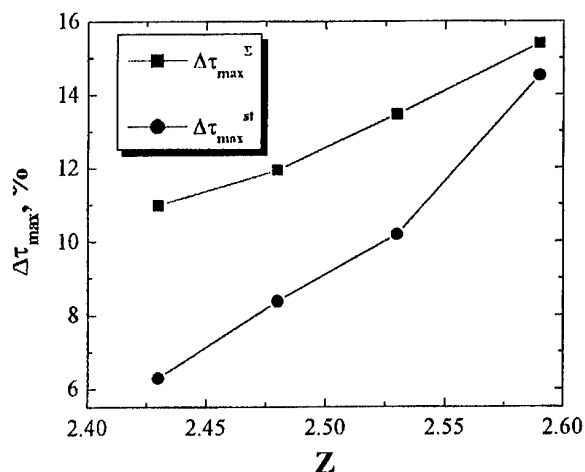
Fig. 1. Dependence of quantitative parameters of total ($\Delta\tau_{max}^{\Sigma}$) and static ($\Delta\tau_{max}^{st}$) RIOE for stoichiometric As_2S_3-GeS_2 section of As-Ge-S system on the average coordination number Z.
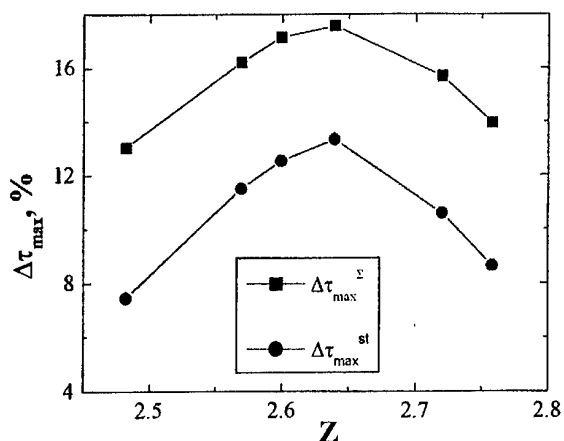
Fig. 2. Dependence of quantitative parameters of total ($\Delta\tau_{max}^{\Sigma}$) and static ($\Delta\tau_{max}^{st}$) RIOE for non-stoichiometric As_2S_3-Ge_2S_3 section of As-Ge-S system on the average coordination number Z.

As expected, the linear increasing of $\Delta\tau_{max}$ with Z is observed for stoichiometric compositions. Higher sensitivity of Ge-enriched glasses to γ-irradiation is well explained by the corresponding decreasing of compactness δ (see Fig. 3). It can be assumed that radiation-induced defects become stabilize easier inside of the voids (at the increasing of "free" volume) in comparison with more compact structure when the nearness of other atoms promotes the quick healing of these defects.

Calculations of δ for non-stoichiometric compositions revealed the minimum value for this parameter at $Z \approx 2.7$ (Fig. 4 [11]). Such feature agrees with the behaviour of $\Delta\tau_{max}^{\Sigma}(Z)$ and $\Delta\tau_{max}^{st}(Z)$ dependencies which demonstrate the maximum RIOE at this point. In the case under consideration the

joint contribution of compactness and bonds concentration into the mechanism of RIOE must be taken into account using the parameter ω [7]:

$$\omega = C\delta, \tag{2}$$

where C- concentration of main chemical bonds, which take part in the radiation-induced defects formation.
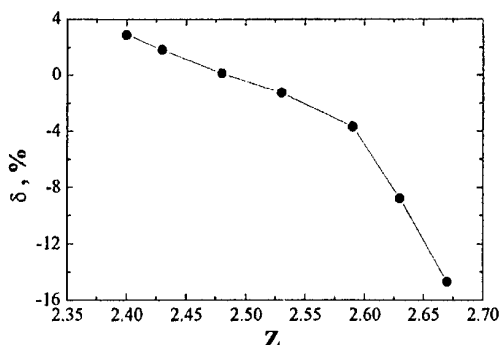
Fig. 3. Dependence of atomic compactness δ on average coordination number Z for As_2S_3-GeS_2 stoichiometric section.
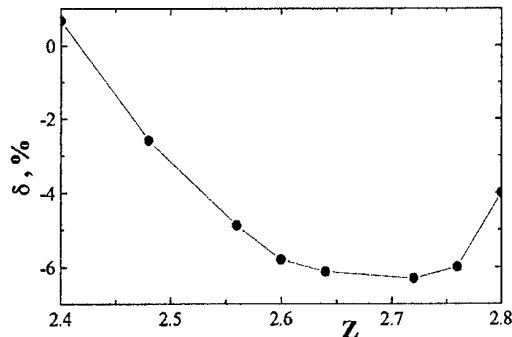
Fig. 4. Dependence of atomic compactness δ on average coordination number Z for As_2S_3-Ge_2S_3 non-stoichiometric section [11].

3.2. Sb-Ge-S system

One more representative of A^{IV}-B^{V}-C^{VI} type ternary systems is Sb-Ge-S. The $\Delta\tau_{max}(Z)$ dependencies of total RIOE and its static component for stoichiometric Sb_2S_3-GeS_2 and non-stoichiometric Sb_2S_3-Ge_2S_3 sections are presented in Fig. 5 and Fig. 6, respectively. In both cases Sb-enriched samples do not reveal any RIOE. This is connected with the nature of Sb atoms, which exhibit exceptional ability to the passivation of RIOE by the preventing of radiation-induced defects stabilization. Such ability is associated with the high level of metallization in Sb-containing chemical bonds and the high compactness of these glasses. The δ(Z) curve has a similar shape as in the case of As-Ge-S. As the consequence, for this non-stoichiometric section, in contrast to As_2S_3-Ge_2S_3, the characters of $\Delta\tau_{max}(Z)$ and δ(Z) dependencies mismatch.
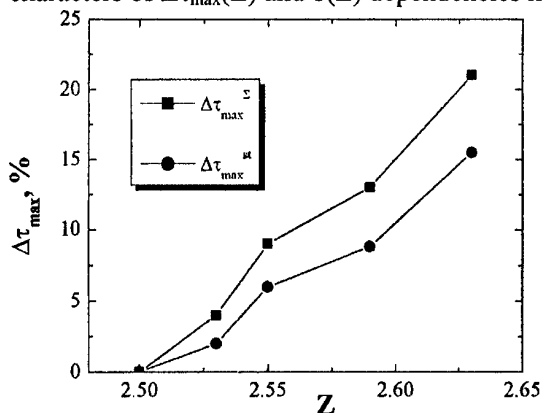
Fig. 5. Dependence of quantitative parameters of total ($\Delta\tau_{max}{}^{\Sigma}$) and static ($\Delta\tau_{max}{}^{st}$) RIOE for stoichiometric Sb_2S_3-GeS_2 section of Sb-Ge-S system on the average coordination number Z.
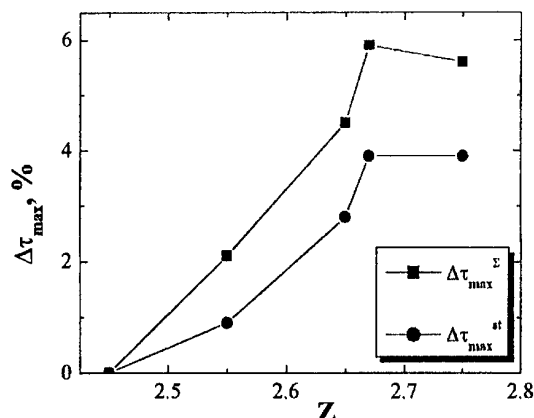
Fig. 6. Dependence of quantitative parameters of total ($\Delta\tau_{max}{}^{\Sigma}$) and static ($\Delta\tau_{max}{}^{st}$) RIOE for non-stoichiometric Sb_2S_3-Ge_2S_3 section of Sb-Ge-S system on the average coordination number Z.

3.3 As-Ge-Se system

In order to analyse the features of RIOE in the whole range of Z variation the γ-induced changes of optical transmittance in $As_xGe_ySe_{1-x-y}$ system was studied. Extremum points can be observed at Z≈2.4 and Z≈2.7. First point undoubtedly represents the well-known rigidity transition

[15,16]. Second point is the subject of discussions up and it is often attributed to 2D-3D topological phase transition [13] or to the phase separations [17].
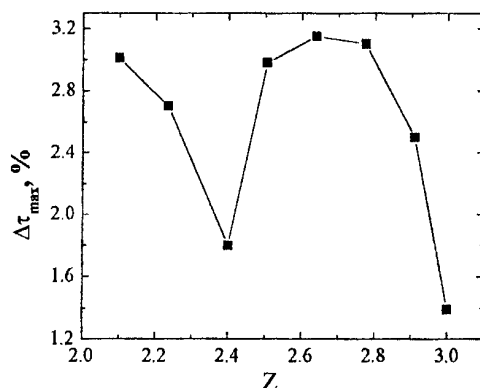
Fig. 7. Dependence of maximal radiation-induced change of transmittance on the average coordination number Z for non-stoichiometric $As_xGe_ySe_{1-x-y}$ family of As-Ge-Se system.

3.3. As-Bi-Se system

Sometimes even small quantities of additions cause the essential radiation-induced changes of optical transmittance. On of such examples is the chemical modification of stoichiometric As_2Se_3 by Bi. Maximal RIOE takes place when the Bi concentration is ~0.5 at. % (Fig. 8) and, as it is assumed, the concentration of (Bi_2^-, Se_3^+) and (Bi_4^+, Se_1^-) defect pairs is highest.
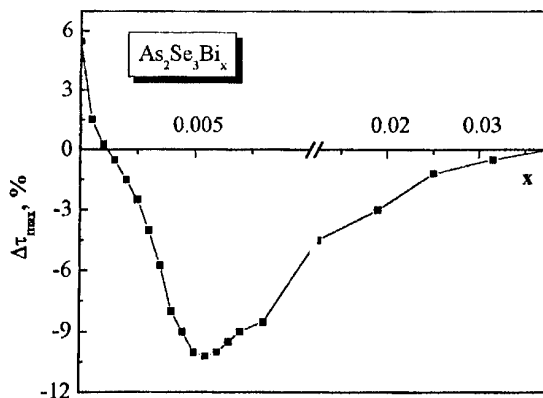
Fig. 8. Dependence of maximal radiation-induced change of transmittance on the content of Bi for stoichiometric As_2Se_3 chemically modified by Bi.

Taking into account that in some glasses addition of Bi can change the type of electrical conduction, it is important to clear the mechanism of Bi entering of into the glass matrix. The most popular explanations are the change of Bi coordination in dependence on its concentration and the increasing of disequilibrium between the concentrations of positively and negatively charged defects [19]. So, the mechanism of RIOE in $As_2Se_3Bi_x$ glasses is intricate problem and needs an additional detail studies.

4. Conclusions

Investigations of γ-induced changes of optical transmittance show that mechanism of RIOE consists in the coordination defects formation under the radiation treatment. The peculiarities of this process are determined by structural features of glass, its composition, stoichiometry, parameters of

free volume, concentration of main chemical bonds as well as by the origin of constituent chemical elements.

Acknowledgement

References

[1] O. I. Shpotyuk, A. P. Kovalskiy, E. Skordeva, E. Vateva, D. Arsova, R. Ya. Golovchak, M. M. Vakiv, Physica B, **271**, 242 (1999).

[2] O. I. Shpotyuk, R. Ya. Golovchak, T. S. Kavetsky, A. P. Kovalskiy, M. M. Vakiv, Nuclear Instruments and Methods in Physics Research B - Beam Interaction with Materials & Atoms, **166-167**, 517 (2000).

[3] E. Skordeva, D. Arsova, V. Pamukchieva, E. Vateva, R. Golovchak, A. Kovalskiy, O. Shpotyuk, Journal of Optoelectronics and Advanced Materials, **2**, 259 (2000).

[4] T. S. Kavetskyy, A. P. Kovalskiy, V. D. Pamukchieva, O. I. Shpotyuk. Infrared Physics & Technology, **41**, 41 (2000).

[5] O. Shpotyuk, T. Kavetskyy, A. Kovalskiy, V. Pamukchieva, Proc. SPIE, **4415**, 272 (2001).

[6] O. I. Shpotyuk, R. Ya. Golovchak, A. P. Kovalskiy, M. M. Vakiv, V. D. Pamukchieva, D. D. Arsova, E. R. Skordeva, Physics and Chemistry of Glasses, **42**, 95 (2001).

[7] M. Vlcek, M. Frumar, A. Vidourek, J. Non-Cryst. Solids, **90**, 513 (1987).

[8] M. Vlcek, M. Frumar, J. Non-Cryst. Solids, **97&98**, 1223 (1987).

[9] I. P. Kotsalas, D. Papadimitriou, C. Raptis, M. Vlcek, M. Frumar, J. Non-Cryst. Solids, **226**, 85 (1998).

[10] E. Savova, E. Skordeva, E. Vateva, J. Phys. Chem. Solids, **55**, 575 (1994).

[11] E. R. Skordeva, D. D. Arsova, J. Non-Cryst. Solids, **192&193**, 665 (1995).

[12] G. Saffarini, Physica B, **253**, 52 (1998).

[13] Ke. Tanaka, Phys. Rev. B, **39**, 1270 (1989).

[14] L. Tichy, H. Ticha, J. Non-Cryst. Solids **189**, 141 (1995).

[15] J. C. Phillips, J. Non-Cryst. Solids, **34**, 153 (1979).

[16] M. F. Thorpe, J. Non-Cryst. Solids, **57**, 355 (1983).

[17] P. Boolchand, J. Grothaus, J. C. Phillips, Solid State Commun., **45**, 183 (1983).

[18] C. Vautier, Solid State Phenomena, **71**, 249 (2000).

RADIATION DEFECTS IN AMORPHOUS As-Ge-S STUDIED BY POSITRON ANNIHILATION TECHNIQUES

O. I. Shpotyuk[a,b], J. Filipecki[b], R. Ya. Golovchak[a,c], A. P. Kovalskiy[a,d], M. Hyla[b]

[a]Scientific Research Company "Carat", Stryjska str. 202, 79031 Lviv, Ukraine
[b]Physics Institute, Pedagogical University, Al. Armii Krajowej 13/15, 42201 Czestochowa, Poland
[c]Lviv I.Franko National University, Physics Department, Dragomanova str. 50, 79005Lviv, Ukraine
[d]National University "Lviv Polytechnics", Bandera str. 12, 79646 Lviv, Ukraine

The nature of coordination defects in chalcogenide vitreous semiconductors of As-Ge-S system have been analysed before and after γ-irradiation using the results of positron lifetime measurements. The correlations between the positron lifetime data, the structural features and the chemical compositions of glasses have been established. The identification of negatively charged point defects has been carried out.

1. Introduction

A good sensitivity of positron annihilation method to the changes in local structure of solids, to the presence of point defects, inhomogeneities and phase transitions makes it an important source of information, which allows to verify and to complete the results obtained by various experimental techniques. Sometimes, as in the case of chalcogenide vitreous semiconductors (ChVS), it is one of the exclusive experimental methods, which provides us with the qualitative and quantitative characteristics of the defect configuration [1-3]. ChVS are characterized by the presence in glass matrix of the specific oppositely charged diamagnetic D^+–D^- coordination defects (CD) [4], which usually cannot be identified by the traditional techniques for the defects detection (ESR, luminescence, etc.). Such defects lead to the appearance of localized electronic states lying at the edges or inside of the ChVS band gap [5] that determines their main physical properties. The positron annihilation method was used for the investigation of CD nature practically in all of the known binary ChVS systems (As-S, As-Se, Ge-S, Ge-Se, Ge-Te and others) [1-3,6,7]. As a rule, two positron lifetimes were revealed for these ChVS. The first component (short-lived) was normally associated with the free positron annihilation, and the second (long-lived) one was attributed to the positron annihilation on the negatively charged point defects. At the same time, in some glasses the third component (with even greater lifetime) was observed. The last was connected with positronium formation inside of glass "free volume" [6]. Taking into account these results, positron annihilation studies for some elemental amorphous materials (such as Se [1]) as well as the data of other defect-sensitive methods the proper CD were identified for almost all binary ChVS. However, the ternary ChVS systems, which are more complicated from the structural point of view, are studied insufficiently in this context. The features of radiation-induced effects, intensively studied in last years, are determined by D^+–D^- CD formation processes too [8,9]. Fair identification of these defects in ChVS before and after the radiation treatment is an important step to the understanding of the mechanism of induced changes. However, such investigations were not performed up to now.

In this connection, the positron lifetime measurements were performed for "stoichiometric" $(As_2S_3)_y(GeS_2)_{1-y}$ and "non-stoichiometric" $(As_2S_3)_x(Ge_2S_3)_{1-x}$ ChVS systems before and after γ-irradiation. The analysis of possible CD formation processes was carried out taking into account the γ-induced optical changes in the fundamental absorption edge region.

2. Experimental

The bulk samples of stoichiometric $(As_2S_3$-$GeS_2)$ and non-stoichiometric $(As_2S_3$-$Ge_2S_3)$ cross-sections of correspondent glass forming region were prepared by the melt quenching method using the

mixture of high purity (99,9999%) Ge, As and S elements. The initial ingredients were sealed in quartz ampoules (10^{-3} Pa) and heated gradually up to 1200 K. The furnace was rocked for 24 hours to obtain the most homogeneous melt. Then the obtained ingots were quenched on air at the ambient temperature. All ampoules were annealed additionally at the temperature of 20-30 K below softening point (T_g) to remove the mechanical strains. The amorphous state of the obtained materials was controlled by character conch-like fracture, data of X-ray diffraction study and IR microscopy. Finally, all ingots were sliced into 1 mm thick disks and polished for precision optical measurements. The ChVS samples were irradiated by γ-quanta at the power of exposure dose of 20 Gy/sec. The radiation treatment was performed in the normal conditions of the stationary radiation field, created in the closed cylindrical cavity owing to the concentrically established ^{60}Co (E=1.25 MeV) sources. The accumulated dose of 2.82 MGy was chosen taking into account previous investigations of radiation-induced effects in binary chalcogenide glasses [8,9]. The optical absorption coefficient $\alpha(h\nu)$ was calculated from the transmission characteristics $\tau(h\nu)$ (as described elsewhere [10]) measured before and after γ-irradiation using two-beam "Specord M-40" spectrophotometer (200-900 nm). Measurements of positron lifetimes were carried out using an ORTEC spectrometer of the resolution FWHM (full width at half maximum) = 270 ps. ^{22}Na isotope positron source with 0.74 MBq activity was situated between two identical samples, forming a "sandwich" system.

3. Results and discussion

As it is known [11,12] the exponential character of the fundamental absorption edge (or so-called Urbach tail of absorption) is caused by the stochastic electrical fields of charged defect centers. As it was stated above in ChVS the D^+–D^- CD can play the role of such defects. The typical absorption spectra $\alpha(h\nu)$ at the region of fundamental absorption edge before and after γ-irradiation for the investigated glasses are shown in Fig. 1. It is clearly seen that after radiation treatment with 2.82 MGy dose the edge shifts towards the low energy values for all studied ChVS. This shift is accompanied with the changes in the edge slope and depends on the chemical composition of the sample. According to [13], the edge slope is directly connected with CD concentration. Thus, we can conclude that γ-irradiation leads to the redistribution of defects in investigated ChVS. It was assumed previously [10] that radiation treatment of As-Ge-S glassy system causes the appearance of new D^+–D^- CD, but the quantitative and qualitative description of this process was not carried out.
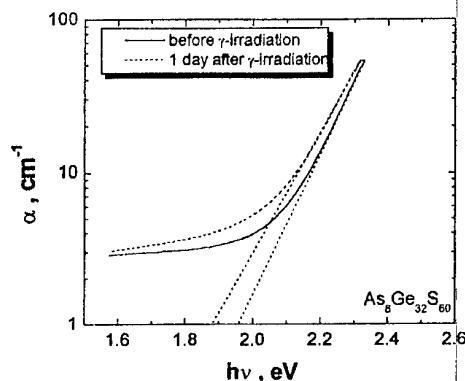
Fig. 1. The typical spectral dependence of absorption coefficient $\alpha(h\nu)$ before and after γ-irradiation with 2.82 MGy dose for As-Ge-S ChVS system.

Positron annihilation lifetime measurements show that before the γ-irradiation all stoichiometric compositions (data for two of them with the maximal content of As_2S_3 and GeS_2 components are presented in the Table 1) are characterized by the lone mean lifetime of positrons ~0.36 be ns. This usually happens, when the channels of comparable intensities and close lifetimes cannot be resolved by the computer. According to [14,15], the above lifetime value is formed as a superposition of lifetimes corresponded to the free positron annihilation (~0.2 ns), to the annihilation on dangling bonds of Ge_3^- CD (~0.42 ns), of

S_1^- CD (~0.32 ns) and of As_2^- CD (~0.37 ns) (the upper index in the defect signature means the electrical charge of atom, and the lower one – the number of nearest covalent-bonded atoms). Because of small concentration of free carriers in most of ChVS (~10^8 cm^{-3} [16]) in comparison to D^+–D^- CD concentration (~10^{16}-10^{19} cm^{-3} [13,16]), the free positron annihilation component should bring a small contribution into the mean lifetime. Therefore, it can be concluded that before the γ-irradiation the amounts of Ge_3^-, S_1^- and

As_2^- CD in stoichiometric ChVS are of the comparable concentration. The changes in optical spectra after the γ-irradiation (Fig. 1) are the evidence of the additional CD formation. The qualitative analysis of measured lifetimes shows the existence of two lifetime components after γ-treatment: short- and long-lived (τ_1 and τ_2, respectively). The first one ($\tau_1 \sim 0.28$ ns) seems to be responsible for the annihilation on S_1^- CD. The second lifetime ($\tau_2 \sim 0.39$ ns) is attributed to the superposition of the annihilations on dangling bonds of Ge_3^- and As_2^- CD. According to the ratio of short- and long-lived components intensities (see Table 1), it can be concluded that in the case of As_2S_3-enriched compositions the S_1^- γ-induced CD creation is preferred. With the increasing of GeS_2 content in the investigated ChVS the role of Ge_3^- and As_2^- CD in radiation-induced optical effects becomes more essential.

Table 1. Positron lifetime characteristics of the samples from stoichiometric $(As_2S_3)_y(GeS_2)_{1-y}$ ChVS system measured before and after γ-irradiation with 2.82 MGy dose.

Chemical composition	Before γ-irradiation		After γ-irradiation (2.82 MGy)	
	Experimental values	Mean lifetime	Experimental values	Mean lifetime
$As_{28.6}Ge_{9.5}S_{61.9}$ y=0.6	$\tau_1 = 0.3638 \pm 0.0002$	$\tau = 0.3638 \pm 0.0002$	$\tau_1 = 0.277 \pm 0.002$; $I_1 = 0.67 \pm 0.01$ $\tau_2 = 0.386 \pm 0.003$; $I_2 = 0.33 \pm 0.01$	$\tau = 0.313 \pm 0.003$;
$As_{6.25}Ge_{28.125}S_{65.625}$ y=0.1	$\tau_1 = 0.3644 \pm 0.0004$	$\tau = 0.3644 \pm 0.0004$	$\tau_1 = 0.282 \pm 0.009$; $I_1 = 0.53 \pm 0.05$ $\tau_2 = 0.397 \pm 0.010$; $I_2 = 0.47 \pm 0.05$	$\tau = 0.336 \pm 0.010$;

The results of positron lifetimes measurements for two non-stoichiometric ChVS compositions are presented in Table 2. As-enriched glasses are characterized by a lone mean lifetime of positrons (~ 0.34 ns) before the irradiation. The most probably, this value is a superposition of positron lifetimes connected with the annihilation on dangling bonds of the same CD (S_1^-, Ge_3^- and As_2^-) [14,15] as in the case of stoichiometric samples. The ChVS with greater Ge content are characterized by two lifetimes. The short-lived component ($\tau_1 \sim 0.24$ ns) is connected with superposition of positron annihilation on the dangling bonds of S_1^- CD and positron annihilation on the trapping sites formed by the open volume defects such as the As, S or Ge vacancies (~ 0.25 ns) [17]. Since Ge-enriched samples of non-stoichiometric ChVS system are characterized by an excess of four-fold Ge atoms, we suppose a large number of such vacancies to be formed. The greater open volume, associated with clusters of above vacancies, is also assumed, but it can contribute only into τ_2 (long-lived component of positron lifetimes) according to [17]. Besides it, $\tau_2 \sim 0.39$ ns lifetime component includes the positron annihilation on dangling bonds of Ge_3^- and As_2^- CD [15]. It should be noted, that in the case of stoichiometric samples the contribution into measured lifetime from positron annihilation processes inside of microvoids (vacancies or their clusters) is of less order. The reason is that the stoichiometric ChVS compositions predict the saturation of all chemical bonds due to their main structural units – $AsS_{3/2}$ pyramids and $GeS_{4/2}$ tetrahedra and, as a result, the more compact ChVS structure. In the non-stoichiometric glasses (especially those with high Ge content) the construction of optimal number of such structural units is complicated that favor the formation of open volume defects. Two positron lifetimes were observed after the γ-irradiation of non-stoichiometric ChVS samples. The short-lived component ($\tau_1 \sim 0.27$ ns) was connected with positron annihilation on the trapping sites of As, S or Ge atoms and with annihilation on the dangling bonds of S_1^- CD. The long-lived one ($\tau_2 \sim 0.39$ ns) was attributed to the positron annihilation processes in the microvoids of a greater volume as well as to the annihilation on dangling bonds of Ge_3^- and As_2^- CD. Owing to the intensities ratio of these lifetime components in the investigated non-stoichiometric ChVS, it can be concluded that the γ-radiation produces the additional number of $D^+–D^-$ defects and favors the microvoids formation.

Table 2. Positron lifetime characteristics of the samples from non-stoichiometric $(As_2S_3)_x(Ge_2S_3)_{1-x}$ ChVS system measured before and after γ-irradiation with 2.82 MGy dose.

Chemical composition	Before γ-irradiation		After γ-irradiation (2.82 MGy)	
	Experimental values	Mean lifetime	Experimental values	Mean lifetime
$As_{16}Ge_{24}S_{60}$ $x=0.4$	$\tau_1 = 0.3396\pm0.0003$	$\tau = 0.3396\pm0.0003$	$\tau_1 = 0.275\pm0.010;$ $I_1=0.55\pm0.06$ $\tau_2 = 0.392\pm0.013;$ $I_2=0.45\pm0.06$	$\tau = 0.328\pm0.013;$
$As_8Ge_{32}S_{60}$ $x=0.2$	$\tau_1 = 0.239\pm0.006$ $I_1=0.43\pm0.02$ $\tau_2 = 0.385\pm0.005$ $I_2=0.57\pm0.02$	$\tau = 0.322\pm0.006$	$\tau_1 = 0.243\pm0.017;$ $I_1=0.33\pm0.05$ $\tau_2 = 0.387\pm0.009;$ $I_2=0.67\pm0.05$	$\tau = 0.339\pm0.017;$

4. Conclusions

It is established, that γ-irradiation of all investigated samples leads to the low-energetic shift of the fundamental absorption edge. This shift is caused by the additional D^+-D^- defects formation. In the case of stoichiometric $(As_2S_3)_y(GeS_2)_{1-y}$ ChVS compositions, the measured positron lifetimes correspond to the diamagnetic S_1^-, Ge_3^- and As_2^- coordination defects. The additional essential contribution of microvoids into the lifetime characteristics of non-stoichiometric $(As_2S_3)_x(Ge_2S_3)_{1-x}$ ChVS system is assumed.

Acknowledgements

References

[1] O. K. Alekseeva, V. I. Mihajlov, A. P. Chernov, V. P. Shantarovich, Sov. Solid State Physics, 19, 3452 (1977) (in rus.).
[2] O. K. Alekseeva, V. I. Mihajlov, V. P. Shantarovich, Phys. Stat. Sol., A48, K169 (1978).
[3] H. E. Hansen, K. Petersen, Appl. Phys., A26, 35 (1981).
[4] N. F. Mott, E. A. Davis, Electronic Processes in Non-Crystalline Materials, Clarendon Press, Oxford (1971).
[5] N. F. Mott, E. A. Davis, R. A. Street, Phil. Mag., 32, 961 (1975).
[6] B. V. Kobrin, R. M. Kupriyanova, V. S. Minaev, E. P. Prokopiev, V. P. Shantarovich, Phys. Stat. Sol., A73, 321 (1982).
[7] A. D. Mokrushin, E. P. Prokopiev, V. S. Minaev, K. Badru, R. M. Kupriyanova, Physics and Technics of Semiconductors 14, 1271 (1980) (in rus.).
[8] V. O. Balitska, O. I. Shpotyuk, J. Non-Cryst. Solids, 227-230, 723 (1998).
[9] O. I. Shpotyuk, Phys. Stat. Sol., A145, 69 (1994).
[10] O. I. Shpotyuk, A. P. Kovalskiy, E. Skordeva, E. Vateva, D. Arsova, R. Ya. Golovchak, M. M. Vakiv, Physica B: Condensed Matter, 271, 242 (1999).
[11] J. D. Dow, D. Redfield, Phys. Rev., B5, 594 (1972).
[12] V. L. Bonch-Bruevich, Sov. Progress in Physical Sciences, 140, 583 (1983).
[13] M. Babacheva, S. D. Baranovskiy, V. M. Lubin, M. A. Tagirdganov, V. A. Fedorov, Sov. Solid State Physics, 26, 2194 (1984) (in rus.).
[14] B. V. Kobrin, V. P. Shantarovich, Phys. Stat. Sol., A83, 159 (1984).
[15] B. V. Kobrin, V. P. Shantarovich, J. Non-Cryst. Solids, 89, 263 (1987).
[16] A. Feltz, Amorphous and Vitreous Inorganic Solids, Mir, Moscow, (1986) (in rus.).
[17] K. O. Jensen, Ph. S. Salmon, I. T. Penfold, P. G. Coleman, J. Non-Cryst. Solids, 170, 57 (1994).

GLASSY TRANSFORMATION AND STRUCTURAL CHANGE IN Ge$_2$Sb$_2$Te$_5$ STUDIED BY IMPEDANCE MEASUREMENTS

E. Morales-Sánchez[a,b], J. González-Hernández[a], E. Prokhorov[a]

[a]Centro de Investigación y de Estudios Avanzados del IPN, Unidad Querétaro, Ap. Postal 1-798, 76001, Querétaro, Qro., Mexico.
[b]División de Estudios de Posgrado, Facultad de Ingeniería, UAQ, Querétaro, Mexico.

The transition form amorphous-to-crystalline (fcc) has been investigated in Ge$_2$Sb$_2$Te$_5$ thin film alloys. This composition is the most frequently used for erasable optical memory devices. The phase transition was monitored using *in situ* impedance measurements as a function of temperature. The results were analyzed using the Maxwell-Wagner and brick models. From the impedance measurements it is possible to detect the appearance of nucleation centers in samples heated at temperatures below crystallization. In samples treated at temperatures above crystallization, the increase in the volume fraction of crystalline material due to the increase in the temperature is also deduced from the impedance measurements. From our investigation we have shown that impedance measurements are a sensitive method to analyze the crystallization process in chalcogenide materials.

1. Introduction

Glassy chalcogenide semiconductors have been studied extensively due to their applications in optoelectronics and electronics. Some of these applications are based on the difference in the optical and/or electrical properties between the amorphous and crystalline phase. The Ge:Sb:Te ternary alloys are the active materials most frequently used in phase-change optical memory technology, specifically, due to its fast crystallization the Ge$_2$Sb$_2$Te$_5$ composition has been used in commercial optical devices. Upon annealing, amorphous layers of this material first undergo the amorphous-to-crystalline (fcc) transition at about 165 °C and at higher temperatures (at about 230 °C) the crystal (fcc)-to-crystal (hex) transition. The crystallization mechanism in these alloys has been studied by many techniques such as optical [1-3], electrical [4-6], Raman spectroscopy [7,8], coherent phonon spectroscopy [9], X-ray diffraction [7,10], transmission and scanning electron and atomic force microscopy [2, 5, 11, 12]. In general, the aim of these investigations is to determine the activation energy of the phase transformation, the microstructures changes in the material during thermal and laser annealing and the influence of the protecting layers on the crystallization process. However, to our knowledge there is no model that can fully explain the crystallization mechanism in this material.

The aim of this article is to study the crystallization process in amorphous Ge$_2$Sb$_2$Te$_5$ ternary thin film alloys by *in situ* impedance measurements as a function of temperature. This technique is vary sensitive to monitor the phase transition, because: i) the resistance of the amorphous state is several orders of magnitude higher than that of the crystalline state [4,5,6], therefore in the process of crystallization a similar change in the real part of impedance must occur; ii) as it is well established in the literature in some temperature range during the process of crystallization, the amorphous and crystalline phase coexisting and the impedance measurements have been widely used for the investigation of the properties of a two-phase materials [13] and iii) the impedance measurements allow to establish the correlation between the microstructure and electrical properties of the material and to obtain information, such as parameter of grain boundaries, difficult to obtain using other methods.

2. Experimental

The $Ge_2Sb_2Te_5$ thin films were prepared by RF sputtering of the bulk alloy samples onto unheated glass substrate. Film with a thickness ranging from 30 nm to 4.6 micrometers were investigate. The samples were heated using a 300 W resistance cartridge heater. The temperature was controlled with a Watlow's Series 982, 1/8 DIN microprocessor-based, with ramping controller. The temperature controller was programmed to produce a constant heating rate of 4 °C/min and to stops every 5 degree to make the impedance measurements in the frequency range of 40 Hz-110 MHz. The measurement were done with the help of an Agilent Precision Impedance Analyzer model 4294A. The amplitude of the measurement signal was 500 mV. For the impedance studies the   planar configuration was used with evaporated Al or silver paint contacts (distance between contact was varied in the range of 0.7-2 mm). The impedance measurements were carried out in films annealed to temperatures below the fcc-to-hexagonal phase transition. The conductivity of the hexagonal phase is too high for the frequency capacity of our device. The experimental results were fitted using the ZView program to obtain the absolute values of all components of the proposed equivalent electrical circuit.

3. Experimental results

The impedance spectra measured in the samples analyzed in this work depend on the temperature at which the sample is measured. Plots of the imaginary versus real part of the impedance consist of one semicircle (not shown) when the sample is measured at temperatures below approximately 100 °C and of two semicircles in samples measured at higher temperatures (see Fig. 1). In the former case, the material is amorphous and the semicircle is related with the properties of the material. In some cases, amorphous materials show impedance spectra with two semicircles, in which the low frequency semicircle describes the properties of the electrical contacts [14]. >From the semicircle observed in the impedance spectra of samples measured at temperatures below 100 °C a value for the dielectric constant in the range of 12.8-15.6 was calculated. The dielectric constant in similar amorphous materials have been reported before, a theoretical steady-state value of 17.7 [15] and also a reported value of 15.3 determined using IR absorption measurements are in good agreement with the experimentally determined in the present work. This confirms the assignment given to the observed semicircle. The resistivity obtained from collinear four-probe measurements (at the room temperature) differs at the most 30 % from the obtained from the impedance measurements in the same material.
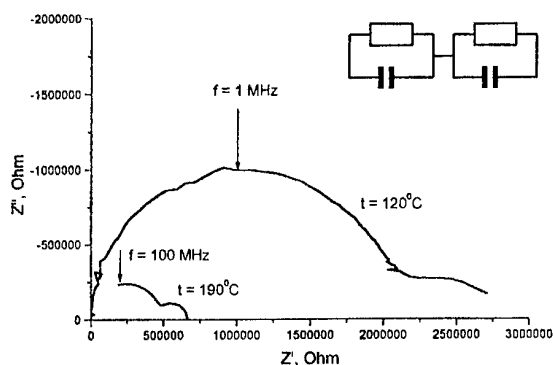
Fig. 1. Impedance spectra obtained at temperatures of 120 °C and 190 °C. The real and imaginary part of the spectra obtained at 190 °C has increased 100 times.
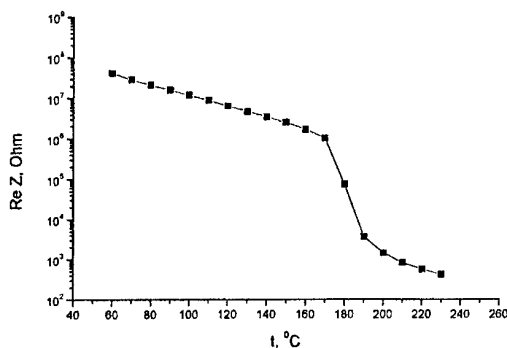
Fig. 2. The temperature dependence of the real part of the impedance.

Arrows show the frequency corresponding to indicate point.

For samples measured at temperatures above 100 °C but below the crystallization temperature T_c, which is 160-175 °C for the material studied, the high frequency semicircle is attributed to the resistance and capacitance of the amorphous material (spectrum at 120 °C in Fig. 1). We suggested that the second semicircle could be due to the appearance of the nucleation centers which start the

crystallization of the amorphous material. This assumption is based on our Temperature-Modulated Differential Scanning Calorimetry measurements in similar $Ge_2Sb_2Te_5$ samples which indicate that the glass transition temperature T_g for this material is at about 100 °C. As has been established in the literature, for many chalcogenide amorphous alloys the nucleation appears at temperatures after T_g [16,17]. At temperatures above T_c one can see (spectrum at 190 °C in Fig. 1) that the impedance spectra also consist of two semicircles, but both semicircles move to higher frequencies. In these spectra, the value of capacitance estimate from the high frequency semicircle is two–three times higher than the value of the capacitance measured for the amorphous material. This is in good agreement with previous results [15] which report that the static dielectric constant of the metastable cubic crystalline phase is 2.2 times larger than that of the amorphous phase. The value of the capacitance determined from low frequency semicircle is about two orders of magnitude larger than the corresponding to the high frequency semicircle, so we suggested that the low frequency semicircle is related with the properties of the grain boundaries. The later is based in two facts: i) our transmission electron microscopy (TEM) measurements in samples heated to temperatures in this range show that the films have a polycrystalline structure [5], and ii) in general the grain boundaries have a higher capacitance than the grain interiors [13]. Fig. 2 shows the temperature dependence of the real part of the impedance spectra, i. e., the resistance of the material as a function of measuring temperature. Qualitative this result is similar to the obtained previously under d.c. [4] or a.c. measurements [5], that is why we do not discuss this dependence.

From the above analysis we can conclude that the structure of samples heated in the range between T_g and temperatures below the crystal-to-crystal transition are formed by a mixture of two phases: at lower temperatures the mixture consists of amorphous and crystalline nuclei, and at higher temperatures the mixture is grains with the fcc structure and grains boundaries. The electrical properties of materials with a structure composed of two phases can be described by an equivalent circuit consisting of two in series RC circuit (this circuit is shown as insert in the Fig. 1).
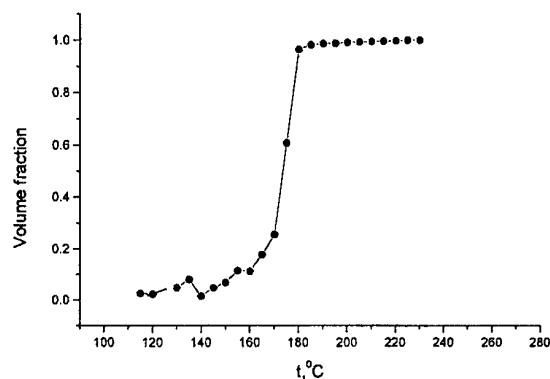
Fig. 3. The temperature dependence of crystalline volume fraction.
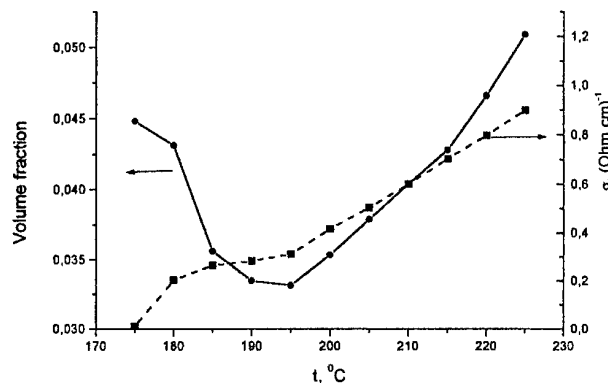
Fig. 4. The temperature dependencies of grain boundaries volume fraction (solid line) and conductivity (dot line).

The electrical properties of continuous medium containing uniformly distributed spheres of a different phase are well described by Maxwell–Wagner model. It was shown [18] that this model is equivalent to the two in series RC circuit shown in Fig. 1. Using the Maxwell–Wagner model we can calculate the change in the crystalline volume fraction for temperatures above 100⁰ C. This dependence is shown in Fig. 3. For samples heated at temperature above the amorphous–to-crystalline transition, we can use the brick model [13], which assumes that cubic-shaped grains are separated by flat grain boundaries. Such physical model agrees with the TEM micrographs which show that the material consists of randomly orientated crystallites [5]. Using this model the volume fraction and conductivity of grain boundaries were calculated and are shown in Fig. 4. The relatively high conductivity of the grain boundaries may be explained assuming the appearance of about 20 % of vacancies at the grain boundaries [10].

4. Discussion

Our results have shown that in $Ge_2Sb_2Te_5$ thin films, the amorphous-to-crystalline transformation occurs after heating at temperatures higher than T_g. In the temperature range between T_g and T_c the

nucleation centers appear and increase as the heating temperature approaches T_c. At the initial stages of nucleation, X-ray diffraction measurements did not detect any crystalline peaks, diffraction peaks corresponding to the fcc phase appear when the volume occupied by the crystalline material is of few percentage, this suggest that the nucleation centers have the cubic phase. The impedance spectra of samples treated above T_c consist of two semicircles (Fig. 1). Similar spectra are found when the sample is cooled down to room temperature. The resistance of samples heated above T_c was measured at room temperature using the four-probe method and the results are close to those determined from the room temperature impedance spectra. This implies that these semicircles describe the microstructure properties of the material. According to previous consideration we concluded that low frequency semicircle describes the electrical properties of the grain boundaries. However, applying the brick model to our experimental resells, we have obtained unexpected results: in Fig. 4, the volume fraction of grain boundaries first decreases and than increases with the increase in temperature. In previous studies in similar samples annealed above crystallization it was reported that TEM observation show that the grain size increases with the increase in temperature [2,5]. In principle, this implies that the volume fraction of grain boundaries must decrease. An explanation to the increase in the volume fraction of grain boundaries could be the following. In the reference [10] have shown that the X-ray diffraction data of crystallized $Ge_2Sb_2Te_5$ films contain two phases: one is the $Ge_2Sb_2Te_5$ crystalline phase and another minority phase of elemental Sb which remain in the amorphous phase at the grain boundary. According to this results [10] we proposed that above certain annealing temperature (about 200 °C), the increase of some atomic segregation to the grain boundaries such as Sb or other impurities could be responsible for the increase in the volume fraction of grain boundaries.

5. Conclusion

It has been shown that the impedance measurements are a high sensitive method by means of which it is possible to determine the structural change in the process of an amorphous-to-crystalline transition. In addition, the impedance study allows to detect the presence of nucleation centers in the early stages of crystallization and to characterize the structural parameters after crystallization.

Acknowledgments

Reference

[1] A. Mendoza-Galván, J. González-Hernández, J. Appl. Phys. **87**, 1, (2000).
[2] N. Oshima, J. Appl. Phys. **83**, 5244 (1998).
[3] C. A. Volker, M. Wutting, J. Appl. Phys. **86**, 1808 (1999).
[4] I. Friedrich, V. Weidenhof, W. Njoroge, P. Franz, M. Wutting, J. Appl. Phys. **87**, 4130 (2000).
[5] J. González-Hernández, E. Prokhorov, Yu.Vorobiev, J. Vac. Sci. Technol. A, **18**, 1694 (2000).
[6] J. González-Hernández, V. Castaño, A.del Real, E. Morales-Sánchez, E. Garsía-Garsía, A. Mendoza-Galván, E.Prokhorov, Yu.Vorobiev, Inorganic Mat. **36**, 1219 (2000).
[7] J. González-Hernández, B. S. Chao, D. Strand, S. R. Ovshinsky, D. Pawik, P. Gasiorowski, Appl. Phys. Com. **11**, 557 (1992).
[8] J. Tominaga, N. Atoda. Jpn. J. Appl. Phys. **38**, L322 (1999).
[9] M. Forst, T. Dekorsy, C. Tappe, M. Laurenzis, H. Kurz, Appl. Phys. Lett. **77**, 1964 (2000).
[10] N. Yamada, T. Matsunaga, J Appl. Phys. **88**, 7020 (2000).
[11] N. Nobukuni, M. Takashima, T. Ohno, M. Horie, J Appl. Phys. **78**, 6980 (1995).
[12] V. Weindenhof, I. Fiedrich, S. Ziegler, M. Wutting, J Appl. Phys. **86**, 5879 (1999).
[13] J. R. Macdonald. Impedance spectroscopy, John Wiley & Sons. Inc. (1977).
[14] E. Morales-Sánchez, J. González-Hernández, E. Prokhorov, Yu. Vorobiev, M. Becerril, Abstract of Int. Mat. Research Congress, Cancun 2000, p. 16.
[15] R. Yokota. Jpn. J. Appl. Phys. **28**, 1407 (1989).
[16] A. Elshafie, A. Abdel-All. Physica B, **269**, 69 (1999).
[17] Y. Calventus, S. Suriñach, M. D. Baró, J. Mat. Res. **12**, 1069 (1996).
[18] N. Bonanost, E. Lilley, J. Phys. Chem. Solids **32**, 943 (1981).

THERMALLY-INDUCED STRUCTURAL CHANGES
IN COPPER-CONTAINING CHALCOGENIDE THIN FILMS

S. R. Lukič, D. M. Petrovič, N. Cvejič, A. F. Petrovič, F. Skuban

Faculty of Sciences, Institute of Physics, Trg Dositeja Obradovič a 4, 21000 Novi Sad, Yugoslavia

Thin-film samples of the system $Cu_x(AsSe_{1.4}I_{0.2})_{1-x}$, x<15 at%, were prepared by the method of thermal evaporation on "cold" substrates in vacuum, using a specially constructed quartz cell as evaporation chamber. The method of transmission electron microscopy was employed to follow the structural changes taking place in the course of thermal treatment of the freshly deposited film samples. It was found that the contents of selenium and copper in the starting glass have a decisive role in determining the structure and properties of the material. The observed microgranular two-phase structures of thin films have a grain size of the order of 10 nm. Heating of the samples to the softening temperature yields the structural transformation in the films from the starting amorphous phase to a new amorphous phase. Also, the temperatures were determined at which partial crystallization takes place, resulting in the separation of crystalline centers of the elemental selenium.

1. Introduction

In the last decades, thin films of various compositions have become the materials of significant practical applications. Thus, it has been shown that their excellent characteristics are of technological importance, for example in manufacturing cathode tubes and microelectronic circuits. On the other hand, they found equally important application in the industry where they are used as the elements of mass-products as transparent coatings on plastics and textile or sunglasses, for example.

It has been shown that samples of chalcogenide amorphous materials can be relatively easily obtained in the form of thin films, whereby all relevant desirable characteristics of these amorphous systems are preserved. It should be especially pointed out that the photo-induced changes of properties in the chalcogenide glasses could appear even in the absence of classical photochrome components in their composition [1, 2]. Most probably, relatively low energies of the chemical bonds in these structures can ensure the occurrence of photochemical reactions and photo-structural transformations. This holds even for photo-crystallization. All these facts are of invaluable importance for the application of thin films of chalcogenide systems as a medium for information recording that can be erased by thermal annealing at a temperature below the softening point [3]. In view of the fact that optical recording is based on the change of the absorption coefficient of electromagnetic radiation and the coefficient of refraction, primarily as a consequence of structural transformations *amorphous phase ⇔ crystal, amorphous ⇔ amorphous* or, possibly, because of the change of magnetic polarizability, one of the primary tasks is to resolve the question of the mechanism of information recording and erasing. In this work we present the results obtained in a study of the effect of temperature on the structural properties of thin films from the system Cu-As-Se-I.

2. Experimental

Thin-film samples of the $Cu_x(AsSe_{1.4}I_{0.2})_{1-x}$ system were obtained by thermal evaporation and condensation in vacuum of the priorily synthesized glass of the given composition. Because of the

complex composition of the starting glass use was made of a special quartz cell as the evaporation chamber allowing the discrete evaporation at optimal temperatures [4]. The glass was synthesized by the previously described procedure of cascade heating and annealing in air [5]. The films were deposited on the glass plates of the known refraction index, kept at room temperature. The film thickness in the process of vapour-deposition was controlled by optical method based on the interference of the reflected laser beam and it was 1.08, 1.22 and 0.77 mm for the samples with 0, 5 and 15 at.%, respectively, which enabled investigation of the films by the method of transmission electron microscopy (TEM) [6]. The film structure was investigated using an electronic microscope EMV-100B additionally equipped with a camera for electron diffraction of the type EMR-100. The character of the structural transformations taking place in the films with increase in temperature were studied by monitoring the changes resulting from the heating of the freshly-prepared samples from room temperature to 200 °C at a rate of 0.5 °/s.

3. Results and discussion

Mass spectrometry was used to control the relative composition of the vapour in the process of thin-film preparation. It was found that the mass spectra are characterized by those structural units that enter the composition of the corresponding glass. In Figs. 1.a–1.c are presented the TEM photographs of freshly prepared films of the investigated chalcogenide system. The photographs (magnification 40,000) were taken for a sample containing no copper and the samples with 5 and 15 at.% Cu. Figs. 2a–2c illustrate the changes caused by thermal treatment of the same samples.

In the same figures are shown the photographs of electronic diffraction patterns taken for each of the observed situations. As can be seen, electronic microscopy showed that freshly deposited films of the ternary glass $AsSe_{1.4}I_{0.2}$ has a microgranular structure, whereby the grain size is of the order of magnitude of 10 nm. Over the whole film surface there are randomly distributed irregular amorphous forms of Se (Fig. 1a).

In the course of heating to the softening temperature, some structural changes take place in the film from the starting amorphous phase to a new, also amorphous phase (in the figure designated as A0 → A1). At about 105 °C crystallization of Se on the film surface takes place (this is confirmed by the crystalline forms present on the sites of the amorphous ones), as well as in the film itself, which is visible as dark grains over the whole picture (Fig. 2a). Further increase in temperature (to the softening point) yielded no significant changes in the film structure.

The freshly deposited films of the composition $Cu_5(AsSe_{1.4}I_{0.2})_{95}$ have a structure very similar to that obtained for the ternary samples (Fig. 1b). It is also possible to observe the structural change A0 → A1, whereby the amorphous character has been preserved. At a somewhat different temperature ($T_t \sim 110$ °C) Se crystallization in the film takes place, but the dominant character of crystallization differs from the corresponding process observed with the sample containing no copper. Namely, in this case, the process of Se separation and crystallization is dominant in the whole thin-film volume, which confirms the formation of a more distinct grainy structure and uniform increase in the size of dark spots over the whole picture (Fig. 2b).

The film $Cu_{15}(AsSe_{1.4}I_{0.2})_{85}$ is essentially different, still in the initial phase. Namely, the microgranular structure is more clearly formed in which there is no Se on the surface (Fig. 1c). Analogously to the other samples, the transition A0 → A1 (motion of the dark front in the microscope field of vision) is observed, and the heating ($T_t \sim 125$ °C) yields crystallization of selenium, which is evident from the forms characteristic of its crystalline state (Fig. 2c).
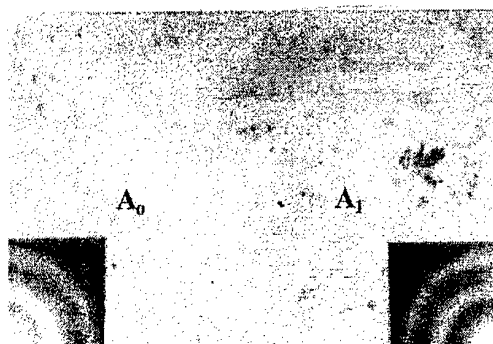
1.a

2.a
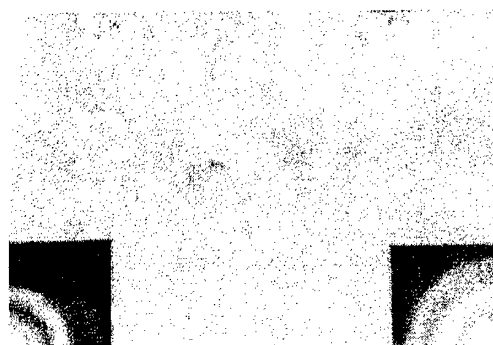
1.b
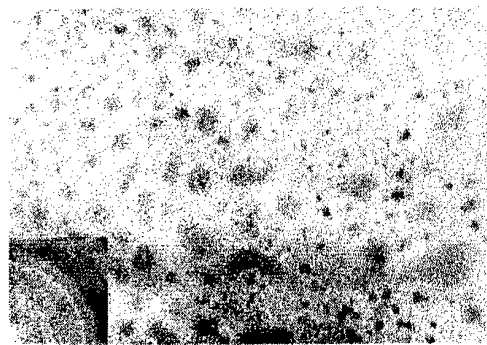
2.b
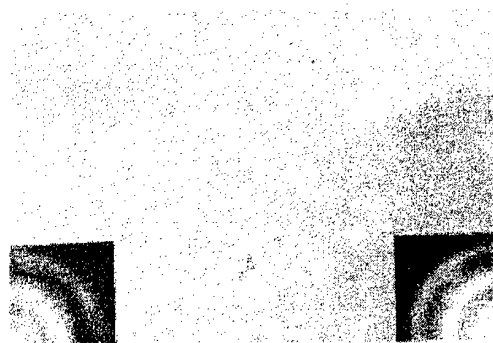
1.c
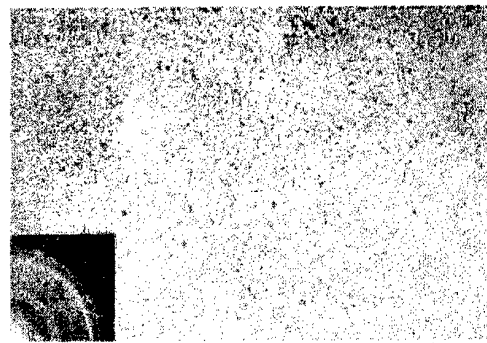
2.c

Fig. 1. TEM micrograph and x-ray diffractogram of as-evaporated thin films:
a – $AsSe_{1.4}I_{0.2}$;
b – $Cu_5(AsSe_{1.4}I_{0.2})_{95}$;
c – $Cu_{15}(AsSe_{1.4}I_{0.2})_{85}$.

Fig. 2. TEM micrograph and x-ray diffractogram of thermally annealed films:
a – $AsSe_{1.4}I_{0.2}$;
b – $Cu_5(AsSe_{1.4}I_{0.2})_{95}$;
c – $Cu_{15}(AsSe_{1.4}I_{0.2})_{85}$.

The identification of two different amorphous phases, that is the corroboration of their existence, is of special importance for the interpretation of photorecording phenomena. It is important to point out that the values of transformation temperatures are in excellent agreement with the softening temperature of the non-crystalline material of the corresponding composition vapour-deposited on a cold substrate, determined by other experimental methods [7,8].

4. Conclusions

The detected changes give the ground to the conclusion that the structure and properties of the films of the Cu-As-Se-I system are mainly determined by the contents of Se and Cu in the starting

glass. It is obvious that lower contents of Se in the sample yield also lower population of individual centres on the film surface, and thus result in a more homogeneous film. This causes the difference in the mode of Se crystallization in the samples of different compositions. On the other hand, the increase in Cu content in the starting glass obviously yields to the increase in the population of the centres that induce structural transformations and crystallization (the temperature of Se crystallization decreases with increase in Cu content of the sample).

References

[1] S. R. Lukič, D. M. Petrovič, I. I. Turyanitsa, O. V. Khiminets, J. Mat. Sci., **26**, 5517 (1991).

[2] S. C. Katyal, S. Okano, T. Bando, M. Suzuki, J. Non-Cryst. Sol., **97/98**, 1195 (1987).

[3] S. R. Lukič, D.M. Petrovič, M. I. Avramov, E. Marquez, J. Mat. Sci. Lett., **16**, 1845 (1997).

[4] I. I. Turyanitsa, I. P. Spasyuk, V. V. Khiminets, E. E. Semrad, Abstr. 2-nd Republ. Conf., Uzghorod, USSR, 134 (1975) (in russian).

[5] S. R. Lukič, D. M. Petrovič, M. I. Avramov, A. F. Petrovič, Proc. 36-th Yugoslav Symp. ETRAN, Ed. D. Uskokovic, Belgrade, Yugoslavia, 35 (1992).

[6] S. R. Lukič, D.M. Petrovič, S. J. Skuban, E. I. Borkach, Proc. 1-st Conf. Electron Microscopy, Novi Sad, Yugoslavia, 205 (1994).

[7] S. R. Lukič, D. M. Petrovič, I. I. Turyanitsa, M. V. Dobosh, J. Therm. Anal., **52**, 553 (1998).

[8] F. Skuban, D. M. Petrovič, S. R. Lukič, M. M. Garič, I. O. Gúth, J. Therm. Anal. Cal., **59**, 877 (2000).

HIGH-PURITY GLASSES BASED ON ARSENIC CHALCOGENIDES

M. F. Churbanov, I. V. Scripachev, G. E. Snopatin, V. S. Shiryaev, V. G. Plotnichenko[a]

Institute of Chemistry of High Purity Substances, Russ. Acad. Sci., 49, Tropinin St.,
Nizhny Novgorod, 603950, GSP-75, Russia
[a]Fiber Optics Research Center at the General Physics Institute, Russ. Acad. Sci., 38,
Vavilov St., Moscow, 117756, V-333, Russia

Low impurity content is the essential requirement to many applications of vitreous arsenic chalcogenides as a material for optoelectronics. Investigations carried out in last ten years increased the knowledge volume about the nature and origin of impurities in chalcogenide glasses, their effect on glass properties, especially on the transmittance in middle IR region and on radiation strength. These properties are most sensitive to impurity presence. The minimum calculated content of impurities, leading to observation of impurity contribution to the property value, is 0.1 - 100 ppb at. for different impurity groups. The effective methods of preparations and analysis of high - purity glasses are developed. The best glass samples contain the impurities of widespread metals and silicon on the level of 0.1 ppm wt., optically active hydrogen - 0.2 -0.05 ppm at., oxygen and carbon - 0.5 - 1 ppm wt., submicron size heterogeneous inclusions - 10^4 - $5*10^6$ cm^{-3}. Impurity content in the glasses of ordinary quality is 10 - 100 times higher. The presence of impurities should be taken into account while investigating both well-known and developed properties and applications of glasses.

1. Introduction

The vitreous arsenic chalcogenides are effective optical materials. They have different attractive properties such as a wide transparency region, low optical losses in the 2-12 µm interval, stability to the atmospheric moisture etc.

Transparency region of glasses measured at the absorption coefficient level of 1 cm^{-1} is 0.62-11.5 µm for As_2S_3 ; 0.85-1.75 µm for As_2Se_3 and 0.75-12.25 µm for $As_2S_{1.5}Se_{1.5}$. The minimum optical losses in As_2S_3 and As_2Se_3 are evaluated as $(6-7)*10^{-2}$ dB/km between 4 and 6 µm. For this reason vitreous arsenic chalcogenides are applicable for the manufacture of optical fibers. There are other fields of arsenic chalcogenides application both traditional and newly developed. Because of stable scientific and applied interest to these glasses the problem of their purity is very actual. The possible effect of impurity presence on the glass properties, which is of especially delicate nature, is relatively not often taken into account.

In the present paper the modern level of purity for the vitreous arsenic chalcogenides and impurity effect on glass properties are considered.

2. Preparation of vitreous arsenic chalcogenides

Bulk samples of vitreous arsenic chalcogenides of optical grade are produced by solidification of the glass forming melt. The initial charge with definite composition is melted in evacuated sealed ampoules made of quartz glass at the time-temperatures modes, which exclude the crystallization, liquation and stria formation. These conditions are individual for different glass systems and determined additionally by mass of the charge melted. For example the values of critical cooling rate for the vitreous As_2S_3, As_2Se_3 and As_2Te_3 approximately differ by three orders of magnitude and equal to $2.4*10^{-6}$; $9*10^{-3}$ and 28 K/s, respectively [1]. It was reflected at the choice of conditions for synthesis and treatment of these glasses.

Different variants for the preparation of initial charge for the glass forming chalcogenide synthesis are possible [2]: from chemical elements (the traditional method); through the decomposition of volatile inorganic hydrides; through the arsenic monosulfide as an arsenic-containing component of charge.

The layers of arsenic selenide may be prepared by plasmochemical decomposition of arsine and selenium hydride [3]. The prepared glass contains a noticeable quantity (several atomic percent) of hydrogen. It is a serious obstacle during heat treatment of glass while manufacturing it into fiber due to blowing up of the melt by hydrogen bubbles evolved. It is serious obstacle at the heat treatment of glass into fiber because of melt distending by hydrogen bubbles evolved. Nevertheless this method may be perspective for the thin films preparation of arsenic selenide. The dependence of the content of arsenic and selenium of different valence states in the layers, prepared at the experimental conditions was established for this process [4].

3. The nature and origin of impurities

The elemental composition, aggregation and chemical forms of impurity presence in vitreous arsenic chalcogenides depend on their macrocomposition, and on conditions of their synthesis. The preparation method and purity degree of initial substances (arsenic, chalcogens) are of importance. A few impurity groups may be isolated at the classification in accordance with element nature and the form of impurity presence in the glass (table 1).

Table 1. Impurity groups in vitreous arsenic chalcogenides.

Principle of classification	Impurity group	Impurity in the group	Typical impurity content, ppm.at.
By elements	Light elements (gas-forming impurities)	Hydrogen, oxygen, carbon, nitrogen	10-100
	Metals	Transition and other metals, silicon	0.1 – 1.0
	Analogues of elements-macrocomponents	Phosphorus, antimony, sulfur, selenium	1 - 100
By the form of presence	Embedded in the glass network	Hydrogen, oxygen, nitrogen, halogens, (OH, SH, SeH, NH, AsH-groups)	0.001 - 10
	Dissolved compounds	CO_2, COS, H_2O, N_2	0.01 - 10
	Heterogeneous inclusions	Carbon, silicon dioxide	$10^6 - 10^9$ cm^{-3}

There are three basic sources of impurities in chalcogenide glasses. First of them is the initial substances used for the glass-forming compound synthesis. Arsenic, chalcogens as pure materials were developed for the semiconductor application. Electrically active impurities, e.g. metallic impurities, were the main object of attention in the first line. For this reason commercial samples of As, S, Se, Te contain of 0.1-0.01 ppm.wt of metallic impurities and more high (1-10 ppm.wt) content of hydrogen, oxygen, carbon and silicon.

The second source of impurities is the material of container used for the synthesis of glass-forming compounds. Impurities having high value of diffusion coefficient, especially hydrogen, enter the chalcogenide melt. It was established [5] that hydrogen from quartz glass, containing 100 ppm of hydrogen, enters the melt of chalcogenide glass starting from 650 °C. The dependence of hydrogen entry rate, υ (g cm^{-2}s^{-1}), on temperature is described by the expression

$$\ln \upsilon = -11,2-(15300/T)$$

(1)

$$(873 \text{ K} \le T \le 1023 \text{ K})$$

Chemical interaction of chalcogenides and some impurities (CS_2, TeO_2) with the quartz glass at high temperature leads to the thin layers formation of new compounds on the inner surface of container and to the appearance of heterogeneous inclusions in chalcogenide melt.

The third source of impurities is the surrounding atmosphere and residual gas of vacuum used at the glass synthesis and glass treatment procedures.

Arsenic and chalcogens have tendency to oxidation at elevated temperature. As it follows from thermodynamic evaluation and from mass-spectrometric investigations of oxide vapors, the equilibrium partial pressure of oxygen at dissociation of arsenic, selenium and tellurium oxides at ~1000 K is at the level of 10^{-4} - 10^{-6} Pa (10^{-6} –10^{-8} mm of Hg). This value will be lower at temperature decrease. For this reason the oxidation of chalcogens and arsenic in the open vacuum system will be excluded at the vacuum better then 10^{-4} - 10^{-6} Pa.

Impurities in vitreous arsenic chalcogenide are present in different forms (Table 1). Atoms of impurity elements may be embedded in glass networks as non-bridging and bridging atoms. The stable impurity compounds (CO_2, CS_2, COS, N_2 etc.) are present in dissolved state in the form of instant solution. Both these forms are well known. Heterogeneous inclusions are the less studied impurity form. They consist of substances which are hardly soluble in the melts of chalcogenides. The particle size depends on the glass sample origin and is distributed between 0.05 and several microns (see Fig.1). Inclusions in arsenic chalcogenide consist of carbon and silicon dioxide. Impurities in this form enter the glasses from initial substances and are also formed by interaction of chalcogen, arsenic, chalcogenides with the apparatus material [6,7].
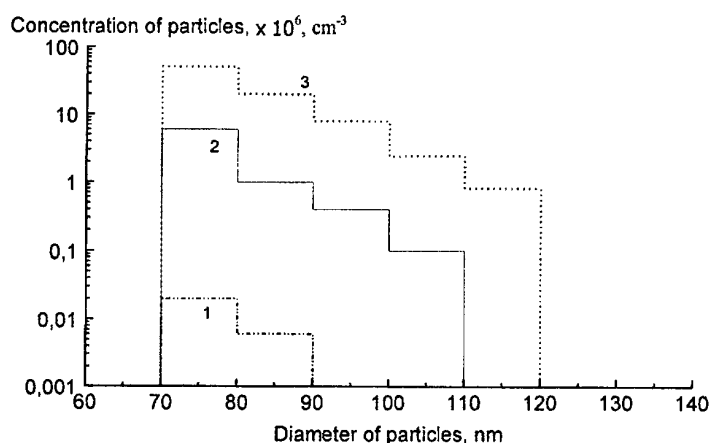
Fig. 1. Histograms of the distribution of impurity particles in glasses: 1- As_2S_3; 2 - As_2Se_3;
3- $As_2Se_{1.5}Te_1$.

Some impurities may present in the glasses in several forms. Carbon compounds (oxides, sulfide and oxysulfide) are dissolved in the glass. Elementary carbon has low solubility in arsenic chalcogenide melts and is present as heterogeneous inclusions.

The oxygen in arsenic selenide present as a cage molecule As_4O_6 and as a polymer formed by structural units $AsO_{3/2}$. In the As_2Se_3 melt monomeric and polymeric forms are in equilibrium, that is frozen at the cooling melt. Taking into account the peculiarities of mutual solubility of polymers it will be reasonable to assume the presence of polymeric arsenic oxide in the form of inclusions. At the melt solidification polymeric arsenic oxide may crystallize. The evidence to this follows from observation of absorption bands characteristic of the transmission spectra of individual arsenic oxide in the form of glass, claudetite and As_4O_6 molecules in the transmission spectra of oxygen containing As_2Se_3 [8-10].

4. Impurity effect on optical properties of glasses

In general case the property of solid material of a given macrocomposition depends on the content of impurities and structural defects. Property value may be presented as the sum

$$P=P_0+P_i+P_d+P_{ii}+P_{dd}+P_{id}, \tag{2}$$

where P_0 is the value for the impurity and defect free hypothetical substance, P_i and P_d – increments caused by impurities and defects, respectively, $P_{ii,}P_{dd}$ - increments caused only by mutual interaction of impurities and defects, P_{id} – increment caused by the interaction of impurities and defects.

P_0 is calculated usually on the base of model conception. For example, the calculated theoretical value of the minimum optical losses in As_2S_3 and As_3Se_3 are equal to (6-7) 10^{-2} dB/km between 4 and 6 μm [11]. The impurities, embedded into the glass network or the dissolved impurities, manifest themselves in the spectra of the total optical loss of optical fibers as the bands of selective absorption. Position of the absorption band is determined by the nature of impurity. Table 2 gives the positions of the maxima of impurity absorption bands in vitreous arsenic sulfide and arsenic selenide.

Table 2. The maxima of absorption bands for the main impurities in As-S and As-Se glasses [12].

Compound or functional group leading to absorption	Position of the maximum of the absorption band, μm
OH⁻	2.92
S-H	4.01; 3.65; 3.11; 2.05
Se-H	7.8; 4.57; 4.12; 3.53; 2.32
Ge-H	4.95
As-H	5.02
P-H	4.35
H_2O	6.31; 2.86; 2.79
Ge-O	12.8; 7.9
P-O	8.3
CO_2	4.33; 4.31; 15.0
COS	4.95
CSe_2	7.8
CS_2	6.68; 4.65
Arsenic oxides (different forms)	15.4; 12.7; 9.5; 8.9; 7.9; 7.5
Se-O	10.67; 11.06
Si-O	9.1-9.6
Non-identified bands supposedly due to carbon presence	4.65; 5.17; 5.56; 6.0

It follows from Table 2 that a considerable number of impurity absorption bands are present in the transparency range. The extinction coefficient is a quantitative measure for estimation of impurity effect on the optical loss in glasses. The values for the extinction coefficient are known only for the limited number of impurities in chalcogenide glasses (Table 3).

Fig.2 gives the spectral dependence of the extinction coefficient of SeH-group, As_2O_3 and of sulfur in As_2Se_3. It follows from the Tables 2, 3 and from Fig.2 that the impurity effect of hydrogen-containing substances is mostly pronounced at 2.5-6.5 μm spectral range, and of the oxygen impurity in the longer wave range (7 – 14 μm). The effect of sulfur impurity, embedded in the network of selenide and selenide-telluride glass, is substantially weaker than in the form of SH-groups. In view of experimental values of the extinction coefficient for SH, the SeH-group, CO_2, COS, CS_2 and As_2O_3 the content of these impurities in glasses with optical losses at the level of the intrinsic values should not exceed 0.1 – 10 ppb (see Table 3).

Table 3. The values of extinction coefficients for the impurities in chalcogenide glasses.

Impurity compound or functional group	Glass	The maximum of absorption band, μm	Extinction coefficient, dB/km/ppm*	Calculated content of impurity leading to the optical loss equal to the intrinsic one, ppb*
SH	As_2S_3	4.0	2500	0.3
SeH	As_2Se_3	4.5	1000	0.1
CO_2	As_2S_3	4.33	15625	0.05
COS	_"_	4.95	10^5	0.008
CS_2	_"_	6.68	477400	0.2
As_2O_3	As_2Se_3	12.65	43560	100
		9.5	1030	400
Se-O	_"_	10.6	380	2000
S	_"_	10.6	0.52	10^6
S	$As_2Se_{1.5}Te_{1.5}$	14.5	32	10^4

I* - the intrinsic loss of glass is estimated accounting for "the weak absorption tail" [14]
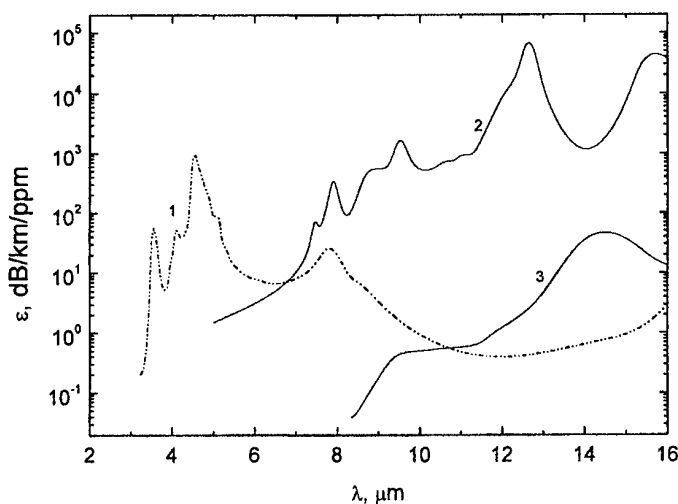
Fig. 2. Spectral dependence of the extinction coefficient of SeH groups (1) [12], oxygen (2) [13] and sulfur (3) [14] in As_2Se_3 glass.

The presence of impurities in the form of heterophase inclusions of submicron size leads to additional optical loss due to absorption and scattering which effect depends on the content of particles and on their distribution by size. Mechanical strength and especially damage threshold of optical fibers are also sensitive to presence of impurities in the form of heterophase inclusions. The energy threshold of the volume damage of As_2S_3 glass increases by two orders of magnitude under the effect of YAG-Er-laser pulse radiation with lowering of the content of submicron-size particles in glass from 10^6 to $10^4\,cm^{-3}$ (see Fig.3). The As_2S_3 glass samples with the particle content lower than the detection limit were not damaged by the pulses with energy more than 1 J [15].

The glass designated for power optics applications, in the ideal case should not contain any particle in the volume illuminated by intense radiation flux. The value of $10^3 - 10^4\,cm^{-3}$ may be accepted as the upper limit of particle content at present time.
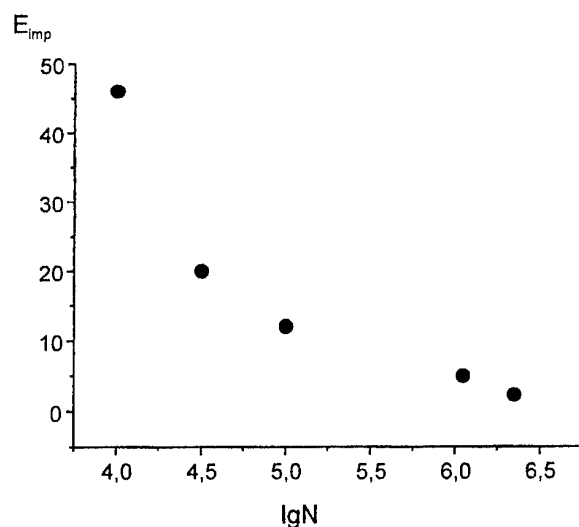
Fig. 3. The dependence of YAG-Er-laser damage threshold upon the content of submicron particles in As-S glass. N - particle content, cm^{-3}, E_{imp} - pulse energy, mJ.

5. Preparation of high purity glasses based on arsenic chalcogenides

At the present time there are two efficient ways for the preparation of arsenic chalcogenide melts with low content of impurities, solidification of which gives the homogeneous high-purity glasses. First of them is synthesis of glass forming compounds or their mixture by vacuum melting of the charge prepared by the above-mentioned methods. This variant can be used while manufacturing all chalcogenide glasses.

The existing problems are connected with a rather high (up to tens ppm) content of the impurities of oxygen, carbon and hydrogen in the commercial samples of specially pure chalcogens and arsenic. Selenium, tellurium and arsenic can oxidize at the contact with environment even at room temperature. That is why the starting high-purity substances are loaded into the container for glass synthesis by evaporation under oil-free vacuum.

Ultrapurification of arsenic and selenium from submicron particles, consisting mainly of carbon, by the method of vacuum sublimation or distillation is of low efficiency at the acceptable evaporation rates [16]. Arsenic monosulfide As_4S_4 was used as an arsenic-containing component of the charge to manufacture the glasses with the ratio of As/S equal to 1/1 and less. This compound is more suitable for the ultrapurification from submicron particles because of low viscosity of melts. Two- and three-component glasses were manufactured by melting the purified arsenic monosulfide with the required amount of chalcogens, e.g.

$$As_4S_4 + S_2 \rightarrow 2\ As_2S_3 \tag{3}$$
$$As_4S_4 + Se_2 \rightarrow A\ As_2S_2Se \tag{4}$$

The second way includes the purification of glass-forming arsenic compounds of technical quality by chemical and distillation methods, melting of some distillate fractions up to homogeneous state achievement and melt solidification. Vacuum distillation in an open and closed system allows a 3-10 times decrease of the content of impurities of highly volatile substances and of submicron particles [17]. Particles behave themselves as hardly volatile impurities, and their content is increased in the lost fraction of a distillate. The purification efficiency is very sensitive to the evaporation rate and to the melt viscosity. Depending on the type of distillate fraction taken for the subsequent treatment it is possible to prepare the glasses with different content of different impurities. The glass from the first distillate fraction is enriched by hydrogen and oxygen compounds, from the lost one - by heterogeneous particles. To remove some impurities (carbon, oxygen) the preliminary chemical treatment of arsenic chalcogenide may be used. To remove the oxygen, chemically bound with glass macrocompo-

nents, a small amount of magnesium (aluminum, rare-earth elements) was added to the melt of the compound being purified which binds oxygen into magnesium oxide. After heating at 700-800°C the melt was subjected to vacuum distillation. To reduce the carbon content similar procedures with addition of small amounts of arsenic and selenium oxides may be applied. A special feature of the process is the difference in macrocomposition of the distillate and of the initial chalcogenide melt. Arsenic chalcogenide evaporate with dissociation and it leads to separation of vapour components at their condensation. In Fig.4 the average distillate composition is given as function of the part of evaporated loading at the As_2S_3 vacuum distillation in the closed system. It is seen that As_2S_3 distillate is enriched with arsenic during vacuum distillation. This phenomenon should be taken into account at the preparation of arsenic chalcogenide layers by condensation of their vapour.
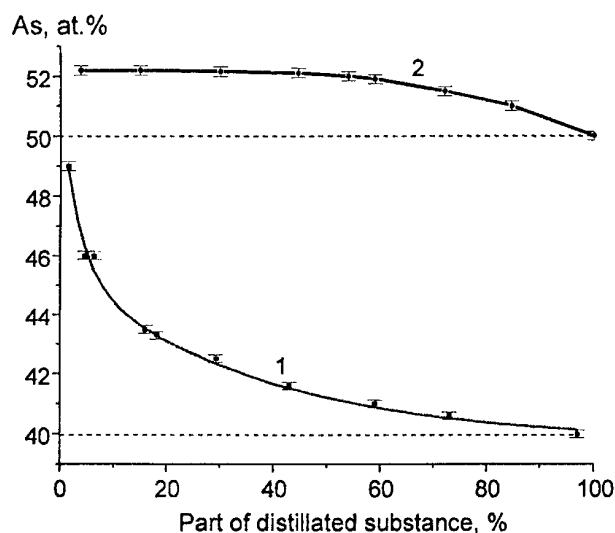
Fig. 4. Average distillate composition as a function of evaporated substance at vacuum distillation of As_2S_3 (1) and As_4S_4 (2).

A practically important question is the stable reproducibility of the glass properties from one sample to another one. The background for the variation of the glasses properties from synthesis to synthesis is a high sensitivity of the glass properties to impurities.

An absolute and relative content of impurity compounds and groups in the glasses can change because of variations in the impurity content in the initial substances and difference in conditions of the glass synthesis and melt solidification (vacuum quality, time-temperature modes). The relative content of the glass network defects, such as "chalcogen-chalcogen" and "arsenic-arsenic" bonds is also affected by the variations of the conditions. For example, the presence of sulfur at the level of several at.% in selenide glass will not noticeably effect its transparence in the 7-11 μm wavelength region. But the impurity hydrogen will change its chemical form. The main part of hydrogen will be bounded with sulfur atoms because of the higher strength of the S-H bond as compared to that of the SeH bond. The intensity of SeH band will reduce considerably but the intensity of SH band will increase. Fig.5 shows the spectra of absorption in the range from 3000 to 1500 cm^{-1} for As_2Se_3 (1), As_2S_3 (2) and $(As_2Se_3)_{0.95}(As_2S_3)_{0.05}$ (3) prepared from glasses 1 and 2. [18].

Thus, for the preparation of vitreous arsenic chalcogenide with the reproducible optical properties a strict identity of the impurity content in the initial substances as well as of the glass preparation conditions should be provided.

In Table 4 the content of impurities in the arsenic chalcogenide glasses is given. It is seen that the content of wide-spreaded metals and silicon is of 0.1-1.0 ppm wt. The content of oxygen and carbon determined by reaction gas-chromatography method and by activation method for the best glass samples is equal to 0.2-0.6 ppm at. Hydrogen content in the form of SH, SeH and OH groups determined by IR-spectroscopy of bulk samples and fibers is equal to 0.02-0.2 ppm at. The content of particles with diameter of 0.1 μm and lower is less then $1 \cdot 10^4$ cm^{-3} for As_2S_3 glass as a result of addi-

tional efforts directed on particles removing [19]. In As-Se and As-Se-Te glasses the particle content is equal to $1 \cdot 10^5$ - $5 \cdot 10^6$ cm^{-3}. The level of transparency in the middle IR-region corresponding to the achieved purity degree of arsenic chalcogenide glasses is given in Table 5. It is obvious that the difference between predicted and real optical losses is of two orders of magnitude.
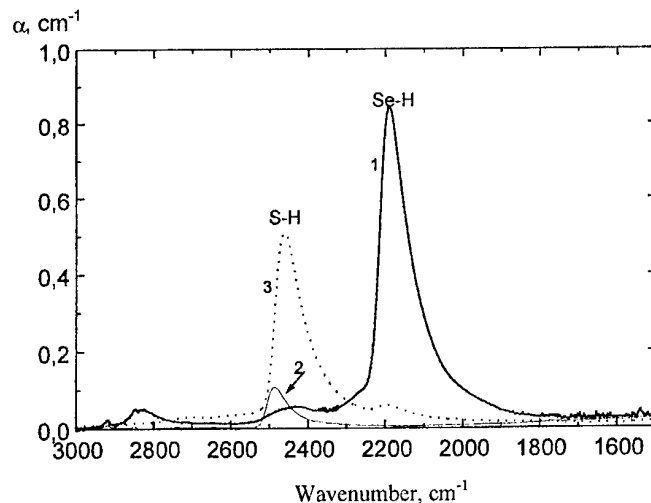
Fig. 5. A hydrogen transfer from Se to S in the mixed As_2S_3-As_2Se_3 glasses. 1, 2 ,3 - absorption spectra of As_2Se_3, As_2S_3 and $(As_2Se_3)_{0,95}(As_2S_3)_{0,05}$ glasses, respectively.

Table 4. Impurity content in the prepared arsenic chalcogenides.

Impurity	Method of determination	Impurity content, in:		
		As_2S_3	$As_2S_{1.5}Se_{1.5}$	As_2Se_3
Hydrogen in the form of SeH- and SH-groups	Spectroscopy of a fiber	0.05 ppm at.	1 ppm at.	0.5 ppm at.
Carbon	Radioactivation and Gas-Chromatographic	$\leq$ 0.2 ppm wt.		6 ppm wt.
Oxygen	Radio-activation analysis	1 ppm wt.		0.9 ppm wt.
Submicron size particles 0.06-0.2 μm	Laser ultramicroscopy	$\leq$ $2 \cdot 10^4$ cm^{-3}	$1 \cdot 10^7$ cm^{-3}	$2 \cdot 10^6$ cm^{-3}
Al, Fe, Ni, Cr, Mg Mn, Ni	Emission spectroscopy	1-100 ppb wt.	<0.2-2 ppm wt	1-100 ppb wt.

Table 5. Optical transparence of the best samples of vitreous arsenic chalcogenides.

Glass	Minimum optical losses		At laser wavelength, dB/km				
	β, dB/km	λ, μm	2.08 μm	2.9 μm	3.7 μm	5.6 μm	10.6 μm
As_2S_3	23	2.4	400	160	140	230	-
$As_2S_{1.5}Se_{1.5}$	190	4.8	1000	3800	400	200	-
As_2Se_3	78	4.2	160	160	80	85	650
$As_2Se_{1.5}Te_{1.5}$						1000	3500

6. Conclusions

The accordance with theoretical evaluation of the impurity effect on optical properties of glasses may be observed at the impurities content from 1 to 0.01 ppb. The content of limiting impurities in chalcogenide glasses obtained up-to-date is not less than 50-100 ppb. That is why the impurities contribution into the investigated glass properties is considerable. For the development of optoelectronic materials, based on high purity arsenic chalcogenides, the 1-2 order decrease in the impurities content is required now. It will become possible if the efforts will be concentrated on the preparation of arsenic and chalcogens with the lower content of impurities, on the development of more sensitive method of the impurities determination and on the improvement of the glass preparation technique.

Reference

[1] M. D. Mikhailov, Yu. S. Tverjanovich, Russian Journ. "Fiz. Khim. Stekla" (Physics and Chemistry of Glasses), 12, 3, 274 (1986).

[2] M. F. Churbanov, in EMIS Datareviews Series, 22. Properties; Processing and Applications of Glass and Rare Earth-Doped Glasses for Optical Fibers. Published by ISPEC, the Institution of Electrical Engineers, London, UK, 340 (1998).

[3] N. I. Voronin, G. G. Devyatykh, E. M. Dianov et.al., Russian Journ. "Dokl. AN SSSR" (Reports of the USSR Academy of Scirnces), 281, 4, 845 (1985).

[4] G. G. Devyatykh, B. E. Ulevaty, M. F. Churbanov, E. M. Dianov, V. G. Plotnichenko, Proc. Intern. Conf. "Amorphous semiconductors-84", September 17-22, Gabrovo, Bulgaria, 2, 153 (1985).

[5] M. F. Churbanov, J. Non-Cryst. Solids, 184, 25 (1995).

[6] G. G. Devyatykh, E. M. Dianov, V. G. Plotnichenko et.al., Russian Journ. "Vysokochistye Veshestva" (High-Purity Substances), 4, 753 (1990).

[7] I. V. Scripachev, G. E. Snopatin, V. G. Plotnichenko et.al., Russian Journ. "Vysokochistye Veshestva" (High-Purity Substances), 4, 186 (1993).

[8] R. G. Behrens, G. M. Rosenblatt, J. Chem. Thermodynamics, 4, 175 (1972).

[9] J. T. Edmond, M. W. Readfearn, Proc. Phys. Soc., 81, 378 (1963).

[10] D. Lezal, K. Konak, J. Non-Cryst. Solids, 192-193, 187 (1995).

[11] M. E. Lines, J. Appl. Phys. (USA), 55, 4058 (1984).

[12] V. G. Borisevich, V. V. Voitsekhovsky, I. V. Scripachev et.al., Russian Journ. "Vysokochistye Veshestva" (High-Purity Substances), 1, 65 (1991).

[13] M. F. Churbanov, V. S. Shirjaev, S. V. Smetanin et.al., Inorg. Materials, 2001 (to be published).

[14] M. F. Churbanov, V. S. Shirjaev, S. V. Smetanin et.al., Inorg. Materials, 35, 12, 1438 (1999).

[15] V. A. Kamensky, I. V. Scripachev, G. E. Snopatin et.al., Appl. Optics, 37, 24, 5596 (1998).

[16] G. G. Devyatykh, M. F. Churbanov, V. S. Shirjaev et.al., Inorg. Materials, 34, 9, 1081 (1998).

[17] M. F. Churbanov, J. Non-Cryst. Solids, 140, 324 (1992).

[18] M.F. Churbanov, V.S. Shirjaev, I.V. Scripachev et.al., J. Non-Cryst. Solids, 2001 (to be published).

[19] G. G. Devyatykh, M. F. Churbanov, I. V. Scripachev et.al., J. Non-Cryst. Solids, 256&257, 318 (1999).

OPTICAL AND MECHANICAL CHARACTERISTICS OF FIBERS MADE OF ARSENIC CHALCOGENIDES

I. V. Scripachev, M. F.Churbanov, V. V. Gerasimenko, G. E. Snopatin, V. S. Shiryaev,
A. A. Pushkin, I. E. Fadin, V. G. Plotnichenko[a], Yu. N. Pyrkov[a]

Institute of Chemistry of High Purity Substances, Russ. Acad. Sci., 49, Tropinin St., Nizhny Novgorod, 603950, GSP-75, Russia
[a]Fiber Optics Research Center at the General Physics Institute, Russ. Acad. Sci., 38, Vavilov St., Moscow, 117756, V-333, Russia

Optical and mechanical characteristics of optical fibers made of high-purity chalcogenide glasses of As-S, As-S-Se, As-Se and Ge-As-Se systems, intended for operation in the middle IR, are given. The fibers from As-S glass will be useful for transmission of IR-radiation in the 1-7 microns spectral region, the fibers on the basis of As-Se and Ge-As-Se glass systems - in the 2-12 microns region. The multimode fibers from arsenic-sulfide and arsenic-selenide glasses have the minimum optical losses equal to 23 ± 8 dB/km and 79 ±10 dB/km at 2.4 and 4.5 microns, respectively. The average bending strength of As-S glass fibers (with diameter of 350-400 microns) is from 1.0 up to 1.2 GPa, and from 0.4 up to 0.8 GPa for the fibers made of As-Se and Ge-As-Se glasses. The single-mode fibers from As-S glasses have the minimum optical losses from 200 up to 400 dB/km in the 1.3 - 3 microns wavelength region. The choice of the glasses compositions for the fiber core and reflecting cladding which provides the given numerical aperture and the mode parameters in the required spectral region is discussed. The features of modal distribution of radiation along the arsenic-sulfide fiber length were explored.

1. Introduction

For various practical applications the fibers based on high purity arsenic–sulfide and arsenic-selenide glasses distinguished in structure, waveguide characteristics, in a level of optical losses in the required spectral range, in mechanical strength, aperture and other parameters are required. These are multimode fibers with a reflecting cladding from relevant chalcogenide glass, fibers with a reflecting polymeric cladding, fibers without a reflecting cladding, and also single-mode fibers.

The number of checked parameters for the fibers reaches ten. It is a diameter of a core of a fiber, ratio of diameters of a core and reflecting cladding, concentricity of an arrangement of a core and cladding, concentricity of a secondary coat, the numerical aperture, mechanical strength, the minimum permissible radius of bending, continuous length of a fiber, level of optical losses in the required spectral range etc. At development of installations for the fiber drawing from high purity chalcogenide the main problem was the possibility to control all the fiber parameters.

The fibers from high purity sulfide- and arsenic-selenide glasses were made by drawing from ordinary and double crucible.

A primary coating from fluoroplastic F-42 was applied on a fiber during drawing. A fiber was passed through an applicator with a solution of F-42 in methyl-ethyl kethone and further through a pipe heater, where the solvent was evaporated.

A secondary protective coating was applied by drawing the fiber with a primary coating through an applicator with PVC plastizole with the subsequent thermal solidification in the furnace. This process carried out as an additional independent stage after the drawing of a fiber.

The total mass of a glass loaded into double crucibles was from 400 up to 800 grams, that allowed to draw from 500 up to 1000 m of optical fibre with its diameter from 500 up to 300 microns.

To form the optical fiber structure it is necessary to ensure a relative difference of refractive index of the core and the cladding materials of a fiber. Depending on this difference value the numerical aperture of a fiber NA changes:

$$NA = \sin \theta = (n^2_{core} - n^2_{clad})^{1/2} \qquad (1)$$

where NA is the numerical aperture of a fiber, θ is the permissible half-angle of input of radiation into a fiber, n_{core} is the refractive index of a core material, n_{clad} is the refractive index of a cladding material.

The necessary ratio of these parameters is provided by the relevant difference in composition of glasses.

2. Fibers based on a high purity arsenic-sulfide glasses

The core glass of multimode fibers had composition from $As_{40}S_{60}$ up to $As_{38}S_{62}$. Compositions for the core and cladding were selected in view of the required NA. For cladding a glass with a smaller content of arsenic was taken in comparison with glass of the core.

The expression for calculation of a numerical aperture of fibers from arsenic-sulfide glasses was derived on the basis of [1]:

$$NA = \{(0.00018(x^2_{core} - x^2_{clad}) + 0.05131(x_{core} + x_{clad}) + 7.32986\}^{1/2} \qquad (2)$$

where x_{core} and x_{clad} is the content of arsenic, at. %, in the glass of core and cladding, respectively.

Both low-aperture fibers with a ratio of compositions of a core and cladding not exceeding 1 at. %, and high-aperture fibers, with a ratio of compositions up to 5 at. % were made. The compositions of glasses of core and cladding for a single-mode fiber were selected so that the well-known expression describing a single-mode condition of a fiber was satisfied:

$$(2\pi a/\lambda)(n^2_{core} - n^2_{clad})^{1/2} \le 2.4 \qquad (3)$$

where a is the radius of a core of a fiber, λ is the wavelength, n_{core} and n_{clad} is the refractive index of a core and cladding material of a fiber, respectively.

For values of a core diameter in the interval from 5 up to 6 microns, the difference of refractive indices of a core and cladding materials should be from 0.2 to 0.3 %. It follows from expression (2), that the glass of a cladding should differ from a glass of a core with the contents of arsenic not more than 0.4 - 0.6 at. %. For the $As_{40}S_{60}$ core material composition the glass cladding of a single-mode fiber had the composition of $As_{39.5} S_{60.5}$.

At manufacturing a single-mode fiber two procedures of fiber drawing was used. At first by the method of a double crucible the two-layer fibers with a diameter from 0.8 up to 1 mm with a ratio of diameters of a core and cladding 1:5 were obtained. Then from a cladding glass the tubes with a diameter of 8 mm with ratio of inner and outer diameters equal to 1:10 were prepared. A piece of a two-layer fiber inserted into this tube and the obtained "rod-in-tube" preform was drawn into a single-mode fiber with a diameter of a core equal to 5 - 8 microns, with the total diameter equal to 250 microns.

The second procedure is based on a direct drawing of a fiber from a double crucible. The microphoto of a cross-section of a single-mode fiber made in such a way, is given in Fig. 1.
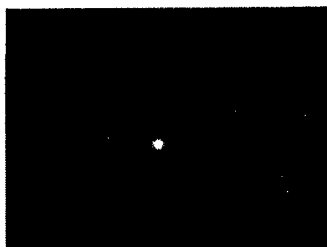
Fig. 1. A microphoto of a cross-section of a single-mode fiber. A diameter of a core is 6 microns, diameter of a cladding - 125 microns.

β, dB/km
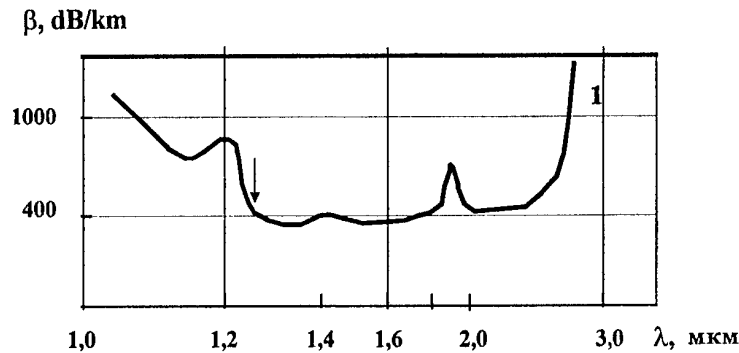
Fig. 2. Spectral dependence of the total optical losses in a single-mode fiber made of high-purity arsenic-sulfide glass with $As_{40}S_{60}$ core [2], the arrow shows the cutoff wavelength .

The spectrum of total optical losses of a single-mode fiber, made on the first procedure, is given in Fig.2. A spectrum of total optical losses of a multi-mode fiber from glasses of the same composition is given in Fig. 3.

From Figs. 2 and 3 it can be seen that the minimum optical losses in a single-mode fiber are much higher than in a multi-mode fiber. Higher losses in a single-mode fiber can be explained by the imperfection of core – cladding boundary in a single-mode fiber. Now optical losses in single-mode fibers from a arsenic-sulfide glass were reduced by us to 250-300 dB/km.
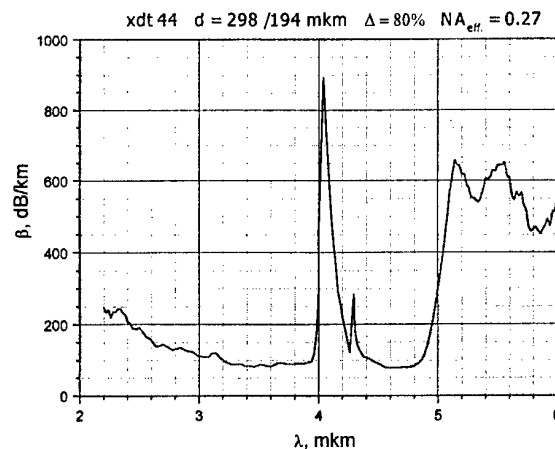
Fig. 3. Spectral dependence of the total optical losses in a multi-mode fiber made of high purity arsenic-sulfide glass with $As_{40}S_{60}$ core.

In Table 1 the main parameters are given for the multi-mode and single-mode fibers based on high purity arsenic-sulfide glass [3].

Table 1. Main parameters of the optical fibres from high-purity As-S glasses.

Type of optical fibre	Continious length	Core/Clad diameter ratio/(μm)	NA	Minimum loss at 2,2 - 4 μm/ (dB/km)	Core concentricity/ (%)	Bending strength/(GPa)	Notes
Multimode	Up to hundreds of meters	300/400, 130/250	0.13 - 0,4	20 - 100	≥ 85	0,8-1,2	Intensity of OH<0.3 dB/m SH < 1 dB/m
Single-mode	tens of meters	8/200 6/125	Not measured	400	≥ 85	0,4-0,6	Cut-off wavelength : 1.1 - 1.5 μm

3. Study of numerical aperture (NA) of the fibers made of arsenic - sulfide glasses

In various instruments and devices the fibers with length from 1 up to 20 m are used. The choice of a fiber for specific application requires a detailed knowledge of its optical parameters.

In many cases the fibers are used which length is insufficient for achievement of a stationary modal distribution at an arbitrary distribution of a radiation power at the input of a fiber. An information on the values of a numerical aperture for short pieces of chalcogenide fibers is scarce. We investigated behavior of a numerical aperture of infrared fibers made of As_2S_3 glass at unsteady modal distribution depending on the aperture of exciting radiation.

Numerical aperture of fibers was determined by the far-field method. The method is based on measurement of a spatial distribution of a radiated power coming out of a fiber, at a distance from an output fiber end being much greater than diameter of a fiber.

For carrying out an experiment the two-layer multi-mode fibers with the diameter of a core of 300 microns and thickness of a reflecting cladding 50 microns were used. Glasses of compositions $As_{40}S_{60}$ and $As_{39}S_{61}$ were respectively used as a material of a core and the claddings, with a difference of refractive index equaled to 0.013. Total optical losses at 5.5 microns wavelength were 800 dB/km. The end faces of fibers were prepared by the method a notch–breakage with the subsequent quality control of the cut with a microscope.

In Figs. 4 and 5 the results of measurement of the aperture of a fiber NA_{eff} are submitted depending on the aperture of excited radiation NA_{in} and length of a fiber. It follows from Fig. 4 that NA_{eff} for fibers with length 1 m is much more than with length of 15 m. At increase of a fiber length the NA_{eff} decreases and tends to the calculated value. The calculated curve is obtained from expression (1) in which the values of refractive index of a core glass are used.

The dependences NA_{eff}, submitted in Figs. 4 and 5, are explained as follows: in a multi-mode fiber with a step-by-step profile of refractive index each spreading mode has a reduction factor, and the modes of the highest order are spreading at angles, close to ultimate, and have optical losses by tens times higher than modes of the lowest order. In case when the radiation is inlet at large angles into short fibers, the modes of the highest order are not completely damp and give the contribution into value NA_{eff}. At a radiation transmission along a fiber the differential losses are partially compensated by modal conversion. When total compensation is achieved, each mode has identical attenuation and the transmission goes at a stationary modal distribution at which the attenuation in a fiber is an exponential function of its length. The measure of achievement of a stationary modal distribution is an invariance of a directional diagram of radiation, coming out of fiber end, in the far-field region under different conditions of excitation. It can be seen from Fig. 5 that it is reached at fiber lengths more than 15 m.

For study of the contribution of the highest order modes into final value of a numerical aperture, the NA measurements of the fiber with an immersion coating at reflecting cladding were carried out. As an immersion medium a chalcogenide glass was used with refractive index slightly exceeding the refractive index of a cladding glass. An immersion coating was applied on a section of a fiber with length 5 cm at 15 cm from an input fiber end face. It was found that the stationary modal distribution is reached at more short lengths of a fiber, about 3 m.

The numerical aperture of a fiber with a primary metal coating was determined. On a fiber glass reflective cladding the layer of indium with thickness 10 microns was applied. The stationary modal distribution for a fiber with a metal coating was achieved at lengths less than 1 m (Fig. 6, curve 3). The metal coating assists the decay of modes of the highest order in a reflecting cladding along the whole fiber length, excluding their influence on NA_{eff}. The refractive index of indium is higher than refractive index of chalcogenide glass ($n_{In} = 10$, $n_{ch.glass} = 2.4$), therefore the total internal reflection at the "reflecting cladding - indium coating" boundary is absent, and the radiation along the cladding is spreading only due to mirror reflection with a coefficient $R \leq 0.97$. At angle close to the critical and the value $R = 0.97$ lengths, on which the radiation intensity in a cladding will decrease by 2 orders, is equal to approximately 10 cm.

As a result of the investigation the lengths of stationary modal distribution for fibers with primary coatings from fluoroplastic F-42, from metal indium and for a fiber with immersion at the

input end face were determined. At unsteady modal distribution the value of a numerical aperture of a fiber depends on the aperture of input radiation, length of a fiber and of a kind of a primary coating. The results obtained are useful at selecting the optimal length of fibers at measurement of its optical losses by a standard double point method and at a selection of the type and parameters of fibers at their practical application.
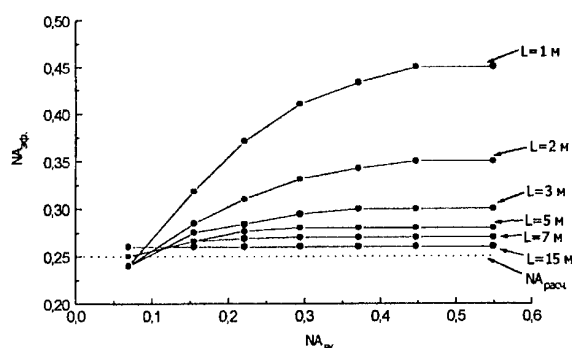
Fig. 4. Dependence of the effective numerical aperture of a fiber NA_{eff} on a numerical aperture of exciting radiation NA_{in}. A primary coating- fluoroplastic F-42, thickness 10 microns.
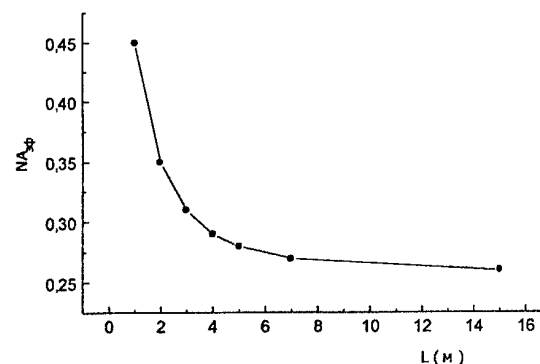
Fig. 5. Numerical aperture NA_{eff} of a fiber versus fiber length for $NA_{in} = 0.55$. A primary coating-fluoroplastic F-42, thickness 10 microns.
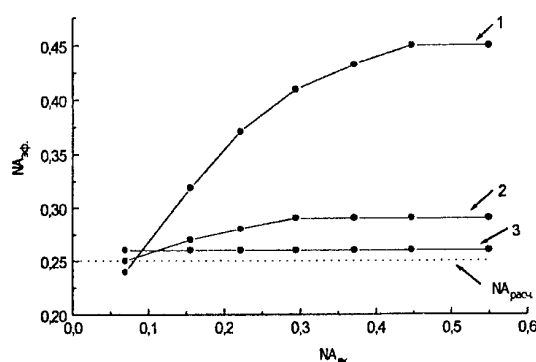
Fig. 6. Numerical aperture of a fiber NA_{eff} versus numerical aperture NA_{in} of exciting radiation for 1 meter length: 1 is with fluoroplastic F-42 coating, 2 is with glass immersion, 3 is with metallic indium coating.

4. Multi-core fibers based on arsenic-sulfide glass

For coupling with IR-radiation detectors, with systems of thermal imaging and IR-introscopes, the flexible fiber bundles consisting of a number of regularly located fibers of a small diameter are required at present time. Such multi-core fibers can be used for assembly of regular optical fiber bundles. The fibers from high purity glassy arsenic sulfide are suitable for operation in a spectral range from 1 up to 6.5 microns, the fibers on the basis of arsenic-selenide glasses and up to 11-12 microns in case of the fibers based on arsenic-selenide glasses.

By the method of drawing from a quartz double crucible having an output nozzle of square shape, the rectangular fibers having a core and reflecting cladding from arsenic-sulfide glass has been obtained. The side of the square fiber was from 250 up to 500 microns.

From such fibers the assemblies 8x8, containing 64 regularly located fibers, with length up to 15 cm were obtained. Then these assemblies were drawn into multi-core fibers with a length up to several tens of meters, with the size of a square equal to 250 microns.
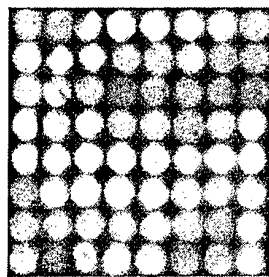
Fig. 7. A square shaped multi-core (8x8) fiber.

5. Mechanical strength of fibers made of arsenic-sulfide glasses

Strengths of the optical core-clad fibers were measured by the method of two-point bending between parallel plates, described in [4]. The results of measurement of strength of the optical fiber are represented in the form of Weibull plots showing the dependence of probability, F, of failure of the optical fibers upon the applied stress, σ. Measurements were carried out at room temperature. The velocity of the plate movement was 1 mm/s; the number of samples in each series of measurement was not less than 30; the fibre diameter was 400 mm. Fig. 8 shows a Weibull distribution plot for the fiber made of high-purity As-S glass (curve 3).

The stability of parameters of fibers at various conditions is of interest. The character of variations in a spectrum of the total optical losses was studied, numerical aperture and mechanical strength at bending of fibers with a core from $As_{40}S_{60}$ glass and reflecting cladding from $As_{39}S_{61}$ glass after action it by high-pressure.

The core diameter was equal to 300 microns, the thickness of reflecting cladding was 50 microns. The fiber had a protective polymeric coating from fluoroplastic F-42 with thickness of 10 mkm and secondary coating from PVC with thickness of 50 mkm. The fiber in the form of wheel rings was positioned in pressure gasostat. A pure argon was used as a working gas. The fibers were exposed to isostatic pressure equal to 85 and 40 MPa (850 and 400 at).
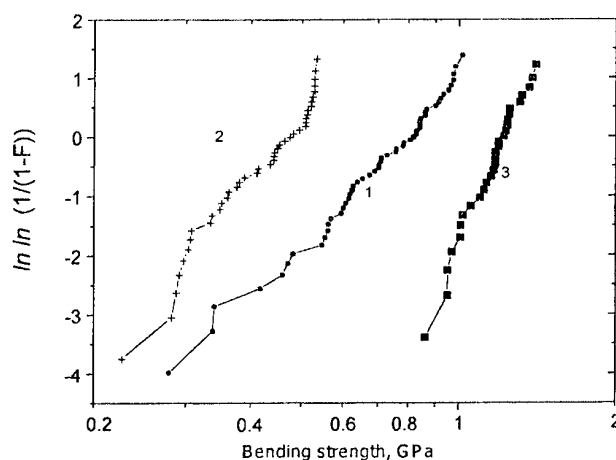
Fig. 8. Weibull distribution of bending strength of the fibers: diameter 400 microns with a primary coating from fluoroplastic F-42. Fibers on the basis of a glass: 1 is As_{40} $S_{30}Se_{30}$, 2 is $As_{40}Se_{60}$; 3 is As_{40} S_{60}.

Variations in value of numerical aperture before and after pressure treatment, with the error limit of measurements equal to 0.02, were not revealed.

The mechanical strength of fibers made of arsenic-sulfide glass subjected to high pressure treatment during one hour under pressure of 85 GPa decreased by 12 %. Weibull curve was biased

into an area of smaller strengths indicating influence of the same type of defects on mechanical strength of fibers before and after action of exterior isostatic pressure.

For two-layer fibers made of high purity As-S glasses, having a core from $As_{40}S_{60}$ glass and glass reflecting cladding from $As_{35}S_{65}$, slight variation of optical losses and bending strength due to pressure action was observed. These fibers had a primary polymeric coating from fluoroplastic F-42 with thickness of 10 microns and secondary polymeric coating from PVC with thickness of 100 microns. The common level of optical losses in such fibers within one year of storage at room temperature has increased on the average from 5 to 7 %, and the average bending strength was decreased on the average by 15 %.

6. Fibers made of high purity sulfoselenide glasses

The fibers from sulfoselenide glasses occupy an intermediate position between fibers from arsenic-sulfide and arsenic-selenide glasses both in a spectral range of optical transmission, and in values of bending strength.

It was shown in [5] that the multiphonon absorption edge for sulfoselenide glass shifts into long wavelength region in comparison with sulfide glass. At replacement of 30 at. % of sulfur for selenium in $As_{40}S_{60}$ glass the shift of a multiphonon absorption edge is about 1 micron and is considerably increased with the further increase of the selenium content.

The two-layer optical fibers on the basis of $As_2 S_{1.5}Se_{1.5}$ glass with a polymeric coating were obtained with the purpose of measurement their optical and mechanical characteristics. The glass of a core had a composition $As_{38}S_{25}Se_{37}$, and glass of a cladding was $As_{38}S_{27}Se_{35}$. For preparation of high purity sulfoselenide glass the direct melting of pure starting elements as well as the purification of sulfur and arsenic through monosulphide of arsenic were used. The two-layer optical fibers were drawn by the method of a double crucible with a ratio of diameters of a core and cladding (in microns) 300/400 and 200/400. The minimum losses measured by the double-point method, were equal to 190 ± 20 dB/km at wavelength of 4.8 microns. In the 4-6 microns spectral range the optical losses were at the level of 200-300 dB/km. It is the best result in this area for the spectrum for two-layer fibers on the basis of chalcogenide glasses.

In Fig.9 the spectrum of the total optical losses in the fiber from As-S-Se glass with a ratio of diameters of a core and cladding of 300/400 and with a polymeric coatings is shown. In the spectrum of the fiber two spectral windows with the losses lower than 300 dB/km are visible: 3.2-4 microns and 4.4-6 microns. There are some peaks of absorption because of SH, CO_2 impurity at 4.31 and 4.34 microns; OH groups at 2.92 microns and traces of molecular water H_2O at 6.33 microns. The intensity of SH at 4.01 microns is 3 dB/m. The impurity band at 4.57 microns bound with absorption of SeH-group, is absent. For comparison the spectrum of the total optical losses for the fiber from As-S glass is given. From this figure the advantage of the fiber from As-S-Se glass is visible in the 5-6 microns spectral range in comparison with fibers from As-S glass. It is necessary to note that in the optical spectrum of fibers from As-S-Se there are no intensive absorption bands with maxima at 5.17 and 5.6 microns, which are characteristic of fibers from As_2S_3.

In Fig. 8 the Weibull distribution of bending strength of the fiber is submitted. The mean mechanical bending strength of the fiber is 0.8 GPa. The Weibull curve for sulfoselenide glass fiber occupies an intermediate position in relation to that for the arsenic-sulfide and arsenic-selenidefibers. The bending strength of a fiber from As-S-Se with fluoroplastic F-42 coating has decreased within 3 days from 0.8 GPa to 0.6 GPa, then there was stabilization, and the average bending strength remained invariable in time.

The effective numerical aperture of a fiber, determined by the angular distribution of output power, was equal to 0.28.

Through 1.5meter fiber with a diameter 400 microns six watts of continuous CO-laser radiation was transmitted. The input laser power was 12 watts.
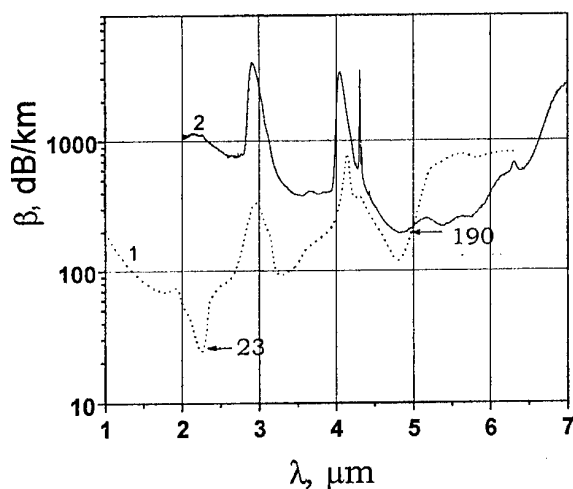
Fig. 9. Comparison of the total loss spectra of two-layer fibers from the glasses of As-S (1) and As-S-Se (2) systems.

The main parameters of arsenic sulfoselenide glass fibers are given in the table 2.

Table 2. Main parameters of optical fibers made of As-S-Se glasses.

Core/clad composition	Continuous length, m	$\varnothing_{clad}/\varnothing_{core}$ μm	A	β_{min} (dB/km) at $\lambda(\mu m)$	β (λ=5.5 μm), dB/km	Transmission of CO-laser radiation, W
$As_{38}S_{25}Se_{37}/As_{38}S_{27}Se_{35}$	>150	400/300 400/200	0.28	190 (4,8)	220	P_{in}=12 W P_{out} = 6 W

7. Fibers made of high purity arsenic-selenide glasses

As a material for manufacturing fibers for the spectrum range of a spectrum 2 - 11 microns the As-Se and Ge-As-Se glasses were used. The contents of germanium was up to 5 at. % (table 3). The fibers with a diameter from 300 up to 400 microns were drawn by the double crucible method.

In the last column the values of losses at λ = 10.6 microns wavelength are given. The intensity of absorption bands of OH - groups (λ=2.9 μm) in the spectra of optical losses of the best samples of fibers did not exceed 0.2 - 0.3 dB/m, molecular water (λ=6.3 μm) - 0.4 dB/m. The minimum optical loss in the unclad fibers made of As_2Se_3 glasses was equal to 76 dB/km at 4.3 μm, and 0.1-0.3 dB/m at 6.7 μm in case of As-Se-Te glass. The optical loss was equal to 3-4 dB/m at 10.6 mm in the best samples.

The average bending strength of two-layer fibers from Ge-As-Se glass with a fluoroplastic F-42 coating is 0.4 – 0.5 GPa and for best samples reaches 0.8 GPa.

Though the fibers on the base of arsenic-selenide glasses have the average bending strength twice smaller in comparison to fibers from arsenic-sulfide glasses, their main advantage consists in a wider range of spectral transmission. The long-wave edge of their transmission reaches10-11 microns, at optical losses in a fiber at a level of several dB/m.

Table 3. Compositions of core and cladding glasses of fibers from high purity arsenic-selenide glasses and the fiber's optical losses, dB/m.

Core glass composition	Clad glass composition	Optical loss, dB/m, at λ (μm)			
		$2 \div 6$	$6 \div 9$	$9 \div 11$	10.6
$As_{40}Se_{60}$	$As_{38}Se_{62}$	$1 \div 1.5$	$1.5 \div 2.5$	$2.5 \div 11$	11
$As_{39}Se_{61}$	$As_{36}Se_{64}$	0.3	$0.3 \div 1.5$	$1.5 \div 8.5$	8.4
$As_{38}Se_{62}$	$As_{34}Se_{66}$	$0.3 \div 0.5$	$2 \div 5$	$2 \div 11$	8.0
$Ge_1As_{39}Se_{60}$	$Ge_2As_{38}Se_{60}$	0.19	$0.3 \div 0.8$	$0.8 \div 7$	5.5
$Ge_2As_{38}Se_{60}$	$Ge_2As_{34}Se_{64}$	$0.9 \div 2$	$2 \div 3$	$3 \div 7$	5.0
$Ge_2As_{38}Se_{60}$	$Ge_4As_{36}Se_{60}$	$0.2 \div 0.3$	$1 \div 1.6$	$1.6 \div 9$	8.0
$Ge_2As_{38}Se_{60}$	$Ge_4As_{36}Se_{60}$	$0.2 \div 0.6$	$0.6 \div 0.8$	$0.8 \div 6$	3.0
$Ge_5As_{34}Se_{61}$	unclad	$0.09 \div 0.3$	$0.3 \div 0.8$	$0.8 - 2.1$	1.6

8. Application of IR fibers based on chalcogenide glasses

One of the most important directions of chalcogenide IR fibers use for the middle IR-range of 2 - 12 microns is concerned with the transmission of powerful laser radiation for the medical and technological purposes. For the radiation transmission of such lasers, such as the HF-laser (λ = 2.7 μm), YAG:Er3+-laser (λ =2.94 μm), DF-laser (λ = 3.8 μm), CO-laser (λ= 5.6 μm) and CO_2-laser (λ=10.6 a μm) IR-fibers are necessary. The level of optical losses in fibers, achieved by us, is given in the Table 4.

Table 4. Basic performances of the best fibers made of high purity glasses of As-S, As-Se and Ge-As-Se systems.

The characteristic of a fiber	Parameter
1. Minimum optical loss (dB/km) at wavelength	23 *(λ = 2.4 μm)* (As-S) 79 *(λ = 4.3 μm)* (As-Se)
2. Optical loss at laser wavelenghts, dB/km YAG:Er^{3+} (λ = 2.94 μm) CO- (λ = 5.5 - 6.3 μm) CO_2- (λ = 9.2 - 11.3 μm)	160 100 - 200 1600
3. Intensity of impurity absorption bands OH SH	60 800
4. The power of radiation transmitted through a fiber YAG:Er^{3+}-laser* CO-laser* CO_2-laser	1.5 kJ/cm^2 10 W 1.5 W
5. Bending strength, GPa	0.5 – 1.2
6. Continuous fiber length	up to 100 m

•) The power, transmitted through a fiber, is limited to maximal output power of commercially available domestic lasers

The two-layer As-S glass fibers with the minimum contents of OH-groups and with the contents of microinclusions less than $2 \cdot 10^4$ cm^{-3} were used for the transmission of YAG:Er^{3+}-laser radiation. Through fibers with a diameter 460 microns which have loss about 250 dB/km at λ = 2.94

microns and length up to 1.5 m the pulses of YAG:Er^{3+}-laser with the duration of 350 μs and with density of power up to 1.5 kW/cm^2 were transmitted [6].

In [7] we describe a system for laser microsurgery of an eye lens, based on use of fiber from high purity arsenic-sulfide glass. The flexible multimode optical fibre with a diameter of 480 microns and length up to 3 m was used for the transmission of YAG:Er^{3+}-laser pulses (λ = 2.94 microns) with power at about 150 mJ and with frequency of 3 Hz. Through a fiber from $As_{35}S_{65}$ glass with a polymeric reflecting cladding with a diameter of 450 microns and length of 1.5 m it became possible to transmit within several hours the radiation of the continuous CO- laser (λ=5-6 mkm) with output power up to 10 W [8]. The power level of transmitting radiation was limited to parameters of the used laser. The optical losses in a fiber were about 700 dB/km at the wavelength of 5.5 microns. In [9,10] the possibility of chalcogenide IR-fibers use in optical pyrometry was shown. Small values of time constant of the described radiometers, and rather high accuracy allows to use them in high-speed scanning systems for the remote measurement of temperature under conditions of strong electromagnetic fields, aggressive mediums or for the supervision of temperature of hard-to-reach objects. The $Ge_5As_{38}Se_{57}$ glass fiber was used for radiation output of miniature cooled semiconductor lasers operating at the 6 - 10 mkm spectral region from a Dewar vacuum flask for the liquid helium storage [11]. The system of a cryostating of lasers with a radiation output through fiber has essentially improved the characteristics of IR-spectrometer for the molecular analysis of high purity volatile substances.

9. Conclusions

The fibers from high purity chalcogenide glasses have passed an initial stage of their development. To the present time the fibers with achieved optical losses and mechanical characteristics are quite satisfactory for their use in devices of new engineering. The main reasons causing the increase of optical losses of fibers and deterioration of their mechanical strength are investigated.

The improvement of the characteristics of IR-fibers from chalcogenide glasses is concerned with the further decrease of impurity level in chalcogenide glasses, improvement of fiber drawing procedures, development of methods of enlightenment and treatment of fiber and search for new strengthening coatings.

References

[1] V. G. Plotnichenko, A. V. Vasiliev, V. V. Voitsekhovsky, Proc. 8-th Intern. Symp. on Halide Glasses, Perros-Guirrec, France, 316 (1992).

[2] G. G. Devyatykh, E. M. Dianov, V. G. Plotnichenko, I. V. Scripachev, G. E. Snopatin, M. F. Churbanov, Quantum Electronics, 25(3), 270 (1995).

[3] G. G. Devyatykh, M. F. Churbanov, I. V. Scripachev, G. E. Snopatin, E. M. Dianov, V. G. Plotnichenko, J. Non-Cryst. Solids, 256-257, 318 (1999).

[4] P. W. France, M. J. Paradine, M. H. Reeve, G. R. Newus, J. Mater. Sci., 15, 825 (1980).

[5] M. F. Churbanov, V. S. Shirjaev, G. E. Snopatin, V. V. Gerasimenko, S. V. Smetaninm, I.E. Fadin, Proc. 12-th Intern. Symp. on Non-Oxide Glasses and Advanced Materials, 10-14 April, Florianopolis, Brazil, 314 (2000).

[6] A. G. Antipenko, N. V. Artem'ev, A. A. Betin, V. R. Kamensky, V. P. Novikov, V.G. Plotnichenko, I.V. Scripachev, G.E. Snopatin, Quantum Electronics, 25(5), 498 (1995).

[7] F. Feldstein, V. Gelikonov, G. Gelikonov, V. Kamensky, K. Pravdenko, N. Artemiev, N. Biturin, I. Scripachev, A. Pushkin, G. Snopatin, Proc. SPIE. 2930, 33 (1996).

[8] E. M. Dianov, V. I. Masychev, V. G. Plotnichenko, V. K Sysoev, P. I. Baikalov, G. G. Devyatykh, A.S. Konov, I.V. Scripachev, M.F. Churbanov, Electronics Letters, 20(3), 129 (1984).

[9] A.V. Vasiliev, G. G. Devyatykh, E. M. Dianov, M. F. Churbanov, I. V. Scripachev et.al., Russian Journ. of Appl. Spectroscopy (in Russian), 42(5), 862(1985).

[10] G. G. Devyatykh, V. A. Ivantsov, V. S. Lebedev, A. R. Radionov, I. V. Scripachev et.al., Russian Journ. "High-Purity Substances" (in Russian), 1, 224 (1991).

[11] I. I. Zasavitsky, G. A. Maksimov, A. R. Radionov, I. V. Scripachev et.al., Russian Journ. "High-Purity Substances" (in Russian), 5, 202 (1987).

OPTO-MECHANICAL EFFECT IN CHALCOGENIDE GLASSES

M. Stuchlik, P. Krecmer, S.R. Elliott

Department of Chemistry, University of Cambridge, Lensfield Road, Cambridge,
CB2 1EW, United Kingdom

The opto-mechanical effect observed in amorphous chalcogenide films deposited onto clamped STM cantilevers [1] has been investigated. In this, bandgap light, incident on the chalcogenide film and linearly polarized either parallel or perpendicular to the cantilever axis, reversibly causes respectively either a contraction or an expansion of the chalcogenide layer, resulting in an optically-actuated displacement of the free end of the clamped cantilever. This effect is electronic, not thermal, in origin, and is believed to be caused by the same photo-induced structural rearrangements that are responsible for the optically induced optical anisotropy observed in chalcogenide glasses. Possible applications of this new all-optical actuation for optical switching will be discussed.

1. Introduction

It is becoming apparent that the next generation of telecom networks, fibre sensors, optical switches or, in the extreme case, also data manipulation, will depend on all-optical technology. At present, one of the major bottlenecks to achieve full photon compatibility in present-day devices is the lack of a suitable all-optical switching capability. Various micro-electro-opto-mechanical systems (MEOMS) are utilised to achieve even better performance; however, ultimately these cannot compete in the long term with all-optical technology. Another issue, distant, but nevertheless progressing, is nanotechnology. It is well recognized that, if nanotechnology is to succeed, our ability to grip, position and release structures on the atomic scale has to improve greatly, not just in terms of precision but, and perhaps more importantly, in terms of scalability and vastly parallel processing. It appears that one of the key factors in the improvement of such future 'SMART' devices, is the mechanical actuation. At present, only a limited number of actuators with sufficient accuracy are available on the market, e.g. using piezoelectric or photostrictive actuation, but they lack sufficient tool-holding capability, as well as being too large and not easily miniaturisable to be made into large arrays of independent actuators.

One of the emerging new technologies with the promise of bridging the gap between nanotechnology and the macroscopic world is opto-mechanical actuation. An anisotropic mechanical effect induced by polarized light was first reported by Krecmer et al. [1]. They showed that, upon irradiation with polarized light, a thin amorphous film of $As_{50}Se_{50}$ deposited on a cantilever, exhibits reversible nanocontraction parallel to the direction of the electric vector of the light and nanodilatation along the axis orthogonal to the electric vector of the light, and a direct correlation of this opto-mechanical effect with the reversible photoinduced optical dichroism was observed. Measurements were made using a cantilever (consisting of an amorphous $As_{50}Se_{50}$ film, 250 nm thick, deposited on a silicon nitride V-shaped AFM cantilever 200 μm long and 0.6 μm thick), which was found to bend reversibly either up or down by up to about ±1μm upon illumination with polarized light (Fig.).

2. Experimental

2.1. Principle

The opto-mechanical effect in chalcogenide glasses (ChG) is, in principle, linked with the well-known phenomenon of photoinduced optical anisotropy [1], where polarized light can cause, in a

previously isotropic chalcogenide bulk or film sample, preferential absorption (and reflection) of the inducing (linearly polarized) light.

Irradiation with polarized light oriented along the axis of the cantilever (the y-axis, E_y) led to the deflection of the cantilever in the +z direction. The opposite effect, i.e. bending of the cantilever in the -z direction was observed when the light was polarized orthogonally to the direction of the cantilever axis (along the x-axis, E_x) (Fig. 1).

a)   b)
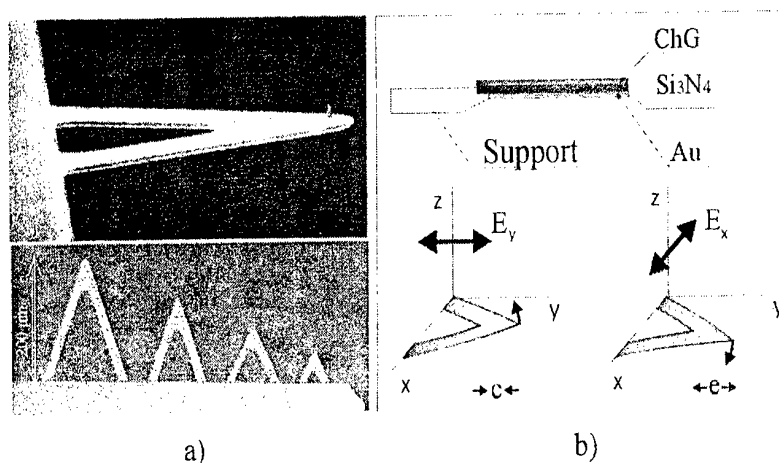
Fig. 1a) Atomic force microscope cantilevers used for the optical-actuation experiments. b) A schematic illustration showing the general structure of the samples used in our experiments and the contraction/expansion of the cantilevers. At the top is a schematic illustration of the gold-Si_3N_4-ChG sandwich. The light in this case is incident on the cantilever from +z direction and its electric vector is polarized either in the y-direction or the x-direction.

The origin of this mechanical polarization effect is not known. Whereas amorphous materials are by nature generally isotropic, some can be made anisotropic by simply illuminating them with polarized light (resulting in them becoming either dichroic or birefringent). The phenomenon of optical anisotropy was first observed in chalcogenide glasses by Zhdanov et al. [2], and the mechanism has since been studied extensively. We can suppose that the microscopic origin of the effect arises from some (anisotropic) structural elements that can be aligned by linearly polarized light. The main problem still remaining to be solved is to identify these structural elements. Krecmer et al. [1] suppose that absorption of polarized light will occur when the E vector of the polarised light is parallel to the main axis of the triangle consisting of a triplet of As-Se-As atoms. After excitation of a lone-pair electron (LP), an electron-hole pair is created, which no longer has the spatial symmetry of the LP orbital, and because of the change of interatomic potential, this leads to a displacement swing of the chalcogen atom. The cooperative swing of many atoms in one direction is then supposed to cause both the mechanical and optical anisotropy [1]. However, there is barely any agreement between different research groups regarding the microscopic structures that are responsible for the optically-induced anisotropy.

2.2. Actuation

Actuators perform useful work on the environment in response to a command or a control signal. The amount of work that they perform and the energy expenditure that they require to do the desired work depend drastically on the method of actuation. These methods can be divided into six categories: electrical, magnetic, thermal/phase, mechanical/acoustic, chemical/biological and optical [3].

Systems, which utilize either an electrical or an optical transduction technique, can be classified as either MEMS (micro-electro-mechanical system) or MOMS (micro-opto-mechanical system). MEMS actuators can employ either piezoelectric, electrothermal or electrostatic means in order to provide the necessary driving force. In contrast to this, MOMS sensing devices may operate

by monitoring either the intensity of light or its wavelength, polarization, or phase. MOMS actuators can utilize either the photothermal effect, the photomechanical effect or radiation pressure [4].

Optical actuation is divided into direct and indirect optical methods. Direct optical methods use light to interact with the active parts of the actuator and cause actuation. Indirect optical methods take advantage of the heating power of the light or its ability to generate an electrical current or to change the resistivity of photo-responsive materials. Several practical benefits distinguish direct optical methods from radiative-thermal processes. Direct optical processes can be much faster than indirect ones, and they can take place at much lower light powers and they permit greater simplicity, versatility and parallelism of the controller.

An interesting feature of both types of optical actuators is that they can be directly interfaced with fibre optics or other forms of waveguides, such as integrated optics [5]. This feature makes optical actuators ideal candidates for smart structures [6], where many actuators are multiplexed (in time or frequency) and located over large areas.

We have discovered a new type of direct optical actuator that uses reversible nanocontraction and dilatation in chalcogenide glasses induced by polarized light [1]. This optomechanical effect was demonstrated on Si_3N_4 V-shaped microcantilevers coated with amorphous $As_{50}Se_{50}$ (see Fig.).

There are several features that make the smart technology of optical actuation involving chalcogenide materials much better than other kinds of actuation:

The opto-mechanical effect is highly reversible.

The effect is wavelength-selective (the maximum response is for light having an energy comparable to the chalcogenide bandgap).

Since light is used as the stimulus, no electricity is needed as in piezoelectric devices. Optical actuators can therefore be used in hazardous environments (e.g. flammable atmospheres) where the use of high voltages (as for piezoelectric devices) would be unsafe.

It is potentially cheap.

Optical actuators lend themselves to miniaturisation, and large arrays of independent cantilevers can be envisaged for applications requiring massively parallel processing.

2.3. Measuring set-up

A vibrational-free optical workplace, together with a temperature stable environment, is the key factor for measurement on nanometer scales. The cantilever is illuminated (from the side coated with the chalcogenide film) with polarized light from laser a He-Ne laser (10 mW). The direction of polarization is adjustable between 0-90 degrees by a $\lambda/2$ waveplate for 632.8 nm. The displacement of the cantilever is detected by measuring the deflection of a laser beam focused on the apex of the cantilever and reflected from the gold surface coating of the other surface of the cantilever. As chalcogenide glasses are sensitive to visible light illumination, the system incorporates a low-power (50 μW) modulated laser diode (655 nm, 119 Hz) as the measuring beam, deflecting from the gold surface onto a position-sensitive quadruple photodiode. The signal is fed into a digital lock-in analyser for enhanced sensitivity of the measurement. Fig. 1 shows a schematic of the measuring apparatus.
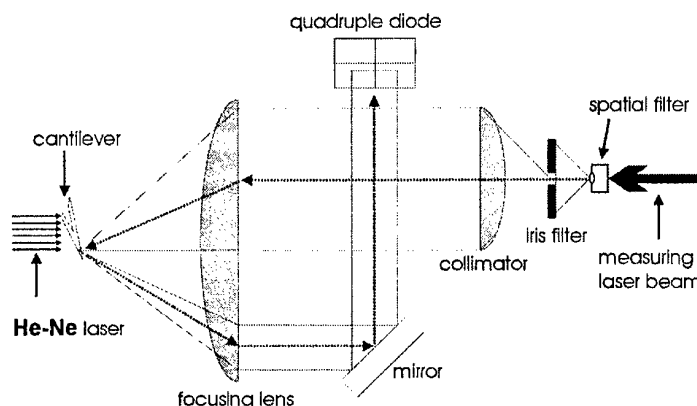
Fig. 1. Illustration of set-up for measurement of the opto-mechanical effect on cantilevers.

3. Results and discussion

The cantilever (consisting of an amorphous $As_{50}Se_{50}$ film, 260 nm thick, deposited on a silicon nitride V-shaped AFM cantilever 200 μm long and 0.6 μm thick) bends reversibly during illumination with a He-Ne laser with different directions of polarization, parallel (||) or perpendicular (⊥) to the cantilever. The polarization-dependent signal is superimposed on a photoinduced scalar expansion, which is shown in Fig. 3a) after switching the incident laser power off. This observation is in accordance with previous measurements [7], and can, in principle, be composed of both a scalar photoexpansion and differential thermal expansion of the glass matrix and the substrate. Fig. 2b) shows the reversibility of the cantilever displacement alternating with change of direction of the laser polarization. This result is in agreement with those carried out earlier on a different apparatus [1].
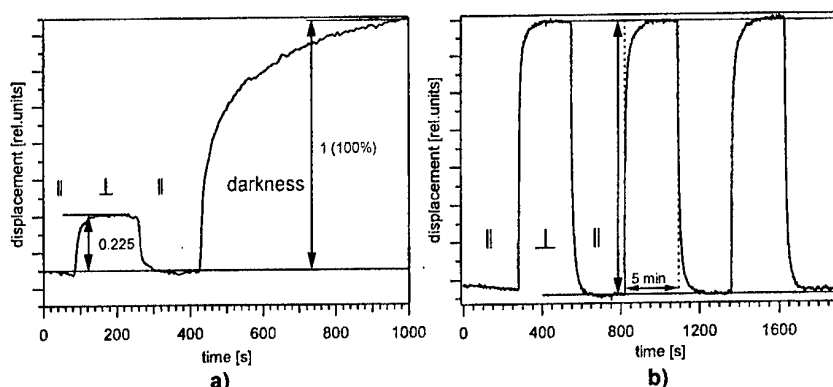
Fig. 2. The changes in relative displacement of the cantilever covered with a 260 nm thick $As_{50}Se_{50}$ film illuminated with a 30 mW·cm^{-2} He-Ne laser. a) The cantilever relaxes to its equilibrium position after the incident laser is switched off. b) Reproducibility of the relative displacement after several polarization plane alternations.

The response of the cantilever depends on the power density of the illuminating laser beam. The experiment was performed with a He-Ne laser with a maximum output power of 200 mW·cm^{-2}. The influence of the laser power on the optomechanical displacement is shown in Fig. 3. The time constant of the fastest curve is of the order of 6-10 s for 200 mW·cm^{-2} input power of He-Ne beam and the given chalcogenide glass/cantilever system. Note that this value is system specific and other systems are now being studied to decrease this time constant to the millisecond range.
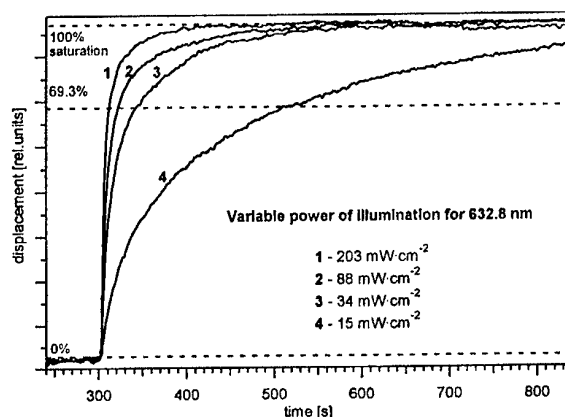
Fig. 3. Variable illumination power causes a certain level of saturation of displacement to the reached in different times. The laser power has been changed neutral density filters.

The illuminating laser power is not the only influence on the bending capabilities of the cantilevers; there is, of course, a size and shape dependency as well. These properties are closely related to different force constants of the cantilevers. This behaviour is shown in Fig. 4, where

cantilevers with various force constants 1) 0.03 N·m⁻¹, 2) 0.06 N·m⁻¹, 3) 0.4 N·m⁻¹, 4) 0.2 N·m⁻¹ covered with the same 260 nm thick $As_{50}Se_{50}$ film have been measured under the same conditions. As expected, the biggest and fastest response has been found for the cantilever with the smallest force constant (curve 1). However, it is also shown that increasing the force constant by a factor of two (curve 2) does not significantly change the relative cantilever displacement or the kinetics. Also increasing the force constant by more than an order of magnitude (i.e. curve 1 vs. curve 3) has a relatively small influence on the displacement (note the lengths of cantilevers 3 and 4 is half that of 1 and 2). These observations suggest the existence of a relatively very strong force constant of the chalcogenide film, and that even thinner chalcogenide films could be used to achieve similar kinetics and displacements. This property is currently under investigation.
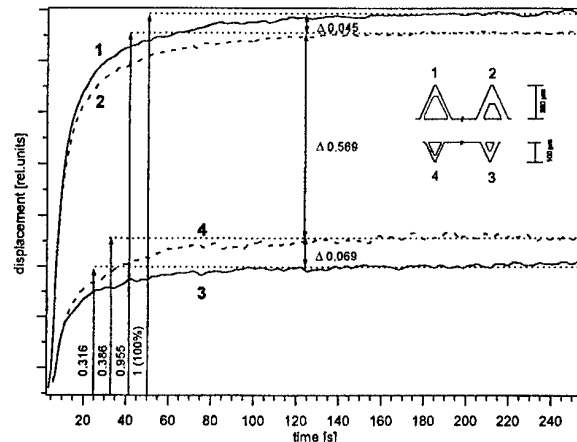
Fig. 4. The effect of cantilever size. The response of the cantilever depends on its force constant, which varies with size and shape of each cantilever 1) 0.03 N·m⁻¹, 2) 0.06 N·m⁻¹, 3) 0.4 N·m⁻¹, 4) 0.2 N·m⁻¹.

Until now we have been concerned with properties of the cantilever illuminated with the laser polarized either parallel or perpendicular to its main axis. However, for the phenomenon to be utilized in micromanipulators, we have investigated the effect of the cantilever displacement of intermediate angles between the light polarization and cantilever axes. Fig. 5 shows that it is possible to drive the cantilever, not only between two extremes, but also its bending can be regulated in intermediate positions simply by changing the angle of polarized incident light relative to the cantilever axis. This property can be very useful in optical-mechanical manipulation (MOMS) applications (e.g. optical tweezers or multi-way optical switches).
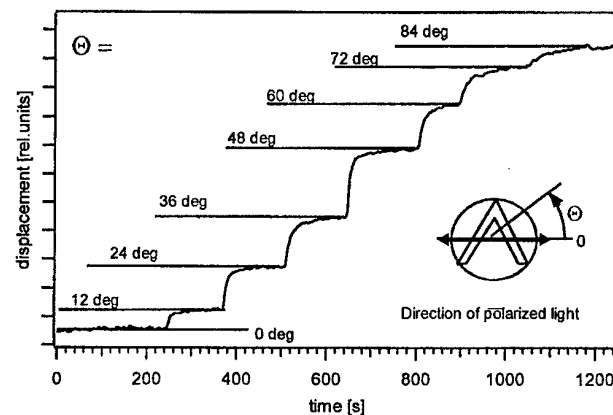
Fig. 5. Dependence of cantilever displacement on angle of polarization of the laser light. The angle of polarization has been changed by rotation of a λ/2 waveplate.

4. Conclusions

One of the major advantages of the opto-mechanical effect in chalcogenide glasses is the direct light-to-mechanical effect coupling without the need for other external sources. In this paper, we have demonstrated the potential of this effect for it to be used in optical switching and micromanipulators. However, if any meaningful structures are to be built, a more detailed analysis of the mechanical characteristics of the composite cantilever with respect to temperature expansion of both materials, differences in modulus, various types of designs, scaling behaviour etc., together with wavelength, temperature, intensity and compositional dependencies need to be investigated. These are currently under investigation.

References

[1] P. Krecmer, A. M. Moulin, R. J. Stephenson, T. Rayment, M. E. Welland, S. R. Elliott, Science, 277, 1799 (1997).
[2] V. G. Zhdanov, B. T. Kolomiets, V. M. Lyubin, V. K. Malinovskii, Physica Status Solidi A, 52, 621 (1979).
[3] M. Tahib-Azar, Microactuators, Kluwer Academic Publishers, Boston, (1998).
[4] A. J. Jacobs-Cook, J. Micromech. Microeng., 6, 148 (1996).
[5] S. Venkatesh, S. Novak, Opt. Lett., 12, 129 (1987).
[6] B. Culshaw, Smart Structures and Materials, Artech House, Boston, (1996).
[7] H. Hisakuni, K. Tanaka, Appl. Phys. Lett., 65, 2925 (1994).

WAVEGUIDES BASED UPON CHALCOGENIDE GLASSES

V. Balan, C. Vigreux, A. Pradel, M. Ribes

Laboratoire de Physicochimie de la Matière Condensée, UMR 5617 CC3 UM II,
34905 Montpellier cedex 5, France

Because of their transparency in the infrared, their high refractive index and their well-known photosensitivity properties, interest in chalcogenide glasses for integrated optics and technological applications related to detection in the IR spectral domain has been growing during the past few years. Our present work is focused on the possibility of integrating chalcogenide glasses in components for two types of applications: spatial interferometry (detection of planets) and environmental metrology (detection of pollutant gases). In both cases, monomode channel or rib waveguides working in the infrared are to be obtained. In this context, first step of our work has been to optimize the chalcogenide films deposition conditions starting from glasses based on germanium combined with antimony and selenium, or with arsenic and selenium. Films with good adherence and controlled composition are currently obtained by RF-sputtering and thermal evaporation. Multimode planar chalcogenide waveguides, based on two external $Ge_{29}As_{12}Se_{59}$ and an inner $Ge_{21}Sb_{18}Se_{61}$ glassy layers deposited on glass or Si/SiO_2 substrates, were then fabricated and proved to guide at 1.55 µm. In order to realize channel or rib chalcogenide waveguides, Ar plasma etching and NH_4OH chemical etching of the films were also investigating and proved to be encouraging.

1. Introduction

Interest in chalcogenide glasses for integrated optics has been growing during the past few years [1-5]. Most of the current research efforts deal with telecommunication applications, at 1.3 or 1.55 µm wavelengths, but chalcogenide glasses present wide transmission windows, from 1 to 20 microns depending on the material composition, high refractive indexes and numerous photoinduced properties (photodarkening, photodissolution of metals,...) which make them also competitive materials for several technological applications related to detection in the IR spectral domain. The present work is focused on two of these potential applications. The first one is spatial interferometry, which implies the use of components working in the far infrared for the detection and the spectroscopic study of extrasolar planets [6]. The second one is environmental metrology. Indeed, the detection of some vibrational modes present in some pollutant gases and located in the wavelengths between 3 and 12 µm would be possible thanks to optochemical sensors working in the infrared. In both cases, monomode channel or rib waveguides must be obtained. In our work, we preliminary focused on the possibility of fabricating multimode planar, channel or rib chalcogenide waveguides working in a large window of wavelengths (between 1 and 15 microns approximately). Adjusting the working wavelength will then only need adjustment of the size of the waveguide.

To date, our work has consisted in the choice of the chalcogenide glasses, the deposition of films with controlled characteristics and the realization of multimode planar waveguides in the continuity of our previous work [7]. The possibility of realizing monomode waveguides has also been investigated: the obtention of monomode structures implies the modification of the initial planar geometry of the films so chemical and plasma etching tests have been performed.

Progress in our investigation is presented in this paper.

2. Experimental

2.1 – Substrates

Two types of substrates were used: microscope slides and Si/SiO_2 substrates (1×1 cm^2) provided by the CNM (Centro de Microelectronica) in Barcelone and which oxidized layer thickness is about 40 nm.

2.2 – Film deposition

Films based on germanium combined with antimony and selenium were deposited by thermal evaporation of powdered $Ge_{28}Sb_{12}Se_{60}$ glass prepared by the conventional melt-quenched method, at a residual pressure of 2×10^{-3} Pa. The layer thickness was controlled by the quantity of powder in the molybdenum crucible (typically 250 mg for a thickness of 1 micron when the crucible is placed at 10 cm of the substrate). The deposition of the films based on germanium combined with arsenic and selenium was performed by RF-sputtering from a $Ge_{33}As_{12}Se_{55}$ commercial target (target called IG2, from VITRON AG), with a constant operating pressure of 5 Pa of argon for non-reactive sputtering. In order to prevent damage of the target, a 30 W RF sputtering power was used, yielding deposition rates of about 10 $nm.min^{-1}$.

2.4 – Film characterization

The adherence of the films on the substrates was verified by the classical adhesive tape test. Their thickness was estimated by profilometry (using a DEKTAK 3) but also by ellipsometric experiments carried out at the ICMAB (Institut de Ciencia dels Materials de Barcelona) in Barcelone and their surface aspect was inspected by Scanning Electron Microscopy (SEM) on a Leica Stereoscan 260. Chemical composition was estimated by Secondary Diffused Electron (EDS). Information about refractive indexes and absorption of the films was provided by ellipsometric measurements performed at the CNM in Barcelone in the range 0.7 to 5 eV.

The experimental setup used for the characterization of the waveguides is composed of a 1.55 micron source from Photonics coupled with a silica fiber which is positioned in front of the planar waveguide. The optical near field collected at the output of the waveguide is focused on a detector using a microscope objective.

Thickness and width of the ribs obtained by etching were measured by profilometry.

2.4 – Film etching

Two ways of etching were tested: (i) chemical (wet) and (ii) physical (dry) etchings.

In both cases, chalcogenide glass films were covered with a thin layer of Microposit® resin of about 2μm thickness by spin coating. After UV insolation through a mask (with 120 or 15 microns line motifs) and resin development in MF320 developer, the samples were annealed 30 minutes at 393 K.

(i) Chemical etching [8, 9]

Several alkaline solutions at different concentrations were tested and a 10^{-3} M NH_4OH solution was finally chosen. After treatment in this solution, layers were dipped in acetone to remove the non-irradiated resin regions.

(ii) Physical etching [10, 11]

After annealing at 393 K, films were introduced in the place of the target in the same sputtering chamber than the one used for depositing them. A 10 W Ar plasma was used (5 Pa Ar) and duration of the etching was chosen according to the required rib depth. After etching, layers were dipped in a commercial removal to remove the remaining resin regions.

3. Results and discussion

Two chalcogenide glasses were chosen for the realization of the future monomode waveguides: $Ge_{28}Sb_{12}Se_{60}$ and $Ge_{33}As_{12}Se_{55}$. Both glasses can be obtained commercially and present satisfying characteristics. They are characterized by high glass transition temperatures (551 K for the first one and 635 K for the second one), that is not negligible for their future utilization. They present a wide transmission window (1-14 microns for $Ge_{28}Sb_{12}Se_{60}$ and 0.8-16 microns for $Ge_{33}As_{12}Se_{55}$) : components based on these glasses could then work in the infrared but also at the telecommunication wavelength of 1.55 µm. These glasses are also characterized by high refraction index (2.6266 for the first one and 2.5469 for the second one at 1.55 µm).

The selected glasses were deposited in the form of thin layers and the deposition parameters were optimized. Good adherence of the films is now currently obtained, whatever the deposition method (RF-sputtering or thermal evaporation) and the substrate (microscope slide or Si/SiO_2) used. Characteristics of the films are also controlled. Two typical examples for films of each composition are given in Table 1.

Table 1. Typical characteristics for the two families of films : composition obtained by EDS, thicknesses, refractive indexes at two different wavelengths and absorption coefficients of two films given by ellipsometry.

Film	e (µm)	n (1.55 µm)	n (He-Ne)	k (He-Ne)
$Ge_{21}Sb_{18}Se_{61}$	1.2	2.78	3.40	~ 0.1
$Ge_{29}As_{12}Se_{59}$	1.9	2.25	2.35	~ 0

These characteristics are representative of all the deposited films. Some comments can be made about them. Film thicknesses obtained either by ellipsometry or by profilometry were proved to be similar. As expected for films deposited by thermal evaporation, composition of the "$Ge_{28}Sb_{12}Se_{60}$" films is quite different from the one of the bulk. The atomic percentage in germanium varies from 20 to 23 percents compared to the expected 28, the one in antimony from 16 to 19 instead of expected 12. The atomic percentage in selenium was proved to be less modified and constant at about 61 percents. Compositions of the "$Ge_{33}As_{12}Se_{55}$" films deposited by RF-sputtering are also somewhat different from the one of the bulk, but quite constant. Refraction indexes of the $Ge_{28}Sb_{12}Se_{60}$ and $Ge_{33}As_{12}Se_{55}$ bulk glasses are known to be 2.6266 and 2.5469 at 1.55 µm respectively. The difference between these values and the ones obtained for our films can be attributed to the difference in composition. To end, the precision in the absorption coefficients is poor (correct values can differ by a factor of 2) because the region in which they have been measured is very close to the absorption edge of the chalcogenide glasses.

Two multimode planar waveguides were then fabricated by stacking different films. They were both constituted of three layers, two external RF-sputtered $Ge_{29}As_{12}Se_{59}$ films constituting the clad and an inner thermal evaporated $Ge_{21}Sb_{18}Se_{61}$ film constituting the guiding core. Thickness of these layers was estimated by profilometry: the two external layers are characterized by a thickness of around 3.5 µm and the inner layer by a thickness of around 4.5 µm. In the waveguide called W_1, the layers were deposited on an oxidized silicon substrate, while in the one called W_2, they were deposited on a microscope slide substrate. After cleavage to obtain plane facets, these two waveguides were tested at 1.55 µm. To date, no guiding test has been performed at higher wavelengths because the sources were not available.

Fig. 1a shows the output of the waveguide W_1 through the inner $Ge_{21}Sb_{18}Se_{61}$ clad layer, and Fig. 1b shows the one of the waveguide W_2: a good guidance of the light is obtained in both cases. The guidance quality is better than the one obtained in a previous work [7]. As shown in Fig. 2, the output of the first planar waveguide made of a core $Ge_{12.5}Sb_{20}Se_{67.5}$ layer and an inferior $Ge_{28}Sb_{12}Se_{60}$ layer constituting the clad with air presented a granulous aspect. The latter was attributed to a damage in the layers during cleavage due to a lack of adherence of the layers on the substrate. On the contrary, the satisfying guidance obtained in the present work testify for a good adherence.

Fig. 1. Injection through the $Ge_{28}Sb_{12}Se_{60}$ core layer : (a) for W_1 ; (b) for W_2.
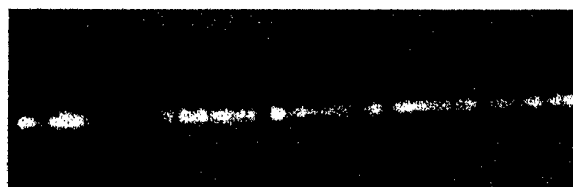
Fig. 2. Injection through the core layer of the waveguide described in reference [7].

Multimode planar chalcogenide waveguides are now currently obtained. The components required for spatial interferometry and environmental metrology applications are to be constituted of monomode waveguides, that is to say channel or rib structures (represented in Figs. 3a and 3b respectively). In both cases, modifying the initial planar geometry of the films is necessary. In this context, etching methods have been investigated.
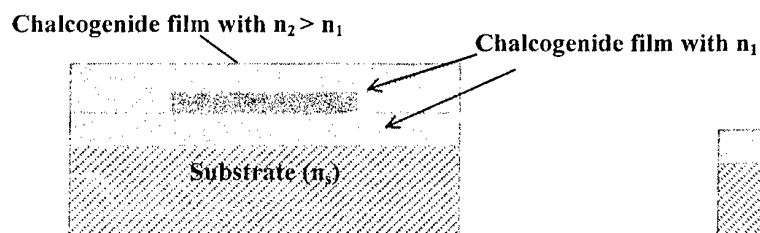
Fig. 3a. Representation of the "channel" structure to be obtained.
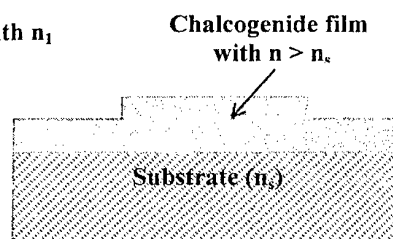
Fig. 3b. Representation of the "rib" structure to be obtained.

Chemical and physical etching tests were performed on $Ge_{29}As_{12}Se_{59}$ chalcogenide films deposited on Si/SiO_2 substrates.

These tests were proved to be very encouraging, since profiles of the as-obtained steps in the glassy films are good. As an illustration, SEM photograph of a physical etched film and profiles of characteristic steps obtained by chemical and physical etchings are presented in Figs. 5 and 6 respectively.
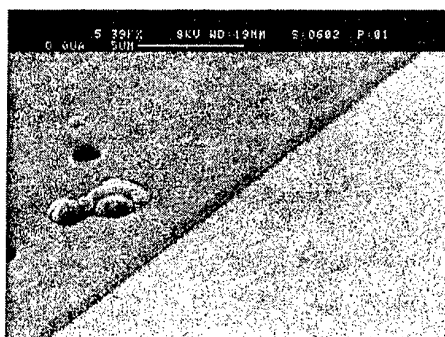
Fig. 5. SEM photograph of the ribs created by plasma etching.
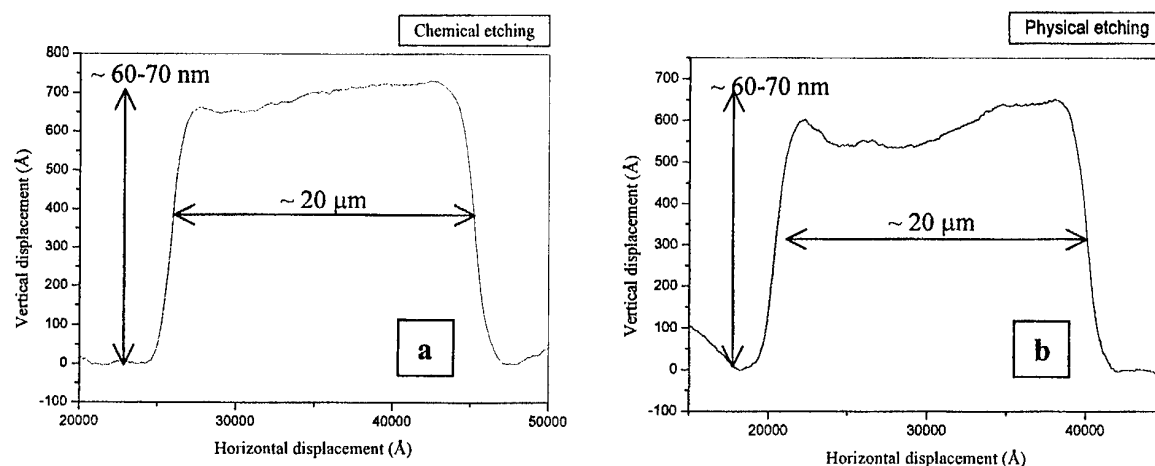
Fig. 6. Rib profiles obtained by profilometry for films: (a) chemically etched; (b) physically etched.

Up to now, tests have been performed with only one mask, so that the width of the steps is constant at 20 μm approximately. The depth of the steps was proved to be controllable and to date the smallest values obtained were 60-70 nm.

4. Conclusion

Films with good adherence and controlled composition are currently obtained, whatever the initial glass composition ($Ge_{33}As_{12}Se_{55}$ or $Ge_{28}Sb_{12}Se_{60}$), the deposition method (sputtering or thermal evaporation) and the substrate (oxidized silicon or microscope slide) are, for thicknesses up to 4 microns. Two multimode planar chalcogenide waveguides based upon $Ge_{29}As_{12}Se_{59}$ / $Ge_{21}Sb_{18}Se_{61}$ / $Ge_{29}As_{12}Se_{59}$ stacked layers were elaborated and proved to guide at 1.55 microns. Guiding quality was good but polishing the entrance surfaces rather than cleaving the substrates could still improve it.

First results related to the realization of channel or rib waveguides and the possibility of modifying the geometry of the films were very encouraging. Indeed, two etching methods (ie Ar plasma etching and NH_4OH chemical etching) were proved to be effective on $Ge_{29}As_{12}Se_{59}$ chalcogenide films.

Optimized dimensions of the waveguides to be suitable as far IR waveguides for astronomical interferometry or as optochemical sensors for environmental metrology are being calculated at the CNM in Barcelone. The next step will be the fabrication and characterization of such components with well defined geometry.

Aknowledgments

References

[1] A. B. Seddon, Journal of Non-Crystalline Solids, 184, 44-50 (1995).
[2] T. V. Galstyan, J. F. Viens, A. Villeneuve, K. Richardson, M. A. Duguay, Journal of lightware

technology, **15**, 1343-1347 (1997).

[3] K. Miura, J. Qiu, H. Inouye, T. Mitsuyu, K. Hirao, Applied Physics Letters, **71**, 3329-3331 (1997)

[4] Y. Mizushima, A. Yoshikawa, JARECT 16: Amorphous Semiconductor Technologies and Devices, 277 (1982)

[5] V. K. Tikhomirov, Journal of Non-Crystalline Solids, **256-257**, 328 (1999).

[6] E. Laurent, I. Schanen, F. Malbet, G. Taillades, in Interferometry in Optical Astronomy, proc. SPIE, (2000).

[7] E. Laurent, I. Schanen, P. Kern, A. Pradel, A. Aggad, proc. ICSO 2000, **497-505** (2000).

[8] H. Nagai, A. Yoshikawa, Y. Toyoshima, O. Ochi, Y. Mizushima, Applied Physics Letters, **28**(3), 145-147 (1976).

[9] M. S. Chang. R. W. Hou, Optics Communications, **24**(2), 220-224 (1978).

[10] A. Yoshikawa, O. Ochi, Y. Mizushima, Applied Physics Letters, **36**(1), 107-109 (1980).

[11] K. L. Tai, R. G. Vadimsky, C. T. Kemmerer, J. S. Wagner, V. E. Lamberty, A. G. Timko, Journal of American Science Technology, **17**(5), 1169-1176 (1980).

CHALCOGENIDE FIBRE DISPLACEMENT SENSOR

S. Miclos, T. Zisu

National Institute of R & D for Optoelectronics INOE-2000, 1, Atomiştilor Str., POB MG-5, 76900 Bucharest-Magurele, Romania

Fibre optic technology offers the possibility for developing of a variety of physical sensors for a wide range of physical parameters. The main advantage of fiber optic sensors lies in their dielectric construction, providing electrical isolation, immunity from electromagnetic fields, small dimensions, and compatibility with optical fibre technology. A large number of fiber sensors in production are based on intensity modulation of the light either outside the fiber or within it. In the case of intensity sensors the physical perturbation to be measured interacts with the fibre or some device attached to the fibre to modulate the intensity of the light as it travels through the fiber. Intensity modulated fiber sensors have been demonstrated to be efficient for different applications. A variation of internal-modulation sensors are the microbending-loss sensors, which are characterized by a relatively simple construction, good performances and compatibility with multimode fibre technology. A very effective configuration for the microbending-loss sensors is that one based on clad mode detection. For clad modes detection the end segment of the fiber is bent and placed in an integrating sphere. The use of chalcogenide rather quartz fibre optic highly increases the sensitivity of the sensor. Experimental set-up, transmission characteristics and technical parameters are presented.

1. Introduction

Fibre optic technology offers the possibility for developing of a variety of physical sensors for a wide range of physical parameters. The use of optical fiber samples for development of optical fibre sensors allows to obtain very high performances in their response to many physical parameters (displacement, pressure, temperature, electric field etc.) compared to conventional transducers [1]. The main advantage of fiber optic sensors lies in their all dielectric construction, giving electrical isolation, immunity from electromagnetic fields, small dimensions, and compatibility with optical fibre technology. Novel approaches based on sensor oriented technology had become very promising for development of fiber sensors with high performances.

A large number of fiber sensors in production are based on intensity modulation of the light either outside the fiber or within it. In the case of intensity sensors the physical perturbation to be measured interacts with the fibre or some device attached to the fibre to modulate the intensity of the light as it travels through the fiber. Intensity modulated fiber sensors have been demonstrated to be efficient for different applications. They are relatively inexpensive, easy to be fabricated and suitable for employment in harsh environments. A variation of internal-modulation sensors are the microbending-loss sensors, which are characterized by a relatively simple construction, good performances [1-4] and compatibility with multimode fibre technology. Depending on the deformer design and material it is possible to make acoustic, magnetic, electric, temperature, acceleration, displacement sensors, etc. Fiber-optic displacement sensors may have different important uses, which exploit the nonelectrical nature of these devices. For example as vibration monitors in generators, fiber sensors guard against costly equipment damage and they are immune to the high electrical noise that plagues piezoelectric vibration sensors. And in explosive atmosphers (e.g. in mines) fiber sensors could safely monitor equipment vibration. The use of chalcogenide rather quartz fibre optic highly increases the sensitivity of the sensor. Experimental set-up, transmission characteristics and

technical parameters of a fiber optic displacement sensor, based on clad mode detection, are presented.

2. Experimental results

It is well known that when an optical fiber is bent, its transmission loss increases as some of the light propagating along the fiber is radiated out. Microbending along the axis of the fibre cause mode Periodic perturbations of the fiber axis result in strong intermodal power transfer when the period of the perturbation corresponds to the difference in propagation constants of the interactng modes. Respectively, the power lost from propagation to radiation modes is maximum, when the fibre spatial bent frequency equals the difference in propagation constants between propagation and radiation modes. It was shown [5], that in the case of fiber with power low index profile, the spacing between the adjacent mode groups is given by the following relation:

$$\delta\beta_m = [2(\alpha\Delta/(\alpha+2))^{1/2}/a]\,(m/M)^{(\alpha-2)(\alpha+2)}, \tag{1}$$

were m is the mode group number, α is the index profile parameter, Δ is the parameter characteri-zing the difference between core and clad indices, a is the radius of the fiber, M^2 is the total num-ber of modes,

$$M^2 = [\alpha/(\alpha+2)](n_0\kappa a)^2\Delta. \tag{2}$$

Parabolic graded index fibers which have a constant difference in propagation constant between neighbouring modes are used to enhance the sensitivity in sensor applications. In the case of optical fiber with a parabolic index profile the formula for a mode group spacing is given by the relation (5):

$$\delta\beta = (2\Delta)^{1/2}/a \tag{3}$$

If the microbendings are formed along the fiber axis with a periodicity Λ that satisfies the relation of resonance

$$\delta\beta_c = 2\pi/\Lambda_c , \tag{4}$$

a complete conversion of guided modes to radiation modes takes place[2]. The critical period of microbends Λ_c is determined from the relation (5):

$$\Lambda_c = 2\pi a/(2\Delta)^{1/2} \tag{5}$$

In the case of small distortions, optical power in the fibre clad is attenuated proportionally to the displacement amplitude.

We have proposed a modified sensor configuration based on clad modes detection[6]. The experimental setup is presented in Fig. 1. It consists of a segment of transmitting optical fibre, coupled to a segment of a multimode fibre, which serves as a sensor element, a light source, a conventional deformer and a fotodetector coupled to the end of the sensor fiber. The optical fibre which serves as a sensor element is a multimode graded index fibre. For effective clad modes detection the end segment of the fiber is bent as represented in Fig. 1, to allow the clad modes out. This bent segment of the fiber is placed inside the integrating sphere in front of the photodetector. The output end face of the fiber is positioned outside of the integrating sphere, to let the core modes out. By monitoring the light power in the clad modes the applied displacement can be detected.
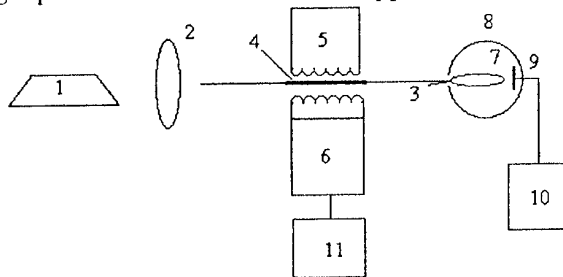
Fig. 1. Experimental set-up: 1 - light source; 2 - microobjective; 3 - optical fibre; 4 -glycerine;
5 - deformer; 6 - piezoelectric transducer; 7 - the bent segment of the fiber; 8 -integrating
sphere; 9 - photodiode; 10 - lock-in amplifier; 11 - generator.

The deformer represents two grooved plates with five teeth. One plate of the deformer is fixed, and the other can be displaced relatively to the other by manually adjusting the differential micrometer or by means of piezoelectric transducer. For transmission measurements a set of grooved plates of different periodicity, covering the range from 1.4 to 4.0 mm with a step 0.2 mm, was used. Optical transmission characteristics of the fiber were measured with different light sources: a He-Ne laser, a luminiscent diode, a diode laser, etc. The fibre segment, suffering the microbending, is covered with glycerene, in order to facilitate the clading modes out. Optical transmission characteristics for different microbending periods are presented in Fig. 2. It can be seen that experimental plot lnT vs. displacement amplitude changes drastically with the microbending period Λ. For small distorsion amplitudes the transmittance characteristic has a good linearity (Fig. 3).

Microbending losses depend in a high degree on the coupling conditions. In order to investigate the dependence of transmittance characteristics on modes exciting conditions we examined the behaviour of microbending induced optical losses vs. the position of injection of light beam along the input fiber face. A monomode fiber was used for selective modes excitation in a multimode fiber. For this purpose the end segment of the monomode fiber was displaced transverse relatively to the input end face of the multimode sensor fiber to allow different modes group excitation. It should be mentioned that the number of modes, excited in a graded index fiber increases by incresing the distance from the fiber axis to the point of light beam focusing. In this case an He-Ne laser was used as a light sourse. The microbending induced losses increses with incresing the distance of light spotfrom the fiber axis. The character of this increasing is almost a monotonous one in respect to the period of microbends. The experimental dependence lnT vs. microbends period for a constant displacement amplitude is presented in Fig. 4.
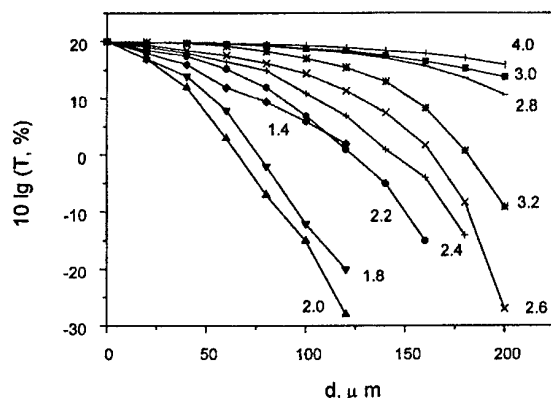
Fig. 2. Optical transmission characteristics vs. displacement amplitude for different microbend periods.= 1.4-4.0 m. The light source was a He-Ne laser coupled through a 90x microobjective.
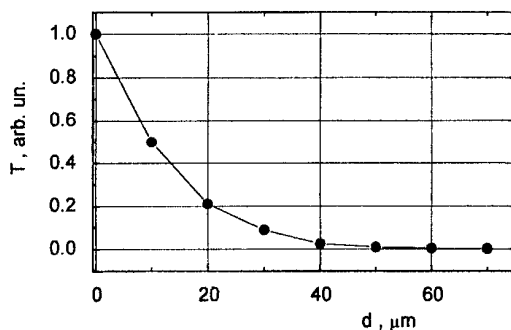
Fig. 3. Optical transmission characteristic for microbending period 1.8 mm.
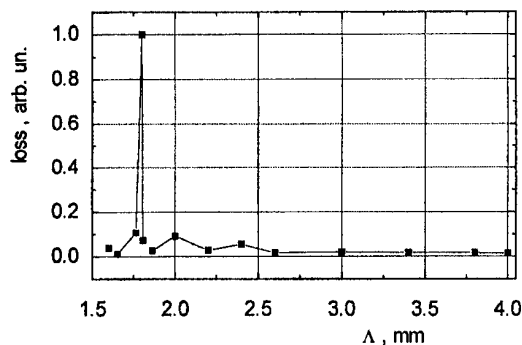
Fig. 4. Transmission vs. microbend period value for a constant deformation amplitude d = 100 μm.

An important resonant character of this dependence may be remarked. The microbending induced losses reach the maximum value for distortion period Λ = 1.8 mm. The character of the curve presented in Fig. 4 correlates with experimental results presented elsewhere [5].

For practical application of fiber sensor for displacement detection the linear part of transmission characteristics can be used (Fig. 3).
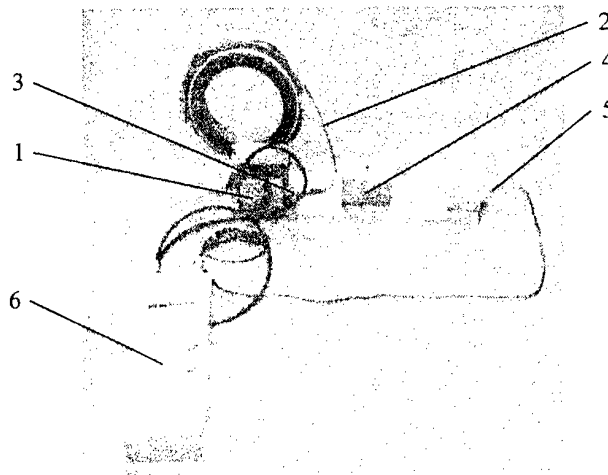
Fig. 5. The fibre optic displacement sensor. 1 - laser diode; 2 - transmitting optical fibre;
3 - conection; 4 - deformer; 5 - photodiode; 6 - electronic package.

On the basis of experimental results we have developed a compact model of fibre-optic displacemenml sensor, presented in Fig. 5. It consists of a diode laser, a photodiode and an electronic package. A diode laser is coupled to a multimode transmitting fibre through a standard optical connector. The transmitting fibre, about 10 m long, is connected to a segment of the sensor fibre. The electronic package includes the power supply, the preamplifier, a A/D convertor, and a digital display.

The performances of the sensor are presented below:
- The range of displacement amplitudes : 0 - 60 μm;
- Sensitivity : 0.1 mV/ μm;
- The dynamic range : ~ 55 dB;
- Resolution : 0.1 μm;
- Deviation from the linearity : ~ 6 %;
- Error : 2.8 %.

References

[1] A. L.Harmer "Optical fiber sensors". VTT Symposion, No. 46, 5-76 (1984).
[2] A. D.Kersey, A. Dandridge, "Applications of fiber optic sensors". 39th Electron.Compon.Conf., Houston, Tex., May 22-24, 1989, (N.Y.), 472-478 (1989).
[3] N. Lagakos, T. Litovitz, P. Macedo, R. Mohr, R. Melster, "Multimode optical fiber displacement sensor", Applied Optics, vol.20(2),167-168 (1981).
[4] S. S. Sai, K. Srinivasan, "A novel fibre-optic integrated cladding mode detector for displacement sensing", Rev.Sci.Instruments, V.65, Nr.1, 242 (1994).
[5] J. N. Fields, "Attenuation of a parabolic--index fiber with periodic bends", Applied Physics Letters, vol. 36(10), 799-801 (1980).
[6] A. M. Andriesh, I. P. Culeac, V. Binchevici, V. Abaskin V. Schitsko "Fiber opticsensors for displacenment and vibration detection", 16th Annual Sem.Conf., CAS'93, October 1993, Sinaia, Romania, p.499.

LIGHT-STIMULATED STRUCTURAL TRANSFORMATIONS
AND OPTICAL RECORDING IN AMORPHOUS NANO-LAYERED STRUCTURES

A. Kikineshi

Uzhgorod National University, Uzhgorod, 88000, Ukraine

The investigations of light-stimulated structural transformations in chalcogenide glasses are expanded towards multilayer structures with nanometer-scale components. The results of optical recording experiments and the new details of the recording mechanisms are reviewed.

1. Introduction

Amorphous semiconductors emerge in a wide class of glasses, amorphous organic and inorganic materials. They are attractive objects for theoretical and applied investigations on structure-dependent optical, electrical and other characteristics in bulk or thin film structures, owing to the existing general problems of ordering-disordering in materials science, charge localisation and transport phenomena or to the applications in optics, optoelectronics [1-3]. Advanced nanotechnologies and nanophysics widely use amorphous semiconductors as basic components in atomic engineering of new materials, electronic devices [4,5]. Amorphous Si, Ge, Se and chalcogenides are the most known and investigated in connection with the problems of tailoring optical and electrical parameters due to the nanometer scaling [6-9]. Experimental investigations are mostly conducted on a superlattice-type structures, which allow us to simplify the sample technology and the analysis of the results [10,11].

Optical recording processes have become of special interest besides usually investigated degradation, shift of the optical absorption edge, luminescence in nanostructures.

a-Se/ As_2S_3 nanolayered structures (NLS) seems to be up tonow the most interesting for amplitude-phase optical recording in a real time-scale [12,13], while Se_xTe_{1-x}-containing NLS are promising as photoconductive materials for electrophotography [14,15]. Both electrophotography and amplitude-phase relief formation on a sensitive chalcogenide layer are optical recording processes or non-silver photography, but the first is determined by the light-stimulated electron movement while the last depends on the light- or heat-stimulated atomic displacement, structural transformations within one phase (amorphous-amorphous) or between different states (amorphous-crystalline). The mechanism of these processes may be effectively tailored in nanostructures, thanks to the changes in electron spectra, thermodinamical and mechanical parameters (defect states, temperature of crystallisation T_c, diffusion, stress). Most of them have not been well examined so fare. It is the goal of this paper to review the results of experimental investigations of the above-mentioned nanostructures in regard to the well known electrophotography process, structural transformations in As-(S,Se,Te)-type homogeneous layers and to the less investigated interdiffusion processes in amorphous multilayers, all of which can be modified by light-stimulated transformations and used for optical recording.

2. Materials, technology and investigation methods

According to the known publications and experience in amorphous NLS production the existing vacuum technology seems to be the most reasonable both in quality and in price. Cyclic magnetron sputtering or thermal evaporation can be used first of all [9,16-18], but pulsed laser or e-

beam evaporation are also applicable for chalcogenides and other amorphous semiconductors. The quality of NLS in all cases is comparable with the results, obtained by plasma CVD for a-Si:H NLS [5]. Small-angle X-ray diffraction (SAXD) and TEM investigations support the conclusion that 3-10 nm layer spacing (periods Λ=6-20 nm) may be kept up to the total thickness of NLS d=0.5-4 μm with 0.5-2 nm thick transition layers in the interfaces for different types of combined materials. Of course, it is difficult to imagine such amorphous nanolayered structure as ideal crystalline superlattice like those produced by MBE. Most likely they are well correlated layers, the external surface of which has an average roughness about 0.5-1 nm, as measured by AFM on NLS, deposited from different chalcogenide glasses (ChG) onto Si-wafer, Corning 7059, sapphire substrata.

Structural investigations are usually provided by HRTEM (cross-sections) and SAXD, but optical (Raman scattering, visible- or IR-transmission spectra and optical recording) and electrical measurements (conductivity) are also good indirect methods for monitoring structural changes (crystallisation, interdiffusion) in NLS. Since we are interested in light-stimulated structural transformations, comparison must be done between the results, obtained at different radiation energy densities on the NLS surface and at the simple thermal treatment, annealing. Combining the above-mentioned direct and indirect methods of structural investigations the reliable information can be obtained about the complex changes in optical, electrical, geometrical parameters and the structure of NLS, since optical image relief depends on all of these parameters.

Most of our optical recording experiments were performed with He-Ne laser (λ=0.63 μm, output capacity density P=0.8 W/cm^2), but Ar-ion laser (λ=0.51 μm, $P\approx$50 W/cm^2) and even pulsed nitrogen laser (λ=0.32 μm) or AlGaAs LEDs were used in optical recording experiments.

3. Optical recording processes

Non-silver photography or optical recording processes may be realised in amorphous chalcogenides both in the form of electrophotography due to the charging- optical discharging or in the form of amplitude-phase optical relief formation due to the light-stimulated structural transformations. Electrophotographic recording mode is well investigated and applied in copying machines, laser printers in which a-Se-based photoreceptors were used besides novel organic materials. Expanding the electron transport investigations in amorphous materials, especially the application possibilities of ChG, electrophotographic recording mode was performed on Se$_x$Te$_{1-x}$-containing NLS [14,15] and used for determination of the influence of multiple heterostructure formation on the sensitivity, discharge processes. It was established that combining narrow- and wide-gap ChG in a periodical structure Se$_x$Te$_{1-x}$/As$_y$Se$_{1-y}$ (0.6$\leq$ x $\leq$ 0.95, 0.06 $\leq$ y $\leq$ 0.5) the total sensitivity may be increased up to one-two orders of magnitude in comparison with a homogeneous layer of mixed composition, especially in the near-infrared spectral range (see for example Fig.1). The dark decay of the surface potential slows down while the light-stimulated discharge accelerates, the drift mobility of holes increases [19].

Additional tuning of these parameters is possible by step-by-step annealing, which enhances interdiffusion and leads to the formation of multiple heterostructures with variable bandgaps up to the total intermixing of NSL components [11]. Thus NLS creation from appropriate photoconductive ChG and additional stimulated structural transformations in it are effective methods for tailoring the parameters of photoreceptors for electrophotography [14].
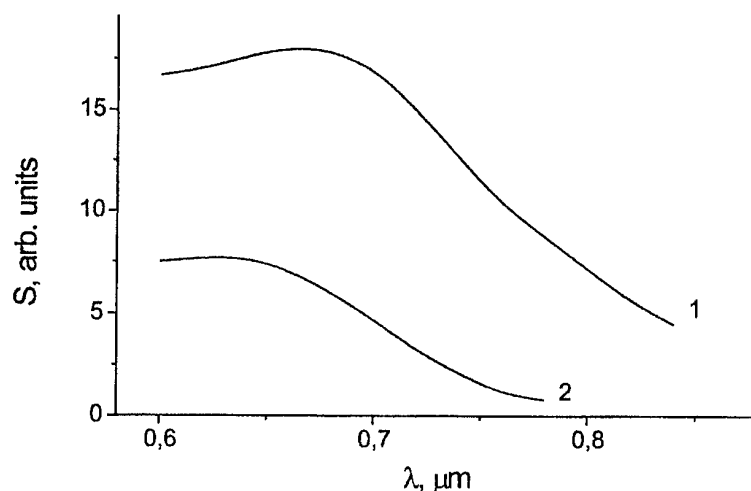
Fig. 1. Spectral dependence of electrophotographic sensitivity of $Se_{0.8}Te_{0.2}/As_{0.06}Se_{0.94}$
NLS (1) and of the homogeneous multicomponent layer of the same composition (2).

As far as the interdiffusion is enhanced by thermal annealing, optical recording of bits or amplitude-modulated image relief ($\Delta\alpha$, ΔR) may be realised on the same or similar NSL due to the heating by the focused light beam. More over, the method may be expanded to the wide class of effectively intermixing materials, for example Si/Ge NLS [18]. The problem lies in the stability of the structure in the dark at the given temperatures, i.e. triggering of the diffusion is necessary for wide applications, since the sensitivity of the process does not differ essentially from the known process of laser-induced amorphisation-crystallisation in Te-containing ChG films. It was supported by our experiments on a number of Te-based ChG NLS.

The main attention in our experiments was devoted to the optical recording due to the pure light-stimulated effects. Investigations were performed in NLS both in a simple amplitude-modulation mode ($\Delta\alpha$, ΔR) and in a phase-modulation mode, which was realised in a holographic experiment. The first is an easy method to control the type (photo-darkening, photo-bleaching), sensitivity (usually the exposition in J/cm^2, which is necessary for achieving certain contrast of $\Delta\alpha/\alpha$, $\Delta R/R$), dynamic range of stimulated changes.
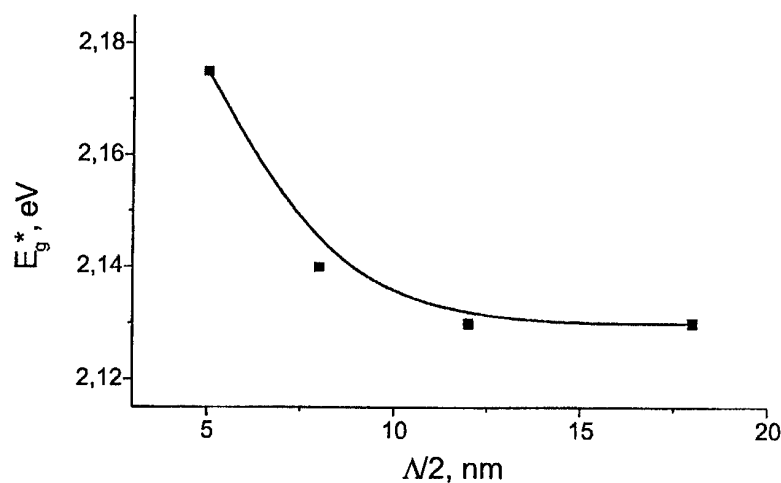
Fig. 2. The optical gap E_g^* as a function of layer spacing in a-Se/As$_2$S$_3$ NLS.

Since the changes in α, R and n are connected in semiconductors [1,20], the more complete information about the light-stimulated structural transformations in NLS may be obtained from writing-readout-erasing experiments. The latter were investigated mostly in a-Se/As$_2$S$_3$, AsSe/ As$_2$S$_3$, As$_x$Se$_{1-x}$/Se$_y$Te$_{1-y}$ NLS due to their sensitivity at the He-Ne laser radiation wavelength. In general, it is important to adjust the optimal spectral range of sensitivity to the recording laser-light wavelength. It was established for ChG NLS that the fundamental absorption edge shifts towards the increasing E_g^* with decreasing layer spacing, i.e. modulation period Λ. This shift is well-pronounced for $\Lambda<14$ nm (see. Fig.). So the NLS with As$_2$S$_3$ or other wide band-gap barriers may be adjusted to the optimum absorption at the recording wavelength. The relative change in $\Delta\alpha/\alpha$, $\Delta R/R$ after maximum illumination is about 30-50%, therefore certain NLS are well applicable for digital optical recording.

There were not large differences between the amplitude (photodarkening) or amplitude-phase (holographic) recording efficiency at 294 K in homogeneous As$_2$Se$_3$, AsSe layers and AsSe/As$_2$S$_3$-type NLS. It is not surprising, since the light-stimulated structural transformations are connected the chalcogen bridge atom and the medium-range order dimensions determine the structural transformations and the resolution limit of optical recording in ChG [14,21]. The interdiffusion, internal stress is small in this type of NLS. Not so in the a-Se/As$_2$S$_3$,

As$_x$Se$_{1-x}$/Se$_y$Te$_{1-y}$ and even a-Si/Ge NLS, where photo-bleaching takes place and interdiffusion is intensive. More over, giant deformations (thickness changes up to 4-5%) occurs under the rather low-intensity laser illumination in a-Se/As$_2$S$_3$ NLS, similarly to the expansion effects observed in ChG layers at high-power illumination [22]. The photo-expansion in a-Se/As$_2$S$_3$ NLS is opposite to the small photo-contraction, observed in homogeneous ChG layers and even in a-Se layers [23], and both are applicable for surface relief hologram recording, as it is demonstrated in Fig.3.
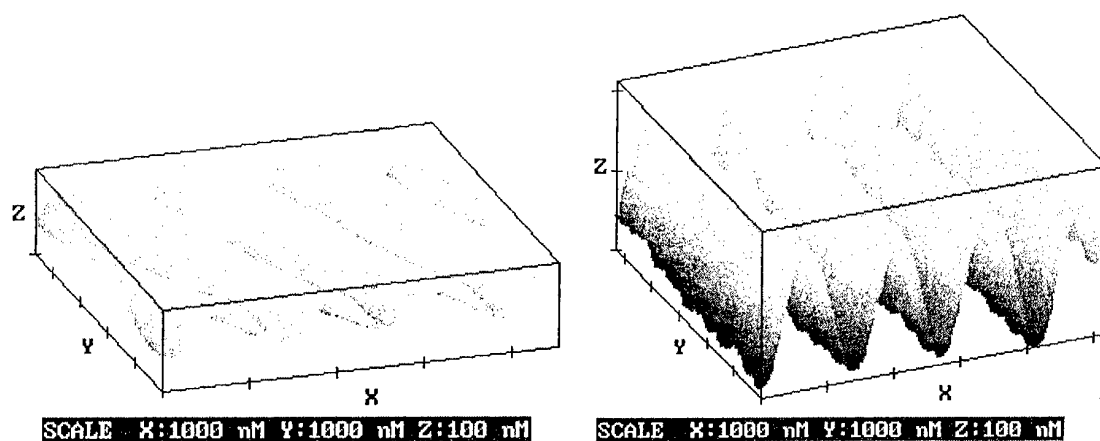
Fig. 3. AFM picture of surface holograms recorded on a-Se layer (left) and a-Se/As$_2$S$_3$ NLS (right).

Interdiffusion, stress relaxation, combined with the known photoplasticity effects in ChG [24] may be involved to the explanation of such expansion effects in NLS. Interdiffusion is better pronounced in Te-based NLS, where it is easily activated [17]. Stress relaxation must also be used for explanation of the short-period grating relaxation under annealing.

The model of the surface grating formation by illumination and its erasing by heating in a-Se/As$_2$S$_3$ NLS was developed. The physical basis of the process is the interdiffusion of a-Se and As$_2$S$_3$ resulting the total volume increase in comparison with a total volume of separated sub-layers. and the effective intermixing of components at short, nanometer-size distances. The concentration profile $C(x)$ along the surface (x-axis) during the interdiffusion in z-direction may be written as:

$$C(x) = \sum_{i=0} A_i^0 \exp\left\{-D\left(\frac{2\pi i}{\Lambda}\right)^2 t \sin\left(\frac{2\pi i}{\Lambda}x\right)\right\},$$ (1)

where A_i^0 is coefficient, D-the diffusion coefficient, Λ- the period of the NLS, t- the illumination time. Thus at the given dependence of D on illumination [24] and the known dependence of the volume (density) on Se concentration in As_2S_3-Se system it is possible to calculate the stimulated thickness changes within one bilayer (see. Fig. 4) and in the NLS. The results fit experimental data of AFM investigations well.
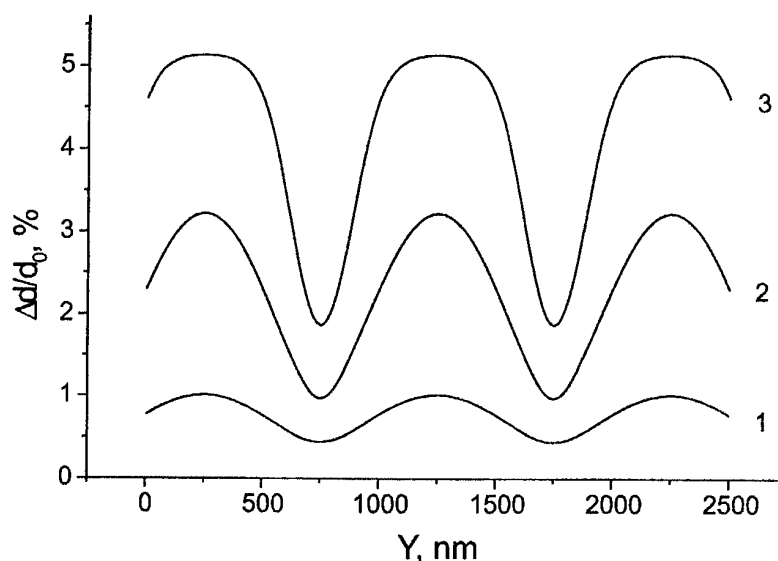
Fig. 4. The model of surface profile formation during hologram recording: 1- t=100 s,
2 – t=1000 s, 3 – t=4000 s.

The above mentioned distinctive features of light-sensitive ChG multilayers depend on the composition of combined layers and on the nano-periodicity. They must be investigated by the complex of direct and indirect structure-sensitive methods.

The light-stimulated contraction-expansion effects, especially the giant photoexpansion in a-Se/As_2S_3 NLS are applicable for surface relief hologram recording in the real time scale, without etching. Such relief is stable at 293 K and hard enough to make copies by direct pressing onto the soft polymer.

5. Conclusions

Nanolayered, compositionally modulated structures which consist of combined pairs of light-sensitive and barrier layers made of amorphous semiconductor chalcogenide glasses broaden the possibility of tailoring non-silver photographic processes, optical recording parameters and applications of this class of materials.

References

[1] N. F. Mott, E. A. Davis, Electron Processes in Non-Crystalline Materials, Clarendon Press, Oxford (1979).

[2] A Feltz, Amorphe und Glasartige Anorganische Festkorper, Acad. Verlag, Berlin (1983).

[3] M. I. Maryan, A. Szasz, Self-Organising Processes in Non-Crystaline Materials: From Lifeless to Living Objects, ONCO Therm, Budapest-Uzhgorod (2000).

[4] M. O. Vasylyev, S. I. Sidorenko, Diffusion and Surface Segregation, Kyiv Politechnica, Kyiv (1998).

[5] M. Hirose, S. Miyazaki, JARECT, 22, Amorphous Semiconductors Technology&Devices, OHM North-Holland, 147 (1987).

[6] H. Hamanaka, S. Konagai, K. Murajama, M. Yamaguchi, K. Morigoki, J. Non-Cryst. Sol., 198-200, 808 (1996).

[7] Gy. Radnoczi, B. Petz, Thin.Sol. Films, 232, 68 (1993).

[8] A. Kikineshi, Optical Engineering, 346,1040, (1995).

[9] D. Nesheva, D. Arsova, Z. Levy, Phil. Mag.B,70, 205 (1994).

[10] S. M. Prokes, F. Spaepen, Appl. Phys. Lett., 47, 234 (1985).

[11] A. Sterr, A. Kikineshi, Ukr. Phys. Journ., 35,.599 (1990).

[12] V. Palyok, A. Mishak, I. Szabo, D. L. Beke, A. Kikineshi, Appl. Phys A68, 489 (1999).

[13] A. Kikineshi, V. Palyok, A. Mishak, I. Szabo, D. Beke, Functional Materials, 6, 413 (1999).

[14] A. Kikineshi, Kvantovaja Elektronika (Kijev), 37, 31 (1989) (in Russian).

[15] E. Vateva, I. Georgieva, J. Non-Cryst. Sol., 164-166, 865 (1993).

[16] D. L. Beke, G. A. Langer, A. Csik, Z. Erdelyi, M. Kis-Varga, I. A. Szabo, Z. Papp, Proc. DIMAT-2000, Mat. Sci. Forum, 176 (2000).

[17] A. Imre, V. Fedor, M. Kis-Varga, A. Misak, M. Shiplyak, Vacuum, 50, 507 (1998).

[18] A Csik, M. Malyovanik, J. Dorogovics, A. Kikineshi, D. Beke, I.A. Szabo, G. Langer, Journ. Optoel. and Adv. Materials, 3, 33 (2001).

[19] A. Imre, A. Mishak, V. Fedor, A. Kikineshi, D. Beke, L. Daroczi, J. Steinber, Proc. Int.Conf. EL-100, Uzhgorod, 155 (1997).

[20] A. N. Borets, V. V. Khiminets, I. D. Turjanitsa, A. A. Kikineshi, D. G. Semak, Slozhnije Stekloobraznije Khalkogalogenidi, Vis. Skola., Lviv (1987) (in Russian).

[21] A A. Kikineshi, Optical Memory and Neural Networks, 4, 177 (1995).

[22] Ke. Tanaka, Physics and Applications of Non-Crystalline Semiconductors in Optoelectronics, NATO ASI Series, 3. High Technology, 36, 31 (1997).

[23] A. Kikineshi, V. Palyok, M. Shiplyak, I.A.Szabo, D. L. Beke, Journ. Optoel. and Adv. Materials, 2, 95 (2000).

[24] S. V. Nemilov, K. Tagantsev, Fizika i Khimija Stekla, 7, 195 (1981) (in Russian).

FORMATION OF PROFILED HOLOGRAPHIC DIFFRACTION GRATINGS USING PHYSICOCHEMICAL INTERACTION IN As$_2$Se$_3$-Ag SYSTEM

M. V. Sopinskyy, P. F. Romanenko, I. Z. Indutnyy, E. F. Venger

Institute of Semiconductor Physics, National Academy of Sciences of Ukraine,
Kiev, 03028 Ukraine

The method of blazed holographic diffraction gratings fabrication by transformation of an original symmetric grating grooves into asymmetric ones using inclined vacuum deposition of silver and additional chemical etching have been developed. As photoresist material for gratings recording light-sensitive chalcogenide glassy As$_2$Se$_3$ layers were used. The shape of grating grooves was determined with an atomic force microscope. Angular and spectral dependencies of the diffraction efficiency of the gratings were found, and a relation between optical features and the grating surface pattern was analyzed.

1. Introduction

Profiled (blazed) gratings make it possible to concentrate energy in a given spectrum range. Of special interest are profiled holographic gratings (PHGs), since they combine the advantages of ruled gratings with those of conventional (unprofiled) holographic gratings (CHGs), namely, high diffraction efficiency in a given spectrum range and low level of light scattering. There are two methods of blazed grating production: recording of interference fringe fields in photoresist materials using special exposing techniques, or transformation of conventional holographic gratings with symmetrical grooves into triangular groove grating by ion etching or another additional treatments [1].

The recent trend in CHG technology is the use of light-sensitive chalcogenide glassy semiconductor (CGS) films [2-5]. Vacuum-evaporated layers of chalcogenide glasses (for example As$_2$Se$_3$, As$_2$S$_3$, or As-S-Se composition) have shown to be a good registering media for holographic relief pattern fabrication due to its high resolution, optical uniformity, sensitivity to the irradiation of available lasers and absence of shrinkage under treatment. Due to light-induced structure transformations, their solubility, particularly, in organic alkaline solvents, changes. Based on this effect, high-quality symmetric CHGs were obtained with spatial frequencies in the range of 600 to 3600 mm^{-1} and diffraction efficiencies up to 80% in polarized light [2-5].

One of today's problem in this field is the transformation of symmetric CGS-based CHGs into asymmetric ones. Publication [5] reports PHGs prepared by ion etching of symmetric CHGs formed on CGS films. The unique properties of CGS films allow for other, unusual, methods for transforming their surface pattern. In [6, 7], we developed a method of fabricating blazed holographic gratings. In this method, symmetric grooves of an original grating are made asymmetric by using additional oblique monochromatic or polychromatic irradiation and chemical etching of the irradiated grating.

In this work, we made an attempt to fabricate PHGs through interactions that take place when silver layers are vacuum-deposited onto CGS films. Ag-CGS interaction begins during deposition [8] and continues at a different rate (depending on a specific Ag-CGS system) after the deposition process is terminated [9]. The metal penetrates into the semiconductor to form a metal-enriched (to several tens of atomic percent) phase. This phase differs in properties from both the metal and the semiconductor [10, 11]. Profiling was accomplished by transforming original symmetric (unprofiled) gratings written on CGS films. Here, we took advantage of the fact that the etching selectivity for Ag-doped CGS films is much higher than the photoinduced selectivity.

In this work we used most sensitive As$_2$Se$_3$ layers and amine-based negative etching solution.

The rate of interaction between As_2Se_3 and Ag is one of the highest among CGS-Me systems: intense interaction proceeds both during and after deposition of the metal even at room temperature [9].

2. Experimental procedures

The original holographic gratings were produced as usually by recording of a stationary interference fringe field onto As_2Se_3 films (thickness of 800-1000 nm) deposited onto high-quality polished glass substrates by thermal vacuum evaporation. The interferential pattern was generated by a He-Ne laser (wavelength of 632.8 nm) using the holographic setup assembled by the wave-amplitude division method. The spatial frequency of the gratings was 600 mm^{-1} and radiant exposure was ~10^{-1} J/cm^2. After exposure, the samples were chemically treated in an amine-based alkaline solution to form a relief pattern.

The next step was profiling. A thin (1-10 nm) Ag layer was deposited on the gratings at a certain angle ϕ varying from 10° to 80° with respect to the normal to the grating. The grating was mounted in such a way that the flux of evaporated silver was directed normally to the grooves. Ag penetrates into the As_2Se_3 layer during and after deposition as a result of chemically and thermally stimulated diffusion to form a metal-enriched semiconductor layer (reaction product). The etch rate of Ag-doped CGS films in alkaline etchants is much lower than for undoped ones; therefore, in subsequent etching of the grating, the former served as a protective mask. Unprotected regions of the As_2Se_3 layer were etched off, and the grating grooves became asymmetric. Profiling was performed in the same amine-based etchant, which was used to pattern the original gratings.

To estimate the profiling effect, we recorded angular and spectral dependencies of the absolute diffraction efficiency η for the original and transformed gratings in the first diffraction order (η is defined as the ratio of the first-order diffraction intensity to the incident intensity). Prior to optical measurements, the original and profiled gratings were covered by a 100-nm-thick reflection aluminum film. Angular dependencies (β is the angle of light incident) of η were measured using He-Ne laser (β= 0°-80°). Spectral measurements were carried out using the setup close to the Littrow's autocollimation scheme; the angle between the incident and diffracted beams was about 8°, and the spectral range was 400-800 nm. Both the spectral and angular dependencies of η were measured for s- and p-polarized light (E is perpendicular and parallel to grooves, respectively), as well as for unpolarized light.

The surface pattern of the gratings was examined with a Dimension 3000 scanning probe microscope (Digital Instruments) in the AFM tapping mode.

3. Results and discussion

The geometric and diffraction properties of the as-prepared and profiled gratings show that the effect of profiling depends on many parameters: the groove profile of initial gratings (which, in its turn, depends on several parameters, as well), the angle of deposition and the amount of Ag deposited, time of Ag-As_2Se_3 interaction and additional etching. This allows us to assume that the properties of PHGs thus obtained can be varied in wide limits. On the other hand, it becomes difficult to estimate the relative contribution of the above factors to the PHG performance. In general, they can be subdivided into three groups: those associated with the CGS film (primarily its thickness and deposition rate), those that govern the fabrication of the symmetric grating, and those closely related to Ag-CGS interaction.

The first two have been much studied. Empiric experimental studies and numerical simulation of gratings recording in CGS-based inorganic resists have been performed [2, 3], These experiments and also the simulation of surface patterning suggest that not only the depth but also the shape of the pattern depends on the initial thickness of the layers, their properties, exposure conditions, etch time, and etchant selectivity. Holographic diffraction gratings with grooves of sinusoidal and cycloidal shapes have been obtained.

We performed experiments with gratings that had sinusoidal grooves, which are the most studied. Fig. 1 shows a typical AFM image of the original symmetric grating with a spatial frequency of 600 mm^{-1}. The depth of the grooves is h_0 = 150 nm; hence, the modulation depth h_0/d = 0.09 (the period of the grating is 1667 nm). The mean angle of inclination of the facets (facet angle) is -10°, the steepest being 15°. The spectral and angular dependencies of η of such gratings was symmetrical

(within the accuracy of measurement: 2% for angular and 5% for spectral measurements) when they were irradiated from opposite directions perpendicular to the grooves.
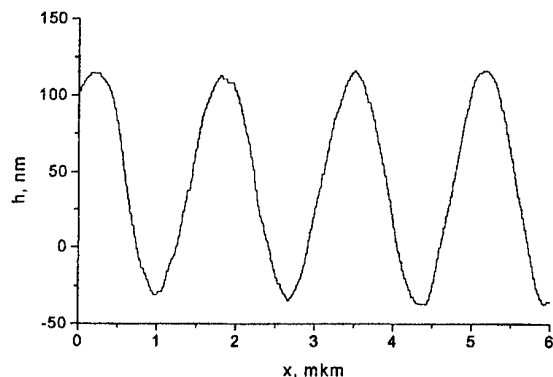
Fig. 1. Groove profile in the initial symmetric holographic grating.
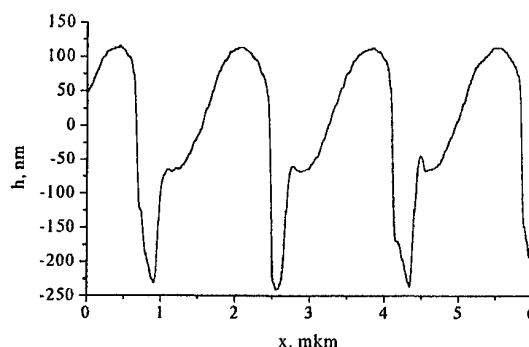
Fig. 2. Groove profile in the grating transformed from the initial grating shown in Fig. 1.

Fig. 2 shows the profile of a typical asymmetric grating made from a symmetric one by additional evaporation of a silver film of thickness $\{h_{Ag}\}$ = 3.6 nm (this value is averaged over the grating area) at 50° to the normal to the substrate surface, and subsequent etching. The groove depth in the asymmetric grating is more than twice that in the initial one, 355 nm, and the modulation depth is $h_0/d \cong$ 0.21. The minimum is 469 nm away from the left peak and 1198 nm from the right one; that is, the projection of the larger facet onto the substrate surface is nearly three-fourths of the grating period. The smaller facet has a gradually increasing steepness with an average angle of 37° with respect to the substrate. The larger facet can be divided into three parts: top (gently sloping), middle (nearly a plateau), and bottom (the steepest portion). The height of the gentle (top) portion somewhat exceeds the groove half-height; here, the average inclination is about 10°. The inclination of the bottom portion is close to the maximum steepness of the smaller facet. On average, the larger facet angle is about 16° with respect to the substrate.

From a comparison between the groove shapes of the initial and transformed gratings, it follows that the front facets of grooves of the initial grating (Ag were deposited onto these facets) remain practically intact after etching. This means that the reaction product nearly completely protected the CGS layer from dissolution during profiling etching. The first (gentle) portion of the larger slope virtually copies the profile of the initial sinusoidal grating. The back facets were affected by etching much more noticeably. Here, small plateaus correspond to the partially etched bottom part of the initial grating relief.
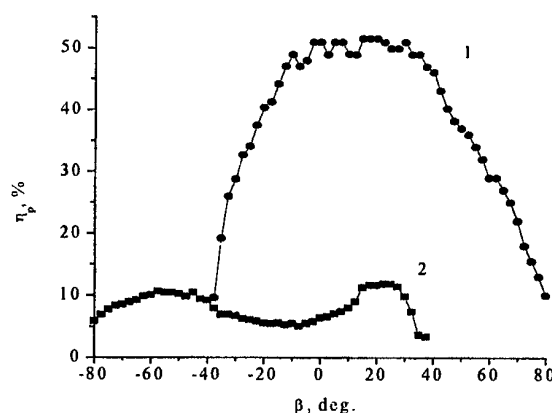
Fig. 3. Angular dependencies of the diffraction efficiency of the PHG for light polarized parallel to the groove direction. Wavelength is 632.8 nm.

The asymmetry of blazed grating is also displayed in angular and spectral dependencies of diffraction efficiency. For p polarization, the angular dependencies are plotted in Fig. 3. Here, curves 1 and 2 were obtained when light was incident on the larger and the smaller facet, respectively. For normal incidence ($\beta = 0$, symmetric arrangement of diffraction orders), the diffraction efficiencies measured on the two facets differ by a factor of 8.5. This points to the considerable asymmetry of the groove shape. For the larger facet, the maximum efficiency was observed when the angle of incidence was close to the mean facet angle. For the smaller one, two peaks appear: the angular position of one of them (-50°) is close to the mean slope of this facet, while that of the other (20°) coincides with the position of the peak from the larger facet and is likely to be associated with rereflections of the light incident on the larger facet. The share of total energy accounted for by conjugate diffraction orders is maximal at 20°; in other words, the maximum amount of light is reflected and rereflected at this angle.

For s-polarization we also obtained asymmetrical angular dependence but unlike p polarization, here distinct anomalies are observed. The anomaly at $\beta = 15°$ is associated with the disappearance (appearance) of the second order; while that at 38°, with the appearance (disappearance) of the conjugate order. The anomalies are more pronounced for the reflection from the smaller facet possibly because of the greater effect of the larger facet on the smaller than vice versa. Thus, the angular dependencies in the case of p polarization more adequately depict the groove shape.

Spectral dependencies of the diffraction efficiency for unpolarized light that were measured in the autocollimation regime for the blazed grating (curve 1 correspond to the bigger facet illumination, curve 2 – to that of the smaller facet), and for the symmetric grating (curve 3) are shown in Fig. 4. Throughout the spectral range (400-800 nm), the diffraction efficiency for the larger facet exceeds that for the smaller one. For wavelengths of 620, 660, and 700 nm, these values differ by a factor of 5.7, 4.5, and 4.5, respectively. Also, the efficiency for the larger facet exceeds that for the symmetric grating, except for the short-wave part of the interval.
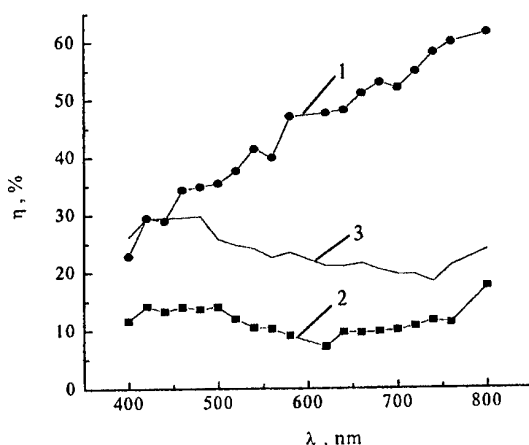
Fig. 4. Spectral dependencies of the diffraction efficiency for unpolarized light.

Simple geometric simulation of Ag deposition will allow us to describe Ag-As$_2$Se$_3$ interaction in quantitative terms. Let the x axis be directed normally to the grooves and the y axis, normally to the substrate (Fig. 5). The density of Ag deposited on the relief surface (and, hence, the thickness of the Ag film) depends on the amount of the metal evaporated and the angle between the Ag flux and each specific deposition area on the surface. Then, the thickness of the metal at a point x in the cross section perpendicular to the grating relief is given by

$$h_{Ag}(x) = K\cos\Theta(x), \tag{1}$$

where K is a proportionality coefficient, which depends on the amount of Ag deposited, and $\Theta(x)$ is the angle of incidence of the Ag flux on the groove surface at the point x.

We also have

$$\Theta(x) = \varphi - \alpha(x) \tag{2}$$

where ϕ is the angle of incidence of the Ag flux on the substrate that is reckoned from the normal to the substrate and $\alpha(x)$ is the groove inclination to the flat surface of the substrate at the point x.

Equation (1) is valid if the sticking coefficient of the metal is independent of the angle of incidence on the CGS film surface and on the amount of the metal deposited. The profile of the initial sinusoidal grating is described by the expression

$$h(x) = (h_0/2)(1 + \cos(2\pi x/d)), \tag{3}$$

where d is the grating period and h_0 is the height of the profile.

The inclination of this grating surface to the substrate surface is then expressed as

$$\alpha(x) = arctan\{[\pi h_0/d][-sin(2\pi x/d)]\}, \tag{4}$$

Fig. 5 illustrates the distribution of the Ag film thickness along the groove of the initial grating. The thickness was calculated by formulas (1), (2), and (4). Comparing this distribution with the distortions of the initial grating due to the metal deposition and subsequent etching, one can conclude that etching is virtually absent for $h_{Ag}(x) > 3$ nm. When $h_{Ag}(x)$ is less than 3 nm, the etch rate sharply grows. Since the Ag films (of thickness less than 10 nm) deposited on the noninteracting substrate are discontinuous (form islands), they could not serve as a protective mask during profiling etching. It appears that protection is provided by the top metal-doped CGS layer. The Ag thickness critical for the formation of the mask is seen to be about 3 nm. This value is close to that obtained earlier upon calculating the Ag amount incorporated into the As_2Se_3 film when the metal is thermally evaporated on this film [8]. The etch rate is maximal at the point one-fourth of the period away from the top of the groove back facet, where the Ag thickness estimated is minimal, 2.3 nm.

Using measurements of the groove shapes of the initial and profiled gratings, an empiric relationship $\Delta h(h_{Ag})$ can be derived, where Δh is the thickness of the As_2Se_3 film dissolved during etching and h_{Ag} is the amount of the Ag deposit. As follows from correlation analysis data, this empiric relationship is fairly accurately approximated by the sum of two exponentials:
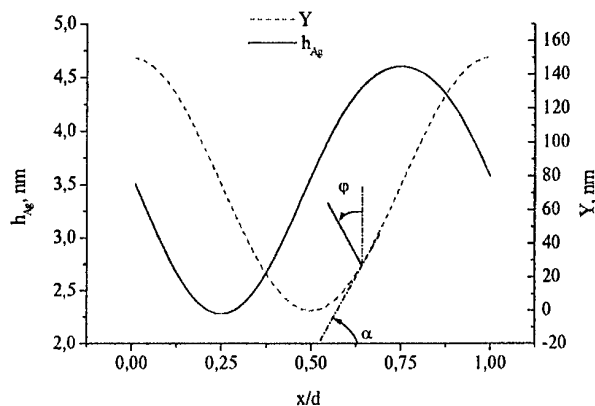
Fig. 5. Groove profile of the sinusoidal grating with $h_0 = 150$ nm and $d = 1667$ nm (Y, dashed line) and the distribution of the Ag deposit along this groove (h_{Ag}, solid line). The average thick-ness of the Ag layer is 3.6 nm.

$$\Delta h(h_{Ag}) = 204.93\exp\{-(h_{Ag}-2.412)/0.125\}$$
$$+ 61.51 \exp\{-(h_{Ag} - 2.412)/1.553\}, \tag{5}$$

With (5), we simulated the transformation of the initial symmetric gratings into asymmetric ones. The initial grating was assumed to be sinusoidal with a modulation depth of $h_0/d = 0.09$. Variable parameters were angle of vacuum deposition of Ag and the thickness of the metal deposited. Fig. 6 shows the results of numerical modeling for the angle of Ag deposition the same as for experimental grating onto Fig. 2, that is 50^0. Variable parameter here is the average thickness of the Ag layer: curve 1 – initial grating, curve 2 - the average thickness of deposited Ag is 4.18 nm, curve 3 – 4.02 nm, curve 4 – 3.86 nm.
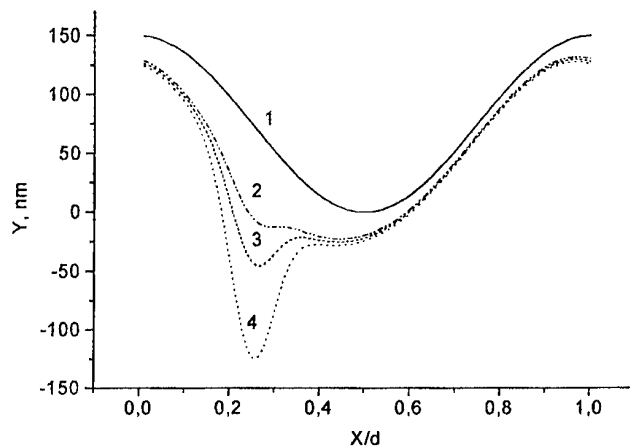
Fig. 6. Groove profile of initial grating (curve 1) and blazed gratings (curves 2, 3 and 4) obtained after Ag deposition and etching. Angle of deposition is equal 50^0.

We can see that as the Ag film gets thinner and etching of the Ag-doped grating becomes selective, the initially symmetric profile transforms into an asymmetric one because of a slight (-0.01d) shift of its maximum and a more considerable (-0.05d) shift of its minimum to the left of the initial grating grooves. The modulation depth remains practically unchanged in this case, since the minimum and maximum lower roughly equally. With further decreasing of Ag thickness, the groove shape can be approximated by an asymmetric trapezoid. The modulation depth in such a grating is somewhat larger than in the initial symmetric one. As Ag thickness continues to decrease, the groove shape becomes nearly triangular, the projections of the groove facets on the x axis being about 0.7d for the larger and 0.3d for the smaller. For an extremely thin Ag film, the larger facet has two drastically differing slopes because of a sharp increase in the etch rate. The maximum ratio of the facet projections is ~0.72d/0.28d in this case.

4. Conclusion

The simple method of PHGs fabrication by additional treatment of initial gratings with symmetrical grooves have been developed. The blaze angle in the PHGs depends on the modulation depth of the initial sinusoidal gratings and also on the angle and the thickness of Ag deposition. The method enables recording of grating with designated blaze angle by changing the original grating formation parameters and the additional treatment conditions. The maximum value of absolute diffraction efficiency of obtained PHGs reached 60% for non-polarized light in the spectral range corresponded to a blaze angle.

References

[1] J. Flammand, F. Bonnemason, A. Thevenon, J. X. Lerner, Proc. SPIE **1055**, 288 (1989).

[2] I. Z. Indutnyi, I. I. Robur, P. F. Romanenko, A. V. Stronski, Proc. SPIE 1555, 248 (1991).

[3] I. Z. Indutnyi, A. V. Stronski, S. A. Kostioukevich. et al., Opt. Eng. 34, 1030(1995).

[4] R. R. Gerke, T. G. Dubrovina, P. A. Dmitrikov, M. D. Mikhailov, Opt. Zh. 64 (11), 26 (1997) [J. Opt. Technol. 64, 1008(1997)].

[5] A. V. Lukin, A. S. Makarov, F. A. Sattarov, et al., Opt. Zh. 66 (12), 73 (1999) [J. Opt. Technol. 66, 1071 (1999)].

[6] P. F. Romanenko, M. V. Sopinski, I. Z. Indvtnyi, Proc. SPIE 3573, 457(1998).

[7] P. F. Romanenko, N. V. SopinskiT, I. Z. Indutnyi, et al., Zh. Prikl. Spektrosk. 66 (4), 587 (1999).

[8] M. T. Kostyshin, V. L. Gromashevskii, N. V. Sopinskii, et al., Zh. Tekh. Fiz. 54 (6), 1231 (1984) [Sov. Phys. Tech. Phys. 29,709(1984)].

[9] I. Z. Indutnyi, M. T. Kostyshin, O. P. Kasyarum, et al., Photostlmulated Interactions in Metal-Semiconductor Structures (Naukova Dumka, Kiev, 1992).

[10] A. G. Fitzgerald, C. P. McHardy, Surf. Sci. 152/153, 1255(1985).

[11] V. Honig, V. Fedorov, G. Liebmann, P. Suptitz, Phys. Status Solidi A 96 (2), 611 (1986).

[12] P. F. Romanenko, I. I. Robur, A. V. Stronskii. Optoelektron. Poluprovodn. Tekh. 27, 47 (1994).

[13] M. C. Hutley, Diffraction Gratings (Academic, London, 1982).

EFFECTIVE HOLOGRAPHIC RECORD ON THIN FILMS
OF CHALCOGENIDE SEMICONDUCTORS

V. Vlasov

Uzhgorod National University, Special Design Office "Quantum" Uzhgorod, 88000, Ukraine

In this work is presented the research on thin films of chalcogenide glassy semiconductors as the medium for relief holograms record. The optimization of photoresist has allowed for an an essential rise in sensitivity to light. $As_{50}Se_{50}$ photoresist composition on which above thousandfold chemical amplification of holographic record is achieved, was used. Diffraction gratings in range of spatial frequencies 600 - 2400 mm^{-1} are submitted. For natural light the magnitude of diffraction efficiency exceeds 70 - 80 % at measurements in autocollimator conditions. The probable cause of differences between continuous and pulse irradiation of thin films of chalcogenide vitreous semiconductors is discussed.

1. Introduction

The change of optical, physical and chemical properties of thin films of chalcogenide vitreous semiconductors (ChVS) under the influence of a band-gap irradiation is a subject of research during more than 30 years. One of the directions of such researches is the analysis of photoresistive properties   [1-4]. The materials from this class was investigated also as electron-beam [5] X-ray [6] and ion-beam resists [7]. As a result of actinic irradiation and subsequent chemical treatment, were obtained structures for microlithography, for the production of holographic diffraction elements, kinoforms and optoelectronic elements [1-9].

The photoresistive properties of the whole class of ChVS thin films were studied. Chemical increase of phase component of an optical record resulted into reduction of exposure necessary for maximum diffraction efficiency. This is equivalent to the increase of material sensitivity. The task to work out photoresistive process was solved not for all investigated structures [10]. A broad spectrum of the characteristics of such inorganic photoresists was obtained [1-4, 8-11]. However it is impossible to consider that the optimization of the photoresists of this type is reached.

The selection of structures for research as photoresists is connected, first of all with the value of photoinduced changes in optical constants. Usually the exposure of ChVS thin films to optical irradiation from a continuous source is investigated. There are few works that report the results of a pulse illumination of such registering medium [12-14]. The parameters of photoresists on the basis of ChVS after the pulse action were not considered by other authors.

The purpose of the present work was the research photoresistive properties for several compositions of thin ChVS films. As a result of the preliminary analysis for optimization the binary structure As-Se is selected. Two regimes of exposure were investigated: continuous and pulse ones. For both cases the reflective holographic diffraction gratings are obtained. In this work their parameters are presented. On the basis of our views on optical record mechanism in the thin ChVS films and available experimental data, the observed difference in sensitivity for a continuous and pulse exposure is discussed.

2. Experimental

For experiments thin ChVS films of several compositions were selected. The initial bulk glasses were synthesized in the vacuum-evacuated quartz ampoules. The thin films were produced by a thermal deposition in vacuum 10^{-3} Pa onto oxide glass substrates. For the production of holographic diffraction gratings the specially produced glass plates with high surface quality were used. The thickness during deposition was controlled by an interference method on a wavelength outside of area of ChVS sensitivity ($\lambda = 1.15$ μm). The uniformity of thickness was reached due to the planetary rotation of samples during deposition. The evaporation was from tantalum effusion cells. The velocity of evaporation was 50-70 Å/s. The composition of initial ChVS and vapour-deposited film was controlled by electron microprobe X-ray spectral analyses. The deviation for As-Se films did not exceed 2 at. %. The holographic diffraction gratings were recorded according to the symmetrical scheme of a double-beam interferometer. The flatness of registration of an interference pattern was set normal to bisectrix of angle between the light beams. In the result the sinusoidal distribution of an interference pattern was converted into a surface relief with a symmetrical profile. The continuous record was carried out on the two wavelengths of the Argon-ion laser (0.48 and 0.51 μm). For a pulse record the phosphate neodymium glass laser irradiation was used. The exposure was made by single-pulses with duration 40 ns on the wavelength 0.53 μm. Besides, the processes of optical record were investigated on wavelengths of He-Ne laser (0.63 μm) and Cu laser (0.51 μm) with pulse repetition frequency 9 KHz. In some cases the dye laser was applied and the wavelength range 0.45 - 0.60 μm was investigated.

In the work we used successive and simultaneous effect of optical irradiation of two wavelengths on one and the same film area. Thus the radiation with the greater wavelength was entered into a film with the help of prism coupling element [15,16].

3. Results and discussion

The maximum ChVS thin films etching selectivity of a number of compositions are given in the Table 1. The selectivity was determined as a velocity ratio of etching of the exposed and not exposed film areas. The exposure was carried out until saturation. All the presented photoresists in the selected conditions of processing by organic alkalis (water and aqueous-alcoholic solutions of amines) were negative.
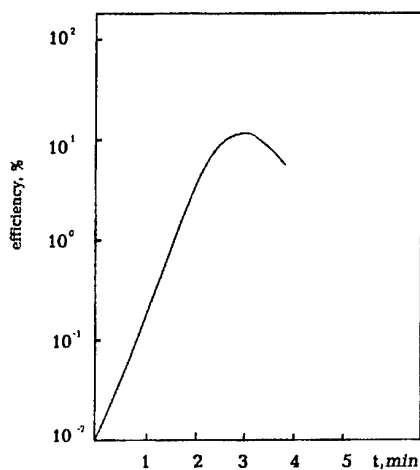

Fig. 1. Diffraction efficiency versus etching time in $As_{50}Se_{50}$ thin films. The best results were got on $As_{50}Se_{50}$ thin films.

Table 1. Experimental values of etching selectivity for some photoresistive ChVS Thin Films.

Composition	Selectivity
$Ge_{22}As_{20}Se_{58}$	5
$Ge_{25}As_{11}Se_{64}$	2
$As_{30}S_{70}$	25
$As_{40}S_{60}$	20
$As_{20}S_{80}$	4
$As_{30}Se_{70}$	5.3
$As_{50}Se_{50}$	60
$As_{40}Se_{60}$	9.3

The films of such composition under irradiation of He-Ne laser (0.63 μm) show considerable changes of optical constants [17]. The comparison of the results of the first record cycle and the subsequent ones demonstrates magnitude comparability of reversible and irreversible changes of optical constants [17]. At application of such ChVS film as a photoresist, the necessity for a preliminary annealing disappears, because both components give the contribution to resultant sensitivity. The selectivity of etching on the annealed film essentially decreases. On as-evaporated $As_{50}Se_{50}$ film the considerable strengthening of a diffraction grating recorded by irradiation of He-Ne laser is reached. In Fig. 1 is shown the dynamics of diffraction efficiency change during etching. The initial value of diffraction efficiency increased, and in a maximum it reached 18 %.

During recording under irradiation from shorter wavelength spectrum area, the sensitivity of the ChVS film increases, but the effective depth of light interaction with material, however, decreases. Therefore, characteristics of a usual amplitude-phase record at such transition is aggravated. At the use of photoresistive process the selectivity of etching of a surface amplitude-phase mask can compensate this drawback. Considerable increase of sensitivity of medium can be reached in this way. The reflective diffraction gratings were obtained in the field of spatial frequencies 600 - 2400 mm⁻¹. Samples by the sizes 200x200 mm are experimentally obtained. The energy density of an exposure was in the interval 0.01 - 0.03 J/cm². The smaller value corresponds to as-evaporated samples, for which the sensitivity drops as a result of relaxation processes [18].

In Fig. 2 and 3 is shown the spectral dependence of diffraction efficiency of reflective diffraction gratings obtained on $As_{50}Se_{50}$ thin films. The diffraction efficiency in the first diffraction order according to auto-collimation scheme [19] was measured. In Fig. 3 besides the results for natural light (curve 3), the values of diffraction efficiency for two polarizations of irradiation are shown: with an electric vector, directed normally (H–polarization, curve 1), and parallel (E–polarization, curve 2) to the grooves of a grating.

Fig. 2. First order diffraction efficiency of refractive holographic grating (spatial frequency 600 mm⁻¹) in As_{50} Se_{50} thin films versus wavelength.
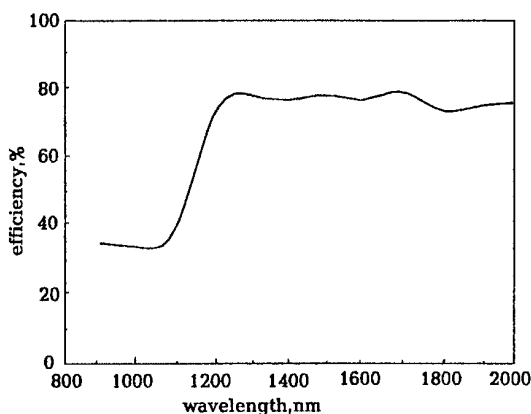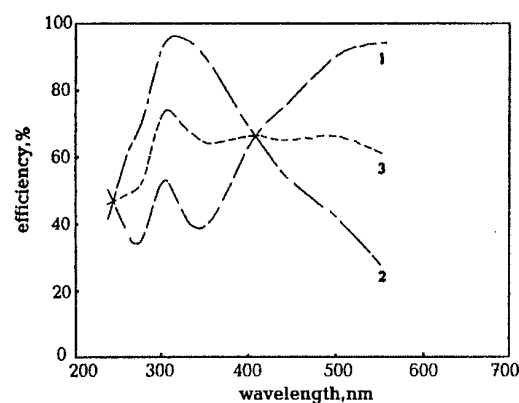
Fig. 3. First order diffraction efficiency of refractive holographic grating (spatial frequency 2400 mm⁻¹) in As_{50} Se_{50} thin films versus wavelength.

In the paper [19] it was shown, that the diffraction efficiency of a grating with a sinusoidal profile is maximum at the altitude of grooves equal 0.3 - 0.4 from the value of grating period.. Thus, if the depth of a relief makes 0.3 from the value of the period, the clearly seen maximum is watched in the field of low wavelengths. If the depth of relief makes 0.4 from the value of the period - broad plateau is seen [19]. All other analysed in the work [19] symmetrical profiles of grating grooves are characterized by sharper spectral maximums of diffraction efficiency. It is possible to conclude, that in all range of spatial frequencies the diffraction gratings with grooved profile, close to sinusoidal and optimum relief altitude, are obtained in $As_{50}Se_{50}$ thin films (see Fig. 2 and Fig. 3). The record of high frequency gratings (2400 mm^{-1}) was made on 0.48 μm wavelength, and the rest of gratings (600 and 1200 mm^{-1}) - on 0.51 μm wavelength of Argon-ion laser.

The maximum of diffraction efficiency of the obtained diffraction gratings in natural light reached 70 - 80 %. Chemical strengthening and transition to record in smaller wavelengths area allowed to increase essentially the medium sensitivity.

Earlier we conducted researches of temperature relations of photoinduced changes of optical constants and effect of thermo-optical erasure on ChVS thin films [17,18]. The conclusion was drawn, that under the influence of actinic light the definite state that corresponds to conditions of exposure and temperature is established each time in the material. The transition between any such states can be carried out by temperature variation of recording media. There can be any direction of transition: additional record, if the medium temperature decreased, or erasure by the same irradiation, if temperature of ChVS thin film increase. So, in such materials during exposure aiming for record the opposite process, erasure, takes place. The saturation of photoinduced changes occurs, when processes of a record and the erasures balance each another. The equilibrium can be shifted in any direction.

Later, in the work [12], the increase of sensitivity of ChVS thin films was revealed for a pulse exposure. Laser irradiation of 40 ns pulse duration was used. It was supposed that if pulse duration and pulse frequency are small enough, it is possible to separate in time the processes of record and erasure. After each pulse, the medium has time to pass into the state, when the opposite transition becomes impossible. It corresponds to our suppositions [17,18]. In Fig. 4 are shown the results regarding the effect on $As_{40}S_{60}$ thin films of Cu laser irradiation and the results obtained at an exposure by continuous Argon ion laser irradiation. The sensitivity and the level of saturation dependence on character of exposure (continuous or pulse) and intensity exposure is studied.

The competition of record and erasure processes is revealed in the effect known under the name "stopping - effect" [15,16].

Intensity of the mode (I) distributing in the ChVS thin film waveguide, in this case $As_{20}S_{80}$ decreases, when the part of a waveguide track is exposed to actinic irradiation (Fig. 5, curve 1) After external exposure stops the intensity of a waveguide mode is restored. The curves 2 - 6 in Fig. 5 correspond to different moments of such exposure ceasing. The greatest mode intensity damping was reached, when the external exposure preceded to the excitation of a waveguide mode. Mode intensity was restored completely, if under mode influence the external exposure ceased (Fig. 5, curve 8), or was established on a level corresponding to simultaneous effect of the both factors (Fig. 5, curve 7).

It is enough to compare saturation state on curves 1 and 8 in Fig. 5. This is equivalent to separation of processes of a record and erasure on two wavelengths. If pulse exposure and the subsequent chemical treatment is applied, the energetic gain will be considerable. In the work the exposure was done by a single-pulses with duration 40 ns on a wavelength of Phosphate neodymium glass laser (0.53 μm). The holographic diffraction gratings formed in the range of spatial frequencies 100 - 2400 mm^{-1}. Diffraction efficiency of the got elements was 45 % in the first diffraction order after metallization a grating surface .The exposure was 3×10^{-3} J/cm^2.

With the purpose to define the extreme parameters of investigated photoresists the range of the wavelength 0.45 - 0.60 μm of a recording radiation was studied. The exposure was done by single-pulses with duration 10 ns by the Dye laser. It is found out, that the latent image can be developed already at 2×10^{-4} J/cm^2. Exposure and the level of chemical strengthening were determined as a function of a holographic optical element. Thus, they can be varied in a wide range.

Apart from periodic structures such as reflective diffraction gratings in the work other types of the relief - phase holograms were obtained for usage as master matrixes in processes of mass replication of the holograms on the plastic films.

EXPOSURE (E,J/cm²)
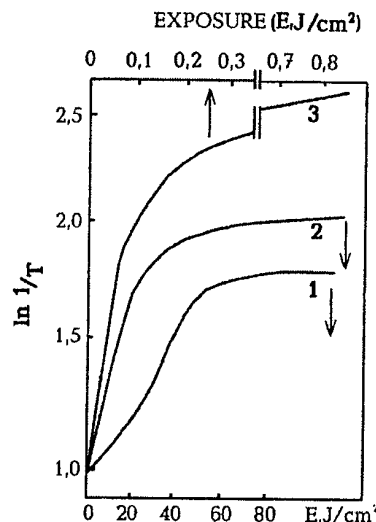
Fig. 4. Characteristic curves of the sample As₄₀S₆₀ thin film under band-gap irradiation 1, 2 – Argon ion laser irradiation 0.2 W/cm² and 1.0 W/cm², respectively.: 3 – Cu laser irradiation, 4x10³ W/cm².
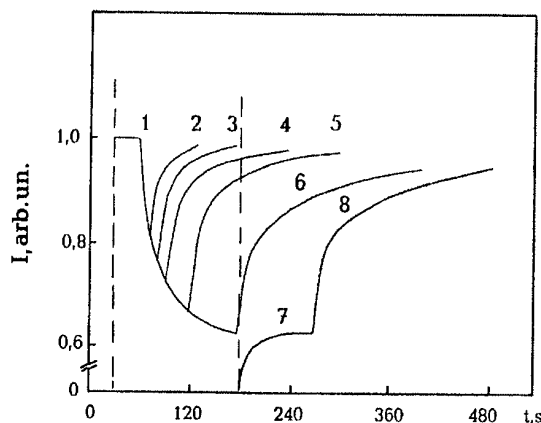
Fig. 5. Light-operated waveguide in As₂₀S₈₀ thin films: dynamics of switch and recovery.

4. Conclusions

In this work the prospects of usage As₅₀Se₅₀ thin films is shown. Such photoresist films is characterized by low exposure both in continuous, and in a pulse regime of a record and, simultaneously, high operational parameters.

On As₅₀Se₅₀ thin films the different kinds of holographic optical elements and holograms are realised with high diffraction efficiency.

The experimental data confirm the supposition about a competition of processes of a record and erasure during exposure of the thin ChVS films, that allows to vary the sensitivity of such materials.

The controlled vacuum deposition, repeatability and uniformity of parameters on the film surface, and the absence of deformation are characteristic to organic photoresists during the processing, and are the padding factors, which are important for future applications of the chalcogenide photoresists.

References

[1] S. Keneman, Thin Solid Films, **21**, 28 (1974).
[2] Y. Utsugi, S. Zembutsu, Appl. Phys.Lett., **27**, 508 (1975).
[3] S. Zembutsu, Y. Utsugi, T. Sakai,Optics. Comm., **17**, 28 (1975).
[4] A. Stronski, M. Vlček, P. Shepeliavyi, et al., Semicond. Phys., Quantum Electron.& Optoelectron., **2**, 111 (1999).
[5] T. Shuhara, H. Nishihara, IEEE J. Quantum Electron., **QE-22**, 845 (1986).
[6] K. Saito, Y. Utsugi, A. Yoshikawa, J. Appl., Phys. **63**, 565 (1988).
[7] H. Lee, H. Chang, J. Korean Phys. Soc., **32**, 171, (1998).
[8] A. Klimin, E. Pen, V. Remesnik, Avtometriya, 1, 70 (1979).
[9] S. Kurita, Y. Seto, T.Yayi, Opt. and Quantum Electron., **12**, 179 (1980).
[10] V. Koronchevich et al., Avtometriya, 1, 4 (1985).
[11] R. Kunzke, Lieemann, J. Inf. Rec. Mater., **14**, 395 (1986).
[12] Yu. Bykovskii, A. Maimistov, A. Mironos, V. Smirnov, Quantum Electronics, **9**, 786 (1982).
[13] J. Teteris, Ja. Ekmanis, Quantum Electronics, **5**, 1611, (1978).
[14] Y. Aoyagi, Y. Segawa, S. Namba et al., Phys. Stat. Sol. (a), **67**, 669 (1981).
[15] M. Kikushi, A. Matsuda, Proc. 6th Int. Conf. Amorphous and Liquid Semicond., Leningrad, USSR, p. 35, 1976.
[16] V. Vlasov, A. Kikineshi, D. Semak, D. Chepur, Ukranian J. Phys., **22**, 1199 (1977).
[17] V. Vlasov, D. Semak, D. Chepur, Izvestiya Vuzov, Ser. Phys., 12, 48 (1978).
[18] V. Vlasov, V. Krishenik, K. Lesik, G. Suran, Proc. Non-crystalline Semicond.-89, Uzhgorod, v.II, p. 201, 1989.
[19] R. Gerke, I. Golubenko, T. Dubrovina, G. Savitsky, Optics and Spectroscopy, **58**, 1201 (1985).

EVANESCENT – WAVE RECORDING IN VERY THIN LAYERS

S. Sainov, J. Dikova[a], R. Stoycheva-Topalova[a]

Bulgarian Academy of Sciences, Central Laboratory of Optical Storage and Processing of Information, 1113 Sofia, P.O.Box 95, Bulgaria
[a]Bulgarian Academy of Sciences Central Laboratory of Photoprocesses, 1040 Sofia, Bulgaria

The theoretical background of optical holographic recording in very thin films is given. The interference fringes are stored by surface – propagating evanescent waves. Such waves are created by the total internal light reflection (TIR). The experimental verification of the theory is made. The holographic grating with 454nm period has been recorded in 29, 39 and 74 nm thick As$_2$S$_3$ films. The diffraction efficiency dependence on the time is investigated. The polarization behavior of TIR surface holograms is similar to that of the thick Bragg gratings. The possible applications of this holographic recording are also discussed.

1. Introduction

Arsenic trisulfide (As$_2$S$_3$) films possess interesting optical characteristics that enable them to be used as holographic storage media. For the first time Keneman [1] has reported such grating recording in evaporated As$_2$S$_3$ films. The diffraction efficiency (DE) of 80% is obtained in 10 μm and several percent – in 2μm thick film.

Later on, Japanese scientists using waveguide technique [2] have successfully made the recording in 250 nm As$_2$S$_3$ film. In thinner films the holographic recording is possible using the total internal reflection (TIR) method, first reported by Stetson [3] The recording is realized by the interference between TIR reference wave and plane object wave. Earlier, we have demonstrated TIR grating recording in 70 nm As$_2$S$_3$ film [4].

In this paper we present for the first time the TIR holographic recording in 29, 39, and 74 nm evaporated thin As$_2$S$_3$ films.

We first describe the principle of the surface TIR recording in thin layers. Then, we show experimental results involving the exposure dependence on DE and polarization characteristics of the recorded gratings. Some possible applications of this holographic recording are finally discussed.

2. Theoretical background

Let us consider the interference between plane wave,

$$E_p = E_{0p}.\exp\left(i\frac{2\pi}{\lambda_0} n_1 z \right)$$

and TIR referent wave

$$E_{TIR} = E_{0TIR}.\exp\left(-\frac{z}{z_0} \right).\exp\left(i\frac{2\pi}{\lambda_0} n_1 x.\sin\varphi \right)$$

as it is shown in Fig.1.

The angle of incidence φ condition for TIR at the interface between optically denser first medium with refractive index n_1 and second with n_2 is $\varphi > \arcsin\left(\dfrac{n_2}{n_1} \right)$ and the characteristic length z_0, where electric field amplitude E falls to e^{-1} of its value is given by

$$z_0 = \frac{\lambda_0}{2\pi n_1 \left(\sin^2 \varphi - n_{21}^2\right)^{1/2}}$$ (1)

λ_0 is the vacuum wavelength, $n_{21} = \dfrac{n_2}{n_1}$
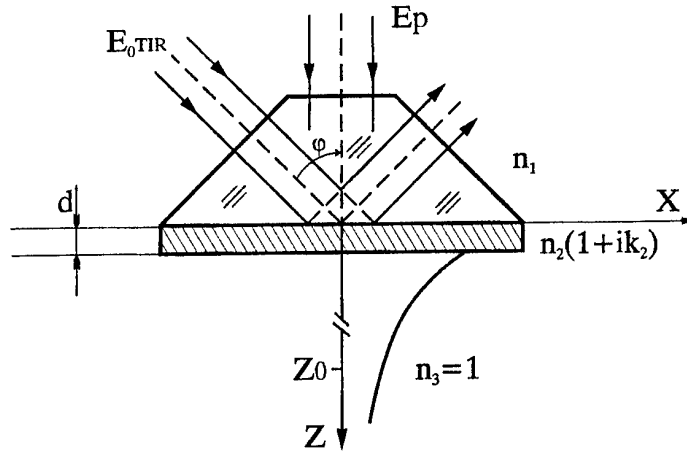
Fig. 1. Optical configuration for TIR surface holographic recording with an evanescent reference wave.

Near the reflecting surface $z = 0$ the interference pattern is described by

$$E_{12} = E_{0p=}^2 + E_{0TIR}^2 \cdot \exp\left(-\frac{2z}{z_0}\right) + 2E_{0p}E_{0TIR}\exp\left(\frac{-z}{z_0}\right)\cos\Phi$$ (2)

with the phase $\Phi = 2\pi\left(\dfrac{n_1 x \sin\varphi}{\lambda_0} - \dfrac{z n_2}{\lambda_0}\right)$

If the second, optical recording medium is much thinner that z_0, i. e. $d \ll z_0$ the interaction between the interference pattern and the recording medium (with complex refractive index $n_2^* = n_2(1 + i\kappa_2)$) can be described, following Harrick [5], with a "effective thickness", given by

$$d_e = \frac{4 d n_2 n_1 \cos\varphi}{\left(n_1^2 - 1\right)}$$ (3)

It is very interesting that, in the case when $\dfrac{2\pi d n_1}{\lambda_0} \ll 1$ and $\kappa_2 \ll 1$ the TIR does not depend on the refractive index of the second, recording medium, that can be higher than the refractive index of the first medium. In this case, the TIR condition is $\varphi > \arcsin\left(\dfrac{1}{n_1}\right)$. For $n_1 = 1.5$, $n_2 = 2.5$, and $\varphi = 45^0$ we have $\left(\dfrac{d_e}{d}\right) = 8.5$ and the plane wave – recording medium interaction can be neglected. In this case, the interference term can be written as

$$E_{12} = E_{0p=}^2 + E_{0TIR}^2\left(1 - \alpha d_e\right) + 2E_{0p}E_{0TIR}\left(1 - \alpha d_e\right)\cos\Phi$$ (4)

here the phase Φ and the absorption coefficient α are, respectively $\Phi = \dfrac{n_1 x \sin\varphi}{\lambda_0}$ and $\alpha = \dfrac{4\pi n_2 \kappa_2}{\lambda_0}$. The grating period Λ over X – axis is

$$\Lambda = \frac{\lambda_0}{n_1 \sin\varphi}$$ (5)

Supposing $E_{0p} = E_{0TIR} = E_0$, the relation (4) can be written as $E_{12}^2 = E_{12(\alpha=0)}^2(1 - \alpha d_e / 2)$, where

$$E^2_{12(\alpha=0)} = 4E_0^2 \cos^2 \pi n_1 x \sin \varphi / \lambda_0 \qquad (6)$$

3. Results and discussion

3. 1. Sample preparation

The experiments are performed with as – deposited thin films of an As_2S_3 having thickness between 5 and 75 nm. The samples are prepared in the Central Laboratory of Photoprocesses, Bulgarian Academy of Sciences. The films have been obtained by a vacuum deposition of high purity As_2S_3 at a residual pressure in the order 6.10^{-4} Pa. A deposition rate of 0.1 nm/s has been achieved at an evaporation temperature of 240°C. The film thickness is measured by Talystep profilograph, Code 112/1037 M-S, produced by Rank Taylor Hobson Ltd.

3. 2. Optical recording and measurements

The optical arrangement is shown in Fig. 2. Ar^+ - ion laser has been used as a light source. The beam intensities are adjusted for an optimal 1 : 1 ratio (10 mW/cm^2 each) with a beam splitter (BS) and gray filter (GF).
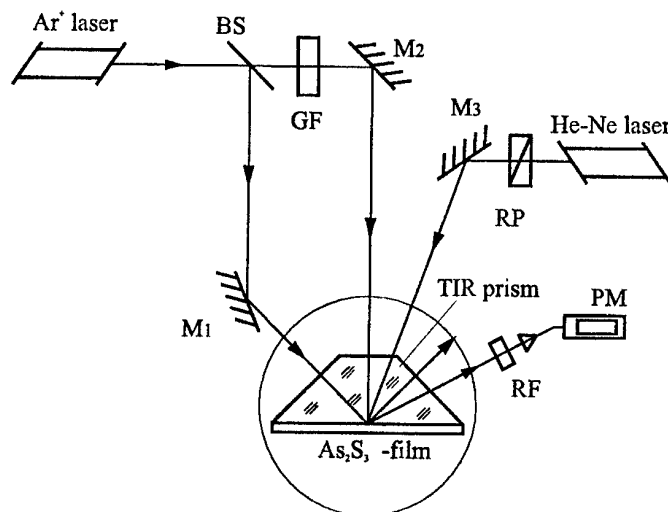
Fig. 2. Optical arrangement for evanescent holographic recording.

Our TIR prism is made of light crown K – 8 with refractive index $n_1 = 1.522$ for $\lambda_0 = 488$nm. The angle of incidence φ is 45°, to which grating period $\Lambda = 454$nm, or spatial frequency 2200line/mm is corresponded. The polarization of the monitoring He – Ne laser is changed from s to p – polarization with rotator (RP). The diffraction efficiency is measured with an Ealing 911 powermeter through a red filter (RF).

The exposure time is changed in 0.5 – 20s region, that correspond to 10 – 400mJ/cm^2 exposure. In Fig. 3a the diffraction efficiency dependence on the exposure is shown for three different thickness of the recording medium – 29, 39 and 74nm. The best result is obtained for 39 nm thin film, where 0.15% efficiency has been measured. The recorded grating in As_2S_3 – Cr film is shown about three times lower efficiency, as it is clear from Fig. 3 – b. The observed shift to higher exposures is possible to be explained with the Cr layer, acting as a density filter.

The polarization properties of the recorded TIR surface gratings are similar to that of thick Bragg holograms. The theoretical treatment of Gasvik [6] ^{gives} following simple relation

$$I(\Theta)/I_s = (1-B)\cos^2 \Theta, \text{ where } B = I_p / I_s \qquad (7)$$

The polarization dependence of the diffracted intensity $I(\Theta)$ is shown in Fig. 4. The solid curve represents the theoretical calculation after (7) for thick Bragg grating. The azimuth angle of 0° corresponds to s – polarization and angle 90° – to the p – polarization. The square points are measured

values with the accuracy of 5%. Within this accuracy limit good agreement between experiment and calculation is observed.
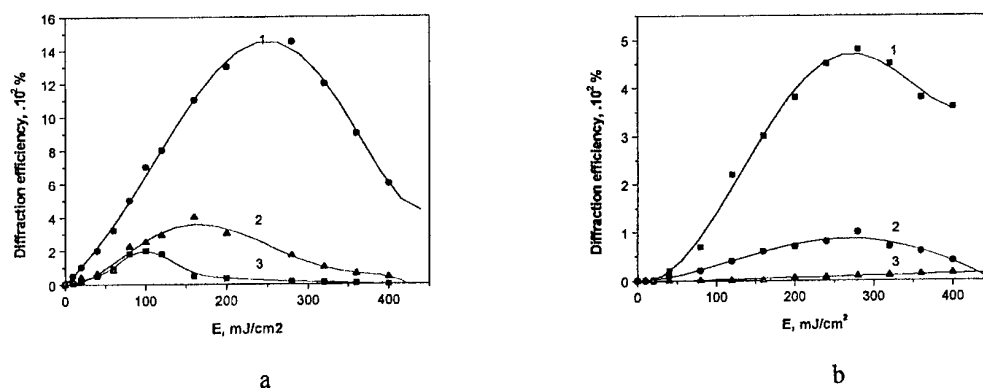
Fig. 3. The exposure dependence of the diffraction efficiency, recorded in: a) – As_2S_3 film;
b) – As_2S_3 – Cr film. The corresponding thickness are: 1- d = 74nm; 2 – d = 39nm;
3 – d = 29nm.
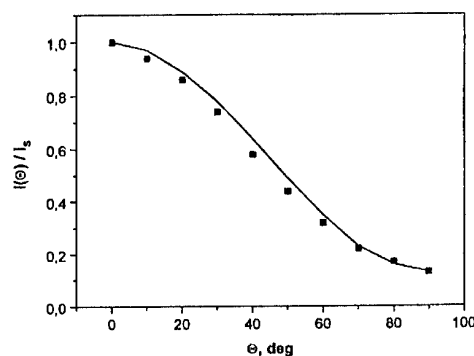
Fig. 4. The polarization azimuth dependence on the normalized diffraction intensity.

4. Conclusions

We have demonstrated for the first time a surface holographic recording in chalcogenide glass using as an optical storage medium. Very thin evaporated As_2S_3 films have been used for its large photo - induced refractive index change. The recorded TIR holograms have shown full analogy to the thick Bragg gratings.

The independence of the TIR from the refractive index of the optical storage medium is also shown which is very important for the future applications of the TIR holographic grating techniques for surface investigations. Such recording possesses also potential applications in near – field optics, submicrometer lenses, optical lithography, etc.

References

[1] S. Keneman, Appl. Phys. Lett., **19**, 205.(1971).
[2] T. Suhara, H. Nishihara, J. Koyama, Opt. Communs., **19**, 353 .(1976).
[3] K. Stetson, Appl. Phys. Lett., **11**, 225. (1967).
[4] S. Sainov, R. Stoicheva, Pl. Markovski, Kv. Electron., **7**, 641 (1980) (in Russian).
[5] N. J. Harrick, Internal Reflection Spectroscopy, Interscience, N.Y., p. 50. 1967.
[6] K. Gasvik, Optik, **39**, 47, 1973

HOLOGRAPHIC RECORDING IN NANO-SIZED As₂S₃ FILMS

S. Sainov, V. Sainov, J. Dikova[a]

Central Laboratory of Optical Storage and Processing of Information,
Bulgarian Academy of Sciences, 1113 Sofia, POBox 95, Bulgaria
[a]Central Laboratory of Photoprocesses, Bulgarian Academy of Sciences, 1040 Sofia, Bulgaria

The diffraction gratings in 10, 15 and 20nm thick As₂S₃ films are holographically recorded with a totally reflected reference wave. The maximum measured values of the diffraction efficiency are 0.0005%, 0.004% and 0.007%, respectively. The exposure dependence on the diffraction efficiency is investigated. Despite of the relatively low efficiency, we succeed in the focal plane quasi-Fourier USAF test target holographic recording and reconstructed.

1. Introduction

It is well known that chalcogenide glasses are widely used as holographic storage media [1]. For example, thick As₂S₃ films exhibit large photoinduced changes of its optical characteristics essential for the optical recording. The value of the refractive index change $\Delta n = 0.13$ has been reported in [2]. This enable achieving the diffraction efficiency value up to 80% for the holographic grating, recorded in 10μm thick As₂S₃ films [3] even in one of the first experiments [3]. In the same publication Keneman reports several percent efficiency in 2μm thick film. The reason is that the photoinduced refractive index change Δn rapidly decreases with the thickness diminishing and for 970nm thick As₂S₃ films is 0.056 [4]. On the base of spectrophotometric investigations has been established that the absorption coefficient increasing (photodarkening) disappears for thinner than 50nm As₂S₃ films [5]. On the strength of the Kramers-Kroning relations, could be expected that it is the lower limit for photoinduced changes caused by usual, plane or focused homogeneous waves.

For the rapidly developping field of nanotechnology [6] is very useful not only the application of the holographic grating measuring methods [7], but also for the nano-scale information recording. Evidently, a new optical method has to be used in order to record holographic (interference) information in nano-sized photosensitive media. The application of surface propagating evanescent waves, as it has proposed for the first time by H. Nassenstein enable the holographic recording in a very thin layer near the recording medium surface [8]. Recently, one of the authors has reported a holographic recording in 39nm thick As₂S₃ films, using a total internal reflection for the creation of the evanescent reference wave [9].

In this paper we report a further development of this method illustrated with holographic recordings in 10, 15 and 20 nm thick As₂S₃ films. The exposure dependence of the diffraction efficiency is investigated, showing maximum values of 0.0005%, 0.004% and 0.007%, respectively. The measuring are made with a He-Ne laser at 633 nm. We have recorded also quasi-Fourier hologram of the USAF test target in 20 nm thick As₂S₃ films, using a random phase mask.

2. Experimental

2.1 Sample preparation

The experiments are performed with as-deposited a- As₂S₃ films having thickness' 10, 15 and 20nm. The films are obtained by vacuum condensation of high purity As₂S₃ into planetary rotating substrates in a standard vacuum unit with an oil diffusion pump maintaining residual pressure in the

order of $2 - 4.10^{-4}$ Pa. A resistively heated Ta crucible having a special design is used. It allowed the sublimation and evaporation of As_2S_3 without local overheating thus preventing non-desirable effects of thermal decomposition. The used substrates are pre-cleaned Ca-Na silicate glass plates. The deposition rate is 0.1nm/s at an evaporation temperature of 240°C. The thickness of the growing films and the deposition rate are continuously measured using a quartz crystal monitor MIK1 FFV. The sample thickness is additionally controlled by a surface profile recorder Talystep Rank Taylor Hobson, Code 112/1037 M-S.

2.2. Holographic recording

The holographic recording is made with the evanescent reference wave, created by the total internal reflection (TIR). This is the case, when the later approaches the reflecting interface from the denser medium with the refractive index n_1. We will consider the case of normally polarized to the incidence plane waves. If E_o is an amplitude of the falling plane wave with vacuum wavelength λ_o, the electric field amplitude falls of exponentially in TIR with the distance z into the second, rarer medium as

$$E = \frac{2E_o n_1 \cos\varphi}{\left(n_1^2 - 1\right)^{1/2}} \exp\left(-z/z_o\right) \qquad (1)$$

The TIR condition is the incident angle φ to be greater than the critical angle value φ_c $=arcsin(1/n_1)$. In (1) z_o is the penetration depth, characterizing the decay into the second medium (air).

$$Z_o = \frac{\lambda_o}{2\pi\left(n_1^2 \sin^2\varphi - 1\right)^{1/2}} \qquad (2)$$

The interference between this evanescent and object plane wave with the same amplitude is described by

$$Ie, p(x,z) = \frac{4E_o^2 n_1 \cos\varphi}{\left(n_1^2 - 1\right)^{1/2}} \exp\left(-z/z_o\right)\cos 2\pi n_1\left(x\sin\varphi - z\right)/\lambda_o \qquad (3)$$

If the recording medium thickness d is smaller than the penetration depth, as it is pointed out by Harrick [10], the TIR is not influenced by its refractive index. In this case the interference is confined near the reflecting surface, i.e.

$$Ie, p(x) = \frac{4E_o^2 n_1 \cos\varphi}{\left(n_1^2 - 1\right)^{1/2}} 2\pi n_1\left(x\sin\varphi\right)/\lambda_o \qquad (4)$$

The necessary condition is given by

$$d < z_o < \frac{\lambda_o}{2\pi\left(n_1^2 - 1\right)^{1/2}} < \frac{\lambda_o}{20} \qquad (5)$$

The film thickness could be less than 25nm for grating recording with 488nm wavelength.

3. Results and discussion

The microstructure of the obtained As_2S_3 films is studied by conventional electron microscopic methods. For the purpose metal-carbon replicas from the films surface are prepared by consecutive vacuum deposition of Pt and C. The replicas observation are performed under a transmission electron microscope JEOL, JEM 100 B.

Fig. 1 shows transmission electron micrographs of Pt/C replicas from the surface of a- As_2S_3 films with thickness 10nm (a) and 20nm (b). As it is illustrated in Fig. 1(a) the As_2S_3 film is built up of individual grains separated by well -defined intergrain boundaries. Simultaneously, the halo ring of the electron diffraction is an evidence for the amorphous structure of the films. From the micrograph in Fig. 1(b) a slight increase of the mean grain size is observed for the thicker sample. These structural peculiarities of the samples studied have been already observed in a previous investigation [11].
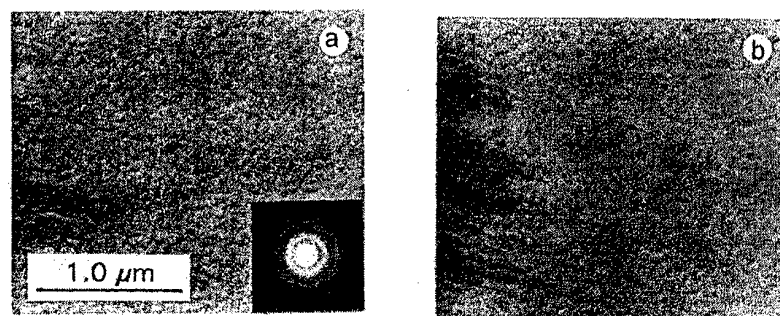
Fig. 1. Transmission electron micrograph of the samples: a-10nm thick film; b-20nm thick.

The experimental set up is sketched in Fig. 2. We have used Ar^+ laser as a light source. The initial intensity is $20mW/cm^2$. For gratings recording the intensity ratio 1:1 is used in order to achieve maximum interference visibility. The object beam after the beam splitter (BS) is incidence normally on the TIR prism (P) with the refractive index 1.522. The glass substrate with the deposited As_2S_3 film is attached at the prism by microscopic oil. When the USAF resolution target is used as an object, the object beam (o) is filtered and expanded with lenses L_1 and L_2. For a noise reduction a random multilevels phase mask (Ph) is used. Reconstructed image or diffracted intensity is monitored through red filter (IRF) with CCD-camera or powermeter (PM). Unexpanded reference wave (r) is falling under incidence angle 45° on the reflecting surface. The critical angle is 41.1° and the penetration depth according (2) is 195nm. A He-Ne laser reconstructs the holographic recording at 633nm.
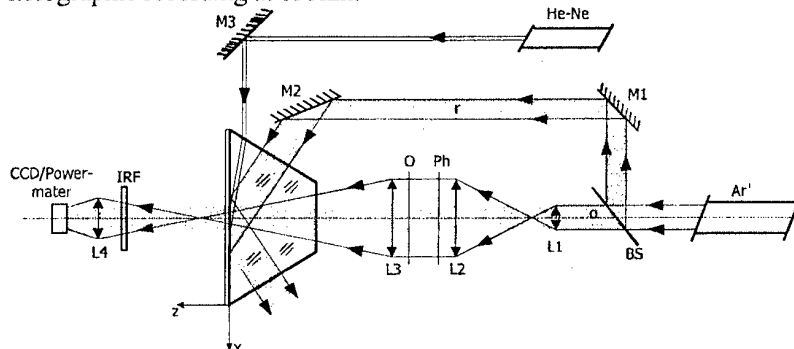
Fig. 2. Optical arrangement for evanescent-wave holographic recording: L-lences; M-mirrors; BS-beam splitter; Ph-phase mask; O-object; IRF-interference red filter.

The exposure dependence of the diffraction efficiency is shown in Fig. 3. The maximum measured values for 10, 15 and 20nm thick As_2S_3 films are 0.0005%, 0.004% and 0.007%, respectively.
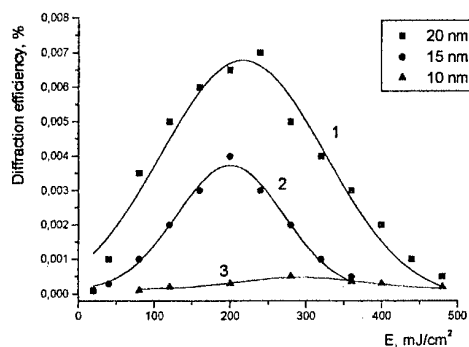
Fig. 3. Exposure dependence of the diffraction efficiency: 1-for 20nm thick As_2S_3 film; 2-for 15nm; 3-for 10nm.

After reaching maximum, the diffraction efficiency is diminishing due to overexposure like in conventional holographic case. It should be noted that optimum exposure is in the range 200-300mJ/cm^2. It is interesting to compare our results with the exposure dependence of the diffraction efficiency of ordinary holographic gratings, recorded in thin As_2S_3 films with Ar^+ laser at 488nm. To the best of our knowledge, for the smallest thickness of 350nm the optimum exposure is 7.6J/cm^2 [12]. In the first experiment, performed in 1969, this value is 3.0J/cm^2 for 450nm thick As_2S_3 films [13]. In recently published paper [14] the authors reported that the dynamic diffraction signal has maximum at 2J/cm^2 for 1100nm thick As_2S_3 film. Obviously, the optimal exposure decreases with the thickness increasing for holographic gratings, recorded with plane waves in the film's volume. On the other hand, in holographic grating recording with surface propagating reference wave, the maximum signal is obtained at lower exposure. Despite of the fact that the optical path of the monitoring red wave is about 3mm, the small photoinduced refractive index change is the main reason for the observed low efficiency. It is most likely that it is due to the adhesive forces, essential in nanoscale thickness. Relatively good signal to noise ratio, estimated roughly to be better than 20:1 enable us in recording of more complicated object. For that purpose we have used the USAF resolution target. The quasi-Fourier hologram is recorded near the focal plane with an evanescent reference wave. In Fig. 4 is shown the reconstructed image of the holographic recording in 20nm thick As_2S_3 films. A random phase mask (Ph) in the object plane is used for diminishing the influence of the recording medium limited dynamic range.
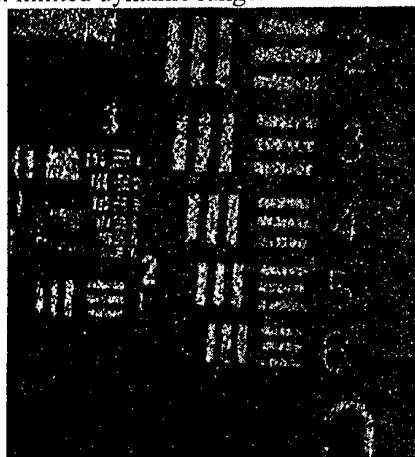
Fig. 4. Reconstructed image of the USAF target.

4. Conclusions

Using surface-propagating evanescent waves it is possible to record holograms in very thin photosensitive media with refractive index higher than input prism/substrate one. This enlarges the recording media limits for the nano-scale optical storage. Another possible application of these holograms is for grating technique that can be used as a sensitive method of investigations in nanotechnology.

References

[1] K. Schwartz, The physics of Optical Recording, Springer-Verlag, Berlin (1993).
[2] K. Tanaka, Y. Ohtsuka, J. Appl. Phys., 49, 6132 (1978).
[3] S. A. Keneman, Appl. Phys. Lett., 19, 205 (1971).
[4] Y. Ohmachi, T. Igo, Appl. Phys. Lett., 20, 506 (1972).
[5] K.Tanaka, Sh. Kyohya, A. Odajima, Thin Solid Films, 111, 195 (1984).
[6] I. Malsch, Nanotechnology, 10, 1 (1999).
[7] J. Wang, J. Xia, J. Phys. Chem., 96, 190 (1990).
[8] H. Nassenstein, Phys. Lett., A28, 249 (1968).
[9] S. Sainov, R. Stoycheva-Topalova, J. Opt. A: Pure Appl. Opt., 2, 117 (2000).
[10] N. J. Harrick, Internal Reflection Spectroscopy, Interscience Publishers, New York (1967).
[11] N. Starbov, K. Starbova, J. Dikova, J. Non-Cryst. Solids, 139, 222 (1992).
[12] T. How, M. Chang, Appl. Opt., 18, 1753 (1979).
[13] R. Brandes, F. Laming, A. Pearson, Appl. Opt., 9, 1712 (1970).
[14] T. Galstyan, J. F. Viens, A. Villeneuve, K. Richardson, M. Duguay, J. Lightwave Technol., 15, 1343 (1997).

RESEMBLANCE OF LASER LIGHT AND ELECTRIC FIELD INFORMATION RECORDINGS ON CHALCOGENIDE GLASSY SEMICONDUCTORS

K. D. Tsendin, E. A. Lebedev, Young-Ho Kim[a], In-Jong Yoo[a], E. G.Kim[a]

A. F. Ioffe Physico-Technical Institute, St. Petersburg, Russia
[a]The University of Suwon, San 2-2, Wawoo-Ri, Bongdam-Myun, Whasung-Kun, Kyunggi-Do, Korea

It is shown that both the effect of laser pulses and electrical pulses, have a thermal basis in the chalcogenide glasses.

1. Introduction

One of the most known reversible memory effect in chalcogenide glassy semiconductors (CGS) is associated with a reversible glass-crystal phase transition. In contrast to the photo-structural effect, which is associated with a reversible structural changes between two metastable disordered glassy states [1], the glass-crystal phase transition in CGS can be initiated and reversed not only by power light but by an electrical voltage also. These facts give us a principle opportunity to combine electric field and laser light pulses for information recording processes in CGS.

The present paper is devoted to peculiarities of information recording based on glass-crystal phase transition in CGS. We discuss the differences and resemblances of the information recording by laser light and electrical voltage pulses. It is shown that recordings based on the reversible glass-crystal phase transition are similar for optical and electrical cases and the main mechanism of phase transition is determined by thermal heating.

2. Experimental details

For the optical recording investigations we have used $Te_{81}Ge_{15}As_4$ films with thickness L = 0.15-0.3 μm prepared by vacuum deposition on a glass substrate. Chalcogenide glassy semiconductors of this and similar compositions with good crystallization properties show a reversible glass-crystal phase transition and find application in electrical and optical memory cells [2]. Argon laser pulse radiation with wavelength $\lambda = 0.51$ μm, time duration $\tau = 1\text{-}0.2 \ 10^{-6}$ s and power up to the 140 mW was used. The laser beam focused on the film surface created a spot with linear dimension ~5-6 μm. The result of the irradiation was controlled by measuring the transmittance of the weak probe laser light beam with $\lambda = 0.63$ μm focused on the spot, on which the recording power beam was incident, and also by subsequent inspection with transmission microscope. Two sets of samples were used for optical recording.

The first set consists of fresh, as-grown glassy films. For these films we determined the pulse power W_a and W_b needed for ~30% and ~ 60% decreasing of transparency. These values are depicted in the Fig. 1A by bars "a" and "b" and will be used for comparison with thermal induced darkening. It is known that thermal darkening originates due to shift of edge of fundamental optical absorption to the long wavelength when glass-crystal phase transition occurs [3].

The second set consists of films that have been subjected to heat treatment at the temperature ~ 540 K, which slightly exceeds the crystallization temperature ~500 K for bulk samples [4]. Full crystallization have been determined from an approximately ~ 90% decreasing in the transmission of the probe light. The onset of glass-crystal transition occurs for thin films due to thermal heating up to only ~350 K and this partly crystallized state corresponds to ~30% decreasing of transparency [5]. A level of 50-60% darkening was achieved for our CGS films by thermal heating up to temperature ~490-500 K which is approximately equals to that one for the bulk samples.

For the electrical voltage pulses recording we used the set of samples with planar geometry. The samples were thin layers of the same $Te_{81}Ge_{15}As_4$ composition, with thickness L = 0.5-1.0 μm and the area size of order 10^{-5} cm^2, which were obtained by evaporation in a vacuum onto Pyroceram substrates with electrodes width l = 10^{-3} cm and gap d = 10^{-2} cm between electrodes. The electrode material was a gold and a thin layer of SiO_2 was applied on CGS films for encapsulation. The as-grown glassy films were subjected to treatment at a temperature of ~500 K for 0.5-1 hour in the same manner as films from the second set used for optical recording. As a result of the treatment the films transformed into the polycrystalline state and their resistance decreased from 10^5 Ω to10^2 Ω.

3. Results and discussion

The optical recording case

For the thermally crystallized films, i.e. for the films from second set, which underwent thermal annealing at ~540 K, we determined, at different τ, the minimum pulse power W_1 needed for hole burning and pulse power W_2 which bleached the film twice as a result of reversed partial amorphization. The dependencies of $W_1(\tau)$ and $W_2(\tau)$ are shown in Fig. 1A. The most important feature of these dependencies is their closeness in the region τ> 10 μs and significant differences for τ approximately less than 1 μs. Let us estimate laser light heating temperature in the region τ> 10 μs. All τ from this region exceed the thermal relaxation time τ_r which is equal ~0.3 μs for L=0.3 μm. Then one may use a steady state approximation W = k(T-T$_0$), where k is external heat transfer factor, T is the temperature of heated spot in a homogeneous approximation and T$_0$ is ambient temperature. From this we obtain W_1/ W_a = (T$_1$-T$_0$)/(T$_a$-T$_0$). For hole burning the temperature T$_1$ must be equal or exceed the melting temperature T$_m$ which equals to ≈ 650 K for bulk CGS under study. Then for $W_1/$ W$_a$ ≈7 (see Fig. 1A) and T$_0$ = 300 K one obtains T$_a$≈350 K. This temperature is very close to the temperature 350 K needed for crystallization initiaton due to pure thermal annealing [5].
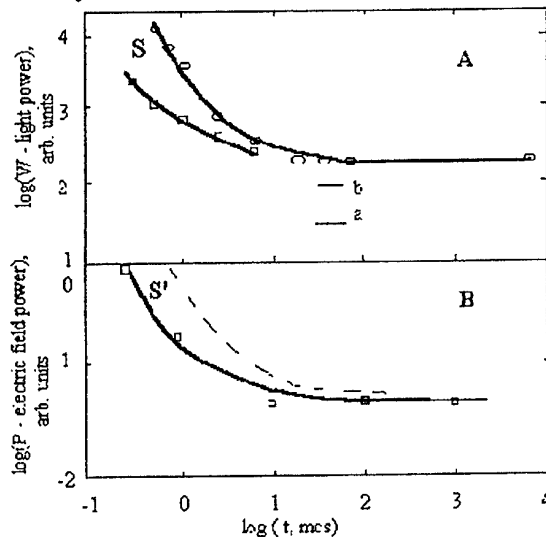
Fig. 1. Pulse power versus pulse length.
A - Laser light pulse recording for films thermally annealed at the ~540 K. The minimum hole burning power W_1 (circles) and the minimum power leading to a twofold increasing in the transmittance W_2 (squares). The horizontal bars labeled "a" and "b" correspond to a decrease in the transmittance by ~30% and ~60% from its value in non-annealed original glassy films.
B – Voltage pulse recording for films thermally annealed at ~500 K. The minimum values of electrical pulses power P (squares) leading to reverse increasing of resistance to initial value of fresh as - grown glassy films. Dashed line corresponds schematically to power leading to film destruction.

In the paper [6] it is emphasized that crystallization which is induced by short laser light pulses is not only thermal phenomenon but excess electron-hole pairs generated by light play important role. This is valid, especially for crystallization kinetics, but coincidence of temperatures needed for ~30% decreasing of transparency either by pure thermal heating or treating by 20-30 μs laser light pulses gives a strong evidence that the main part of a laser light pulse energy spends on pure heating. We have checked this conclusion by using the second bar "b" (Fig. 1A), which corresponds to ~60 % decreasing of transparency due to 20-30 μs laser light pulses. From $W_1/ W_b \approx 2$ one obtains value $T_b \approx 475$ K which is very near to the temperature ~500 K, needed for the same decreasing of transparency in the pure thermal heating case [5]. Thus, in the following we will use the simple estimation of temperature which is induced by short laser light pulses based on pure thermal approximation.

According to this approximation $W_2(\tau)$ dependence for $\tau < 1$ μs. is determined by heating to constant temperature, but in non-stationary regime because $\tau \leq \tau_r$ [7].

It is supposed that this constant temperature equals the melting temperature $T_m = 650$ K, because for "crystal-glass" phase transition this temperature is minimum needed value. The $W_1(\tau)$ dependence for $\tau < 1$ μs is governed by heating also in non-stationary regime, but to temperature considerably higher than T_m [7]. Due to the difference between $W_1(\tau)$ and $W_2(\tau)$ dependencies region S (Fig. 1A) has been revealed. All points of this region $W_1(\tau) > W > W_2(\tau)$ correspond to power W when pulses induced "crystal-glass" phase transition due to heating to temperature higher then T_m, but without film destruction.

These results demonstrate the characteristics of interaction of short laser pulses with thin films of CGS and they show that known advantages of optical recording and re-recording of information using short pulses are possibly related to the existence of a wide power region S for short times whereas this region is appreciably narrower for long times. Then it is very difficult to use appreciated value of W from the interval $W_1(\tau) > W > W_2(\tau)$ in the region $\tau > 10$ μs and it is rather easily to do in the case $\tau < 1$ μs. For this reason we can not depict $W_2(\tau)$ curve in the region $\tau > 10$ μs (Fig.1A).

The electrical recording case

For the comparison of optical and electrical recording, the minimum values of electrical pulses power $P(\tau)$, which needed for reverse increasing of resistance to initial value 10^4-10^5 Ω are depicted in Fig.1B. One can see that this dependence $P(\tau)$ is very similar to the dependence $W_2(\tau)$ of Fig. 1A. It is may be easy understood from the thermal heating point of view, because for reverse transition from crystal value resistance ~10^2 Ω to glass one 10^4-10^5 Ω the heating up to the melting temperature needed. The next interesting and important result in the electrical recording case is the following. In the region $\tau > 10$ μs, if the voltages exceed 10-20% of that ones which correspond to curve $P(\tau)$ then destruction of sample occurs. But in the region $\tau \leq 1$ μs the interval between voltages correspond to curve $P(\tau)$ and that ones, which destroyed the films are 100% and more. We have not systematically measured the destroyed voltages so the curve which is analogous to $W_1(\tau)$ dependence of Fig. 1A is depicted in Fig. 1B schematically by dash line only. But, nevertheless, one can see that region S' exists in the electrical recording case also. This region is wide for short pulse duration, whereas it is appreciably narrower for long pulse duration, as in optical recording case too.

4. Summary

The characteristics of optical and electrical recording of information based on pulse induced "crystal-glass" phase transition are very similar. Laser pulse with power W_2 has bleached locally the film due to "crystal-glass" phase transition. The powerful pulse W_1 has burned the film. It was demonstrated that for pulse with duration τ approximately less than 1 μs there is a wide pulse power interval $W_1(\tau) > W > W_2(\tau)$ or region S, when pulses induced "crystal-glass" phase transition without film destruction. The interval $W_1(\tau)$ - $W_2(\tau)$ decreased with τ and for $\tau > 10$ μs region S became so

narrow that bleaching without destruction was very difficult to get. Similar results have been obtained when "crystal-glass" phase transition was induced by electric field pulses.

It is shown that the effect of laser light and electric field pulses on the chalcogenide materials has mainly a thermal nature.

References

[1] K. Tanaka, S. Iizima, K. Aoki, S. Minomura, Proc 6th Int. Conf. Amorph. Liq.
   Semic. (Leningrad, 1975), v. Structure and Properties of Non- Cryst. Semic. Ed.
   B. T. Kolomiets, Nauka, Leningrad, 442 (1976).
[2] A. Madan, M. P. Shaw, The Physics and Applications of Amorphous Semiconductors Academic
   Press Inc. (1988).
[3] J. Feinleib, S. R. Ovshinsky, J. Non-Cryst. Sol. **4**, 564 (1970).
[4] A. L. Glazov, S. B. Gurevich, N. N. Il'yashenko et al., Pis'ma Zh. Eksp. Teor. Fiz. **12**, 138 (1986).
[5] N. K. Kiseleva, V. I. Kochenov, E. A. Lebedev, Sov. Phys. Solid State **30**, 1135 (1988)
[6] J. Feinleib, J. DeNeufville, S. C. Moss, S. R. Ovshinsky, Appl. Phys. Lett. **18**, 53 (1971).
[7] E. A. Lebedev, K. D. Tsendin, Semiconductors **32**, 838 (1998).

TIME-OF-FLIGHT TECHNIQUE FOR INVESTIGATION
OF AMORPHOUS CHALCOGENIDES AND BARRIER STRUCTURES
ON THEIR BASE

S. P. Vikhrov, N. V. Vishnyakov, A. A. Maslov, V. G. Mishustin

Ryazan State Radioengineering Academy, Russia

It is shown that time – of – flight technique is an efficient method in the investigation of non-crystalline chalcogenide and barrier structures.

The reliability of any electronic device depends on quality of contact between metal and semiconductor. For crystalline semiconductors a contact phenomenon is studied well. For unordered semiconductors as distinct from crystalline ones so far there is no unified theory of formation of metal - unordered semiconductor contact. Therefore investigations of unordered semiconductors and barrier structures on their base are actual scientific and applied problem.

The modified time-of-flight technique is worked out specially for unordered semiconductors like as amorphous chalcogenides and amorphous hydrogenated silicon. The traditional time-of-flight drift-mobility technique measures time during the carriers transit through sample [1]. The modified time-of flight technique measures charge-collection (G) and electrical field distribution $F_i(x)$ in space charge region of the structure metal - amorphous chalcogenide. Method of internal field profile measurement which uses varies the excitation wavelength and apply of reverse field is described [2 - 4].

Conditions for calculations and measurements are as follows:

1. Carriers are generated by the pulse of monochromatic light and distributed in accordance with the light absorption law.

2. Photogenerated charge is small so it does not affect the internal field distribution, i.e.

$$Q_0 << \frac{\varepsilon\varepsilon_0}{d} \int_0^d F_i(x)dx.$$ Satisfaction of this condition may be tested experimentally from independence G from Q_0.

3. The external electric field is subtracted from the internal field, i.e. structure is illuminated by pulse of light after apply of reverse field but before redistribution of internal field. Time of delay between apply of reverse field and pulse of light is RC $< t_{del} < t_{rel}$, where RC is the time constant of measuring eqiupment, t_{rel} is Maxwell relaxation time. Satisfaction of this condition may be tested experimentally from independence G from t_{del}.

4. The influence of surface states in calculations doesn't take in account.

5. Only one type of carriers (electrons or holes) is considered depending on polarity of applied voltage.

6. The work function from metal more than ones from amorphous chalcogenide, i.e. there is depletion layer of semiconductor.

7. The experimental samples are sandwich-type structure with transparent for excitation light electrodes (Fig. 1).
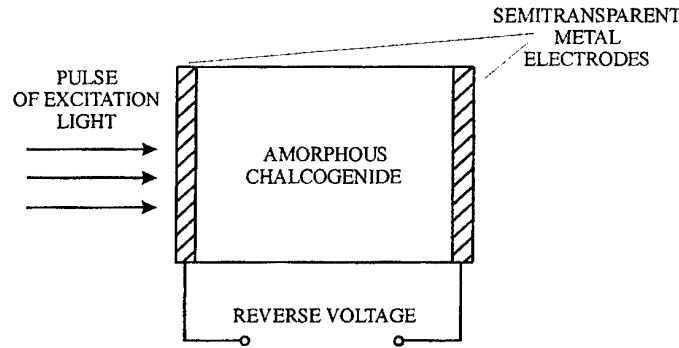
Fig. 1. The experimental sample is sandwich-type structure with semitransparent metal
electrodes.

The main idea of the method is contained in compensation of internal field of depletion
layer of amorphous chalcogenide - metal contact by external pulse of voltage. The value of the in-
ternal electric field is determined by external voltage $V_{G(V,\,\alpha)}$ under which $G(V,\,\alpha) = 0$ under cer-
tain excitation wavelength (α is absorption efficiency, α is function of wavelength).

$$F_i(x_c) = \frac{V_{G(V,\alpha)=0}}{d},\tag{1}$$

where d is the sample thickness [3].

Charge collection G is function of absorption efficiency α and external voltage V. We sug-
gest the following equation for defining the charge-collection:

$$G(V,\alpha) = \frac{(1 - R(V,\alpha))\alpha\mu\tau}{(1 - \exp(-\alpha d))d} \int_0^d \frac{\exp(-\alpha x_g)}{x_c - x_g} \int_{x_g}^{x_c}(F_i(x) + \frac{V}{d})dx \left[1 - \exp\left(-\frac{d}{\mu\tau \frac{1}{x_c - x_g} \int_{x_g}^{x_c}(F_i(x) + \frac{V}{d})dx} \right) \right] dx_g \tag{2}$$

where μ is drift mobility of the carriers, τ is the lifetime of carriers, $R(V,\,\alpha)$ is the coefficient,
which take into consideration diffusion of the carriers against field, x_c is the co-ordinate of stop
drift (in co-ordinate x_c external field compensate internal field so that resultant field
$F_i(x_c) + \dfrac{V}{d} = 0$), and x_g is the co-ordinate of carriers photogeneration.

$$R(V,\alpha) \geq (1 + \frac{\alpha\varphi_T}{F_i(0) + V/d})^{-1},\tag{3}$$

where φ_T is the thermal potential:

$$\varphi_T = kT/e,\tag{4}$$

where k is Boltzmann constant, T is absolute temperature, e is charge of electron [3].

Equation (2) as distinct from analogous [3] takes into account the deep trapping by local-
ized states during photogenerated charge drift. This permit to calculate the co-ordinate x_c and the
internal field profile with the more accuracy than in [3].

The co-ordinate x_c is defined by absorption efficiency and sample thickness, so that x_c is a
function of α and d. In order to get the analytical dependence x_c from α and d it is necessary to
solve the equation (2) under the condition that $G(V,\,\alpha) = 0$. Solution of equation (2) reduces to next
integral:

$$\int_0^d \exp(-\alpha x_g)(x_c - x_g)\left[1 - \exp\left(-\frac{d}{|x_c - x_g|} \right) \right] dx_g = 0.\tag{5}$$

Solution of integral (5) permit to obtain the final equation:

$$x_c\left[1-\exp\left(-\frac{d}{x_c}\right)\right] = \exp(-\alpha d)(d-x_c)\left[1-\exp\left(-\frac{d}{d-x_c}\right)\right].$$ (6)

The dependence of absorption efficiency from excitation wavelength is measured experimentally for specific structure. Equation (6) is solved by numerical method. These permit to obtain the internal field profile of depletion layer (Fig. 3) and charge-collection directly from experiment.

The time-of-flight technique is limited by half the sample thickness (Fig. 2):

$$\lim_{\alpha\to 0} x_c = d/2.$$ (7)

If depletion layer thickness more than a half of sample ones it is necessary to illuminate back side of sample for obtaining internal field profile. This technique is also limited by surface. The experimental results become inaccurate under light absorption depth less than 50 nm because of carrier recombination on the surface states [2].
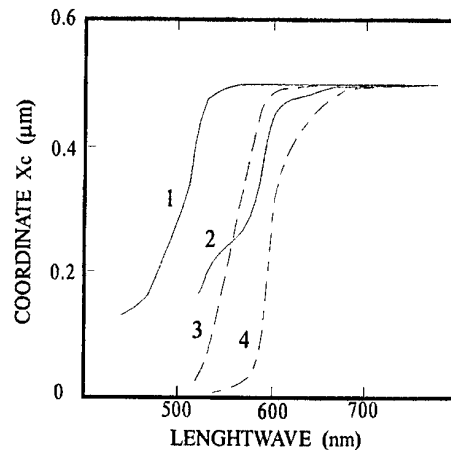
Fig. 2. The x_c (the co-ordinate of stop drift) is calculated for Schottky-barrier in a-silicon (curves 1 and 3) and for a-Si:H p-i-n structure (curves 2 and 4). Thickness of both samples is 1 μm. Curves 1 and 2 are calculated by method of Juska G. [3]; 3 and 4 – are obtained for same samples accordingly by formula (6).

These data allow to calculate the value of μτ, potential profile (Fig. 4) and distribution of the density localized states in mobility gap N(E). So it permits to obtain important parameters, which characterize electrical properties of material and efficiency of devices on its base.
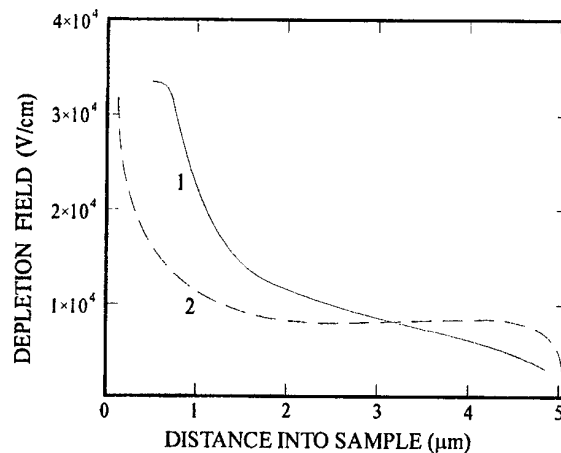
Fig. 3. The profiles of internal depletion field in a-Si:H solar sell (p-i-n structure). Thickness of sample is 5.1 μm. 1– is measured by Juska G. [3], 2 – is calculated by formulas (1) and (6).
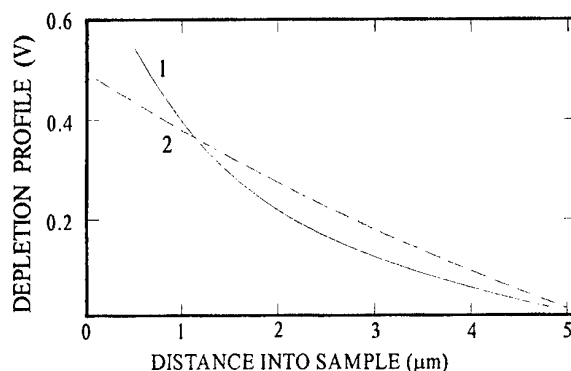
Fig. 4. The depletion profiles in a-Si:H solar sell (p-i-n structure). Thickness of sample is 5.1
μm. 1 – is calculated by Juska G. [3], 2 – is obtained by integration of the internal depletion
field $F_i(x)$ (Fig. 3, curve 2).

The suggested modified time-of-flight technique allows to measure $\mu\tau$ for electrons and
holes the changing polarity of the applied voltage. Equation (2) as distinct from the analogous [3]
takes into account photogenerated charge deep trapping during its drift by localized states. It per-
mits to measure internal field profile and to calculate potential profile and distribution of the den-
sity localized states in mobility gap with the more accuracy than previous methods. It is shown that
our results differ from data obtained in [2 - 4] (Fig. 2 – Fig. 4) and agree with the theory described
in [5, 6] quite well.

With the described modifications the time-of-flight technique becomes a good and effective
instrument for investigation of amorphous chalcogenides and barrier structure on their base. The
technique allows to reveal the process of formation of barrier at the contact between the metal and
the disordered semiconductor.

References

[1] A. Madan, M. P. Shaw, The physics and applications of amorphous semiconductors Boston;
    New York – Sidney – Tokyo, Academic Press, (1988) p. 670.
[2] R. A. Street, Measurements of depletion layers in hydrogenated amorphous silicon, Phys. Rev.
    B. 1983, V.27, No.8. p. 4924.
[3] G. Juska, Collection efficiency in a-Si:H light converters, J. of Non-Cryst. Solids. 90, 247
    (1987).
[4] T. Datta, M. Silver, Schottky – barrier profile in a-silicon alloys, Appl. Physics Letters, 38,
    903 (1981).
[5] S. P. Vikhrov, N. V. Vishnyakov, V. A. Ligachev , The influence of band-gap localized states
    on metal – amorphous hydrogenated silicon contact parameters, Procc. SPIE Intern. Confer. on
    Microelectronics. 1992, No. 1783, p. 600 – 603.
[6] S. P. Vikhrov, N. V. Vishnyakov, A. A. Maslov Determination of barrier capacity and flat bands
    potential on metal – disordered semiconductor contact, Bulletin of the V. Tarasov Center of
    Chemotronics of Glass, No. 1, Mendeleev University of Chemical Technology of Russia, Mos-
    cow, p. 111 – 115 (2000).

FEATURES OF PHYSICOCHEMICAL INTERACTION IN THIN-FILM SYSTEM ON THE BASE OF ARSENIC TRISULPHIDE AND COPPER

M. V. Sopinskyy, M. T. Kostyshin

Institute of Semiconductor Physics of NASU, Kyiv, 45 Prospect Nauki, 03028 Kyiv, Ukraine

Physicochemical interactions in amorphous As_2S_3 - copper thin film systems were studied by the methods of resistometry, ellipsometry, microscopy and by the chemical dissolution. It was shown that considerable variation of chemical process activity observed in these systems is caused by an essential dependence of the physicochemical interaction rate on chalcogenide film stoichiometry and imperfection of its structure. Ellipsometric modeling results indicate that the thickness distribution of the dissolved copper is close to a rectangular shape. It confirms reactionary nature of interaction. Application of our thermochemical model for a probability estimation of quasi-molecular reactions of copper and oxygen with polymerized and non-polymerized fragments in arsenic trisulphide film enabled to give qualitative description of the interaction mechanism. Comparison with As_2S_3-Ag system is made. Results presented in this work indicate some new ways to control physicochemical interaction process in amorphous chalcogenide-metal thin-film systems.

1. Introduction

Thin-film photosensitive systems based on chalcogenide glassy semiconductors (CGS) and some metals (Ag, Cu) [1] have many unique properties. For example, they can be successfully applied in submicron lithography and are very promising in nanolithography as inorganic resists [2]. Among them, the systems containing silver and copper as metal component have the greatest light sensitivity [3].

Thin-film heterogeneous CGS-Me systems, in general, are thermodynamically nonequilibrium ones: there are physicochemical processes in them which cause their ageing. The systems containing silver and ChGS layers based on arsenic, germanium and sulfur are the only ones that are sufficiently sensitive and stable. Most of investigations concerning the nature of the phenomenon, technology of manufacturing, and practical applications have been carried out using above mentioned systems.

The use of ChGS-Cu non-silver systems is difficult due to their chemical instability: the physicochemical interactions (PCI) between CGS and copper are very intensive, what leads to their rapid ageing. Preparation of non-silver systems based on ChGS and copper with performances similar to those of CGS-Ag systems is an urgent problem. Its solution requires detailed investigations of physicochemical transformations in the CGS-Cu systems. Besides, the examination of physicochemical interactions of CGS and metal films is the important topic of research by itself. We have recently demonstrated that these effects can be applied to creation of blazed holographic diffraction gratings [4].

The problems mentioned above require a detailed study of specific features of the interaction in thin-film ChGS-Cu systems. Taking into account that the As_2S_3-Ag system is the most investigated among CGS-Ag systems, the As_2S_3-Cu system as model has been chosen for such examinations. It has allowed to carry out the most complete comparison of the processes of CGS interaction with silver and copper.

2. Experimental

Samples of sandwich-like thin-film CGS-Cu systems were prepared by deposition onto K-8 glass substrates vapours produced by the subsequent thermal vacuum evaporation of the copper load with initial weigh 0.5 g) and that of crashed powdered glassy As2S3 with initial weight 2g) from tantalum boats at residual pressure, P, of $5 * 10^{-3}$ Pa. The deposition rate and amount of deposited substance were measured by the KIT-1 quartz crystal oscillator monitoring system. Thicknesses of Cu and As_2S_3 films were also determined using the MII-4 interferential microscope.

The most universal physical property describing mass transport during solid-state reactions in such systems is the metal layer expenditure, Δh_{Cu}. It was observed by the electrical resistance measurements of the copper film. Specific implementation of this procedure and its metrological substantiation are given in [5].

The ellipsometrical angles of thin-film As_2S_3 -Cu samples and As_2S_3 and Cu control films, ψ and Λ, were measured using the LEF-3M-1 ellipsometer (λ = 632.8 nm) for angles of light incidence in the interval φ_0 = 45°...80°. In order to obtain information about the constitution of samples under investigation, we developed the Fortran-program which enabled to distinguish between various ellipsometrical models. Methodological and metrological aspects of the utilised ellipsometrical modeling method have been described in detail [6, 7].

3. Results

Thickness changes of the copper conductive film in As_2S_3 -Cu samples prepared in the same vacuum cycle began simultaneously with the start of the chalcogenide film deposition on it and continued after completion of the deposition at the same rate (see Fig. 1, chart 3). The change of copper film thickness over the 0...5 min. interval is approximated by the $h = A*t^{1/2}$ formula, where A is a constant. The rate of copper film expenditure, V_e reaches the values of 0.1...0.2 nm/s. When the $\Delta h_{Cu}/h_{As2S3}$ ratio reached the values of 0.25...0...30 (the average concentration of metal in As_2S_3< Cu > layer (interaction products (IP) layer) is 39...46 weight % or 33...37 at. %) the dissolution rate began to drop rapidly.
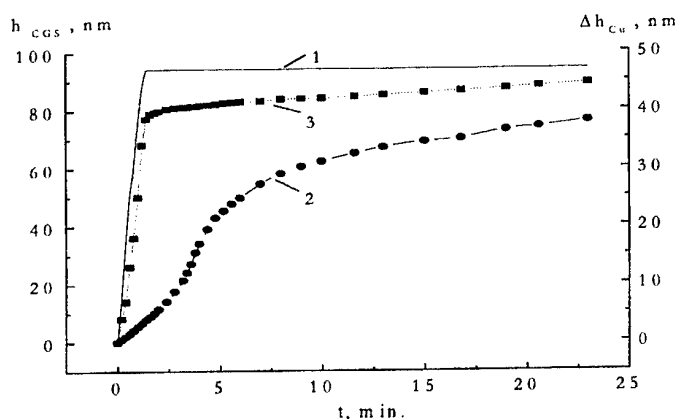
Fig. 1. Dependence of the thickness of the As_2S_3 film being deposited on the deposition time (1). Dependence of the copper film thickness change on the storage time in the vacuum chamber (2 and 3). (Starting from the moment when the CGS film deposition begins.) 3 - Cu film was not annealed on purpose before the As_2S_3 deposition. 2 - Cu film has been annealed before the As_2S_3 film deposition at 100 °C in the presence of glassy As_2S_3 in the chamber.

It has been determined that the physicochemical processes become more intensive when the copper film was deposited on the heated substrate before the formation of the CGS film, or when the copper film has been annealed after deposition at elevated temperatures in the presence of glassy As_2S_3 in the vacuum chamber. In this case the visually appreciable layer is formed on the copper film

surface (apparently, due to the interaction of copper with components of rarefied gaseous medium of chamber).

The formation of such layer proves that the arsenic trisulphide is noticeably volatilized at $P < 10^{-2}$ Pa even at the ambient temperatures. This layer, most likely, consists of copper - sulfur compounds (Cu_xS), because the layer with similar optical and chemical properties is also formed on the surface of copper film annealed in the vacuum chamber in the presence of free sulphur.

During the deposition of As_2S_3 on Cu film covered by Cu_xS layer, V_e was proportional to chalcogenide deposition rate, and the rate of interaction of metal with ChGS reaches 0.8 nm/s. This rate drops sharply when the deposition of CGS film is completed (Fig. 1, curve 2). At this moment, the $\Delta h_{Cu}/h_{CGS}$ ratio for various samples is ~0,4...0,5. Thus, the average concentration of copper in $As_2S_3<Cu>$ is 52...57 weight % or 45...50 at. %. These values are close to the maximum possible concentration of copper in interaction products of copper - amorphous As_2S_3 systems [8].

The results presented above show that for preparation of more stable As_2S_3-Cu systems, it is necessary to evaporate copper and arsenic trisulphide in separate vacuum chambers or in different "vacuum cycles". This should prevent the formation of the CuxS layer on the copper film surface, thus avoiding the facilitation of penetration of the copper atoms from the metal film into the As_2S_3 film through such layer. Subsequently, Cu and As_2S_3 films were deposited in different "vacuum cycles ", between which the copper film was exposed to variable duration free air cycles at temperatures from room and up to 150 °C. Under such conditions the Cu oxide layer is formed on the copper film surface [9, 10]. At the room temperature their thickness reached up to 7 nm [9]. Their thickness grows with rise of oxidation temperature [10].

As opposed to Cu_xS layers, the Cu_2O ones formed by this process have the barrier properties: there is an induction period of PCI in the systems which have intermediate Cu_2O layers. During this period the dissolution rate of the copper film is the lowest (Fig. 2). The general view of Δh_{Cu} (t) dependencies for samples with an oxide-coated Cu film is of the S-type: the induction period is followed by the period of PCI acceleration, then the period of PCI deceleration, and last stage is the saturation of the reaction. The concrete view of $\Delta h_{Cu}(t)$ diagram at various thicknesses of the oxide layer is presented at Fig. 2. The duration of the induction period, the Δh_{Cu} (t) curve inflection point position, the top metal dissolution rate can be used as quantitative parameters in describing the barrier properties of oxide layer. As the thickness of the oxide layer increases, both the duration of the induction period, and the time necessary to reach the inflection point on the Δh_{Cu} (t) curve increase. Thus, the period of reaction acceleration takes place over the wider range of Δh_{Cu} changes, and the maximum value of V_e decreases.
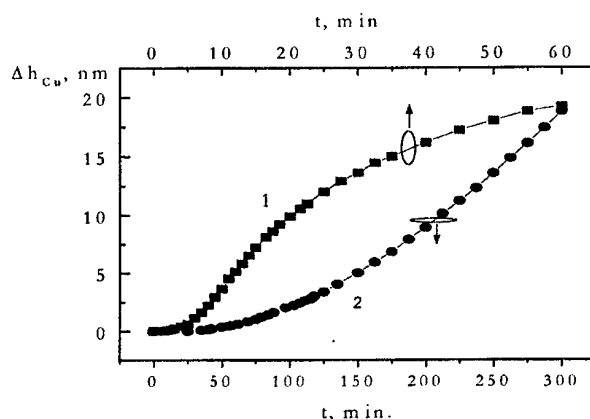
Fig. 2. Copper film thickness change depending on the duration of the As_2S_3-Cu systems storage in vacuum (h_{As2S3} = 150 nm). 1-intermediate Cu_2O layer, h_{Cu2O} = 4 nm; 2-h_{Cu2O} =7 nm.

The As_2S_3-Cu sampleageing rate depends not only on the condition of the interface between the Cu and As_2S_3 films but also on the conditions of preparation of the As_2S_3 film. During the sample storage in vacuum the PCI takes place most intensely when the CGS film obtained by evaporation of primary glassy As2S3, subsequent multiple using of the As_2S_3 load slows down PCI in systems obtained with their evaporation. For example, for samples with ~4 nm thick oxide layer the maximal

value of V_e is 0.4 nm/min. However, as a result of multiple use of glassy As_2S_3 load the V_e gradually decreases down to 0.01 nm/min.

The films obtained by evaporating the previously used As_2S_3 shots have the refraction index that is several percents higher than the films obtained from the fresh load. This has been shown by the ellipsometrical measurements of the reference As_2S_3 films. The evaporator temperature, load mass, deposition rate, and the thickness of obtained As_2S_3 films were similar in all cases considered.

During the gradual heating of the evaporator containing the fresh load of 2 g of the glassy As_2S_3, deposition of small amounts of substance (up to 5 $\mu g/cm^2$) takes place on both the quartz oscillator and substrate. After that, the increase in the mass of deposited substance usually slows down considerably. With the further rise of the evaporator temperature, the deposition rate increases again. When the loads are used again, then the time progression of the mass of the deposited material becomes less obvious. More often, as the temperature rises, the sharp and monotonic increase of the mass of deposited substance is observed.

The stability of As_2S_3-Cu systems depends also on the storage conditions: in vacuum or in air. The character of atmospheric influence significantly depends on the conditions of CGS film production.

In As_2S_3-Cu systems with the films obtained from the fresh shots, the PCI in air is slower than in vacuum (Fig. 3, curves 1 and 2). From the comparison of these results, we can see that atmosphere has little influence on the duration of the induction period, and only slightly moves the inflection point position of the $\Delta h_{Cu}(t)$ dependence towards smaller times. However, V_e in air is much less than in vacuum. Also, $\Delta h_{Cu}(t)$ dependence for the air stored system is closer to linear than that for the vacuum stored one. Hence, the atmosphere has less influence on the barrier properties of copper oxide layer itself, but it slows down the velocity of transition of copper particles through copper/CGS interface area.
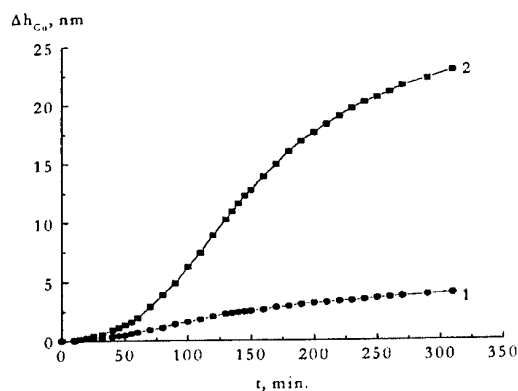
Fig. 3. Change of the Cu film thickness in the As_2S_3-Cu system. System was being stored in air (1) and in vacuum (2). (Thickness of the As_2S_3 film is 180 nm, thickness of the intermediate oxide layer is 5.5 nm.)

On the contrary, in As_2S_3-Cu systems, in which ChGS films are obtained from earlier used material, the PCI rate in air is higher than in vacuum. Fig. 4 shows the $\Delta h_{Cu}(t)$ dependencies for the sample, in which CGS film was deposited from the glass sample whose weight was equal to approximately 30 % of initial mass. In vacuum the initial V_e is ~ 0.1 nm/min. and gradually decreases (close to square law, curve 2). In the sample taken from vacuum on air right after the deposition, the Vd is higher and is practically stationary (curve 1). Longer storage of the sample in vacuum (before placing it in air) gradually causes the low V_e initial period to occur (equal to the copper expenditure rate in vacuum at the moment of extraction). It also causes the decrease of the metal expenditure rate during the main (close to linear) stage of $\Delta h_{Cu}(t)$ dependence (curve 3).

An additional information about Cu-As_2S_3 thin-film interactions was obtained from their ellipsometrical investigations, and also from the investigations of their stability in etchtants as well as their mechanical properties.
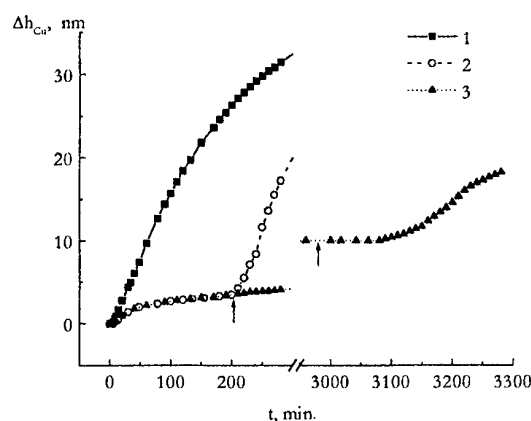
Fig. 4. Time dependencies of copper film thickness change for As_2S_3-Cu_2O-Cu system over the vacuum-and air-keeping. The As_2S_3 film has been obtained by the evaporation of load used earlier in four evaporations. The pre-evaporation weight was approximately ~30% of the initial weight. 1 - keeping in air. 2, 3 - keeping in vacuum (up to the time moment ↑) and in air (after the time moment ↑). (Thickness of the As_2S_3 film is 106 nm, thickness of the intermediate oxide layer is 5 nm.)

Ellipsometrical investigations were carried out immediately after the removal of the systems from vacuum chamber and also during their storage in air. The systems under investigation were modelled as multilayer structures with sharp layer interfaces. Such elipsometrical models have been successfully used for the description of interactions in CGS-Ag thin film systems [11].

Angular $\Delta(\varphi_0)$ and $\psi(\varphi_0)$ dependencies for the systems stored in vacuum chamber depending on storage duration are described with good accuracy by the "copper substrate - homogenous layer of reaction products " or by the "copper substrate -homogenous layer of reaction products - homogenous ChGS layer" models. Transition from the former model to the latter one correlate with the stage of $\Delta h_{Cu}(t)$ kinetic dependence when the metal dissolution rate V_e rapidly decreases. This makes it possible to explain this rapid decrease by the fact that the outer surface of the semiconductor film was reached by the reaction front. Moreover, from the resistometrical and ellipsometrical data the next equation follows:

$$\Delta h_{Cu} + h_{As2S3} = h_{As2S3 <Cu>}$$

Below we represent the details on ellipsimetrical investigations of the acceleration of PCI in air phenomenon. As an example, let us consider the system, kinetics of the copper layer expenditure of which is presented in Fig. 4 (curve 3). Calculations showed that the experimental angular $\Delta(\varphi_0)$ and $\psi(\varphi_0)$ dependencies measured immediately after the system removal from vacuum (time moment ↑ on curve 3, Fig. 4) are described by the "copper substrate - two homogenous layer" model with 0.07 grad. accuracy. Calculated thicknesses, refraction (n) and absorption (k) indexes of these layers are: h = 50 nm, n = 2.57, k = 0.01 for the upper layer and h = 66 nm, n = 3.48, k = 0.43 for the lower one. This clearly demonstrates that the upper part is As_2S_3 layer, whereas the lower one is the As_2S_3 <Cu> reaction products layer. These ellipsometric modeling results indicate that the thickness distribution of the dissolved copper is close to rectangular shape. It confirms reactionary nature of interaction.

Dynamics of the thickness changes for these copper-doped and non-doped CGS layers during further storage in air is demonstrated in figure 5. From the modeling it is also obtained that, as the thickness of doped layer increases, the optical constants of this layer increase as well. This proves, obviously, the gradual change of a composition or/and a structure of the layer of reaction products. By the moment of the deceleration of dark interaction caused by the reaching of the doping front the external surface of As_2S_3 film the values of optical constants of Cu doped layer were: n = 3.6, k = 0.8. The accuracy of the description of $\Delta(\varphi_0)$ and $\psi(\varphi_0)$ dependencies by "copper substrate - homogenous layer of interaction products" model was 0.3 grad.. This points out that the composition and/or structure of reaction products somewhat change(s) along the doped layer.
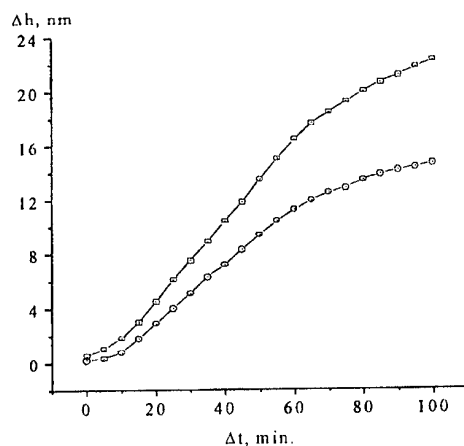
Fig. 5. Thickness change of non- doped (1) and copper-doped (2) parts of CGS film during the storage of the As_2S_3-Cu_2O-Cu system in air. The CGS film was obtained with the load of glassy As_2S_3 that had been previously used four times.

Further, in this system even slower changes take place. The gradual increase of values of optical constants of this layer has been observed. This points to the further increase of concentration of copper in doped layer. Thus, the precision of the description of system by the "copper substrate - homogeneous layer of interaction products" model also has gradually improved. After the dark reaction having reached the saturation point, the optical constants of As_2S_3 <Cu> layer were: n = 4.0, k = 1.3. The thickness of products layer was approximately 1.5 times more than the initial thickness of film. Accuracy of the description of system by the "copper substrate - homogeneous layer of interaction products" model slightly exceeded 0.1, which is 1.5 times worse than the accuracy of the description of system in which the interaction took place in vacuum.

Doping As_2S_3 films by copper is accompanied by a change of their dissolution rate in various alkaline etchants, in particular, in the aqueous solutions of NaOH and KOH. Their adhesion to the underlying Cu film also is reduced in comparison with the adhesion of the initially deposited non-doped As_2S_3 film. It enabled also to study changes occurring in Cu films during their interaction with As_2S_3 films. The mechanical or chemical removal of As_2S_3 <Cu> products layer from the surface of copper film and measuring the $\Delta(\varphi_0)$ and $\psi(\varphi_0)$ dependencies on the remaining Cu film were done for this purpose upon the end of interaction.

It was ascertained that the $\Delta(\varphi_0)$ and $\psi(\varphi_0)$ values after removal of As_2S_3 <Cu> layer in the majority of systems are close to $\Delta(\varphi_0)$, $\psi(\varphi_0)$ values for the reference Cu films. This proves that during the interaction of copper film with CGS one the state of the copper film surface and a volume structure of this film have not undergone essential changes.

As opposed to the previous cases, the copper films in systems stored in air, in which the As_2S_3 film is obtained from repeatedly utilised shots, had lower $\Delta(\varphi_0)$, values and especially the $\psi(\varphi_0)$ values, compared to the control copper films after removal of As_2S_3 <Cu> layer. This causes the growth in the effective refraction index values and reduction in the effective absorption index values of such copper films. For example, in the above described systems with a sulfur deficiency in the As_2S_3 film, the n grows from 0.15 to 0.44, and k drops from 3.20 to 3.03. The k/n ratio drops from 21.3 for the control Cu film to 6.9 for the residual Cu film after the reaction and mechanical removal of the As_2S_3 <Cu> layer. This should demonstrate the reduction of the film packing density [12].

The conclusion obtained with using ellipsometrical investigations is confirmed by observation of the surface of unreacted part of Cu film in reflective optical microscope. For Cu films with low $\Delta(\varphi_0)$ and $\psi(\varphi_0)$ values compared to the reference Cu films, the increase in the scattered light level and roughness are observed. The lower reflectivity spots are observed in the microscope' field of view. All this demonstrates that the dissolution of Cu films is non-uniform across the surface. As a consequence, the copper film becomes heterogeneous, with reduced volume content of metal.

Apparently, it is necessary to assume the presence of the spots too small to be visible in the optical microscope used in this study (x600). The presence of macroscopic as well as microscopic

defects in the copper film also should result in the lower specular reflectivity and greater surface roughness. It affects the values of ellipsometrical parameters of copper film as well.

Thus, the results obtained show that the physicochemical processes during the interactions of the metal and ChGS films in As_2S_3-Cu systems have the complex dependency on such factors as the Me/CGS interface state, conditions of CGS film preparation, and composition of the environment.

4. Discussion

Comparison of interaction rates in As_2S_3-Ag [13] and As_2S_3-Cu (Fig. 1) thin-film specimens without intentionally formed intermediate layers shows that interaction rate of arsenic trisulphide film with the silver one is about four orders of magnitude lower than with the copper film. Thus, the difference in PCI kinetic shape is also observed in these systems.

For As_2S_3-Ag the kinetics of metal thickness change may be described by square-root time dependence, $\Delta h(Cu) \sim t^{1/2}$ [13]. This points out that the dark interaction is being controlled by diffusion. On the other hand, for As_2S_3-Cu the dependence is close to linear over the considerable part of the kinetics curve (Fig. 1, curve 2).

The explanation of such a substantial difference between chemical process rates can be based on heats of formation of silver, copper, and arsenic sulphides. Let us note that the similar approach has been used before by Phillips [14], when he proposed his thermochemical model of photodoping for ChGS-Ag systems. The relative heats of formation are given in Table 1 in kcal/mole chalcogen per formula unit in accordance with [14].

Table 1. Relative heats of formation for arsenic, silver and copper sulphides and arsenic, silver, copper and sulphur oxides.

Compound	ΔH_f, Kcal/[mole×{number of chalcogen or oxygen atoms per formula unit}]	Compound	ΔH_f, Kcal/[mole×{number of chalcogen or oxygen atoms per formula unit}]
As_2S_2	15.95 [16]	SO_2	35.48 [17]
As_2S_3	13.3 [15]; 10.0 [16]	SO_3	36.83 [17]
As_2S_5	7.0 [16]	S_3O_9	34.9 [17]
Ag_2S	7.837 [15]	S_2O_7	27.75 [17]
CuS	12.7 [15]; 12.1 [16]	Cu_2O	41.4 [17]
α-Cu_2S	19.0 [15]; 19.6 [16]	CuO	38.72 [17]
$Cu_{1.96}S$	17.83 [15]	As_2O_3	52.13 [17]
$Cu_{1.8}S$	17.24 [15]	As_4O_6	53.04 [17]
Ag_2O	7.44 [17]	AsO_2	43.9 [17]
Ag_2O_2	2.95 [17]	As_2O_4	47.77 [17]
S_2O	26.11 [17]	As_2O_5	44.28 [17]
SO	-0.098 [17]		

For arsenic trisulphide and silver sulphide the following is true: (see Table 1)

$$|\Delta H_f (As_2S_3)| > |\Delta H (Ag_2S)|.$$

In other words, chemical reaction between silver and arsenic trisulphide is endothermic (is not beneficial energetically). That is why for As_2S_3-Ag compositions, most probably, one can expect only the diffusion intermixing of atoms of copper and ChGS layers, caused by an entropic component of Gibbs' free energy. This makes it possible to explain square-law dependence observed in [13] for As_2S_3-Ag thin-film systems.

For arsenic trisulphide and cupric sulphides the following is true:

$$|\Delta H_f (As_2S_3)| = |\Delta H_f (CuS)|, \tag{1}$$

$$|\Delta H_f (As_2S_3)| < |\Delta H_f (Cu_2S)|, \tag{2}$$

$$|\Delta H_f (As_2S_3)| < |\Delta H_f (Cu_{2-\delta}S)| \tag{3}$$

From (2, 3) it follows, that, when copper and arsenic trisulphide contact, the fast exothermic exchange reactions should take place, producing the Cu_2S and $Cu_{2-\delta}S$ compounds. An interaction rate

is determined by an enthalpy and entropy of reactions and by the kinetic factors. (Taking into account the propensity of silver and copper to form the triple compounds with arsenic and sulfur [18], strictly speaking, heat of dissolution of sulphides of these metals in arsenic trisulphide should be taken into account too, when the probability of reaction between silver and copper, on the one hand, and arsenic trisulphide, on the other hand, is estimated.)

Apparently, the almost-linear kinetics for the main stage of $\Delta h_{Cu}(t)$ dependence (Fig. 1, curve 3) means [19] that the surface reactions (at $Cu/As_2S_3<Cu>$ or $As_2S_3<Cu>/As_2S_3$ boundaries, in our case) control the interaction rate between CGS and copper as-deposited films. The slowdown of V_e begins at those concentrations of copper in the products layer, at which the electron diffraction pattern similar to that of pure $a-As_2S_3$ had already disappeared [8], and different amorphous diffraction pattern was observed. One can conclude that the above mentioned slowdown is caused by the $As_2S_3<Cu>$ reaction product front reaching the external surface of As_2S_3 film. This conclusion is also confirmed by our ellipsometrical examinations.

The presence of Cu_xS layer on the surface of copper film considerably improves the interaction conditions at this surface. The interaction of copper particles diffused through the Cu_xS intermediate layer with As_nS_m (n, m = 0, 1, 2, 3 ...) molecular fragments being deposited from vapour phase [20, 21], most likely, controls the rate of Cu layer expenditure in this case.

When the copper oxide layer separates the metal and ChGS films, the interaction between them takes place in a different manner (Fig. 2). The decrease of the maximum value of V_e, and increase of linear-like part of the $\Delta h_{Cu}(t)$ dependence with increase of oxide layer thickness point out that this layer loses its barrier properties only partially. Hence, the copper oxide layer slows the PCI down from the beginning to the end.

The existence of the correlation between the refraction index of the as-deposited As_2S_3 film, and the state (fresh or already used) of the glassy sample of arsenic sulphide explains the influence of thermal history of glassy As_2S_3 on its interaction with copper. It is known from [22, 23] that the violation of stoichiometrical composition and structure of As_2S_3 being precipitated due to change of fragmentary composition of vapour phase causes changes of optical properties of the arsenic trisulphide films. In particular, this violation changes its refraction index.

Apparently, multiple evaporation of glassy As_2S_3 causes changes in composition of its vapour phase. As the evaporator temperature gradually increases from room temperature and up to melting temperature, the vapour phase composition appears to become enriched with sulfur from near-surface areas of the shots. At the melting point and above the intensive evaporation of other molecular fragments begins. Those fragments are produced by the decomposing As_2S_3. The dominant evaporation of more volatile sulfur-enriched fractions takes place, apparently, during the subsequent cooling of an evaporator loaded with the crashed As_2S_3. Hence, for these reasons one can assume that the near-surface layer of As_2S_3 shots gradually loses sulfur when taken through several heatings and coolings cycles (multiple partial evaporation). The average gross - composition of the obtained films gradually changes from sulfur-enriched to sulfur-deficient compared to the stoichiometrical composition. Since (see Table 1),

$$|\Delta H_f (As_2S_5)| < |\Delta H_f (As_2S_3)| < |\Delta H_f (As_2S_2)| \qquad (4)$$

one should expect intensification of interaction between the copper and the sulfur-enriched films obtained during the first evaporation of arsenic trisulphide load. This has been confirmed experimentally.

There are reports on the influence of the environment on interaction of metal and CHGS [3, 24, 25]. It has been observed before [3] that for As_2S_3-Ag thin-film compositions the interaction between metal and ChGS slows down in air compared to vacuum. On the contrary, the [24] shows that the silver penetration into the arsenic sulphide plate for air annealed samples increases by several times compared to the vacuum annealed one.

The slowdown of physicochemical interaction in air is explained in [3] as follows: during the storage in vacuum the mobility of free sulfur in As_2S_3 film is higher. As a result, the sulfur diffuses into the Ag film and reacts with it, while in air the slow bi-directional diffusion of metal and As_2S_3 film material takes place. The results obtained by us do not contradict such explanation of this effect for $As_2S_3-Ag(Cu)$ systems in case when As_2S_3 films are enriched with sulfur. Besides, it is necessary to take into account the penetration of atmospheric oxygen into the CGS film, and the possibility of its chemical interaction with sulfur. Such interaction is energy favourable (see Table 1).

On the contrary, in As_2S_3-Cu systems with lower free sulfur content, the amplification of the PCI processes (fig. 4) is observed in air, similarly to the effect of silver thermodiffusion increase in monolithic glassy arsenic trisulphide. The existence of a correlation between metal film expenditure rate in air and the duration of preliminary exposure to vacuum (Fig. 4) allows us to state that it is the activity of atmospheric gases that influences the rate of metal-CGS interaction. From data shown in Fig. 4, it is also possible to conclude that atmospheric oxygen causes acceleration of process activity taking place in the copper - IP interface, or in the IP layer. However, it does not accelerate the processes that undergo at the IP -ChGS interface. In the latter case, the duration of initial period of $\Delta h_{Cu}(t)$ dependence in air should have been decreased as the vacuum exposure is increased. This is due to the approach of IP -CGS boundary to the outer surface of CGS film. Besides, it is possible to make the conclusion that the IP layer formed during the vacuum storage of the system impedes the access of atmospheric gases to the Cu - CGS<Cu> interface.

Thus, close-to-square-root Δh_{Cu} (t) dependence for thin-film vacuum-kept specimens (Fig. 4, curves 2, 3 - up to the arrow mark) points to the dominant role of copper atoms diffusion processes through the gradually thickening product layer. At the same time, the slowest stage of interaction process in air is the reaction at the copper-IP boundary. This is the cause of the linear $\Delta h_{Cu}(t)$ dependence.

Ellipsometry and optical microscopy data show that the acceleration of interaction under influence of the atmospheric gases primarily occurs in those areas of the Cu/As_2S_3 interface where the access of atmosphere gases is facilitated. These areas are characterised by the presence of macrodefects due to the non-ideal technological conditions of preparation of structures, by the presence of pores, hollows, microdefects in as-deposited As_2S_3 films. These data support the conclusion that the Cu/IP interface performs the control function in the air-kept As_2S_3 -Cu systems without surplus of sulfur in As_2S_3 film.

The atmospheric influence effects can also be explained in the non-contradictory manner in terms of the thermochemical approach. In Table 1 the heats of formation for oxides of silver, sulfur, copper and arsenic are given. The analysis of these data shows that the exothermic effect of the 3-, 4-, 5-valence arsenic atoms reaction with oxygen is greater than the oxygen-copper and oxygen-sulfur reactions, and greater yet than the oxygen-silver reaction. This exothermic effect is also greater than that characteristic to silver, arsenic or copper atoms reactions with sulfur. This enables to assume that the overall PCI rate in air increases specifically due to the interaction of atmospheric oxygen with arsenic atoms. This interaction results in release of sulfur, which in turn interacts with atoms of copper or silver. Oxygen stimulated increase of Cu_x S compounds content in products layer should increase its n, k values. That explains the results of ellipsometrical studies.

The acceleration of the PCI interaction processes should be especially noticeable in samples without excess sulphur, such as monolithic samples of glassy As_2S_3 or thin-film samples without surplus of sulfur. According to [24], for glassy As_2S_3-Ag film systems stimulated by atmospheric oxygen, the silver expenditure rate from the film can be several times greater than that caused by the diffusion intermixing of components in such heterogeneous structure. Our experimental data show that for sulfur-deficient As_2S_3-Cu systems the sulfur expenditure rate can increase several times under the influence of the atmospheric oxygen. In this case we deal with the increase of the chemical process rate which, however, remains lower than rate of PCI processes in As_2S_3-Cu samples containing surplus of sulfur, and taking place in vacuum.

It is also possible to explain the results of work [25] by the chemical interaction of atmospheric oxygen with arsenic atoms. In [25] it was observed that there is considerable difference of properties of the photostimulated interaction products obtained by illumination of the As_2S_3--Ag composition in vacuum and in air. At the same time, there was small difference in properties for two such types of products inherent to the As_2S_5 - Ag system. There is clear correlation between the degree of an atmospheric influence and atomic concentration of arsenic in CGS film.

5. Conclusions

The results obtained in this work demonstrate the considerable range of chemical process activity that takes place in the As_2S_3-Cu system. It has been ascertained that the specific type of physicochemical interaction between copper and ChGS essentially depends on composition and

structure of ChGS film, and also on the presence of intermediate layers between the film and the metal.

Based on the analysis of heats of formations of sulphides and oxides of silver, copper, and arsenic, the existing experimental data, as well as the data obtained in the present work can be explained. (on interaction of copper and silver with arsenic sulphide.)

The results of the present work pave the way to the precise control over stability of CGS-Me systems that is necessary for producing competitive silverless CGS-Me media.

Acknowledgements

References

[1] M. T. Kostyshin, E. V. Mikhailowskaya, P. F. Romanenko, Sov. Phys. - Solid State 8, 451 (1966).
[2] A. V. Stronski, Microelectronics Interconnections and Assembly, NATO ASI Ser. 3, High Technology, 54, 263 (1996).
[3] I. Z. Indutnui, M. T. Kostyshin, O. P. Kasyarum at al. (Naukova Dumka, Kiev, 1992) (in russ.)
[4] M. V. Sopinskyy, P. F. Romanenko, I. Z. Indutnyy, E. F. Venger, Journ. of Optoelectronics and Advanced Materials 3 (2),   (2001).
[5] N. V. Sopinskii, I. Z. Indutnyi, M. Yu. Gusev, Zhurn. Nauch. i Prikl. Fotogr. (in russ.) 41 (1), 32 (1996)
[6] N. V. Sopinskii, Optoelectronics, Instrumentation and Data Processing (Avtometria) 1, 95 (1997).
[7] N. V. Sopinskii Russiann Microelectronics 30 (1), 35 (2001).
[8] A. G. Fitzgerald, Thin Solid Films 98 (1), 101(1982).
[9] T. Scimeca, G. Anderman, W. K. Kuhn, Appl. Surf. Sci. 37 (2), 167(1989).
[10] M. R. Pinnel, H. G. Tompkins, D. E. Heath, Appl. Surf. Sci 2 (4), 558(1979).
[11] V. Honig, V. Fedorov, G. Liebmann, P. Suptitz, Phys. Stat. Sol. A96 (2), 611(1986).
[12] G. A. Al-Jumaily, S. R. Wilson, L. L DeHainaut et al., J. Vac. Sci. Technol. A5 (4), 1909(1987).
[13] M. T. Kostyshin, S. A. Kostioukevich, P. E. Shepeljavi, Ukr. Fiz. Zhurn. (in russ.), 29 (9), 1417(1984).
[14] J. C. Phillips, Proc. Intern. Symp. "Physics Latent Image Form. Silver Halide", Singapore, 297, 1984.
[15] Physico-chemical Properties of Semiconductor Substances. Reference Book. (Moscow, Nauka, 1979) (in russ.).
[16] Thermodynamical Properties of Inorganic Substances. Reference Book./ Ed. O.P. Zefirov. Moscow, Atomizdat, 1965. (in russ.).
[17] Physico-chemical Properties of Oxides. Reference Book. Ed. by G.V. Samsonov (Moscow, Metallurgiya, 1978) (in russ.)
[18] R. G. Kuryaeva, Fiz. i Khim. Stekla (in russ.) 12(2), 240 (1986).
[19] Bernard Delmond, Introduction a la cinetique heterogene. Paris: EDITIONS TECHNIP, 969.
[20] N. Tohge, M. Kimoto, T. Minami, M. Tanaka, J. Ceram. Soc. Japan. 90 (1039), 133(1982).
[21] Z. Cimpl, F. Kosek, J. Janos, M. Mikhailov, Phys. Stat. Solidi A88 (2), K111 (1985).
[22] K. White, B. Kumar, A. K. Rai, Thin Solid Films, 161 (1), 139(1988).
[23] I. M. Pecheritcin, I. I. Kryzhanovskii, M. D. Mikhailov, Fiz. i Khim. Stekla (in russ.) 24 (6), 721 (1998).
[24] A. Simanovskis, S. V. Stolyarova, J. Teteris, Phys. Stat. Solidi A95 (2), K105(1986).
[25] M. T. Kostyshin, P. E. Shepeljavi, A. M. Kovaltschuk, Ukr. Fiz. Zhurn. (in russ.), 25 (2), 181(1982).

PREPARATION AND PROPERTIES OF NON-CRYSTALLINE GLASSES IN THE SYSTEM Se-I

S. Zamfira, D. Ursutiu[a]

Department of Precision Michanics and Mechatronics, University "Transylvania", 2200-Brasov, Romania
[a]Department of Physics, University "Transylvania", 2200-Brasov, Romania

Vitreous Se_xI_{1-x} samples (x=0.1; 0.15; 0.20) have been prepared and studied by thermal analysis, iodometry, X-ray diffraction and optical transmission. The results show that part of iodine remains unbonded in the structure while another part saturates the ends of selenium chains. The main effect of the iodine atoms upon the selenium matrix configuration consists in the shortening of the selenium chains and occupation of the short chain ends by atomic iodine.

1. Introduction

In 1981 Shanabrook et al. [1] reported the preparation of the first zero-dimensional solid: amorphous iodine (a-I) exhibiting one-fold coordination. The predominant inter-molecular bonding in a-I is probably a delocalized metallic-like bonding. The system Se-I is important both for the structural, specific problems of the zero-one dimensional configurations and for the control of the defects in the non-crystalline selenium with high relevance in applications.

The stoichiometric crystalline compounds Se_2I_2 and SeI_4 are prepared by stirring selenium with a solution of iodine in CCl_4, or selenium with a solution of C_2H_5Br [2].

We report in this paper the results on preparation and properties of several Se-I alloys in the vitreous state.

2. Experimental

The Se_xI_{1-x} alloys (x=0.1;0.15;0.20) have been prepared by melting under vacuuum in glass ampoules mixture of selenium (Hobboken 99.9999%) and iodine (Carlo Erba 99.9999%) in corresponding proportions. The ampoules were heated with the rate of 5°C/min up to the temperature of 300 °C and maintained 7 hours. During the thermal treatment the ampoule was rotated with 10 turns/min. The vitreous samples were obtained by throwing the melt into water.

The samples looked grey-dark and showed a visco-plastic character immediately after preparation. The visco-plastic property decreases slowly in the interval 1÷6h, as a function of composition.

The optical microscopy investigations and X-ray diffraction diagrams proved the vitreous state of all the samples.

3. Results

3.1. Iodometric results

Iodine was determined by titration with a solution of natrium thriosulphate ($Na_2S_2O_3$) in presence of amidin (starch) as indicator.

It was found that not all iodine used in preparations is situated in the bonded state. For the samples $Se_{0.8}I_{0.2}$ and $Se_{0.85}I_{0.15}$, after melting and rapid cooling the concentration of non-bonded iodine

is 14.86 at.% and 9 at.%, respectively. The amount of non-bonded iodine firstly decrease rapidly and after 2-3 days its amount remains practically unchanged.

3.2. Thermal analysis

The thermal differential analysis carried out in the interval 20-250 °C (Fig.1).
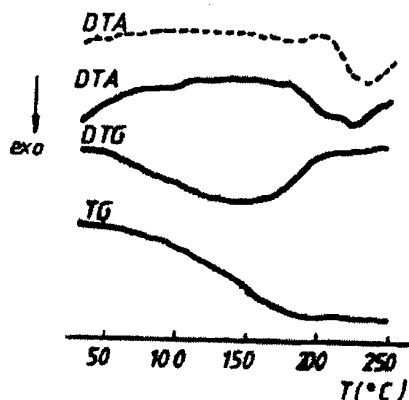
Fig. 1. DTA, DTG and TG curves for the sample $Se_{0.8}I_{0.2}$ heating rate: 5°C/min - $Se_{0.8}I_{0.2}$ ---Se.

Endothermal transformations are evidenced. The softening of the melts is produced in large temperature intervals (100-200 °C). The thermogravimetric curves reveal important loss of material (iodine) of the same order of magnitude as for the losses observed by iodometry measurements.

3.3. X-ray diffraction

X-ray diffraction patterns taken on the as-quenched samples $Se_{0.8}I_{0.2}$ and $Se_{0.9}I_{0.1}$, corrected and normalized, are shown in Fig. 2.
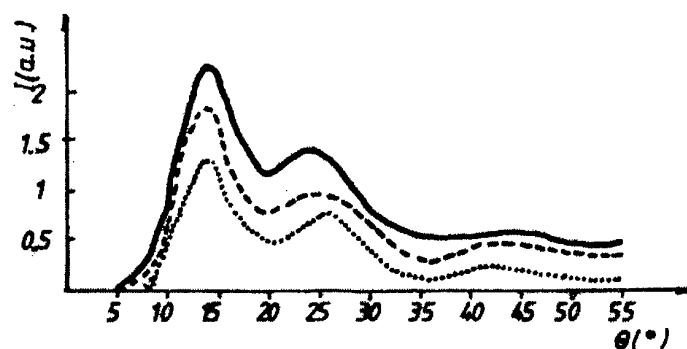
Fig. 2. X-ray scattered intensity for samples in the system Se-I.
--- $Se_{0.9}I_{0.1}$; —— $Se_{0.8}I_{0.2}$.

Cu K_α radiation and digital recording in the angular interval $2\theta = 3 \div 113°$ were used. The measurements were carried out in a Siemens-Kristalloflex IV diffractometer.

The reduced electron density distribution curves (REDD) are shown in figure 3.
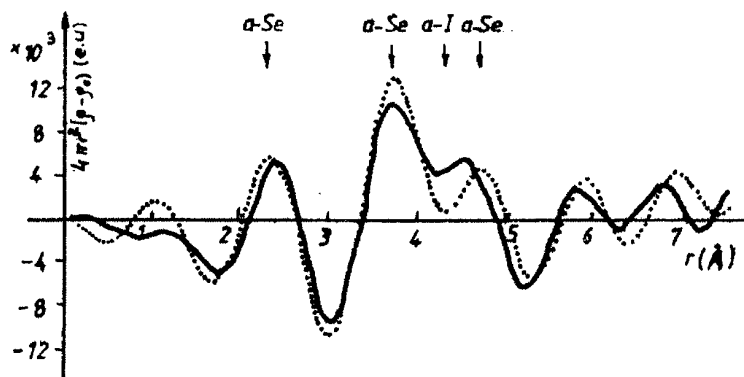
Fig. 3. REDD curves in the system Se-I.
--- $Se_{0.9}I_{0.1}$; ⎯ $Se_{0.8}I_{0.2}$.

Careful analysis of the REDD of the vitreous samples allows to conclude that iodine strongly influence the third peak situated at ~ 4.5 Å. In selenium this third peak (situated at ~ 4.75 Å) is related to the chain configuration. For a-Se-I the third peak shifts towards smaller r and its intensity increases when the iodine amount increases. In an old paper, Richter [3] has shown that amorphous iodine exhibits its third peak in REDD at 4.40 Å.

3.4. Optical transmission spectra

Optical transmission of the vitreous Se-I samples has been recorded with a SPECTROMASTER apparatus in the infrared range (400 cm^{-1} - 4000 cm^{-1}). Figure 4 shows the results. For large wavelengths two absorptions peaks are evidenced for pure a-Se (480 cm^{-1} and 743 cm^{-1}) and they are interpreted as two-phonons and three-phonons bands of Se_8. A new absorption peak, revealed at ~860 cm^{-1} in $Se_{0.9}I_{0.1}$ is given probably by Se-I bond vibration.
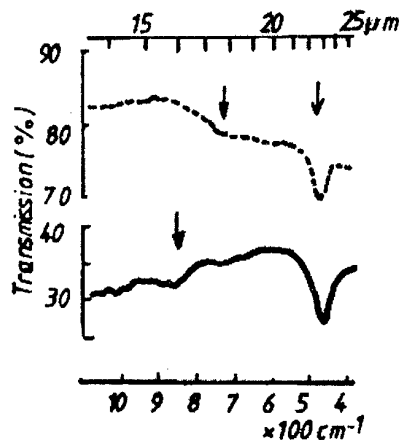
Fig. 4. Infrared transmission spectra for samples in the system Se-I.
⎯ $Se_{0.9}I_{0.1}$ ---a-Se.

3.5. Electrical resistance

We have measured the electrical resistance of the sample with maximum amount of iodine: $Se_{0.8}I_{0.2}$. Two measurements were carried out. The first one was made immediately after preparation and the change of resistance in time was followed (Fig 5a). The second one was made after 20 days of storage (Fig. 5b).

The rapid drop of the electrical resistance immediately after preparation can be due to two causes: a partial crystallization and the release of iodine. The second cause seems to prevail, because

the non-bonded iodine in fresh samples is in high amount. For long time storage, a partial crystallization is produced, as evidenced by X-ray diffraction (peaks ascribed to iodine (I_2 crystallites) were revealed).
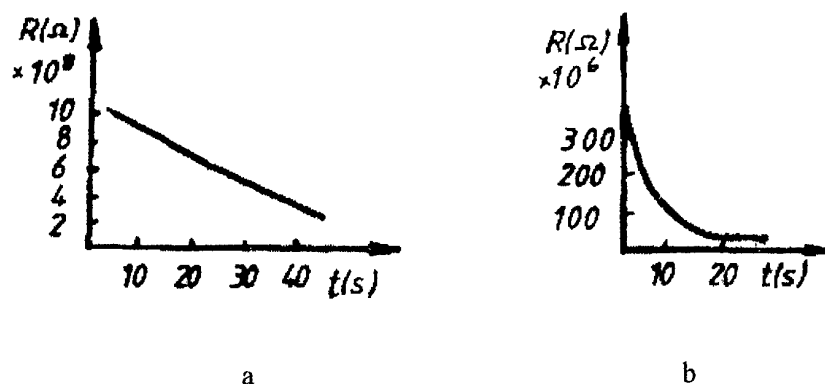
Fig. 5. The evolution of the electrical resistance in the $Se_{0.8}I_{0.2}$ vitreous sample
    a)   immediately after preparation
    b)   after 20 days of storage.

4. Discussion

The properties of vitreous Se-I alloys are strongly influenced by the iodine content. The fresh samples rich in iodine are not stable due to non-bonded iodine accumulated in between the selenium configurations. Selenium and iodine form a simple eutectic for 52 at%Se, with the melting temperature 58 ± 1 °C [4]. After Golubkova and Petrov [5] the solubility of iodine in selenium does not exceed 2 at.%.

The stabilization of the vitreous Se-I alloy is reached for low iodine content and long storage at room temperature. In this case the iodine is strongly bonded with selenium. Klapötke and Passmore [6] succeeded to prepare a number of salts of selenium iodine cations, all of which contain covalent Se-I bonds. The average selenium-iodine bond distance is 2.51 Å and is near to the sum of the covalent radii of Se and I (2.493Å). The existence and stability of selenium-iodine cations suggest the possibility to find such configurations in vitreous Se-I. Because the structure of Se-I may be thought as a disordered packing of selenium chains, with iodine occuping the possitions at the end of these chains, the iodine doping may be useful for the investigation and control of the defect states in non-crystalline selenium.

5. Conclusions

The properties of Se-I glassy are determined by the iodine content. Part of iodine is bonded to the ends of selenium chains while the other part (molecular I_2) can be released spontaneously (at room temperature) or by heating. A minimum amount of iodine cannot be eliminated and, therefore, only Se-I alloys poor in iodine are convenient in applications.

References

[1] B. V. Shanabroook, J. S. Lannin, I. C. Hisatsune, Phys. Rev. Lett. **46**, 130 (1981).
[2] D. Jecu, S. Zamfira, T. Petre, Bulletin of the University of Brasov, Series C, Mat. **24**, 55 (1982)
[3] H. Richter, Fortschritte der Physik, **8**, 493 (1960).
[4] M. Popescu, Non-crystalline chalcogenides, Solid State Science and Technology library, vol.8, Kluwer Acad. Press, 2000.
[5] V. G. Golubkova, E. S. Petrov, Izv. Sibir. Otdel. Ak. Nauk, SSSR, Ser. Him. Nauk, **2**, 114 (1975).
[6] T. Klapötke, J. Passmore, Acc. Chem. Res. **22**, 234 (1989).

STRUCTURE AND PROPERTIES OF CHALCOGENIDE GLASSES IN THE SYSTEM $(As_2S_3)_{1-x}(Sb_2S_3)_x$

F. Sava

National Institute of Materials Physics
Bucharest-Magurele, P.O. Box MG. 7, Romania

The glass system $(As_2S_3)_{1-x}(Sb_2S_3)_x$, $0 \leq x \leq 0.65$, has been studied by X-ray diffraction and microhardness measurements. The long-time irradiation of the samples by ultraviolet rays has been carried out and its structural effect was investigated. The substitutional model and the microphase separation model have been discarded. A new intermediate model, whose main feature is the formation of mezoscopic Sb_2S_3 clusters, has been advanced.

1. Introduction

The chalcogenides glasses are important due to their remarkable properties, which make them useful in optoelectronics for infrared elements and devices for acusto-optic devices, for electrical switches, holography and information storage media [1,2]. Arsenic trisulfide (As_2S_3) is the most studied chalcogenide glass and deserves applications in infrared optics and optical coatings because of its excellent IR transmission, large glass-forming tendency, and resistance to moisture and chemicals [3]. Antimony trisulfide (Sb_2S_3) and the non-stoichiometric compositions (as e.g. SbS_4) prepared as thin amorphous films have found applications for information storage media [4]. A graded refractive index, which is required in some applications, may be produced in the non-crystalline As_2S_3 of both bulk and thin film forms by gradually replacing the arsenic component with chemically similar antimony atoms [5]. This approach will fail if the resultant glass crystallizes or undergoes a gross phase separation, because these phenomena cause light scattering. The glass-forming tendency is very different in As_2S_3 and Sb_2S_3. While for As_2S_3, even melt cooling by simply removing the sample from the furnace at room temperature, the glassy Sb_2S_3 can be obtained only for high cooling rates by using the so-called splat-cooling techniques [6]. A special method for getting glassy Sb_2S_3 by a conventional melt quenching method was demonstrated by Dalba et al. [7]. If Sb_2S_3 is added to As_2S_3 then the glass-forming ability of the mixture is greatly enhanced and, thus, a broad range of glassy As_2S_3-Sb_2S_3 alloys is obtained. Although the structure of the non-crystalline state in the binary system As_2S_3 and Sb_2S_3 is satisfactorily known, the atomic configuration in the alloys As_2S_3-Sb_2S_3 is controversial. Some authors interpreted the EXAFS, XANES, IR data and the Mössbauer experimental data on the atom [121]Sb in the frame of a model with random substitution of the arsenic atoms by antimony atoms with the formation of As-S-Sb bridges [8-11]. Other authors interpreted the IR, XRD, crystallization kinetics and optical gap data in the frame of a model with mixture of As_2S_3 and Sb_2S_3 microphases exhibiting weak interaction or without interaction at all [5, 12, 13]. The effect of the light of energy above the gap, in particular ultraviolet radiation in the system As_2S_3-Sb_2S_3 is poorly investigated. Hayashi et al. [14] have shown that in As_2S_3 and other chalcogenide glasses the UV irradiation produces a change in the optical absorption edge, two orders of magnitude higher than for the band-gap irradiation. While in the last case the photodarkening is caused by changes in atomic coordinations [14] and positions resulting from exciting lone pair electrons, in the case of UV irradiation an Auger process may take place, too, and, therefore, bond breaking or ionisation of atoms are more easy to occur, leading to layer change in local structure of the non-crystalline network. In this paper are reported the results obtained in the study of the glassy system $(As_2S_3)_{1-x}(Sb_2S_3)_x$ $0 \leq x \leq 0.65$ by X-ray diffraction and microhardness measurements. A structural model for the glassy materials was proposed.

2. Experimental

Glasses were prepared by melting stoichiometric mixtures of glassy As_2S_3 and polycrystalline Sb_2S_3 in sealed silica ampoules, previously evacuated at 10^{-5} Torr. Melting was carried out at 850 °C for ~

8 hours in a rotating furnace in order to ensure homogeneity. Glasses were then obtained by water-quenching the silica ampoules. The following glassy ingots were obtained: $(As_2S_3)_{1-x}(Sb_2S_3)_x$ x = 0; 0.05; 0.25; 0.45 and 0.65.

The densities of the ingots were determined by the Archimede's method.   The   microhardness of the ingots were determined with a PMT-3 tester provided with diamond indentation prism. Indentation loads between 10 g and 50 g were used. The structure of the samples has been determined by X-ray diffraction in a TUR-M62 diffractometer equipped with a copper target tube. The samples were prepared by grinding chunks of ingots in a mortar and then pressing the powder in a special support to be mounted in the diffractometer. The X-ray diffraction patterns for every sample were recorded in the frame of a step by step method with the measuring time per angular position of 40s. The angular step was 0.05°. The parameters of the first sharp diffraction peak (FSDP) were carefully extracted by a computing procedure. The whole X-ray diffraction curves measured in the range 7.25°-74.25° (θ) were processed and the radial electron density distribution curves (REDD) were obtained with special computing programs written in FORTRAN language.

3. Results

3.1 Density

The exact values of the densities of the chalcogenide glasses are important both for the computation of the radial electronic density distribution curves and for the explanation of the photostructural effects which are in many cases accompanied by volume changes [15,16].

Moreover, in order to check various models of the atomic scale structure it is necessary to have accurate determinations of the material density.

The densities of the glassy ingots have been determined by the Archimede's method. Special attention was paid to the elimination of air bubbles during immersion in water. The accuracy of the mass determination was ±0.0001g, and the accuracy of the densities was ±0.01g/cm³. The results are shown in Fig. 1.
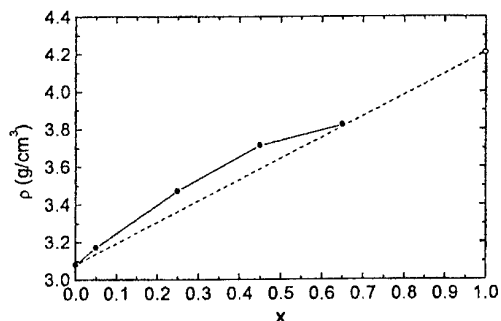
Fig. 1. -•- The density of the glassy samples in the
          system $(As_2S_3)_{1-x}(Sb_2S_3)_x$;
          --- Theoretical densities in the case of
          phase mixture (As_2S_3 and Sb_2S_3).
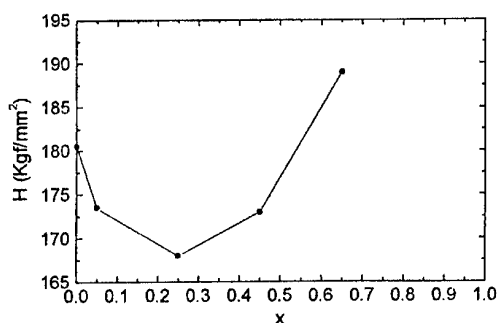
Fig. 2. The microhardness in the glassy system
          $(As_2S_3)_{1-x}(Sb_2S_3)_x$;

While the theoretical curve for the case of the mechanical mixture of two phases (As_2S_3 and Sb_2S_3) corresponds to the linear variation with x of the densities, the experimental values show a significant deviation from the linearity in the glass-forming region. This effect speaks in favour of the preserving of the basical structural arrangement of As_2S_3 during alloying with Sb_2S_3 for the range of the possible glassy state in the system As_2S_3-Sb_2S_3 for the range of glassy alloys. For x = 0.65 the density of the sample approaches that corresponding to a mixture of arsenic and antimony based sulfides. The Sb_2S_3 density was that reported in [6].

3.2. Microhardness

One of the parameters, which offer informations on the strength of the interatomic bonds, is the microhardness. The microhardness of the glassy ingots was determined with the help of a PMT-3 microhardness tester provided with diamond indentation prism. The tester gives the hardness in Vickers (Kgf/mm²) or in gigapascals (GPa). The hardness values of the glassy samples in the system As_2S_3-Sb_2S_3 are situated in the range 120-190 kgf/mm²). Large number of indentations (20-30) has

been performed for 50 g load. The mean value of the hardness was taken as the experimental value. An accuracy of ± 5 Kgf/mm² was estimated from the distribution of the measured hardness values. Fig. 2 shows the glass microhardness in the system As_2S_3-Sb_2S_3 as a function of Sb_2S_3 concentration.

Hardness measurements involve complex flow mechanisms; the observed increase of hardness with x indicates structural changes leading to smaller molecular or configurational mobility.

3.3 X-ray diffraction

3.3.1 First sharp diffraction peak

The X-ray diffraction patterns of the chalcogenide compounds and alloys exhibit as a fundamental feature a narrow diffraction peak situated at low diffraction angles. Figure 3 shows the experimental X-ray diffraction curves, smoothed and aligned in order to evidence the changes produced when antimony substitutes arsenic in glassy alloys. A strong decrease of the first peak with the composition x is observed.
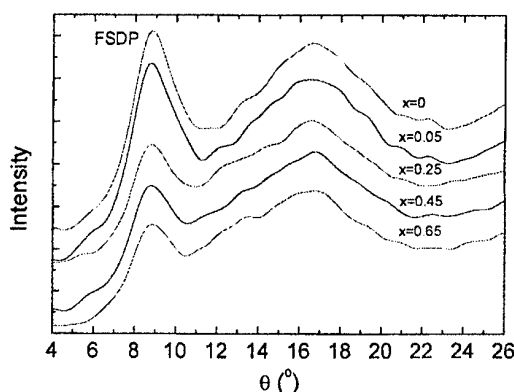
Fig. 3. X-ray diffraction patterns for glassy samples in the system $(As_2S_3)_{1-x}(Sb_2S_3)_x$.

This first sharp diffraction peak (FSDP) was explained as a "signature" of the medium range or intermediate-range order in the non-crystalline matrix. In the investigated compositions FSDP exhibits significant modifications a function of antimony content. Three parameters have been carefully measured: the peak area, peaks position on the angular scale and peak width. The last two parameters allow for calculation of the quasi-periodicity, d, and the correlation size, D, in the material, respectively. Fig. 4 shows the results.
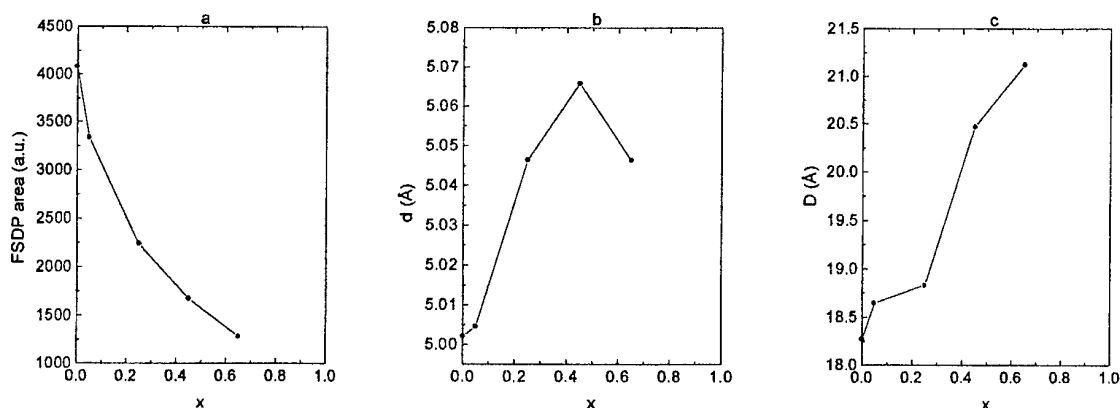
Fig. 4. The evolution of FSDP characteristics when As atoms are substituted by Sb in the glass-forming domain of the pseudo-binary system $(As_2S_3)_{1-x}(Sb_2S_3)_x$.
a- FSDP integral intensity (area);   b- Quasi-periodicity, d;   c- Correlation length, D.

The area of the FSDP strongly decreases with x. The quasi-periodicity in the glass raises up to x = 0.45, then decreases. The correlation length, that is related to the range of ordering of large configurational entities increases with x.

3.3.2 Radial electron density distribution (REDD)

The method based on the calculation of the so-called radial distribution function is the most powerful technique used to determine the local structure of non-crystalline materials.

The measured X-ray diffraction intensities for the largest possible angular theta range (7.25-74.25)° were corrected for polarization and then converted into electron units. The reduced interference function i(Q) where $Q = (4\pi\sin\theta)/\lambda$ was calculated from the corrected and converted I, as follows:

$$i(Q) = \frac{I- <f^2>}{<f>^2} \tag{1}$$

where $<f>$ stands for the mean atomic scattering factor averaged over the atomic concentrations.

By a Fourier transformation of Qi(Q) the correlation function G(r) is obtained:

$$G(r) = \frac{2}{\pi} \int_0^\infty Qi(Q) \sin(Qr)dQ \tag{2}$$

Both the REDD(r) and the pair distribution function, g(r), can be calculated;

$$REDD(r) = 4\pi r^2 \rho_0 + rG(r) = 4\pi r^2 \rho_0 g(r) \tag{3}$$

where ρ_0 is the mean electronic distribution density. The Fourier transformation was carried out in the range $Q = 1.03$ to $Q = 7.84$ Å^{-1}.

Fig. 5 shows the REDD curves obtained for the investigated glassy composition.
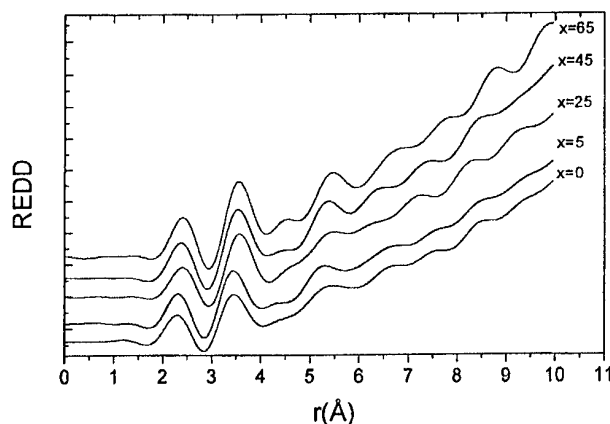
Fig. 5. The radial electron density distribution curves in the system $(As_2S_3)_{1-x}(Sb_2S_3)_x$
$\lambda_{CuK\alpha}=1.54$ Å. Integration range: $1.03 \div 7.84$ Å^{-1}.

The most important characteristic of the REDD curves are related to the position, area and breadth of the first 3-4 peaks.

Careful analysis of the REDD curves allowed for getting the numerical data in Table 1.

Table 1. The most important characteristic of the REDD curves in the system $(As_2S_3)_{1-x}(Sb_2S_3)_x$.

Sb_2S_3 (x)	First coordination peak			Second coordination peak			r_2/r_1
	r_1 (Å)	Half breadth $\sigma(r_1)$	Area (u.e.)	r_2 (Å)	Half breadth $\sigma(r_2)$	Area (u.e.)	
0.00	2.250	0.588	1456	3.460	0.600	3827	1.538
0.05	2.274	0.558	1493	3.451	0.584	3984	1.518
0.25	2.349	0.606	2005	3.563	0.597	5227	1.517
0.45	2.325	0.597	2156	3.539	0.617	5628	1.522
0.65	2.361	0.587	2407	3.55	0.577	6093	1.504

4. Discussion and structural model

X-ray diffraction data have been reported for As_2S_3 glass by a number of workers [17, 18].

There is general agreement that the As-S bond length is similar to that in the crystal and that the radial distribution functions are consistent with three fold coordination of sulfur atoms about arsenic atoms. Yhe existence of a sheet-like structure in the glass has been suggested on the basis of the correspondencin position of the FSDP and the (020) reflection of orpiment (c- As_2S_3), but there is no feature in the RDF for the glass corresponding to the cross ring c_0 distance in the crystal, showing that the sheets are more or less disordered in the glass. Chemical and difraction studies on a variety of glass compositions in the arsenic-sulfur system [18] have shown that the presence of arsenic in excess of the As_2S_3 composition increases the layer separation in glass, while sulphur in excess gives rise to discrete S_8 rings.

The crystalline structure of Sb_2S_3 is a complex one. Atoms forms thread-like molecules, neighbouring molecules are coupled to form a ribbon along the b axis. The band themselves are combined into layers (double ribbons) which are parallel to the b-axis. The double ribbons have the composition $(Sb_4S_6)_n$. The ribbons represent deformed positions of a rock salt structure, somewhat reminiscent of the SnS structure. The coordination number of the Sb atoms is hard to define, it is at least three [19].

For the Sb_2S_3 glass, Zacharov and Gerasimenko [20] reported the number of S(Sb) atoms surrounding a Sb(S) atom as 4(2.7). The higher coordination numbers that in the corresponding crystalline phase were explained as a result of the absent atoms at the distances 3.15 Å and 3.20 Å which reflects the manner of joining Sb-S-Sb-S ... chains into ribbons.

Tatarinova [21] has shown from electron diffraction data on thin Sb_2S_3 amorphous films that the number of S(Sb) atoms surrounding a Sb(S) atom was 6(4). A dense octahedral packing of Sb and S atoms was proposed. Resetnik [22] reported coordination numbers 5.9(3.95) for an amorphous Sb_2S_3 film.

As regarding the system As_2S_3-Sb_2S_3 Tichý et al. [23] have shown that in the first approximation it is a nearly ideal solution of the As_2S_3 and Sb_2S_3 microstructural species, while Kawamoto and Tsuchihashi [12] concluded from the results of the study of the various properties and structure of glasses that the structure is composed of As_2S_3 and Sb_2S_3 regions which are joined together by linkages like As-S-Sb. On the other hand Vinogradova [24] has shown from the diagram of state that in the system takes place eutectic interaction because the eutectics is degenerated. The system do not have solid solution region, nor ternary compounds. The liquidus curve shows the tendency to separation in the system [24].

The FSDP measures the spacing in layered molecular clusters (quasi-periodicity) or can be associated with certain forms of long-range order in the structure [25]. The ordering of the quasi-layers is measured by the correlation length, D. The increase of D with x shows an increasing ordering when Sb_2S_3 is added to As_2S_3.

The quasi-periodicity increases up to x = 0.5 (Fig. 3.b). This seems to be the limit of insertion of Sb into the As_2S_3 network (by substituting As). Then Sb dominates and so the typical Sb_2S_3 structure imposes its pattern to the amorphous alloy.

It is remarkable that the REDD curves (fig.5) show a well evidenced peak at distances as high as ~5.5 Å and this MRO feature can be related to the particular feature in the diffraction pattern at the position of FSDP.

The above described features can be related to the evolution of density with x. The deviation of ρ from the linear low corresponding to the model with phase separation can be explained by the model with substitution of As by Sb when the As-S bonding length becomes smaller as shown by Durand et al. [26] (from 2.286 Å for x = 0 to 2.283 Å for x = 0.75). So, the density becomes higher than for the case of simple substitution. For x>0.5 the density tends to the value with a mixture of glassy microphases: As_2S_3 and Sb_2S_3.

The weak diminishing of microhardness when the Sb_2S_3 is added can be interpreted as a bond weakening during As substitution by Sb. For higher content of Sb x>0.45 the prevalence of Sb_2S_3 microphase, increases the microhardness (as observed in Fig. 2). Further insight into the structure of As_2S_3-Sb_2S_3 glassy systems can be obtained from the REDD curves.

The position and the area under first peak (r_1 and A_1) gives information on the first atomic coordination sphere in the system. Fig. 6a and 6b shows the evolution of the position of the first atomic coordination in the system and of the area (in electronic units) compared to the theoretical data assuming a linear variation of these parameters with the composition (the case of a phase mixing in the system).

The electron density data for As_2S_3 and Sb_2S_3 in the first coordination sphere were calculated for the case of 3-fold and four-fold coordination of As and respectively Sb in the frame of a random covalent model, according to the formulas:

$$A_3 = 2[3xZ_{As}Z_S + (1-2x)Z_S^2]$$
$$A_4 = 2[2x^2Z_{Sb}^2 + (1-x)^2Z_S^2 + 3x(1-x)Z_{Sb}Z_S]$$

where Z_{As}, Z_{Sb}, and Z_S are the number of electrons on As, Sb and S, respectively.

From Fig. 6 we may conclude that antimony enters into the alloy with a coordination number higher than 3. The second peak in REDD curves gives the distances directly related to the bond angle on As, Sb and S atoms.
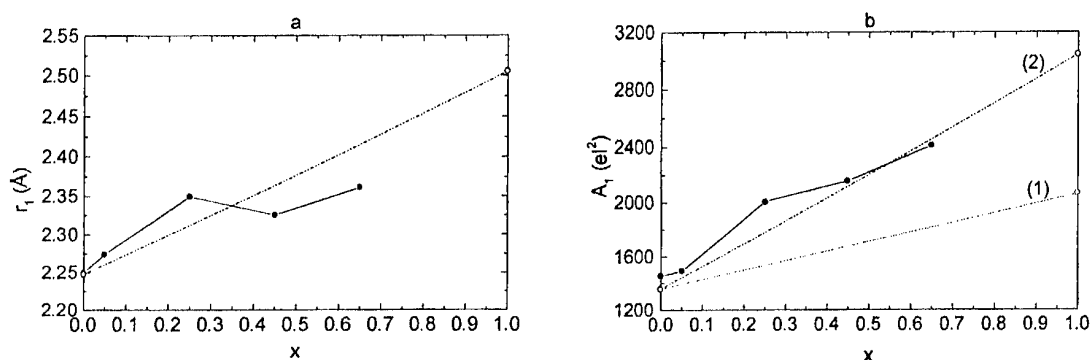
Fig. 6. First coordination (position (a) and magnitude (b)) in the system $(As_2S_3)_{1-x}(Sb_2S_3)_x$ from REDD.

-●- experimental data;
-o- (a) data from literature [6];
-o- (b) calculated values for three coordinated atoms As and Sb (case 1) and three-coordinated As and four-coordinated Sb atoms (case 2).

Fig. 7 a, b shows the experimental numerical values for the position and area of the second peak of REDD, together with the calculated data and those from literature.

The second coordination peak in the system follows the general trend of increasing with x. Nevertheless the lower values in the glass-forming region speak in favour of a more distortion of the basical pyramidal configurations $As-S_3$ and $Sb-S_3$ that lead to lower bonding angle on the atoms. This feature is correlated with the higher density of glassy alloys.

The area under the second peak (A_2) can be compared with the theoretical curves for three cases, as calculated in [6]:

case C: crystalline-like radial distribution (Sb_2S_3);
case L: layer-like radial distribution based only on interlayer distances (Sb_2S_3);
case B: band-like radial distribution based only on interband distances (Sb_2S_3).

In the case C, Sb has as second neighbours 8 Sb atoms in an anisotropic coordination; in the case L a highly anisotropic second coordination with 6 Sb do exist; in the case B a Sb atom is coordinated to 4 Sb atoms in the second coordination sphere. It is remarkable that our experimental points are situated near the layered case. It must be concluded that the real amorphous structure is consistent with a model with configurations similar to those in crystalline Sb_2S_3. In the same time glassy Sb_2S_3 can be classified as different if compared to the layered structure of As_2S_3 and more closed to the continuous random structure of the type As_2Te_3.

Fig. 7. The position and area of the second peak in REDD compared with the theoretical models (-o- data from literature [6]).

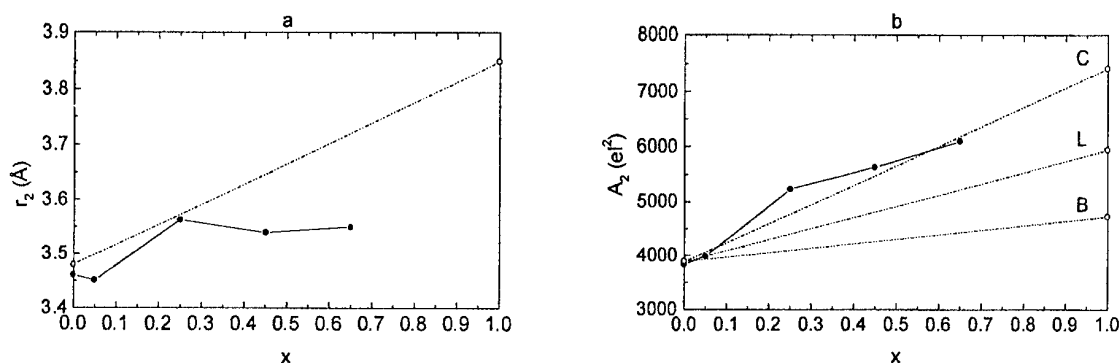The amount of disorder in the system can be investigated by means of the half breadth (σ) of the distance distribution in the coordination spheres, as resulted from REED.

Fig. 8 shows the widths of the coordination spheres for the investigated samples in the system. The width of both coordination remains practically unchanged when Sb_2S_3 is added to As_2S_3.

No significant modification of MRO is produced when x increases, as proved by the decreasing tendency of σ.
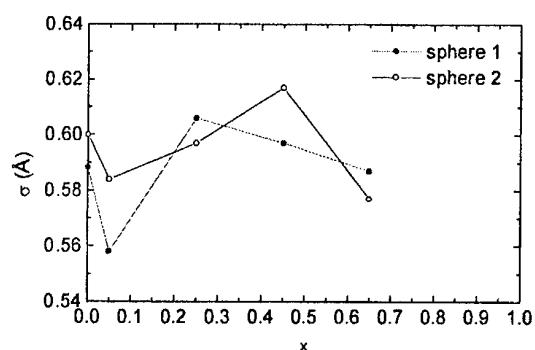
Fig. 8. The variation with x of the breadths of the first two coordination spheres in the system $(As_2S_3)_{1-x}(Sb_2S_3)_x$.
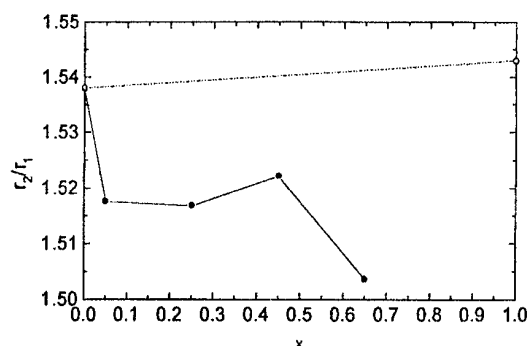
Fig. 9. The evolution of the ratio r_2/r_1 in the system $(As_2S_3)_{1-x}(Sb_2S_3)_x$ -o- data from literature.

The mechanism of transition from layered to continuous random network with x can be understood on the basis of Fig. 9. In this figure is plotted the ratio of the position of the first two coordination spheres for various x.

It is remarkable the general tendency towards lowering of the bond angles in the glassy system when Sb is added. The non-orpiment configurations develop up to x = 0.65. As-S-Sb bridges lead to chain branching and folding and to the interconnections of layer-like As_2S_3 configurations.

From infrared reflectance spectrometry Kapoutsis et al [27] have found that the destruction of As-S-As bridges with increasing Sb_2S_3 content is accompanied by the creation of mixed As-S-Sb bridges, which reach maximum abundence at x = 0.45. After x = 0.65 the Sb_2S_3 configurations dictate the structure, and the ratio r_2/r_1 increases up to Sb_2S_3 value.

5. Conclusions

The system As_2S_3-Sb_2S_3 in glassy form represents an interesting transition from the layer-like structure of As_2S_3 that incorporates step by step more Sb atoms on the As sites to continuous random structure similar to As_2Te_3 structure. The transition to three dimensional structure (at x = 0.45) is accompanied with a more and more advanced separation of Sb_2S_3 clusters. Therefore, the transition with x signifies the formation of a more homogeneous structure at the atomic scale, although clusters of Sb_2S_3 bands are practically sandwiched with As_2S_3 fragments.

The intercalation of Sb atoms into the As_2S_3 layer up to saturation is proved by the increase of the quasi-periodicity. The intercalation of Sb_2S_3 configurations is proved by the decrease of the FSDP area. A model with disordered configurations, intermediary between the Sb_2S_3-like compacted bands where some As are included, and layer-like configurations, seems to be realistic for this system.

Acknowledgements

References

[1] A. B. Seddon, J. Non-Cryst. Solids **184**, 44 (1985).
[2] M. Popescu, Non-Crystalline Chalcogenides, Chapter 4, Kluwer Academic Publishers, Solid State and Technology Library, Volume 8, (2000).
[3] D. R. Uhlmann, N. I. Kreidl, Glass Science and Technology, Vol.1, Glass-forming systems, Academic Press, New York (1983).
[4] A. Madan, P. Shaw, The Physics and Applications of Amorphous Semiconductors, Academic Press, New York (1988).
[5] K. White, R. L. Crane, J. A. Snide, J. Non-Cryst. Solids **103**, 210 (1988).
[6] L. Červinka, A. Hrubý, J. Non-Cryst. Solids **48**, 231 (1982).
[7] G. Dalba, P. Fornasini, G. Giunta, E. Burattini, A. Tomasi, J. Non-Cryst. Solids **97&98**, 411 (1987).
[8] M. A. El Idrissi Raghni, P. E. Lippens, J. Olivier-Fourcade, J. C. Jumas, J. Non-Cryst. Solids **192&193**, 191, 364 (1995)
[9] J. M. Durand, P. E. Lippens. J. Olivier-Fourcade, J. C. Jumas, M. Womes, J. Non-Cryst. Solids **194**, 109 (1996).
[10] E. Bychkov, G. Wortmann, J. Non-Cryst. Solids **159**, 162 (1993).
[11] M. Kato, S. Onari, T. Arai, Jap. J. Appl. Phys. **22**, 1382 (1983).
[12] Y. Kawamoto, S. Tsuchihashi, Yogyo-Kyokai-Shi **77**, 328 (1969).
[13] L.Tichy, A. Triska, M. Frumar, H. Ticha, J. Klikorta, J. Non-Cryst. Solids **50**, 311 (1982).
[14] K. Hayashi, D. Kato, K. Shimakawa, J. Non-Cryst. Solids **198-200**, 696 (1996).
[15] B. Singh, S. Rajagopalan, P. K. Bhat, D. K. Pandhya, K. L. Chopra, J. Non-Cryst. Solids, **35&36**, 1053 (1980).
[16] M. D. Mikhailov, E. A. Karpova, Z. Cimpl, F. Kosek, phys. stat. sol. (a) **117**, 467 (1990).
[17] A. A Vaipolin, E. A. Porai-Koshits, Fiz. Tv. Tela (russ.) **5**, 178 (1963).
[18] S. Tsuchihashi, Y. Kawamoto, J. Non-Cryst. Solids **5**, 286 (1971).
[19] F. Hulliger, Structural chemistry of layer-type phases, Ed. F. Lévy, D. Reidel Publ. Dordrecht-Holland/Boston-USA, 1976, p.65.
[20] V. P. Zacharov, V. S. Gerasimenko, Structure and properties of semiconductors in amorphous state (russ.), Izd. Naukova Dumka, Kiev, 1976, p.124.
[21] L. I. Tatarinova, Electronography of amorphous materials (russ.), Izd. Nauka, Moscow, 1972, p.61.
[22] A. M. Resetnik, Kristalografia (russ.) **4**, 926 (1959).
[23] L. Tichý, A. Tříska, M. Frumar, H. Tichá, J. Klikorka, J. Non-Cryst. Solids **50**, 371 (1982).
[24] G. Z. Vinogradova, Glass formation and phase equilibrium in chalcogenide systems (russ.), Ed. Nauka, Moscow, 1984.
[25] J. C. Philips, J. Non-Cryst. Solids **43**, 37 (1981).
[26] J. M. Durand, P. E. Lippens, J. Olivier-Fourcade, J. C. Jumas, J. Non-Cryst. Solids **192&193**, 364 (1995).
[27] J. A. Kapoutsis, E. I. Kamitsos, I. P. Culeac, M. S. Iovu, in Physics and Applications of Non-Cryst. Semic. in Optoelectronics, Kluwer Acad. Publ. 1997, p. 307.

COMPOSITIONAL DEPENDENCE OF THE OPTICAL PROPERTIES OF THE Ge–Se-Ga GLASSES

Y. Nedeva, T. Petkova[a], E. Mytilineou[b], P. Petkov

Department of Physics, Univ.Chem.Tech. & Metall., 1756 Sofia, Bulgaria
[a]Centr.Lab.Electrochem.Power Sources, BAS, 1113 Sofia, Bulgaria
[b]Department of Physics, University of Patras, 265 00 Patra, Greece

Optical properties of the glasses from the systems with a constant ratio of Ge/Se and different concentrations of gallium are investigated. The spectral dependence of the absorption coefficient α, is calculated from transmission spectra. The optical band gap, E_g^4, found to increase with the addition of gallium. This variation is explained by the increase of the average bond energy that occurs with the addition of Ga into the alloys. The optical constants, were also calculated from the transmission spectra, using a method proposed by Swanepoel.

1. Introduction

Chalcogenide glasses are promising optical materials due to their transparency in the IR region, relatively good thermal, mechanical and chemical properties and the low optical losses. Germanium chalcogenides with the addition of Sb [1], As [2] and In [3] have already investigated. These studies have mainly focused on the improvement of the optical transmission of the alloys in the IR region [4] and attention has mainly given on the choice of the proper modifier or on the improvements of the preparation conditions.

In the present study we investigate the effect of the addition of Ga in two amorphous systems where the ratio of Ge/Se was kept constant. Mitkova and Boncheva [5] have studied the glass-forming region of the Ge-Se-Ga system. They found that good glasses are prepared having concentrations as high as 35 at.% of Ge and 20 at.% of Ga.

We report the dependence of the optical absorption coefficient, of the refractive index and of the extinction coefficient on the Ga content. On the base of the results we discuss a correlation between the composition and the optical properties in terms of the chemically ordered covalent network model [8].

2. Experimental

We investigated bulk and thin films of $(GeSe_4)_{1-x}Ga_x$ and $(GeSe_5)_{1-x}Ga_x$ systems, with up to 20 at % Ga. Bulk glasses were prepared with the melt-quenched technique, using 4N purity elements of Se, Ge and Ga. Evacuated ampoules with the initial substances were heated in a rotated furnace. The synthesizes were carried out with a constant heating ratio of 3 K/min up to a final temperature 1200 K. Glasses were obtained after a quenching in a mixture of water and ice.

Thin films were evaporated on glass substrates in a standard vacuum installation, using the respective bulk composition as a source material. The residual pressure was $1.33 \cdot 10^{-5}$ Torr, the distance source-substrate was 0.12 m, and the temperature of the evaporation source was 800-900 K. The typical thickness was about 0.5 μm. The amorphicity of both bulk and thin films was examined by the X-ray diffraction technique.

Optical transmission of the bulk samples was measured in the spectral region 400-900 nm or 1.2-1.8 eV, using a 75 W halogen lamp and a monochromator. The intensities of the incident, I_0 and transmitted light, I, were measured with a silicon detector at the shorter and a germanium detector at

the longer wavelengths. The transmission of the thin films was measured in the energy range of 2.1-3 eV, using two independent techniques: one was similar to that used for the bulk samples and the other was by a double channel spectrophotometer in VIS and NIR regions. The refractive index and the extinction coefficient are obtained using a computer program based on a method described by Swanepoel [6].

3. Results and discussion

The optical absorption coefficient, α, is calculated from the transmission, $T= I_0/I$ and using the relation

$$\alpha=1/d \ [\ln (1-R)^2 \ / \ T] \qquad (1)$$

where, d is the thickness and R the reflectivity. The energy variation of the absorption coefficient gives an indication of the distribution of the density of states in the energy gap. The low energy region, 1.2-1.8 eV, which is obtained by measuring transmission through the thick bulk samples, gives an estimate of the density of the deep defects states at mid-gap. The absorption spectra of the thin films one are determined at the high-energy region, 2.1-3 eV, obtained by measuring transmission through the thin films. In the region with energies higher than 2.5 eV, the absorption coefficient shows a parabolic variation on the photon energy, while up to 2.5 eV, it depends exponentially on the photon energy [7],

$$\alpha=\alpha_0 \exp (h\nu/E_0) \qquad (2)$$

where α_0=const and E_0 is the so-called Urbach slope. Variations in the width of the exponential region, E_0, provide information about the relative changes of the structural disorder induced by an additive. For a good chalcogenide material, a typical value of the slope, E_0, is around 50 meV. Higher values of E_0 indicate that the addition of Ga increases the disorder. In this region the optical band gap of the material is also determined. The optical band gap, E_g, of amorphous materials [7] is usually defied as the energy at which α has a value between 10^4–10^5 cm^{-1}. In our case, where the interference fringes start to dominate the photon energy range below 2.1 eV, we take as an optical gap, E_g^4, the energy where α=2×10^4 cm^{-1}.
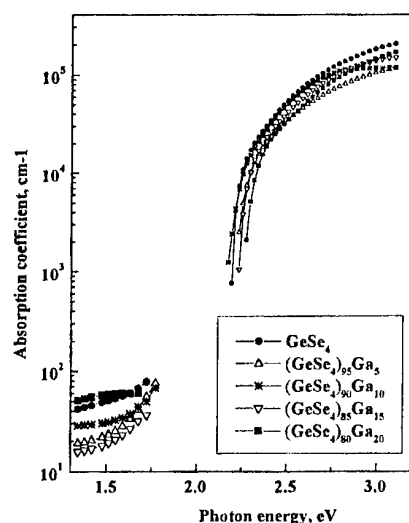

Fig. 1. Spectral dependence of the absorption coefficient for $(GeSe_4)_{1-x}Ga_x$ system.

In Fig.1 are plotted the spectra dependence of the absorption coefficient, α, for bulk (at the low energy range) and for thin films (at the high energy range) of $(GeSe_4)_{1-x}Ga_x$ with x = 0, 5, 10, 15 and 20. As it can seen the optical gap increases slightly with the gallium content.
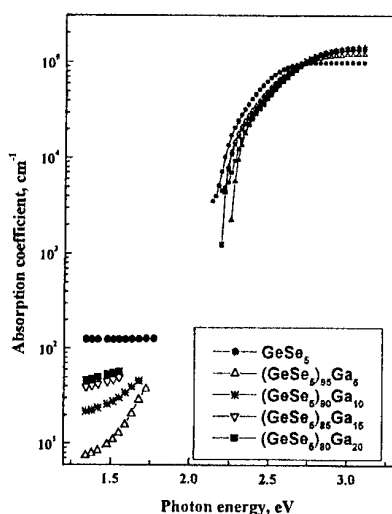
Fig. 2. Spectral dependence of the absorption coefficient for $(GeSe_5)_{1-x}Ga_x$ system.
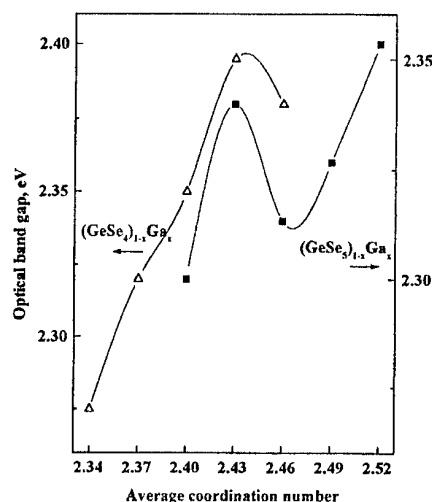
Fig. 3. Optical band gap versus gallium content.

Fig. 2 shows the spectral dependence of the absorption coefficient of bulk and thin films with compositions $(GeSe_5)_{1-x}Ga_x$, where x= 0, 5, 10, 15 and 20. We can see that the addition of up to 5 at.% Ga decreases the midgap absorption, and also the optical gap. The addition of higher concentrations of Ga seems to increase the absorption gap and the midgap absorption. Due to the similar compositions, the variation of the optical band gap with the Ga content for the alloys of the system $(GeSe_5)_{1-x}Ga_x$ is very similar to that of the $(GeSe_4)_{1-x}Ga_x$ alloys. In Fig. 3 is plotted the variation of E_g^4, as a function of the Ga content. The observed increase of the band gap can be explained in terms of structural arguments. It is known that the structure of the Ge-Se-Ga glasses is made up from tetrahedral $GeSe_2$ and pyramidal Ga_2Se_3 units [8]. According to the chemically ordered covalent network model [9] the $GeSe_2$ and the Ga_2Se_3 units are connected with extra Se atoms. The excess Se atoms are connected in chains. Ge-Ge bonds are not expected to form up to 33 at. % Ge. According to ref. 10, the bond energy of Ga-Se bonds (65 kcal/mol) is bigger than Ge-Se bond energy (55.4 kcal/mol), which indicates that the increase of the Ga content, the average bond energy of the system will increase. The formation of stronger bonds could be the cause of the increase of the optical band gap. The optical constants of the thin films were calculated from the transmission spectra, using a method proposed by Swanepoel [6]. The spectral dependence of refractive index, n and extinction coefficient, k for $(GeSe_4)_{1-x}Ga_x$ and $(GeSe_5)_{1-x}Ga_x$ are shown in Fig. 4 and Fig. 5.
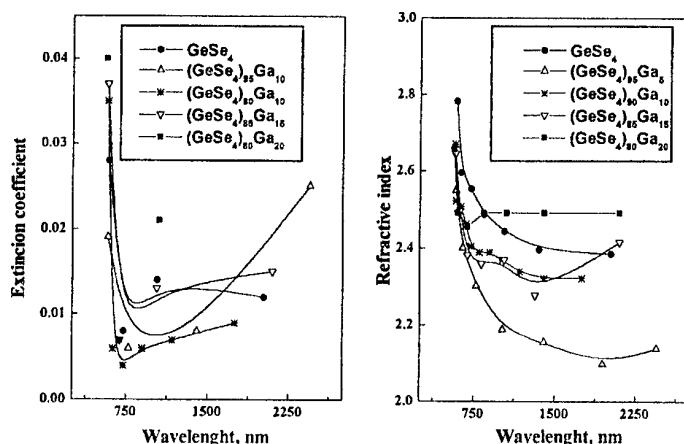
Fig. 4. Extinction coefficient and refractive index for $(GeSe_4)_{1-x}Ga_x$ system.
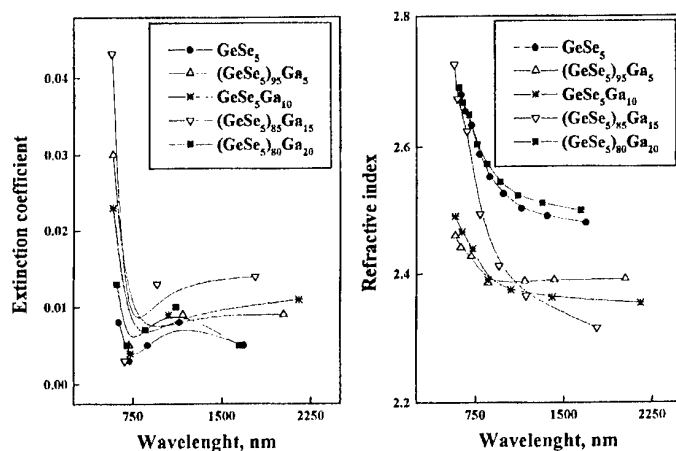
Fig. 5. Extinction coefficient and refractive index for $(GeSe_5)_{1-x}Ga_x$ system.

It is found that, at small wavelengths, both k and n decrease drastically and then remain practically constant. The values of k and n decrease slowly with the increase of the gallium concentration. This trend of lower values with increasing Ga content could assume to be connected with structural transformations. The appearance of new Ga_2Se_3 units changes the density of the material, which is consistent with optical constants' values.

4. Conclusions

Optical properties of the glasses from the systems with a constant ratio of Ge/Se and different quantities of gallium are investigated. The optical gap found to increase with the addition of gallium. This variation could be explained as due to the increase of average bond energy of the alloys that occurs with the addition of Ga.

Acknowledgment

References

[1] P. Klocek, L. Colombo, Index of refraction, dispersion, bandgap and light scattering in GeSe and Ge-Sb-Se glasses, J. Non-Cryst.Solids, 93, 1 (1987).
[2] M. Fadel, The physical properties and the chemical bond approach for Se-Ge-As amorphous chalcogenide glasses, Vacuum, 48(1), 73 (1996).
[3] S. Saffarin, Compositional trends of the compactness in ternary chalcogenide glasses of the Ge-In-Se system, Physica B, 253, 52 (1998).
[4] B. Kolomiets, Y. Rukhlyadev, V. Shilo, The effect of gallium, indium and thallium on the photoelectric ptoperties of glassy arsenic selenide, J. Non-Cryst. Solids, 5, 402 (1971).
[5] M. Mitkova, Z. Boncheva, Compt. Glassforming region in the Ge-Se-Ga system, Rend. Acad. Bulg. Sci., 28, 189 (1975).
[6] R. Swanepoel, Determination of thr thickness and optical constants of amorphous silicon, J. Phys. E: Sci. Instrum. 16, 1214 (1983).
[7] N. F Mott, E. A Davis, Electronic Processes in Non-Crystalline Materials, Claredon Press (1971).
[8] S. Mahadevan, A. Giridhar, Coexistance of topological and chemical ordering effects, Journal of Non-Crystalline Solids, 152, 42 (1993).
[9] G. Lucovsky, F. Galeener, R. Keezer, R. Geils, H. Six, Phys. Rev B, 10, 5134 (1974).
[10] Gmelin Handbuch anorganischer Chemie, Se, B2, Springer Verlag, (1984).

PHOTOELECTRET PROPERTIES AND HIGH-FIELD POLARIZATION IN CHALCOGENIDE GLASSES AND THIN FILMS

E. Skordeva

Institute of Solid State Physics, Bulgarian Academy of Sciences,
72 Tzarigradsko Chaussee blvd, 1784 Sofia, Bulgaria

The paper is dedicated to the 90th anniversary from the birth of my father, the late Prof. Razum Andreichin. It is dedicated also to the 20th commemaration from the death of the Academician Georgy Nadjakov, the discoverer of the photelectret state (PES). A short historical review on the invention of PES is followed by a brief presentation of the matter of the photoelectret state and the high-field polarization. The most part of the results obtained from Prof. Andreichin and co-workers during investigations of PES in chalcogenide glasses, mainly As_2S_3 and As_2S_3–based ones, is summarized.

1. Introduction

1.1. Short historical presentation

The term "electret" was introduced at the end of the 19th century by O. Heaviside [1] as a counterpart of the term "magnet". The first representative of the great family of the electrets was the thermoelectret, discovered by Eguchi [2]. The electrets family contains nowadays a number of different members -- thermoelectrets, photoelectrets, thermophotoelectrets, radioelectrets, magnetoelectrets etc. One of them, the photoelectret, was discovered by the Bulgarian physicist G. Nadjakov in 1937 [3]. In that time Prof. Andreichin was a Ph.D. student of Prof. Nadjakov. He kept the interest to that matter all his life. There was a strong "photoelectret" school in Bulgaria leaded by Prof. Nadjakov (Chetkarov, Andrejchin, Kashukeev, Antonov et al). A great deal of the contribution to the photoelectret state investigations has the Russian School (Fridkin, Zheludev, Adirovich, Tartakovskii etc). There was a group of researchers in India (Pillai, Jain et.al.) which has also contributted to the investigation of the photoelectret state. Researchers from all over the world have worked in this scientific region because of the large application possibilities it gives (PES is widely used nowadays in the technique - in the electrophotography, xerography, electrofax technique etc.).

The first material in which the photoelectret state was proved was polycrystalline sulfur. Later this state was found in many other wide-band-gap materials, crystalline or amorphous. Several reviews on photoelectrets are listed in references [4-7]. The first publication on photopolarization and photoelectret state in vitreous semiconductors was reported in 1962 by B. Kolomiets and V. Lyubin [8]. In the same time investigations have been carried out in the laboratory of Prof. Andreichin in Sofia. Their first results concerning the existence of a pronounced photoelectret state in vitreous arsenic sulfide were published in 1965 [9]. A great part of the investigations on the photoelectret state in amorphous chalcogenide has been summarized by R. Andreichin in Ref. [10].*
In the present review published [11-16] and unpublished results of the investigation on photoelectret properties of As_2S_3-based glasses and thin films carried out in the laboratory of Prof. Andreichin are used.

---

* In the present paper parts of this publication are used with the special permission of the subsidiary Rights Manager of Elsevier Science.

1.2. Photoelectret state

The photoelectret state is characterized by a prolonged preservation in darkness of the photopolarization called photoelectret polarization. The photopolarization P is the total polarization obtained for an illuminated sample. The analysis of the polarization/ depolarization phenomena leads to a conclusion that they consist of three components (related to 3 processes):

(a) *A dark high-field polarization*, which is independent on the illumination. It disappears for a comparatively short time. The process begins at once after the removal of the field. This polarization is supposed to be caused by relatively shallow traps in the semiconductor.

Wide-band-gap amorphous semiconductors manifest the high-field polarization in darkness with both blocking and injecting electrodes. The latter show that the dark polarization is not only surface, but also bulk phenomena.

(b) *A high-field light polarization*. It has the same character as the dark one but the initial current and the accumulated charge are greater. The corresponding depolarization begins also immediately after removal of the field but it decays more slowly in darkness. This polarization is probably due to a higher concentration of filled levels at the same (or slightly greater) depth as the dark polarization.

Both high-field depolarizations are supposed to be the consequence of thermal recombination.

(c) *Photoelectret polarization* – the permanent polarization of samples kept in darkness. In this process the charge is stored for a long time and deep traps are filled. The depolarization at room temperature after removal of the field begins only when the semiconductor is illuminated again.

It is hard to trace a sharp boundary between light and photoelectret polarization in any real photoelectret and moreover for the disordered ones: the zone between the shallow and deep states is smeared. However, as will be pointed later, a relative decision of this problem can be found.

2. Experimental

Since the formation of the photoelectret state requires a wide band gap, different type of electrometers must be used. The first used in the laboratory electrometers were the constructed by the Academician G. Nadjakov mechanical ones. The kinetics of the polarization and depolarization was investigated using the electronic electrometers of the German Vakutronik and of the Keithley type.

Bulk samples in the form of plates 0.1-1 mm thick were investigated with both gap plane and sandwich type electrodes. Thin films evaporated on mica or teflon with a wide gap between the electrodes were also used.

In the early years of investigation of the electrical properties of the amorphous semiconductors it was believed that no problems with contacts or special effects associated with surfaces exist. Fritzsche has pointed that in several cases this statement is not right [17]. Very high contact resistances are usually encountered in wide gap (larger than 1.5 eV) amorphous semiconductors such as Se, As_2Se_3, and As_2S_3. E.g. when the electrode is allowed to oxidize before it is covered with the amorphous film, it gives rise to a larger contact resistance. In some cases a hole blocking contact is formed at larger biases (V~0.5 volt) - the oxidized contact passes electrons from the metal into the amorphous semiconductor but not reverse. When the electrode, however, is a non-oxidizing metal, the low voltage ohmic region corresponds to the bulk resistance of the amorphous material [17]. The type of the contact is usually evaluated by measuring the U(I) characteristics of the measured sample. The currents should be linear in field indicating the absence of space-charge limitations when electrical resistivity is the aim of the investigation. Another way to check the "reliable" contact provide the comparison of measured I(T) curves obtained by increase and decrease of the temperature. The "hysteresis", however, can be also due to some experimental mistake.

In the light of the mentioned above difficulties it should be stressed that in any case it will be necessary to choose carefully the type of electrodes for any composition.

Our experience has shown that it is very hard to find ohmic contacts for the wide-band-gap semiconductors. Silver contacts are ohmic but diffusion into the sample occurs not only under illumination and heating but even at room temperature. Using gold is a little better. However diffusion of the contact material into the sample is observed by high temperatures. The aquadag contacts are ohmic (injecting) and have been used for bulk samples. Thin films however have been damaged (partially solved in the vicinity of the contact). These problems are not actual when polarization properties are studied. In fact, when using blocking electrodes, both dark and photopolarization are more clearly manifested and considerably stronger. Relatively good blocking contacts have been obtained by evaporating aluminum on the films and

bulk samples. Blocking electrodes have been also formed simply by pressing small metal lamellae to well polished bulk samples. Sometimes we put highly isolating spacers under the lamellae.

In some of the experiments a combination of one blocking and one injecting contacts was used.

3. Results

All of the investigated As_2S_3-based samples have shown typical polarization/depolarization curves at room temperatures. A more detailed analysis of the kinetic of these curves has shown that they are multi-exponential and can be presented as a sum of several currents with different initial values and relaxation times [11]. For the depolarization currents

$$I_d(t) = \Sigma I_{oi} \, e^{-b_i t} \qquad (1)$$

For polarization and depolarization in the dark the sum of the exponents can be satisfactorily reduced to a sum of two components, a rapid one and a slow one. In the case of injecting electrodes the first component decreases very rapidly. By depolarization under illumination the decay curve can be resolved into at least three components. The number of the components depends on the composition. The relaxation times remain almost the same even after keeping the sample for a long time Δt in darkness. The initial current I_o depends on the polarization conditions and decreases with the time. An example of photodepolarization current expansion of As_2S_3 is presented in Table 1. The addition of Ag and Cu to As_2S_3 leads to a decrease of the number of the components and to changes in their relaxation times. The addition of Sn and Ge does not change significantly the kinetics, although the time constants differ with the compositions (e.g. $b_1 \approx 0.026$, $b_2 \approx 0.073$ and $b_3 \approx 0.354$ for $As_2S_3+1.5$ at.% Sn and $b_1 \approx 0.015$, $b_2 \approx 0.054$ and $b_3 \approx 0.14$ for As_2S_3+2 at.% Sn). The kinetics of the polarization and depolarization currents depends also on the technological pre-history of the samples.

Table 1. Kinetics of photodepolarization current of vitreous As_2S_3.

Δt [hours]		0.5		24	95	P
I_{o1} [a. u.]	106.3	132.6	95.5	91.3	69.2	88.3
I_{o2} [a. u.]	1652	1245	959.8	745.7	477.1	1306
I_{o3} [a. u.]	1227	877	687.7	609.6	376	1764.9
I_o [a. u.]	2885	2136.6	1743	1446.6	922.3	3159.2
b_1	0.071	0.071	0.071	0.071	0.071	0.055
b_2	0.258	0.203	0.190	0.205	0.203	0.228
b_3	0.643	0.485	0.457	0.523	0.512	0.559
Q	22600	19900	17900	14000	9300	22800

$$Q = \sum_{i=1}^{n} Q_i = \sum_{i=1}^{n} \int_0^{\infty} I_{oi} e^{-bt} dt = \sum_{I=1}^{n} \frac{I_{oi}}{b_i} \qquad (2)$$

Differences have been observed not only in the kinetics of the polarization/depolarization currents. Changes in the value of the polarization in dark (P_d) or in light (P_l) when new elements are added to the basic glass matrix have also been registered [12-15]. E.g., P_d and P_l shows an upward tendency with an increase in silver concentration and the photopolarization $(P_l - P_d)$ decreaeses, like the photoconductivity [9].

$$P = U \frac{I_0 - I_1}{I_0} \qquad (3)$$

A measure of the photodepolarization P can be the ratio I_{od}/I_{op}, or, even better, Q_d/Q_p. I_{od} and I_{op} are the initial currents of depolarization and polarization, Q_d and Q_p are the charges released by the depolarization and accumulated during the polarization, resp. Since a sharp boundary between light- and photoelectret- polarization cannot be drawn, the decay curve of the photoelectret charge $Q_d/Q_p(t)$ could be usable. When the ratio approaches a constant value, the polarization remaining is due solely to the photoelectret state (Fig. 1). Q_d/Q_p depends also on the composition of the electret (Table 2).

Table 2 . Qd/Qp for bulk samples with different compositions.

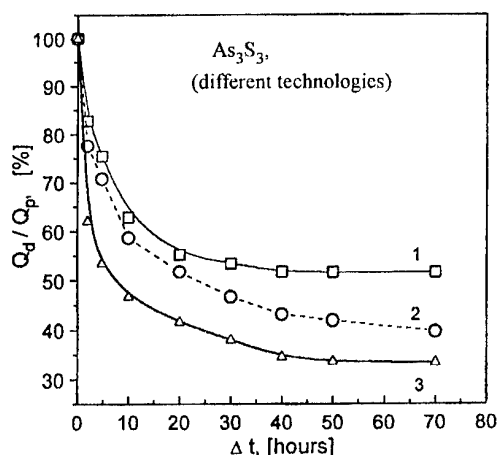|	Sn			Cu				Ag		
At. %		1.5		2.5	0.5				0.5	1	2
Light	80	55	40	30	20	41	58	56	15	10	15
Dark	40				12	28	30	28	30	10	15

Fig. 1. Dependence of the photo-polarization on the time Δt for bulk samples obtained by different cooling technologies. Curve 1 - the ampoule with the melt was kept 24 hours at 200°C, curve 2 – the cooling was performed in the furnace, curve 3 – cooling in the air [16].

Powerful methods for investigation of the charge created in the deep traps of the electrets are those using thermally stimulated discharge. The method of thermally stimulated currents can be used and, also, the method of the thermally stimulated depolarization. In the latter the heated sample is cooled under illumination and applied voltage. Then on re-heating of the electret without applied voltage, the stored charge is released. The discharge $I(T)$ curves are registered as "glow peaks". The shape of these peaks is supposed to be similar to the uniform density of the previously stored in the traps charge. Although the position of the discharge peaks depends on the experimental details (applied voltage, spectral characteristics and intensity of the used light, the velocity of the temperature change etc.), a qualitative scheme of the deep band-gap-states distribution can be drawn. The bad site of this method is that it does not give a complete picture of the whole band structure but only of a small part of it.

Fig. 2 and 3 represent several discharge curves obtained using the method of the thermally stimulated depolarization. The curves are normalized toward 100% for the higher extremum in order to elucidate the differences in the shape and the position of the maxima. The shape of the obtained maxima varied with the composition, both with the amount and the type of the added to the arsenic sulfide metal. A rough evaluation of the parameters of the traps, that are potentially connected with these maxima, gives the values of 0.4-0.78 eV for the depth (from the top of the valence band) and a minimal concentration of the filled traps about 10^{11}. [12-15]. Similar results have been obtained by other authors in chalcogenide glasses when photoluminescence was investigated. The presence of two groups of levels: one close to the band edge, and another about 1 eV deep in chalcogenide glass has also been reported by Kolomiets. et. al. [18].

Photoelectret state and photopolarization have been found not only in the mentioned above materials. We have also observed them in glasses of the As_2S_3-As_2O_3, As_2S_3-GeS_2 , $As_2S(Se)_3$-$Ge_2S(Se)_3$ and other systems. Investigation of thin films evaporated from these glasses has shown that, although less pronounced, the same polarization phenomena as in bulk samples are present. Evaporated layers of the same composition as bulk materials show much weaker photoelectret properties. However, for technological reasons thin films are successfully used in the electrophotography.
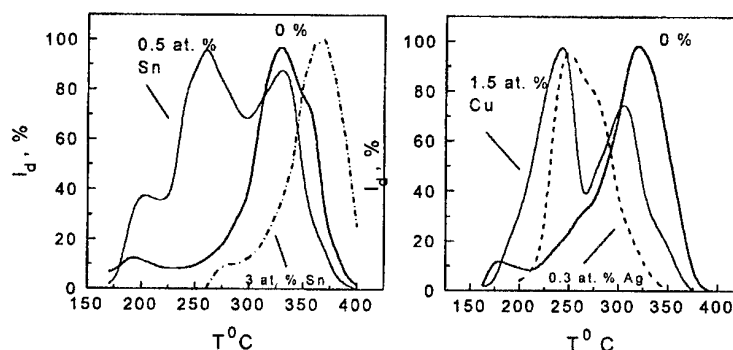
Fig. 2. Depolarization curves obtained for bulk As_2S_3-based glasses with different additivities.

4. Discussion

The photoelectret properties of As_2S_3-based glasses are characterized by all the common features of the crystalline photoelectrets: (1) For a constant light intensity the accumulated charge Q depends linearly on the applied field up to a certain value (e.g. 3 kV/cm) and then tends to saturation; (2) For a constant external electrical field Q is proportional to the illumination; (3) For both constant field and illumination Q depends initially linearly on the irradiation time, after wich becomes saturated; (4) The reciprocity law is obeyed to a certain high value of the radiant energy. The difference between the crystalline and amorphous photoelectrets consists mainly in the lack of a broad interval without traps in the latter ($\Delta E > 0.4$ eV is needed, according to the photoelectret theory [5]). It is obvious, however, that despite of the hypothesis about the large area of traps distribution in the band gap in the amorphous semiconductors, the presence of photoelectret state is possible. The undoubted result obtained by the summarized above investigations is the non-uniform distribution of the traps in the band gap.

Shallow traps are related to the dark and light high-field polarization. The results of the performed current expansion allow to suppose different trapping levels for the different current components. They may differ either in depth, or in mechanisms of accumulation, trapping cross-section etc. It is not necessary to connect these traps with the band tails, but it is very probable that they are. As_2S_3 glasses cooled with different rates have shown, differences in the grade of their PES, as well as in the amount of P and Q_d/Q_p (Fig. 1, the cooling rates are respectively $v_1 < v_2 < v_3$). Long time annealing or low rate of cooling lead to greater order and decrease of the band tails. When metal additions are included in the glass matrix of As_2S_3, the medium and long-range order are also damaged. The addition of Ag disturb the chain-like and layer-like structure. New shallow traps become active and the accumulated by the polarization charge is released faster. The addition of Sn may help the formation of longer layers and decrease the amount of shallow traps. The band tails decrease and the gap between them and the deep traps increases. As a result the photoelectret properties of the materials becomes better pronounced. The change of the composition leads to changes of the size of the semiconductor band gap. This process can also increase or decrease the assumed gap between the deep traps and the next ones taking part into the conductivity. Not only the position but also the density of the mentioned traps could be changed in a similar way.

The results of the thermally stimulated depolarization have shown that somewhere around the middle of the band gap a non-uniform distribution of deep traps also exists. Probably all the intermediate states are localized and do not allow a thermal recombination to the bands until a sufficient energy is absorbed. However, the attempt to do a spectral dependence of the photopolarization at room temperature has shown that the polarization considerably increases only when the photon energy is greater than the band gap. This discrepancy might not be connected only with the slight intensity of the used light (see the last paragraph of this section).

The deep gap states might originate from dangling bonds, defects and random deviations from the network structure. As_2S_3 has a local structure spread to the dimensions of the middle-range order. Independently on the fact are the As_2S_3-pyramids connected simply in layers or clustered, many uncompensated free states can be present at their ends. The addition of new elements leads to the formation

of new structural units and changes the charge and the amount of those states. That is the reason for the different behavior of the glasses containing Ag and Sn. In both cases, however, the stoichiometry was disturbed. As a result the position of the thermostimulated depolarization peaks changes. (All the experimental conditions were equal).

In the same experimental conditions the depolarization curves of As_2S_3-As_2O_3 glasses have not shown any significant changes with the composition. This is probably due to the fact that both molecular components are stoichiometric, isomorphic and the parameters of the local order do not differ essentially.

The thin evaporated films are essentially more disordered than the parent glasses. Many new shallow traps are formed in their band gap and the accumulated during the polarization charge is easily released.

Several authors have supposed a relation between the dark conductivity and the position and height of the corresponding peak of the depolarization current [19, 20]. According to P. Muller, if the depolarization is caused by equilibrium charge carriers the position (temperature of the maximum) and the height of the TSD peak can be predicted. P. Muller has supposed that the bulk conductivity determines accumulation of depletion of charges in the surface, adjacent to the blocking electrodes regions. Although such a model seems not applicable for our experimental results, it is worth to turn the attention of the future investigations towards the correctness of all types of interpretation of the TSD results. Moreover, since this paper is written as a review of works performed in the past, it would be advisable to use new contemporary methods to elucidate all the discrepancies and unclear items.

5. Conclusions

The present review has shown that the polarization and photoelectret phenomena in in As_2S_3-based amorphous semiconductors do not differ phenomenologically from those in the corresponding crystalline semiconductors. The explanation of this phenomena based on the band theory for crystalline or amorphous semiconductor, however, meets with some difficulties and requires much more investigations.

References

[1] O. Heaviside, Electrical Papers (USA) 1, 488 (1892).
[2] M. Eguchi, Proc. Math. Soc. Jap., 1, 326 (1919).
[3] G. Nadjakov, Chem. Rev. 204, 1865 (1937).
[4] V. M. Fridkin, I. S. Zheludev, "Photoelectrets and the Electrophotographical Process", AN USSR, Moskow, (1960) (in Russian).
[5] V. M. Fridkin, "The Physics of the Electrophotographical Process", Focal Press, New York,-1973
[6] P. K. C. Pillai and Malti Goel, Phys. Stat. Sol. (a), 6, 9 (1971)
[7] "Electrets", ed. By G. M. Sessler, Springer-Verlag, Berlin-Heidelberg-New-York, (1980)
[8] B. T. Kolomiets and V. M. Lyubin, Sov. Phys. Solid State, 4, 291 (1962)
[9] R. Andrejchin, P. Simidchieva and M. Nikiforova, C.R. Acad. Bulg. Sci, 18, 1079 (1965).
[10] R. Andreichin, Journal of Electrostatics, 1, 217 (1975).
[11] R. Andreichin, M. Nikiforova, E. Skordeva, M. Baeva, L. Yuroukova, S. Alexandrova, Bul. de l'Institute de Physique et de Recherche Atomique, Academie Bulg. des Sciences, 24, 13 (1973) (in Bulgarian).
[12] R. E. Andreichin, V. L. Averyanov, E. R. Skordeva, Bulg. J. Phys. 2, 229 (1975) (in Russian).
[13] E. Skordeva, Ph.D. thesis, Physico-Technical Institute, Leningrad, (1975).
[14] R. Andreichin, V. Aver'yanov, E. Skordeva, Bulg. J. Phys. 2, 345 (1975) (in Russian).
[15] E. Skordeva, R. Andreichin, M. Nikiforova, B. Kolomiets, T. Mazets, Proc. Conf. on Amorphous Semiconductors, Balatonfured, ed. Kosa-Somogyi, Publ. House of the Hungarian Academy of Sciences, Budapest, 1978, p. 145.
[16] E. Skordeva, M. Nikiforova, R. Andreichin, Proc. Int. Conf. on High-resistance Semiconductors, Photoelectrets and Electrophotography, Varna, eds. V. Kusev and A. Vavrek, Bulg. Acad. Sci., p. 76, 1974, (in Russian).
[17] H. Fritzshe, in "Electronic and Structural Properties of Amorphous Semiconductors", ed. P.G. Le Comber&J. Mort, Academic Press London and New York, (1973).
[18] B. T. Kolomiets, T. F. Mazets, Sh. M. Efendiev, A. M. Andriesh, J. Non-Cryst. Solids 4, 45 (1970).
[19] P. Muller, Phys. Stat. Sol. (a) 23, 165 (1974).
[20] P. Muller, Phys. Stat. Sol. (a) 28, 521 (1975).

SPECTROSCOPIC STUDIES OF BULK As$_2$S$_3$ GLASSES AND AMORPHOUS FILMS DOPED WITH Dy, Sm AND Mn

M. S. Iovu, S. D. Shutov, A. M. Andriesh, E. I. Kamitsos[a], C. P. E. Varsamis[a], D. Furniss[b], A. B. Seddon[b], M. Popescu[c]

Center of Optoelectronics, Str. Academiei 1, MD-2028 Chisinau, Moldova
[a]Theoretical and Physical Chemistry Institute, HNRF, 11635 Athens, Greece
[b]Novel Photonic Glasses Group, University of Nottingham, Nottingham N67 2RD, UK
[c]National Institute for Physics of Materials, Bucharest-Magurele, Romania

The effect of rare earth (Dy and Sm) and transition metal (Mn) luminescent impurities on the optical properties of As$_2$S$_3$ glass is studied in a wide spectral region. The Raman, infrared, band-to-band and edge absorption spectroscopies are employed to obtain information about the incorporation of impurity ions in the host glass structure and the corresponding changes in intrinsic optical characteristics. The effects of light-soaking and thermal treatment on the doped As$_2$S$_3$ glasses were examined as well. In the fundamental absorption region a reflectivity maximum at 2.98 eV shows blue (Dy, Sm) or red (Mn) shift depending on the electronegativity of the impurity, in accordance with the corresponding variations of the glass structure. Near the edge absorption the impurity affects strongly the slope and the magnitude of the weak absorption tail. In the wide range of transparency the addition of impurity suppresses several absorption bands indicating the interaction of dopants with the host glass contaminations. Some variations of the characteristic Raman spectra under light exposure and thermal ageing of doped glasses were registered. The observed effects of metal dopants on the As$_2$S$_3$ glass are discussed in connection with the expected behaviour of the impurities in the glass.

1. Introduction

Glassy As$_2$S$_3$ is a promising candidate for optoelectronics applications because of its high transmission in the infrared (up to 10 μm), high refractive index (n≈2.4) and low phonon energy [1,2]. Special interest for applications is connected with glassy As$_2$S$_3$ doped with optically active rare-earth and transition metal ions, because they alter optical, photoelectrical and transport properties of the host material [3-5]. The bandgap of arsenic sulphide lies in the visible region of the spectrum (E$_g$≈ 2.4 eV), and thus optical transitions involving conduction bands and edge tail states overlap with some electronic transitions due to the discrete levels of the rare-earth ions (Pr^{3+}, Nd^{3+}, Sm^{3+} or Dy^{3+}). For this reason, the photon energy absorbed in the broad band region in rare earth doped As$_2$S$_3$ glasses is partially transferred to rare earth ions, and this results in the enhancement of the pumping efficiency of luminescence. This is an important effect for applications such as in fibre optics amplifiers operating at the 1.3 μm telecommunication window [6,7].

X-ray diffraction results as well as optical, electrical and photoelectrical characteristics have been reported for As$_2$S$_3$ and As$_2$Se$_3$ glasses doped with Dy, Sm and Mn [8]. It was shown that doping affects the interlayer distance and leads to creation of additional localised states in the forbidden gap of the chalcogenide glass. These effects are manifested by changes in electrical and photoelectrical characteristics of glass, while doping stabilises the glassy matrix with respect to light exposure and thermal treatment [9].

The aim of this paper is to study further the effect of metal impurities (Dy, Sm and Mn) on the structure of As$_2$S$_3$ glass and the optical properties measured over a wide spectral region. The influence of metal impurities on the medium range order (MRO) structure of glass was studied by X-ray diffraction, while infrared and Raman spectroscopies were applied to reveal changes in the short range order (SRO) structure. The effect of doping on the optical characteristics of As$_2$S$_3$ glass was

investigated by UV-visible spectroscopy. Combination of these experimental techniques may elucidate the way metal ions are incorporated in the glassy network, and could help to optimise chalcogenide glass compositions with the desired optical properties. Finally, the effect of illumination and annealing of arsenic sulphide bulk glasses and thin films doped with Dy, Sm and Mn was investigated by infrared and Raman spectroscopies.

2. Experimental

Chalcogenide glasses As_2S_3:Me (Me:Dy, Sm and Mn) were synthesised using elements of 6N (As, S) and 5N purity (Dy, Sm, Mn). Conventional melting in evacuated (p~10^{-5} Torr) and sealed silica ampoules was carried out at two temperature steps, 600÷650 °C for 2 h and 800÷850 °C for 8 h, and was followed by quenching in cold water. The nominal concentration of glass in metal ion dopants was 0.1 and 0.5 at. % (Table 1). The colour of the obtained glasses varies from yellow-red for pure As_2S_3, to dark-red for As_2S_3 doped with Dy and Sm, and to black for As_2S_3 doped with Mn. The glass transition temperature, T_g, of As_2S_3:Me glasses was measured by differential thermal analysis (DTA) and was found to be $T_g \approx 200$ °C (Table 1), as compared to $T_g = 151$ °C for the pure As_2S_3 glass [8].

As_2S_3:Me glass samples doped with various amounts of metal ions were investigated by X-ray diffraction on a Siemens Kristalloflex IV diffractometer, which was equipped with copper target tube, a graphite monochromator and a NaI(Tl) water cooled scintillation counter. It is noted that very accurate recording of the diffraction patterns was necessary because of the nature of the glass diffractograms (i.e. existence of a few broad maxima), and the expected weak structural modifications due to the low level doping with metal ions. The samples were prepared as powders, by crushing chunks of the chalcogenide glasses, and were pressed in special supports for X-ray measurements. High precision diffraction curves were obtained using the step by step method in recording the X-ray intensity. The number of X-ray quanta was counted for 20 s at every angular position, using an angular increment (2θ) from 0.0050 to 0.020.

The bulk glasses were cut into plates of 2÷3 mm in thickness using a low speed diamond saw, and then polished to yield samples with high quality flat surfaces suitable for optical measurements. As_2S_3:Me thin films of thickness 2.0 to 8.85 μm were prepared by thermal evaporation in vacuum onto K-8 glass substrates. A SolarBox-1500 device equipped with a Xenon lamp and infrared and ultraviolet cutting filters was used as light source for exposing bulk and thin film samples to radiation in the spectral region 0.7 to 0.4 μm, where As_2S_3 glass exhibits its optical bandgap (2.4 eV). Annealing bulk As_2S_3:Me glasses was accomplished by heating in an open air furnace in a step-by-step mode at 160 °C, 190 °C and 210 °C for 3 h, 2 h and 1 h, respectively. The as-deposited and irradiated As_2S_3 thin film samples were annealed at 160 °C for 1 h.

Infrared transmittance and specular reflectance (11° off-normal) spectra were recorded on a Fourier-transform vacuum spectrometer (Bruker IFS 113V). Appropriate sources (Hg arc and globar) and detectors (DTGS with polyethylene and KBr windows) were used to cover the infrared region from 30-4000 cm^{-1}. Five Mylar beam splitters of variable thickness (3.5 to 50 μm) were used in the far infrared, 30-700 cm^{-1}, and a KBr one in the mid-infrared range, 400-4000 cm^{-1}. The entire infrared spectrum was obtained by merging the six spectral segments, each one corresponding to the optimum beam splitter throughout. All spectra were measured at room temperature with a resolution of 2 cm^{-1} and represent the average of 200 scans. The reflectance data were analysed by employing the Kramers-Kronig technique to yield the optical response functions of the glass, i.e. the complex refractive index and dielectric function. The absorption coefficient spectra were calculated from the expression $\alpha = 4\pi k\nu$, where k is the imaginary part of refractive index and ν is the frequency in cm^{-1}.

Raman spectra were measured on a Fourier-transform spectrometer (Bruker RFS100) in a back-scattering geometry and resolution of 2 cm^{-1}. The 1064.4 nm line of a Nd-Y laser was used for excitation and this leads to Raman spectra free of luminescence background. UV-visible room temperature reflectance and absorption spectra were recorded on a Perkin-Elmer spectrometer (Lamda 19) in the spectral range 0.2 to 3.2 μm.

3. X-ray diffraction patterns

The measured diffraction curves have shown that all chalcogenide compositions considered in this work are completely amorphous. The main difference between the measured diffraction curves was found in angular region comprising the first sharp diffraction peak (FSDP) as shown in Fig. 1. This finding suggests that doping influences primarily the medium range order structure of the glassy network. A shift of the FSDP from its position in pure As_2S_3 glass can be observed in the diffraction curves of doped glasses (Fig. 1), the direction of which depends on the type of doping metal. We have employed the position of the FSDP in each glass to calculated the per cent relative change of the interlayer distance between As_2S_3 layers in the glassy network, $\Delta d/d$ (%), as a function of metal ion type and content.

The obtained change of interlayer distance was found to depend linearly on the per cent ionicity of the metal-sulphur bond, suggesting a direct influence of Me-S bonding on the MRO structure of glass. The As_2S_3 disordered layers are distorted locally by insertion of metal ions that bond to sulphur atoms. Me-S interactions of high covalency give rise to strong directional bonding that makes the layers more rigid, while the stiffness of layers decreases when the Me-S bonding is mainly ionic and therefore weaker. Thus, the intralayer ordering and the interlayer packing are dependent on the type of metal ions introduced in As_2S_3 glass. Samarium and dysprosium exhibit electronegativities lower than manganese, and thus assume the role of network modifier ions with ionic Me-S bonding. This effect allows for a better packing of the disordered As_2S_3 layers, which can now assume a smaller interlayer distance with respect to pure As_2S_3 glass.
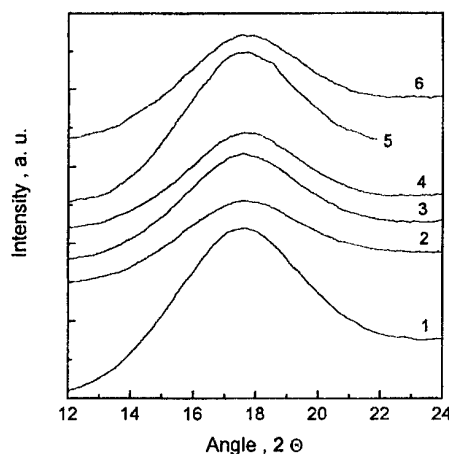

Fig. 1. X-ray diffraction curves of bulk glasses in the region of the first sharp diffraction peak (FSDP); As_2S_3 (1), As_2S_3+0.1 at.% Dy (2), As_2S_3+0.1 at.% Sm (3), As_2S_3+0.5 at.% Sm (4), As_2S_3+0.1 at.% Mn (5), and As_2S_3+0.5 at.% Mn (6).

The higher covalency of Mn-S bonding renders the Mn ions a network former role, and thus the disordered layers become stiffed by the insertion of manganese ions. This leads to an increase of the effective layer thickness and a consequent increase of the interlayer spacing. The effect of the low metal ion contents on the As_2S_3 glass can be explained by co-operative effects. Insertion of few dispersed ions in the layer structure can induce a (dis)ordering effect on a scale larger than the distance of the first co-ordination sphere and, therefore, the interference between the induced zones can amplify the (dis)ordering effect.

4. UV-VIS reflectivity spectra in the fundamental absorption region

The reflectivity spectra of the bulk glassy samples with composition As_2S_3 and As_2S_3:Me (Me:Sm, Dy, Mn) are presented in Fig. 2. The spectra of As_2S_3:Me glasses are normalised to the As_2S_3 spectrum at the photon energy of 2.6 eV, which is near the fundamental absorption edge. This

normalisation procedure removes difference in reflectivity of about 8 % due to surface imperfections of the glass samples.

In the photon energy interval between 2.5 and 6.2 eV a broad double reflectivity peak is observed in accordance with results of earlier studies [2, 10-12], and can be attributed to electronic transitions from the valence band to the conduction band minimum. According to band structure calculations in a tight-binding approximation [13,14], the states near the valence band edge of As_2S_3 result predominantly from the p-orbital electron lone-pair of the chalcogen atom (low-energy side of the reflectivity peak in Fig.2), and the high-energy side of the peak is due to p- and σ- orbital states of chalcogen. In addition to chalcogen orbitals, both parts contain contributions of the p- and s-orbitals of arsenic. In this approximation the shape of the spectra is governed by the SRO structure of glass.

Watanabe et al. [15] have pointed out the important role of intermolecular interactions in chalcogenide glasses, which are responsible for the strong dependence of the optical gap on external pressure. The inclusion of intermolecular interactions leads to marked changes in the density-of-states spectra of the valence bands, resulting in the smoothing and broadening of their characteristics. Such changes are observed in the reflectivity spectra in Fig. 2 with addition of metal impurity. Introduction of rare earth Sm and Dy ions causes the broadening of the main reflection feature, especially around its high-energy peak at 3.5 eV, as quoted in earlier studies [10].
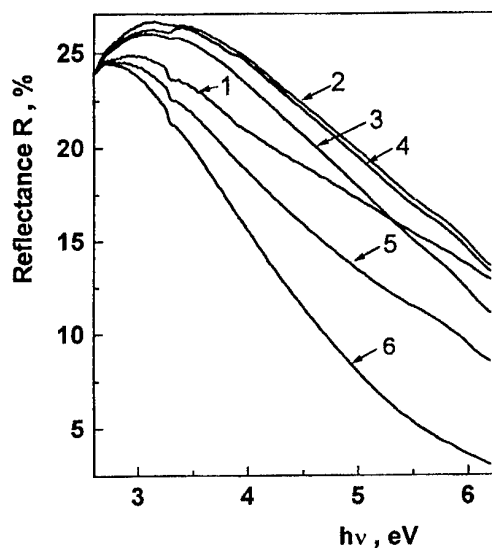

Fig. 2. Reflectance spectra of bulk glasses; As_2S_3 (1), As_2S_3+0.1 at.%Dy (2), As_2S_3+0.1 at.%Sm (3), As_2S_3+0.5 at.%Sm (4), As_2S_3+0.1 at.%Mn (5) and As_2S_3+0.5 at.%Mn (6).

However, addition of the transition metal Mn ions to As_2S_3 glass decreases the reflectivity and bandwidth of the aforementioned band. As shown in Fig. 2, the induced changes by metal ion doping increase with increasing impurity content from 0.1 to 0.5 at. % Sm and Mn. The fall of reflectivity in the 5 to 6 eV energy range in the presence of metal impurities may be associated with the effect of impurities on the degree of intermolecular interactions, which influence significantly the density of states in this energy range [15]. The changes in intermolecular interactions were found to be reflected in the increase (Mn) or decrease (Sm and Dy) of the interlayer distance as discussed earlier in this work. However, these observations are insufficient to provide a quantitative explanation of the impurity effect on the presented reflectivity spectra since the magnitude of shifts predicted in [15] is not observed here. This may suggest that the effect of metal ion impurities is considerably more complex.

5. Fundamental edge absorption

In chalcogenide glasses the absorption edge is broader than in crystalline analogues and this is caused by a broad energy distribution of electronic states in the band gap due to disorder and defects. The absorption edge in the high absorption region ($\alpha > 10^4$ cm^{-1}) is described by a quadratic function

$$\alpha \propto \frac{1}{h\nu}(h\nu - E_g)^2,$$ (1)

and when plotted in the Tauc co-ordinates $(\alpha \cdot h\nu)^{1/2}$ vs. $(h\nu)$ [16] gives the value of the optical gap, E_g, determined as the energy difference between the onsets of exponential tails of the allowed conduction bands [17]. For amorphous As₂S₃ the value of band gap was found to be $E_g = 2.35 \div 2.4$ eV [2].

The optical absorption edge spectra of As₂S₃ doped thin films are presented in Fig. 3a. As in the case of bulk glasses, doping the evaporated As₂S₃ thin films affects strongly the optical absorption edge spectra, as evidenced by the pronounced shift to lower energy values.
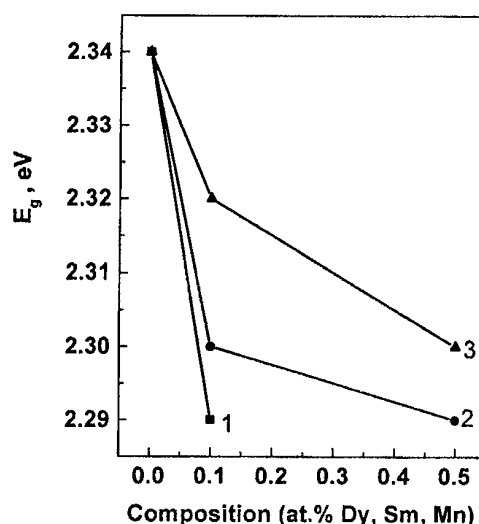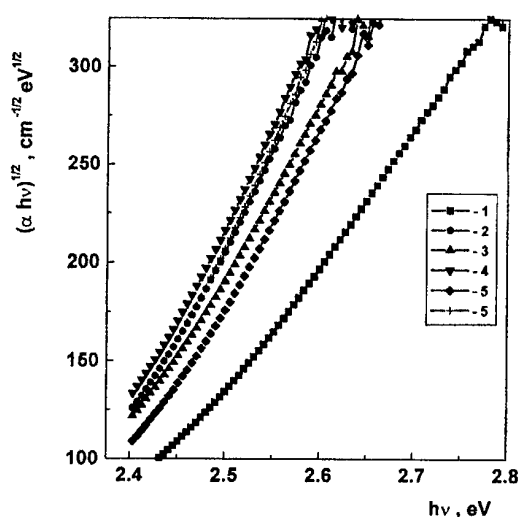

Fig.3a. Absorption spectra of thin films; As₂S₃ (1), As₂S₃+0.1 at.% Dy (2), As₂S₃+0.1 at.% Sm (3), As₂S₃+0.5 at.% Sm (4), As₂S₃+0.1 at.% Mn (5) and As₂S₃+0.5 at.% Mn (6).

Fig. 3b. Dependence of the optical band gap, E_g, for As₂S₃ doped thin films on the type and content of metal ion impurity; Dy (1), Sm (2) and Mn (3).

The optical gap E_g determined by extrapolation of the straight-line portions of the $(\alpha \cdot h\nu)^{1/2}$ vs. $(h\nu)$ graphs was found to be 2.34 eV for As₂S₃ (Fig. 3b and Table 1), in good agreement with previously reported data [2]. Doping As₂S₃ glass with metal impurities was found to decrease E_g (Table 1), with the new optical gap value being dependent on the nature and concentration of the metal ion dopant (Fig. 3b).

Table 1. Glass transition temperature, T_g, optical band gap, E_g, and Δ_1, Δ_2 values of As₂S₃ doped glasses.

Glass Composition	T_g, °C	E_g, eV	Δ_1, eV	Δ_2, eV
As₂S₃	151	2.34	0.056	0.31
As₂S₃+0.1 at.% Dy	205	2.29	0.11	0.31
As₂S₃+0.1 at.% Sm	213	2.30	0.07	1.02
As₂S₃+0.5 at.% Sm	207	2.29	0.07	1.02
As₂S₃+0.1 at.% Mn	196	2.32	-	0.31
As₂S₃+0.5 at.% Mn	197	2.30	-	-

Absorption coefficient spectra, α, of bulk glasses were calculated from transmittance, T, and reflectance, R, measurements according to:

$$\alpha = \frac{-\ln T}{d} + \frac{2\ln(1-R)}{d},$$

(2)

where d is the thickness of the sample, and are shown in Fig.4. In the Urbach edge region ($\alpha \approx 1 \div 10^3$ cm^{-1}) the absorption coefficient spectra depend exponentially on the photon energy

$$\alpha \propto \exp(\frac{h\nu}{\Delta_1}),$$

(3)

where Δ_1 is the parameter which characterises the distribution of localised states in the band gap. In this region the experimentally obtained α spectrum for vitreous As$_2$S$_3$ is similar to that reported earlier [16]. In addition, the Δ_1 value for amorphous As$_2$S$_3$ found in this work, Δ_1=0.056 eV, is in good agreement with the reported value of 0.05 eV [16], whereas for As$_2$S$_3$ doped with Dy and Sm Δ_1 is found to be somewhat higher (Table 1). For As$_2$S$_3$ doped with Mn the absorption coefficient in this region is very high, and almost frequency independent for the 0.5 at. % Mn glass. The broadening of the Urbach tail is caused probably by the formation of new impurity metal-based structural units, which add compositional disorder to the existing structural disorder. The reason for such behaviour and the role of disorder in the formation of the Urbach edge is still under discussion [18]. This effect is possibly responsible for the drastic increase of absorption in samples doped with Mn, where new Mn-based structural units with lower optical threshold energy may be formed resulting in the decrease of the mean value of the gap as in the case of alloys.
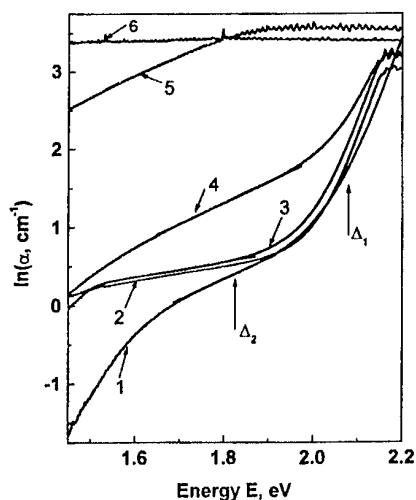

Fig. 4. The absorption spectra of bulk glasses; As$_2$S$_3$ (1), As$_2$S$_3$+0.1 at.%Sm (2), As$_2$S$_3$+0.5 at.%Sm (3), As$_2$S$_3$+0.1 at.%Dy (4), As$_2$S$_3$+0.1 at.%Mn (5) and As$_2$S$_3$+0.5 at.%Mn (6).

The absorption coefficient spectra in the region of weak absorption (α<1 cm^{-1}) are also included in Fig. 4 and show that doping with Sm and Dy results in an increase of the absorption coefficient. The effect of Mn doping is much more pronounced and leads to very high absorption coefficient values. It is known that in this region the absorption coefficient depends strongly on the conditions of sample preparation and the impurities present, and this is often described by an exponential dependence:

$$\alpha \propto \exp(\frac{h\nu}{\Delta_2}),$$

(4)

where Δ_2>Δ_1 [16]. The value of Δ_2 for vitreous As$_2$S$_3$ obtained in this work is $\Delta_2 \approx 0.31$ eV, and this in good agreement with the reported value of 0.3 eV [2]. Doping As$_2$S$_3$ was found to affect drastically Δ_2 as shown by the values reported in Table 1.

The nature of the weak absorption tails in chalcogenide glasses remains to be investigated. It is demonstrated that the absorption in this region is sensitive to impurities, though the tail is still

observed in specially purified samples. This weak absorption may be attributed to additional states created by defects and/or impurities, or to the increase in the average amplitude of the internal electric fields produced by the introduction of additional charged centres. The latter interpretation can be applied to the present case since Sm/Dy and Mn dopants enter the host glass as three- and two-fold charged ions, respectively. It is noted that the As₂S₃ glass studied in this work shows absorption in the region under consideration which is about an order of magnitude higher than that of specially purified samples employed for fibre-optic applications. .
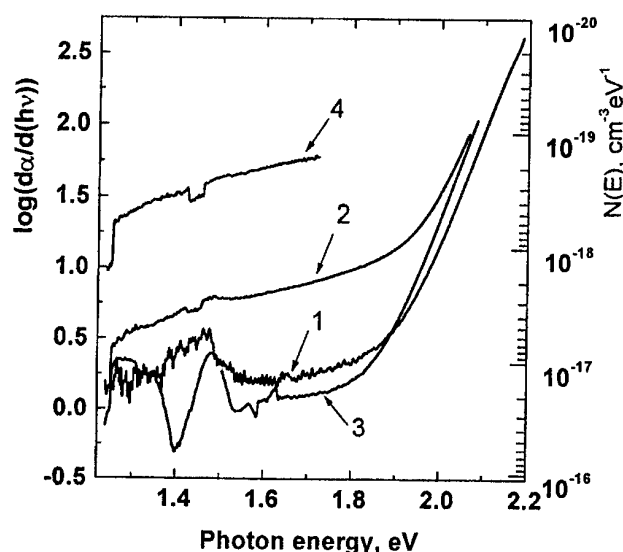

Fig. 5. Derivative of absorption spectra reported in Fig. 4. Right scale gives the order of the density of states. Spectral numbering corresponds to glass compositions given in the caption of Fig. 4.

For the evaluation of the density of states distribution associated with the weak absorption region we follow the approach of Ref. [19]. By using standard simplifying assumptions the relation between the density of states $N(E)$ and absorption spectrum $\alpha(hv)$ takes the form [20]:

$$N(E_c\text{-}hv) = M[d\alpha/d(hv)], \tag{5}$$

where $M \approx 10^{17}$ cm⁻². The density of states $N(E)$ calculated from the differentiation of the $\alpha(hv)$ spectra are shown in Fig. 5 for the As₂S₃:0.1at.% Me glass samples. It is observed that the Sm doped sample modifies slightly the density of states in the depth of the gap, while doping with Dy and especially Mn produces a substantial increase in the whole energy range. This procedure provides reasonable values for the density of states of active centres, and this is ca. 10^{17} cm⁻³eV⁻¹. As shown in Fig. 5 Dy and particularly Mn ions are more effective in producing optically active centres in As₂S₃ than Sm ions.

6. MID infrared transmittance

The mid-IR transmission spectra of As₂S₃ and As₂S₃:Me doped glasses are shown in Fig. 6 and are characterized by several well resolved absorption bands. These bands are observed in the frequency ranges 839÷993 cm⁻¹ (As-OH), 1500÷1587 cm⁻¹ (O-H), 2487÷2493 cm⁻¹ (S-H), and 3539÷3625 cm⁻¹ (O-H), and are summarized in Table 2. The characteristic absorption bands for pure As₂S₃ are measured at about 993, 1587, 2487, and 3539÷3625 cm⁻¹, and are significantly reduced upon doping with Sm, Dy and Mn. For the As₂S₃+0.5at.% Sm glass additional absorption bands are measured at 2025 and 1500 cm⁻¹. The observed changes upon doping in the mid infrared region are most likely related to interactions of a portion of the introduced metal ion impurities with the inherent

impurities of the host glass, such as hydrogen and oxygen atoms. Such interactions result in the reduction of the relative intensity of bands associated with O-H. S-H, As-O and As-H bonds in the parent glass.
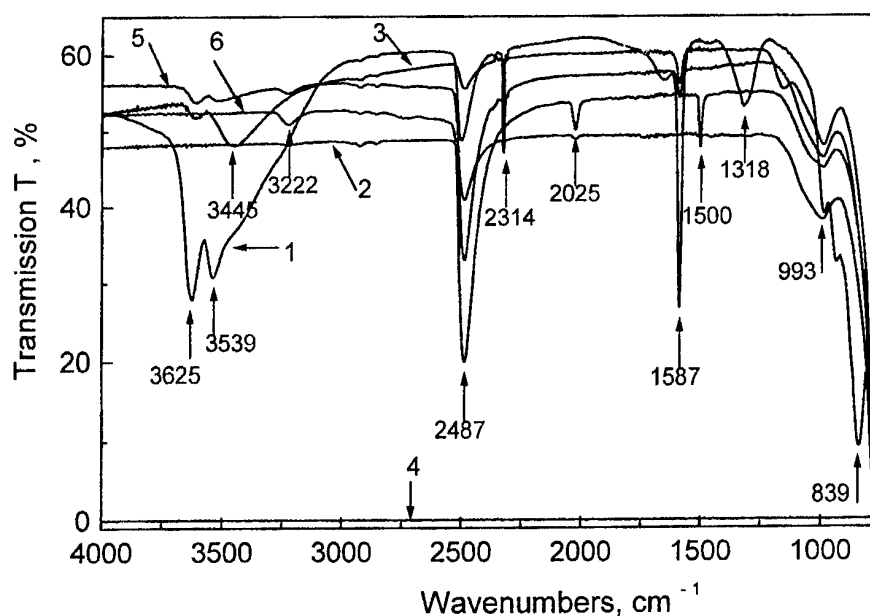

Fig. 6. Mid infrared transmission spectra of glasses As_2S_3 (1), As_2S_3+0.1 at.% Dy (2), As_2S_3+0.1 at.% Mn (3), As_2S_3+0.5 at.% Mn (4), As_2S_3+0.1 at.% Sm (5), and As_2S_3+0.5 at.% Sm (6).

Table 2. Assignments of characteristic vibrational bands for vitreous As_2S_3 doped with Dy, Sm and Mn.

Glass	Infrared frequency (cm^{-1}) and assignments					
composition						As–O
	O-H	S- H	?	O-H	As_4O_6	As–H
As_2S_3	3539-	2487	2314	1587	1318	839
As_2S_3+0.1 at.% Dy	3625	2493	-	-	-	993
As_2S_3+0.1 at.% Sm	-	2493	2325	1590	-	989
As_2S_3+0.5 at.% Sm	3623	2493	2024	1500	-	990
As_2S_3+0.1 at.% Mn	3623 3460	2493	-	1590	-	988

Additional treatment of glasses by irradiation for 6 hours and annealing at 210 °C was found to cause no significant changes in the infrared transmission spectra. This fact manifests the high stability of As_2S_3-based bulk glasses towards thermal and visible light-irradiation treatments. However, a recent study of bulk As_2S_3 glass has shown that wavelength-selective infrared irradiation can cause a significant reduction of the intensity of vibrational modes associated with CH_x impurities [21]. Thus, the method of wavelength-selective infrared irradiation may provide a novel non-thermal treatment for the reduction of infrared absorption attributed to impurities in As_2S_3-based glasses.

7. Raman spectra

a). Raman spectra of As₂S₃ doped glasses

The measured Raman spectra of As_2S_3 and As_2S_3:Me doped glases are reported in Fig.7. The Raman spectrum of vitreous As_2S_3 is similar to that reported in the literature [22,23], and is dominated by the strong band at ca. 345 cm⁻¹ attributed to the symmetric stretching vibrational mode of $AsS_{3/2}$ pyramids [24]. Besides this strong band at 345 cm⁻¹, there are additional features (shoulders) at ca. 310 and 380 cm⁻¹ and can be assigned to the asymmetric stretching modes of $AsS_{3/2}$ pyramids and As-S-As bridges, respectively [24]. The presence of sulphur in excess is indicated by the weak band at 485÷495 cm⁻¹ associated with the S-S stretching vibration in S_8 rings. Weak bands situated at 188 and 235 cm⁻¹ can be attributed to the bending modes of $AsS_{3/2}$ pyramids and S_8 and As_4S_4 molecules [23,24].
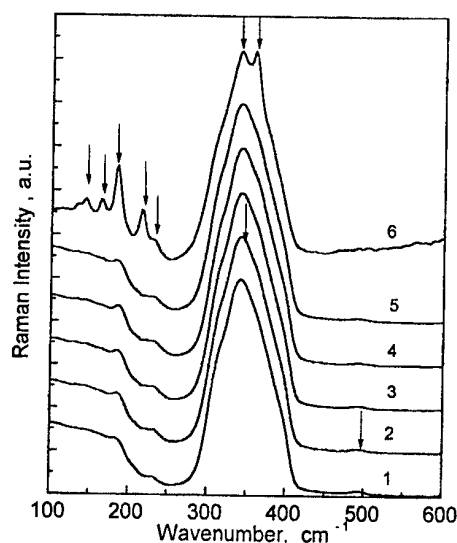

Fig. 7. Raman spectra of chalcogenide glasses; As_2S_3 (1), As_2S_3+0.1 at.% Dy (2), As_2S_3+0.1 at.% Sm (3), As_2S_3+0.5 at.% Sm (4), As_2S_3+0.1 at.% Mn (5), and As_2S_3+0.5 at.% Mn (6).

Doping As_2S_3 glass with Dy and Sm causes a slight increase of the intensity of bands located at 235 and 185 cm⁻¹, as opposed to the drastically changed Raman spectrum of the As_2S_3+0.5 at.% Mn glass. In particular, introduction of Mn leads to the appearance of a number of narrow bands in the frequency region 130 to 220 cm⁻¹ which may be associated with the formation of a new sulphur-containing units, like the MnS clusters. In addition, the most intense peak at 345 cm⁻¹ splits into two bands characteristic of the presence of As-rich molecular units (As_4S_4 type molecules), as reported elsewhere [23]. Such new molecular fragments can be formed by a Mn-induced dissociation $2As_2S_3 \rightarrow As_4S_4+S_2$. A similar dissociation process was suggested by the Raman spectral profiles of freshly evaporated amorphous chalcogenide films in the As-S system [23].

b). Raman spectra of light irradiated As₂S₃ doped bulk glasses

With the exception of the As_2S_3+0.5 at.% Mn glass, irradiation with light in the visible was found to cause no effect on the Raman spectra of all other compositions. Similar observations were reported in a recent study of photodarkening effects in glassy As_2S_3 [25]. Irradiation with light of energy near the optical band gap (λ=514.5 nm) for 230 hours resulted only in subtle differences in the measured NMR spectra [25]. It is pointed out that an increase of the relative intensity of the broad

band situated at 345 cm^{-1} during irradiation was observed in the Raman spectra of crystalline As_2S_3 samples and was ascribed to a crystal-to-amorphous state transition [17].
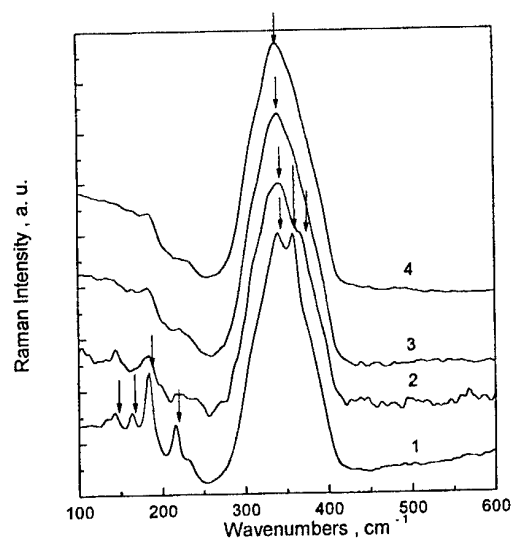

Fig. 8. Raman spectra of As_2S_3+0.5 at.%Mn glass before anealing (1) and after annealing at T=150 °C for 3 hours (2), at T=190 °C for 2 hours (3), and at T=210 °C for 1hour (4).

c). Raman spectra of annealed As_2S_3 doped glasses

The Raman spectrum of As_2S_3 glass was found to remain the same after annealing at temperatures T=150 °C (t=3 hours), T=190 °C (t=2 hours) and T=210 °C (t=1 hour). Frumar et al. [26] suggested that the As_2S_3 glass does not crystallise even after annealing for several months at temperatures near or above the glass transition temperature. These findings indicate again the high thermal stability of As_2S_3 glass, probably because of similarities in the short range order structure and Gibbs free energy in the glassy and crystalline states of arsenic sulfide.

The same behaviour was observed for the doped As_2S_3 glasses with the exception of the As_2S_3+0.5 at. % Mn glass. As shown in Fig.8, upon increasing annealing temperature the splitting of the peak at ca. 345 cm^{-1} gradually disappears, and is completely removed with annealing at 210 °C. This effect is accompanied by the progressive decrease of the intensity of the sharp bands in the 130 to 220 cm^{-1} region. Thus, the dissociation process $2As_2S_3 \rightarrow As_4S_4+S_2$ seems to be reversed by annealing. Similar effects were reported in photodarkening studies of glassy As_2S_3 where changes induced by irradiation at 514.5 nm for 230 h were found to be reversed by annealing at 200 °C for 1.75 h [25].

d). Raman spectra of light irradiated As_2S_3 thin films

The Raman spectrum of the as-evaporated As_2S_3 thin film measured in this work was found to be similar to that reported in a previous study [28]. This spectrum exhibits strong bands at 345 and 365 cm^{-1}, and several sharp features in the region 100 to 250 cm^{-1} (Fig. 9a), which can be assigned to molecular species of the As_4S_4, As_4 and S_n type.

Irradiation of As_2S_3 thin films prepared by thermal evaporation was found to cause a photodarkening effect, as manifested by measurements of the absorption edge of thin films (L=8.85 µm) before and after irradiation. It was found that irradiation causes a shift of the absorption edge in the Urbach region to lower energies. This shift is equal to $\Delta\lambda$=6.3 nm when the film is irradiated for 20 min, and increases to $\Delta\lambda$=16.8 nm when the film is irradiated for 6 hours.

As shown in Fig.9a, irradiation treatment for 20 and 40 min causes the decrease in the intensity of bands at 364 and 495 cm^{-1} and those in the frequency region 100 to 250 cm^{-1}, in agreement with results reported in previous works [27,29]. When the irradiation time was increased

to 6 hours the glass exhibited a broad Raman spectrum with a pronounced feature at 231 cm⁻¹ (Fig. 9a), which may by associated with As clustering in the glass [19]. Such changes may be interpreted in terms of optical polymerization of As_4S_4 structural units into the glassy network, as reported previously in a study of photoinduced changes in the infrared spectrum of amorphous As_2S_3 films [30].
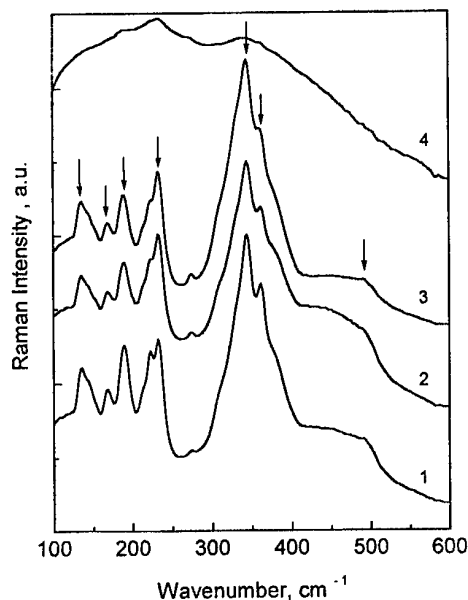

Fig. 9a. Raman spectra of the as-deposited As_2S_3 thin film (1), and after irradiation for 20 min (2), 40 min (3), and 6 h (4).
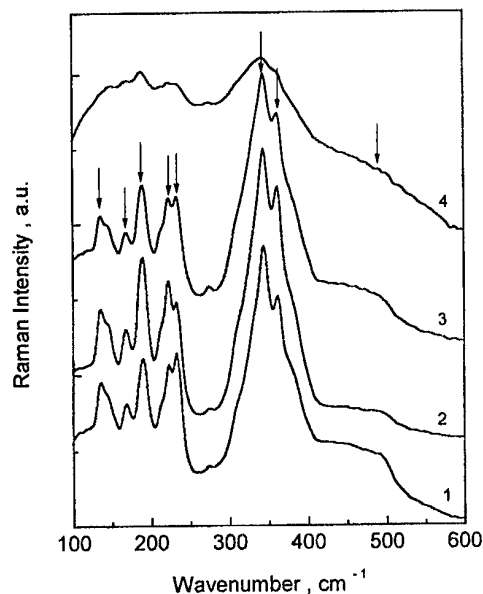
Fig. 9b. Raman spectra of as-deposited As_2S_3 thin film (1), as-deposited and annealed As_2S_3 thin film (2), after irradiation for 40 min and annealing (3) and after irradiation for 6 h and annealing at 160 °C (4).

e). Raman spectra of annealed As₂S₃ thin films

The effect of annealing on the as-evaporated and irradiated As_2S_3 thin films has been also investigated by Raman spectroscopy, as shown by typical spectra in Fig.9b. Annealing thin films which were irradiated for times up to 40 min causes the increase of the relative intensity of the band at 364 cm⁻¹ and the decreases of the intensity of the band at ca. 495 cm⁻¹, while the features in the region 100 to 250 cm⁻¹ remain relatively unaffected. The spectrum of the annealed As_2S_3 thin film which was irradiated for long time (6 hours) shows pronounced differences, and this can be understood in terms of reversing the dissociation process $2As_2S_3 \rightarrow As_4S_4 + S_2$ as in the case of bulk glasses.

8. Conclusions

The effect of rare earth (Dy and Sm) and transition metal (Mn) luminescent impurities on the optical properties of the As_2S_3 glass is studied in a wide spectral region. Raman, infrared and band-to-band reflectance, and edge absorption spectroscopies are used to obtain information regarding the incorporation of impurity metal ions in the host glass structure and the corresponding changes in the intrinsic optical characteristics. The effects of light-soaking and thermal treatment on the doped As_2S_3 glasses were examined as well. In the fundamental absorption region a reflectivity maximum at 2.98 eV shows blue (Dy, Sm) or red (Mn) shift depending on the electronegativity of the impurity, in accordance with corresponding variations of the glass structure. Near the edge absorption the impurity strongly affects the slope and the magnitude of weak absorption tail. In the wide range of infrared transparency the addition of impurity suppresses several absorption bands indicating the interaction of dopants with host glass contaminations. Illumination for 6 hours in the visible and prolonged annealing at 210 °C did not affect substantially the shape and intensity of the main vibrational bands of the investigated bulk glasses, with the exception of the As_2S_3+0.5 at.% Mn composition. The

observed effects of metal dopants on the spectroscopic properties of As_2S_3 glass were discussed in connection with the chemical characteristics of the impurity metal ions.

Acknowledgment

References

[1] A. Madan, M. P. Shaw. The Physics and Application of Amorphous Semiconductors, Academic Press, 1988.
[2] M. Popescu, A. Andriesh, V. Chumash, M. Iovu, S. Shutov, D. Tsiuleanu, The Physics of Chalcogenide Glasses, Ed. Stiintifica Bucharest - I.E.P.Stiinta, Chisinau, 1996.
[3] S. R.Elliott, Adv. Phys. **36**, 135 (1987).
[4] A. Andriesh, M. Popescu, M. Iovu, V. Verlan, S. Shutov, M. Bulgaru, E. Colomeyco, S. Malcov, M. Leonovici, V. Mihai, M. Steflea, S. Zamfira, In: Proc. 18th Annual Semicond. Conf. CAS'95, Sinaia (Romania), Oct. 1995 (**Vol.1**, p.83).
[5] M. S. Iovu, N. N. Syrbu, S. D. Shutov, I. A. Vasiliev, S. Rebeja, E. Colomeyco, M. Popescu, F. Sava, Phys. Stat. Sol.(a), **175**, 615 (1999).
[6] S. Tanabe, J. Non-Cryst. Sol. **259**, 1 (1999).
[7] S. G. Bishop, D. A. Turnbull,B. G. Aitken, J. Non-Cryst.Sol. **266&269**, 876 (2000).
[8] M. Iovu, S. Shutov, M. Popescu, D. Furniss, L. Kukonnen, A. B. Seddon, J. Optoel. Adv. Mater. **1**, 15 (1999).
[9] M. S. Iovu, S. D. Shutov, S. Z. Rebeja, E. P. Colomeyco, M. Popescu, Phys. Stat. Sol. (a) **181**, 529 (2000).
[10] A. M. Andriesh, V. V. Sobolev, I. N. Lerman, Izv. AN MSSR, Ser.fiz.-mat.nauk, **6**, 91 (1967).
[11] R. Zallen, M. L. Slade, A. T. Ward, Phys. Rev.B **3**, 4257 (1971).
[12] N. F. Mott, E. A. Davis, Electron Processes in Non-crystalline Materials (Clarendon Press, Oxford) 1979.
[13] S. G. Bishop, N. J. Shevchik, Phys. Rev. B **12**(4), 1567 (1975).
[14] D. W.Bullet, Phys.Rev. B (1976), **14**(4), 1683
[15] J. Watanabe, H. Kawazoe, M. Yamane, J. Non-Cryst.Sol. **95&96**, 365 (1987).
[16] D. L. Wood, J. Tauc, Phys. Rev. **B5**, 3144 (1972).
[17] W. B. Jackson, S. M. Kelso, C. C. Tsai, J. W. Allen, S.-J. Oh, Phys. Rev. **B31**, 5187 (1985).
[18] J. Ihm, Solid State Commun. **53**, 293 (1985).
[19] K. Pierz, H. Mell, J. Terukov, J. Non-Cryst. Solids, **77&78**, p.1, 547 (1985).
[20] $\alpha(hv)$ is governed by optical transitions from the filled localised states into the free states of the conduction band; dipole matrix element of a transition is energy independent; the distribution of delocalized states is approximated by a step function.
[21] P. Hari, C. Cheney, G. Leupke, S. Singh, N. Tolk, J. S. Sanghera, I. D. Aggarwal, J. Non-Cryst. Sol. **270**, 265 (2000).
[22] G. Lucovsky, R. Martin, J. Non-Cryst. Solids **8&10**, 185 (1972).
[23] M. Frumar, Z. Polák, Z. Černošek, J. Non-Cryst. Solids **256&257**, 105-110 (1999).
[24] E. I. Kamitsos, J. A. Kapoutsis, I. P. Culeac, M. S. Iovu, J. Phys. Chem. **B101**, 11061 (1997).
[25] P. Hari, T. Su, P. C. Taylor, P. L. Kuhns, W. G. Moulton, N. S. Sullivan, J. Non-Cryst. Solids **266&269**, 929 (2000).
[26] M. Frumar, A. P. Firth, A. E. Owen, J. Non-Cryst. Sol. **192&193**, 447 (1995).
[27] I. M. Pecheritsyn, I. I. Kryzhanowsky, M. D. Mikhailov, Glass. Phys. Chem, **24**, 508 (1998).
[28] M .Frumar, A. P. Firth, A. E. Owen, Philos.Mag. **B50**, 463 (1984).
[29] A. V. Stronski, M.Vlcek, A. I. Stetsun, A. Skelenas, P. E. Shepeliavy, J. Non-Cryst. Sol **270**, 129 (2000).
[30] H. Strom, T. P. Martin, Solid State Communic. **29**, 527 (1979).

DONOR- AND ACCEPTOR-LIKE CENTER REVEALING
BY PHOTOCONDUCTIVITY OF AMORPHOUS THIN As$_2$Se$_3$ FILMS

A.M. Andriesh, V. I. Verlan

Center of Optoelectronics, Institute of Applied Physics, Academy of Sciences
of Moldova, Academiei 1, Chisinau, MD-2028, Moldova Republic

Measurements of photoconductivity and relaxation of positive and negative charge in amorphous thin As$_2$Se$_3$ layers are discussed. Photosensitive donor- and acceptor-like centers of 1.05 eV and 0.76 eV energies from valence band were revealed. These energies are constant and independent of light intensity in the range 1.5×10^9 - 1.5×10^{15} quanta/(cm^{2}s) and of energy of quanta. Wide quasicontinuously distribution trap centers with maximums at 0.62, 0.87 and 1.05 eV were found by relaxation measurements of positive and negative charge.

1. Introduction

The measurement of a photoconductivity (PhC) is applied to determination of the different information about semiconductors, as the photosensitivity of a material and its spectral distribution law, the identification centers of trap, recombination of free charge carriers, etc. [1]. Detailed measurements of PhC glass semiconductors was studied for the first time in the paper of Kolomiets et al. [2], who have found the main PhC properties dependence of temperature and intensity of excited light.

Recently, in connection with development of the new concept about pair centers D$^+$ and D$^-$ with variable valence and negative bond energy [3] and concept of "soft potentials" in disordered semiconductors [4] the attempt of combination of the data on photoconductivity, on optical and photoinduced optical absorption and on photoluminescence in common description scheme was made.

E.g., for massive glass semiconductor a-As$_2$Se$_3$, levels of 1.40 eV and 1.65 eV from valence band were revealed by measuring optical absorption [5], levels of 0.8-0.9 eV were revealed by measuring photoluminescence [6], and levels of 0.60 eV and 1.05 eV were revealed by measuring PhC dependence of temperature and light intensity at mono- and bimolecular recombination. These data are explained through configuration electron-phonon interaction diagram. Energy of interaction obtained for bulk a-As$_2$Se$_3$ is U$_c$ = -0.45 eV [5].

We were interested in investigation of PhC for thin amorphous layers As$_2$Se$_3$ obtained by vacuum thermal evaporation which are in more disbalanced conditions than voluminous samples, to compare different experimental data on trap and recombination centers of free charge carriers. On this topic, a few published data exist.

In the present paper we investigate photoconductivity dependence on temperature and light intensity in a large interval of intensities and relaxation of positive and negative charge.

2. Experimental technique

We investigated properties of stationary PhC at the planar geometrical configuration of electrodes, because it characterizes properties of a sample more adequately, introduces less errors in calculation of PhC, do not depend of non-uniformity, of volume illumination, contact effects, etc. [1]. Monochrome He-Ne laser light (λ= 0.63 μm) was used for PhC excitation with maximal intensity F$_0$ = 1.5 $\times$ 10^{15} quanta/(cm^{2}s), which was loosened more than to 6 orders by neutral gauged filters. The spectral PhC dependence was measured at different temperatures using MDR-4 monochromator at illumination by a halogen lamp.

Amorphous As_2Se_3 films of thickness about 1.2 - 1.5 μm on glass substrates were investigated. They were obtained by thermal evaporation in vacuum. The source As_2Se_3 for evaporation was prepared by synthesis of elemental As and Se with cleanness not less than 10^{-5} %. On films, the Au contacts were made by thermal deposition in vacuum.
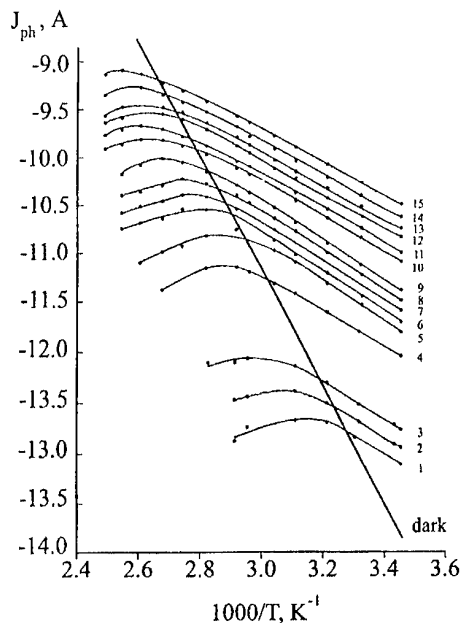

Fig. 1. Photoconductivity dependence of temperature for As2Se3 films at different light intensities (λ = 0.63 μm). Lines 1 – 15 correspond intensities from 1.5×10^{10} to 1.5×10^{15} quanta/cm^2.
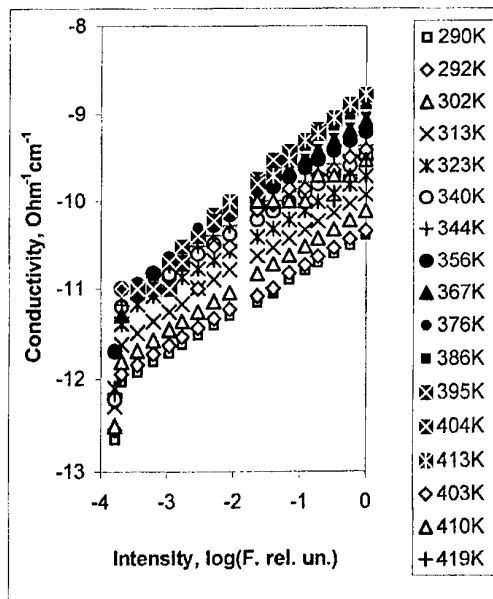
Fig. 2. Photoconductivity dependence of intensity for As_2Se_3 films at different temperatures (Lux-Ampere characteristic; λ = 0.63 μm)

The non-steady electrophotographic spectroscopy deep levels (NESDL) measurements were executed by a standard technique described in [7].

Before PhC measurements, films were subject to heat treatment in vacuum during 2 hours at 160 $^\circ$C, to guarantee stationary properties of the material. Due to the strong dependence of electrical properties of amorphous As_2Se_3 films of humidity [8], and to eliminate effects of air humidity, all measurements were carried out in vacuum (10^{-5} bar). The maximum of applied electrical field for a sample was 600 V/cm. The sizes of contacts were about 1.5×0.3 cm^2, and distance between them was about 0.5 cm.

3. Results

It was found that for all measured samples the current-voltage characteristics were linear, and the Ohm's law was always satisfied. Hence we concluded the lack of influence of contacts to PhC measurements in a-As_2Se_3 layers. The measured stationary PhC in the temperature interval 286 - 413.4 K and at sample illumination intensity in range F_0 - 10^{-6} F_0 are shown in Fig. 1. Measurements of dark conductivity are shown also.

The measured dark conductivity is presented by a straight line in log σ_d – (10^3/T) coordinates for all temperatures. Energy of activation corresponding to energy of a Fermi level (E_F) measured trough the conductivity of amorphous layers a-As_2Se_3 is 0.85 ± 0.03 eV.

PhC dependence of (10^3/T) has mixed character, i.e., in the dependence of temperature exist positive and negative slopes, to which donor- and acceptor-like levels correspond. It was found that with increase of light intensity σ_{ph}(10^3/T) is shifted without slope change. Even as light intensity is varied on 6 orders, the activation energy remain constant: ΔE_m = 0.20 ± 0.04 eV for donors and ΔE_m = 0.38± 0.02 eV for acceptors. The maximum of σ_{ph}(10^3/T) moves to higher temperatures at increase of light intensity (Fig. 1).

Lux-Ampere characteristic ($\sigma_{ph}(F)$) of thin films a-As_2Se_3 is shown on Fig. 2. At temperatures higher than 404 K the dependence is linear in coordinates $\log\sigma_{ph}$ - $\log F$, i.e., is of the type $\sigma_{ph} = \sigma_0\ F^\gamma$, where σ_0 is a constant and γ is a constant slope at given temperature. At temperatures higher than 404 K, the dependence $\log\sigma_{ph}$ - $\log F$ has is a second slope with $\gamma > 0.5$. It is necessary to note sharp transition from $\gamma = 1$ to $\gamma = 0.5$. These slopes correspond to monomolecular and bimolecular recombinations of photoexcited carriers [1]. The γ dependence of temperature in coordinates $1/\gamma$ - T is non-linear (Fig. 3). At low temperatures it is almost constant and changes from 0.5 till 0.65 for all temperatures. The drawn average straight line slope corresponds to the slope at the characteristic temperature T_0 = 590 K.
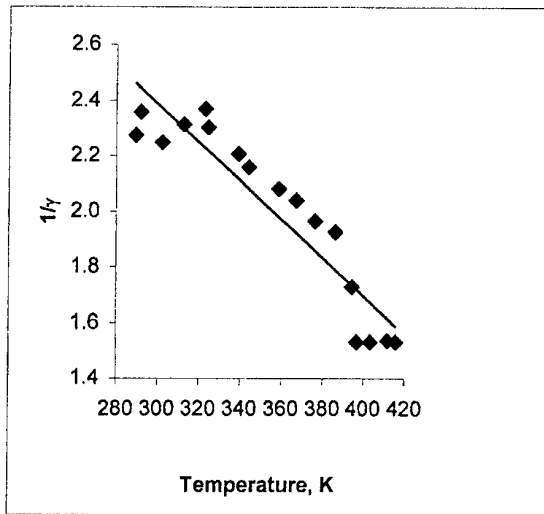

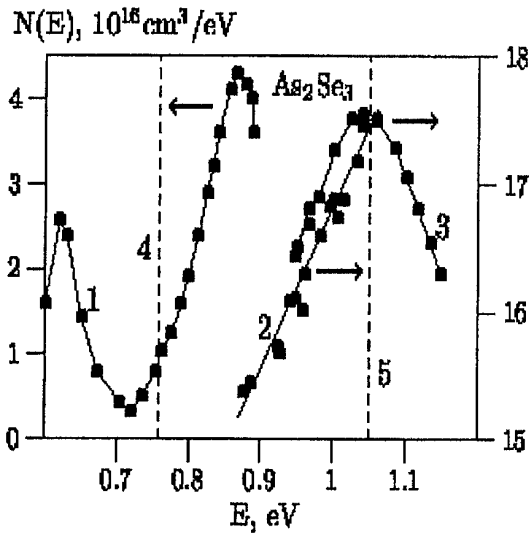Fig. 3. Parameter γ dependence of temperature.

Fig. 4. Energy distribution of trap centers density in a- As_2Se_3. Data 1–3 got by NESDL technique, data 4–5 got form PhC.

The PhC dependence of temperature at different excitation energies in the interval of 1.8 - 2.5 eV is alike to the similar data obtained at He-Ne laser excitation, namely, PhC also has mixed character, and the activation energies do not depend on a wavelength of excited light. We investigated more detailed PhC properties using excitation by He-Ne laser, because it permits to vary light intensity in a large range.

The measurement results for relaxation of accumulated positive or negative charges by a method of the electrophotographic spectroscopy on thin amorphous layers As_2Se_3 in electrode mode are shown in Fig.4. More detailed description of the experimental technique and calculation of density of the localized condition is given in our paper [7]. Broad quasi-continuous power distribution of trap centers of donor and acceptor type with maxima was retrieved at 0.62, 0.87, 1.05 eV by measurements of relaxation of accumulated charge.

4. Discussion of measurements

We can conclude from experimental data that at least two types of centers (donors and acceptors) participate at PhC. The photoconductivity stipulated by acceptors predominates at lower temperatures and at large intensities of light. The increase of light intensity yields PhC increase and shift of its maximum to higher temperatures. It is necessary to note that energies of activation levels are constant and do not depend on intensity and energy of exciting light quanta.

The PhC dependence of light intensity and temperature was calculated in two-level (donors and acceptors) model inside the conduction band [9]. Two different PhC areas are analyzed:

$$J_{ph} = q\ \mu\ E\ F/(v\ \sigma_t\ N_t)\exp((E_F-(E_D-E_v))/kT)$$

$$J_{ph} = q\ \mu\ E\ (FN_0\ /(v\ \sigma_t\ N_t))^{1/2}\ \exp((E_A-E_v)/(2kT))$$

The activation energies are: $\Delta E_m = (E_D - E_V) - E_F$ and $\Delta E_b = (E_A - E_V)/2$.

Here q is the charge of an electron, k is Bolzmann constant, μ is mobility, E is electric field intensity, F is light intensity, v is thermal velocity of free carriers, σ_t is capture cross-section of centers, E_A and E_D are, correspondingly, energies of acceptor and donor centers, which are situated at different sides of the Fermi level, E_V is the energy at the edge of the valence band.

We obtained $E_A = 0.76$ eV, $E_D = 1.05$ eV, and the bond energy of centers $D1^+$ and $D2^-$ is equal $E_A - E_D = -0.29$ eV.

Lux-Amper characteristics exhibits the monomolecular, bimolecular and mixed recombination of charge carriers. The slope of acceptor type in the dependence $\sigma_{ph}(10^3/T)$ is $\gamma \approx \frac{1}{2}$. Lux-Amper characteristics described above characterize also model of trap centres quasicontinuously distributed inside the forbidden band of the semiconductor. The dependence $\gamma(T)$ is of a kind $1/\gamma = T/T_0 - 1$ with characteristic temperature $T_0 = 590$ K. It means the distribution close to exponential inside the forbidden band [10].

The constant position of activation energy of both types of levels and its independence of energy of quanta of exciting light is apparently connected to transportation of carry with repeated trap. This transportation is dominant and is responsible for a current in amorphous semiconductors and is determined by exchange of carriers between zones and traps irrespective of places where this carrier was generated. At energies equal or higher than threshold, there is apparently an excitation $D1^+$ or $D2^-$ centers which results in neutral charge $D1^0$ or $D2^0$. These ones are thermally ionized and return the charge carrier in the conductivity or valence band. The further identification of the center model will be made after researches of photoconductivity, optical, luminescent and other properties.

Let's remark that in paper [7] PhC measurements in massive samples showed the results close to ours. The activation energies E_A and E_D given in that paper are 0.60 and 1.05 eV, correspondingly. The difference of these values is due to the relative unbalance of the thin amorphous layers comparatively to voluminous massive samples.

The obtained results of PhC measurements and electrophotografical spectroscopy led us to the dependence of energy distribution of centers inside a forbidden band in amorphous As_2Se_3 films shown in Fig. 4.

5. Conclusions

The PhC dependence of temperature dependence and of wide range of intensities $(1.5 \times 10^9 - 1.5 \times 10^{15}$ quanta/(cm^{2}s)) and relaxation of accumulated positive and negative charges were measured in thin amorphous a-As_2Se_3 layers. The photosensitive centers of donor and acceptor types with activation energies 1.05 eV and 0.76 eV relative to valence band were retrieved, whose energies are constant and do not depend neither on intensity, nor from energy of exciting light in rather broad range of intensities and energies. The broad quasi-continuous energy distribution of trap centres of a donor and acceptor type with maxima was retrieved at 0.62, 0.87, 1.06 eV from measurements of relaxation of the accumulated charge.

References

[1] S. M. Ryvkin, Semicond. Photoelectr. Phenomens, Moscow, Phys.-Math. Liter. Publ. House, 1963.

[2] B. T. Colomieţ, Yu. V. Ruchleadev, V. P. Şilo, J. Non Cristal. of Solids., 5,. 389, 482 (1971).

[3] T. C. Anderson Phys. Rev. Lett., 34, 953 (1975).

[4] M. I. Clinger, V. G. Carpov, JETF (Russia), 82, 1687 (1982).

[5] M. Hammam, G. J. Adriaenssens, J. Non-Cryst. Solids. 18, 2151(1985), 119, 89 (1990).

[6] S. P.Depina, B. C. Cavenett, Lamb N. E. Phil. Mag 47, 99 (1983).

[7] A. M. Andriesh, S. A. Malkov, V. I. Verlan, Physica Status Solidi (b) 169, K39 (1991).

[8] A. M. Andriesh, M. S. Iovu, V. I. Verlan, et.al., Semicond. device and materials, Kishinev, Shti intsa Publish. House, 133 (1987).

[9] J. G. Simmons, G. W. Taylor. J. Phys. C: Solid State Phys., 7, 3051(1974). J. G. Simmons, M. C. Tam. Phys. Rev. B, 7, Nr. 8, 370 6(1973).

[10] Rose A., Concepts in Photoconductivity, Moscow, Mir Publishing House, 1966.

HOMOGENEITY THRESHOLD IN SULPHUR RICH Ge-S GLASSES

Z. Černošek, J. Holubová, E. Černošková[b], M. Frumar

Research Centre of University of Pardubice and Institute of Inorganic Chemistry of Academy of Sciences of Czech Rep., nám. Legii 565, CZ-532 10 Pardubice, Czech Republic
[b]Joint Laboratory of Solid State Chemistry of Czech Academy of Sciences and University of Pardubice, Studentská 84, CZ-532 10 Pardubice, Czech Republic

The glassy Ge-S system was analysed on the basis of Raman spectra with the aim to find the compositional dependence of cyclo-octo-sulphur and polycatena sulphur.

1. Introduction

Ge_xS_{1-x} glasses have been intensively studied for many years. Great effort was paid to the study of short-range order (SRO) in these materials. Several structural models have been proposed to describe SRO: random-covalent-network model (RCNM), generalised chain crossing model (CCM) [1,2] and Philipp's model [3]. All these models were used by Lucovsky and co-workers [4] for interpretation of Raman spectra of Ge-S glasses. For glasses with sulphur overstoichiometry authors have found that analysis of IR and Raman spectra supports CCM model rather than a RCNM model. Based on these results authors [4] supposed that mostly two atoms of sulphur link Ge atoms and that the excess of sulphur separates as new phase. But this approach led to discrepancy between computed and experimental data for increasing overstoichiometry of sulphur. The SRO models based only on statistics of chemical bonds don't seem to be good approximation and they don't successfully correlate the properties of materials with their structure. For that reason authors [5] proposed the SRO-model for Ge-S glasses which is based on the assumption that atom in excess of the stoichiometric composition GeS_2 is considered to be the central atom of the respective structural units in this system. The homopolar bonds between atoms in understoichiometry don't originate. For sulphur rich glasses of Ge-S system the sulphur is central atom of structural units and thus Ge-Ge bonds don't exist. It means that germanium can only takes part in $GeS_{4/2}$ units. Three basic structural units may be considered: (Ge-S-Ge), (Ge-S-S) and (S-S-S). Their ratio bears on the properties of the material. From the dependence of relative population of above mentioned structural units on decreasing atomic fraction of germanium, x, the equivalent relative concentration of all kinds of structural units is reached for x = 0.2 and for x < 0.2 only the content of (S-S-S) units increases [5]. One can expect, in accordance with [4,6], that properties of Ge-S system could differ in regions x < 0.2 and x > 0.2. The main aim of this paper is analysis of Raman spectra of glassy Ge-S system with sulphur overstoichiometry with respect to compositional dependence of cycloocta-sulphur and polycathena-sulphur and testing of SRO-model [5] applicability.

2. Experimental

Bulk samples were prepared by direct synthesis from high purity elements in evacuated quartz ampoules in a rocking furnace. The melt was quenched in water (glasses with x > 0.20), respectively in air (x = 0.20 and 0.15). Chemical composition of glasses was checked by X-ray microprobe (Kevex). Raman spectra of glasses and both sulphur allotropes were measured under laboratory temperature in the back scattering geometry using FT spectrometr (Bruker IFS-55 with FRA-106). The excitation line 1064 nm (Nd:YAG laser) and Ge detector cooled with liquid nitrogen were used. Specific density of bulk glasses was measured by conventional pycnometric method.

Polycathena-sulphur S_n was obtained as a rest after dissolving the cycloocta-sulphur from high purity sulphur (5N) in distilled carbon disulphide. Soxhlett's extraction apparatus was used.
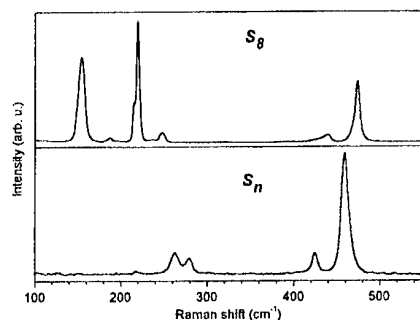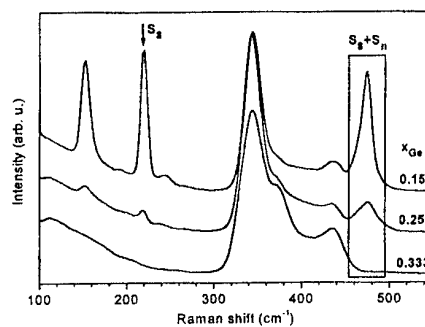
Fig. 1. Raman spectra of S_8 and S_n sulphur.

Fig. 2. Reduced Raman spectra of Ge_xS_{1-x} glasses. Labelled bands were used for the study.

3. Results

Lucovsky at al. [4] identified two species in Raman spectra, a network structure based on a local $GeS_{4/2}$ configuration and molecular species S_8. We assumed that indispensable concentration of linear chains S_n could be also present in the glass, especially when the glass is quickly quenched. To confirm this assumption we measured the Raman spectrum of sulphur S_n, because its spectrum was not available in literature. Raman spectra of S_n and S_8 sulphur are shown in Fig. 1. Spectrum of S_n consists of four well-resolved bands (263, 279, 424 and 459 cm^{-1}). At the spectra of Ge-S glasses only the most intensive band of S_n at 459 cm^{-1} can be identified as a shoulder on 473 cm^{-1} band of cycloocta-sulphur, see part labelled 'S_8+S_n' in Fig. 2.

Raman spectra of Ge_xS_{1-x} glasses were measured for x = 0.15, 0.20, 0.25, 0.30 and 0.333. Obtained spectra are shown in Fig.2. Raman bands labelled in this figure were used for our study from following reasons:

i) S_8 sulphur band at ~ 220 cm^{-1} is very intensive and has not considerable overlap with surrounding bands,

ii) in the region ~ 460 – 490 cm^{-1} both sulphur S_n and S_8 bands are found and can be easily separated.

All Raman spectra obtained were computer separated into bands. Integral intensities of labelled bands (Fig. 2) were normalised to the strength of Raman band at 343 cm^{-1} to provide a measure of their compositional dependence, analogously to [4]. This relative normalisation is based on an assumption that this mode is associated with the vibrations of Ge-S bonds and its strength scales as x. Compositional dependence of normalised integral intensities was compared with compositional dependence of (S-S-S) species of the SRO-model [5], see Fig. 3.

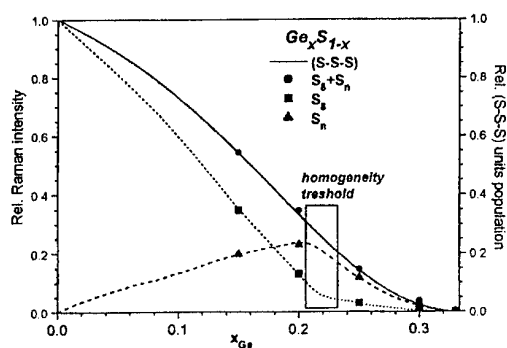Specific densities of studied glasses are in Fig. 4.

Fig. 3. Compositional dependence of obtained Raman relative intensities of monitored sulphur bands and (S-S-S) species population computed according to the SRO-model [5].

4.Discussion

We found the lower values of normalised relative intensities in the case of S_8 in comparison with [4] probably bears on the fact that authors [4] replaced integral intensities of bands by their heights. The good agreement was achieved between compositional dependence of general S_8 and S_n content in glasses with its theoretical prediction based on the SRO-model [5], Fig. 3. Obtained dependence shows that there is considerable concentration of S_n chains in the glasses with sulphur overstoichiometry. For $x = 0.2$ their content reaches $\sim 66\%$ of total (S-S-S) units population, see Fig. 3. In contrast to S_8 molecules, which have to separate, it isn't possible, however, to determine if the S_n chains are separated into individual phase or if they are built in any structure containing germanium.
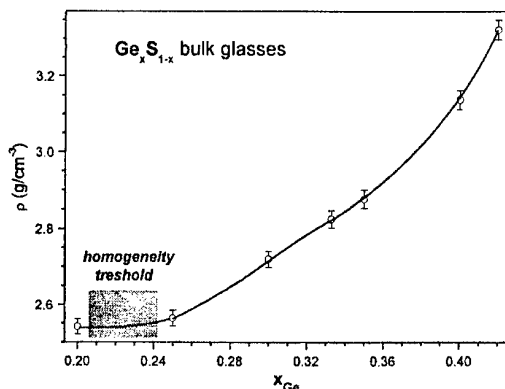

Fig. 4. Specific densities of Ge_xS_{1-x} glasses.

From the compositional dependencies, Fig. 3, it results that with increasing overstoichiometry of sulphur in glasses Ge_xS_{1-x}, approximately over 76 at.% S, the concentration of S_8 sulphur increases very quickly to the detriment of S_n sulphur. Thus if glasses with sulphur content more than 80 at.% (x < 0.20) are prepared the cooling rate has to be risen up sufficiently to prevent $S_n \rightarrow S_8$ transition and its following separation into microcrystalline phase. This assumption is in agreement with DSC results [7]. It is known that increasing overstoichiometry of chalcogen over ~ 80 at.% is accompanied with decrease of glass-forming ability of Ge-X melts, see e.g. [8].

On basis of these results we conclude that glassy system Ge_xS_{1-x} seems to be microheterogeneous for x less than approx. 23 at. % Ge. Its structure is built up by $GeS_{4/2}$ tetrahedra partly linked with S_n chains, and by microcrystalline sulphur S_8. This concept corresponds well with gradual break of compositional dependence of density near $x \sim 0.23$, Fig. 4. The lower volume of microcrystalline sulphur contrary to amorphous sulphur can be good explanation of this break. Our homogeneity threshold at $x \sim 0.23$ corresponds also with rigidity transition threshold near $x = 0.23$ of Ge_xSe_{1-x} glasses found by Boolchand [9].

5. Conclusions

The analysis of Raman spectra of Ge_xS_{1-x} glassy system has shown, that in the region $0.20 \leq x < 0.33$ the S_n chains are present and the concentration of co-existing cycloocta-sulphur S_8 is very low. S_n chains probably act as linkage of $GeS_{4/2}$ units and they are stabilised by this way. With increase overstoichiometry of sulphur, however, the number of such kind of structures decreases and thus the content of free sulphur increases and sulphur chains can phase-separate. In this phase of polycathena-sulphur the transition of the $S_n \rightarrow S_8$ occurs and the microcrystalline S_8 phase creates. It is demonstrate that the SRO-model [5] describes well compositional dependence of relative population of (S-S-S) units. It is shown that these units are parts of S_8 molecules as well as of S_n chains.

Acknowledgement

References

[1] F. Betts, A. Bienenstock, S. R. Ovshinsky, J. Non-Cryst.Solids **4**, 554 (1970).

[2] F. W. Fawcett, C.N.J.Wagner, G.S.Cargill III, J.Non-Cryst. Solids **8-10**, 369 (1972).

[3] H. R. Philipp, J.Non-Cryst.Solids **8-10**, 627 (1972).

[4] G. Lucovsky, F. L. Galeener, R. C. Keezer, R. H. Geils, H. A. Six, Phys.Rev. **B19**, 5134 (1974).

[5] Z. Černošek. E. Černošková, phys.stat.sol.(b) 122 (1984) 405.

[6] P. Boolchand, W. J. Bresser, M. Zhang, Y. Wu, J. Wells, R.N. Enzweiller, J. Non-Cryst.Solids **182**, 143 (1995).

[7] L. Tichý, N. Ryšavá, A. Tříska, H. Tichá, J. Klikorka, Solid State Commun, **49**, 903 (1984).

[8] J. C. Phillips, J.Non-Cryst.Solids **34**, 153 (1979).

[9] P. Boolchand, D. Selvanathan, Y. Wang, D. G. Georgiev. W. J. Bresser, in: Properties and Applications of Amorphous Materials, NATO Science Series, Kluwer Academic Publishers (eds. M.F. Thorpe, L. Tichy) vol. **9**, 97 (2001).

THERMAL PROPERTIES OF As-S GLASSES IN THE GLASS TRANSITION REGION

E. Černošková, Z. Černošek[a], J. Holubová[a], M. Frumar[a]

Joint Laboratory of Solid State Chemistry of Czech Acad.of Sci. and Univ. of Pardubice, Studentská 84, CZ-532 10 Pardubice, Czech Republic
[a]Department of General and Inorganic Chemistry, University of Pardubice, nám. Legii 565, CZ-532 10 Pardubice, Czech Republic

The compositional dependence of T_g, C_p and relaxation enthalpy in the glassy system As-S was investigated. The observed modifications are related to the change of coordination polyhedra.

1. Introduction

Glass transition is usually characterized by a phenomenological value T_g and by a width of so-called glass transition region. In this region the diffusive motion of the melt begins to freeze in, before a glassy structure is achieved with viscosity values typical of solids 10^{14} Ns m^{-2}. Glasses are metastable solid materials without long range order. They lack translation and rotation symmetry. The nature of glass transition is complex and even today remains poorly understand. Numerous studies have been devoted to measurements and understanding of the glass transition temperature T_g which is influenced by experimental conditions. There is not consensus yet if structural or thermodynamic factor are responsible for determining of T_g.

2. Experimental

The glasses of the $As_xS_{(100-x)}$ system, where x = 33 - 42 at.%, were prepared by direct synthesis from the pure elements. The differential scanning calorimetry (DSC) experiments in the heating regime were performed using DSC Pyris 1 (Perkin-Elmer). The StepScan software (Perkin-Elmer) was used to separate steady state thermodynamic and kinetic processes in the glass transition region.

3. Results

Using the StepScan method the glass transition temperatures, T_g, were obtained. Main benefit of method used is ability to separate the heat capacity, C_p, representing the changes associated with the rapid molecular motion in the material in the time scale of experiment and enthalpy changes (thermodynamic component), ΔH_{Tg}, associated with slow irreversible processes (kinetic component) in the glass transition region. The quantities characterizing thermodynamic part of the glass transition are plotted in Fig.1. The dependencies of the specific heat capacity difference in the glass transition region, $\Delta C_{p,Tg}$, of the configurational entropy difference in the glass transition region, ΔS_{Tg}, and of the Gibbs free energy difference in the glass transition region, ΔG_{Tg}, on arsenic content were calculated from experimental DSC data.
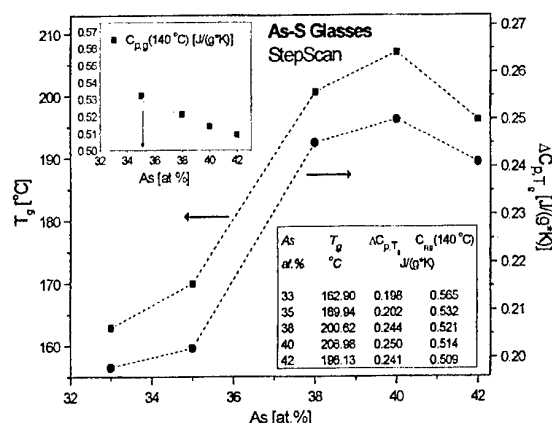
Fig. 1. The dependence of thermodynamic component of the glass transition (T_g, $\Delta C_{p,Tg}$) on arsenic concentration. In the insert: the compositional dependence of $C_{p,g}$ at the temperature 140 °C is shown. The curves are only for eye guidance.

The entropy difference in the glass transition region ΔS_{Tg} was calculated from the measured temperature dependence of C_p for all prepared glasses according to relation:

$$\Delta S = S_{T1} - S_{T2} = \int_{T1}^{T2} \frac{C_p}{T} dT , \tag{1}$$

temperature T_1 corresponds to the temperature of the beginning of the glass transition and T_2 temperature is the temperature of the melt at the end on the transformation. For result see Fig. 2.

Gibbs free energy difference in the glass transition region, ΔG_{Tg}, for all prepared samples was calculated:

$$\Delta G_{Tg} = \Delta H_{Tg} + T_{Tg} * \Delta S_{Tg} , \tag{2}$$

ΔH_{Tg} corresponds to so-called relaxation overshoot (the kinetic component). Gibbs free energy differences in the glass transition region, ΔG_{Tg}, for studied glasses are in Fig. 3. The strong discontinuity for glasses with 35 –38 at.% of arsenic is found for both dependencies.

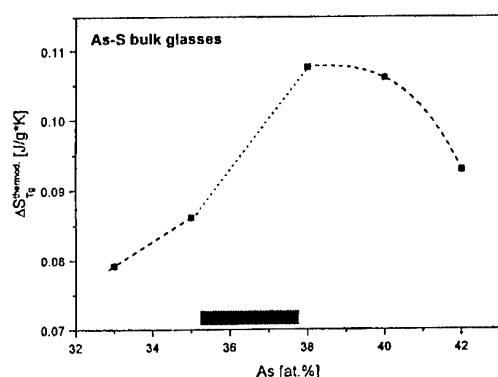Fig. 2. The dependence of the configuration entropy difference, ΔS_{Tg}, in the glass transition region on the arsenic content.
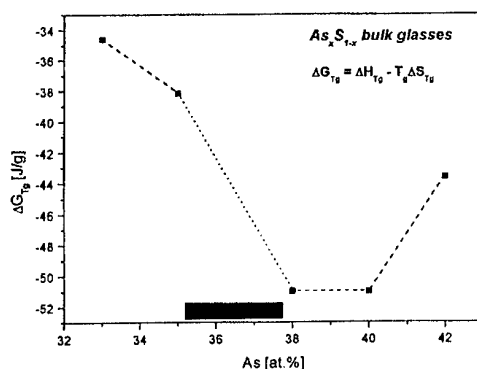
Fig. 3. The dependence of Gibbs free energy difference in the glass transition region ΔG_{Tg} on the concentration of arsenic.

Similarly strong change was observed by Borisova [1] for composition dependence of the thermal expansion coefficient α, see Fig. 4.

All results obtained were also plotted as functions of the mean coordination number $<r>$, Fig. 5.
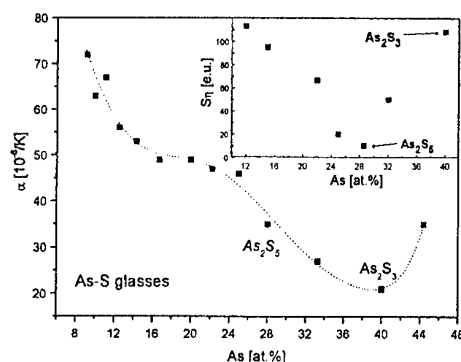

Fig. 4. The temperature dependence of the thermal expansion coefficient α on the concentration of arsenic. Inset shows the dependence of viscous-flow activation entropy on arsenic content [1].
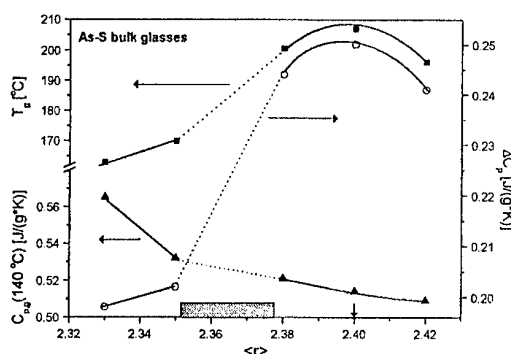
Fig. 5. The dependence of obtained thermodynamic quantities in the glass transition region as function of $<r>$ for 3-fold arsenic.

4. Discussion

The glass transition temperatures were determined from measured $C_p(T)$ dependencies, Fig. 1. It was found that T_g reaches maximal value for stoichiometric composition As_2S_3. The calculated dependence of the heat capacity difference at T_g, $\Delta C_{p,Tg}$, reaches maximum for As_2S_3 as well as in the case of As-Se glasses, see [2]. The concentrational dependence of $C_{p,g}$ at 140 ^0C, i.e. at temperature lower than onset of the glass transformation temperature, is shown in the inset into Fig. 1. It is obvious that for chemical compositions close to $As_{35}S_{65}$ the strong change of the slope of dependence of $C_{p,g}$ on As concentration takes place. From the compositional dependence of the configuration entropy difference, ΔS_{Tg}, in the glass transition region (Fig. 2) it is possible to conclude that the change of the basic structural units probably takes place in the studied glasses.

Borisova [1] supposes for 28.57 at.% of arsenic existence of quasi-tetrahedral units which correspond to As_2S_5 glass composition, and pyramidal units $AsS_{3/2}$ for the stoichiometric As_2S_3 composition. In the region between these two limit compositions the transformation of quasi-tetrahedral units into pyramidal units takes place, a vice versa. On going from As_2S_5 to As_2S_3 the value of viscous-flow activation entropy S_η increases which represents, according to [1], a transition from tetrahedral to trigonal coordination of arsenic in As-S glasses (see Fig.4, inset). Studied glasses predominantly fall in this transformation region. X-ray and neutron diffraction measurements shown that structure of As-S and As-Se glasses are very similar in the range of compositions x = 0 – 70, [3]. On the base of changes of T_g slope on concentration of arsenic it is concluded [4] that two fractions of chemical composition could coexist in this region of chemical compositions. Authors [4] suppose that two possible oxidation states of arsenic can exist in the studied covalent glasses, i.e. As^V and As^{III}. One fraction of the above mentioned glasses can be created by 4-fold coordinated As^V with quasi-tetrahedral local configuration with three bridging Se atoms and one double bonded Se. In the second one there are preliminary units with 3-fold coordinated As^{III} in pyramidal configuration. The change of $C_{p,g}$ slope on composition for x = 35 at.% As was observed, see Fig. 1, inset. We suppose structural units changing close this composition. Providing that all arsenic is 3-fold coordinated (As^{III}) the mean coordination number $<r>$ = 2.35. If all arsenic is 4-fold coordinated (As^V) the mean coordination number $<r>$ would be 2.7. It is necessary to point out that these two limited values are very close to the values for so-called chemical and/or topological transitions i.e. $<r>$ = 2.4 or 2.65 [5,6]. According to the constraint theory it is suggested [5] that valence forces (bond-stretching and bond-bending) can serve as the atomic constrains in the covalent network. It is supposed that glass formation would be optimal (ideal mechanical stability) when the number of constrains per atom equals 3 (3 degrees of

freedom per atom in 3D network). These ideas lead to the recognition that glass network becomes for $<r> = 2.4$ elastically rigid. The rigid clusters can percolate and a phase transition (so-called rigidity transition) can take place. The feature observed at $<r> = 2.67$ was understood using the structural transition model as well [6]. It was established by topological consideration using medium-range structures and it is attributed to the transition from essentially layered structure to 3D network arrangement due to the cross-linking. The dependence of obtained thermodynamic quantities in the glass transition region as function of $<r>$ is shown in Fig. 5. There are shown studied dependencies for the case when only pyramidal structural units are present in the glasses. Strong discontinuities are evident again. Pyramids are also supposed to be main structural units in As-Se glasses with $x \le 40$ at.% As, [7].

It is not possible to prepare crystalline analogs of As-S glasses, except of As_2S_3 [8] and so it is necessary to bear on indirect data only for their analysis, unfortunately.

5. Conclusions

Compositional dependence for $As_xS_{(100-x)}$ ($x = 33 - 42$ at.% As) of T_g, C_p and relaxation enthalpy in the glass transition region were measured. Obtained data show that the changes of oxidation state and associated changes of the coordination number of arsenic take place very probably in the studied region of chemical compositions. Changes in the studied quantities reflect the changes of coordination polyhedra (short-range order change). Observed changes are in good agreement with published structural studies dealing with the above mentioned glasses.

Acknowledgement

References

[1] Z. U. Borisova, Glassy Semiconductors, Plenum Press, New York p. 128 (1981).
[2] P. Boolchand, D. Selvanathan, Y. Wang, D.G. Georgiev, W.J. Bresser, Onset of Rigidity in Steps in Chalcogenide Glasses, NATO Sciences Series, Properties and Applications of Amorphous Materials, Kluwer Academic Publishers (ed.M.F. Thorpe, L. Tichý), vol. .9 p. 97 (2001).
[3] A. J. Leadbeter, A. J. Apling, J. Non-Cryst.Sol. **8-10**, 250 (1974).
[4] M. Micoulaut, G. G. Naumis, Europhys. Lett. **47**, 568 (1999).
[5] J. C. Philips, M. F. Thorpe, Solid State Commun. **53**, 699 (1985).
[6] K. Tanaka, Phys. Rev. **B39**, 1270 (1989).
[7] P. F. Mutolo, H.Eckert, Abstracts of Papers of the American Chemical Society **218**, 40 (1999).
[8] Z. Černošek, E. Černošková, L. Beneš, Mat. Letters **38**, 336 (1999).

CARRIER TYPE REVERSAL IN Pb$_x$Ge$_{42-x}$Se$_{58}$ AND Pb$_{20}$Ge$_y$Se$_{80-y}$ GLASSES EXHIBITED IN THERMAL DIFFUSIVITY MEASUREMENTS

R. Ganesan, B. Thangaraju, K. S. Sangunni, E. S. R. Gopal

Department of Physics, Indian Institute of Science, Bangalore –560012, India.

Bulk Pb$_x$Ge$_{42-x}$ Se$_{58}$ (x = 0, 2.5, 5, 7.5, 9, 10 & 15 at.%) and Pb$_{20}$Ge$_y$Se$_{80-y}$ (y = 17, 19, 21, 23 and 25 at.%) homogeneous glasses have been prepared by melt quenching. The thermal diffusivity has been measured by the photoacoustic technique using a laboratory built non-resonant photoacoustic cell. The composition dependence of thermal diffusivity shows an anomalous behavior at x = 9 at% of Pb in Pb$_x$Ge$_{42-x}$Se$_{58}$ and y = 21at.% of Ge in Pb$_{20}$Ge$_y$Se$_{80-y}$ glasses, the composition at which a p- to n- conduction transition generally occurs. The reported electrical conductivity and optical band gap measurements are used to explain the minimum thermal diffusivity value obtained at the transition threshold in these glasses. These results have been explained with the Kolobov model on the basis of modification of the charged defect states due to the addition of metallic elements.

1. Introduction

The melt quenched chalcogenide glasses are semiconductors, which are useful in several potential applications like threshold and memory switching devices and the reverse phase change optical recording memories [1-3]. These glasses generally exhibit p- type electrical conduction due to the pinning of the Fermi level arising from the trapping of charge carriers at localized gap states [4,5]. Once it was believed that there is no possibility to prepare n- type chalcogenide bulk glasses. But in 1979, Tohge et al. [6,7] observed for the first time p- to n- type electrical conduction reversal in Bi doped Ge-Se glasses. After eight years, the same group [8] have observed the carrier type reversal in yet another system PbGeSe glasses. Since then, the mechanism of carrier type reversal has been in debate. There are two series in the PbGeSe glasses which exhibit p- to n- conduction change: one is Pb$_x$Ge$_{42-x}$Se$_{58}$ (I) and the other is Pb$_{20}$Ge$_y$Se$_{80-y}$ (II). Apart from these two series, Murugavel and Asoken [9] have observed n-type conduction in Pb$_x$Ge$_{42-x}$Se$_{48}$Te$_{10}$ glasses and Mehra et al. [10] have found the conduction change in Pb$_x$In$_{25-x}$Se$_{75}$ glasses.

Over the past few years the photoacoustic (PA) technique has developed into a powerful tool for studying the optical and thermal properties of solids [11]. In PA technique [12], the sample to be studied is placed inside a closed cell containing air and a sensitive condenser microphone. The sample is then illuminated with a modulated beam of monochromatic light. The sample absorbs the incident energy; some of the energy levels in the sample are excited and subsequently de-excite through non-radiative relaxation processes. This periodic optical excitation of the sample results in a periodic heat flow from the sample to the surrounding gas. This in turn results in a periodic pressure oscillation within the cell, which is detected by a microphone as an acoustic signal. In recent years, a great deal of effort has been spent to understand the role of certain element in controlling the mechanism of electrical conduction in glassy chalcogenide semiconductors. Tohge et al. [7,8] have reported the results on electrical conductivity, thermoelectric power and drift mobility studies on both the series of PbGeSe glasses. Rabinal et al. [13,14] have carried out DSC measurements and optical properties on Pb$_x$Ge$_{42-x}$Se$_{58}$ glasses. The ac conductivity and dielectric relaxation studies have been reported by Bhatia et al. [15,16]. Rahman et al. [17] have reported the dc conductivity measurements and current – voltage behavior of the Pb$_{20}$Ge$_y$Se$_{80-y}$ glasses and the origin of the carrier type reversal has been analysed by Vaidhyanathan et al. [18] using thermal, electrical and structural studies.

Many researchers [6-10,13-18] have analyzed the mechanism of carrier type reversal but no concrete explanation has been reached so far. A study of thermal properties is on of the techniques used to obtain an understanding of the conduction mechanism in chalcogenide glasses. It is established that the PA technique is highly sensitive to the topological threshold, rigidity percolation and carrier type reversal in chalcogenide glasses [19,20]. The composition dependence of the thermal diffusivity values on the glasses will help to reveal the mechanism of carrier type reversal [20]. To throw more light on understanding the electrical conduction changes in these glasses, we have undertaken thermal diffusivity measurements of both the series using the PA technique.

2. Experimental details

Many researchers have studied systematically the glass forming region of Pb-Ge-Se systems [8,21,22] and they found that the homogeneous glass formation is confined to two series of compositions. The I series is restricted around 58 at.% of Se, the maximum Pb content being 22.5 at.%. The II series is limited at 25 at.% of Ge with 20 at.% of Pb. In this study, we prepared $Pb_xGe_{42-x}Se_{58}$ ($x = 0, 2.5, 5, 7.5, 9, 10$ & 15 at.%) and $Pb_{20}Ge_ySe_{80-y}$ ($y = 17, 19, 21, 23$ & 25 at.%) homogeneous glasses by melt quenching.

Appropriate amount of high purity (99.999 %) elements of Pb, Ge and Se are sealed in quartz ampoule. The ampoule is evacuated to better than 5×10^{-5} Torr, then kept inside the tubular furnace. The ampoules are heated in two stages to avoid the sudden evaporation and deposition of the selenium to the inner wall of the quartz tube. The ampoules are heated slowly and maintained at 600 °C for about 24 hours with continuous rotation. The temperature is then subsequently raised to 1000 °C and kept under constant rotation for 36 hours to facilitate the homogenization of the sample. Then the ampoules are quenched rapidly in a continuous flow liquid Nitrogen bath, in order to avoid the vapour thermal isolating envelope around the ampoules, therefore increasing the efficiency and reproducibility of the fabrication process. The amorphous nature of the samples is verified by the absence of sharp peaks in X-ray diffraction spectra.

The thermal diffusivity measurement of various compositions of both the series have been carried out. The description of the photoacoustic cell developed here, the experimental setup and the procedure of the measurement have been reported elsewhere [20,23].

3. Results and discussion

The log-log plot of chopping frequency versus PA signal amplitude is shown in Fig. 1 for the samples of different compositions. The thermal diffusion length at 100 Hz, thermal diffusivity and characteristic frequency with corresponding thickness of the samples have been listed in Table 1.

Borisova in 1981 [24] has suggested that the reason for the p- type electrical conduction in chalcogenide glasses is that the conduction band is formed by antibonding orbitals, whereas the valence band is formed by nonbonding orbital. The disorder is more dominant in antibonding states than in the nonbonding states, which results in a deeper tail for the conduction band states. So the electrons are localized stronger than the holes leading to p- type electrical conductivity.

Table 1.

Composition	Sample thickness $l(\mu m)$	Characteristic frequency $F_c(Hz)$	Thermal diffusivity $\alpha = f_c l^2$ $\times 10^{-2}$ cm^2 s^{-1}	Thermal diffusion length at 100 Hz $\mu = (2\,\alpha/\omega)^{1/2}$ $\times 10^{-2}$ cm
$Ge_{42}Se_{58}$	230	170.5	09.02	1.70
$Pb_{2.5}Ge_{39.5}Se_{58}$	280	140.8	11.04	1.88
$Pb_5Ge_{37}Se_{58}$	275	140.8	10.65	1.84
$Pb_{7.5}Ge_{34.5}Se_{58}$	275	150.6	11.39	1.90
$Pb_9Ge_{33}Se_{58}$	245	130.2	07.82	1.58
$Pb_{10}Ge_{32}Se_{58}$	273	190.0	14.16	2.12
$Pb_{15}Ge_{27}Se_{58}$	270	170.8	12.45	1.99
$Pb_{20}Ge_{17}Se_{63}$	265	120.9	08.49	1.64
$Pb_{20}Ge_{19}Se_{61}$	280	150.6	11.81	1.94
$Pb_{20}Ge_{21}Se_{59}$	270	130.5	09.51	1.74
$Pb_{20}Ge_{23}Se_{57}$	280	140.8	11.04	1.88
$Pb_{20}Ge_{25}Se_{55}$	275	140.4	10.62	1.84

The origin of p- type conduction has been explained with the charged defect states recently by Kolobov [25]. The lowest energy defects in a chalcogen are charged pairs consisting of a singly coordinated negative site (C_1^-) and a triply coordinated positive site (C_3^+). The subscript refers to the coordination, the superscript refers to the charge state and the C refers to the chalcogen. The charged defects C_3^+ and C_1^- have been called by Kastner [26] as a valence alteration pair (VAP). According to the Kolobov model [25], due to the thermal excitation of C_3^+ center with one of its neighbors C_2^0, an electron-hole pair is created. The electron is attracted and trapped by the C_3^+ defect center and converts it into a C_3^0 center, which is unstable and easily decays to a C_1^0 center.

$$C_3^+ C_2^0 \rightarrow C_3^0 + C_2^0 + h; \quad C_3^0 \rightarrow C_1^0 + h$$
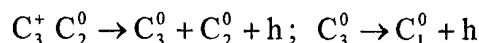
The hole created in the valence band is mobile and contributes to the conductivity. So, the process ends with the conversion of a C_3^+ center into a C_1^0 center with simultaneous creation of a hole in the valence band. In principle, the excited hole can recombine with its original C_3^+ and C_2^0 sites, but here the recombination is not possible because the structure of the defect has been modified. Hence, the process is irreversible and the excited hole is left in the valence band as a free carrier.

$$C_1^- C_2^0 \leftrightarrow C_1^0 + C_2^0 + e; \quad C_1^- \leftrightarrow C_1^0 + e$$
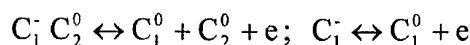
In the case of C_1^- center excited with its neighbor C_2^0, the process becomes

In the singly coordinated defect, no structural reconstruction takes place in the defect site. So, the process is reversible since the created electron is recombined. As a consequence of these processes, the long-lived holes in the valence band due to the thermal excitation of positively charged defects become the origin of the p-type electrical conduction in the chalcogenide glasses. It is now fairly well established that the metallic additives such as Bi enters the network as charged species, altering the concentration of valence-alteration pairs [27,28]. When the concentration of charged additives exceeds that of valence-alteration pairs, the chalcogenide glasses exhibit the carrier type reversal.
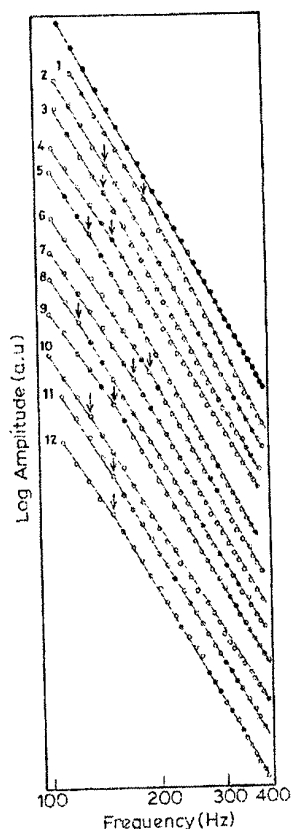
Fig. 1. Log – log plot of photoacoustic amplitude versus chopping frequency.
(● - Thick sample, 1. $Ge_{42}Se_{58}$, 2. $Pb_{2.5}Ge_{39.5}Se_{58}$, 3. $Pb_5Ge_{37}Se_{58}$,
4. $Pb_{7.5}Ge_{34.5}Se_{58}$, 5. $Pb_9Ge_{33}Se_{58}$, 6. $Pb_{10}Ge_{32}Se_{58}$, 7. $Pb_{15}Ge_{27}Se_{58}$, 8. $Pb_{20}Ge_{17}Se_{63}$,
9. $Pb_{20}Ge_{19}Se_{61}$, 10. $Pb_{20}Ge_{21}Se_{59}$, 11. $Pb_{20}Ge_{23}Se_{57}$, 12. $Pb_{20}Ge_{25}Se_{55}$.

Fig. 2 and 3 show the variation of thermal diffusivity with Pb and Ge concentration respectively. It can be clearly seen from the figures that an anomalous behavior is observed, in $Pb_xGe_{42-x}Se_{58}$ glasses at 9 at.% of lead and in $Pb_{20}Ge_ySe_{80-y}$ glasses at 21 at.% of Ge, at the compositions showing a transition from p- to n- type conduction. The change is more prominent in I series than in the II series of glasses. This may be due to the difference in the way of changing the composition between the series. In II series Ge is substituted with Se atom, but in I series, Pb is substituted with Ge atom. The transition at the specific Pb and Ge composition in the glasses agrees well with the reported thermoelectric power measurements [8].

An attempt is made to explain the anomalous behavior of thermal diffusivity values with Pb and Ge addition of I and II series glasses respectively. Calculations of covalent bond concentrations of these series have been reported by Tohge et al. [8]. The reported radial distribution function [29] showed that Pb is present as Pb^{2+} ions in these glasses, necessarily accompanying nonbridging selenium (-Se⁻). The possible bonds are Ge-Ge. Ge-Se, Pb-Se and Se-Se. In I series, the concentration of calculated covalent bonds Ge-Se and Ge-Ge changed gradually with relative increase in Pb-Se ionic bonds. But in II series, besides Pb-Se ionic bonds, the Se-Se bonds decreases and completely vanish at x = 20 at.% of Ge, while at this composition the concentration of Ge-Se bonds reaches maximum and Ge-Ge bonds start to appear. With further addition of Ge, the Ge-Ge bonds gradually increase and Ge-Se bonds decrease. It is speculated in this II series that the disappearance of Se-Se homopolar bonds causes the electrical conduction changes from p- to n- type. In I series the minimum value obtained at the transition can be attributed to the addition of Pb, where a decrease in the number of Ge-Se and Ge-Ge covalent bonds leads to an increase of Pb-Se ionic bonds. It is worth to mention here that the conduction change in both the series is at the specific compositions $Pb_9Ge_{33}Se_{58}$ and $Pb_{20}Ge_{21}Se_{59}$. The Pb and Ge concentrations are not the same but the Se at.% is almost equal in the two series.
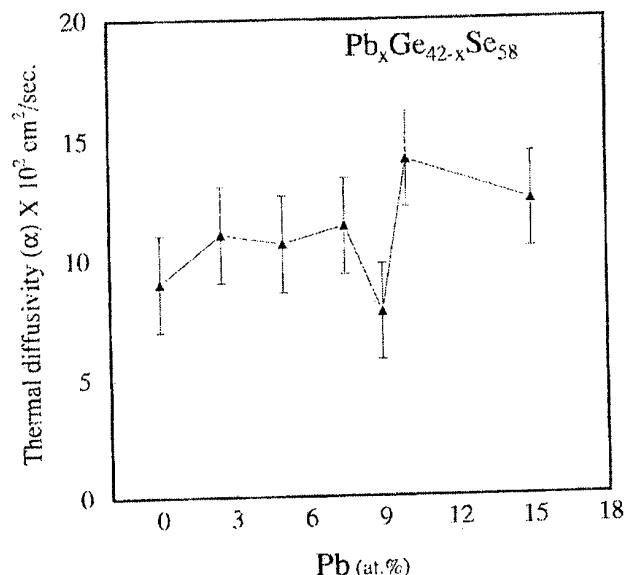
Fig. 2. Variation of thermal diffusivity with Pb concentration.

The similar trend of anomalous behavior of thermal diffusivity measurement with the composition of GeBiSe and Ge Bi Se Te glasses has already been observed by Thangaraju et al. [20]. The Ge Bi Se Te and I series glasses show the drastic change in thermal diffusivity value at the p- to n- transition. The changes are more prominent than in the GeBiSe and II series glasses. A perusal of these figures reveals that the thermal diffusivity value decreases at the time of transition then increases with increasing Bi in GeBiSe and Ge Bi Se Te glasses and, with Pb and Ge in I and II series glasses respectively. The electrical conductivity values [8] show that the specific composition where the electrical conductivity is a minimum agrees with that where the conduction type changes from p- to n-.

After the transition the conductivity increases with addition of respective Pb and Ge atomic concentration in I and II series glasses, which is reflected in the thermal diffusivity value also.

The minimum electrical conductivity during the p- to n- transition may be due to the maximum value of the optical band gap. Rabinal [30] has observed that the band gap value increases along with increasing Ge content in $Pb_{20}Ge_ySe_{80-y}$ glasses, the Eg value reaches maximum at y = 21 at.% and then decreases. We have reported the comparison of thermal diffusivity with electrical conductivity in the GeBiSe and Ge Bi Se Te glasses [20]. In solids, thermal conductivity is due to the heat transport by both phonons and charge carriers. The thermal diffusivity is directly proportional to the thermal conductivity [12]. Since at the p- to n- transition, the optical band gap is higher, the excited concentration of electrons from valence band to conduction band is appreciably low, which results in a lower carrier concentration. After the critical composition, the Eg value decreases and as a result the electrical conductivity and thermal diffusivity both increase. Further increasing the Pb and Ge concentration in I and II series respectively, the decreasing thermal diffusivity value may be due to a decrease in the phonon mobility arising out of scattering and phonon collisions due to the defects present in the 3-d structure.
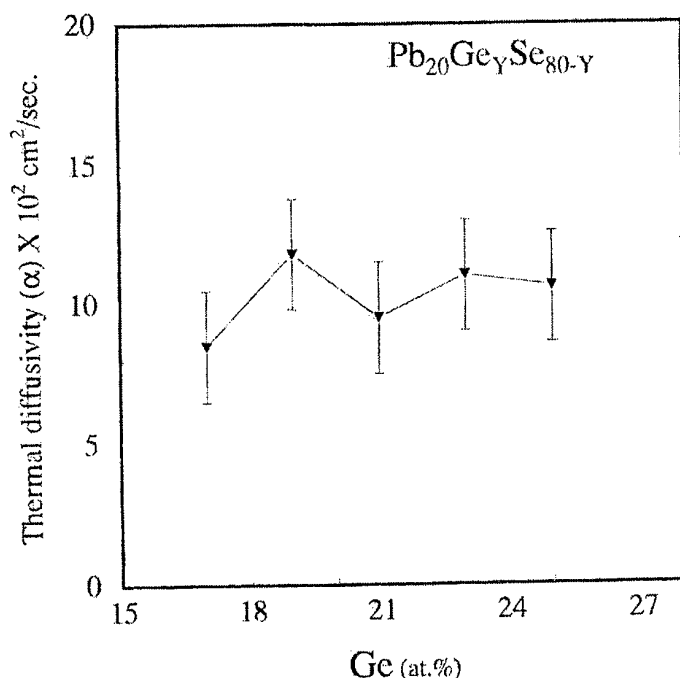
Fig. 3. Variation of thermal diffusivity with Ge concentration.

According to the Kolobov model [25] by the addition of Pb in Ge-Se glasses, the concentration of C_3^+ center decreases rapidly with a corresponding increase in C_1^- centers. So after a certain Pb and Ge composition in these glasses, C_1^- centers act as majority carriers, which result in n-type electrical conduction. From the above discussions, it is concluded that after the specific composition of Pb and Ge the Fermi level E_F moves towards the conduction band, which is assumed to be a consequence of the formation of Pb-Se ionic bonds. The addition of Pb atoms create the formation of negatively charged Se centers, which disturb the equilibrium between the Se^- and Se_3^+ centers by the law of mass action and hence causes the unpinning of Fermi level. Mehra et al. [10] have proved this unpinning of Fermi level in Pb added Se-In chalcogenide glasses with the studies of the activation energy of electrical conductivity and optical band gap.

4. Conclusion

The composition dependence of the thermal diffusivity of $Pb_xGe_{42-x}Se_{58}$ and $Pb_{20}Ge_ySe_{80-y}$ glasses has been studied by the photoacoustic technique. The measurements show an unusual behavior at p- to n- conduction changes. In $Pb_xGe_{42-x}Se_{58}$ glasses the change is more prominent than in the $Pb_{20}Ge_ySe_{80-y}$ glasses. Like the electrical conductivity measurements, the thermal diffusivity value shows minimum at the p- to n- transition threshold and then increases with corresponding increases of Pb and Ge concentration in I and II series glasses. The addition of Pb disturbs the equilibrium between Se_3^+ and Se^- centers, thus unlocking the Fermi level. This results in the E_F shifting toward the conduction band and in the p- to n- conduction changes in these glasses.

Acknowledgement

References

[1] D. Adler, Amorphous Semiconductors, CRC, Butterworths, London, 1971.
[2] S. Murugavel, S. Asokan, Phys. Rev. B., **58**, 33 (1998).
[3] K. Ramesh, S. Asokan, K. S. Sangunni, E. S. R. Gopal, Appl. Phys. A., **96**, 421 (1999).
[4] R. A. Street, N. F. Mott, Phys. Rev. Lett., **35**, 1293 (1975).
[5] A. I. Gubanov, Sov. Phys. Solid State, **3**, 1964 (1962).
[6] N. Tohge, Y. Yamamoto, T. Minami, M. Tanaka, Appl. Phys. Lett., **34**, 640 (1979).
[7] N. Tohge, T. Minami, M. Tanaka, J. Non-Cryst. Solids, **37**, 23 (1980).
[8] N. Tohge, M. Matsuo, T. Minami, J. Non-Cryst. Solids, **95-96**, 809 (1987).
[9] S. Murugavel, S. Asoken, Phys. Rev. B., **58**, 4449 (1998).
[10] R. M. Mehra, S. Kohli, A. Pundir, V. K. Sachdev, Mathur, P. C., J. Appl. Phys., **81**, 1997, 7842.
[11] K. N. Madhusoodanan, J. Philip, G. Parthasarathy, S. Asokan, E. S. R. Gopal, Phil. Mag., **B58**, 123 (1988).
[12] A. Rosencwaig, Photoacoustics and Photoacoustic Spectroscopy, Wiley, New York, 1980.
[13] M. K. Rabinal, N. Ramesh Rao, K. S. Sangunni, E. S. R. Gopal, Phil. Mag., **B70**, 89 (1994).
[14] M. K. Rabinal, K. S. Sangunni, E. S. R. Gopal, S. V. Subramanyam, Physica B, **205**, 403 (1995).
[15] K. L. Bhatia, S. K. Malik, N. Kishore, S. P. Singh, Phil Mag., **B66**, 587 (1992).
[16] K. L. Bhatia, S. K. Malik, Phys. Stat. Sol. (b), **168**, K51 (1991).
[17] S. Rahman, M. V. Ramana, G. S. Sastry, Phys. Chem. Glasses, **33**, 209 (1992).
[18] B. Vaidhyanathan, S. Murugavel, S. Asokan, K. J. Rao, J. Phys. Chem., **101**, 9717 (1997).
[19] R. Ganesan, K. N. Madhusoodanan, A. Srinivasan, K. S. Sangunni, E. S. R. Gopal, Phys. Stat. Sol. (b), **212**, 223 (1999).
[20] B. Thangaraju, R. Ganesan, K. S. Sangunni, E. S. R. Gopal, Sol. Stat. Commun., **108**, 301 (1998).
[21] A. Feltz, L. Snef, Z. Anorg. Allg. Chem., **444**, 195 (1978).
[22] D. Linke, M. Gitter, F. Krug, Z. Anorg. Allg. Chem., **444**, 217 (1978).
[23] B. Thangaraju, R. Ganesan, N. Asha Bhat, K. S. Sangunni, E. S. R. Gopal, J. Optoelect. & Adv. Mat., **2**, 91 (2000).
[24] Z. U. Borisova, Glassy Semiconductors, Plenum, New York, 294 (1981).
[25] A. V. Kolobov, J. Non-Cryst. Solids, **198-200**, 728 (1996).
[26] M. Kastner, D. Adler, H. Fritzsche, Phys. Rev. Lett., **37**, 1504 (1976).
[27] N. Tohge, T. Minami, Y. Yamamoto, M. Tanaka, J. Appl. Phys., **51**, 1048 (1980).
[28] K. L. Bhatia, G. Parthasarathy, A. Sharma, E. S. R. Gopal, Phys. Rev. B, **38**, 6342 (1988).
[29] S. C. Rowland, F. Ritland, D. Hafer Burns, A. Bienenstock, Amorphous and Liquid Semiconductors, ed. Spear, W. E., Edingburg, 135 (1977).
[30] M. K. Rabinal, Ph. D. Thesis, Indian Institute of Science, Bangalore, India, 1993, p.105 (un published).

PHOTOCONDUCTIVITY AND TRANSPORT PROPERTIES OF As-Se THIN FILMS

M. A. Iovu, M. S. Iovu, S. D. Shutov, E. P. Colomeyco, S. Z. Rebeja

Center of Optoelectronics, Institute of Applied Physics, Academy of Sciences of Moldova
Str. Academiei 1, MD-2028 Chisinau, Moldova

Steady-state and transient photoconductivity characteristics of thermally and laser-beam deposited chalcogenide amorphous films $As_{40}Se_{60}$ and $As_{50}Se_{50}$ are studied at varied light intensity and temperature. The lux-ampere characteristics are shown to change the power exponent from a value greater than 0.5 at low intensities to the value less than 0.5 at high intensities, indicating the change in recombination reaction. The transient photocurrents in step-function mode of excitation were found to be consistent with the model of trap-controlled non-stationary capture and recombination in exponentially distributed in energy hole traps. Evaluating of the trap energy distribution parameter independently from the photocurrent transients as well as from the dependence of steady-state photoconductivity measurements yields consistent results.

1. Introduction

Amorphous films of chalcogenide glassy system As_xSe_{100-x} are currently of interest as materials for optoelectronic devices and optical information storage [1-3]. The composition $As_{50}Se_{50}$ of this system exhibits high light sensitivity in photostructural transformations due to the presence of homopolar As-As bonds [4-6]. Excess of As in $As_{50}Se_{50}$ relative to stoichiometry composition $As_{40}Se_{60}$ leads to increase of optical gap E_g (from 1.90 eV to 1.95 eV for bulk $As_{40}Se_{60}$ and $As_{50}Se_{50}$, respectively) and of other related energy intervals [7,8]. The evaporated films are shown to have large degree of structural disorder depending on the deposition procedure. In the present paper the results of systematic study of steady state and transient photoconductivity characteristics of thermally deposited amorphous films $As_{50}Se_{50}$ and $As_{40}Se_{60}$ are described. The obtained data are analysed on the base of multiple trapping model and some parameters of the localised state energy distribution are derived from the experimental results.

2. Experimental

The thin film samples were prepared in sandwich configuration with aluminium or gold electrodes. The $As_{50}Se_{50}$ and $As_{40}Se_{60}$ films with thickness from 1 to 6 µm were obtained by flash thermal deposition in vacuum of the starting bulk material onto glass substrates kept at $T_s=375\div400$ K. In some cases the laser ablation was used for obtaining amorphous films. He-Ne laser LGN-108 ($\lambda=0.63$ µm) was used as a light source with photon flow $F=6.5\cdot10^{14}$ $cm^{-2}s^{-1}$; the light intensity was controlled by calibrated neutral density filters. A shutter was used to switch the light on/off with time constant of about 10^{-3} s. The photoconductivity relaxation was registered with a time constant not greater than 0.1 s by a co-ordinate recorder ENDIM 622.01. The spectral distribution of steady-state photoconductivity was obtained with the aid of spectrophotometer SPM-2 with a tungsten lamp as a light source.

3. Results and discussion

3.1. Steady state photoconductivity

Lux-ampere characteristics of steady-state photoconductivity σ_{ph} for all investigated amorphous films in a wide intensity (F) interval at various temperatures (T) are sublinear and may be approximated by a power law:

$$\sigma_{ph} = B \cdot F^{\gamma}, \tag{1}$$

where B is the constant weakly dependent on temperature, and γ is the power index. For each σ_{ph} vs. F curve an inflection point is observed corresponding to the transition of the power index γ from the values $\gamma_L = 0.60 \ldots 0.73$ in the low-intensity interval to lower values $\gamma_H = 0.5 \ldots 0.3$ at higher excitation intensities (Fig. 1a). With the temperature increasing, γ_L and γ_H first remain constant up to 350 K and then γ_L increases while γ_H decreases. This kind of behaviour appears to be unusual as γ_L as a rule decreases with temperature increasing while γ_H is weakly temperature dependent. The intensity dependence of photoconductivity at all temperatures shows a kink (Fig. 1a), at which the power exponent γ is changed from $\gamma > 0.5$ to $\gamma < 0.5$. It is commonly accepted that this kink is due to change of excess-carrier recombination mechanism at increasing of excitation, i.e. to transition from the monomolecular (MR) reaction to the bimolecular (BR) one. Sublinear power γ_L is then associated with variation of the recombination rate during movement of the quasi-Fermi level through a region of quasicontinious exponential gap-state distribution (A.Rose [9]), that is $\gamma_L = T_0/(T_0+T)$, where T_0 is the characteristic temperature of the gap-state distribution ($T_0 > T$) and $0.5 \le \gamma_L \le 1$.
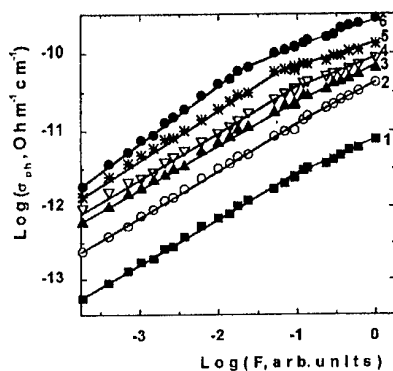

Fig. 1a. The steady state photoconductivity σ_{ph} dependence on. light intensity F of the $As_{50}Se_{60}$ films. Temperature T, K: 1-289; 2-321; 3-341; 4-351; 5-365; 6-388. $F_0 = 6.5 \cdot 10^{14}$ cm$^{-2} \cdot$s^{-1}.
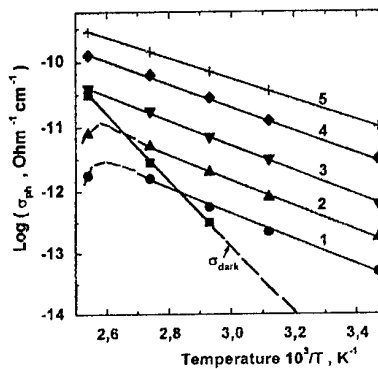
Fig. 1b. The steady state photoconductivity σ_{ph} dependence on temperature T of the $As_{40}Se_{60}$ films. Light intensity F, cm$^{-2} \cdot$s^{-1}: 1- 6.5·10^{10}; 2-6.5·10^{11}; 3-6.5·10^{12}; 4-6.5·10^{13}; 5-6.5·10^{14}. The temperature dependence of dark conductivity σ_{dark} is also shown.

The obtained value of γ_L=0.6 leads to T_0=450K, which is lower than T_0=550K obtained for the characteristic temperature of the state distribution in the valence-band tail of the stoichiometry composition $As_{40}Se_{60}$ [10]. The observed independence of γ_L up to 350K and its further rise at increasing of the temperature could be understood in the frames of the mentioned model if we suppose that T_0 is also increased with the temperature, i.e. the hole quasi-Fermi level crosses the region of quasicontinious distribution of localised states with varying steepness. At high temperatures and intensities of light the power exponent γ_H deviate from the standard value γ_H=0.5 characteristic for bimolecular recombination and takes lower values, which indicate the participation of another recombination path. Low γ_H values (γ_H<0.5) are expected for tail-to-tail or tail-to-defect tunnelling recombination (a-Si:H [11,12]) or in the case of light absorption in the metal-semiconductor contact region for sandwich-cell samples (a-$As_{40}Se_{60}$ [13]).

The temperature dependence of steady-state photoconductivity (Fig. 1b) is activated with an activation energy E_b= 0.33 eV, which becomes somewhat lower (0.30 eV) at highest light intensity. In the high-temperature region a tendency to change of the recombination mechanism is observed. The estimation of the transition temperature T_m from the expression [14]:

$$T_m = (\sigma_{ph}/\sigma_{dark})E_a/2k \tag{2}$$

yields the temperature about 400K, which is out of the interval of measurements.

According to the model of quasidiscrete gap states of charged defects the activation energy of photoconductivity in low-temperature region (T<T_m, σ_{ph}>σ_d) accounts for the position of the acceptor-

like level E_2-E_v = $2E_b$ [8,12,15]. For the $As_{50}Se_{50}$ films E_2-E_v = 2x0.33 eV = 0.66 eV, in agreement with the similar results for the films of stoichiometric composition $As_{40}Se_{60}$ [8]. This value is also close to the results of time-of-flight drift mobility measurements [16], in which there was found that the drift mobility activation energy in $As_{50}Se_{50}$ films equals to 0.69 eV and sharply increases with further growth of As content (0.97 eV for $As_{55}Se_{45}$).

The spectral dependence of photoconductivity for the $As_{50}Se_{50}$ and $As_{40}Se_{60}$ films represents a curve with a broad peak (Fig. 2). The films demonstrate high photosensitivity in the visible region of the light spectrum (from 0.50 μm to 0.8 μm at the half-peak level) with light-to-dark conductivity ratio more than 10^2 at F= $5 \cdot 10^{14}$ cm^{-3} s^{-1}.
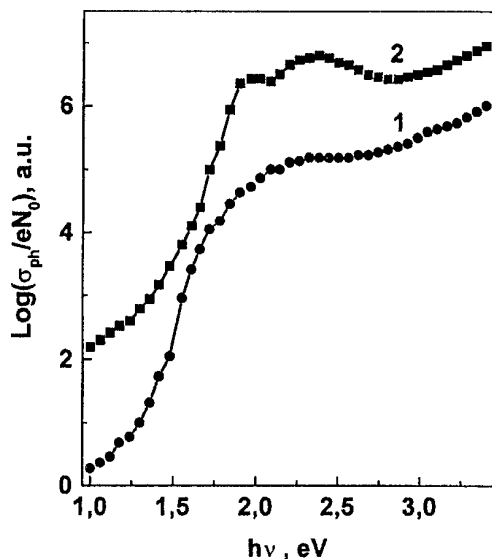
a)   b)
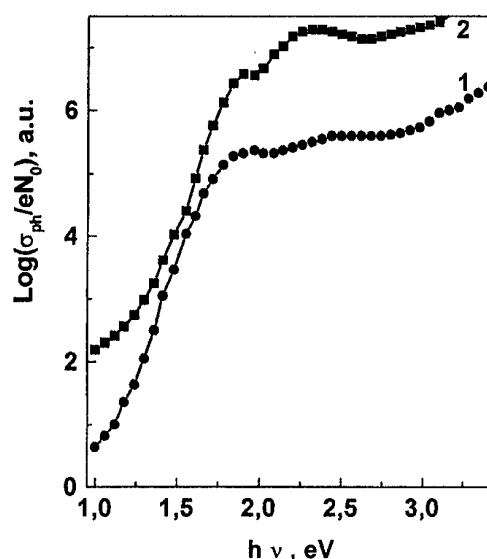

Fig. 2. The spectral dependence of the photoconductivity of laser (1) and thermal (2) deposited $As_{40}Se_{60}$ (a) and $As_{50}Se_{50}$ (b) thin films. The positive voltage is applied to the top illuminated electrode.

The position of the main peak of the photoconductivity spectrum of the amorphous arsenic selenide films at hv=1.97 eV corresponds to the optical gap E_g at the absorption coefficient α=10^4 cm^{-1}. This value coincides with E_g=1.95 eV [7] obtained from optical measurements in bulk samples.

The photoconductivity spectra contain information about generation, transport, and recombination processes of the non-equilibrium carriers:

$$\sigma_{ph}=(1/d)e\mu_d\tau\beta N_0[1-exp(-kd)],$$ (3)

where N_0 is the number of the incident photons, d is the thickness of the sample, β is the generation rate, μ_d is the drift mobility, k is the absorption coefficient, and τ is the lifetime.

In the region of high absorption coefficients $(exp(-kd)<<1)$, for the negligible low surface recombination, the photoconductivity weakly depends on the photon energy

$$\sigma_{ph}=(1/d)e\mu_d\tau\beta N_0,$$ (4)

For the weak absorption region $(exp(-kd)\approx1-kd)$ the photoconductivity spectra are described as

$$\sigma_{ph}=e\mu_d d\tau\beta N_0,$$ (5)

In this region the slope of the photoconductivity spectra expresses the parameter of the localised states $E_0=kT_0$, which depends on composition and on the preparation method of the amorphous thin film ($E_0\approx0.07$ eV for $As_{50}Se_{50}$, and $E_0\approx0.06$ eV for $As_{40}Se_{60}$). For the $As_{50}Se_{50}$ and $As_{40}Se_{60}$ thin films prepared by laser deposition an increase of photosensitivity in all investigated spectral domain is observed.

3.2. Transient photoconductivity

Long-term relaxation of photoconductivity in the amorphous $As_{50}Se_{50}$ and $As_{40}Se_{60}$ films under light excitation in step-function mode are shown in Fig. 3 at various laser light intensities. Illumination by the He-Ne laser corresponds to the absorption coefficient near 10^4 cm^{-1} therefore the incident light is totally and nearly uniformly absorbed in the film volume. As it is seen from the Fig. 3, at low intensities the photocurrent rises in monotonous manner up to the steady-state value. At higher intensities an overshoot appears on the increasing portion of the transient, i.e. the steady state is reached after passing a peak on the rise [17,18].
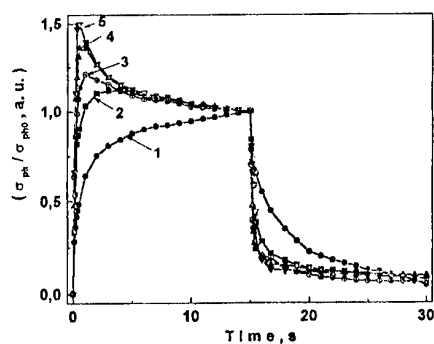

Fig. 3a. Photoconductivity relaxation curves in Au-$As_{40}Se_{60}$- Al thin films (L=9.7 µm) at T=290 K. Light intensity F, %: 1-0.008; 2-2.2; 3-13; 4-37; 5-100. $F_0=6.5\cdot10^{14}$ cm^{-2}·s^{-1}, λ=0.63 µm.
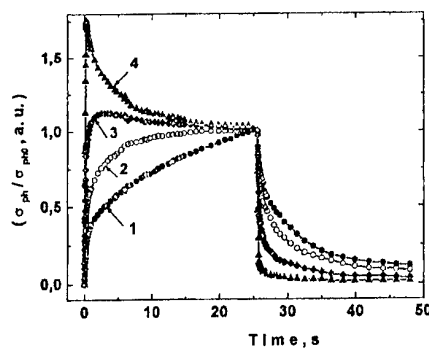
Fig. 3b. Photoconductivity relaxation curves in Au-$As_{50}Se_{50}$-Al thin films (L=5.87µm) at T=290 K. Light intensity F, %: 1 - 0.008; 2 - 0.3; 3 - 2.2; 4 - 100. $F_0=6.5\cdot10^{14}$ cm^{-2}·s^{-1}, λ=0.63 µm.

Photoconductivity relaxation in amorphous chalcogenides has gained satisfactory interpretation in frames of the model of multiple trapping in gap states quasicontiniously distributed in the mobility gap of an amorphous semiconductor [10,18,19]. Application of this model allows understanding also some other nonequlibrium processes specific for the chalcogenide glassy semiconductors such as dispersive transport and induced optical absorption. An analysis of these processes leads to an exponential form of the energy distribution N(E) of localised state density of the form:

$$N(E) = (N_t/E_0)\exp(-E/E_0), \qquad (6)$$

where N_t is the total gap-state density and $E_0=kT_0$ is the distribution parameter.

The theoretical consideration of the photocurrent relaxation in frames of the multiple-trapping model with gap states exponentially distributed in energy allows revealing several definite time domains in transient curves [18]. Each of these domains corresponds to a power dependence of photocurrent upon time and is determined by capture of free carriers in traps or by their recombination in monomolecular (MR) or bimolecular (BR) regimes. These processes govern the dependencies of relaxation both on excitation intensity and on the temperature. The detailed calculations and relaxation patterns have been presented in Ref. [19]. In Fig.4 the rise and decay curves for $As_{50}Se_{50}$ thin films are replotted in double-logarithmic scale to visualise the power-law portions of the transients discussed below.

Over the initial portion up to the moment t_1 the photocurrent rise is governed by the capture process, while recombination so far is not significant: $i_{ph} \sim G \cdot t^\alpha$, where G is the generation rate and $\alpha=(T/T_0=kT/E_0)$ is so called dispersion parameter. Further behaviour of the transients depends on excitation intensity. At low intensities (corresponding to MR) the photocurrent monotonously increases and reaches the steady-state value. At higher exposure intensities a quasistationary portion is observed, which at certain moment is followed by a decreasing portion of the transient, where the BR mechanism is dominant. Along this portion $i_{ph} \sim G^{1/2} \cdot t^{(1-\alpha)/2]}$. At highest excitation level the relaxation is governed by BR and the quasistationary portion of photocurrent is absent ("an overshoot", see Fig.4a).
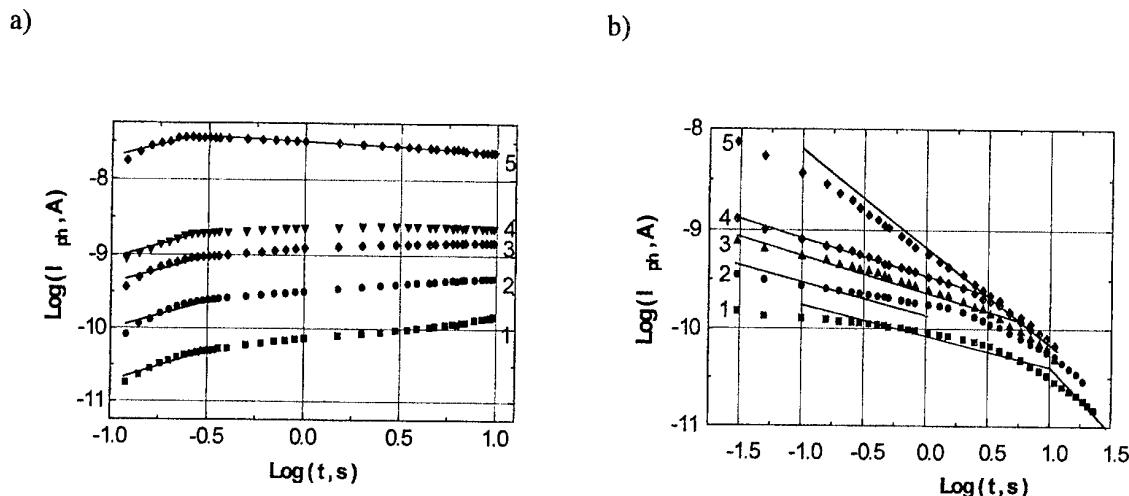
a)   b)

Fig.4. Double-logarithmic plot of photocurrent rise (a) and decay (b) in the $As_{50}Se_{50}$ film at various light intensities F, $cm^{-2} \cdot s^{-1}$: 1 - $5.3 \cdot 10^{11}$, 2 - $2.4 \cdot 10^{12}$, 3 - $6.6 \cdot 10^{12}$, 4 - $1.5 \cdot 10^{13}$, 5 – $6.5 \cdot 10^{14}$. Straight-line portions are calculated with $\alpha = 0.67$ (see text for details).

The photocurrent decay depends on the initial density of photogenerated charge carriers. If during the generation pulse the total filling of gap states is not achieved then an initial portion of the decay governed by capture process exist and the recombination is delayed. Over this portion $i_{ph} \sim i_{ph0} \cdot t^{(1-\alpha)}$ where i_{ph0} is the photocurrent at the moment when the light is switched off. At low generation intensities (MR regime) the starting portion turns into final decay, along which $i_{ph} \sim i_{ph0} \cdot t^{e-(1+\alpha)}$. If the generation intensity provides the BR regime, then an intermediate portion exists, where $i_{ph} \sim i_{ph0} \cdot t^{-1}$. The above-described behaviour of photocurrent kinetics is in good agreement with the experimental curves of transient photocurrent for a set of generation rates presented in Fig.4. The dispersion parameter α was determined from the experimental relaxation curves as an asymptotic of the power-law portions of the rise and decay of the photocurrent plotted in double-logarithmic co-ordinates. Using the experimentally calculated values of the dispersion parameter α, the parameter of localised states distribution E_0 was estimated, which increase from E_0=0.037 eV (T_0=429 K) for $As_{50}Se_{50}$ up to E_0=0.046 eV (T_0=533 K) for $As_{40}Se_{60}$, respectively.

The value of the parameter T_0=533 K for amorphous $As_{40}Se_{60}$ films is in a good agreement obtained by Vaninov and co-workers [20] ($T_0 \approx 550$ K<$T_g \approx 450$ K) from the relaxation curves of the transient photocurrent in a-$As_{40}Se_{60}$ thin films. This parameter was studied in dependence of the nature of the metal dopants in a-$As_{40}Se_{60}$ (Ga, Na, Ag, Cu, Tl, In). Unfortunately the obtained results for different metallic dopants don't permit to obtain an adequate interpretation. For-example, the value of the dispersion parameter α for different dopants is different: $\alpha(As_{40}Se_{60}:In) > \alpha(As_{40}Se_{60}) > \alpha(As_{40}Se_{60}:Tl)$. The indium impurity (In) increases the value of the parameter $\alpha \approx 0.65$, while the impurity of thallium (Tl, $N_A \sim 10^{20}$ cm^{-3}) decreases it down to α=0.45 with respect to that for undoped a-$As_{40}Se_{60}$ (α=0.54). According to [20], the parameter T_0 reflects the temperature at which the impurities or the fluctuations of the potential are frozen at the cooling process of the chalcogenide glass. That means that the value of the parameter T_0 determined for different impurities reflects the temperature for which the diffusion coefficient of the impurities became negligible small [21].

The parameters α, T_0 and E_0 were estimated from the relaxation curves of the photocurrent as well as from the lux-ampere characteristics for $As_{50}Se_{50}$ and $As_{40}Se_{60}$ amorphous thin films and compared with the data from optical absorption [22] (Fig. 5). In Fig. 5 there are also presented the values of the parameter α, determined from the relaxation curves of the photoconductivity and photoinduced absorption for different values of the parameter T_0 for the exponential distribution of the localised states according to [23].
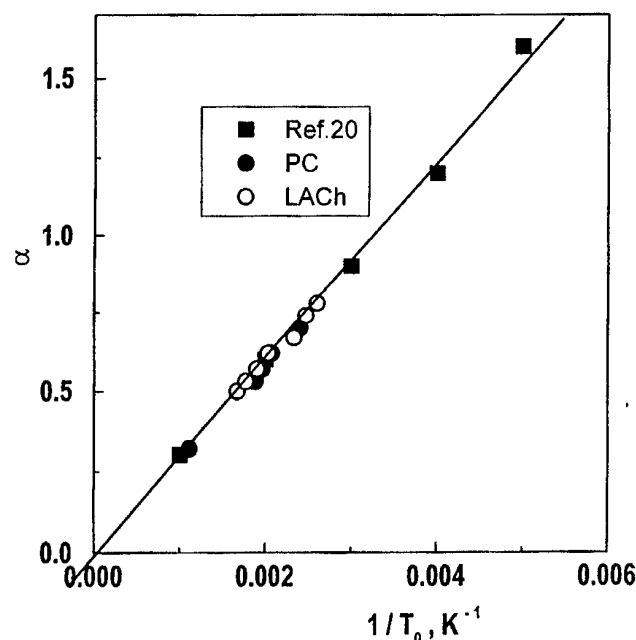
Fig. 5. The dependence of the dispersion parameter α vs. T_0 for $As_{50}Se_{60}$, and $As_{40}Se_{60}$ films determined from the transient photocurrent (•), from lux-ampere characteristics (O), and according to Ref. [23] (■).

The fact that the complex picture of the photocurrent kinetics can be described by single parameter justifies the use of the model of multiple-trapping controlled recombination. The variation of the kinetics with temperature corresponds to the predictions of the model as well, as the transition moment t_i is exponentially shifted to shorter times as the temperature is increased. It is worth noting the important role, which capture plays in photoconductivity of amorphous semiconductors, determining the specific initial portions of relaxation. Capture enhancement leads to the delay of recombination and to shift of the moment t_i to longer times. The shortest time t_i, corresponding to the onset of recombination in investigated glasses, appears for the stoichiometry composition $As_{40}Se_{60}$ ($t_i = 10^{-2}$ s), it is about 3.3 s in $As_{50}Se_{50}$ films (containing excess As atoms).

4. Conclusion

The steady-state and transient characteristics of photoconductivity in amorphous thermally deposited chalcogenide $As_{50}Se_{50}$ and $As_{40}Se_{60}$ films were studied at various light intensities and temperatures. The set of photoconductivity characteristics are adequately interpreted in the frame of the multiple-trapping model, according to which transport and recombination of non-equilibrium holes are controlled by multiple capture in exponentially distributed in energy hole traps. Evaluating of the trap energy distribution parameter kT_0 independently from the photocurrent rise and decay as well as from the dependence of steady-state photocurrent on light intensity yields consistent results. The photoconductivity occurs under condition that the thermal equilibrium between fractions of delocalized and localised charge carriers has not been established, similar to the situation characteristic for the dispersive transport of photoinjected carriers. By this reason the activation energies of photoconductivity and of drift mobility have close values. Spectral distribution of steady-state photoconductivity was shown to depend from the thin-film deposition technology.

References

[1] V. Aiyah, S. D.Kasap, B. Polischuk, A. Bailie, J. of Non-Cryst. Solids, **164-166**, 777 (1993).

[2] A. I .Buzdugan, M. S. Iovu, A. A. Popescu, P. G. Cherbari, Balkan Phys. Letters, **1**, 7 (1993).

[3] A. M. Andriesh, M. S. Iovu, E. G.Khanchevskaya, Balkan Phys.Letters, **4**, 1 (1996).

[4] V. M. Lyubin, J. of Non-Cryst.Solids, **97-98**, 47 (1987).

[5] G. Pfeiffer, M. A. Paesler, S. G. Agarwal, J. of Non-Cryst.Solids, **130**, 111 (1991).

[6] Z. M. Zallen, G. A. Williams, P. C. Taylor, Phys.Rev.B, **40**, 10557 (1990).

[7] H. Hurst, E. A. Davis. In 'Amorphous and Liquid Semiconductors', ed. J. Stuke and W. Brenig (London: Taylor and Francis), 349 (1974).

[8] M. Hammam, G. J. Adriaenssens, W. Grevendonk, J. Phys. C: Solid State Phys., **18**, 2151 (1985).

[9] A. Rose. Concepts in Photoconductivity and Allied Problems (Interscience Publishers, N.-Y.-London), (1963).

[10] J. Orenstein, M. A.Kastner, V. Vaninov, Phil.Mag, **B46,23**, (1982).

[11] J. -H. Zhou, S. R. Elliott, Phys.Rev, **B48**, 1505, (1993).

[12] A. Vomvas, H. Fritzsche, J. Non-Cryst. Solids, **97-98**, 823, (1987).

[13] M. Hammam, G. J. Adriaenssens, J. Non-Cryst.Solids, **59-60**, 961, (1983).

[14] J. G. Simmons, G. W. Taylor, J. Non-Cryst. Solids, **8-10**, 947 (1972).

[15] C. Main Proc.of the Conf."Amorphous Semiconductors'84", Gabrovo, Bulgaria, Sept.17-22,1984, and A.E.Owen. In "Electronic and Structural Properties of Amorphous Semiconductors", ed. P.G. Le Comber and J. Mort (London, Academic Press) (1973), p. 527

[16] L. Toth. In: Proceed. Conf. Amorphous Semiconductors'84, Gabrovo (Bulgaria), Sept. 17-22, 1984, V.1, p. 236.

[17] M. S. Iovu, E. P. Colomeyko, S. D. Shutov, Semiconductors 31(7), 710 (1997).

[18] M. S. Iovu, S. D. Shutov, V. I. Arkhipov, S. Z. Rebeja, M. G. Bulgaru, E. P. Colomeyko, Proceed. of the 20-th Int.Semicond.Conference CAS'97, Sinaia, Romania, 1997, p. 53.

[19] V. I. Arkhipov, M. S. Iovu, A. I. Rudenko, S. D. Shutov. Sov.Phys. Semicond., **19**, 61, (1985).

[20] V. Vaninov, J. Orenstein, M. A. Kastner, Phil. Mag. **B45**(4), 399, (1982).

[21] M. A. Kastner, Phil. Mag. B37, 127, (1978).

[22] M. S. Iovu, N. Syrbu, S. D. Sutov, I. A. Vasiliev, S. Rebeja, E. Colomeico, Phys. Stat. Solidi (a), (1999), **175**, 615, (1999).

[23] S. Grobtchak, M. Cocivera, Phil. Mag. **B79**(6), 881, 881, (1999).

OPTICAL AND ELECTRICAL PROPERTIES OF AMORPHOUS (GeS$_2$)$_{100-x}$Ga$_x$ THIN FILMS

Z. G. Ivanova, P. Petkov[a], V. S. Vassilev[a]

Institute of Solid State Physics, Bulgarian Academy of Sciences, 72 Tzarigradsko Chaussee, 1784 Sofia, Bulgaria
[a]University of Chemical Technology and Metallurgy, 8 Kl. Ohridski blvd., 1756 Sofia, Bulgaria

Results from the study of basic optical and electrical parameters of semiconducting (GeS$_2$)$_{100-x}$Ga$_x$ (x=0, 4, 8, 12 at.%) amorphous layers have been summarized. The investigation of the optical absorption has shown that the introduction of Ga leads to a shift in the absorption edge towards lower energies in comparison with GeS$_2$. The spectral distribution of the refractive index n, accounting the influence of photoexposure, has been specified. The optical energy gap E$_g^{opt}$ has been determined from the Tauc plot $\alpha h v = B(E_g^{opt} - h v)^2$. The electrical energy gap E$_g^{el}$ has been obtained from the thermal dependence of the conductivity. Both the values of E$_g$ decrease with increasing Ga content. From the current-voltage characteristics, the effective electron mass m in the conduction band, the electron work function χ at the Al/Ge-S-Ga interface and the relative dielectric permitivity ε have been determined. The experimental data are in agreement with Christov's theory for injected electron currents into dielectric or semiconducting materials. The observed regularities are related to some structural peculiarities in the Ge-S-Ga system studied.

1. Introduction

Amorphous chalcogenide semiconductors possess a lot of interesting phenomena, which reveal possibilities for using them in microelectronics and optoelectronics - as ovonic threshold and memory switching devices, inorganic photoresists, optical memory disks, etc. The increased interest in them has been connected mainly with their unique peculiarity to record information by irreversible or reversible structural transformations between a disordered and a more ordered state. Exposure to band gap light causes photoinduced changes, which have been studied in detail by K. Tanaka [1,2]. Especially, amorphous Ge-S thin films exhibit remarkable irreversible photo- and thermo-bleaching effects, caused by illumination and annealing, respectively [2,3].

Recently, Ge-S-Ga glasses have been intensively investigated as host materials for fiber-optic amplifiers and infrared lasers by doping with rare-earth elements [4-6]. They have good chemical durability, low phonon energy, high refractive indexes and good glass-forming ability. Besides, reversible and/or irreversible photoinduced effects have been observed in them, which are more pronounced than those in the binary Ge-S system [7,9].

The glass-forming boundaries and basic physicochemical parameters of the ternary Ge-S-Ga system have been determined earlier [10]. The largest photoinduced changes in the optical and physicochemical properties have been found for amorphous (GeS$_2$)$_{100-x}$Ga$_x$ thin films [7,8]. The aim of this paper is to summarize the data on basic optical and electrical properties exactly for such compositions (x = 4, 8, 12 at.% Ga), which are important both from fundamental and practical point of view.

2. Experimental

Bulk Ge-S-Ga glasses were synthesized by melting the initial elements (purity of 5N) inside evacuated and sealed quartz ampoules in a rocking furnace. The suitable temperature regime was

determined depending on the composition [10]. The enriched in sulphur samples were heated to ~ 780 °C, held at that temperature for 7-8 h and then quenched in ice-water (Ge-enriched compositions were heated to ~ 1000 °C). The homogeneity of the glasses was confirmed by optical and electron microscopy. Amorphous thin films were prepared by thermal evaporation (vacuum ~ 2.10^{-5} Pa) onto glass substrates. The special design of the evaporator prevented eventual fractional decomposition [11].. The structure of the films was investigated by electron diffraction and the thickness was measured with an interference microscope. The composition was determined by Auger electron spectroscopy and the data showed that it is identical with that of the bulk glasses, with an accuracy ~ 1 at%, according to the used method (Fig. 1).
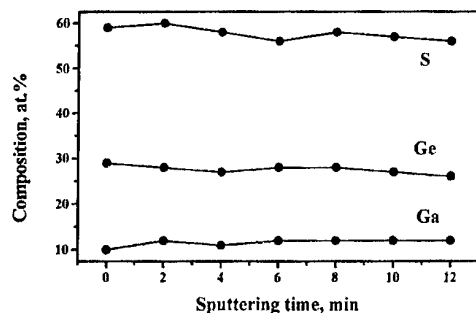
Fig. 1. Profilogram of the $Ge_{35}S_{53}Ga_{12}$ composition.

The optical transmission was measured in the spectral range of 400 ÷ 1300 nm and the refractive index was obtained using a computer program based on a method described by R. Swanepoel [12]. The electrodes were made of extremely pure aluminium (5N) by vacuum deposition. The capacitance and dielectric losses were measured at room temperature with a precise RCL bridge at a frequency of 8 kHz. In order to assess the response of the films to band gap light, half of each film was exposed in air at ambient pressure and temperature by mercury lamp HBO-500 with intensity of about 0.6 Wcm^{-2}.

3. Results and discussion

3.1. Optical properties

It has been found from the investigation of the optical transmittance of amorphous Ge-S-Ga thin films that exposure to band gap light causes a photobleaching effect [8]. The absorption edge shift $\Delta\lambda$ towards shorter wavelengths is accompanied by substantial increase of the integrated transparency of the exposed films. It has been established that $\Delta\lambda$ is maximal for compositions with a ratio of S/Ge=2 and about 10 at% Ga (Fig. 2).

Fig. 2. Compositional dependence of the absorption edge shift.

Fig. 3. Compositional dependence of the optical band gap.

The optical energy gap E_g^{opt} has been determined by extrapolating the dependence $(\alpha h\upsilon)^{1/2}=f(h\upsilon)$ to the intersection with the abscissa. The E_g^{opt} values decrease from 2.95 eV to 1.97 eV with increasing Ga

concentration, following an weak exponential relation after results fitting (Fig. 3). The refractive index n changes in the same way and its spectral distribution has shown that after illumi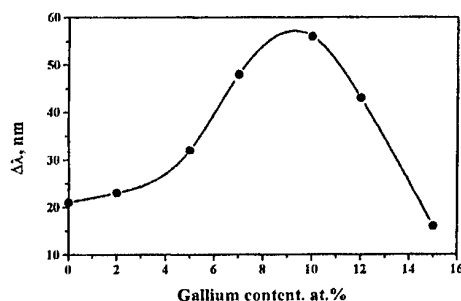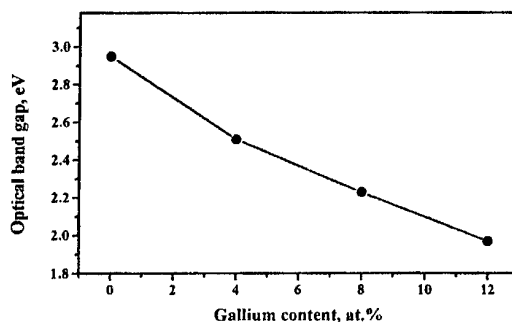nation n decreases (Fig. 4). The difference Δn between non-illuminated and illuminated films is largest for the composition with 8 at% Ga, which is in accordance with the maximal shift $\Delta\lambda$ (Fig. 2).

It has been found from the Raman spectroscopic study of these films that the photobleaching effect is associated with a certain degree of ordering in the local structure without formation of new phases [13]. This is expressed by enhanced orientation of existing bonds and/or extension of the short range order. Introduction of Ga in the binary Ge-S system results in stronger bleaching, i.e. larger shift of the optical absorption edge to shorter wavelengths The formed Ge-Ga and/or Ga-Ga bonds are weaker, therefore exposure breaks them to form the basic Ge-S bonds and to bring about a stabilization of the structure. Unfortunately, the Ge- and Ga-containing bonds cannot be distinguished because of their close vibration frequencies and overlapping of the bands.
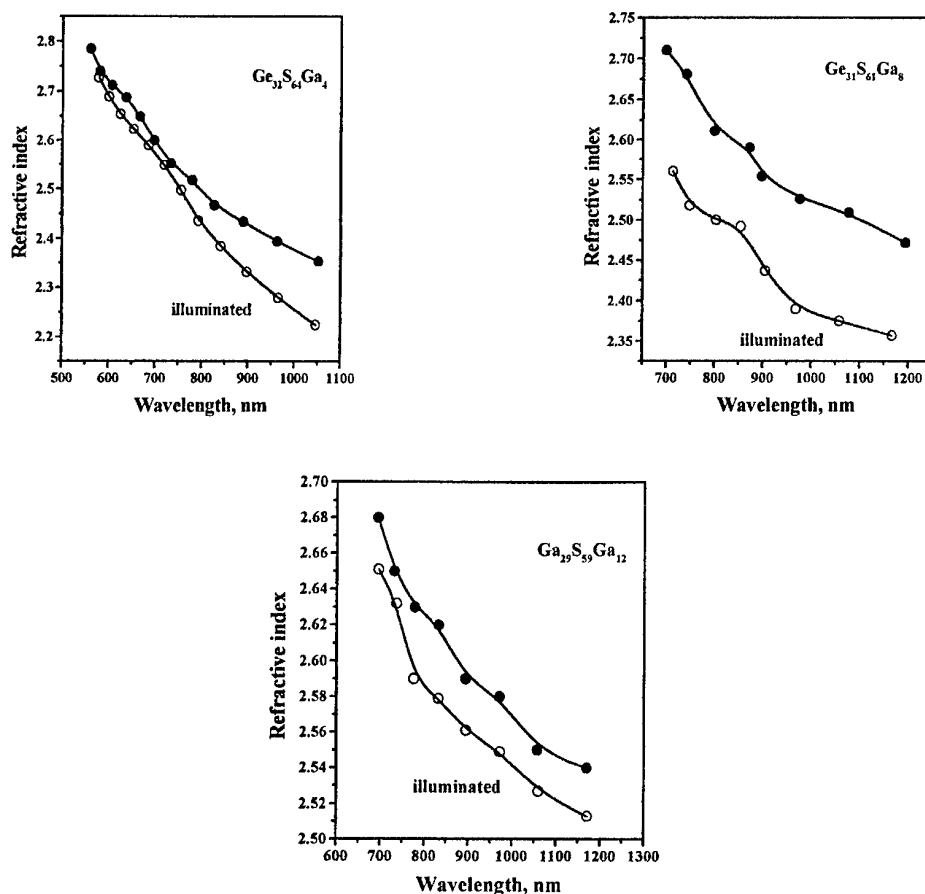
Fig. 4. Spectral distribution of the refractive index.

3.2. Electrical properties

From the current-voltage characteristics, the effective electron mass m* and electron work function χ at the Al/Ge-S-Ga interface have been determined (Table 1) [14]. An increase of the m* values at higher gallium content has been observed. The values of the dielectric losses and relative dielectric permitivity are tan δ < 0.03 and ε = 6.2±0.1, respectively. According to Christov's theory [15], thermionic (T) and thermionic-field (TF) emission regions have been investigated. On the boundary between them, determined by the condition Tk=1.76 T (Tk is Christov's characteristic temperature and T is the experimental one), the T and TF components of the current have been obtained to be equal. The temperature measurements of the conductivity have been limited by the glass transition temperature

of the glasses studied [10], because of thermocrystallization processes. The activation energy of the conductivity E_a has been determined from these dependences (Fig. 5).

Table 1. Effective electron mass and electron work function for thermionic and thermionic-field emissions of the studied samples.

Composition	m*	c_T	c_{TF}
$Ge_{33}S_{67}$	0.51	0.81	0.81
$Ge_{32}S_{64}Ga_4$	0.55	0.82	0.81
$Ge_{31}S_{61}Ga_8$	0.68	0.81	0.80
$Ge_{29}S_{59}Ga_{12}$	0.99	0.80	0.79

Fig. 5. Compositional dependence of the activation energy of the conductivity.

Subsequently, the band gap E_g^{el} can be calculated by the formula $\sigma = \sigma_0 \exp(-E_a/kT)$. The observed decrease of E_a with increasing Ga can be explained by the local ordering structure of the studied glasses [16]. The formation of Ga-Ga bridges at highest Ga contents leads to creation of defect states, resulting in an increase of the electron density in the conduction band.

4. Conclusion

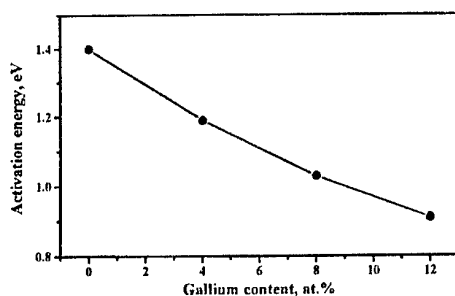The complex investigation of the optical and electrical properties of amorphous $(GeS_2)_{100-x}Ga_x$ thin films shows that the introduction of Ga into glassy GeS_2 does not influence significantly the glass. The results from the electrical transport in the thermionic and thermionic-field emission regions support Christov's theory for injected electron currents in insulators and semiconductors. The studied films are characterized by their basic optical (band gap, refractive index) and electrical (effective electron mass, electron work function, activation energy of the conductivity, etc.) properties.

References

[1] K. Tanaka, Reviews of Solid State Science (World Scientific Publishing Company, 1990) p. 641.
[2] K. Tanaka, Y. Kasanuki, A. Odajima, Thin Solid Films, 117, 251 (1984).
[3] T. Kawaguchi, S. Maruno, K. Masui, J. Non-Cryst. Solids, 97&98, 1219 (1987).
[4] K. Kadono, H. Higuchi, M. Takahashi, Y. Kowamoto, H. Tanaka, J. Non-Cryst. Solids, 184, 309 (1995).
[5] K. Abe, H. Takebe, K. Morinaga, J. Non-Cryst. Solids, 212, 143 (1997).
[6] J. Heo, J.M. Yoom, S.Y. Ryou, J. Non-Cryst. Solids, 238, 123 (1998).
[7] Z.G. Ivanova, V.S. Vassilev, Phys. Chem. Glasses, 33, 1, 28 (1992).
[8] Z.G. Ivanova, Thin Solid Films, 256, 257 (1995).
[9] Z.G. Ivanova, V.S. Vassilev, J. Non-Cryst. Solids, 192&193, 439 (1995).
[10] Z. Boncheva Mladenova, Z.G. Ivanova, Proc. Intern, Conf. Amorph. Semicond., Pardubice (Czech Republic) 1978, vol. I, p103.
[11] C. Vodenicharov, A. Stanchev, Bulgarian Patent No 31375 (1975).
[12] R. Swanepoel, J. Phys., E16, 1214 (1983).
[13] C. Raptis, Z.G. Ivanova, J. Appl. Phys., 64, 5, 2617 (1988).
[14] P. Petkov, Z.G. Ivanova, V. Vassilev, Thin Solid Films, 304, 315 (1997).
[15] S. G. Christov, Phys. Status Solidi (a), 15, 655 (1973).
[16] Z. G. Ivanova, J. Molec. Struct., 245, 335 (1991).

EXTENDED X-RAY ABSORPTION FINE STRUCTURE STUDY
ON Bi MODIFIED GeS BULK GLASSES

G. Saffarini, J. M. Saiter[a], A. Zumailan[a*]

Department of Physics, University An-Najah National, Nablus, Palestine via Israel
[a]Laboratoire d'Etude et de Caractérisation des Amorphes et des polymères, Faculté des Sciences, Université de Rouen, 76821 Mont Saint Aignan CEDEX, France
[*]Permanent address: Department of Physic, Faculty of Sciences and Education, University of Aden, Republic of Yemen.

EXAFS measurements have been performed from the Ge K edge and Bi L_{III} edge on GeSBi glasses with 6, 8 and 16 Bi at. %, and on crystalline Bi_2S_3. As expected, Ge is found to be fourfold coordinated with S atoms. It is also found that Bi is only coordinated with S with a coordination number CN = 4. This result for the CN of Bi contradicts the conclusion of Elliot and Steel. On the basis of the obtained CN of Bi, it is possible to exclude the presence of Bi_2S_3 microcrystalline inclusions and to assert that these glasses are homogeneous at the microscopic level.

1. Introduction

The first paper that dealt with the addition of bismuth in a cholcogenide matrix was published by Bowman and Schottmiller [1] in 1968. The goal was the preparation of new infrared photodetectors. At the same time, it was discovered that small amount of Bi atoms incorporated in a selenium matrix changes the electrical conductivity from p to n type [2]. More recently, the possibility of making an all chalcogenide glass p-n junction based on the ability of Bi to change the conductivity type was demonstrated [3,4]. Since the Schotmiller and co-workers results, many studies were performed to propose an explanation for the origin of this specific property that Bi atom seems to posses. Different atomic configurations were proposed. Most of these works were recently discussed in a synthesis paper of Vautier [5]. In regard to this last paper, one of the conclusions was that after more than 30 years of researches and debates, the origins of this specific property are not yet completely elucidated. In fact, one of the main problems is the lack of direct structural investigations of atomic Bi surrounding. Indeed, except the EXAFS works of Elliot et al [6] performed on GeSBi and GeSeBi glasses at the Bi absorption edge, to our knowledge no further direct investigations of the local surrounding of Bi atoms incorporated in a chalcogenide matrix were proposed.

In this work, structural results obtained on a series GeSBi glassy materials by means of EXAFS experiments are presented. The Ge and Bi absorption edges are explored.

2. Experiments and fitting procedure

Glasses were synthesised by direct melting of the ad-hoc amounts of high purity elements in vacuum sealed (10^{-3} Pa) silica ampoules at 900°C for 72 hours with continuous agitation. Glasses were obtained by quenching the tube in cold ice-water mixture.

EXAFS measurements in the transmission mode were performed at the Ge K edge (11103 eV) and Bi L_{III} edge (13440eV), at the EXAFS III station using the beam delivered from the bending magnet at DCI in LURE (Orsay France). The Si 311 monochromator was used to select the beam energies for Ge K and Bi LIII edge experiments. Experiments were performed at room temperature. Data were collected with an energy step of 2eV and 3eV for respectively Ge k and Bi LIII edges, using ionization chambers as detectors. Three spectra were obtained for each sample. The samples

used in absorption measurements were prepared by crushing and grinding the materials into particles finer than 20 μm, which were homogeneously pressed on kapton tapes.

The EXAFS spectra analyses were performed through a chain of programs written by Michalowicz [7]. The normalised EXAFS oscillations X(k) were obtained with the Lengeler-Eisenberger formula [8] with a linear model for the pre edge background removal and a five degree polynomial function to reproduce the post edge absorption. The EXAFS oscillation are approximately described by the following formula:

$$X(k) = \sum_j \frac{F_j(2k)N_j}{kr_j^2} \cdot \exp\left(\frac{-\Gamma_j r_j}{k}\right) \cdot \exp\left(-2\sigma_j^2 k^2\right) \cdot \sin\left(2kr_j + \Psi(k)\right) \qquad (1)$$

$F_j(2k)$ is the backscattering amplitude from each N_j neighbouring atoms of the jth type located at a distance r_j from the photoexcited atom (here Ge and Bi) and $\Psi_j(k)$ is the total phase shift experienced by the photoelectron. Both $F_j(2k)$ and $\Psi_j(k)$ are chemically sensitive, σ_j is the Debye-Waller factor that is the standard deviation in interatomic distances relative to their mean value r_j. The damping factor $\exp\left(-\Gamma_j r / k\right)$ is due to inelastic losses in the scattering process where Γ_j is related to the mean free path of the photoelectron.

Through the EXAFS analysis, the information about N_j, r_j, and σ_i around the photoexcited atom can in principle be obtained for each coordination shell. The modulus of the sine Fourier Transform (FT) of equation 1 gives a pseudo radial distribution function (RDF) in real space. In our data treatment, the Kaiser window function is used, which is defined by $\tau = 2.5$ in the range 3.5 eV to 12 eV. The FT of the k^2 weighted EXAFS spectra were obtained. For these ternary chalcogenide based alloys, ab-initio calculations cannot be performed because of the lack of a reference material. Thus to simulate the EXAFS oscillations, we used theoretical phase and amplitude functions from Mac Cale et al. [9] which introduce a correction term ΔE for the absorption edge.

3. Results

The Fourier transform of the experimental EXAFS signal obtained at the Ge K edge exhibits, for the entire studied samples, the same shape. Basically, as exemplified by Fig. 1, only one oscillation is observed. Fig. 2 shows as an example the experimental and the calculated filtered EXAFS signals obtained on $Ge_{20}S_{64}Bi_{16}$ at the Ge K edge. The comparison of these two curves, show that the experimental data are well fitted by the set of parameters given in Table 1. The same conclusions are obtained if comparisons are performed on the Fourier Transformed k^2 weighted EXAFS spectra. The same procedure performed on $Ge_{26}S_{68}Bi_6$ leads to the same remarks and the set of parameters are also given in Table 1.
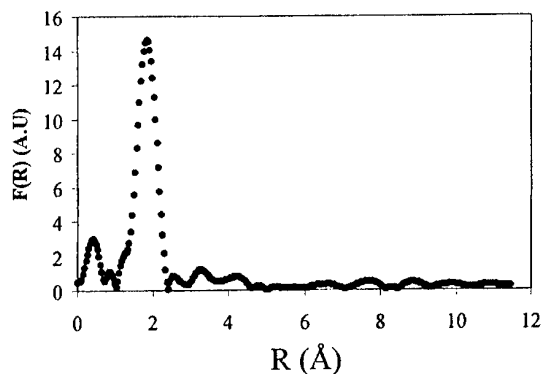
Fig. 1. Experimental Fourier transform of the EXAFS signal obtained at the K edge for $Ge_{20}S_{64}Bi_{16}$.
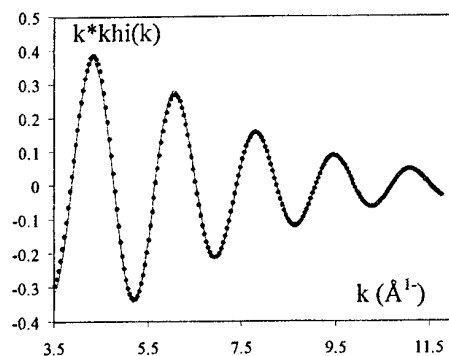
Fig. 2. Experimental (points) and calculated (line) of the filtered EXAFS signal obtained at the Ge K edge for $Ge_{20}S_{64}Bi_{16}$.

Table 1. Results obtained after the fitting procedure given the surrounding of Ge atoms.$\chi 2$ is the quality factor.

Material	N	r	σ	Γ	ΔE	χ^2
$Ge_{20}S_{64}Bi_{16}$	4	2.24	0.066	0.43	10.4	$7x10^{-4}$
$Ge_{26}S_{68}Bi_6$	4	2.24	0.076	0.51	9.8	$5x10^{-4}$

Fig. 3 shows the experimental EXAFS signal obtained at the Bi LIII edge for all the studied samples. From these signals the filtered EXAFS signals corresponding to the first shell are obtained and simulated. The experimental data and the results obtained from the fitting procedures are displayed on Fig. 4. The sets of parameters obtained are given in Table 2. We may notice at this stage of the data presentation, that in any case the parameters used to fit the Bi_2S_3 crystalline structure are able to fit the data corresponding to the ternary glassy alloys.
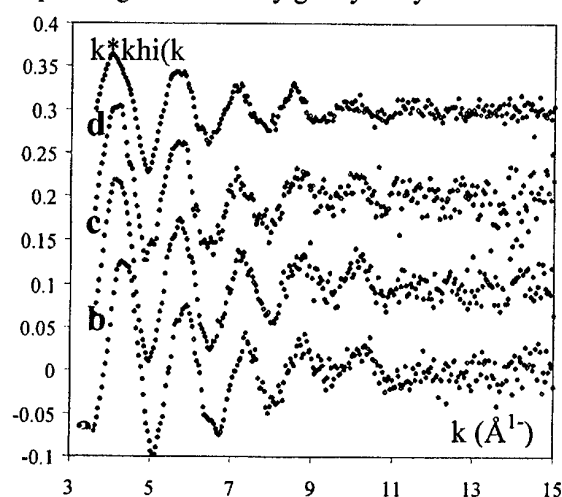
Fig. 3. Experimental EXAFS signal obtained at the Bi LIII edge for glasses a) $Ge_{26}S_{68}Bi_6$, b) $Ge_{26.7}S_{65.3}Bi_8$, c) $Ge_{20}S_{64}Bi_{16}$ and for crystal d) Bi_2S_3.

Fig. 4. Experimental (points) and calculated (line) of the filtered EXAFS signal obtained at the Bi LIII edge for all the studied samples.

Table 2. Results obtained after the fitting procedure given the surrounding of Bi atoms.
Results for $Ge_{20}S_{77}Bi_3$ and $Ge_{20}S_{70}Bi_{10}$ come from ref. 6.

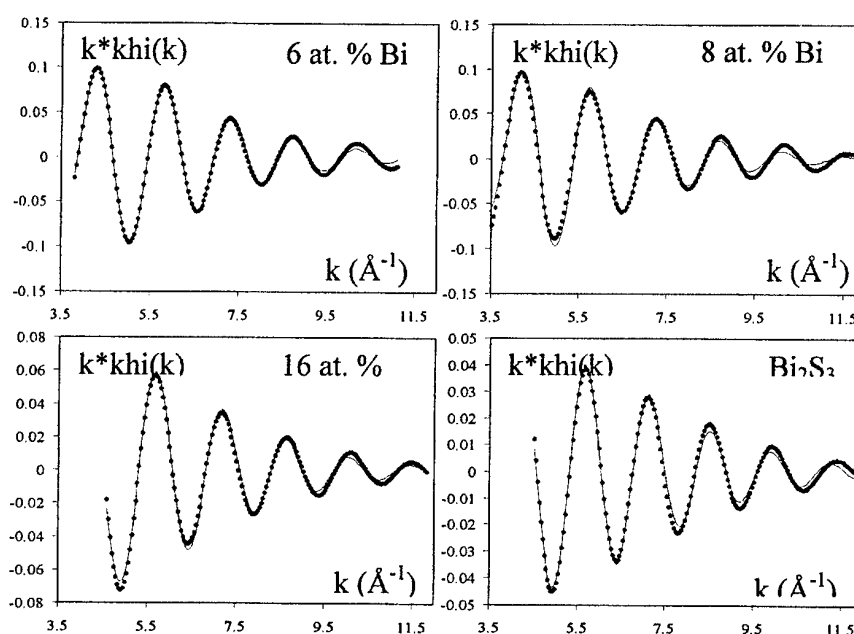| Material	N	r	σ	Γ	ΔE	X^2
Bi_2S_3	3.02	2.65	0.10	1.4	6.25	2.2×10^{-5}
$Ge_{26}S_{68}Bi_6$	3.90	2.59	0.10	0.92	5.1	6.3×10^{-5}
$Ge_{26.7}S_{65.3}Bi_8$	3.85	2.60	0.11	0.87	3.2	2.5×10^{-4}
$Ge_{20}S_{64}Bi_{16}$	4.02	2.60	0.11	1.28	1.97	3.2×10^{-5}
$Ge_{20}S_{77}Bi_3$	3±0.5	2.54	0.06			
$Ge_{20}S_{70}Bi_{10}$	3±0.5	2.56	0.08			

4. Discussion

From data reported in Table 1, we observed that Ge atoms are fourfold coordinated with S atoms located at 2.24 Å. No homopolar Ge-Ge or heteropolar Ge-Bi bonds exist in these glassy ternary alloys. This result is not surprising and is basically found for all the Ge-chalcogenide alloys as GeSe [10,11] and GeTe [12,13], as far as the Ge content remains low enough. Thus as in most cases the local surrounding of Ge atoms in chalcogenide based alloys leads to the formation of GeX_4 tetrahedral units (X being the considered chalcogenide atoms).

From data reported in Table 2, Bi atoms are also found fourfold coordinated with S atoms located at 2.60 Å. this coordination number for Bi atoms is found for both low andr high Bi content. Moreover, the values of the other parameters resulting from the fitting procedure i.e. the Debye-Waller factor, the Γ factor are also found very similarl. In Table 2 the results obtained by Elliot et al. [6] on other compositions are presented. These authors have found that the coordination number of Bi was 3±0.5 with a first coordination shell located at $\approx 2.55 \pm 0.02$ Å for 3 at. % and 10 at. % Bi. Differences occur between these two compositions only on the Debye-Waller factor values, which is twice when composition passes from 3 at. % to 10 at. % Bi. We believe that this discrepancy between these two sets of experimental results could come from two different ways. The first concerns the sample preparation. Indeed, as previously mentioned on other glassy chalcogenide alloys [14-16], small differences in: the values of the upper temperature used for melting operation; the maintenance times at this temperature; the value of the cooling rate (never well known); can lead to important differences in the local order of the resulting glass. Basically, this problem is insoluble. The second concerns the fitting procedure. Indeed, as we have well observed on the GeSeIn system [17,18], different sets of N, r, σ, Γ values can lead to the same apparent good fit of experimental data. This point is rarely mentioned in the literature but is often the source of many problems. To carry out the data fitting procedure, we have performed the following steps:

i)   The number of nearest neighbours N is fixed in such a way that the amplitude of the experimental signal is approximately fitted.

ii)   The radius r of the first coordination shell is also fixed.

iii) ΔE is the first quantity allowed to vary

iv)   r is the second quantity allowed to vary then both ΔE and r vary simultaneously.

v) σ varies, then σ, ΔE and r vary simultaneously.

vi) Γ varies, then Γ, σ, ΔE and r vary simultaneously.

vii)   Finally N is allowed to vary, then all quantity vary simultaneously.

The last step is repeated until the quality factor (χ^2) reaches a constant minimum value. We have to say, that with this fitting procedure, the EXAFS signal cannot be fitted with N = 3 or N = 3.5. On the other hand, as observed by Elliot et al [6], we find that there is no similarity between the EXAFS spectra for Bi doped glasses and the crystalline structure (Bi_2S_3). Thus in agreement with Elliot et al. and at the difference of other ternary chalcogenide systems as GeTeSb [12,13], or GeSeIn [17,18], any significant proportions of microcrystalline regions (clusters or micro clusters) are found. With other words, Bi atoms are well dissolved and from an homogeneous way in the chalcogenide matrix.

5. Conclusion

As a conclusion we may propose the structure presented on Fig. 5 for GeSBi glassy alloys. The latter may be resumed as follow. Ge atoms are covalently bonded to four S atoms forming tetrahedra units. In regards to the studied composition most tetrahedra must be connected together by common S atoms leading to a tetrahedra formed network. Bi atoms are connected to four tetrahedra by making bonds with S atoms. One consequence is that the disorder supposed to be produced by the introduction of Bi atoms does not concern short-range order or medium or long range order but modification of the $GeTe_4$ tetrahedra network.
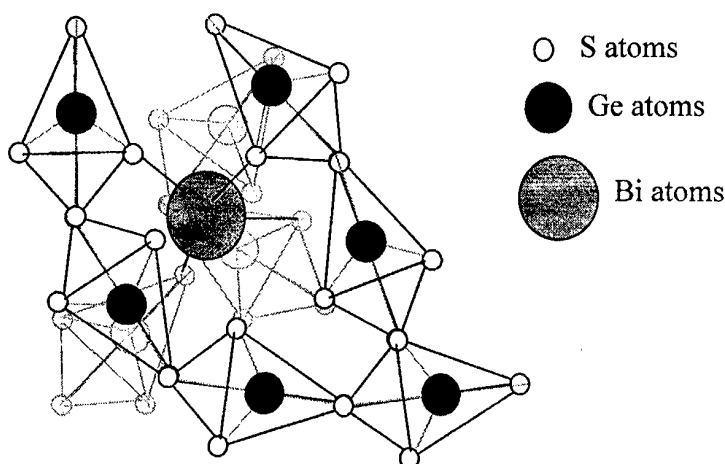
Fig. 5. Structural model proposed for Ge S Bi glassy alloys.

Acknowledgements

References

[1] D. L. Bowman, J. C. Schottmiller, J. Appl. Phys., 39, 1659 (1968).
[2] J. C. Schottmiller, D. L. Bowman, C. Wood, J. Appl. Phys., 39, 1663 (1968).
[3] S. Okano, M. Suzuki, T. Himura, A. Hiraki, Jpn J. Appl. Phys. 24, L445 (1985).
[4] N. Tohge, K. Kanda, T. Minami, Appl. Phys. Lett., 48, 1739 (1986).
[5] C. Vautier, Sol. State Phenomena, 71, 249 (2000).
[6] S. R. Elliot, A. T. Steel, Phys. Rev. Let., 57, 1316 (1986).
[7] A. Mickalowicz, Logiciels pour la chimie, Société Française de Chimie, Paris, P.102, 1991.
[8] B. Lengeler, P. Eisenberger, Phys. Rev. B21, 4507 (1980).

[9] A. G. Mc Kale, B. W. Veal, A. P. Paulikas, S. K. Chan, S. Knapp, J. Am. Chem. Soc., **110**, 3763 (1988).

[10] M. L. Theye, A. Gheorghiu, C. Senemaud, M. F. Kotkata, K. M. Kandil, Phil. Mag., **B69**, 209 (1994).

[11] M. M. Hafiz, F. H. Hammad, N. A. El-Kabany, Physica **B183**, 392, (1993).

[12] J. M.Saiter, Qing Ma, S. Benazeth, M. Belhadji, C. Vautier, Mater. Lett., **19**, 287 (1994).

[13] J. M.Saiter, S. Benazeth, Qing Ma, M. Belhadji, C. Vautier, J. Non-Crystalline Solids, **192-193**, 369 (1995).

[14] J. M. Saiter, J. Ledru, A. Hamou, A. Zumailan, Mater. Lett., **33**, 91 (1997).

[15] J. M. Saiter, K. Chebli, A. Hamou, Physica **B293**, 98, (2000).

[16] K. Chebli, J. M. Saiter, J. Grenet, A. Hamou, G. Saffarini, Physica B, (2001) (in press).

[17] J. M. Saiter, J. Ledru, G. Saffarini, S. Benazeth, Mater. Lett., **28**, 451 (1994).

[18] J. Ledru, J. M. Saiter, G. Saffarini, S. Benazeth, J. Non-Crystalline Solids, **232-234**, 634 (1998).

CORRELATION BETWEEN MECHANICAL PARAMETERS
FOR AMORPHOUS CHALCOGENIDE FILMS

T. N. Shchurova, N. D. Savchenko

Uzhgorod National University, Department of Engineering
13 Kapitulna St., Uzhgorod 88000, Ukraine

Young's modulus, linear thermal expansion coefficient, stress, microhardness, wear resistance, adhesion and cohesion strength for thin films of As_2S_3, As_2Se_3, $Ge_{28}Sb_{12}Se_{60}$, $Ge_{33}As_{12}Se_{55}$ and $Ge_{36}As_4S_{60}$ chalcogenide glasses thermally deposited onto unheated zinc selenide substrates have been determined. The interrelationship between mechanical parameters of the films has been studied. Wear resistance of chalcogenide films has been found to be related to the adhesive force and mechanical parameters used in the formal theory of glass strength. The effect of the additional stress arising in result of the temperature increase under friction on the wear resistance of the films has been shown.

1. Introduction

Thin films deposited from chalcogenide glasses, are applicable in opto- and microelectronics for different purposes: protective, passivating and optical coatings [1], electrical switches [2], heterojunctions [3], data recording, etc. Mechanical strength determination is of great importance for the application of the films. The main mechanical properties of special interest are microhardness, wear resistance, adhesion and shear strength, which are related to the Young's modulus and linear thermal expansion coefficient. Mechanical properties for the films of this type of materials have been studied episodically. The available papers as a rule give information on the one of the named characteristics only and for the certain film material (see, e.g., [4 - 7]).

In this work the combined studies of the mechanical properties for thin chalcogenide films aimed to define the correlation between wear resistance and basic mechanical parameters of the films have been performed. The following glass compositions that are used for IR optical components, design of multilayer film structures for varied applications, and available from different manufacturers [2, 8] have been picked up for the studies: As_2S_3, As_2Se_3, $Ge_{28}Sb_{12}Se_{60}$, $Ge_{33}As_{12}Se_{55}$ and $Ge_{36}As_4S_{60}$.

2. Experimental

Deposition of thin films has been performed by thermal evaporation of the bulk glasses from the effusion cells onto unheated ZnSe [9] and Si (111) substrates in vacuum deposition unit of VUP-5 type (Sumy, Ukraine) at pressure of 10^{-4} Pa and deposition rate of about (6.0 ± 0.1) nm/s. The bulk glass samples were prepared by the melting of As, Se and Ge high-purity components mixture (99.999 %) in evacuated ampoules with the subsequent quenching of the melt. Thickness of thin films under investigation was about 1.5 μm. Microhardness has been measured on the films of at least 4 μm thick. Optical thickness monitoring for thin film during the deposition process has been conducted by the interference technique.

The Young's moduli and linear thermal expansion coefficients have been determined from the results of the measurement of thermal constituent of the stress, arisen under heating in the films

deposited onto the substrates measured $25.0 \times 5.0 \times 0.2$ mm^3 with different linear thermal expansion coefficients (ZnSe and Si).

Stress in thin films has been determined from the measurement of the deflection of free edge of the substrate supported as a cantilever during film deposition or heating of film - substrate system. Substrate deflection and linear thermal expansion coefficient measurements have been conducted by laser dilatometer ($\lambda = 0.63$ μm) with the accuracy of $\pm \lambda/4$ [10].

The linear thermal expansion coefficient values for thin films have been calculated from the equations:

$$\alpha_f = \frac{\alpha_{s1} - \alpha_{s2} A}{1 - A}, \tag{1}$$

$$A = k \frac{E_{s1} \ (1 - v_{s2}) \ \delta_2}{E_{s2} \ (1 - v_{s1}) \ \delta_1}, \tag{2}$$

where k is geometrical factor close to the unit; $\alpha_{s1} = 8.52 \times 10^{-6}$ K^{-1} and $\alpha_{s2} = 2.51 \times 10^{-6}$ K^{-1} for ZnSe and Si, respectively; $E_{s1} = 6.49 \times 10^{10}$ Pa and $E_{s2} = 18.0 \times 10^{10}$ Pa, $v_{s1} = 0.28$ and $v_{s2} = 0.262$ - corresponding Young's modulus and Poisson's ratio values; δ_1 and δ_2 - substrate deflection of the film - substrate system under heating from $T_1 = 303$ K, to $T_2 = 363$ K ($\Delta T = T_2 - T_1 = 60.0 \pm 0.3$) K.

The value of the substrate Young's modulus has been defined from the measurement of the deflection of the loaded substrate edge [11]. Poisson's ratio values were taken from literature [12]. The error of the linear thermal expansion coefficient determination for thin films was not higher than 5 %.

Thin film Young's modulus has been computed from the equation

$$E_f = \frac{E_{s1} d_s^2 \delta_1 (1 - v_f)}{3(1 - v_{s1}) l^2 d_f \Delta T (\alpha_f - \alpha_{s1})}, \tag{3}$$

where $d_s = 2.0 \times 10^{-4}$ m - substrate thickness; $d_f = 1.5 \times 10^{-6}$ m - film thickness; l - the length of the deformed portion of the substrate (the gauge length); v_f - Poisson's ratio of film material.

For the selected film and substrate thicknesses the corrections for the equations (1) - (3), accounting for the film and substrate Young's modulus and thickness ratio have been not higher than 0.5 % (see [13]). Young's modulus determination error was not higher than 7 %.

Microhardness for thin films ($H_{\mu f}$) has been measured on PMT-3 device (Minsk, Belarus) with the accuracy better than 5 % at indentation depth not higher than 2/3 of the film thickness. The microhardness number has been derived from 9 microhardness indentations. The coefficient of variation was not higher than ± 10 %.

Wear resistance measurements have been performed with the help of the device described in [14]. Samples have been rubbed by application of the force of about (2.00 ± 0.01) N to the film via the rubbing tip at a distance of $r_o = 5 \times 10^{-3}$ m from the rotational axis of the sample rotating at an angular speed of 500 RPM. Thin films were rubbed by the batiste cloth moving at a speed of 5.0×10^{-4} m/s. The device provides removal of the wear products from the zone of friction and allows determination of revolutions number of stood by the sample up to the moment when the scratch cuts through the film. To determine the relative wear resistance for the films the experimental data have been rated to the wear resistance for Ge$_{16}$Sb$_{24}$Se$_{60}$ film taken for a unit. Wear resistance has been determined with the accuracy better than 3 %. The coefficient of variation was about ± 7 %.

Adhesion and shear strengths have been determined by the normal pull-off method [15]. Pins have been resin bonded to the films. The sum of the force breaking away the film from the substrate and the shearing force around the pin perimeter has been measured with the help of mechanical-to-electric transducer. Force values have been measured to an accuracy of 0.1 N [8]. The pins of two different radii have been used $r_1 = 2r_2 = 2 \times 10^{-3}$ m. For this case adhesion and shear strengths have been calculated from the equations:

$$\sigma_a = \frac{F_1 - 2F_2}{2\pi r_2^2},$$ (4)

$$\sigma_{sh} = \frac{4F_2 - F_1}{4\pi r_2 d_f},$$ (5)

where F_1 and F_2 - the sum of the breaking and shearing forces for the pins with r_1 and r_2 face radius, respectively. Adhesion and shear strengths have been estimated from the data of 5 measurements for each film, coefficient of variation being not higher than $\pm$ 5 %.

3. Results and discussion

Tables 1 - 3 present the mechanical parameters for thin films and the data from literature for the corresponding chalcogenide glasses. The following correlation between film and bulk glass parameters has been found:

$$E_f = 0.92E_s,$$ (6)

$$\alpha_f = 1.12\alpha_s,$$ (7)

$$H_{\mu f} = 0.29H_{\mu s}.$$ (8)
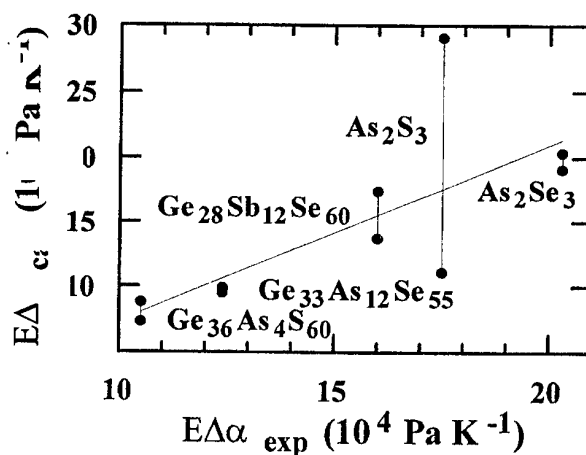
Fig. 1. Theoretical $E\Delta\alpha$ value $(E\Delta\alpha_{calc})$ versus experimental $(E\Delta\alpha_{exp})$. The line corresponds to the proportionality factor equal to the unit.

These relationships between bulk material and film mechanical parameters closely coincide with the ones observed for SiO_2, SiN and Si_3N_4 thin films. The authors of the reference [23] have attributed the decrease in the $E_f/(1 - v_f)$ value for thin films against the bulk material to the packing density that is the ratio between film density ρ_f and density of bulk material ρ_b (ρ_f/ρ_b).

The higher linear thermal expansion coefficient values for the films with respect to bulk materials and their dependence on the substrate material for ZnS, ZnSe, SrF_2 and BaF_2 films ascribed to the structural peculiarities of the films have been observed earlier [24]. Substantially lower thin film microhardness as opposed to that for bulk glass and its dependence on the annealing temperature has been reported for As_2S_3 [25] and SiO_2 films [26].

Table 1. The Young's moduli (E) and linear thermal expansion coefficients (α) for chalcogenide glasses and thin films on their base.

Compound	E, 10^{10} Pa			α, 10^{-6} K^{-1}		
	Bulk glass	References	Film	Bulk glass	References	Film
As_2S_3	1.62	[2]	1.0	22.4	[5]	26.0
	1.38	[13]		23.7	[2]	
	0.8	[5]		26	[6]	
As_2Se_3	1.83	[17]	1.5	19	[13, 5]	22.0
$Ge_{28}Sb_{12}Se_{60}$	2.14	[5]	2.0	15.0	[5, 6]	16.5
	2.07	[13]		15.8	[18]	
	2.18	[17]				
$Ge_{33}As_{12}Se_{55}$	2.07	[13]	1.8	13.3	[6]	15.0
				13	[13]	
$Ge_{36}As_4S_{60}$	2.10	[17]	1.9	12.0	[17]	14.0

Table 2. Poisson's ratio (ν) and microhardness (H_μ) for chalcogenide bulk glasses and thin films.

Compound	ν		H_μ, 10^7 Pa		
	Bulk glass	References	Bulk glass	References	Film
As_2S_3	0.305	[18]	09	[16; 19]	33
			134	[22]	
As_2Se_3	0.289	[20]	140-156	[22]	34
	0.297	[18]	114	[19]	
$Ge_{28}Sb_{12}Se_{60}$	0.265	[20]	150	[19]	45
$Ge_{33}As_{12}Se_{55}$	0.266	[20]	171	[19]	50
$Ge_{36}As_4S_{60}$	0.250	[20]	200	[20]	58

Table 3. Relative wear resistance (ε), initial stress (σ_o), adhesion and shear strengths (σ_a and σ_{sh}) for chalcogenide thin films.

Compound	ε, relative units	σ_o, MPa	σ_a, GPa	σ_{sh}, MPa
ZnSe	6.2	8.2	4.8	29 - 49
As_2S_3	3.1	-1.3	1.8	26
As_2Se_3	3.5	2.1	2.6	30
$Ge_{28}Sb_{12}Se_{60}$	1.0	-4.2	1.5	33
$Ge_{33}As_{12}Se_{55}$	4.5	12.0	4.0	35
$Ge_{36}As_4S_{60}$	4.9	11.4	3.5	39

Information on the Young's modulus and linear thermal expansion coefficient is necessary for computation of thermal stress in thin films. Fig. 1 shows the interrelation between the value of the $E\Delta\alpha$ product determined experimentally for thin films deposited onto ZnSe substrates and calculated from the literature data.

Data from different references on the ZnSe crystal parameters ($E_s = 4.1 \times 10^{10}$ Pa [19] and $E_s = 7.1 \times 10^{10}$ Pa [27]; $\alpha_s = 7.8 \times 10^{-6}$ K^{-1} [28] and $\alpha_{s2} = 8.5 \times 10^{-6}$ K^{-1} [17]) have been used in calculations for comparison. The discordance in ZnSe parameters is related to anisotropy and the difference in crystal perfection. For the glasses, the discrepancies between parameters given in Tables 1 and 2, as a rule, are attributed to the peculiarities in glass preparation technique.

As it is seen from Fig. 1, there is substantial difference between experimental and computed $E\Delta\alpha$ values.
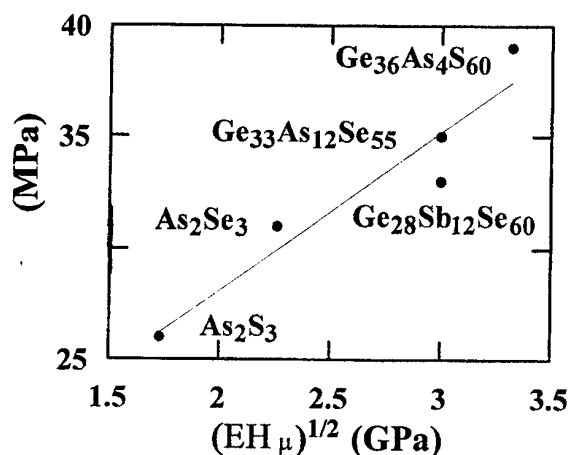

Fig. 2. Shear strength, σ_{sh} (MPa), versus $\sqrt{EH_\mu}$ (GPa) for thin chalcogenide films.

It is known that the adhesive and cohesive forces define mechanical strength of thin film. According to the formal theory of the glass strength [29], the strength of the glass is described by the equation:

$$\sigma_{sh} = C_0 \sqrt{EH_\mu},$$ (9)

where $C_0 = 1.1 \times 10^{-2}$ is a constant, determined from the experiment.

Fig. 2 shows the dependence of the shear strength for thin films on the $\sqrt{EH_\mu}$ value. From this dependence the constant C_0 in eq. (9) for thin films under investigation has been found to be about 7.5×10^{-3}. In view of the found relationships (6) and (8) this constant is equal to 5.8×10^{-3} that is in agreement with experimental results with the accuracy of 23 %.

The dependences of the relative wear resistance for the films on the adhesion strength and $\sqrt{EH_\mu}$ value are given in Fig. 3 and 4, respectively. The highest deviation from the straight line in Fig. 3 has been found to be over ± 45 %.
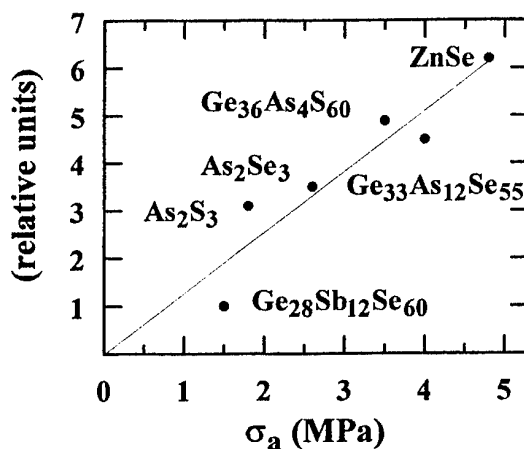
Fig. 3. Relative wear resistance, ε, for chalcogenide films versus adhesion strength, σ_a. The line is drawn by the least-squares technique.

Experimental data shown in Fig. 4 (with the exception of $Ge_{28}Sb_{12}Se_{60}$ films) can be described by the linear dependence with a slope of 1.2×10^{-9} Pa^{-1}. The significant deviation from the linear dependence given in Fig. 4 of the relative wear resistance for $Ge_{28}Sb_{12}Se_{60}$ films can be associated with the thermal stress resulting from thermal spike under the work done by frictional forces.

Fig. 4. Relative wear resistance, ε (relative units), versus $\sqrt{EH_\mu}$ (GPa) for chalcogenide films.

The computations of the contact temperature under rubbing of the films (carried out following the equations of ref. [30]) gave the temperature increase possible in the near-surface region of the sample of about $\Delta T_c = 40 - 60$ K. Fig. 5 shows theoretical dependence of the relative wear resistance on the total stress, that can arise in thin films unde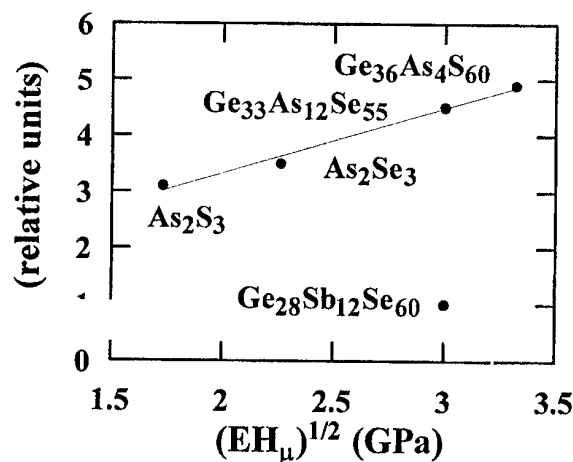r investigation with temperature increase in 60 K. It is seen that in result of the heating the highest compressive stress arises in $Ge_{28}Sb_{12}Se_{60}$ films.

The calculations have revealed that for the above-mentioned conditions of the experiment the wear resistance of the films is additionally affected by an external compressive stress of about 1.0×10^7 Pa grown up in the zone of friction. Thus the origination of the high compressive stress $\sigma_T = E \alpha \Delta T_c$ exceeding the flow limit, reducing the adhesion strength and the wear resistance is characteristic of $Ge_{28}Sb_{12}Se_{60}$ films.

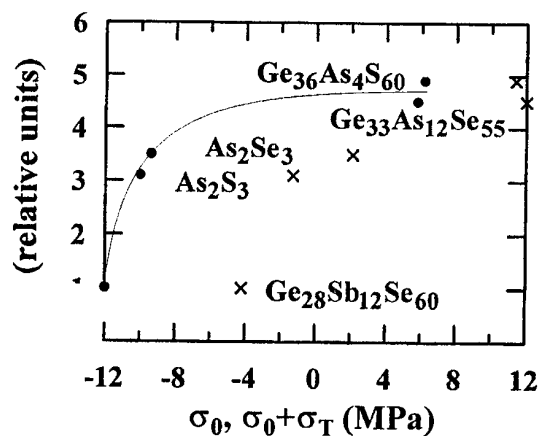Fig. 5. Calculated dependence of the relative wear resistance, ε, for chalcogenide films on the value of the total stress $\sigma_0 + \sigma_T$. Crosses show the initial stress σ_0.

4. Conclusions

The interrelation between mechanical properties of As_2S_3, As_2Se_3, $Ge_{28}Sb_{12}Se_{60}$, $Ge_{33}As_{12}Se_{55}$ and $Ge_{36}As_4S_{60}$ chalcogenide glasses and thin films on their base has been determined. The necessity of the combined studies of the mechanical properties for the prediction of the wear resistance has been shown. The effect of the additional stress originating under friction should be taken into account in the explanation of the deviations from the found relationships between wear resistance and mechanical parameters.

References

[1] S. V. Svechnikov, V. V. Khiminets, N. I. Dovgoshey, Non-crystalline Multinary Non-crystalline Chalcogenides and Their Application in Optoelectronics, Naukova Dumka, Kiev (1992).
[2] A. Madan, M. P. Shaw, The Physics and Application of Amorphous Semiconductors, Academic Press, Inc., Boston (1988).
[3] A. M. Andriesh, Russ. J. Phys. & Techn. Semicond., 32, No. 8, 970 (1998).
[4] N. I. Dovgoshey, V. V. Onopko, I. E. Kacher, A. B. Kondrat. Ukr. J. Vacuum technique and technology, No. 2, 39 (1996).
[5] N. Savchenko, T. Shchurova, M. Trunov, A. Kondrat, V. Onopko, Proc. SPIE, 3182, 319 (1997).
[6] N. D. Savchenko, Proc. SPIE, 3890, 385 (1999).
[7] M. L. Trunov, J. Non-Crystal. Sol., 192&193, 431 (1995).
[8] Optics in Ukraine. Science and Production Guide, Kyiv (1996).
[9] G. G. Deviatykh, V. A. Sidorov, E. M. Gavrishchuk, A. N. Moisejev, High Purity Substances, No. 4, 54 (1992).
[10] M. L. Trunov, A. G. Anchugin, N. D. Savchenko, V. M. Rubish, Proc. SPIE, 2113, 186 (1994).
[11] Handbook of Thin Film Technology, vol. 2, McGraw Hill Hook Company, New York (1970).
[12] W. A. Brantley, J. Appl. Phys., 44, 534 (1973).
[13] A. V. Dobrynin, Sov. J. Techn. Phys. Letters, 23, No. 18, 32 (1997).
[14] A. G. Anchugin, N. D. Savchenko, G. S. Salishchev, M. A. Shakhaida, Yu. Yu. Firtsak, The Method and the Device for Determination of Coating Wear Resistance, Patent USSR No. 1528121, dated 08. 08. 1989.
[15] A. D. Zimon, Adhesion of Thin Films and Coatings, Chemistry, Moscow (1977).
[16] E. M. Voronkova, B. N. Grechushnikov, G. I. Distler, I. P. Petrov, Infrared Optical Materials, Science, Moscow (1965).
[17] T. F. Deutsch, J. Electron. Mater., No. 4, 663(1975).
[18] A. Feltz, Amorphe und Glasartige Anorganische Festkörper, Academie - Verlag, Berlin (1983).
[19] A. R. Hilton, J. of Electron. Mater., 2, No. 2, 211 (1973).
[20] A. R. Hilton, D. V. Hayes, J. of Non-Crystal. Solids, 17, 339 (1975).
[21] J. A. Savage, J. of Non-Crystal. Solids, 17, No. 2, 101 (1975).
[22] Z. U. Borisova, Semiconductor Chalcogenide Glasses, Leningrad University Publ., Leningrad (1983).
[23] A. K. Sinha, H. J. Levinstein, T. E. Smith, J. Appl. Phys., 49, No. 4, 2423 (1978).
[24] E. A. Nesmelov, A. G. Gusev, O. N. Ivanov, R. M. Validov, Sov. J. Opt. & Mechan. Industry, No. 9, 50 (1986).
[25] I. P. Manika, Ya. A. Teteris, in "The Topical Problems for Micro Indentation Physics", Shtiintsa, Kishinev, 168 (1989).
[26] A. Ya. Kuznetsov, E. V. Solovjeva, Sov.J. Opt. & Mechan. Industry, No. 9, 32 (1983).
[27] Monocrystals. Optics and Scintillators, Merck, Dormstadt (1987).
[28] A. A. Blistanov, V. S. Bondarenko, V. V. Chkalova et al., Acoustic Crystals, Science, Moscow (1982).
[29] A. V. Ivanov, The Strength of Optical Materials, Machine Building Publ., Leningrad (1989).
[30] Yu. N. Drozdov, V. G. Pavlov, V. N. Puchkov, Friction and Wear under Extreme Conditions, Machine Building Publ., Moscow (1986).

RESEARCH OF A MICROPLASMA BREAKDOWN IN THIN FILMS OF GLASSY SEMICONDUCTORS

A. R. Fairushin

Moscow Power Engineering Institute, Semiconductor Electronics Chair, Moscow, Russia

Experiments were carried out to detect presence of a microplasma in thin films of glassy chalcogenide semiconductors. Films of As_2Se_3 and As_2SeTe_2 were investigated. In the regime of a "soft" breakdown time series of current and voltage of the samples based on As_2Se_3 were measured and then processed by spectral analysis. Films of As_2SeTe_2 were used for experiment with long discharge space. This experiment resulted in observation of oscillating streamer discharge. A model was suggested to explain the phenomenon.

1. Introduction

Investigation of electronic processes occurring at high electrical fields in thin films of vitreous semiconductors is of great interest both for theory of carrier multiplication in amorphous semiconductors [1], and for practical application of this material for pulse generation of acoustic and optical radiation [2]. At high current concentration density of free charge carriers become so large that electron subsystem have to be considered as a plasma media or, speaking other words, a microplasma, because these regions are localized in solid state. The main feature of a microplasma by analogy with gaseous plasma is collective behavior of involved charge carriers. This effect results in the presence of nonlinear processes in microplasma media. Such processes can have the resonant or oscillatory nature depending on different conditions.

In the given work the results of experimental investigation of an electrical instability arising in a mode of "soft" and irreversible breakdown of thin films of vitreous semiconductors are presented. Films of As_2Se_3 and As_2SeTe_2 were under study. Experimental procedure with the samples based on As_2Se_3 included dynamic measurement of I-V (current-voltage characteristics) and pulse measurements of sample's current and voltage series for constant voltage of the generator. Films of As_2SeTe_2 were used for registration of the spatial distribution of the energy, developing in the sample at an irreversible streamer breakdown.

2. Experimental

Samples with films of As_2Se_3 presented sandwich-like structure Au–Vitreous semiconductor–In_2O_3–Glass substrate. One contact to the amorphous film was In_2O_3 layer, and the other one was pinch gold contact with an area of $2.5 \cdot 10^5$ μm^2. The thickness of films for different samples was made varying from 0.2 to 1 μm. Samples with As_2SeTe_2 film had rather different structure and thickness of the chalcogenide film. The structure consisted of a glass substrate with chalcogenide film deposited upon it and planar metallic electrode strips with the distance between them 0.2 mm deposited on the surface of the semiconductor film. The thickness of the chalcogenide films was 1 – 5 μm. All the chalcogenide films were produced by vacuum evaporation.

Investigation of samples based on As_2Se_3 was conducted as follows. At first, single saw teeth-like pulse of voltage was applied to the sample during 5 ms. Measurement of current and voltage of the sample started simultaneously with the beginning of the pulse. After the I-V characteristic is defined, several square voltage impulses of different amplitude with high duration were applied to the sample. The pulse must be long enough to measure sufficient amount of current and voltage data for statistical processing. Amplitude of the pulses covered all voltage range of the earlier measured I-V characteristic. The length of the measured time series was 5000 values. One should mention that in this case the voltage applied not exceeded breakdown threshold. The aim was to measure time series near the breakdown threshold, which was defined by strong noise on the I-V characteristic. Time se-

ries were subjected to spectral analysis. Above-mentioned experiment was carried out in such conditions, when amorphous material was not subjected to irreversible changes. Other extreme case was the experiment on observation of a streamer breakdown in lengthy interelectrode gap. For this experiment a samples based on As_2SeTe_2 were used. At the beginning of the experiment the pulse of voltage, with leading edge less than duration of all characteristic processes in structure, was applied to the structure. The duration of the pulse must be large for the completion of the streamer process [3]. The track pattern was influenced by parameters of electric impulse: amplitude, the rate of voltage increasing, impulse duration and resistance of the generator.

3. Results and discussion

Processing of series for the several As_2Se_3 samples showed that there was special threshold on the I-V characteristic at the forward bias (when potential on the In_2O_3 electrode was positive). If the amplitude of the square pulse was greater than threshold then spectral analysis showed low frequency chaotic oscillations for voltage series. Presented in this work results concerned the film of As_2Se_3 with thickness of 0.3 μm. I-V characteristic for the sample is shown on Fig. 1. Investigation had shown that the threshold of oscillations approximately equaled to 1 V while the irreversible breakdown began approximately at 1.5 V. The curves of spectral analysis for the current and voltage series before oscillation threshold looked like curves shown on Fig. 2 for voltage 0.8V at the forward bias. Fig.3. shows curves of spectral analysis for forward voltage 1.1V. All the curves for reverse bias had shape of white noise with a rise at low frequencies.
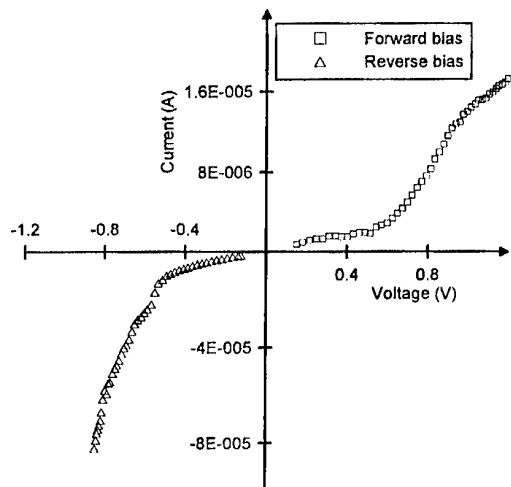
Fig. 1. The I-V characteristic for As_2Se_3 s ample, measured before studying time series.
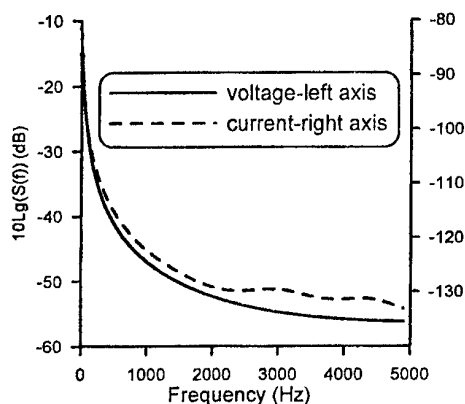
Fig. 2. Curves of spectral analysis for time series of current and voltage at the mean forward voltage of 0.8V.

Figures with results of spectral analysis show distribution of spectral density S(f) for the time series of current and voltage, expressed in decibels. Dependence of the spectral density on frequency is defined by the expression:

$$S(f_k) = \frac{\Delta}{n} \left| \sum_{i=1}^{n} x_i \cdot \exp(-2\pi i f_k t) \right|^2 \qquad (1)$$

Where n is length of the series, $k=0,1,2...n/2$, f_k are the discrete Fourier frequencies, x_i – time series of current or voltage.

Fig. 3. Curves of spectral analysis for time series of current and voltage at the mean forward voltage of 1.1V.

Fig. 4. Traces left in the material by pulsating head of a streamer.

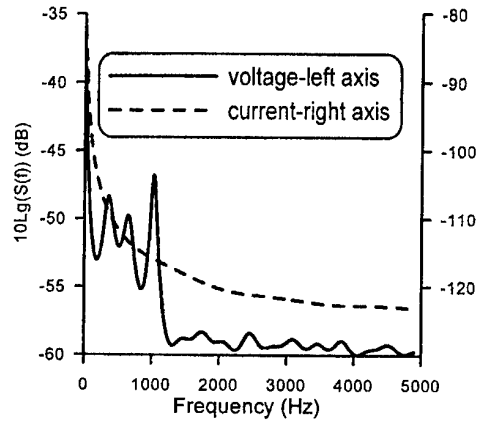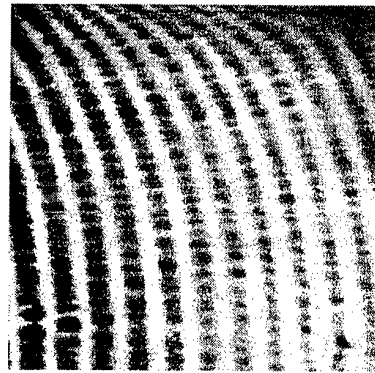Presence of close several peaks on spectral curves (Fig. 3) points to at least three periodic processes in volume of the structure. These oscillations are supposed to be due to microplasma generation and damping. The generation of a microplasma region leads to a local rising of carriers. As the pulse generator in that case acted as current source so changes in carriers had resulted in detected potential oscillations.

Results obtained with As_2SeTe_2 samples enabled us to recognize microplasma generation by traces in the chalcogenide film. The energy dissipation during impulse breakdown was registered visually by the view of the melted material track. To demonstrate reproducibility of that mode, the breakdown was executed by sequence of similar pulses, so Fig. 4 shows a number of parallel channels.

In order to explain this effect we proposed that two concurrent processes take place in the streamer head: the electron-hole generation and the heating, which reduces generation.

Streamer breakdown is rather complicated process and has some consequence steps. We considered the some main stages. During delay time τ_d the forming of the cathode streamer head takes place, after that the wave of plasma generation spreads from cathode to anode and forms a current channel. As a result of this process the potential jump and the high field region occurs near anode. At the next stage double injection of hot carries into depletion region takes place from the anode and the channel. The level of injection is so high, that impact Auger recombination becomes dominated. The current through channel enlarges at several orders. The head of anode streamer generates plasma and moves toward the cathode. The recombination process in the anode streamer head is accompanied by phonon generation [2] and the hot spot becomes powerful source of phonon stream modulated by periodic oscillation

This process is similar to leader breakdown of gases. This stage of breakdown used to call spark breakdown because the temperature of the leader head is so high that it emits light.

In the discussion of possible nature of oscillations we exclude the initial and final stages of anode blazing up and cathode blazing down. We consider only the period, when the leader head (hot spot) moves to cathode with a constant velocity. In that case it is possible to use stationary approximation, because the average energy dissipated by the hot spot is equal to the energy of supply. The equation of the charge balance is standard:

$$\frac{dQ}{dt} = G - U - div(J),$$

(2)

Q – charge of carriers, G – generation part, U – recombination part, J – current density.

In order to calculate the concentration of carriers in the head we assume that the volume of the head is constant. After integration and differentiation we shall get:

$$\frac{d^2N}{dt^2} = \frac{dG}{dt} - \frac{dU}{dt}$$

(3)

Where N - concentration of electrons in the head of the leader. As we can see the balance of generation and recombination rates determines the change of carriers. If we take into consideration heating and temperature dependence of Auger recombination we can write non-linear system:

$$y_1' = y_2$$
$$y_2' = -ay_1^2 - by_1 + c$$

(4)

Where y_1 - normalized concentration, y_2 - rate of concentration variation, constants "a", "b" and "c" are determined by material properties. The numeric decisions of equation were determined under different conditions. The phase diagram for one of variants is at the Fig. 5. It shows the possibility of existence not only divergent but also periodic solutions in accordance with different initial conditions. We marked (A, B, C) three different possible cases, demarcated by phase lines, which from our point of view are similar to some of our experimental results.
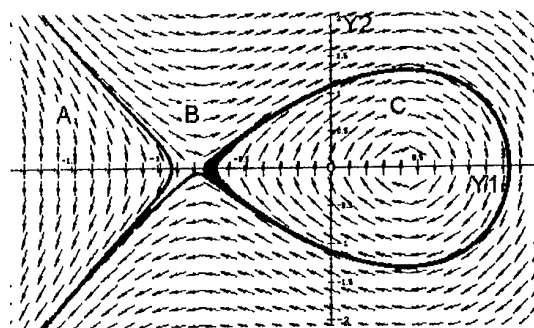

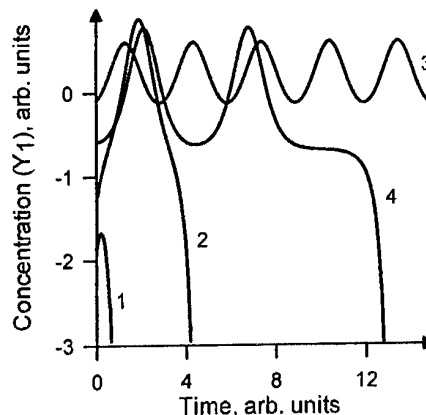Fig. 5. The phase diagram of numeric solutions.

Fig. 6. The solutions, which demonstrate the existence of not only divergent (1,2,4), but periodic (3) solutions.

The four different solutions, which are corresponded to the marks on phase diagram, are represented at Fig. 6.

Solution "1" corresponds to region A (Fig.), solution "2" to B, solution "3" to C and solution "4" to the border between B and C. Cases "1" and "2" could be correlated with well-known solid trace of melted material during spark breakdown. Solution "4" could explain breakdown channel with two (or other discrete number) hot spots. The most interesting case is "3", which, from our point of view, causes tracks of fig.4. The picture demonstrates that the periodic oscillatory breakdown is rather reproducible. But we must pay attention that the range of initial conditions that produces periodic oscillations is rather narrow, as possible to notice at Fig. 5.

4. Conclusion

The performed investigation confirms the existence of electrical instabilities at high electric fields. In our case, the study of time series of current and voltage revealed low frequency chaotic oscillations, which can be explained by generation and damping of several microplasma regions.

Another experiment on observation an irreversible spark breakdown in long discharge gaps demonstrated that, depending on initial conditions, breakdown in chalcogenides has an oscillating character, which must be accompanied by powerful periodically modulated stream of phonons. According to the suggested model this never known before effect is explained by competition between processes of carrier's generation and recombination, resulting in periodical generation of a microplasma in streamer's head.

Acknowledgement

References

[1] V. I. Arkhipov, S. O. Kasap, J. of Non-Cryst. Solids, 266-269, 959 (2000).
[2] E. N. Voronkov, Semiconductors, 33, #8, 906 (1999).
[3] E. N. Voronkov, Bulletin of the V. Tarasov Center of Chemotronics of Glass №1, Moscow, Medeleev University of Chemical Technology of Russia, 2000, p.116.

NEW CHALCOGENIDE GLASSES IN THE GeSe$_2$ -As$_2$Se$_3$-CdTe SYSTEM

S. V. Boycheva, V. S. Vassilev, P. Petkov[a]

University of Chemical Technology and Metallurgy, Department of Semiconductors, 8
Kl.Ohridski blvd., 1756 Sofia, Bulgaria
[a]University of Chemical Technology and Metallurgy, Department of Physics
8 Kl.Ohridski blvd., 1756 Sofia, Bulgaria

Glass-forming region in the GeSe$_2$-As$_2$Se$_3$-CdTe system has been determined by visual, X-ray diffraction and electron microscope analyses. Glasses have been obtained in the GeSe$_2$-rich region. Glass-formation has been situated wholly on the GeSe$_2$- As$_2$Se$_3$ and partially on the GeSe$_2$-CdTe and As$_2$Se$_3$-CdTe (0 - 15 Mol. % CdTe) sides in the Gibbs diagram. The maximal dissolution of CdTe in the glasses has been found up to 20 Mol. % CdTe. The temperatures of glass transition (T$_g$), crystallization (T$_{cr}$) and melting (T$_m$) of the glasses have been examined in the temperature range 20÷950 °C. Two exothermic effects have been registered at 440 and 565 °C, which are connected with GeSe$_2$ and CdTe crystallization, respectively. The endothermic effect observed at 680±20 °C is related to the previous crystallized GeSe$_2$ phase. A small deviation from the melting temperature of GeSe$_2$ (T$_m$=740 °C) is probably due to a solid solution formation on the base of GeSe$_2$+As$_2$Se$_3$. According to the rule $\Delta t=T_c-T_m>100$ °C the glasses have been obtained stable. The density and microhardness of the glassy samples have been measured to be in the range 4.36÷4.58 g/cm^3 and 85-125 kgf/mm^2, respectively. It has been calculated some characteristics of synthesized glasses as follows: module of elasticity (E), minimal micro-voids volume (V$_h$) and micro-voids formation energy (E$_h$). The relations properties-average coordination number (Z) were clarified in terms of glassy network structure.

1. Introduction

Recently, multicomponent chalcogenide glasses are widely applicable in the field of semiconductor technics. The great interest of these materials is due to their simply obtaining technology in bulk forms and thin films; chemical and radiation durability; their transparency and photosensitivity in IR and VIS spectral regions, as well as the possibility of wide varying of properties with the composition. That determine the possibilities for their application - for optical covers and optical fibers preparation, photoresists, optical recording media, threshold and memory-switching devices and so on. Multicomponent chalcogenide glassy materials have recently been used successfully in ion-selective potentiometry as functional membranes in ionselective electrodes for determination of heavy metal ions [1]. Chalcogenide glassy membranes are more stable and durable in corrosion media in respect to crystalline ones [2]. In this connection chalcogenide glasses are often used as membrane materials in ionselective electrodes for determination of Ag(I)-, Pb(II)-, Fe(III)- and Cu(II)-ions [2÷5].

The investigation of new glassy materials on the basis of Ge-chalcogenides and/or As with MeCh (Me=Zn, Cd, Ni, Sn, Tl, Cr and so on; Ch=S, Se, Te) provokes the scientific interest for new membranes materials production.

The aim of the present work is to synthesize multicomponent chlacogenide glasses in the system GeSe$_2$-As$_2$Se$_3$-CdTe and to investigate their physico-chemical properties. The idea of CdTe addition in glassy matrix is to increase the ionic conductivity [6]. It is expected the new synthesized glasses to be a suitable material for Cd^{2+}-ionselective electrodes.

2. Experimental

The glass-forming region was determined by the help of 24 synthesized compositions. The starting materials were Ge, As, Se with 5N purity and CdTe (Coating quality, BALZERS 99.999%). The starting compounds $GeSe_2$ and As_2Se_3, as well as the samples from the investigated system were prepared by direct monotemperature synthesis at 850-1000 °C depending on the CdTe content. The melts were kept for about 2 hours at the highest temperature of the synthesis and vibrational stirring was applied, and after that the melts were quenched in a ice-water mixture.

The glassy state of the obtained samples were checked by a visual, X-ray diffraction (diffractometer TUR – M 61 with CuK_{α} radiation and a Ni filter) and electron-microscope (Philips) analyses. The density of the samples (d) was measured by a hydrostatic method using toluene as immersion fluid and the microhardness (HV) was measured by Vickers' method. A thermograph (DTA) was used to record the thermal characteristics of the samples.

3. Results

The synthesized bulk samples from the $GeSe_2$ -As_2Se_3-CdTe system are dark colored with a strong lustre. The results from the X-ray diffraction show that several compositions (group A) are typical glasses without peaks on the diffractograms – these compositions form the glass-forming region. Some other compositions (group B) show diffraction peaks with small intensity (compositions on the region's boundary). The diffractograms of the samples from group C show strong peaks, these samples are crystalline and outside the glass-forming region.

The electron microscopic observation shows a smooth and homogeneous surface of the samples form group A. Small crystalline regions are shown on the surface of the samples from group B while the samples placed outside of the glass-forming region (group C) are completely crystallized. Thermal characteristics of the samples - temperatures of glass transition (T_g), crystallization (T_{cr}) and melting (T_m) were determined by DTA-analysis and the results are summarized in Table 1. The obtained values for density and microhardness are given in Table 1.

Table 1. Thermal and physical properties of the $(GeSe_2)_x(As_2Se_3)_y(CdTe)_z$ glassy samples, where x+y+z=100.

Composition			m	T_g, °C	T_{cr}, °C	T_m, °C	d, g/cm^3	HV, kgf/mm^2
x	y	z						
90	0	10	0.0	155	445	680	4.40	125
81	9	10	0.1	140	445,565	685	4.44	120
63	27	10	0.3	125	445,565	685	4.49	115
45	45	10	0.5	120	440,565	675	4.50	104
27	63	10	0.7	120	440,565	670	4.56	96
9	81	10	0.9	120	440	665	4.60	89
0	90	10	1.0	130	440	660	4.62	85

4. Discussions

4.1. Glass-forming region

The glass-forming region was determined on the basis of the results from the visual, X-ray diffraction and electron microscopic analyses of the samples from ternary $(GeSe_2)_x$ $(As_2Se_3)_y(CdTe)_z$ system, where x+y+z = 100 and m = y/(x+y) - Fig. 1. The region is situated in the $GeSe_2$ –rich region and lies wholly on the $GeSe_2$- As_2Se_3 side partially on the $GeSe_2$-CdTe and As_2Se_3-CdTe sides from 0 to 17 Mol.% CdTe. The glasses dissolves up to 20 Mol.% CdTe - Fig. 1.
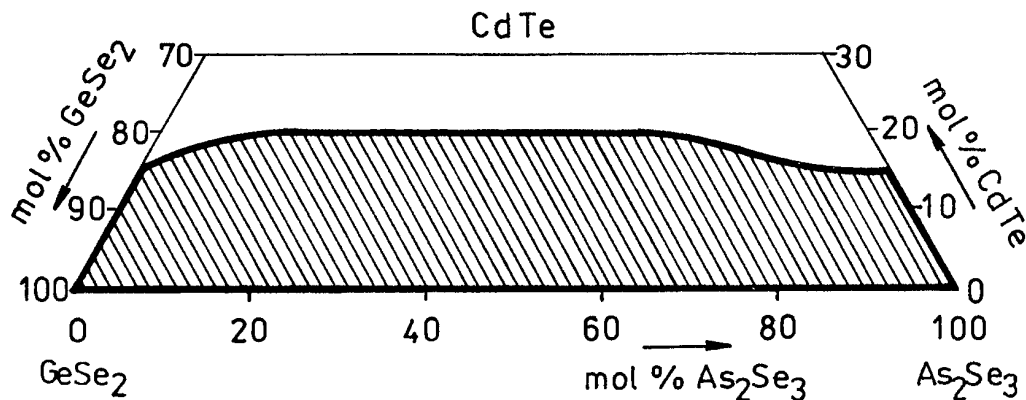
Fig. 1. The glass-forming region in the GeSe$_2$-As$_2$Se$_3$-CdTe system.

4.2. Thermal characteristics

Three different effects are observed in the thermograms of the glasses: the first endothermic effect is connected to the glass transition temperature (T_g), next exothermic effect is related to the crystallization temperature (T_{cr}) (part of samples show two consecutive exothermic peaks), and last endothermic effect correspondent with melting of the crystallized phases (solid solutions). Glass transition temperatures, T_g, of the glasses decreases with increasing of m (z = const). The obtained T_g values are in the range 120÷150 °C. The influence of the composition variation on the crystallization temperature is negligible, it is evidence that identical phases are crystallized at the all compositions. The quantity of the glassformers GeSe$_2$ and As$_2$Se$_3$ have no influence on T_{cr}. It is observed one or two crystallized phases under glassy samples heating. The first crystalline phase was observed at (440±5)°C and the second at (565±5)°C, respectively. We supposed that the low temperature crystallized phase belongs to GeSe$_2$ and high temperature crystallized phase corresponds to CdTe, taking into account that the melting point of starting compositions are as follows: $T_m^{GeSe_2}$ =740 °C, $T_m^{As_2Se_3}$ =360 °C and T_m^{CdTe} =1095 °C.

The melting effects are probably connected to the melting of the crystallized solid solutions of GeSe$_2$. Melting temperatures are independent on the composition of the samples.

4.3. Density and microhardness

The density values of the samples are in the range 4.40 - 4.62 g/cm^3. The results are given in Table 1. The values increase with As$_2$Se$_3$ content when z = const. These results are expected because the density of As$_2$Se$_3$ is bigger compared to these of GeSe$_2$ (d_{GeSe_2} = 4.34 g/cm^3 [7], $d_{As_2Se_3}$ = 4.8 g/cm^3 [8], d_{CdTe} = 5.86 g/cm^3[9]). The density values increase with CdTe content at a constant value of m since the density of CdTe is bigger in respect to the density values of GeSe$_2$ and As$_2$Se$_3$.

The values obtained from microhardness (HV) measurements are in the ranges 85÷125 kgf/mm^2 and depend on the glassy compositions – Table 1. An increase of the microhardness is observed in cases when As$_2$Se$_3$ content increases (m decreases and z is constant), as well as when CdTe content decreases (z –decreases and m is constant). This relation is determined by the higher microhardness of GeSe$_2$ and As$_2$Se$_3$, respectively compared to the microhardness of cadmium telluride (HV_{GeSe_2} = $HV_{As_2Se_3}$ =150 kgf/mm^2 [7,10] and HV_{CdTe} = 60 kgf/mm^2 [7]).

4.4. Thermo-mechanical characteristics

According to the free-volume theory Sanditov [11] proposed a follow equation for microhardness of glasses:

$$HV = \frac{E_h}{V_h},\tag{1}$$

where E_h is the energy of micro-void creation in a volume V_h. According to Bartenev [12] and Nemilov [13] the microhardness is related to the module of elasticity (E) and a Poison's coefficient, μ, by the relation:

$$HV = \frac{1-2\mu}{6(1+\mu)} E \tag{2}$$

On the other hand [11]:

$$\Delta\alpha.T_g = 3(1-2\mu).\frac{HV}{E}, \tag{3}$$

where $\Delta\alpha = \alpha_f - \alpha_g$ is the variation of the coefficient of thermal expansion at T_g and

$$\Delta\alpha.T_g \cong 0,1 \tag{4}$$

The equation (4) is given by Simh-Boyer and it is valid for the glasses possessing equal values of Poison's coefficients. Combining the equations (2) and (3) we can write the relation:

$$\Delta\alpha.T_g = \frac{(1-2\mu)^2}{2(1+\mu)} \tag{5}$$

According to Bartenev and co-authors [15]:

$$\Delta\alpha.T_g = f_g \ln\left(\frac{1}{f_g}\right). \tag{6}$$

Thus at $T=T_g$ the partition of fluctuational free volume, f_g, depends also on the Poison's coefficient $fg=f(\mu)$.

$$HV = \left(\frac{gk}{V_h}\right)T_g, \tag{7}$$

where k is the Boltzmann's constant and $g=\ln\left(\frac{1}{f_g}\right)$. It is logical to expect existing the correlation

between HV and T_g values for the glasses from one and the same type which possess $V_h \cong const$ and $g(f_g) \cong const$.

Integration of the equations (1) and (7) gives the relation of T_g, as well as HV, towards f_g and E_h:

$$T_g = \left(\frac{1}{gk}\right)E_h, \tag{8}$$

From the equations' systems (4) and (5), and (4) and (6) we can determine $\mu=0.25$ and $f_g \cong 0.028$ ($g \cong 3.58$). In order to determine V_h, E_h E the relations (7), (8) and (2) we can be written as:

$$V_h = 3.58\, k\, \frac{T_g}{HV}; \quad E_h = 3.58\, k\, T_g; \quad E = 15\, HV, \tag{9}$$

Table 2 presents the calculated values of V_h, E_h, E as a function of the glassy composition (m) and average coordination number ($Z=x_i z_i$, x_i, z_i - are the molar part and coordination number of ith component of the glass).

Table 2. Thermo-mechanical characteristics of glasses from $(GeSe_2)_x(As_2Se_3)_y(CdTe)_z$ system.

Composition			m	Z	T_g, °C	HV, kgf/mm²	V_h, Å³	E_h, kJ/mol	E, 10³ kgf/mm²
x	y	z							
90	0	10	0.0	2.60	155	125	17.26	13.15	1.88
81	9	10	0.1	2.58	140	120	17.35	9.65	1.80
63	27	10	0.3	2.53	125	115	17.44	8.60	1.73
45	45	10	0.5	2.48	120	104	19.05	8.45	1.56
27	63	10	0.7	2.43	120	96	20.63	8.45	1.44
9	81	10	0.9	2.38	120	89	22.26	8.45	1.34
0	90	10	1.0	2.36	130	85	23.89	8.75	1.28

The graphical presentation of $V_h(Z)$, $E_h(Z)$ and E(Z) shows a kink at Z = 2.53 which corresponds to a composition $(GeSe_2)_{63}(As_2Se_3)_{27}(CdTe)_{10}$ (more gradual changes in V_h and E are observed when Z>2.53 while E_h increases significantly) – Fig. 2.
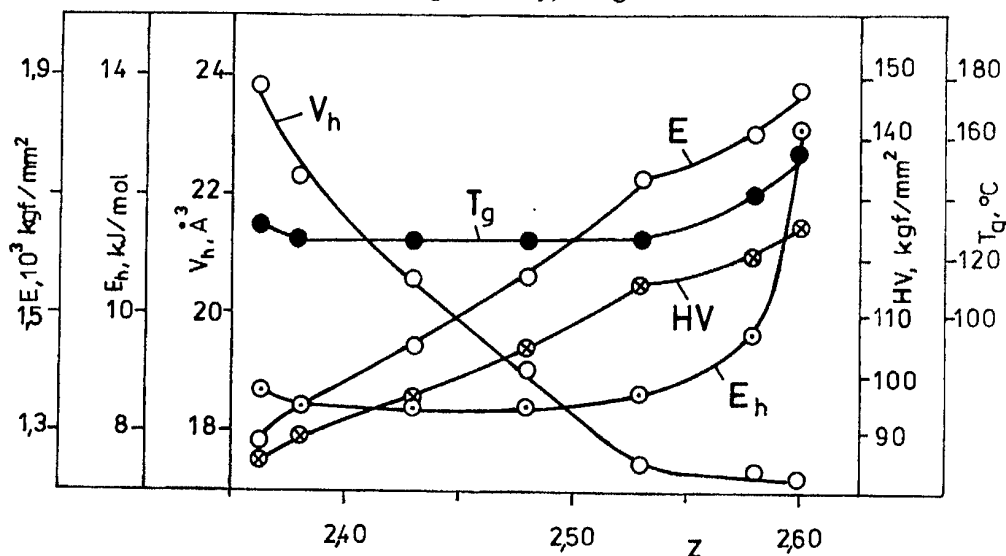
Fig. 2. Dependencies of V_h, E_h and E on Z of glasses.

The trend of the V_h curve could be explained by the cross-linking process of the glassy structure and saturation in the glassy network with bonds of tethraedrical $GeSe_{4/2}$ units. The further increase in $GeSe_2$ content is not related to a variation in the minimal sizes of micro-voids. The structure corresponds to an optimal energy of interatomic forces and system equilibrium. The deviation from these conditions is connected with a structure resistance and increase of energy values necessary for free volumes densification. In this reason the negligible decreasing in V_h at Z>2.53 corresponds to a quite increasing in values of necessary energy for micro-voids formation - Fig. 2. The values of elastic module presented in Fig. 2 show dependence similar to those of microhardness which is predictable result from eq. 9.

4. Conclusions

New chalcogenide glasses from the systems $GeSe_2$-As_2Se_3-Sb_2Se_3-CdTe are synthesized. The basic physico–chemical characteristics of the glasses are investigated – density, microhardness and temperatures of transformation, crystallization and melting. A compositional dependence of these properties is shown. A correlation between glassy structure and thermo-mechanical properties is proposed based on the structure deviations at Z=2.53. The relation is connected with saturation of the glassy network.

References

[1] H. Hirata, K. Higashiyama, Talanta 19, 391 (1972).

[2] Y.G. Vlasov, E.A. Bychkov, Ion-Selective Electrode Rev., 9, 5 (1987).

[3] Y.G. Vlasov, Fresenius' Z. Anal. Chem., 335, 92 (1989).

[4] C.E. Koenig, E.W. Grabner, Electroanalysis, 7, No 11, 1090 (1995).

[5] E. Pungor, Anal. Sci., 14, 249 (1998).

[6] Y. G. Vlasov, E.A. Bychkov, A.M. Medvedev, Anal. Chem. Acta, 185, 137 (1986).

[7] Z. U. Borisova, Chalcogenide Semiconducting Glasses, Leningrad: Leningrad University Press, 1983 (in Russian).

[8] S. A. Dembovski, A. A. Vaipolin, Solid State Phys. 6, 1388 (1964) (in Russian).

[9] P. H. Hamilton, Semicond. Prod. and Sol., State Technol., 7, No 6, 15 (1964).

[10] A. A. Ivanko, Microhardness, Book of Russ. Acad. Sci., "Naukova dumka" K. 1968 (in Russian).

[11] D. S. Sanditov, "Novelties in the field of investigations of microhardness", 236, "Nauka", M., 1974 (in Russian).

[12] G. M. Bartenev, "Superstrength and higherstrength inorganic glasses", "Stroiizdat", M., 1974.

[13] S. V. Nemilov, "Glassy State", 126, "Nauka", L. (1971).

[14] R.Simha, R. Boyer, J.Chem. Phys., 37, 1003 (1962).

[15] G. M. Bartenev, D. S. Sanditov, I. V. Razumovskaia, I. A. Lukianov, Ukr. Phys. J., 14, 152 (1969).

X-RAY EXCITED LUMINESCENCE AND X-RAY IRRADIATION EFFECT ON CdS$_{1-x}$Se$_x$ NANOCRYSTALS OPTICAL ABSORPTION

A. V. Gomonnai, A. M. Solomon, Yu. M. Azhniuk, M. Kranjčec[a,b],
V. V. Lopushansky, I. G. Megela

Institute of Electron Physics, Ukr. Nat. Acad. Sci, Universytetska St. 21, Uzhhorod, 88000, Ukraine
[a]Ruđer Bošković Institute, Zagreb, P.O.Box 1016, 10000 Zagreb, Croatia
[b]University of Zagreb, Geotechnical Faculty Varaždin, Hallerova aleja 7, 42000 Varaždin, Croatia

X-ray excited luminescence and X-ray irradiation (10–3240 Gy) effect on the optical absorption spectra of CdS$_{1-x}$Se$_x$ nanocrystals in borosilicate matrix are studied. The parameters of the luminescence bands are analyzed with the account of the luminescence of the host matrix itself. The observed smearing of quantum-size-related maxima and absorption edge blue shift with the irradiation dose increase are related to the X-ray ionization of the nanocrystals with charge-carrier transfer between the nanocrystals and the host matrix. The radiation-induced changes completely vanish at post-irradiation annealing to 575 K.

1. Introduction

CdS$_{1-x}$Se$_x$ nanocrystals (quantum dots) embedded in glass matrices are extensively studied in the recent years by optical techniques, providing important information on the nanocrystal parameters. Optical absorption, Raman scattering and photoluminescence (PL) enable one to derive the nanocrystal composition, size and energy parameters, complementing the methods of electron microscopic studies, small-angle X-ray scattering and Auger spectroscopy [1–5]. PL spectra are known to be essentially dependent on the excitation energy and power [1, 6–8], hence it seems interesting to investigate X-ray excited luminescence (XL) as well. The luminescent properties of the glass matrix itself should be also taken into account at the analysis of the observed spectra of the glass-embedded nanocrystals.

Only a few studies devoted to the variation of quantum dot parameters under irradiation with X-rays [9, 10] and high-energy electrons [11] are reported. It should be noted that X-ray irradiation effects have been discussed only for CdS quantum dots in the interband absorption range, no detailed dose dependences being shown, especially for the spectral range where specific quantum-size effects in the absorption spectra are revealed.

Here we report the results of XL spectroscopic studies as well as the influence of X-ray irradiation upon the optical absorption spectra of CdS$_{1-x}$Se$_x$ nanocrystals embedded in borosilicate glass matrix.

2. Experimental

CdS$_{1-x}$Se$_x$ quantum dots were embedded in a matrix of SiO$_2$–B$_2$O$_3$–ZnO–K$_2$O–Na$_2$O glass by conventional solid-state precipitation technique generally similar to those described in [3, 12, 13]. About 5×5 mm^2 plates with the thickness down to 0.13 mm were prepared for optical measurements.

X-ray irradiation and X-ray luminescence excitation was provided by a molybdenum anti-cathode tube (40 kV, 20 mA) with the irradiation dose rate of 0.15 Gy/s what enabled us to achieve the irradiation dose D up to 3240 Gy, its value was determined by LiF thermoluminescent gauges.

The interval between the irradiation and the beginning of the measurement procedure was 1 h. Optical absorption measurements were performed at room temperature on a LOMO MDR-23 monochromator with FEU-100 and FEU-62 phototubes in the range 300–800 nm.

3. Results and discussion

XL spectra of $CdS_{1-x}Se_x$ nanocrystals in the glass matrix are shown in Fig. 1. The XL of the borosilicate glass matrix itself, measured separately, is presented by the dashed curve. The band, centered at 470 nm (2.64 eV) is related to intrinsic and radiation-induced centres in glass. Note that a similar luminescence band is observed in glassy SiO_2 under X-ray excitation [14] and in alkali borosilicate glasses under N_2-laser excitation [15]. Having subtracted the host matrix contribution from the experimentally measured spectra of the glass-embedded nanocrystals, we obtained the spectra, shown by solid curves, whose simulation by elementary Gaussian contours (dotted curves) provided the energy position and halfwidth values of $CdS_{1-x}Se_x$ nanocrystal XL bands. Thus, in the XL spectra the bands centered at 2.04 and 2.36 eV with the halfwidths 0.35 and 0.54 eV, respectively (for $CdS_{0.4}Se_{0.6}$), and at 1.92 and 2.21 eV with the halfwidths 0.30 and 0.38 eV, respectively (for $CdS_{0.22}Se_{0.78}$), have been detected.

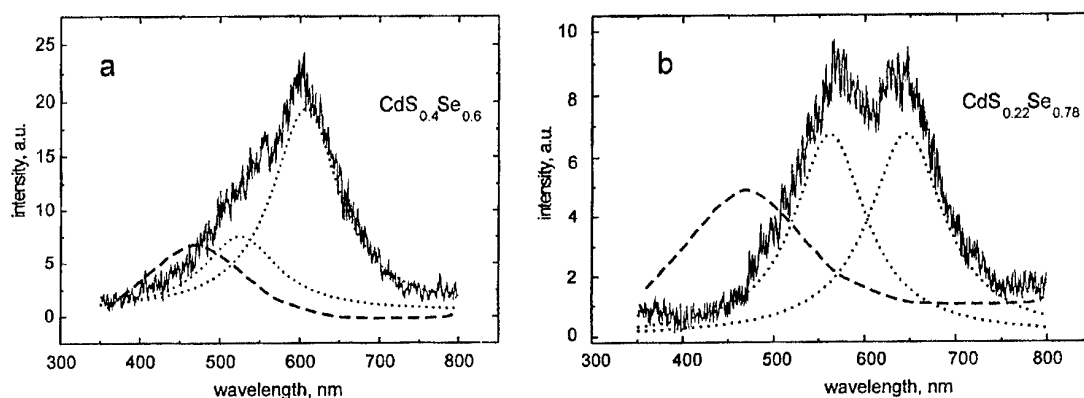Fig. 1. X-ray excited luminescence spectra of $CdS_{0.4}Se_{0.6}$ (a) and $CdS_{0.22}Se_{0.78}$ (b) nanocrystals embedded in alkali zinc borosilicate glass matrix: dashed curves – XL of the host matrix itself; solid curves – the experimentally measured spectra of the samples after subtraction of the matrix luminescence; dotted curves – simulation of the nanocrystals spectra by Gaussian contours.

It should be noted that the composition of $CdS_{1-x}Se_x$ nanocrystals in the glass matrix was determined from the measured Raman scattering spectra (room temperature, 488.0-nm laser excitation, LOMO DFS-24 double grating monochromator). Since $CdS_{1-x}Se_x$ mixed crystals are characterized by the two-mode type of phonon spectrum compositional transformation, having compared the observed CdS-related (285 and 275 cm^{-1}) and CdSe-related (200 and 208 cm^{-1}) LO phonon frequencies with the known results for $CdS_{1-x}Se_x$ nanocrystals in a broad compositional range [16–18], we obtained for the samples under investigation the values of x=0.6 and 0.78, respectively.

The effect of X-ray irradiation on the optical absorption spectra of $CdS_{1-x}Se_x$ nanocrystals in borosilicate glass matrix is shown in Fig. 2. The additional singularities revealed in the non-irradiated samples spectra (solid curves in Fig. 2, a, b) are known to arise due to charge-carrier confinement in case the semiconductor nanocrystal characteristic size not exceeding the exciton Bohr radius [1]. This has enabled us to derive, based on [5], from the experimentally observed spectra the average radius r = 2.76 nm and 3.08 nm for $CdS_{0.4}Se_{0.6}$ and $CdS_{0.22}Se_{0.78}$ nanocrystals, respectively.

In $CdS_{0.4}Se_{0.6}$ nanocrystals the confinement-related absorption maxima are observed at X-ray irradiation with the dose D up to 135 Gy (Fig. 2, a). With the further increase of the irradiation dose they smear and vanish. At $D \geq 540$ Gy the absorption edge is smooth and gradually shifts towards higher energies with the irradiation dose increase (See Fig. 2, a).
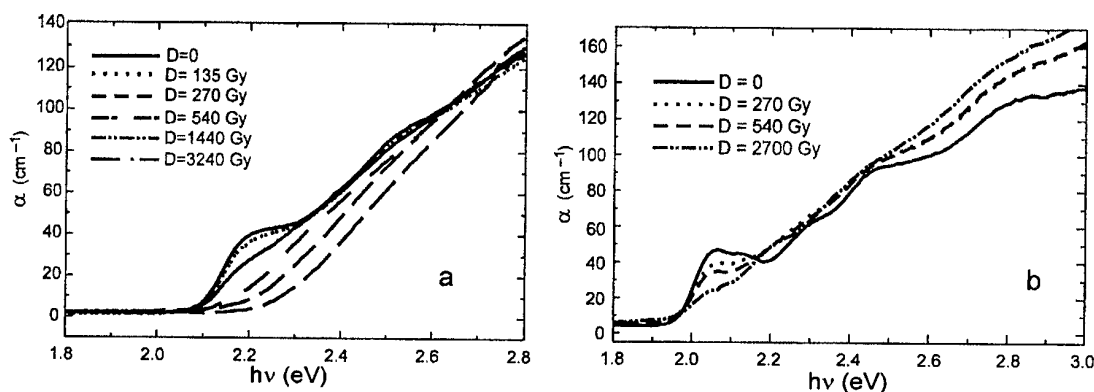
Fig. 2. X-ray irradiation effect on the optical absorption spectra of CdS$_{0.4}$Se$_{0.6}$ (a) and CdS$_{0.22}$Se$_{0.78}$ (b) nanocrystals embedded in alkali zinc borosilicate glass matrix.

As seen from Fig. 2, b, in CdS$_{0.22}$Se$_{0.78}$ nanocrystals the X-ray irradiation effect is also revealed in the quantum-size absorption maxima smearing. However, this applies mostly for the first (lowest-energy) and second maxima, though these two features do not vanish completely even at the highest achieved irradiation dose values (2700 Gy). Besides, the second maximum, whose energy position (2.28 eV) remains unchanged at D≤270 Gy, smears almost completely with the further increase of the irradiation dose, and at D≥1080 Gy arises again at 2.20 eV. The energy of the first quantum-size maximum also shifts downward, though much less. Meanwhile, the higher-order features in the absorption spectrum remain unchanged even at 2700 Gy. The dependence of the energy positions of the quantum-size maxima on the X-ray irradiation dose is illustrated by Fig. 3.
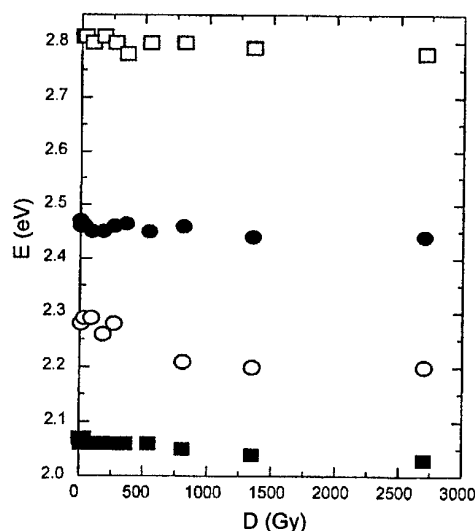

Fig. 3. Dependence of the energy positions of the confinement - related maxima in the optical absorption spectra of CdS$_{0.22}$Se$_{0.78}$ nanocrystals on the X-ray irradiation dose.
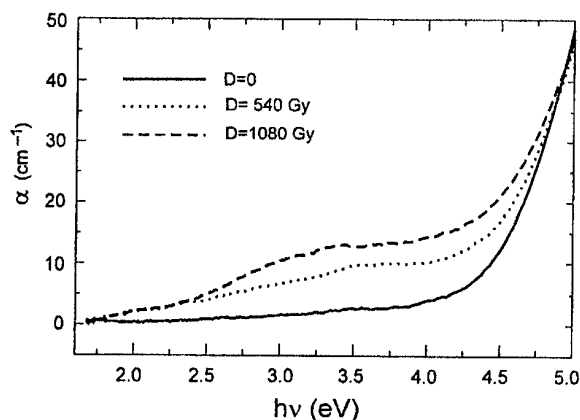
Fig. 4. X-ray irradiation effect on the optical absorption spectra of alkali zinc borosilicate glass matrix.

The effect of X-ray irradiation on the absorption spectra of alkali zinc borosilicate glass matrix itself is shown in Fig. 4. The broad irradiation-induced absorption increment can be simulated by a superimposement of three Gaussian contours centered at 1.75, 3.04 and 4.29 eV. Such bands are known to appear in silicate glasses under UV, X-ray, γ- and electron irradiation and are attributed to colour centres in glass [19–21].

It should be noted that in X-ray irradiated CdS$_{1-x}$Se$_x$ quantum dots in the borosilicate glass matrix the irradiation-induced blue shift of the absorption edge whas observed to decrease slightly after storage at room temperature. In particular, as seen from Fig. 5, for the most heavily irradiated

(3240 Gy) $CdS_{0.4}Se_{0.6}$ sample the absorption edge position shifts by 0.045 eV after six-day (150 h) storage, the major part of this value arising from the first 24 h. Note that further storage during 1000 h results in no changes in the absorption spectrum. Such effect can be attributed to the post-irradiational relaxation which is generally typical for dielectric glass matices [22].
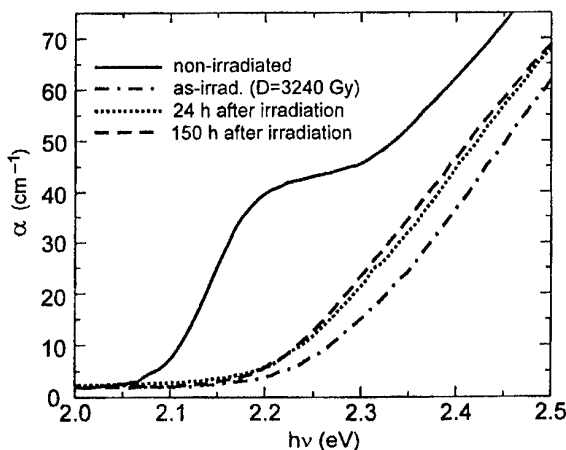

Fig. 5. Post-irradiation storage effect on the optical absorption spectrum of 3240-Gy X-ray irradiated $CdS_{0.4}Se_{0.6}$ nanocrystals embedded in alkali zinc borosilicate glass matrix.
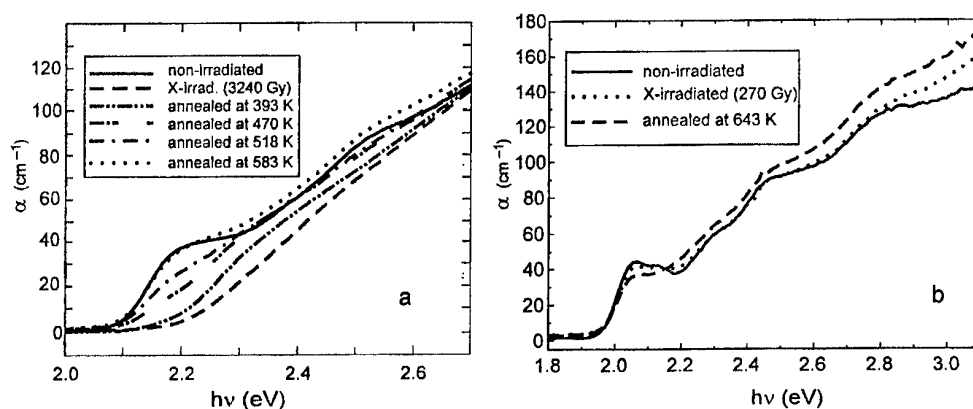

Fig. 6. Isochronal (20 min) annealing effect on the optical absorption spectra of $CdS_{0.4}Se_{0.6}$ (a) and $CdS_{0.22}Se_{0.78}$ (b) nanocrystals after X-ray irradiation with 3240 Gy (a) and 270 Gy (b).

The samples of $CdS_{0.22}Se_{0.78}$ and $CdS_{0.4}Se_{0.6}$ nanocrystals, irradiated with 270 and 3240 Gy, respectively, were chosen for isochronal (20 min) annealing studies, performed after durable storage of the irradiated samples. The initial absorption spectra of $CdS_{1-x}Se_x$ quantum dots were observed to recover gradually in the temperature range 375–575 K. For $CdS_{0.4}Se_{0.6}$ the increase of the annealing temperature T_a first leads to the reverse, red shift of the absorption edge, and at $T_a > 500$ K the quantum-size-related features gradually begin to reveal. After annealing to 575 K the initial spectrum shape is restored (See Fig. 6, a), though for $CdS_{0.22}Se_{0.78}$ nanocrystals the structure of the lowest-energy confinemen-related features is not restored completely even at $T_a = 643$ K (Fig. 6). Note that the irradiation-induced absorption increment in the glass matrix itself is also annealed within the range of 375–575 K.

Generally, several factors can be responsible for the observed behaviour of $CdS_{1-x}Se_x$ nano-crystals absorption spectra under X-ray irradiation and annealing. The gradual smearing of the size-quantum features, observed for both samples, can be attributed to the X-ray induced ionization of the quantum dots due to electron (hole) transfer between the nanocrystals and irradiation-activated electron (hole) traps in the host matrix. With the increase of the irradiation dose the transferred charge-carriers occupy the confinement-related levels in the nanocrystals, gradually disabling the lower-energy transitions. Therefore, in $CdS_{0.22}Se_{0.78}$ quantum dots the irradiation-induced changes affect

only the lower-energy features. In the case of $CdS_{0.4}Se_{0.6}$ nanocrystals the discussed effect results in the observed blue shift of the absorption edge.

Note that a similar effect (the blue shift of the absorption edge) was observed in CdS nano-crystals under X-ray irradiation [9] and CdSe quantum dots under intense light irradiation [23], though the transformation of the quantum-size-related maxima is not reported in any of the quoted references. In both cases the blue shift is explained by photoionization of the quantum dots, the pho-toelectrons leaving the microcrystals and being captured by the traps in the glass [9, 23]. However, one should note that, as follows from the results of photoluminescence and ESR studies of X-ray ir-radiated CdS quantum dots in borosilicate glass, the X-ray induced defects in the quantum dots differ from the photoinduced defects [10].

However, there are at least two more possible explanations for the absorption edge blue shift in the irradiated $CdS_{1-x}Se_x$ nanocrystals. At normal conditions, $CdS_{1-x}Se_x$ quantum dots in borosilicate glass matrix already sustain hydrostatic pressure from the matrix which is caused by the difference in the values of thermal expansion coefficients for the matrix and $CdS_{1-x}Se_x$ [5, 6]. X-ray irradiation can result in the additional hydrostatic pressure upon the nanocrystals due to the known phenomenon of radiation swelling of the glass matrix [24]. However, since the pressure-induced energy gap shift dE_g/dp values for $CdS_{0.22}Se_{0.78}$ and $CdS_{0.4}Se_{0.6}$ nanocrystals embedded in the borosilicate glass are rather close, as follows from our measurements [25], and no blue shift is observed in X-ray irradiated $CdS_{0.22}Se_{0.78}$ samples, one may conclude that the role of additional hydrostatic pressure in this case is negligible.

It should be also noted that, since the host borosilicate matrix in our case contains a consider-able (13 mass %) amount of ZnO, the blue shift of the absorption edge can also be related to the in-corporation of zinc into the quantum dots where it can substitute Cd, forming quaternary $Cd_{1-y}Zn_yS_{1-x}Se_x$ mixed nanocrystals. Such possibilities are reported to occur at thermal annealing of $CdS_{1-x}Se_x$ quantum dots in Zn-containing silicate glass matrix [3, 26, 27]. However, the completely reversible character of the absorption spectrum variation observed at the post-irradiation annealing excludes the possibility of X-ray induced Zn diffusion from the glass to $CdS_{1-x}Se_x$ quantum dots. Note that the isochronal annealing temperature in our case (below 600 K) is much lower than the temperatures at which zinc diffusion into the nanocrystals is reported ($T_a > 850$ K [26, 27]).

4. Conclusions

XL spectra of $CdS_{1-x}Se_x$ nanocrystals embedded in a borosilicate matrix were measured, the XL band parameters being analyzed with the account of the luminescence of the host matrix itself.

X-ray irradiation is shown to result in the smearing of the quantum-size-related maxima in the absorption spectra of $CdS_{1-x}Se_x$ quantum dots and subsequent absorption edge blue shift. The ini-tial spectrum of the samples is completely restored at annealing in the temperature range 375–575 K. The observed transformation of the quantum-size-related features in the optical absorption spectra of $CdS_{1-x}Se_x$ quantum dots under X-ray irradiation can be attributed to the ionization of the nanocrystals with charge-carrier transfer between the quantum dots and the electron (hole) traps in the host matrix.

References

[1] A.I. Ekimov, A. A. Onushchenko, JETP Lett.. **40**, 1136 (1984).
[2] A. I. Ekimov, I. A. Kudryavtsev, M. G. Ivanov, Al.L.Efros, Fiz. Tverd. Tela (russ.), **31**, No 8, 192 (1989).
[3] H. Yükselici, P. D. Persans, T. M. Hayes, Phys. Rev., **B52**, 11763 (1995).
[4] S. V.Gaponenko, Fiz. Tekhn. Polupr. (russ.), **30**, 577 (1996).
[5] N. R. Kulish, V. P. Kunets, M. P. Lisitsa, Fizika Tverdogo Tela (russ.), **39**, 1865 (1997).

[6] P. D. Persans, L. B. Lurio, J. Pant, H. Yükselici, G. Lian, T. M. Hayes, J. Appl. Phys., **87**, 3850 (2000).

[7] G. Mei, J. Phys: Condens. Matt., **4**, 7521 (1992).

[8] M. Ya. Valakh, N. R. Kulish, V. P. Kunets, M. P. Lisitsa, G. Yu. Rudko, Ukr. J. Phys. (russ.), **38**, 1667 (1993).

[9] V. Ya. Grabovskis, Ya. Ya. Dzenis, A. I. Ekimov, A. I. Kudryavtsev, M. N. Tolstoi, U. O. Rogulis, Sov. Phys. Solid State, **31**, 272 (1989).

[10] T. Miyoshi, H. Furukawa, K. Nitta, H. Okuni, N. Matsuo, Sol. St. Commun., **104**, 451 (1997).

[11] A. V. Gomonnai, Yu. M. Azhniuk, D. B. Goyer, I. G. Megela, Ukr. J. Phys. (ukr.), **45**, 1225 (2000).

[12] N. F. Borelli, D. Hall, H. Holland, D. Smith, J. Appl. Phys., **61**, 5399 (1987).

[13] B. G. Potter, J. H. Simmons, Phys. Rev., **B37**, 10838 (1988).

[14] L. Skuja, J. Non-Cryst. Sol., **149**, 77 (1992).

[15] A. O. Volchek, A. O. Gusarov, A. P. Zhevlakov, D. O. Leshchenko, Opt. i Spektroskopiya (russ.), **80**, 439 (1996).

[16] A. Tu, P. D. Persans, Appl.Phys.Lett., **58**, 1506 (1991).

[17] A. Roy, A. K. Sood, Phys. Rev., **B53**, 12127 (1996).

[18] A. Ingale, K. C. Rustagi, Phys. Rev., **B58**, 7197 (1998).

[19] D. L. Griscom, J. Ceram. Soc. Jap., **99**, 923 (1991).

[20] V. I. Arbusov, Fiz. Khim. Stekla (russ.), **22**, 228 (1996).

[21] A. V. Gomonnai, Yu. M. Azhniuk, D. B. Goyer, I. G. Megela, V. V. Lopushansky, J. Optoelectr. Adv. Mater., **3**, 37 (2001).

[22] A. I. Gusarov, A. V. Dmitryuk, A. N. Kononov, V. A. Mashkov, JETP (russ.), **97**, 525 (1990).

[23] A. I. Ekimov, A. L. Efros, Phys. Stat. Sol., (b) **150**, 627 (1988).

[24] L. B. Glebov, V. G. Dokuchayev, N. V. Nikonorov, G. T. Petrovskii, Fiz. Khim. Stekla (russ.), **12**, 345 (1986).

[25] V. S. Shusta, A. V. Gomonnai, A. G. Slivka, O. I. Gerzanich, Yu. M. Azhniuk, V. V. Lopushansky (to be published in this issue).

[26] M. Rajalakshmi, T. Sakuntala, A. K. Arora, J. Phys.: Condens. Matter, **9**, 9745 (1997).

[27] P. D. Persans, L. B. Lurio, J. Pant, G. D. Lian, T. M. Hayes, Phys. Rev., **B63**, 115320 (2000).

VARIATION OF $CdS_{1-x}Se_x$ NANOCRYSTAL PARAMETERS UNDER HYDROSTATIC PRESSURE

V. S. Shusta, A. V. Gomonnai[a], A. G. Slivka, O. I. Gerzanich,
Yu. M. Azhniuk[a], V. V. Lopushansky[a]

Uzhhorod National University, Pidhirna St. 46, Uzhhorod, 88000, Ukraine
[a]Institute of Electron Physics, Ukr. Nat. Acad. Sci.,
Universytetska St. 21, Uzhhorod, 88000, Ukraine

The effect of hydrostatic pressure on the optical absorption spectra of $CdS_{1-x}Se_x$ nanocrystals embedded in borosilicate glass matrix is studied. The energy gap pressure coefficients and compressibility values for $CdS_{0.4}Se_{0.6}$ (average size 2.76 nm) and $CdS_{0.22}Se_{0.78}$ (3.08 nm) samples are obtained. The effect of the glass matrix pressure upon the nanocrystals is discussed.

1. Introduction

$CdS_{1-x}Se_x$ nanocrystals (quantum dots) are of extensive scientific interest in view of wide possible applications as well as due to quantum-size effects arising from the spatial confinement of charge carriers [1–4]. A special attention is paid to the hydrostatic pressure effect on the optical properties of the nanocrystals, whose investigations enable the nanocrystal parameter behaviour versus pressure to be traced. Such studies were carried out for CdSe [5–10] and CdS [8, 11–14] quantum dots, both capped [5–11] and embedded in borosilicate [8, 12] and germania [13, 14] glass matrices. The performed experiments enabled not only the values of pressure variation coefficients for energy parameters to be determined, but also the phase transitions in nanocrystals from hexagonal to cubic phase to be reached, the transition pressure values being estimated from the Raman measurements [5–9, 11–14]. Much less investigated are pressure effects for mixed $CdS_{1-x}Se_x$ nanocrystals [8, 11, 15].

Here we report the influence of hydrostatic pressure on $CdS_{1-x}Se_x$ nanocrystals embedded in borosilicate glass matrix studied by optical absorption spectroscopy.

2. Experimental

$CdS_{1-x}Se_x$ quantum dots were embedded in a matrix of SiO_2–B_2O_3–ZnO–K_2O–Na_2O glass by conventional solid-state precipitation technique generally similar to that described in [4]. About 5×5 mm^2 plates with the thickness down to 0.13 mm were prepared for optical measurements.

The spectra were measured in a three-window optical pressure cell, benzene being used as a pressure medium. The pressure was varied in the range from 0 to 0.4 GPa in increasing and decreasing mode. A LOMO MDR-2 monochromator with a FEU-106 phototube was used.

Low-temperature absorption measurements at normal pressure were carried out on a LOMO MDR-23 monochromator with a UTREX cryostat.

3. Results and discussion

The optical absorption spectra of $CdS_{1-x}Se_x$ nanocrystals in the glass matrix at different hydrostatic pressure and temperature values are shown in Figs. 1, 2. The composition of the nanocrystals was determined from the Raman measurements of the LO phonon frequencies, corresponding to

the CdS- and CdSe-sublattices of the two-mode solid solutions [16], by comparing them with the known Raman results for $CdS_{1-x}Se_x$ nanocrystals in a broad compositional range [17–19]. The features in the absorption spectra, related to the quantum-size effects (charge-carrier confinement) (See Fig. 2), enabled us to determine, according to [20], the mean radius of the nanocrystals as 2.76 nm (x=0.6) and 3.08 nm (x=0.78).
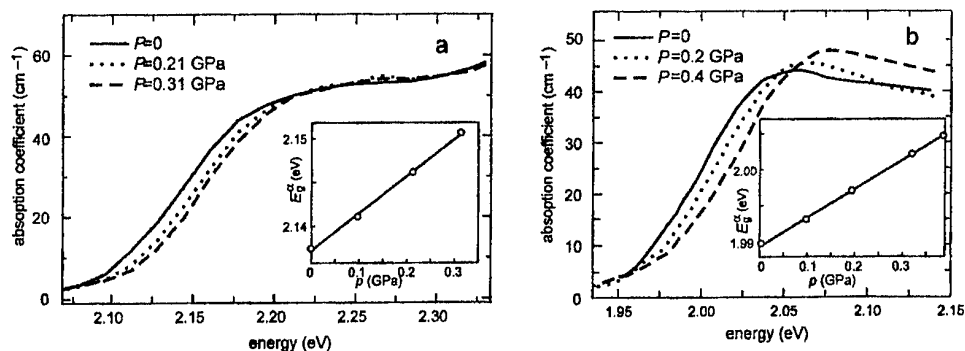

Fig. 1. Hydrostatic pressure effect on the optical absorption spectra of $CdS_{0.4}Se_{0.6}$ (a) and $CdS_{0.22}Se_{0.78}$ (b) nanocrystals in borosilicate glass matrix. The inserts show the dependences of the energy gap E_g^{α} on the pressure value.

It should be noted that while scaling in Figs. 1, 2 the absolute values of absorption coefficient α, we mean the absorbance of the samples (borosilicate glass with the quantum dots embedded), not of the quantum dots themselves. The actual absorbance of the microcrystals should be much higher, since the effective thickness of the quantum dots themselves is considerably smaller than the sample thickness, taking into account the concentration of $CdS_{1-x}Se_x$ in the samples which follows from the content of the relevant components in the initial mixture (about 1 %). Hence, the actual absorption coefficient of the nanocrystals is by about two orders of magnitude higher than that of the composite, displayed at the vertical axes.
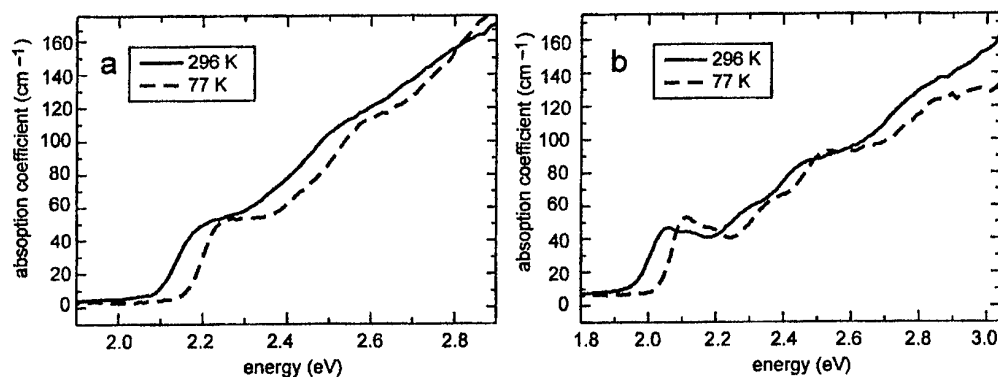
Fig. 2. Optical absorption spectra of $CdS_{0.4}Se_{0.6}$ (a) and $CdS_{0.22}Se_{0.78}$ (b) nanocrystals in borosilicate glass matrix at 77 and 296 K.

One more point that should be taken into account, concerns the determination of the band gap value E_g in the nanocrystals. Generally it is calculated from the experimental spectra by extrapolation of the $\alpha^2(h\nu)$ plot for allowed direct optical transitions. However, especially in disordered materials, when the density-of-states tails may smear the shape of the absorption edge, while studying the edge variation under different factors often a substitutive parameter E_g^{α} is introduced, being determined as the energy position of the fixed absorbance value α_f [21, 22]. Usually for bulk materials α_f is taken of the order of 10^2–10^3 cm^{-1}. In our case, due to the above discussed difference in the absorbance of the samples and the actual absorbance of the nanocrystals, we have chosen for defining E_g^{α} the value $\alpha_f = 25$ cm^{-1}, what corresponds to the middle of the edge part of the spectra.

The increase of pressure is observed to result in a blue shift of the optical absorption edge of the nanocrystals. This is illustrated by Fig. 1 where only the edge part of the spectra is shown. In the investigated pressure range the absorption edge shift is linear (as seen from the insert in Fig. 1) and equals to 0.041 eV/GPa for CdS$_{0.4}$Se$_{0.6}$ and 0.039 eV/GPa for CdS$_{0.22}$Se$_{0.78}$ samples. These results are consistent with the band gap pressure coefficients dE_g/dp for CdS$_{1-x}$Se$_x$ nanocrystals measured by other authors [5, 8, 10, 14] which vary from 0.027 to 0.061 eV/GPa, depending on the nanocrystal size, composition and host media. It should be noted that dE_g/dp values for the bulk crystals also fall into this interval, ranging from 0.033 [23] to 0.058 [24] eV/GPa for CdS and from 0.037–0.040 [23, 24] to 0.058 [25] eV/GPa for CdSe.

The measurements were performed at increasing and decreasing pressure, no hysteresis being observed in the investigated pressure range. This indicates that CdS$_{1-x}$Se$_x$ nanocrystals are in direct contact with the glass matrix. It should be noted that at normal conditions CdS$_{1-x}$Se$_x$ quantum dots in borosilicate glass already sustain hydrostatic pressure from the host matrix caused by the specific features of their preparation [26, 27]. While being cooled from the synthesis temperature to the room temperature the quantum dots are compressed by the matrix since the value of thermal expansion co-efficient for the latter ($A_g=1.02\times10^{-5}$ K^{-1}) considerably exceeds those for II–VI semiconductors. Then the hydrostatic pressure of the glass matrix Δp upon the nanocrystals is given by [27]

$$\Delta p = \frac{\left(A_g - A_\parallel\right)\Delta T + 2\left(A_g - A_\perp\right)\Delta T}{2S_{11} + 2S_{12} + 4S_{13} + S_{33}}, \qquad (1)$$

where A_g is thermal expansion coefficient for the glass, $A_\parallel$ and $A_\perp$ – thermal expansion coefficients for CdS$_{1-x}$Se$_x$, $\Delta T = T_s - T_m$ – the variation of temperature from the synthesis temperature T_s to the measurement temperature T_m, S_{ij} (i, j=1, 2, 3) – elastic constants of CdS$_{1-x}$Se$_x$ lattice. Note that Eq. (1) is applicable when the pressure is supposed to be independent of the nanocrystal size and the nano-crystals are large enough to preserve hexagonal crystal structure, what in the case of CdS$_{1-x}$Se$_x$ quantum dots is valid in case their mean radius exceeding 1.5–2.5 nm [1, 7, 8]. In this case the values for bulk semiconductor materials can be applied, for the case of the mixed CdS$_{1-x}$Se$_x$ crystals they can be obtained by interpolation of the corresponding values for pure CdS and CdSe which are listed in Table 1.

Table 1. Relevant parameters of bulk CdS and CdSe crystals.

Parameter	CdS	CdSe	Reference
dE_g/dp, eV/GPa	0.033	0.037	[23]
	0.058	0.040	[24]
		0.058	[25]
$A_\parallel$, K^{-1}	2.6×10^{-6}	2.9×10^{-6}	[27]
$A_\perp$, K^{-1}	4.6×10^{-6}	4.9×10^{-6}	[27]
S_{11}, N^{-1}·m^2	2.069×10^{-11}	2.338×10^{-11}	[28]
S_{12}, N^{-1}·m^2	−0.999×10^{-11}	−1.122×10^{-11}	[28]
S_{13}, N^{-1}·m^2	−0.581×10^{-11}	−0.572×10^{-11}	[28]
S_{33}, N^{-1}·m^2	1.697×10^{-11}	1.735×10^{-11}	[28]
dE_g/dT, eV/K	−4.4×10^{-4}	−4.6×10^{-4}	[29]
	−3.8×10^{-4}		[30]
	−5.5×10^{-4}		[31]

Using the quoted parameters for the bulk crystals and Eq. (1), the hydrostatic pressure of the borosilicate glass matrix upon CdS$_{1-x}$Se$_x$ nanocrystals for the range of compositions under investigation was calculated as $\Delta p\approx0.55$ GPa [27].

Since the borosilicate matrix pressure Δp upon CdS$_{1-x}$Se$_x$ quantum dots depends on the sample temperature, its temperature variation could be estimated from the optical absorption edge measurements at different temperatures. Fig. 2 shows the relevant spectra at ambient atmospheric pressure at 77 and 296 K. As seen from the figure, cooling of the samples results in the absorption edge shift by 0.07 eV for both nanocrystal compositions; note that the features related to the quantum-size effects also shift in energy by the same value. It should be noted that both above mentioned methods of

estimating the absorption edge shift – by $\alpha^2(h\nu)$ plot extrapolation and by using a substitutive parameter E_g^{α}, corresponding to $\alpha_f = 25$ cm^{-1}, gave the same value of the temperature-induced absorption edge shift.

Since the temperature shift of the absorption edge for CdS$_{1-x}$Se$_x$ quantum dots in the glass matrix results from the combination of the proper temperature-related edge shift and the edge shift due to the temperature-related increase of the pressure of the host matrix, both of them shifting the edge to the higher energies, it could be expected, in case the above assumption of applicability of the bulk parameters for the nanocrystals being valid, that the corresponding calculations would enable us to separate the contributions of these two effects into the temperature shift of the absorption edge. However, the experimental results have shown the absorption edge shift in CdS$_{1-x}$Se$_x$ nanocrystals in borosilicate glass matrix at the temperature decrease from 296 to 77 K (0.07 eV) to be smaller than that estimated using the interpolated values for the bulk crystals (0.09–0.12 eV) even without the account of the host matrix pressure variation. Hence, the values of the relevant parameters (dE_g/dT, dE_g/dP) for the bulk crystals cannot be applied for quantitative estimation of temperature and pressure effects of semiconductor nanocrystals, since in the latter confinement-related changes in electron-phonon coupling may occur as well as surface-(interface-) related effects can be revealed much stronger due to much higher surface-to-volume ratio what is manifested as the decrease of phonon frequencies in Raman spectra of CdS$_{1-x}$Se$_x$ nanocrystals [18, 19].

The energy gap temperature variation at constant pressure can be described as [32]

$$\left(\frac{dE_g}{dT}\right)_p = \left(\frac{dE_g}{dT}\right)_V - \frac{3A}{\beta}\left(\frac{dE_g}{dp}\right)_T , \qquad (2)$$

where A is the volume thermal expansion coefficient and β is compressibility. The first term in this expression corresponds to the contribution of electron-phonon coupling into the energy gap variation, and the second one – to the gap variation due to the crystal volume change. The performed experiments enabled us to obtain compressibility values 1.73×10^{-11} Pa^{-1} and 1.8×10^{-11} Pa^{-1} for CdS$_{0.4}$Se$_{0.6}$ and CdS$_{0.22}$Se$_{0.78}$ nanocrystals, respectively. Hence, from Eq. (2) the contribution of the electron-phonon coupling was about 4×10^{-4} eV/K for both samples while the gap variation due to the nanocrystal volume size was about 8.5×10^{-5} eV/K.

We have studied the effect of hydrostatic pressure on the optical absorption spectra for the sample of CdS$_{0.4}$Se$_{0.6}$ nanocrystals in the borosilicate glass matrix subjected to annealing at 925 K during 6 h, which was performed in order to increase the nanocrystal size in the matrix. The measurements have shown the pressure variation of the optical gap to decrease ($dE_g/dP = 0.03$ eV/GPa) with respect to the initial value. Hence, while describing the effects of external factors on CdS$_{1-x}$Se$_x$ quantum dots in glass matrices, the correct account of the nanocrystal size and composition should be carried out instead of using the relevant parameters for the bulk crystals.

4. Conclusions

The performed optical studies of influence of hydrostatic pressure effect on the absorption edge of CdS$_{1-x}$Se$_x$ quantum dots has enabled us to obtain the energy gap pressure coefficients $dE_g/dP=0.041$ eV/GPa for CdS$_{0.4}$Se$_{0.6}$ ($r=2.76$ nm) and 0.039 eV/GPa for CdS$_{0.22}$Se$_{0.78}$ ($r=3.08$ nm) samples which agree well with the corresponding values for bulk and nanocrystalline CdS and CdSe.

The investigation of hydrostatic pressure and temperature effect on the optical spectra of CdS$_{1-x}$Se$_x$ nanocrystals in borosilicate glass matrix has shown that the correct description of the observed effects requires the dependence of the corresponding parameters on the nanocrystal size and composition to be taken into account.

References

[1] A. I. Ekimov, A. A. Onushchenko, JETP Lett., **40**, 1136 (1984).

[2] D. J. Norris, M. G. Bawendi, Phys. Rev., **B 53**, 16338 (1996).

[3] S. V. Gaponenko, Fizika i Tekhnika Poluprovodnikov (russ.), **30**, 577 (1996).

[4] A. Ekimov, J. Luminesc., **70**, 1 (1996).

[5] S. H. Tolbert, A. P. Alivisatos, Z. Phys., **D26**, 56 (1993).

[6] S. H. Tolbert, A. B. Herhold, C. S. Johnson, A. P. Alivisatos, Phys. Rev. Lett., **73**, 3266 (1994).

[7] S. H. Tolbert, A. P. Alivisatos, J.Chem. Phys., **102**, 4642 (1995).

[8] J. Schroeder, P. D. Persans, J. Luminesc., **70**, 69 (1996).

[9] J. N. Wickham, A. B. Herhold, A. P. Alivisatos, Phys. Rev. Lett., **84**, 923 (2000).

[10] J. Li, G. H. Li, J. B. Xia, J. Zhang, Yu. Lin, X. Xiao, J. Phys.: Condens. Matter., **13**, 2033 (2001).

[11] J. Schroeder, L. W. Hwang, M. R. Silvestri, M. Lee, P. D. Persans, J. Non-Cryst. Sol., **203**, 217(1996).

[12] X. S. Zhao, J. Schroeder, A. P. Persans, T. Bilodeau, Phys. Rev., **B43**, 12580 (1991).

[13] T. Makino, M. Arai, K. Matsuishi, S. Onari, T. Arai, J. Phys.: Condens. Matter., **10**, 10919 (1998).

[14] T. Makino, M. Arai, S. Onari, K. Matsuishi,T. Arai, Phys. Stat. Sol., (b) **211**, 317 (1999).

[15] M. Silvestri, J. Schroeder, J. Phys.: Condens. Matter., **7**, 8519 (1995).

[16] A. V. Gomonnai, A. M. Solomon, V. A. Yukhimchuk, V. V. Lopushansky, Yu. M. Azhniuk, I. I. Turok, Ukr. J. Phys. Opt., **2**, 31(2001).

[17] A. Tu, P. D. Persans, Appl.Phys.Lett., **58**, 1506 (1991).

[18] A. Roy, A. K. Sood, Phys. Rev., **B53**, 12127 (1996).

[19] A. Ingale, K. C. Rustagi, Phys. Rev., **B58**, 7197 (1998).

[20] N. R. Kulish, V. P. Kunets, M. P. Lisitsa, Fizika Tverdogo Tela (russ.), **39**, 1865 (1997).

[21] N. F. Mott, E. A. Davis, Electronic Processes in Non-Crystalline Materials, Clarendon Press, Oxford, 1979.

[22] I. P. Studenyak, M. Kranjčec, Gy. S. Kovács, V. V. Pan'ko, D. Desnica, A. G. Slivka, P. P. Guranich, J. Phys. Chem. Solids, **60**, 1897 (1999).

[23] A. L. Edwards, H. G. Drickamer, Phys. Rev., **122**, 1149 (1961).

[24] P. Cervantes, Q. Williams, M. Côté, O. Zakharov, M. Cohen, Phys. Rev., **B54**, 17585 (1996).

[25] J. R. Mei, V. Lemos, Sol. St. Commun., **52**, 785 (1984).

[26] P. D. Persans, L. B. Lurio, J. Pant, H. Yükselici, G. Lian, T. M. Hayes, J. Appl. Phys., **87**, 3850 (2000).

[27] V. P. Kunets, Ukr. Fiz. Zh. (ukr.), **43**, 64 (1998).

[28] F. Cerdeira, G. S. DeWitt, U. Rossler, M. Cardona, Phys. Stat. Sol., **41**, 735 (1970).

[29] Tables of Physical Values: Handbook, Ed. by I.I.Kikoin (russ.), Atomizdat, Moscow (1976).

[30] Numerical Data and Functional Relationshiprs in Science and Technology, Ed. by O.Madelung, Vol. III-17b, Springer, Berlin (1982).

[31] T. Komatsu, T. Nakagawa, K. Matusita, J. Mater. Sci. Lett., **14**, 1023 (1995).

[32] J. F. Nye, Physical Properties of Crystals. Their Representation by Tensors and Matrices, Clarendon Press, Oxford (1964).

VISIBLE LIGHT EMISSION FROM $Cd_{1-x}Mn_xS$ NANOCRYSTALS

V. Ghiordanescu, M. Sima, M. N. Grecu, L. Mihut

National Institute of Materials Physics, PO Box MG-7
76900 Bucharest-Magurele, Romania

The luminescence spectra of some $Cd_{1-x}Mn_xS$ nanocrystals have been measured at room and liquid nitrogen temperature. The Mn^{2+} ions give rise to a broad emission band centered at about 580 nm, between the emission bands of CdS host.

1. Introduction

Optical properties of the nanocrystaline semiconductors were extensively studied in the last years. Due to the quantum confinement, the large surface/volume ratio and the high density of the surface states, these materials differ from the bulk crystals. Most
studies were performed on the pure semiconductors [1-5]. To improve emission activity have been performed researches on the doped nanocrystaline semiconductors like ZnS: Mn [6-8] or CdS:Mn [9-11]. The d-electronic states of the Mn^{2+} ions act as the luminescence centers emitting in the green part of the visible spectrum; the efficiency increases by energy transfer from s-p states of the host nanocrystal. On the other side, recent studies [7,8] showed that the emission intensity increases as a result of surface modification, which appears when the nanocrystals are imbedded in an acrylic polymer.

In our paper we report some results of the study concerning the influence of Mn^{2+} ion and poly(p-aminobenzoic acid) (PABA) matrix on the optical properties of
$Cd_{1-x}Mn_xS$ nanocrystals.

2. Synthesis

$Cd_{1-x}Mn_xS$ nanoparticles were prepared at room temperature by H_2S bubbling into H_2O/THF (tetrahydrofuran) (1:4 vol.) solution containing $CdCl_2$ and $MnCl_2$ in different molare ratios; the concentration of the cations, $[Cd^{2+}] + [Mn^{2+}]$ was kept at 10^{-3} M. The pH of the solution before treatment with hydrogen sulfide was 8.5. Sodium thioglycollate (10^{-3}M), as stabilizing agent was added in this solution. The precipitated nanoparticles were maintained in this medium during 48 h and then separated. To obtain a composite film PABA/$Cd_{0.95}Mn_{0.05}S$ the nanocrystals were redispersed into H_2O/THF (9:10 vol.) and were mixed with PABA; the polymer was prepared using the procedure described in [12]. For optical measurements the $Cd_{1-x}Mn_xS$ nanoparticles and the composite were deposited on the quartz glass substrate. The $Cd_{0.95}Mn_{0.05}S$ particles dimension was estimated to be ~10 nm from the micrograph (Fig.1) obtained with a Philips EM 301 electron microscope.

3. Results and Discussion

Fig. 2 shows *the absorption spectra* at room temperature (RT) for $Cd_{0.95}Mn_{0.05}S$ (a), $Cd_{0.75}Mn_{0.25}S$ (b) and PABA/$Cd_{0.95}Mn_{0.05}S$ composite film (c). Curves (a) and (b) show a main peak due to CdS, near 400 nm and several weak superimposed structures (Table 1) which can be attributed to Mn^{2+} ions, according to literature data [13-15]; the 405 and 414 nm absorption peaks are due to transitions of excited CdS states [3] . Curve (c) doesn't show these absorption peaks; a nanoparticles' agglomeration process can be produced in composite sample. The assignments of the Mn^{2+} transitions given in Table 1 are in agreement with literature data [13-15].
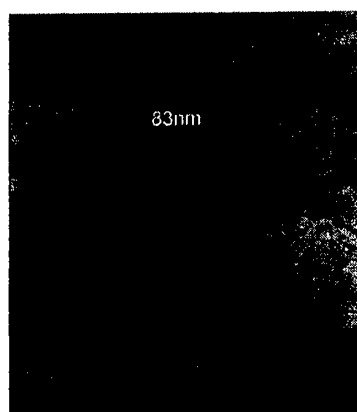
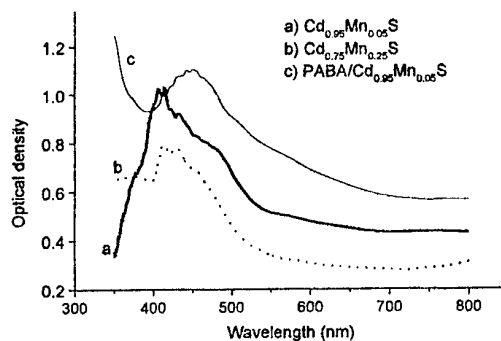Fig. 1. Transmission electron micrograph of $Cd_{0.95}Mn_{0.05}S$ nanoparticles.

Fig. 2. Absorption spectra of $Cd_{0.95}Mn_{0.05}S$, $Cd_{0.75}Mn_{0.25}S$ nanoparticles and PABA/ $Cd_{0.95}Mn_{0.05}S$ composite film, at RT.

Table 1. The Mn^{2+} absorption and photoluminescence excitation (PLE) maxima for $Cd_{1-x}Mn_xS$ nanoparticles.

$^1A_6 \longrightarrow$		$^4T_1(^4G)$	$^4T_2(^4G)$	$^4E, ^4A_1(^4G)$	$^4T_2(^4P)$	$^4E(^4P)$	$^4T_2(^4D)$
$Cd_{0.6}Mn_{0.4}S$, crystal [13]		510	480	445	-	-	-
$Zn_{0.95}Mn_{0.05}S$, crystal [14]		531	498	466	429	389	-
$Zn_{0.94}Mn_{0.6}S^*$, film [15]		550	500	465	430	380	-
$Cd_{0.95}Mn_{0.05}S$, our results	Abs. (Fig.2)	-	485	463	430	373	360
	PLE (Fig.4)	508	490	465	429	373	361

*estimated from transmission spectrum

The photoluminescence (PL) spectra were registered at RT and liquid nitrogen temperature (LNT) using the exciting light from an Ar^+ laser (λ=457.9 nm) and a SPEX double monochromator with EMI 9658 A photomultiplier. The geometry was 90^0 and the registration by photon counting.

Table 2 presents the positions of the maxima and their intensities observed on the PL spectra (Fig.3). Assuming that the emission spectrum is composed by three Gaussian curves, the maximum centered at 510 nm at LNT is attributed to CdS band to band transition [1]. The red luminescence (652-673 nm) is due to CdS defect states. The emission maximum (576-596 nm) located between CdS bands is attributed to the Mn^{2+} ions ($^4T_1 \rightarrow ^6A_1$ transition), in accordance with [9-11].

The relative efficiency of manganese PL increases as far as temperature and Mn^{2+} concentration decreases (Table 2).

Table 2. PL intensity (I) and peak position (λ, nm) of the $Cd_{0.95}Mn_{0.05}S$ (a), $Cd_{0.75}Mn_{0.25}S$ (b) nanoparticles and PABA/ $Cd_{0.95}Mn_{0.05}S$ composite film(c), obtained by deconvoluting the PL spectra.

		a)		b)		c)	
		λ	I	λ	I	λ	I
		510	1.3	518	1.6	509	2.3
LNT		586	22.1	596	5.9	576	4.0
		652	10.5	673	8.9	663	4.0
		539	1.0	525	0.3	523	0.7
RT		579	1.2	564	0.8	573	2.0
		659	1.2	674	0.7	670	1.9
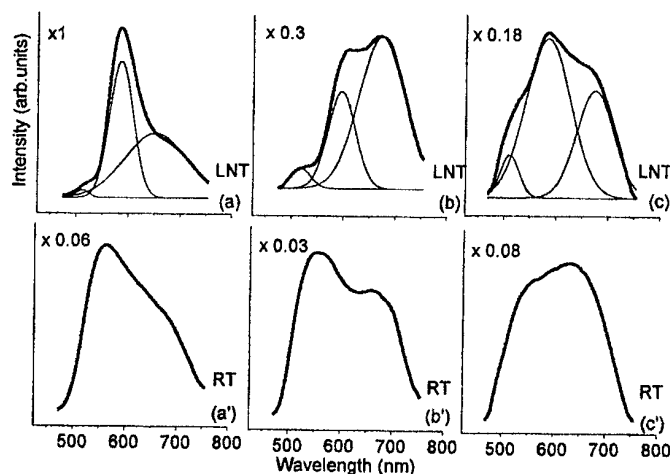
Fig. 3. Photoluminescence spectra of $Cd_{0.95}Mn_{0.05}S$ (a,a'), $Cd_{0.75}Mn_{0.25}S$ (b,b') nanoparticles and PABA/ $Cd_{0.95}Mn_{0.05}S$ (c,c') composite film, at RT and LNT.
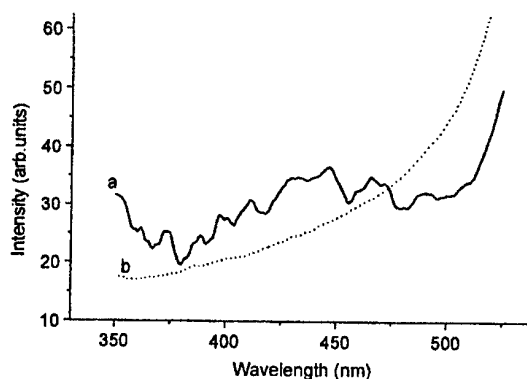

Fig. 4. Photoluminescence excitation spectra of $Cd_{0.95}Mn_{0.05}S$ nanoparticles in the 570 nm (curve a)and 750 nm (curve b) spectral region, at RT.

The photoluminescence excitation (PLE) spectra (Fig. 4) were obtained in the 320-550 nm range, using a SPM-2 monochromator with tungsten lamp and EMI 6558 QB photomultiplier. The sample was irradiated in the 45^0 geometry arrangement using a cut filter and interferential filters, which permit detection at the 570 nm and 750 nm. The data were corrected using a $BaSO_4$ diffuser as reference.

One can observe in the Fig. 4, curve (a) the presence of several weak peaks, which are attributed to the Mn^{2+} absorption [13-15]. The supplementary peaks from 446, 411, 396 and 388 nm can be attributed to CdS host [3]. The CdS luminescence from 510 nm is a result of these absorptions and it is superimposed on the $^1A_6 \rightarrow {}^4T_1$ Mn^{2+} absorption; an energy transfer from CdS host to manganese emitting centers can be produced. The shape of the curve (b) (Fig. 4) registered for the red emission follows filter transmission; the presence of very weak peaks in the 400 nm region confirms that the red emission is due to some defects' states in the gap of CdS.

X-band EPR spectra were recorded at room temperature for $Cd_{1-x}Mn_xS$ nanoparticles deposited on quartz plate. In figure 5 are shown broad EPR signals in three samples with different concentrations of manganese ions: 5%, 25%, respectively 5% and dispersed in polymer. Absorption is mainly observed in the region of $g_{eff} = 2.01$. No resolved hyperfine structure is observed. The broadening of the EPR line width increases with the concentration of manganese ions from 12 mT (in sample with 5% Mn) to 19 mT (for 25% Mn). The sample dispersed in polymer has a narrower line (11 mT). We note that these values are much smaller than those reported in [16]. Besides, the EPR spectra for samples with low concentration of Mn ions are changing in time. In figure 5(a) one can see such a behaviour; the spectrum of two distinct EPR signals observed for fresh samples is drastically

modified after six weeks, the sample being kept at room temperature. Such modifications are associated with an aggregation process of the $Cd_{1-x}Mn_xS$ nanoparticles deposited on quartz glass substrate.
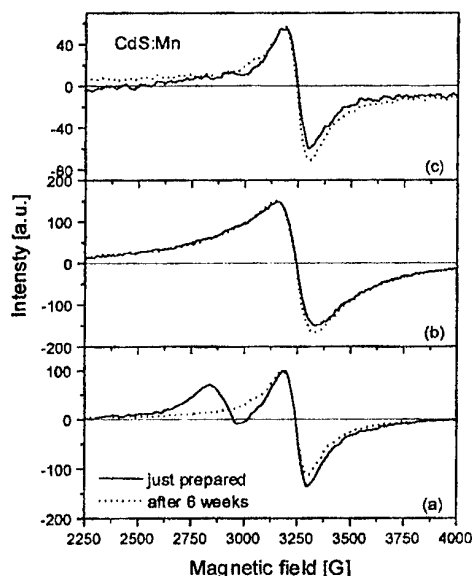

Fig. 5. Room temperature EPR spectra of $Cd_{0.95}Mn_{0.05}S$ (a), $Cd_{0.75}Mn_{0.25}S$ (b) nanoparticles and PABA/ $Cd_{0.95}Mn_{0.05}S$ (c) composite film.

4. Conclusions

The absorption spectra of $Cd_{1-x}Mn_xS$ particles show a main absorption due to CdS host and several weak peaks superimposed on it; some of them are attributed to Mn^{2+} ions in accordance with the PLE spectrum of the yellow-green emission.

The PL spectra show three components in the 500-800 nm spectral region. Their intensities at RT are at the same order of magnitude.

Our results show an energy transfer from CdS host to manganese dopant.

EPR and emission spectra confirm two manganese location; they apear due to nonuniform distribution of Mn^{2+} ions inside nanoparticle.

References

[1] J.J. Ramsden, M. Grätzel, J.Chem.Soc.,Faraday Trans, 1, 80, 919 (1983).
[2] A.P. Alivisatos, A.L. Harris, N.J. Levinos, M.L. Steigerwald, L.Brus, J.Phys.Chem., 89, 4001 (1988).
[3] K.K. Nanda, S.N. Sarangi, S. Mohanty, S.N. Sahu, Thin Solid Films, 322, 21 (1998).
[4] S. Pethkar, R.C. Patil, J.A. Kher, K. Vijayamohanan, Thin Solid Films, 349, 105 (1999).
[5] T. Nakanishi, B. Ohtani, K. Uosaki, J. Phys. Chem., 102, 1571 (1998).
[6] R.N. Bhargava, D. Gallagher, T. Welker, J. Lumin., 60, 275 (994).
[7] T. Igarashi, T. Isobe, M. Sena, Phys. Rev., B56, 6444 (1997).
[8] T. Kezuka, M.Konishi, T. Isobe, M.Sena, J. Lumin., 87-89, 418 (2000).
[9] L. Levi, N. Feltin, D. Ingert, M.P. Pileni, J. Phys. Chem., B101, 9153 (1997).
[10] L. Levi, N. Feltin, D. Ingert, M.P. Pileni, J. Cryst. Growth, 184/185, 377 (1998).
[11] N. Feltin, L.Levi, D. Ingert, M.P. Pileni, J. Phys. Chem., B103, 4 (1999).
[12] K. S. Alva, Macromol. Rapid Commun., 17, 805 (1996).
[13] M. Ikeda, K. Itoh, H. Sato, J.Phys.Soc. Japan, 25, 455 (1968).
[14] D. S. McClure, J.Chem.Phys., 39, 2850 (1963).
[15] V. Dimitrova, J.Tate, Thin Solid Films, 365, 134 (2000).
[16] Shu Man Liu et al., Solid State Commun., 115, 615 (2000).

CHEMICALLY PREPARED NANOCRYSTALLINE PbS THIN FILMS

E. Pentia, L. Pintilie, I. Matei, T. Botila, E. Ozbay[a]

National Institute of Materials Physics, Bucharest, Magurele P.O.Box MG-7, R-76900, Romania
[a]Department of Physics, Bilkent University, Ankara 06533, Turkey

PbS nanocrystalline thin films were prepared by Chemical Bath Deposition (CBD) technique. A comparative study between "standard" and "nanocrystalline" PbS thin films was performed. We denoted "standard" the PbS film with a good photosensitivity for to use as IR detector. This film was deposited after 1 hour from chemical bath containing reducing agent and Bi ions as doping element. The "nanocrystalline" film was obtained at shorter reaction time (after 17 minutes) from reducing bath without doping element. The other parameters: concentration of the reactants, pH, temperature were kept constant for the all depositions. The morphological properties of the films were determined by SEM analysis. Also, the electrical and photoelectrical behaviors were investigated for the both types of PbS films. The "nanocrystalline" film had a very high electrical resistance (10^{10} -$10^{11} \Omega/\square$) compared with the "standard" film (10^5-$10^6 \Omega/\square$). Both types of films proved to be sensitive to the surrounding atmosphere, air or vacuum. Thermally Stimulated Current (TSC) measurement had shown the presence of trap concentration in the both cases, probably due to the large amount of disordered regions.

1. Introduction

A variety of physical properties of nanoparticles semiconductors have been reported in the literature [1-5]. Many authors have predicted for nanoparticle semiconductors enhanced nonliniarities resulting from quantum confinement effects [6-8]. The materials application that has attracted considerable attention relates to nonlinear optics 9,10]. Most studied nanocrystalline semiconductors belong to the II-VI and IV-VI groups as they are relatively easy to synthesize and are generally prepared as particles or in thin film form. In the last years, several methods to synthesize PbS nanoparticles, semiconductor from IV-VI group, were studied such as grown in a glass, glass-ceramic, polymer matrix respectively [11-13]. PbS is a semiconductor with band gap about 0.41 eV at room temperature and 0.29 eV at liquid-N_2 temperature. For PbS, the size effect can be observed for a crystallite as large as 180Å, which contains over 10^5 atoms [4].

Chemical Bath Deposition (CBD) is a very comfortable method for deposition polycrystalline PbS thin films with a good photoconductive properties. By CBD method, the dimensions of the crystallites can be varied controlling deposition parameters: reaction time, temperature, pH, and presence of impurities in the solution. Most of the works on nanosize semiconductor particles reported so far have been restricted to optical absorption. The absorption edge has been found to be blue shifted as the particle size reduced. Only o few studies of electrical and photoelectrical properties of these kind of materials have been presented in the literature.

This article presents some comparative preliminary results between two types of PbS films "standard" and "nanocrystalline", prepared by CBD method. The morphology of the films was investigated by scanning electron microscopy (SEM). Also, we have investigated the electrical and photoelectrical properties of the films.

2. Experimental

Two sets of PbS samples were prepared: "standard" and "nanocrystalline" thin films. The PbS film deposition was performed on glass substrates by CBD method. The substrates were very carefully cleaned using oxidant mixing ($K_2Cr_2O_7$: H_2SO_4; 1:10), HNO_3, 1% EDTA and successive rinsing with bidistilled water. The cleaning state of the substrate surface is very important for the quality of the film formation. The substrates were introduced vertically in the chemical bath.

The deposition bath contained an aqueous solution, consisting of: $Pb(NO_3)_2$ 0.06M, thiourea $SC(NH_2)_2$ 0.24M, NaOH 0.6M and reducing agent (hydroxylamine hydrochloride, $NH_2OH \cdot HCl$ 0.1M). The concentration of the reagents, pH (12.7) and temperature (24^0C) were kept constant for all depositions.

In the alkaline medium, the thiourea decomposed and released S^{2-} ions, which precipitate Pb^{2+} ions from the solution:

$$SC(NH_2)_2 + OH^- \rightarrow CH_2N_2 + H_2O + HS^-$$
$$HS^- + OH^- \rightarrow H_2O + S^{2-}$$
$$Pb^{2+} + S^{2-} \rightarrow PbS$$
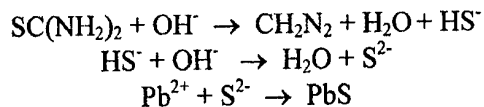
Hydroxylamine hydrochloride seems to accelerate the chemical deposition reaction so that acceleration causes a decrease in the size of the crystallites.

For "standard" film the precipitation took place in the presence of Bi ions ($Bi(NO_3)_2$ $2.06 \cdot 10^{-4}$M). It is known that PbS film with a good photoconductivity had an average grain size of 300nm [14,15]. Optimum proportion between hydroxylamine hydrochloride and Bi as doping element allowed us to obtain quality films with average grain size of 250-300nm. The films prepared by above mentioned procedure had very good photoconductivity and can be used in IR detection.

To impede the growth of crystallites, the "nanocrystalline" film was deposited without doping, at shorter reaction time (17 minutes). Our previous studies shown that a small amount of Bi ions in the deposition bath lead to the enhance of the grain size [16]. This was reason that in case of "nanocrystalline" film preparation we have eliminated the doping element from deposition bath.

For the electrical and photoelectrical measurements gold electrodes in a coplanar configuration, were evaporated in vacuum on the surface of the PbS for both type of films. The distance between electrodes was 6 mm. After that the samples were annealed at 80^0C for several (24-30) hours to improve the sensitivity of the films and stabilize the parameters.

The set-up presented in Fig.1 was used to perform the photoconductive measurements. The radiation source was a SYLVANIA lamp (30 W electrical power). The collimated radiation beam passed through a Carl Zeiss monochromator, with LiF prism, and falls on the surface of the PbS film. For photoconductivity measurements on " standard" PbS films, the incident light was modulated with an ITHACO 383A type mechanical chopper. The measurements were performed at 200Hz. The photosignal was taken from a load resistance (see Fig. 1) and measured with a UNIPAN 233 nanovolmeter. Because of the high dark resistance and a small photosignal the photoconducive measurements on "nanocrystaline" films were performed without light modulation.
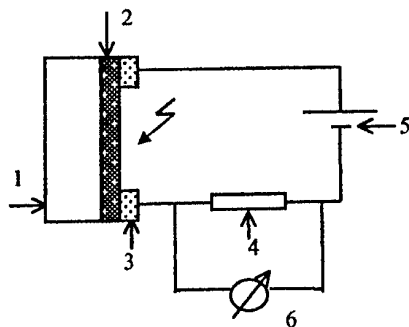

Fig. 1. The experimental setup for the photoconductive measurement. 1) glass substrate; 2) PbS film; 3) gold electrodes; 4) load resistance; 5) current source; 6) amplifier.

For TSC measurements, the samples were irradiated with light ($5mW/cm^2$ optical power) for 5 minutes at liquid–nitrogen (N_2) temperature. During the heating, with constant rate (0.1 K/s), a constant potential (25V) was applied between the coplanar electrodes situated on the PbS film surface. The current was measured with a KEITHLEY 6517 electrometer.

3. Results and discussion

A very adherent film with gray-black color and metallic aspect was obtained in case of the "standard" film. SEM photographs (Fig. 2) of the "standard" PbS film reveal existence of a continuous compact polycrystalline film with grain size around 250-300nm. The thickness of the film is about 500nm and was determined by interpherometric method.

Fig. 2. SEM photograph of "standard" PbS film deposited on glass.

The SEM photo of the "nanocrystallite" film (Fig. 3) showed a continuous layer with grain size around 50nm and less. This film is also very adherent on the glass substrate and had a brown color.
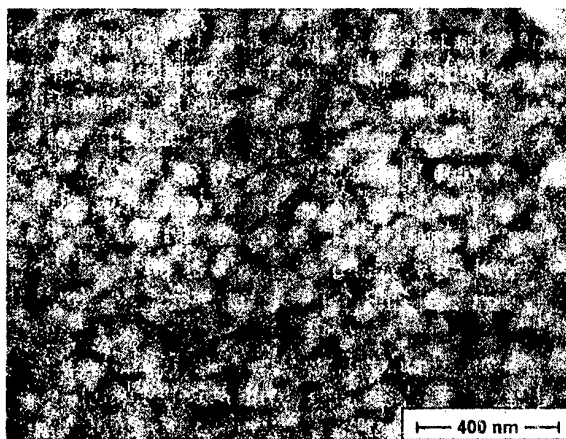
Fig. 3. SEM photograph of PbS "nanocrystalline" film deposited on glass.

The dark resistance of the "nanocrystalline" film had a high value, 10^{10}-$10^{11}\Omega/\square$, comparing with "standard" films when dark resistance not exceeded 1-2 $10^6\Omega/\square$.

Correlating these values with SEM photo, we can claim that the high resistance of the "nanocrystalline" film is due to the small crystallite sizes. Change in crystallite size will mainly affect the mobility of the carriers and so change the resistance [17].

Both the "nanocrystalline" and "standard" PbS films presented p-type conductivity, determined by "hot probe" method. Spectral distribution measurements of photoconductive signal revealed a shift of the maximum sensitivity towards shorter wavelenghts for "nanocrystalline" PbS

film. (Fig. 4 b). Thus, "standard" film presented one maximum of sensitivity at 2.55μm and another at 2,2 μm, while "nanocrystalline" films show maximum at 1.8 and 0.8μm (Fig. 4a and b).

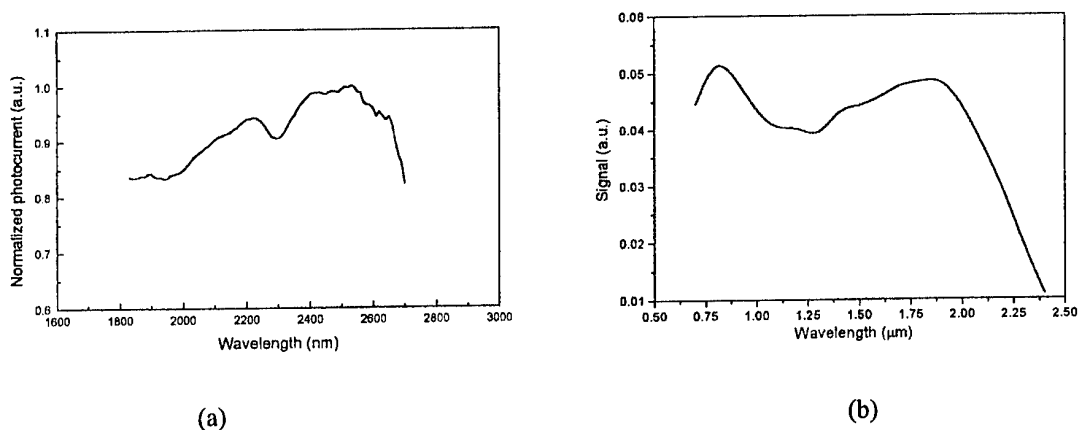(a)   (b)

Fig. 4. Spectral distribution of photoconductive signal normalized to the incident power for PbS films: (a) "standard" film measured in modulated light; (b) "nanocrystalline film measured in permanent light.
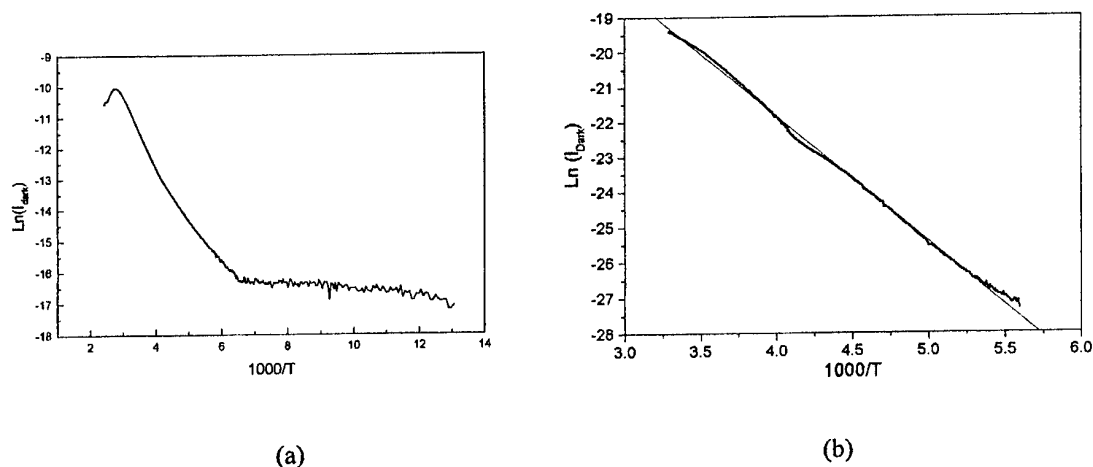

(a)   (b)

Fig. 5. Dark current vs temperature for (a) "standard" and (b) "nanocrystalline" PbS films.

The thermally activation energy E_a for both type of films was determined from the slope of dark current curve vs temperature (Fig. 5 a and b). This energy, for "standard" film, was estimated to be about 0.196 eV and for "nanocrystalline" film 0.3 eV. Considering that E_a represent ½ from band gap energy E_g, it can evaluated that E_g = 0.4eV for "standard" film and E_g = 0.6 eV for "nanocrystalline" film.

Thermally Stimulated Current (TSC) is a method used to obtain information about the energy level in the band gap, associated with the various defects in semiconductors. Fig. 6 a and b are presenting the TSC curves for " standard and "nanocrystalline" films. Two levels are observed for "standard" sample. The activation energy of the first level was estimated to be about 0.16 eV and second 0.19 eV using the empirical formula, for activation energy of trapping level, $E_a = nkT_m$ (k is the Boltzmann constant, T_m is the peak temperature and n= 19 is assumed). In the "nanocrystalline" film are observed three peaks in the TSC current but two of them appeared at a higher temperatures. The activation energy estimated for these two levels were 0.36 eV and 0.45 eV. We are noted that the

band gap of PbS is 0.41 eV at room temperature. Comparing the second activation energy of trap level (0.45 eV) of "nanocrystalline" film with band gap energy of PbS, it can be supposed that for this film the band gap energy was larger that of "standard" film, in accordance with value obtained from dark current vs temperature measurement.
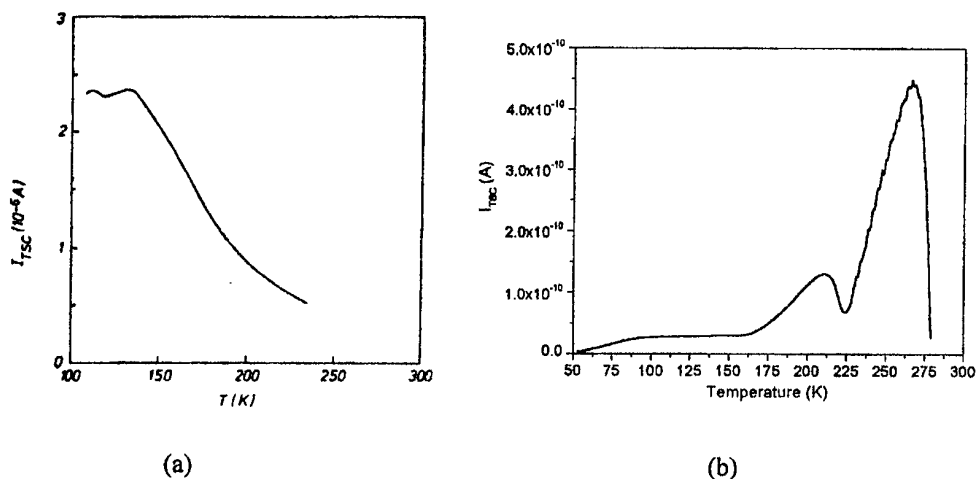

(a)   (b)

Fig. 6. TSC curves for a) "standard" PbS film b) nanocrystalline PbS films.

4. Conclusion

Several conclusions can be drawn on the basis of the experimental data. The CBD method can be used for the preparation of nanocrystalline PbS films. Comparative studies on the electrical and photoelectrical properties of "standard" and "nanocrystalline" film have shown important differences between them. Our results suggest that the shift of the maximum of photosensitivity to shorter wavelengths and the larger value of E_g can be ascribed to nanoparticles size effect.

Acknowledgements

References

[1] A. L. Efros, L. Efros, Fiz. Tekh. Poluprovodn., 16, 1209 (1982).
[2] M. L. Steigerwald, L. E. Brus, Annu. Rev. Mater. Sci. 19, 471 (1989).
[3] Y. Wang, N. Harron, W. Mahler, A. Suna, J. Opt. Soc. Am. B 6, 808 (1989).
[4] Y. Wang, N. Herron, J. Phys. Chem., 95, 525 (1991).
[5] D. Chakravorty, A. K. Giri, Chemistry of Advanced Materials, edited by C. N. R. Rao (Blackwell Sci. Publications, Oxford), 217 (1992).
[6] P. H. Roussingnol, D. Ricard, C. H. R. Flytzanis, Appl. Phys. B51, 437 (1990).
[7] H. Minti, M. Eyal, R. Reisfeld, G. Berkovic, Chem. Phys. Lett. 183, 277 (1991).
[8] K. Fukumi, A. Chayahara, K. Kadono, T. Sakaguchi, Y. Horino, M. Miya, J. Hayakawa, M. Satou, Japn. J. Appl. Phys. 30, L742 (1991).
[9] R. Vogel, P. Hoyer, H. Weller, J. Phys. Chem. 98, 3184 (1994).
[10] R. Konenkamp, R. Henninger, P. Hoyer, J. Phys. Chem. 97, 7328 (1993).
[11] M. Mukherjee, A. Datta, D. Chakravorty, Appl. Phys. Lett. 64, 1159 (1994).

[12] P. Hoyer, R. R. Konenkamp, Appl. Phys. Lett. **66**, 349 (1995).

[13] M. Mukherjee, A. Datta, D. Chakravorty, J. Mater. Res. **12**, 2507 (1997).

[14] G. P. Kothiyal, B. Ghosh, R. Y. Deshpande, J. Phys. *(D)* **13**, 869 (1980).

[15] T. Botila, E. Pentia, M. L. Ciurea, P. Pausescu, C. Sirbu, Proc. Annual Conf.Sem.Proc (Romania) p. 51 (1985).

[16] E. Pentia, Ph. D. Thesis, I.F.A. Bucharest, Romania, 2000.

[17] N. F. Mott, Contemp. Phys, **10**, 125 (1969).

IDEAS CONCERNING THE NON-CRYSTALLINE MATERIALS
OBTAINMENT BY MELT UNDERCOOLING

P. Balta

University "Politehnica" Bucharest

A short selective review of concepts and ideas concerning the conditions in which the melts may be undercooled in vitreous state is presented. The important role of the cooling rate in the broadening of the glass forming domains, encouraging the apparition of the new ultra high cooling rate techniques, is underlined. Correlation between the undercooling in the vitreous state tendency and basicity (pB in %) is demonstrated. The new evidenced fact that the classic glass formers are located in the central field of the basicity scales, i.e. approximately between 40 and 60 % of pB, is discussed. The speed of the heath dissipation V_{hd}, as a very general glass forming condition, is defined. The fulfilling of this condition allows obtaining every liquid or melt in vitreous state. The two new possibilities of melts undercooling tendency estimation are easily utilisable the necessary data being accessible.

1. Introduction

To obtain non-crystalline solids energy must be injected during the material processing. Many genesis routes may be used depending on the energy nature [1, 2, and 3]. These possibilities are suggested by the genesis routes triangle presented in figure 1, where S = solids, L = liquids, G = gases, V and V* are different resulting vitreous structures. For example, using thermal route, the solid is melted and the obtained L is undercooled to non-crystalline solid V.
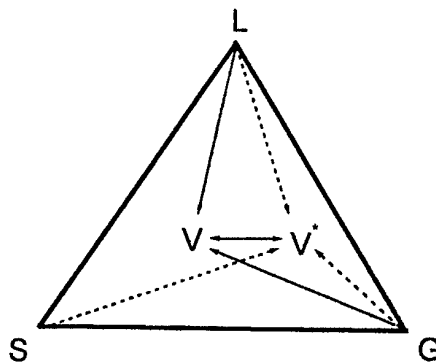
Fig. 1. Genesis routes triangle.

For thousand of years the main energy used for glass producing is the thermal one. After obtaining a melt it must be cooled up to the room temperature avoiding the crystallization to conserve the structural disorder. Because the nucleation and the crystallization processes devolve in time the cooling rate is one of the most important factors.

In the usual industrial technological conditions a reasonable slow cooling rate is necessary to allow the normal processing of glass products. For some glasses, like chalcogenide, metallic and others, interesting and important from scientific and application points of view, new technologies were elaborated.

In this work an attempt to update the ideas concerning the undercooling of melts in glassy state is presented.

2. A short review of the concepts concerning the possibilities of the melts undercooling tendency estimation

Efforts were made during the time to theoretically estimate the melt undercooling in vitreous state tendency. Many research workers approached this problem by following, mainly, two ways: 1) the consideration of the melt structure and of the nature of the chemical bonds and 2) the study of the kinetics of the crystallization process.

The first way resulted in the elaboration of rules, stepwise enriched with the progress of the glass chemistry. As examples, the Zachariasen rules are well known and also the use in this aim of the cation field strength introduced by Dietzel. Other attempts in this sense together with the use of the accumulated knowledge in the field of chemical bonds and of melt structure are presented in [1, 2, and 4]. Three categories of oxides are defined: glass formers, intermediates and modifiers. It was proved that these rules must be adjusted when new scientific and experimental data are accumulated. Thus, many compositionally new glasses and those obtained by the use of some ultra rapid cooling techniques made necessary a re-definition of the above mentioned three categories. For example, in chalcogenide glasses the role of modifiers seems to be played by the halogen atoms, which break the chalcogen bridges. In that concerns the formers this concept is less clear defined and consequently less used.

On the crystallization kinetics line the efforts were concentrated to express as correctly as possible the probability of nuclei apparition and the crystallization development. One of the early obtained results is a glass forming condition expressed by means of the so-called kinetic barriers for nucleation $\Delta G'$ and for crystallization $\Delta G''$, related to the viscosity influence increase, during the melt temperature decrease, on activation energies [1, 5]. For the case when the nucleation rate is of the order of 1 nucleus·cm^{-3}·s^{-1} and the crystal growth rate is less than 10^{-5} atomic dimensions per second, one obtain that the undercooling of a melt in vitreous state is possible when:

$$\Delta G' \approx \Delta G'' \geq 20 \cdot R \cdot T_m \tag{1}$$

where R is the gas constant and T_m is the melting temperature. That means that only the melts with a complex enough structure and with strong, active chemical bonds may be undercooled in vitreous state. Obviously the relationship (1) has been conceived mainly for usual industrial glass melting conditions. Taking into account the melt structural complexity and the chemical bonds energy the condition (1) is applicable to chalcogenide glasses too. However, many new glasses cannot be obtained in such conditions.

Stevels and collaborators [6] defined the notion of critical cooling rate CCR as the minimal cooling rate at which a melt with a given composition still can be obtained in vitreous state. Such experimentally accumulated information may be used to identify the compositions that can be processed in the usual industrial conditions without the risk of crystallization. However, getting such experimental data is laborious.

Uhlmann [1, 7, and 8] had the idea to establish the minimum crystal volume, detectable in glass by the usual techniques, which may make doubtful the quality of the given material as a glass. This volume fraction has been estimated at 10^{-6}. Uhlmann proposed a relation for the volume fraction of crystal calculation taking into account the nucleation frequency and the crystallization rate. Finally it may be drawn the so-called T-T-T curves, representing the temperature dependence of the time interval necessary for a given degree of melt-crystal transformation took place.

Using this kind of curves it may be approximated the cooling rate necessary for avoiding the formation of the previously established crystal volume fraction and even the thickness of the sample obtainable in vitreous state. A precious information is obtained in this way, as results from the table 1 [7, 8], that concentrates a part of the few data acquired in this field. It is evident the traditional glass forming character of SiO_2 and GeO_2 and the diminution of this property towards metal.

The knowledge concerning the melts nucleation and crystallization are considerable enriched in the time passed after the elaboration of the above ideas.

Table 1. Information obtained by means of T-T-T curves.

The substance	CCR (K·s⁻¹)	The thickness of the sample obtainable in vitreous state
SiO_2	2.10^{-4}	400 cm
GeO_2	7.10^{-2}	~7 cm
Salol	50	0,07 cm
H_2O	10^7	~1 μm
Ag	10^{10}	1000 Å

It must be noted the importance of transient phenomena in the nucleation process and the role of non-steady state time lag in nucleation, outlined especially by Gutzow and collaborators [4]. A simple relationship was deduced for critical cooling rate (denoted in this case as q_c) calculation in the case of a catalyzed nucleation:

$$\log q_c \cong 17 - \frac{U(T_m)}{RT_m} \qquad (2)$$

where $U(T_m)$ is the activation energy at the melting temperature. Taken into account the correlation between this activation energy and the molar enthalpies of evaporation and of sublimation one obtain:

$$\log q_c \cong C - \frac{\Delta H_{subl}}{RT_m} \qquad (3)$$

where C is a constant. If a quite reasonable value of 1 K·s⁻¹ is considered for q_c then results the condition:

$$\frac{\Delta H_{subl}}{RT_m} \geq C \qquad (4)$$

that may be used to conventionally separate the glass formers or "vitroids" from "crystalloids" [4]. The correlation possibility with melt structure and with chemical bonds is maintained.

The practical use of these ideas, of a high theoretical interest, encounters difficulties especially in the acquisition of the necessary for calculation data.

3. The use of basicity for the undercooling tendency estimation

As it is known, for solids the Lewis's theory of basicity seems to be the most adequate. In oxide glasses, oxygen is the basic partner donating the electrons needed for the bond. A simple image of such a bond offered by Lewis in 1916, cited and used by Pauling too [9], supported the idea that the shared electron pair is in general attracted more strongly by one than by other of two unlike atoms, according to the respective electronegativity values. The established equilibrium position of the electron cloud has important consequences, among them: a kind of mean electronegativity value, some partial charges on the partner atoms, a certain amount of ionic character of the bond etc. It is evident that the electron donating power of the oxygen atom and the acceptor ability of the partner atom must change too, the significance being a change in the basicity value.

The consequences may be seen also in certain modification of the electron levels (molecular orbitals), reflected by the electron transitions, by the polarizability values, by the refractive index and finally by all properties of glasses and all other oxidic materials. it is not surprising that many such influences have been proposed or used, with more or less success, as tools to measure the basicity.

The pB concept was published for the first time in a Romanian textbook of glass technology in 1984 [2] and then in English in 1985 [10]. Accepting the fact that oxygen is the basic part in oxides the amount of the ionic character (I_c), as defined by Pauling [9] was chosen to measure the electron donating power denoted, in this aim, pB. The immediate advantage was the possibility to calculate this magnitude by means of the known Pauling's relation, using the electronegativity (X_A and X_B) values:

$$I_c = 1 - e^{-0.25(X_A - X_B)^2} \qquad (5)$$

To consider also the co-ordination number CN and to use the ionisation potential of the cation

in the given oxide or glass instead of electronegativity a new relationship was elaborated for the amount of the ionic character, i. e. for pB, calculation.

$$\log pB = 1.9(CN)^{0.02} - 0.023\frac{P_i}{CN} \qquad (6)$$

The P_i values are easily accessible from tables based on calculated or experimentally determined data. The P_i value (in eV) used in (6) accounts for the oxidation state (OS) of the cation too, which has an important influence on the amount of the ionic character. For oxides having the same OS and CN the amounts of the ionic character calculated by means of electronegativity(5) or with (6) are identical [10].

The formula (6) gives pB values in percents, the pB = 100 % being the value of a free O^{2-} ion, that is, an ideal, not achievable, limit of electron donating power. The expressing of basicity in percent has the advantage to make easier the comparisons and correlation. The acronym pB prompts, in principle, the analogy with pH and pO^{2-} and also the expressing in %.

For complex glasses and oxidic materials the pB value is obtained from:

$$pB_g = \sum_i pB_i \cdot c_i \qquad (7)$$

c_i being the weight fraction of the oxide i and pB_i the respective basicity.

By means of the explicitly or implicitly included magnitudes, the basicity scale pB takes into consideration the properties of the atom (electronegativity, ionization potential), of the ion (oxidation state) and also the local chemical structure (coordination number CN) [2, 10-12]. For this reasons pB correlates in a direct and simple manner with all properties of glasses. The correlation between pB and the undercooling in the vitreous state tendency is illustrated by the data in the table 2.

The glass former, in the classical sense, oxides have pB values up to approximately 60 %, the intermediates between 60 and 70 % and modifiers over 70 %. It is interesting to note that the most different industrial glasses have pB values in the range of glass formers, up to 63 %. Because the pB scale was elaborated only for oxidic materials the basicity values of chalcogenides were obtained using the relationship (5) for the amount of ionic character calculation function of electronegativity.

Table 2. Basicity (pB) values for some compounds and glasses.

Oxides	pB (%)	Industrial glasses	pB (%)
P_2O_5 - former	38	BaO - modifier (CN =8)	89,5
B_2O_3 - former (CN = 3)	44.8	Schott C_1 solder glass	50.0
SiO_2 - former	49.4	Simax (Pyrex, Duran)	52.2
As_2S_3 - former	6.0	Solder glass for Kovar	54.1
GeS_2 - former	11.6	Schott C_{15} solder glass	57.1
Al_2O_3 - interm. (CN = 4)	61.6	Glass for high tension insulators	58.9
Al_2O_3 - interm. (CN = 6)	72.4	Window glass	60.0
Na_2O - modifier (CN =6)	89.0	E fiber glass	60.9
K_2O - modifier (CN =9)	94.2	Philips, for TV screen glass	62.8
CaO - modifier (CN=7)	88.4	Sovirel S 000,01 solder glass for Fe	63.0

As it is known and seen in the table 1, the amount of the ionic character of chalcogenides is small, that is, the basicity is low. Considering the pB values the examined chalcogenides are glass formers. This statement is valuable for many other chalcogenide compositions.

The increase of the amount of basicity over 60 % indicates the diminution of the glass forming tendency in the usual industrial conditions. However, the vitreous state may be obtained but only using rapid or ultra rapid cooling techniques.

The available CCR data [8] allow checking the correlation with pB. In the figure 2 were represented in semilogarithmic coordinates the CCR values calculated for the case of a homogeneous nucleation and for the case of a heterogeneous nucleation and contact angles of 100° and of 60°, versus basicity. The drawn curve evidences for the first time the existence and the nature of this correlation.

Although the available data are few it is showed the inedited fact that the crystallization tendency is minimal, respectively the undercooling in vitreous state tendency is maximal in the central zone of the basicity scale. The CCR increase by the basicity increase over about 60 % is known and easy explainable but the CCR increase when the basicity decreases, i.e. when the amount of the covalent character of the chemical bonds increase is unexpected.
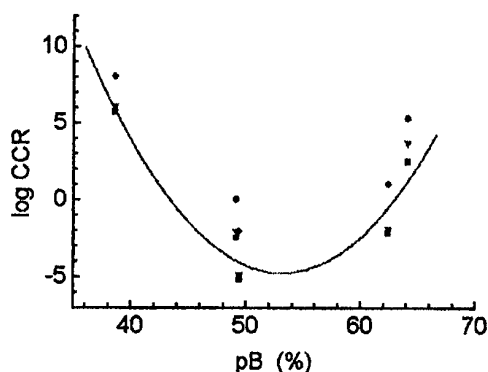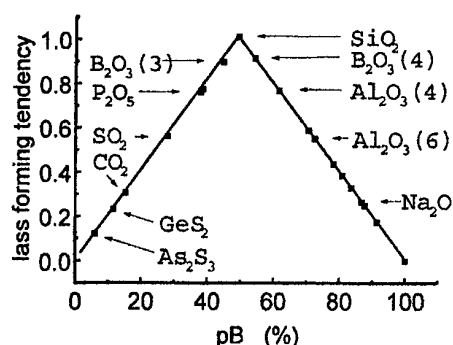

Fig. 2. The CCR dependence on pB.

Fig. 3. Glass forming tendency and pB.

To discuss these new aspects figure 3 was drawn based on the idea that SiO_2 is the best glass former in usual industrial conditions, at a pB value of about 50 %. In principle, figure 3 offers a more suggestive image, comprising also B_2O_3, P_2O_5, SO_2, CO_2, GeS_2 and As_2S_3 as examples. To obtain glasses from more basic compositions, with less complex ionic structures the rate of melts cooling must be correspondingly increased. As was shown above, at pB values between about 60 % and 40 % the glass-forming tendency is high and the respective materials may be quite easily undercooled.

The new revealed effect of the increase of the amount of the chemical bonds covalent character upon the undercooling in the vitreous state tendency deserves a deeper examination in the future. For the moment one may advance the hypothesis that the oxide glass forming tendency diminution towards smaller pB values is probably determined by a certain structure simplification continued, at lower basicities, by the formation of some small, isolated molecules, less active towards exterior. As a result the volatility increases in the same direction up to gases like SO_2 and CO_2. The diminution of the polymerization ability and the increase of volatility seems to be the reasons of the change in the basicity influence on glass forming tendency.

The position of chalcogenides in figure 3 was determined by the practical impossibility to obtain such glasses in the traditional industrial conditions because they important tendency to react with the atmospheric oxygen. In vacuum or in special protective atmosphere they show the glass former property indicated by the low pB values.

4. A new, very general, condition for melt undercooling

The cooling rate of a melt to obtain glass signifies the possibility to dissipate a given heat quantity in a short enough time to preclude crystallization. This process evidently depends on the heat quantity, respectively on the mass of the melt to cool and on the conditions in which the thermal transfer to the environment is realized. In the table 3 some data are presented for two very different situations in which glasses are obtained by undercooling [2, 14].

Table 3. Data for heath dissipation rate V_{hd}. Calculation.

The parameter	Industrial oxidic glasses	Metallic glasses
Cooling rate (C_r) degrees·s^{-1}	10^{-2}	10^5
Undercooled mass, (m) grams	10^6	10^{-1}
Heat capacity (c) J·degrees^{-1}·g^{-1}	0.33 - 1.04	0.12 - 1.13
Heat dissipation rate (V_{hd}) kJ·s^{-1}	3.3 - 10.4	1.2 - 11.3

If in the classical expression of heat transfer the temperature difference is replaced with the cooling rate, i.e. with the temperature difference realized in a second, the transferred heat quantity in the

time unit (V_{hd}) may be calculated:

$$V_{hd} = C_r \cdot m \cdot c \qquad (8)$$

Using the data in table 3, from the last row results the condition:

$$V_{hd} \geq 10^0 \quad (kJ \cdot s^{-1}) \qquad (9)$$

For obtaining glass from any melt heat quantities of the order of units of kJ or greater must be eliminated in each second. Having no terms related to composition, structure, temperature, this condition has a very general character. Only the absence of an adequate technique for rapid heat dissipation may preclude the obtainment of a given melt in glassy state.

On the basis of the figure in the right side of the inequality (9) it may be established a new classification criterion of melts and glasses, taking into account the manner the heat dissipation necessary for undercooling may be realized. For example the present industrial oxidic glasses and also many chalcogenides might be characterized by a V_{hd} smaller than $10^0 kJ \cdot s^{-1}$. Some melts based on heavy element oxides, orthosilicates and metallic alloys might form an intermediate category with V_{hd} of the order of 10^0 $kJ \cdot s^{-1}$. Pure metals might form a category having a greater V_{hd}, value that, eventually, may not yet be realized.

The classification of melts in such categories might indicate in a direct manner in what conditions and with what processing methods become possible their obtainment in a non-crystalline state by undercooling.

5. Conclusions

A brief review of ideas concerning the melts undercooling was done.

In spite of the few available data it was shown the interesting CCR correlation with basicity.

The correlation between the undercooling into vitreous state tendency and melt basicity is outlined. For the first time was evidenced the fact that only the melts with basicities between 40 % and 60 % may be obtained in vitreous state in the present industrial conditions. The diminishing of the glass-forming tendency with the basicity increase above 60 % pB is quite easily explainable by the decrease of the structural melt complexity. When the basicity decreases under about 40 % a new, interesting feature appears, which has to be deeply examined in the future. It seems to be related to the prevalence of covalent bonds resulting in smaller, isolated structures with an increasing tendency to volatilize.

A new very general condition for melts undercooling was deduced, expressed as the rate of heat dissipation V_{hd}. If this condition is fulfilled every melt irrespective of his composition and structure can be obtained in vitreous state. The only restriction is related to the availability of a method able to realize the needed V_{hd}. A possibility of melts classification on the basis of their V_{hd} is suggested.

References

[1] P. Balta, Eugenia Balta, "Physical Chemistry of the Vitreous State", Romanian Academy Press, Bucharest-Romania and Abacus Press, UK, p. 29-58, 177-184, 1976

[2] P. Balta, "Glass technology", Didactic and Pedagogic Press Co., Bucharest, p.19-20, 27-31, 1984 (in Romanian).

[3] C. Spurcaciu, P. Balta, a) Materiale de Constructii, Vol. XV, 3, 162-164 (1985) (in Romanian); b) J. of Non-Cryst. Solids, 84, 120-128 (1986)

[4] I. Gutzow, J. Schmelzer, "The Vitreous State, Thermodynamics, Structure, Rheology and Crystallization" Springer Verlag, Berlin, p. 123-162, 389-411, 1995.

[5] D. Turnbull, M. H. Cohen, in "Modern Aspects of the Vitreous State", London, Butterworths, Vol. 1, p. 38-63, 1960.

[6] A. C. J. Hovermans, H. N. Stein, J. M. Stevels, J. Non-Crystalline Solids, 5, 66 (1970).

[7] D. R. Uhlmann, J. Non-Crystalline Solids, 7, 4, 337 (1972).

[8] Z. Strnad, "Glass-Ceramic Materials", Elsevier, Amsterdam, 19, 1986.

[9] L. Pauling "The nature of the chemical bond", Cornell University Press, Ithaca, New York, 65, 97-102, 1967

[10] P. Balta, C. Spurcaciu, Some new ideas concerning the basicity of glasses, 9-IBAUSIL, Weimar, Sektion 4, 21, 1985.

[11] P. Balta, D. Radu, Rev. Roumaine de Chimie, 40, 10, 977 (1995).

[12] P. Balta, "The basicity of glasses", in Proc. 5th ESG Conference, Prague, June, CD, B4, 3 (1999).

[13] P. Balta, Communication to the Conf. of Chemistry and Chemical Engineering, Bucharest, 1982 (in Romanian).

STRUCTURAL CALCULATIONS FOR AMORPHOUS SYSTEMS USING STRUCTURAL DIFFUSION MODEL

S. Dalgýç, S. Dalgýç, N. Talip, I. Oruç

Department of Physics, Trakya University, 22030 Edirne, TURKEY

We present the results of calculations of the structure factor S(k) and the pair distribution function g(r) for amorphous Iron, Cobalt and Nickel using Structural Diffusion Model (SDM). With the choice of local lattice structure made in this work, the agreement between the calculated and experimental S(k) and g(r) is reasonably good. We suggest that the most promising procedure to choose the local lattice for Structural Diffusion Model calculation of the amorphous systems studied in this work is to start with the fcc crystallographic unit cell.

1. Introduction

This work aimed forwards the studies of the static structure of the amorphous Iron, Cobalt and Nickel using the Structural Diffusion Model (SDM). The most commonly employed description of the structure in amorphous systems is the pair distribution function g(r), which can be deduced by the Fourier inversion of the experimental static structure factor S(k) [1-2]. g(r) is one-dimensional real-space pair distribution function, from which the regeneration of the underlying three-dimensional structure can never be unique.

This work is concerned with a specific model, the Structural Diffusion Model (SDM). It was originally proposed by Baer [3], and has been used to describe the structure of liquids and amorphous solids [4, 5, 6, 7]. At its simplest the SDM characterises the local spatial arrangement of atoms in disordered systems by a lattice L, and viewing the disorder as due to a spatial decay of coherence between local structures, the spatial diffusion process. In its most recent form [8], used in this work, we associate the local structure with a *virtual* lattice L which may include vacancies. The spatial diffusion process is characterised by a statistical parameter, the *structural diffusion* coefficient D. The local lattice is determined by ($3n+1$) parameters - where n is of the order of the number of relevant neighbours- and on a couple of statistical parameters. The latter are determined by an optimisation process, simulated annealing [9], to the local configuration. The expression for the structure factor $S(k)$, or the pair distribution $g(r)$, is related to a spatial, radically evolving, Fokker-Planck equation in reciprocal space. Each of these properties, namely $S(k)$ and $g(r)$, can be evaluated independently, thus avoiding the truncation errors arising from Fourier transforming one into the other. This is precisely what we do in the calculations presented below.

With an increase in complexity of L, namely when the number n approaches $N \approx O\ (10^3)$, the SDM recovers a single configuration, say $\{r^N\} \equiv \{r_1, r_2,..., r_N\}$, produced by the Reverse Monte Carlo Simulation (RMC), originally developed by McGreevy and Pusztai [10]. For $O\ (10^3)$ a single "typical" RMC configuration is expected to give full information on the structure of the system, as far as low order ($n << N$) correlations are concerned. Yet, there is some redundancy in the information contained in $\{r^N\}$. For instance, for two atoms far apart, the atomic positions in the neighbourhood of one atom relative to the other atom become unimportant. Whence if the relevant information sought is on the average configuration, this can be achieved by a distribution law that drastically reduces the number of parameters required. Moreover, while it is hoped that the RMC will eventually "converge" to an optimised structure, both in principle and in practice, this is not always possible. The difficulties of principle, which also apply to the SDM, have been discussed by Evans [11], and by van der Lugt and Winnink [12]. The practical difficulties have been overcome, sometimes, in the RMC method by the introduction of constraints to help with the optimisation procedure. In the end both the RMC and SDM seek to describe the experimental structure factor $S(k)$, or the deduced pair distribution function

g(r). Both these properties are one-dimensional constructs either in reciprocal or real space from which the regeneration of the underlying three-dimensional structure can never be unique.

In this work we have taken the view that the proper choice of local for the description of the pair distribution function of an amorphous system, within the SDM, must be related to the crystallographic structure with which it completes. We specifically propose that a distorted fcc unit cell is proper choice of local lattice structure for amorphous systems whose parent crystallographic structure is fcc.

We show in Section 3 that, in fact, the SDM reproduces the structural of amorphous Fe, Co and Ni. The calculations are carried out by using concise analytical expressions for both $S(k)$ and $g(r)$; these are presented, together with a brief outline of the SDM, in Section 2. This is followed, in Section 3, by the presentation and discussion of our results. Finally, in Section 4, we sum up and briefly comment on the results of our work.

2. Theory

The SDM assumes that the local configuration, i.e., the relative positions of a small group of neighbouring atoms, can always be approximated by a suitable domain in an ordered structure specified by a lattice, L. Further, the spatial disorder is introduced as a random relative displacement of the locally observed lattice structures at different points in space.

The resulting expression for the pair distribution function $g(r)$, has the form of a theta-type infinite series,

$$\rho g(r) \equiv G(r) = \sum_{\nu} G_{\nu}(r) = \sum_{\nu} \rho C_{\nu} \exp\left(-W b_{\nu}\right)\frac{\sin b_{\nu} r}{b_{\nu} r} \tag{1}$$

Here the sum extends over all points (shells) of the reciprocal lattice $L^{*}=\{b_{\nu}\}$, ρ is the density and C_{ν} is a *unit cell structure factor* given by $C_{\nu} = C(b_{\nu})$, where

$$C(k) = \left|\frac{1}{n}\sum \exp\left(i k \cdot a_{\sigma}\right)\right|^{2} \tag{2}$$

with the sum extending over the n points in the unit cell. $W = W(r) > 0$ serves as a *width function* which is a measure of the decay of coherence between local structures at two localities separated by a distance r. $W(r) \approx Dr$ when $r \to \infty$,. Moreover, $W(r)$ decays faster than r when r goes to zero, i.e.

For reasons of convenient analytic evaluation, we make use of the following specific form of $W(r)$,

$$\frac{dW(r)}{dr} \to 0 \quad as \quad r \to 0.$$

previously introduced by Egelstaff and Schofield [13], namely,

$$W(r) = D\left[\sqrt{r^2 + r_0^2} - r_0\right] + W_0 \tag{3}$$

where r_0 is the average exclusion parameter.

For disordered systems such as amorphous solids and liquids, an optimal L is not strictly unique because of an element of randomness present in the local arrangement of atoms. Consequently, it is possible to choose for L increasingly complex lattices possessing larger unit cells, together with coefficients D, giving increasingly accurate modelling for given $S(k)$ data. Indeed, in the limit of a very large cell having the size of the typical volume used in computer simulations with periodic boundary conditions, by putting $D = 0$ we can choose any representative configuration of the atoms as defining the unit cell of L. We denote any such macroscopically complex lattice by L_∞. In practice, the usefulness of the SDM lies in finding a relatively small local structure which reproduces with sufficient accuracy the $g(r)$ data. The details of the structure and its statics are then hidden in the spatial random process, exhibited by $D > 0$.

The expression for $g(r)$ used here is a generalisation of (1) following from the consideration of an additional spatial random process taking into account the effect of vacancies of the local structure. In its simplest version it leads to the consistency requirement

$$g(r) - 1 = \left(\frac{\rho_L}{\rho}\right)^2 [g_L(r) - 1] \quad (g(r) > 0) \tag{4}$$

where $g_L(r)$ is the SDM expression (1) with the correct density ρ_L for L and ρ is the experimental density. We carried out the optimization results with respect to the local structure L and the statistical parameters D and r_0 using (4).

With the above choice we fit directly to the $S(k)$ experimental data and use the fact that the Fourier transform of $g(r)$ can be evaluated analytically, which is particularly important in the low k range [14]. We have

$$S(k) = \sum_v S_v(k) = \sum_v \int G_v(r) \exp(i\mathbf{k}\cdot\mathbf{r}) d\mathbf{r} \tag{5}$$

Moreover, choosing (3) we have

$$S_v(k) = 2\pi r_0^2 D C_v b_v \exp\left[(Dr_0 - W_0)b_v^2\right] \frac{1}{k} \left\{\frac{K_1(X_{v-})}{X_{v-}} - \frac{K_1(X_{v+})}{X_{v+}}\right\} \tag{6}$$

where $K_1(X)$ is the modified Bessel function of the second kind and

$$X_{v\pm} = X_v(\pm k) = r_0 \sqrt{(Db_v^2)^2 + (b_v \pm k)^2} \tag{7}$$

The optimization was carried out with respect to [13],

$$\chi^2 = \sum_i y_i^2 \left[(X(y_i)) - X_{\exp}(y_i)\right]^2 / \sigma^2 \tag{8}$$

where σ is related to the variance at each step of the minimization process.

In Eq (8) $X_{\exp}(y_i)$ denotes either the experimental or simulated structure factor or pair distribution function, y stands for either r or k, and $X(y_i, \mathbf{p})$ the $S(k)$ or $g(r)$ obtained from the SDM with the set of parameters $\mathbf{p}$.

3. Results and discussion

All the systems considered in this work have, in their crystalline state, a fcc crystallographic structure that we take as our initial local lattice. a_i ($i = 1, 2, 3$) denote the elementary vectors, and α_i ($i = 1, 2, 3$) denote the internal angles. We also specify the initial position vectors s_k ($k = 1$, ...,n) of the 8 atoms inside the unit cell. a_{min} denotes the minimum value allowed for nearest neighbour distances during the iteration cycle; any lattice with smaller distances, produced in the iteration cycle, is rejected.

In the simulation annealing process the $(3n+1)$ parameters of L_n, plus the two parameters D and r_0 defining $W(r)$ (we keep W_0 fixed) are varied in random steps, and χ^2 calculated by using Eq (8). The change in the parameters is then accepted or rejected according to the probability law which, say, for move m reads

$$P = \begin{cases} 1 & \chi_m^2 < \chi_{m-1}^2 \\ \exp\left[-\beta\left(\chi_m^2 - \chi_{m-1}^2\right) / \chi_{m-1}^2\right] & \chi_m^2 > \chi_{m-1}^2 \end{cases} \tag{9}$$

Convergence to the present accuracy is normally achieved in about 60 moves.

We only compare directly in Figures 1-3 our results with the experimental data of $S(k)$ and with the $g(r)$ deduced from the same experimental data by Fourier transform.

3.1. Amorphous Iron (a-Fe)

The structure factor of a-Fe has been measured by Lauriat [15]. The latter were measured using both polarized x-ray and polarized neutron scattering on a sample of ex-carbonyl amorphous iron obtained from $Fe(CO)_5$ molecular gas decomposed by continuous electrical discharges in neon at low temperature. Both S(k) are shown in figure(1-a). We note that the differences between the

experimental S(k) in a-Fe not very large, bearing in mind the different techniques used in either sample preparation and types of radiation used. In figure (1-b) we also compare with the x-ray scattering data of Ichikawa [16].

In our calculations we have used fixed bond length the value $2.55\ A^o$, the average exclusion parameter $0.74\ A^o$ and diffusion constant 0.0102. Also our choice of number density is $0.08486\ \text{Å}^{-3}$ [17] and the value of angles is $60\ ^0$.
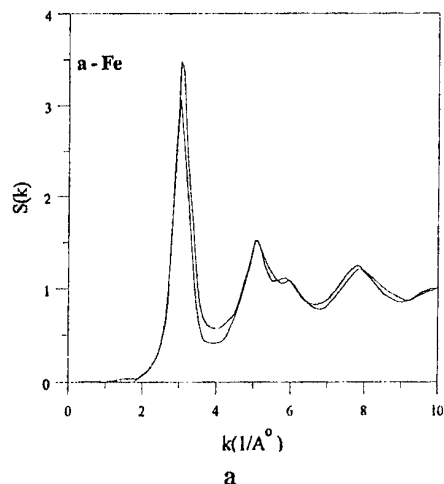

Fig. 1a. Static structure factor for a-Fe using the
Polarized X-ray scattering data and Polarized
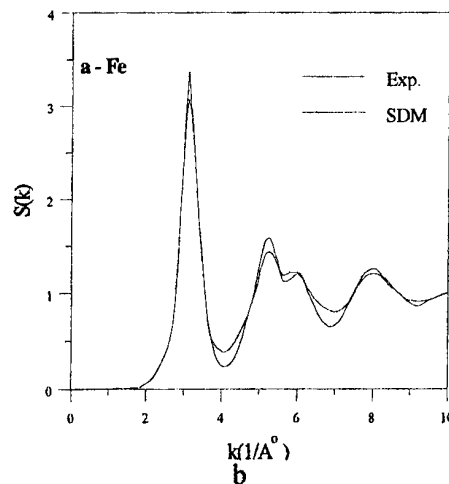neutron scattering data in Ref. [15].

Fig . 1b. Static structure factor for a-Fe using
the X-ray scattering data in Ref. [16].

The results for S(k) using the SDM are reasonably good. The general shape and positions of the peaks are well reproduced in all the system studied here. However the calculated main peak heights are, in most cases, lower than the experimental ones also our SDM calculation do not reproduce in a completely satisfactory manner the full details of the split second peak. Even though the correct trends are always present, it is possible, within the SDM to improve the quality of the calculated S(k)'s by using a more sophisticated dispersion law for W(r) as suggested in a previous work [18].

We have also calculated the corresponding pair distribution function , g(r)'s are obtained by the Fourier inversion of our S(k) results. Our g(r) result is shown in figure(1-c) for a-Fe.

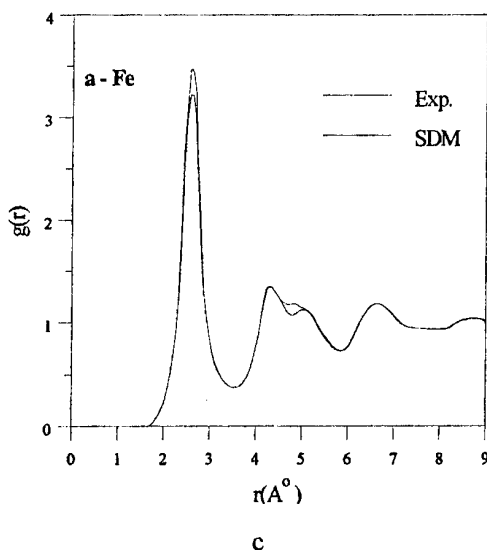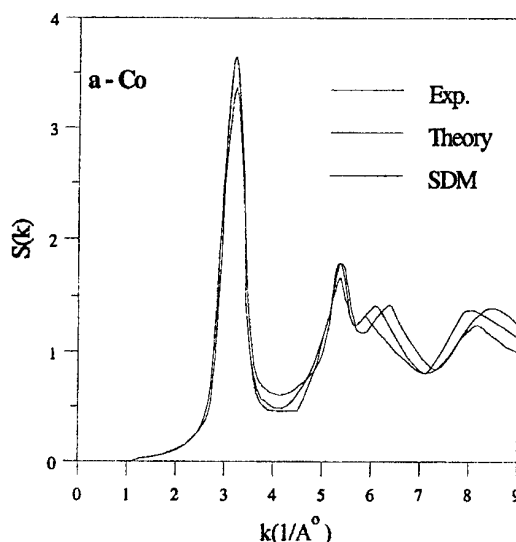
Fig. 1c. Pair distribution function for a-Fe using the X-ray scattering data in Ref. [16].

It is compared with the corresponding g(r) deduced from experimental data. It was obtained from the diffraction pattern of a thin film of amorphous material prepared by law-temperature condensation in high vacuum [16]. Our g(r)'s calculations reproduce well the shape, position and height of the peak of g(r) and account for the small irregularity in the third minimum.

3.2. Amorphous Cobalt (a-Co)

We present, in figure (2-a), the results of our SDM calculation for a-Co. The figures compare our result with the electron diffraction data of Leung and Wright [19]. We have also included, for comparison, the theoretical S(k) obtained by Sadchev and Nelson [20] using a Ginzburg-Landau theory based on the symmetries of a perfect icosahedral solid in a four-dimensional curved space. SDM result shows a lower S(k)-maximum with experimental results. For a-Co, we have used fixed bond length the value 2.45 A^o, the average exclusion parameter 0.72 A^o and diffusion constant 0.0098. Also our choice of number density is 0.09094 $Å^{-3}$ [17] and the value of angles is 60 ^{0}.

a

Fig. 2a. Static structure factor for a-Co using the Electron diffraction data in Ref.[19] and Theoretical calculations in Ref.[20].

We used the SDM result of S(k) to calculate the pair distribution function for a-Co. It is shown in figure (2-b). The results for Co were obtained by scattering electron diffraction of a thin film prepared by ultra-high vacuum at 4 °K [19]. The experimental results for amorphous systems at law temperatures reveal that the width of the first peak of g(r) is more narrow relative to the liquid phase as a result of more restricted particle displacement. For the same reason the short range order extends to large distances than for liquids. Some authors refer to third behaviour as intermediate short range order [21]. Moreover the second peak splits in to two sub peaks. This feature of g(r) has sometimes been taken to be as a sign of the true glassy state [22]. Another common feature of the g(r)'s of amorphous systems is an irregularity is also obtained in the third minimum. This behaviour is also obtained in results of computer simulation. The second peak splits gradually in to two subpeaks as the as the liquid is cooled down to temperatures below freezing [23,24].
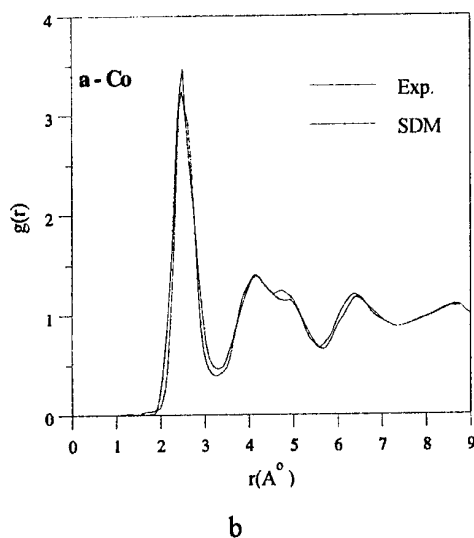
Fig. 2b. Pair distribution function for a-Co using the Electron diffraction data in Ref. [19].

3.3. Amorphous Nickel (a-Ni)

Our SDM fitting of the a-Ni structure factor , figure (3-a) , is in excellent agreement with the experimental data of Ichikawa [16] , except both second peak and minimum the height of the second peak is lower than experiment and also the minima is below experiment; otherwise our fitting follows closely the experimental data. We have used fixed bond length the value 2.48 A^o, the average exclusion parameter 0.69 A^o and diffusion constant 0.0099. Also our choice of number density is 0.09141Å^{-3} [17] and the value of angles is 60 ^{0} for amorphous a-Ni.

Our result for g(r), is shown in figure (3-b) along with the X-ray scattering data [16]. It is very good and it shows a marked shoulder on the high-r side of the second peak. The observed properties for a-Ni are similar to a-Fe and a-Co.
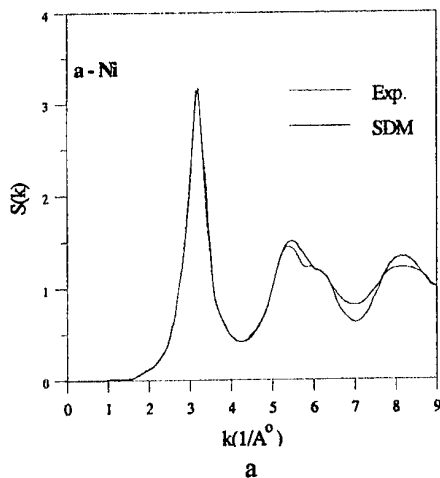

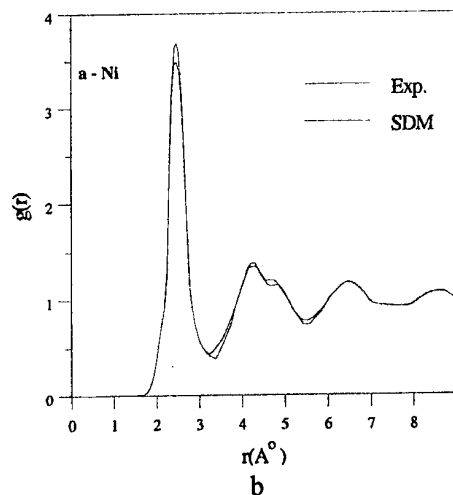Fig. 3a. Static structure factor for a-Ni using the X-ray scattering data in Ref. [16].

Fig. 3b. Pair distribution function for a-Ni using the X-ray scattering data in Ref. [16].

4. Conclusions

We have analysed the structure of a-Fe, a-Co and a-Ni using the Structural Diffusion Model (SDM) which, while based on a similar philosophy, is computationally simpler. We have also described satisfactorily the typical short and intermediate-range order observed in a-Fe, a-Co and a-Ni. Moreover we put forward the proposition that the local lattice structure used in this work is the proper choice of local lattice for a SDM description of the atomic arrangements of all the amorphous solids whose parent crystallographic structure is fcc. It is also likely that a similar choice of local lattice is capable to describe the correct g(r) of amorphous systems whose crystallographic structure is hcp.   As a result of our calculations we suggest that the small peak, or shoulder, following the second peak of g(r) is a real feature that reflects, weakly, the third-neighbour peak in the crystalline phase of the tetrahedrally bonded amorphous systems. Within the SDM description of g(r) it is not possible to assert whether the system is in the amorphous phase or, indeed, how it has reached that phase. For the latter we would need information on the kinetic processes involved in the transition, which no static model or theory of the structure provides.

Finally, the following comments are in order. The structural disorder in an amorphous solid implies a non-zero configurational (structural) entropy, $S > 0$. The SDM offers the possibility of obtaining compact expressions for the structural entropy [25], a property that is difficult to study using standard statistical theories or computer simulations.

The SDM provides a modelling by analytic functions which are computationally convenient and can produce result for both the static structure factor and pair distribution function as well their spectral representations. We propose that the SDM is a convenient, simple model to describe the structure of amorphous systems.

References

[1] G. S. Cargill, Solid State Phys. **30**, 277 (1975).
[2] Y. Waseda, The Structure of Non-Crystalline Materials, McGraw-Hill, New York (1980).
[3] S. Baer, Physica **A87,** 569 (1977); Physica **A91,** 603 (1978); Chem.Phys. **39**, 159 (1979); J.Physique **46,** C9-145 (1955).
[4] S. Baer, E. Canessa, J. M. Lopez, M.Silbert Physica **B154,** 8 (1988).
[5] J. M. Lopez, M. Silbert Solid State Comm **66**, 585 (1989).
[6] S. Baer, J. M. Lopez, M. Silbert J. Non-Cryst Solids **117/118**, 180 (1990).
[7] V. Petkov J. Phys: Condens Matter 7, 5745 (1995).
[8] S. Baer, L. Gutman, M. Silbert J. Non-Cryst Solids **192/193**, 106 (1995).
[9] S. Kirpatrick, C. D. Gelatt, M. P. Vecchi Science **220**, 671 (1983).
[10] R. L. McGreevy, Pusztai Mol.Sim.1, 359 (1989).
[11] R. Evans Mol. Sim.4, 409 (1990).
[12] W. van der Lugt, M. Winnink Physica **B 191**, 217 (1993).
[13] P. Egelstaff, P. Schofield Nucl Sc Eng. **12**, 260 (1962).
[14] L.Gutman, S. Baer Mol. Phys. **73**, 715 (1991).
[15] S. Sachdev, D. R. Nelson, Phys.Rev. **B 32**, 1480 (1985).
[16] T. Ichikawa, Phys. Stat Solidi A **19**, 707 (1973).
[17] C. Kittel, Introduction to Solid State Physics, 6th edition, John Wiley and Sons, Inc. (1986).
[18] E. Canessa, M. Silbert, S. Baer, Z. Phys.Chem. **156**, 463 (1988).
[19] P. K. Leung, J. G. Wright, Phil.Mag. **30**, 185 (1974).
[20] S. Sachdev, D. R. Nelson, Phys. Rev. **B 32**, 1480 (1985).
[21] P. H. Gaskell, J. Physique **46**, C8-3 (1985).

[22] H. R. Wendt, F. Abrahams, Phys. Rev. Lett. **41**, 1244 (1978).
[23] K. J. Smolander, Phys. Scripta **31**, 427 (1985).
[24] S. K. Lai, S. Wang, K. P. Wang, J. Chem Phys. **87**, 599 (1987).
[25] S. Baer, B. Ilan, J. Phys Condens. Matter **9**, 7785 (1997).

POSSIBLE HIGH TEMPERATURE SUPERCONDUCTIVITY IN CHALCOGENIDE GLASSY SEMICONDUCTORS

K. D. Tsendin, A. V. Prihod'ko[a], B. P. Popov[a]

A. F. Ioffe Physico-Technical Institute, Russian Academy of Sciences
194021 Saint-Petersburg, Russia
[a]Saint-Petersburg State Technical University, 195251 Saint-Petersburg, Russia

High T_c superconductivity in composite system of selenium matrix with globular Y-Ba-Cu-O is discussed in relation to the experimental results.

1. Introduction

In our recent paper [1] we have elaborated the model of superconductivity, which may be realized in the system of negative – U centers with a large concentration. The model is based on the theoretical results of paper [2]. It is supposed in [1], that manifestation of negative – U centers model of superconductivity (NUCS – model) may be found in chalcogenide glassy semiconductors, because these substances are known as matters with a large concentration of negative – U centers. Then in the present paper we discuss several experimental results, which might confirm our hypothesis.

2. Analysis of experimental data

The present paper is devoted to investigation of superconductivity of the samples, which consist of globules of well known high temperature superconductor (HTSC) with $Y_1Ba_2Cu_3O_7$ composition which are embedded in glassy Se matrix. The details of samples preparation have been described in [1], and here we briefly remind the most important ones only. A little bubble (volume ~ 1 mm^3) of a-Se mixture with micro-crystalline pieces of $Y_1Ba_2Cu_3O_7$ (or globules) are located between two intersecting wolfram wires. Diameters of wires are equal to 50 μm. The bubble has been melted by Joule heating of wolfram wires, melting substance entered between wires and separated them at distance L. Micro-crystalline pieces of $Y_1Ba_2Cu_3O_7$ – globules- have linear size about several micrometers and occupy approximately 14% of whole volume then all of them have been separated by a-Se. Two sets of samples have been investigated.

The first set consists of low-resistance samples with resistance R at room temperature of order R~1 Ω. This value can be estimated from date of Fig. 1a (curve 1). The distance L between electrodes for these samples has a minimum value L~1 micrometer and so L is less than linear size of globules one can conclude that there are several globules which join two contacts. This conclusion may be confirmed by estimation of the conductivity value σ ~ L/RS. One can obtain for typical square of globule cross-section S ~10 μm^2 the conductivity value of order ~10^3 Ω^{-1} cm^{-1}, which rather well coincides with the conductivity of $Y_1Ba_2Cu_3O_7$ at room temperature. The superconductivity phase transition temperature T_c for these samples approximately coincides with that one for $Y_1Ba_2Cu_3O_7$ ($T_c{\approx}90$ K) [1]. The value of critical current density, which can be estimated from the initial current jump of curve 2 (Fig. 1a) at U=0, equals to ~ 2 A/cm^2 and coincides with known value for HTSC [2].

Then one can conclude, that electrical properties of of low-resistance samples at all temperatures: T>T_c and T<T_c are governed by HTSC.

The second set consists of high-resistance samples with R~10^4 Ω at room temperature (see Fig. 1b, curve 1). The typical distribution of HTSC globules through the sample cross-section obtained by X-ray microanalysis is shown on Fig. 2, which is taken from paper [1]. It is very well seen, that globules are separated and there is not the continuous current path trough them. Solid line has been depicted by authors to show the possible current path through the several globules and a-Se inter-

these layers may be taken as ~10 μm. The distance between electrodes for these samples has a value more than for the low-resistance samples and one can use for estimation the value L~50 μm. If one takes the linear dimension of globule ~5 μm as the diameter of current path cross-section then the conductivity value of order ~10^{-6} Ω^{-1} cm^{-1} may be obtained at room temperature. This value very differs from the value ~10^{-12} Ω^{-1} cm^{-1} for pure a-Se. It is known that conductivity of a-Se very depends on the doping with oxygen [3], then we can suppose that a-Se channels, which join globules and are depicted by solid line (Fig. 2) consist of glassy selenium doped with oxygen catched from air or from globules.

But we would like to emphasize that in any case the resistance of high-resistance samples at room temperature ($T>T_c$) is not controlled by HTSC.

Phase transition temperature T_c for samples from the second set is the same as for $Y_1Ba_2Cu_3O_7$ [1] and one can see the direct superconducting current through whole sample, which existence at U=0 and T=77 K(Fig 1b, curve 2). Hence a conclusion was made in [1] that Josephson contacts are formed between HTSC globules embedded in the a-Se matrix, making possible the superconducting transport in these samples.
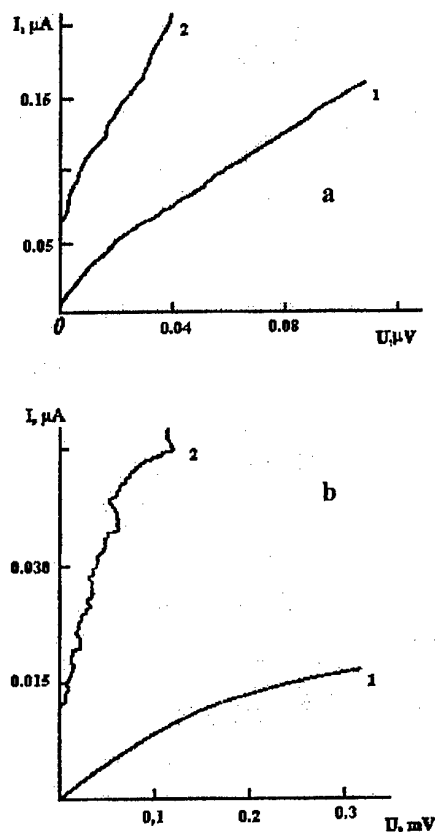

Fig. 1. I-V characteristics of (a) low- and (b) high-resistance samples at temperatures T = 297 (1) and 77 K (2).

The most important fact we would like to emphasize in present paper consists in the following. It is known presently that the correlation length ξ in HTSC materials is small and equals to 10-15 Å [4, 5]. Consequently, the thickness of the Josephson contacts must be of the same order of magnitude. At the same time, it can be seen from Fig. 2 that the a-Se spaces between HTSC globules have linear dimensions of several micrometers, i.e. 10^3 times ξ. Hence follows that the superconducting properties of the sample as a whole can only be accounted for under the assumption that a-Se in spaces between the globules also would possesses superconducting properties with T_c not lower than that of $Y_1Ba_2Cu_3O_7$. This assumption does not refer to the entire volume of selenium known not to

exhibit high-temperature superconductivity. We mean here only the channels appearing between the HTSC globules in electric field as a result of switching, shown schematically, as the guide to the eye, by the solid broken line in Fig. 2. It is known that the transition of a thin Se layer from the state with high resistance to that with low resistance (switching effect) occurs in an electric field with strength on the order of 10^5-10^6 V/cm [6]. At the same time, the external field strength in [1] did not exceed 10^2 V/cm, even with the effective thickness of the a-Se layer taken to be ~0.1 μm. Thus, it can be assumed that a-Se presents between HTSC globules has unusual properties and is switched in weak external electric fields or there are strong internal electric field in the vicinity of HTSC – a-Se boundary.
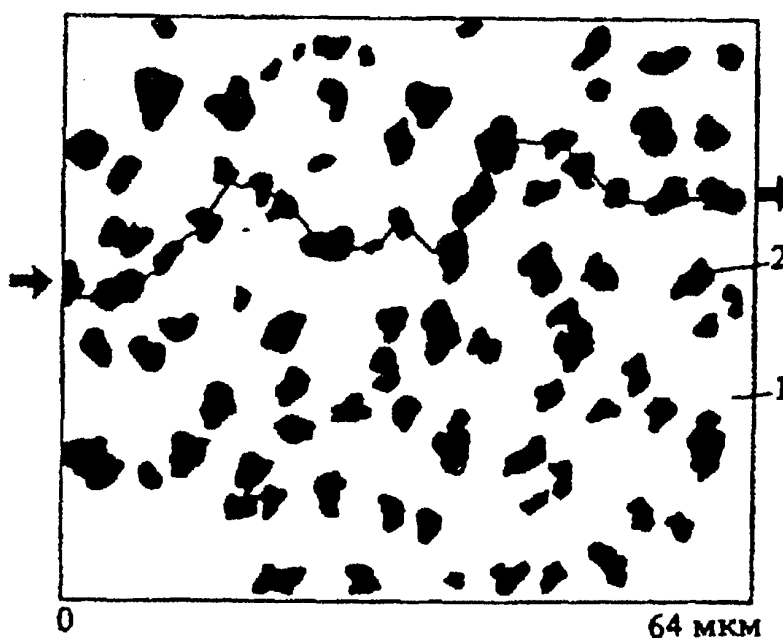

Fig. 2. Distribution of elements over the sample cross-section, obtained by means of X-ray microanalysis (reproduced from [1]). (1) Selenium and (2) HTSC. The solid, broken line showing the path of the through current represents a set of superconducting Se channels connecting adjacent HTSC globules.

It is for channels of this kind, appearing as a result of switching in chalcogenide glassy semiconductors (CGS), whose representative Se is, that a model of superconductivity has been proposed recently [7], based on the concept of centers having negative effective electron correlation energy U (negative-Ucenters). At present, it can be considered a well-established fact that it is the negative-U centers that are the predominant type of native defects in chalcogenide glassy semiconductors. For the reason of negative U, electrons (holes) are effectively attracted when residing on a defect and thus form pairs of electrons or holes, which are bosons. It was assumed in [7] that, at a sufficiently high concentration of negative-U centers, their states may form bands of delocalized pairs of electrons or holes, whose Bose condensation gives rise to superconductivity. Just the simplest CGS - glassy Se, was considered in [7] as an example. Fig. 3 shows schematically the band of electron and hole pairs: D(-) and D(+) bands made of non-superconducting metals exists only in strong electric fields. The parameters of negative-U centers in a-Se can be found from drift mobility measurements. The thermal activation energy of hole drift in the valence band is 0.14 eV [3], which corresponds to capture of holes into states of the electron pair. Therefore, it can be assumed that the center of the D(-) band lies 0.14 eV above the top of the a-Se valence band. The same figure shows the expected energy of optical ionization of the D(-) states, which, according to a simple theory of negative-U centers, must be twice the thermal ionization energy.

Thus, the Bose condensation of delocalized electron pairs in the D(-) band arising from the

D(-) level may be thought of as being responsible for the superconducting properties of the selenium channel connecting HTSC globules. It was believed in [7] that the superconducting channel appearing upon switching in CGS samples with electrodes
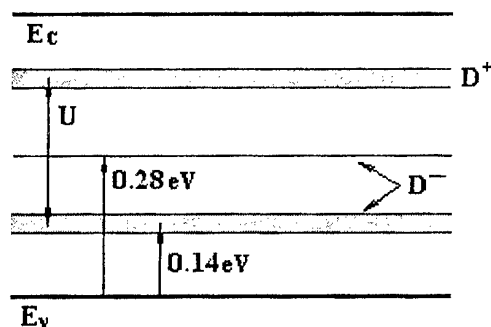

Fig. 3. Band energy diagram of a- Se. The arrows show the thermal and optical transitions of holes to the D^- states of the negative-U center. Two dark bands present the bands of delocalized electron pairs - D^- and D^+ bands, whose Bose condensation is responsible for the superconductivity.

By contrast, in the case in question, it should be considered that the channels between the HTSC globules arise in samples prepared from a mixture of HTSC and a-Se already on applying a weak measuring field. This distinction suggests that the role played by globules located at the channel ends consists in reducing the field strength necessary for superconductivity to appear in the a-Se channel. A large number of negative-U centers may exist in the channel due to self-compensation processes induced by doping with oxygen [8]. Additional concentration of negative-U centers arise during the switching effect in the internal electric field or in the weak external electric field which is used for current observation. The superconductivity in the system of negative-U centers in the channel may be induced by superconductivity phase transition in micro-crystalline pieces of $Y_1Ba_2Cu_3O_7$ which occupy two end of each channel. It was suggested in [7] that a situation similar to that observed in CGS may arise in organic polymers in which negative-U centers also, possibly, exist. The results of recent studies [9, 10] confirm this assumption. In these investigations, as also in the present study, the superconducting state was observed in channels of organic polymers connecting electrodes made of superconducting metals.

3. Conclusion

The experimental evidences of possible high temperature superconductivity in chalcogenide glassy semiconductor Se have been revealed and discussed for samples which consist of globules of well known HTSC with $Y_1Ba_2Cu_3O_7$ composition which are embedded in glassy Se matrix. The superconductivity possibly takes place in Se channels with linear dimension of several microns which arise between $Y_1Ba_2Cu_3O_7$ globules due to may be switching effect. The parameters of channels determined for normal and superconductivity states have been described by negative-U centers model rather well.

References

[1] A. V. Prihod'ko, S. V. Kozirev, V. F. Masterov, Superconductivity: physics chemistry engineering, **3**, 1130 (1990).
[2] I. A. Graboy, A. R. Kaul', Yu. G. Metlin, Him. i tehnolog. VTSP, **6** (Itogi nauki and tehniki VIINITI AN USSR), Moscow, 143 (1989).
[3] G. B. Abdulayev, D. Sh. Abdinov, Fizika Selena. ELM, Baku (1975).
[4] T. K. Worthington, W. J. Gallagher, T. R. Dinger. Phys. Rev. Lett., **59**, 1160 (1987).
[5] L. Forro, J. Y. Henry, C. Ayache, P. Stamp, Phys. Lett. A, **128**, 283 (1988).
[6] A. V.Prihod'ko, A. A. Chesnis, V. A. Bareykis, Fiz. Tehn. Polupr., **15**, 536 (1981).
[7] B. P. Popov, K. D. Tsendin, Tech. Phys. Lett., **24**, 265 (1998).
[8] K.D. Tsendin, the paper in the present issue.
[9] A. N. Ionov, V. A. Zakrevskiy, I. M. Lazebnik. Pis'ma Zh. Tekh. Fiz., **25**, 36 (1999).
[10] A. N. Ionov, V. A. Zakrevskiy, Pis'ma Zh. Tekh. Fiz., **26**, 34 (2000).

THEORETICAL POSSIBILITY OF INCREASING OF SUPERCONDUCTIVITY TRANSITION TEMPERATURE IN HIGH TEMPERATURE SUPERCONDUCTORS BY REPLACING OXYGEN WITH CHALCOGEN

K. D. Tsendin, D. V. Denisov

A. F. Ioffe Physico-Technical Institute, St.Petersburg, Russia

The paper discusses the experimental data that evidence the increase of the critical temperature of superconductivity in Y-Ba-Cu-O system, when doped with chalcogens.

1. Introduction

In the present paper the experimental data which evidence of increasing of superconductivity transition temperature (T_c) in high-temperature superconductor of YBaCuO system doped with chalcogenides have been discussed. The interpretation of experimental data has been done in the frame of the negative-U centers model. The opportunity of changing and, probably, increasing of temperature of superconducting transition in materials such as YBaCuO by replacement of atoms of oxygen by atoms of chalcogenides is considered. It is supposed that if someone could replace large amount of oxygen with chalcogenides (for example sulfur) the significant increasing of T_c can be obtained.

2. Theoretical model and calculations

The $Y_1Ba_2Cu_3O_7$ material is the high-temperature superconductor, its temperature of transition is equal to $\approx 90K$. As it is known, the standard theory BCS [1], describing superconducting transition in metals, explains processes in high-temperature superconductors (HTSC) not very well. So for example, the temperature of transition in BCS is described by the formula

$$T_c = 1,14 \cdot \hbar \cdot \omega_d \, exp(-1/g \cdot v) \qquad (1)$$

Where g is a constant of electron-lattice interactions, v – density of electron states at Fermi level and ω_d – characteristic frequency. If we describe high-temperature superconducting transition with this formula then we obtain T_c approximately twice less than experimental value. Nowadays many alternative models are created for the HTSC description. The present approach are based on concepts of the model of the localized pairs of electrons [2] and negative-U center model [3]. In these models electronic pairs, in contrast to BCS theory, exist already at T > Tc. Using the model [2], it is possible to show how T_c is changing with change of the matrix element of a electron transition from one center of localization to another. It will be shown that adding of chalcogenides into superconductor under studding increases T_c. This statement proves to be true by experiments [4].

The given model is described by Hubbard Hamiltonian

$$H = -U \cdot \sum n_{i\uparrow} \cdot n_{i\downarrow} + \sum t_{ij} \cdot a_{i\sigma}^+ \cdot a_{j\sigma} \qquad (2)$$

Where $n_{i\sigma} = a_{i\sigma}^+ \cdot a_{i\sigma}$ are occupation numbers, $a_{i\sigma}^+$ and $a_{i\sigma}$ are operators creating and annihilating electrons with spin σ on center i, and t_{ij} – matrix element of transition between the nearest centers of localization (negative-U centers). It is considered that U > 0 and $t_{ij} \ll U$. Negative values of -U lead to attraction between electrons with opposite spins on the same negative-U center. At low temperatures Hamiltonian (2) leads to occurrence of superconducting correlation between electron pairs. The second term of Hamiltonian (2) corresponds to kinetic energy of band movement (width of an one electron band $\approx |t_{ij}|$), and the first - to interaction between electrons with energy U. In the BCS model the width of the band is great, and consequently interaction is examined as perturbation. The main difference of investigated model from the BCS model is that the width of the band is considered small in comparison with U, so the second term of Hamiltonian (2) is examined as perturbation.

At T=0 all electrons are in the pairs localized on the negative-U centers. At $T \neq 0$ system represents assembly of empty centers, the centers occupied with one electron, and the centers occupied with two

electrons. Number of negative-U centers occupied with one electron is proportional to $n \cdot \exp(-U/T)$, where n is concentration of electrons. When $T \ll U$, amount of single electrons is a very little in comparison with number of pairs, then concentration of single electrons can be neglected. In this case, solving the Hamiltonian (2), we are obtaining the formula (3) for temperature of superconducting transition [2].

$$T_c = W \cdot (1-2v)/ln(v^{-1}-1) \qquad (3)$$

Where $W = 2zt^2/U$ – width of the pairs band, z – number of the nearest neighbors of the given center, v – relative concentration of electronic pairs (v $= n/2 \cdot N$, N – concentration of negative-U centers).

As it is described in the paper [3] electron-lattice interaction results in negative correlation energy that intrinsic defects (D), being negative-U centers, get a various charge ($D^{+, 0, -}$). Strong interaction of two electrons results in that the reaction $2D^0 \rightarrow D^+ + D^-$ becomes exothermic. Such reactions may occur in superconductors YBaCuO, they are fair for atoms of copper and run under the following circuit (4)

$$2Cu^{2+} \rightarrow Cu^{3+} + Cu^+ \qquad (4)$$

Presence of ions $Cu^{3+, 2+, 1+}$ was confirmed experimentally [5]. From the statistical point of view reaction (4) means that ions of copper is spending equal time in Cu^{3+} and Cu^+ states, exchanging charges with neighbors. It is assumed and proved in [3], that $Cu^{3+, 2+, 1+}$ states may be considered as $D^{+, 0, -}$ states of the negative-U centers. This allows us to count, that ions Cu in lattice YBaCuO (Fig. 1) are the negative-U centers.
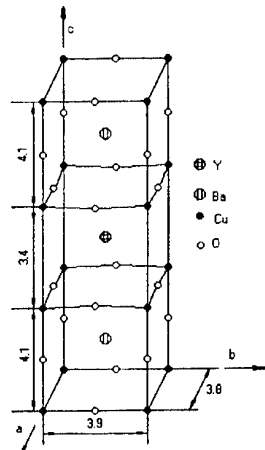

Fig. 1.Structural lattice of $Y_1Ba_2Cu_3O_7$.

Analyzing the formula (3) it is easy to see, that for increasing of the T_c it is necessary to increase t which is a matrix element of electron transition from one negative-U center to another. In structural lattice these centers are separated from each other by oxygen (Cu-O-Cu, direction b), so it is necessary to examine interaction between copper and oxygen. It is needed because a direct matrix element of electron transition from one atom of copper to another (distance between them is 3,9Å) is several times less than the matrix element calculated for atoms Cu and O on distance 1,95Å. The matrix element of this transition will be approximately estimated in two-nuclear molecule CuO.

Possible way of increasing t is replacement of atoms of oxygen by elements of the same group. We examine the sulfur. For calculations of the matrix elements of electron transition from the copper ion to the ion of oxygen or sulfur (6) the electronic functions (5) entered by Slater [6] were used.

$$Cu \ (3d\text{-state}) \ \Psi_{Cu} = (x^2-y^2) \cdot exp \ (-cCu \cdot r/3)$$
$$O \ (2p\text{-state}) \ \Psi_O = x \cdot exp \ (-cO \cdot r/2) \qquad (5)$$
$$S \ (3p\text{-state}) \ \Psi_S = x \cdot r \cdot exp \ (-cS \cdot r/3)$$

Where cCu, cO, cS is the effective shielded charges for the given elements.

$$t_{CuO} = \int \Psi_{Cu}(r) \cdot H(\Psi_O(r-R))dV$$
$$t_{CuS} = \int \Psi_{Cu}(r) \cdot H(\Psi_S(r-R))dV \qquad (6)$$

Where R is a distance between atoms, $H = -\nabla^2 - \dfrac{cCu}{r_1} - \dfrac{cO}{r_2}$, cO in the second integral (6) is

replaced by cS. Matrix elements of transition t_{CuO} and t_{CuS} are showing how transition of electron changes in process of atoms removal from each other (Fig. 2). From Fig. 2 it is seen (distance more than 1,5Å) that realization of a situation when the matrix element t_{CuS} for sulfur will be greater, than t_{CuO} for oxygen, can be obtained. Even a small difference of inter-nuclear distances in bonds CuO and CuS leads to significant difference in values t_{CuO} and t_{CuS}. For example, in the lattice $Y_1Ba_2Cu_3O_7$ distance between atoms Cu and

O 1.95Å, so t_{CuO} is equal -0.609 Ry. If in the same structural lattice we replace some of atoms of oxygen by atoms of sulfur we should gain some increase of T_c, because the matrix element of transition Cu-S on distance 1.95Å is equal -0.929 Ry. In the ideal case the transition temperature (if all atoms would be replaced) would be increased by 2.3 times. But it is not known constants of a structural lattice for full replacement of atoms O by atoms S. If the constant b of the lattice will decrease, that was shown in experiments [4], both t_{CuO} and t_{CuS} significantly would increase, so T_c would be increased sharply. If inter-nuclear distances will increase (this conclusion is possible, comparing molecules CuO and CuS), T_c will exceed 90K up to some critical distance equal 2,26 Å because t_{CuS} is more than t_{CuO}. In Table 1 matrix elements of transition values of examined atoms in various bonds are shown. These data shows that in simple bonds absolute value t_{CuS} normally exceeds t_{CuO}. As we expect, in HTSC will be maintained the same tendency, and T_c will increase in the case of sulfur addition.
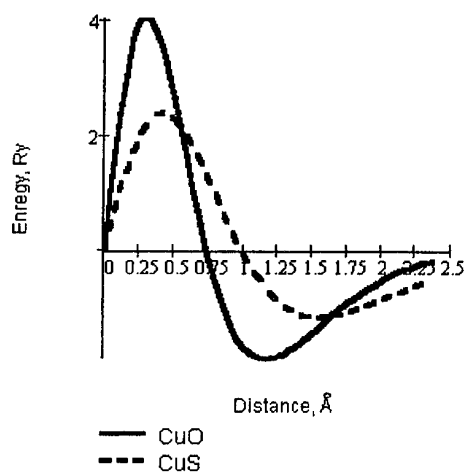

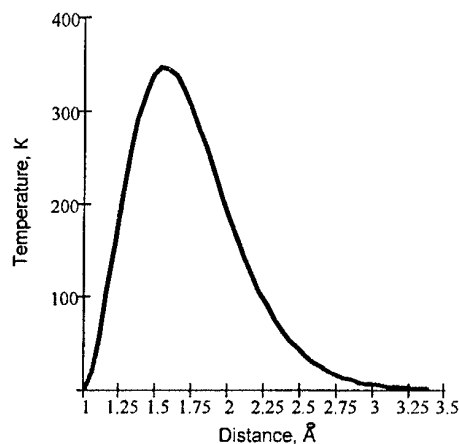Fig. 2. Dependence of matrix element of electron transition from ion Cu to

Fig. 3. Dependence of temperature of superconducting transition on distance between ions Cu and S in the structure YBaCuS.

3. Discussion of experimental dat

The results confirming our assumption have been obtained in the paper [4]. In this paper the small amount of sulfur or selenium was added in structural lattice $Y_1Ba_2Cu_3O_7$, thus the temperature of superconducting transition was increased, and constants of structural lattice were changed (tab. 2). Apparently, additions even a small number of chalcogenides caused substantial increasing of temperature. Reduction of the average inter-nuclear parameter b is probably caused by local increasing of distances between atoms of copper and sulfur in comparison with distances between copper and oxygen. Therefore, a lattice relaxed distances between copper and oxygen have slightly decreased, in comparison with that case where chalcogenides is not present. However it is not necessary to reject variant when the distances between atoms of the given direction have decreased in comparison with initial structure everywhere, including atoms Cu and S.

Table 1. Temperature of superconducting transition depending on values of matrix element of transition at various distances between atoms Cu and O, Cu and S.

Structure	Distance (b) between atoms Cu and O (S)	t, Ry	T_c (t), K
$Y_1Ba_2Cu_3O_7$	1.95Å	-0.609	90
CuO	1.95Å	-0.609	90
CuS (0)	1.95Å	-0.929	209
CuS (1)	2.19Å	-0.680	112
CuS (2)	2.32Å	-0.556	75

In this case, apparently from Fig. 2, it is possible to expect for distances less than 1.95 Å substantial growth of the T_c because of atoms Cu and S, Cu and O have approached to each other and the matrix element of transition t have grown.

Table 2. Experimental data of temperature's of superconducting transition changing in case of addition of chalcogenide elements in YBaCuO [4].

Structure	T_c	ΔT	a, Å	b, Å	c, Å
$Y_1Ba_2Cu_3O_{7-x}$	89.5K	0K	3.83	3.89	11.68
$Y_1Ba_2Cu_3O_{7-x}S_{0.001}$	90.5K	1K	3.83	3.87	11.67
$Y_1Ba_2Cu_3O_{7-x}S_{0.05}$	93K	3.5K	3.84	3.87	11.62
$Y_1Ba_2Cu_3O_{7-x}Se_{0.5}$	91K	1.5K			

We consider a case when only 0.05 amount of sulfur (Table 2) was added to original structure and the inter-nuclear parameter b has decreased on 0.02Å. It is possible to make a conclusion, that distances between ions Cu and O have approximately changed by 0.01Å. Then it is possible to estimate how the temperature will increase depending on change of the matrix element t_{CuO}. The t_{CuS} can be not taken into calculation, because it is much less atoms of sulfur than atoms of oxygen in this new structure.

$$T_c^1 = \left(\frac{t_{CuO}(1.94A)}{t_{CuO}(1.95A)}\right)^2 \cdot 89.5K = 93.7K \tag{7}$$

As it's seen from the formula (7) temperature obtained theoretically coincides rather well with experimental one, which is equal 93 K. Fig. 3 represents dependence T_c on distance between Cu and S calculated by the formula the same as (7). In this case it is considered, that all atoms of oxygen are replaced with atoms of sulfur. It is clearly visible from this diagram that the temperature sharply grows with reduction of inter-nuclear distances. The peak is observed in area near 1.6-1.7Å that corresponds to changing of a constant *b/2* only by 0.3Å. For all *b/2*<2.2Å the exceeding of temperature is possible.

4. Conclusions

Clearly, that practically achievement of such temperatures, as 350K (the maximal value on Fig. 3) by the method described in the given work, most likely is impossible. First of all in the given work only approximate calculations for estimation of T_c were used. However the tendency to increasing of temperature is seen rather clearly and it has proved to be true and in practice.

We shall note two possible variants of increasing Tc, when sulfur are added to YBaCuO, based on fact that the temperature of transition is proportional to the quadrant of matrix element of transition *t*.

· the inter-nuclear parameter *b* is increased. The temperature of transition grows because the matrix element of transition t_{CuS} (distances between ions Cu and S is less than 2.26Å) will exceed t_{CuO} for ions Cu and O in original structure.

· the inter-nuclear parameter *b* decreases. Both t_{CuS} and t_{CuO} are increased, therefore, even if full replacement of oxygen by sulfur is incomplete, strong increase Tc is expecting.

It is necessary to note, that creating of new structures is very difficult, because method used for creating usual HTSC is hard to apply for new materials. For example, addition in YBaCuO large concentration of S or Se lead to appearance of a new dielectric phase, and the samples lose the superconducting properties and become isolator.

We think that it is possible to rely on the model of the negative-U centers, which qualify coincides with experiments [4]. If estimation of T_c, which was calculated using of this model, is true, creating of superconductors with temperature of transition more than 110K is possible.

References

[1] A. A. Abrikosov, Bases of the theory of metals, Science, Moscow (1987).
[2] I. O. Kulik, A. G.Pedan, Sov. Phys.- JETP, **79**, 1469 (1980).
[3] K. D. Tsendin, B. P. Popov. Supercond. Sci. Technol., **12**, 255 (1999).
[4] Shizo Kamble, Maki Kawai, Journal Applied Physics, **27**, L2342 (1988).
[5] V. A. Verjazov, J. E. Kitaev, V. P. Smirnov, R. A. Evarestov, High-temperature superconductivity. Edited by A.A. Kiselev, Mechanical Engineering, Leningrad (1990).
[6] K. Koulson, Valence, Oxford University Press, Oxford (1961).

PHOTOSENSITIVITY IN ANTIMONY BASED GLASSES

M. Nalin[a,b], Y. Messaddeq[a], S. J. L. Ribeiro[a], M. Poulain[b], V. Briois[c]

[a] Laboratório de Materiais Fotônicos, Instituto de Química, UNESP, rua Professor Francisco Degni, Araraquara – SP, Brazil
[b] Laboratoire des Matériaux Photoniques, Université de Rennes 1, Rennes, France
[c] LURE, Université Paris Sud, BP34, 91898 Orsay cedex, France

New glass forming systems based on Sb_2O_3-$SbPO_4$ has been explored. These glasses present higher thermal stability against devitrification and higher refractive index than chalcogenide glasses. Under irradiation, using Ar-laser 350nm wavelength and 50 mW power density, change on the coloration is observed. Structural and electronic modifications around Sb cations induced by such treatment have been characterized by XANES measurements at the L-Sb edges. On the one hand, XANES spectra, at the L_3 edge, show a decrease of the coordination number for Sb atoms induced by exposure to light indicating a breaking of Sb-O bonds in the glassy network. On the other hand, XANES spectra, at the L_1 edge, suggest a change in the oxidation state of Sb atoms. These modifications associated to the photodarkening of the glass is reversible either after a couple of days or after heating the glass at the glass transition temperature, T_g.

1. Introduction

Heavy metal oxide based glasses have been the subject of several studies [1]. Particularly, antimony oxide glasses have been studied as they present extended infrared transmission [2]. Several studies have been focused on optical properties mainly non linear optical properties as they present higher refractive index [3,4].

Several photoinduced processes have been reported in oxide glasses. It is known as photoexpansion, photodarkening, etc. The phenomenon allows the fabrication of different phase structure as example, the Bragg grating obtained by photoimprinting a periodic index modulation [5,6]. The photosensitivity may led also the fabrication of miniature thin film by directly writing a channel waveguide in a photosensitive wafer without the use of chemical process as photoresist or etching. For oxide systems, in the case of silica glasses a volume change is observed. Several studies are reported on thin film Sb_2S_3 in view of its photosensitive and thermoelectric properties [7]. In our Knowledge, no studies are reported in the literature on photoinduced phenomenon on antimony oxide glasses. A photocontration effect is recently observed on thin film Sb_2S_3 under UV irradiation [8]. In this sense antimony based glasses may also be photosensitive under irradiation. One of the reasons that can be considered is the lone pair present in the trivalent antimony ions. The presence of this lone pair in the amorphous network could be accountable for break and formation of bonds during exposure.

This work reports the investigation of new glass compositions which could be photosensitive materials. The structural behaviors of the binary Sb_2O_3-$SbPO_4$ glass systems before and after irradiation have been particularly studied, using mainly as structural tools the XANES spectroscopy.

2. Experimental

2.1. Glass preparation

Starting materials used for glass preparation are Sb_2O_3(Acros 99%) and $SbPO_4$. $SbPO_4$ is prepared in the lab by mixing Sb_2O_3 and H_3PO_4(85%). Details of this preparation is reported on ref.

[9]. Synthesis were carried out by melting starting materials in glassy carbon crucibles in electrical furnace for 10 minutes at 700-1000 °C. Then the melt was cast and glass samples were obtained upon cooling. For less stable glasses, melt was quenched between two brass pieces, which lead to samples of 1 mm or less in thickness. Sample thickness can reach 10 mm for compositions less prone to devitrification by casting the melt into a brass mould preheated around Tg. Large samples were annealed around this temperature for two hours to reduce thermal stresses.

2.2. Physical measurements

Characteristics temperatures (Tg for glass transition temperature, Tx for onset of crystallisation and Tp for maximum of crystallisation peak) were determined by differential scanning calorimeter (DSC) using a SEIKO SSC/5200H equipment. The estimated error on the temperature is 2 K for glass transition and onset of crystallisation which are obtained from tangents intersection and 1 K for the position of the crystallisation peak. Powdered samples were set in aluminium pans under N_2 atmosphere at 10 K/Min heating rate. Infrared transmission spectra were recorded with a BOMEM Michelson Spectrophotometer in the 400-4000 cm^{-1} range. Ultraviolet transmission spectra between 800 and 200 nm were obtained using a Varian spectrophotometer Cary 5. The irradiation process was performed at LURE (Orsay, France) by exposing the samples to a Ar-laser, with wavelength of 350nm and 50 mW power density. Sb L-edge XANES measurements have been carried out at LURE (Orsay, France) on the D44 beam line using a Si(111) double crystal monochromator detuned by 60% in order to reject the harmonics. Measurements have been done in TEY (Total Electron Yield) in grazing incidence ($\approx 5°$) in order to collect electronic and structural information on the surface (about 0.6-0.8μm) of the glasses. Energy calibration has been checked by using a Titanium foil (4966.0 eV) recorded between each glassy sample. $Sb-L_3$ edge (4132 eV) spectra were collected over 340 eV with an energy step of 0.3 eV and counting time of 3s whereas $Sb-L_1$ edge spectra (4698 eV) were recorded over 100 eV with an energy step of 0.3eV and counting time of 1s. For each sample several scans were recorded to improve the signal-to-noise ratio. Sb_2O_3 and $SbPO_4$ powdering samples deposited onto millipore membranes were recorded in TEY as reference compounds. The absorption background was subtracted from the rough XANES spectra using a linear function. Them spectra were normalised far from the edge in a range of pure atomic absorption (4243.5 eV for $Sb-L_3$ edge and 4774.3 eV for $Sb-L_1$ edge).

3. Results

3.1. Vitreous domain

Fig. 1 present the vitreous domain of the binary system Sb_2O_3-$SbPO_4$. The limits of the glass region were determined using quenching technique.
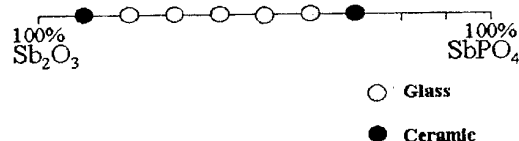

Fig. 1. Vitreous domains of the binary glass system.

3.2. Thermal analysis

Table 1 summarizes the characteristics temperatures obtained from DSC curves for the more stable glass composition. We have also included the thermal stability, Tx-Tg, used as parameter to evaluate the glass stability against devitrification. DSC curves are shown in the Fig. 2 for binary

glasses. From Table 1, we can observe an increase in the Tg values as the SbPO$_4$ concentration increases.
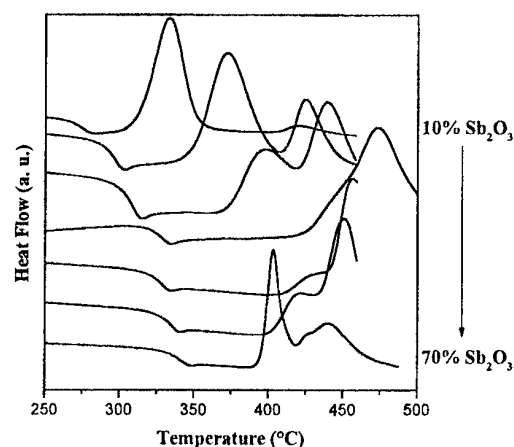

Fig. 2. DSC curves the binary systems.

Table 1. Chemical glass compositions, characteristics temperatures and stability parameter for binary system.

Samples	Glass Compositions (mol %)			Characteristics Temperatures (°C)			Tx-Tg
	Sb$_2$O$_3$	SbPO$_4$	WO$_3$	Tg	Tx	Tp	Tx-Tg
Sbp1	90	10	-	265	312	333	47
Sbp2	80	20	-	287	349	373	62
Sbp3	70	30	-	294	372	394	79
Sbp4	60	40	-	317	424	472	107
Sbp5	50	50	-	318	411	457	93
Sbp6	40	60	-	325	400	451	75
Sbp7	30	70	-	334	396	403	62

3.3. Optical properties

Optical spectra of these glasses are presented in Fig. 3 from UV to infrared range. Absorption band observed at 3400 cm^{-1} can be attributed to stretching, ν of the O-H bonds. The absorption band around 2000 cm^{-1} corresponds to multiphonons absorption of the O-P-O bonds, from the antimony orthophosphate. Also, we may note that the band gap of the binary glass appears around 35000 cm^{-1} (350 nm).
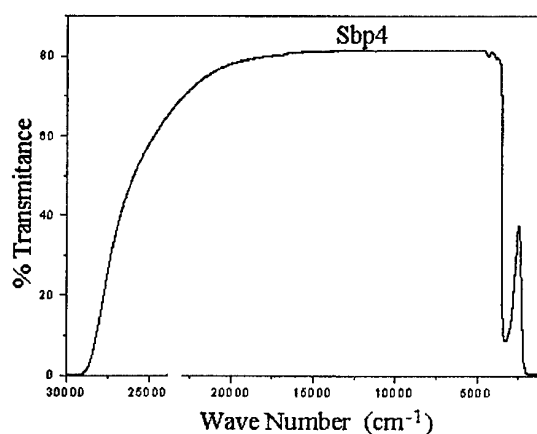

Fig. 3. Optical window in the UV-visible range for the glass compositions Sbp4.

3.4. Laser irradiation and XANES data

Sb L_3-edge data refer to transitions from $2p_{3/2}$ level towards empty d and s states. The pre-peak in the rising edge (≈ 4138 eV) is attributed to $2p_{3/2}$-->5sσ^* transition whereas the main absorption at higher energy (4145 eV) as interpreted as $2p_{3/2}$ -->5d transition. Correlations between the surface of pre-peak and Sb coordination polyhedron are well established[9]. Roughly speaking a decrease of the pre-peak surface means an increasing mean coordination number for Sb atoms as evidenced on the Sb_2O_3 and $SbPO_4$[9]. Sb L_1-edge data refer to transitions from 2s level towards empty p states. The position of the rising edge is informative of the oxidation state of antimony [10] whereas the intensity of the white line (≈ 4704 eV) and the shape above the white line is strongly dependent on the short and medium range order around Sb. For Sb_2O_3 and $SbPO_4$ compounds both rising edges are located at the same energy (≈ 4702.3 eV) attesting to the same trivalent state for Sb whereas the general shape is very different due to the different coordination patterns.

During the irradiation by a laser of 50 mW for seveal hours a change in the coloration of the samples (they pass from yellow to brownish) has been observed but this phenomenon is not permanent and disappears some hours late. Such effect has been long known as photodarkening. We present herein the XANES results obtained on two binary glasses, the Sbp3 and Sbp4 compositions, exposed for 4 and 6 hours, respectively. XANES characterizations on the irradiated Sbp4 sample have been performed immediately after irradiation when the photodarkening is always present, whereas XANES characterizations on the irradiated Sbp3 sample were carried out several days after irradiation. Then the color is turned back to yellow. On the one hand, drastic changes in the shape of both Sb L_3- and L_1- edges are observed for the irradiated Sbp4 sample compared to the non-irradiated film as displayed in Figs. 4a and 5a, respectively. According to the above interpretations for the references, the XANES results at the L_3-edge clearly evidence that a change in the coordination polyhedron of Sb occurs by irradiation. Furthermore, the appearance of a shoulder at ≈ 3 eV above the white line at the L_1-Sb edge could be the evidence of a partial oxidation state change from Sb(III) to Sb(V) upon irradiation. Indeed such energy position is in agreement with the energy of the white line for Sb(V) cations reported in the literature [11]. On the other hand, the structural modifications around Sb after irradiation for the Sbp3 sample, reported in Figs. 4b and 5b, are smaller than those observed on the Sbp4 sample. We note a faint change of the pre-peak intensity at the L_3-Sb edge after irradiation and some modifications in the shape of the XANES resonances above the white line at the L_1-Sb edge. Both effects are indicative to small changes of the local and medium order around Sb cations. Furthermore the oxidation state of Sb is always III.
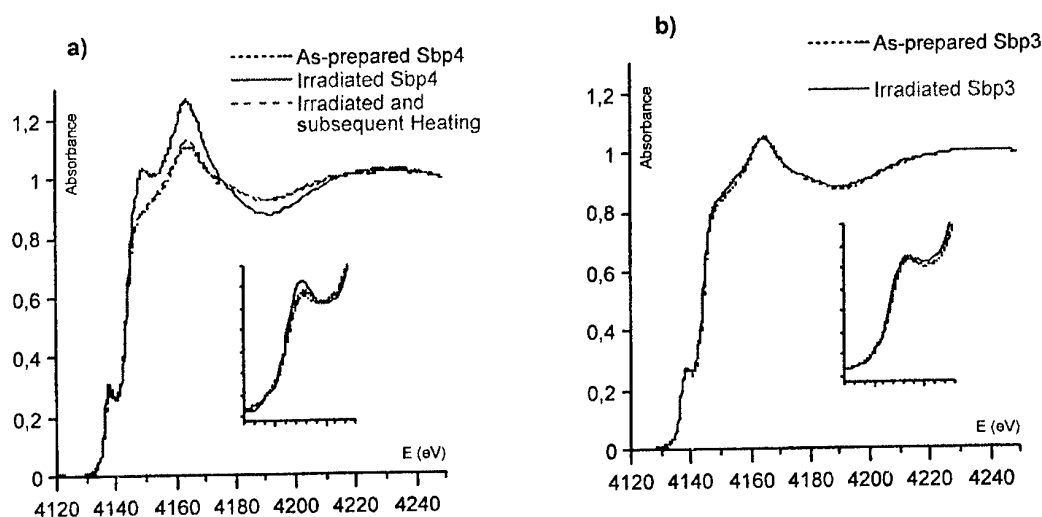

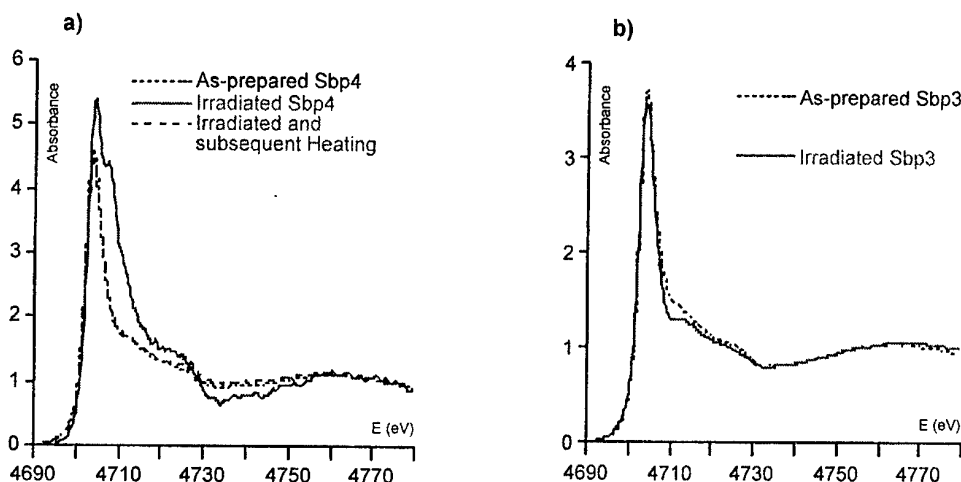Fig. 4 – XANES spectra recorded at the L_3-Sb edge for a) Sbp4 and b) Sbp3.

Fig. 5 – XANES spectra recorded at the L₁-Sb edge for a) Sbp4 and b) Sbp3.

After the XANES characterizations, the Sbp4 sample was immediately heated for 15 hours, in electrical furnace, near Tg. The XANES spectra recorded after the heat treatment are superimposable to the spectra of the non irradiated sample indicating a reversible character of the photoinduced phenomenon providing that an ad-hoc thermal treatment was carried out.

4. Discussion

Homogenous glasses with higher thermal stability have been obtained with the incorporation of polyphosphates. This may be noted from Table 1 data, which indicate higher value of the difference $(T_x - T_g)$ with the incorporation of orthophosphate. This behavior can also be noted from Fig. 1, which indicates a large domain of vitrification in the binary system. It seems that the vitrification is easier with the addition of $SbPO_4$, if we assume that isolated PO_4 exist in the glass. The glass transition temperature increases with increase of orthophosphate. This can be linked with the polymerization of the glass network due to the high concentration of PO_4^{-3} groups. Beside that, both, the temperature of onset of crystallization and the maximum of crystallization values increase from Sbp1 to Sbp4 (see Table 1).

Samples under irradiation in the wavelength region of the absorption edge with 50 mW power density shown a photodarkening effect. This effect is not permanent and disappears rapidly and glass samples regain its original transmitivity. We have evidenced by XANES measurements on the Sbp4 sample that the photodarkening phenomenon induces a breaking of Sb-O bonds in the glassy network: the mean coordination number of Sb in the irradiated film decreases compared to the non-irradiated film. Furthermore, the results at the L₁-Sb edge suggest also a change in the oxidation state of Sb. The XANES investigation on this sample shows also that the structure is totally restored after heating near Tg. The XANES results reported for the Sbp3 sample strongly indicates that the stronger structural and electronic modifications occur during the photodarkening phenomenon. When the darkening has disappears the oxidation of antimony ions is equal to III as evidenced by the shape of the L₁ white line.

Many publication report studies on the photosensitivity behavior of glasses. Such processes are used for several purposes as light modulators, sun-glasses or glare protection glasses [12,13]. In such glasses the mechanism responsible of the photoinduced effect is related to high concentration of defect centers and a high concentration of vacancies which are caused by considerable local energy absorption. Consequence, these can lead to irreversible as well reversible changes in the structure and some properties as refractive index.

In our case, the structural effect is reversible as shown in Fig. 4 and 5. Annealing in the region of the glass transition temperature restores the L₁ spectra to the original position.

5. Conclusion

New photosensitive glasses have been synthesized and characterized in the binary glass system Sb_2O_3-$SbPO_4$. We have shown that phosphates increase the thermal stability of the glass samples. Photodarkening effect is observed after irradiation and is not permanent. XANES measurement indicate that the photoinduced effect can be related to defect centers originated by a change on the oxidation number of antimony.

Acknowledgement

References

[1] M. Ahmed, D.Holland, Glass Techn. 28, 41 (1987).
[2] J. F. Bednarik, J. A. Neely, Glass techn.Ber. 55, 126 (1982).
[3] R. El Mallawany, J. Mat. Sci: Mat. in Electron. 6, 1 (1995).
[4] W. H. Dumbaugh, Phys. Chem. of Glasses 19, 121 (1978).
[5] K. O. Hill, Y. Fujji, D. C. Johnson, B. S. Kawasaschi, Appl.Phys.Lett. 32, 647-649 (1978).
[6] G. Meltz, W. W. Morey, W. H. Glen, Opt. Ett. 14, 823-825 (1989).
[7] K. Y. Raijpure, C. H. Bhosale, J. Phys. Chem. of Solids, 61(4), 561-568 (2000).
[8] F. Vicente, Private communication.
[9] M. Nalin et al. J. Non Cryst. Solids (2001) in press.
[10] J. M. Durand et al. J. Non-Cryst. Solids 194, 109 (1996).
[11] J. Rockenberger, U. zum Felde, M. Tisher, L. Tröger, M. Haase, H. Weller, J. Chem. Phys. 112, 4296 (2000).
[12] W. Vogel, Glaschemie, (1979).
[13] H. Scholze, Glass, its nature, structure and properties, 3rd edition, Springer-Verlag, Berlin, 1988.

THERMO AND PHOTOLUMINESCENCE OF SILICATE LASER GLASS DOPED WITH NEODYMIUM

B. Grigoras, M. Cerchez, L. Ionescu, M. Secu[a], L. Matei[a], A. Trutia[b]

National Glass Institute Theodor Pallady 47, Sector 3 Bucharest, Romania
[a]National Institute of Materials Physics 76900 Bucharest-Magurele, P.O.Box, MG-7, Romania
[b]Faculty of Physics, University of Bucharest, Bucharest, Romania

The luminescence and thermoluminescence have been measured in vitreous materials doped with Nd^{3+}. The luminescence spectra show a maximum at 400 nm and a shoulder at about 440 nm. The measured global thermoluminescence shows a broad band with a maximum at 270 °C, which suggests a continuous distribution of electron traps induced by ionizing radiation. Thermoluminescence measured through two optical filters which transmit at about 400 nm and 440 nm wavelength shows a structured behavior with two glow peaks at 270 °C and 330 °C. This apparently contradictory behavior has been explained by the existence in this material of a continuous distribution of trap levels and a discrete distribution of recombination levels. The 270 °C and 330 °C glow peaks have been interpreted as being due to recombination of the electrons released from electron traps with O^{2-} and Nd^{3+} hole centers. Due to the high stability of the defects induced by the radiation observed from thermoluminescence measurements, this material could be used as a new radiation detector.

1. Introduction

Due to the large applicability in the field of radiation detection and dozimetry, the family of the materials which presents thermoluminescence peaks under X-irradiation, grows continuously.

The most frequently used materials are composites with crystalline powders in plastic matrix. Recently, the researchers attention was canalized on glass materials doped with metals from the rare earth family (Nd and Eu being the most frequently used).

For binary silicate glasses having the composition 71.5% SiO_2 and 28.5% Na_2O, there were reported [1] two thermoluminescence peaks at 75 °C and at 125 °C, for moderate irradiation doses. In the case of high irradiation doses, it was reported a single peak situated at an intermediate temperature (between the two temperatures previously mentioned).

Y. Kirsh [2] has reported a maximum of the thermoluminescence intensity at 130 °C for silicate glass filters doped with Nd and Ge. The corresponding emission spectrum presents two peaks at 400 nm and 520 nm respectively. It was suggested that the 400 nm peak is due to the electrons recombination with trap centers represented by O^{2-} holes and that the 520 nm peak corresponds to the recombination with trap centers represented by Nd^{3+} holes.

2. Experimental results and discussions

This paper presents the results of the photoluminescence and thermoluminescence measurements on a silicate laser glass doped with Nd, obtained in the laboratories of the National Glass Institute, Bucharest, Romania. Measurements have been performed at the National Institute of Materials Physics, Bucharest, Romania. After a previous X-irradiation, the thermoluminescence was measured using an experimental equipment, the heating rate being 1.12 deg/sec. For the fotoluminescence measurements, standard equipment was used.

Fig. 1 presents the global thermoluminescence curve (a), the thermoluminescence curve (b) for a Schott Jena optical filter UG3 transmitting in the "blue" spectral zone and the thermoluminescence curve (c) for a Schott Jena optical filter VG6 transmitting in the "yellow" spectral zone.

The aspect of the (a) curve is typical for amorphous materials having a continuous distribution of the electronic trap energy levels. Table 1 presents the kinetic parameters obtained by fitting the experimental curve with the theoretical one. The analytical expression for the theoretical curve is:

$$I(T) = -\frac{dn}{dt} = S' n^b \exp\left(-\frac{E}{kT}\right) \qquad (1)$$

where I = the luminescence intensity;
       n = the free trap concentration;
       b = the kinetic order;
       S' = the freency factor;
       E = the acti ition energy.
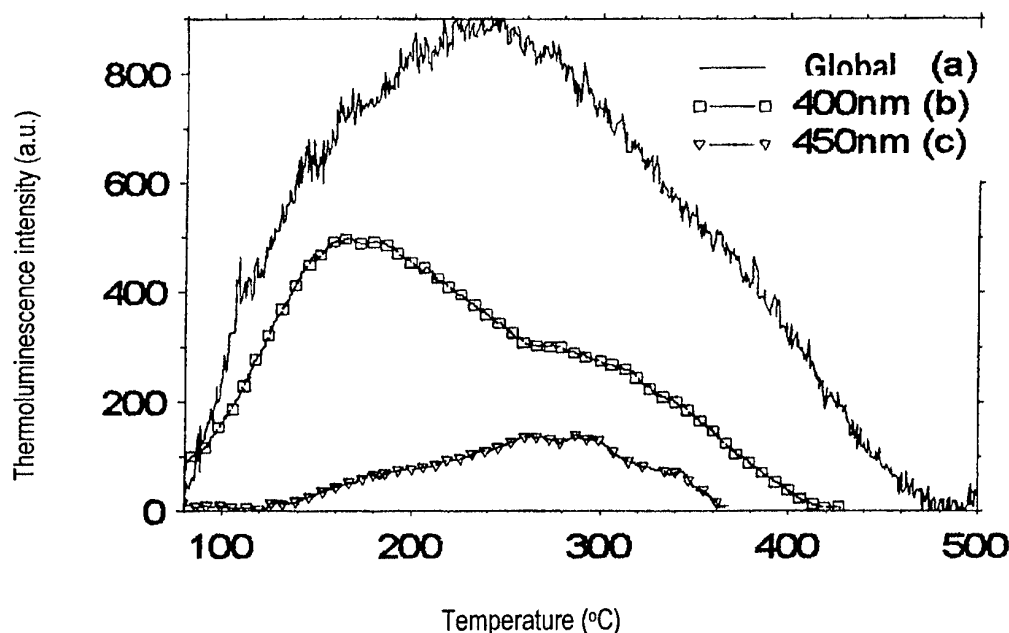
Fig. 1. The thermoluminescence intensity at room temperature for the X-irradiated Nd^{3+} silicate laser glass.

Table 1. Calculated kinetic parameters.

T_m (°C)	S' (s⁻¹)	E (eV)	b
132	$2.0 \cdot 10^{11}$	1.00	2.4
185	$1.8 \cdot 10^{12}$	1.22	2.4
239	$3.2 \cdot 10^{12}$	1.40	2.4
297	$4.8 \cdot 10^{12}$	1.57	2.4
370	$5.2 \cdot 10^{12}$	1.78	2.4

The used method was the "best fit" by the approximation of the experimental thermoluminescence curve with the sum of five individual peaks (Fig. 2). The obtained results give

some qualitative information about the range of the activation energy. For the studied glass this range is 1.0 – 1.8 eV, moderately shifted compared with the reported 0.89 – 1.72 eV activation energy range for silicate optical filters [2]. Another difference is in the intensity and repartition of the peaks.
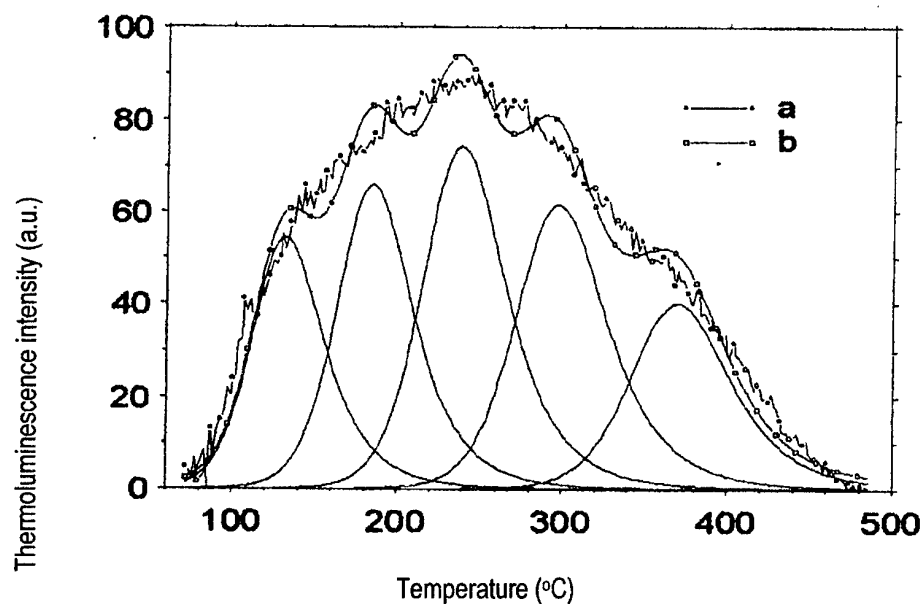

Fig. 2. The decomposition of the thermoluminescence curve using the "best fit" method:
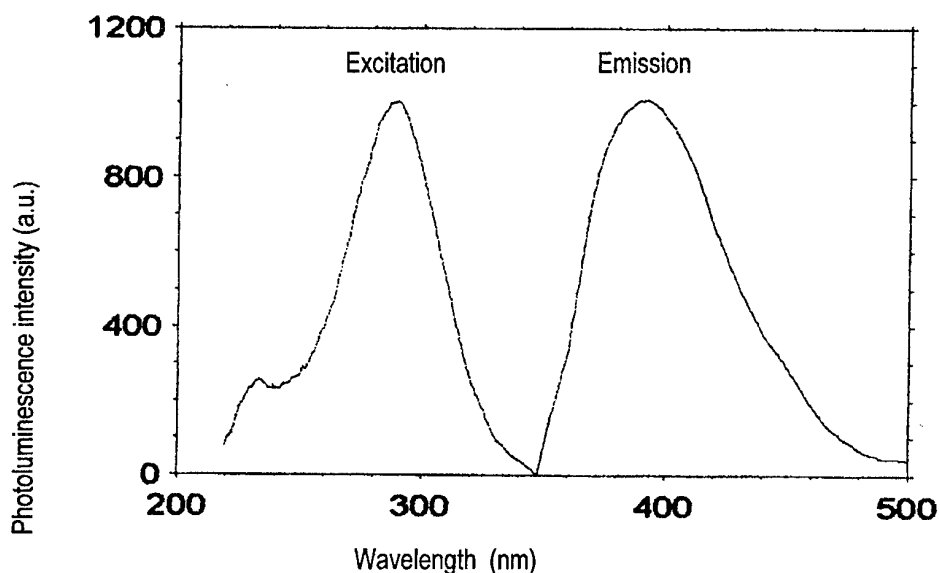a) Experimental curve
b) Theoretical curve

Fig. 3. The photoluminescence of the Nd^{3+} silicate laser glass.

The left part of Fig. 3 presents the excitation of the photoluminescence and the right one, the emission. It can be seen that the excitation of the emission bands is situated in the spectral zone where the material begins to absorb. This zone is known, in the crystalline materials terminology, as the fundamental band edge. In emission, a peak situated at 400 nm and a "shoulder" at 440 nm are observed. The observed thermoluminescence using optical filters that transmit at 4oo nm (Fig. 1b) and

450 nm (Fig.1c) respectively, presents different appearance. This indicates that the energy levels of the recombination centers have a discrete character.

The large number of the chemical components of the investigated glass could explain a continuous distribution of the electronic trap levels.

The luminescence at 400 nm and 440nm are done by the electron recombinations with trap centers represented by O^{2-} and Nd^{3+} holes respectively. This interpretation is in accordance with the results presented in [1].

3. Conclusions

The positioning of the global luminescence curve in a relatively high temperature range demonstrates the thermal stability of the defects induced by irradiation. This observation indicates that the investigated glass could be used as a new radiation detector material.

References

[1] C. Bettinali & G. Ferraresso - Journal of Chemical Physics, **44**, 6, (1966).
[2] J. Kirsh, J. E. Townsend & P. D. Townsend – Phys. Stat. Sol. (a), **114**, 739, (1989).

ANALYSIS OF a-SiO₂/ a-Si MULTILAYER STRUCTURES BY ION BEAM METHODS AND ELECTRON SPIN RESONANCE

N. Tomozeiu[a], J. J. van Hapert, W. M. Arnoldbik, E. E. van Faassen, A. M. Vredenberg, F. H. P. M. Habraken

Debye Institute, Utrecht University, PO Box 80000 3508 TA, Utrecht, The Netherlands
[a]Faculty of Physics, Bucharest University, PO Box 11Mg, Bucharest-Magurele, Romania

Multilayered structures of a-Si/SiO₂ sequences were deposited using a magnetron sputtering system, where Si atoms are sputtered in an Ar-O₂ mixture. All samples have the same total thickness (250nm) and the thickness/layer is between 2 nm and 16 nm. The purpose of this paper is to investigate the inhomogeneity of these films and its limit. The sample composition and thickness were investigated by conventional Rutherford backscattering spectrometry (RBS), high resolution RBS using a magnetic spectrograph and elastic recoil detection (ERD). The analysis of the conventional RBS and ERD spectra has revealed that samples with 16 nm/layer consists of a-Si/SiO₂ sequences. The high-resolution RBS measurements have also shown a multilayered structure for samples with a smaller layer thickness. The composition of the SiO₂ layers for samples with 4 and 2 nm/layer is more SiO$_x$ like, with different values of the x parameter. It seems that the interface region is dominant for these samples with 4 nm/layer and less. The structural study is completed with the ESR measurements, which revealed two paramagnetic species attributed to a-Si dangling bonds and E' centers respectively. The latter are characteristic for SiO₂ material. We found that a-Si DBs are present in all samples, irrespective of the layers thickness. Their spin density amounts to about 10^{20}cm^{-3}. In contrast, the E' centers are not present in the sample with 2 nm/layer.

1. Introduction

The era of nano-technologies and nano-devices offers challenging fields to scientists. As a result, in the last decade many studies have been devoted to multilayered structures of amorphous semiconductors. There is an equal interest in these layered films for both fundamental physics and applications. A very interesting aspect is how the structure of each layer from the stack influences the physical properties of the complete structure. Some amorphous materials from the chalcogenide glass family (e.g. InSe) show particularities as each layer is formed in sublayers in a well-known sequence (e.g. Se-In-In-Se) /1/. Materials from the family of silicon are structurally organized within a tetrahedral basic cell built around a silicon atom. The Si-Si₄ structure has Si-Si bond length of 2.38Å while Si-O₄ is characterized by Si-O bond of 1.66Å /2/. This mismatch at the SiO₂/Si interface, in a structure with thin layers, will play an important role in the behavior of the microelectronic devices.

One very important step in the structural study is the compositional determination with a high accuracy. Using the ~ MeV ion-beam analysis techniques, the elemental composition of layers can be probed as a function of depth by analyzing the spectra of scattered or recoiled ions. The typical depth resolution near the surface varies from 5-10 nm for conventional methods to better than 1 nm using a dedicated high resolution instrument. The concentration of the atoms of which a thin layer consists can be obtained on an absolute scale. No information is obtained about the chemical environment of the probed atoms. The most popular ion-beam analyses techniques used to investigate semiconductor layers are Rutherford backscattering spectrometry (RBS) and elastic recoil detection (ERD).

The nature and the quantity of defects from the material structure are also very important for structural characterization. Electron spin resonance (ESR) is a technique used to determine the paramagnetic dangling bond defects.

In this paper we present results of ion beam analyses methods and ESR on a-SiO$_2$/a-Si multilayer structures. Combining the RBS and ERD results with those from ESR measurements we will find a limit where the a-SiO$_2$/a-Si sequences can be resolved.

2 Experimental

2.1. Sample preparation

Multilayers of a-SiO$_2$/a-Si were deposited in a sputtering system equipped with a 13.56 MHz r.f. magnetron source using a power of 140 W. The deposition chamber was pumped down to a base pressure of less than $2 \cdot 10^{-7}$ mbar before the plasma gas was introduced. Silicon atoms were sputtered from a polycrystalline silicon target. When the SiO$_2$ layers were deposited, the oxygen line was opened. The ratio between Ar and O$_2$ flows was 80:1. For the next a-Si layer the oxygen line was closed while the plasma runs continuously with the same argon flow. In this way samples with 2, 4, 8 and 16 nm/layer were deposited. In order to obtain sharper interfaces, samples with a layer thickness of 2 nm and 4 nm were also deposited by a procedure in which for each layer the following steps have been done: i) a basis pressure of $2 \cdot 10^{-7}$ mbar; ii) the plasma gasses were introduced (the ratio Ar/O was 80/1 for SiO$_2$ layers and for a-Si layers was 80/0); iii) turn on the plasma and keep it to obtain the desired thickness. We denote these samples as "plasma on/off" and the first series of samples as "plasma on". During deposition the pressure was 5.6 μbar. The distance between target and sampler holder is 6 cm. All samples were deposited on both c-Si wafer (for ion beam analyses) and corning glass (for ESR) at room temperature.

2.1. Measurement techniques

__Rutherford Backscattering Spectrometry__ uses a beam of light ions, usually He or H, with high energy (0.5 – 3 MeV), which scatter from the nuclei in the measured layer (target) /3/. The number and energy of scattered ions, usually at a backward angle, in the direction of a particular detector are determined. RBS is used with success to determine the concentration depth profiles of heavy atoms in a matrix of light atoms. The relations between the energies and mass numbers for elastic scattering is determined by the kinematics of the collision. An important parameter is the stopping power defined as the energy loss divided by the atomic areal density of the target (eV/(10^{15} at/cm^2)). This parameter determines the depth sensitivity and the depth resolution. The stopping cross section data have been collected in the Ziegler's tables /4/. Due to the statistical nature of the stopping process the amount of energy lost per unit length fluctuates. For a path length t this spread, called energy straggling increases, with $t^{1/2}$. The RBS spectra are analyzed using a computer program which calculate the spectra for an assumed sample composition taking into account the effects of straggling, detector resolution, multiple scattering, etc /5/. Comparing the calculated spectra with the measured one, in successive approximation the absolute concentration depth profiles for elements from the sample are obtained.

Fig. 1 shows the RBS spectra for a SiO$_2$ thin film deposited by sputtering on c-Si. The depth resolution near the surface is determined by the detector resolution (15 keV), while at a larger depth, de resolution is mainly determined by energy straggling. In this figure the contributions of Ar, a heavier element than Si (the host matrix) and of O a lighter element are well visible. We have to note that the RBS sensitivity is poor for light elements ($\sigma_{RBS} \sim Z^2$, σ is the cross section that characterize the collision event, Z is the atomic number). Also RBS based on He ions has a limited mass resolution and it is difficult to resolve isotopes or neighbouring elements. The solutions for this problems are given by ion-beam analyses techniques by ERD and high resolution RBS (HR-RBS).
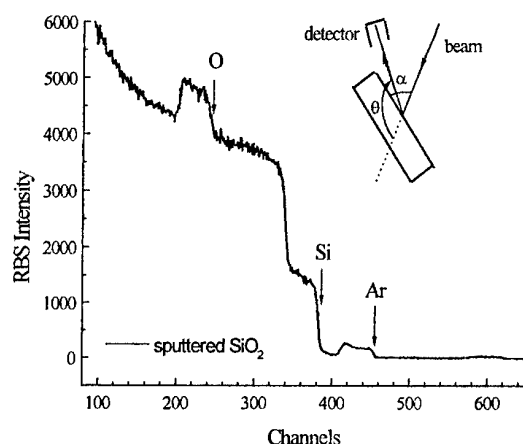
Fig. 1. The RBS spectrum of SiO₂ layer deposited on c-Si. The position of the surface edges for Si, O, N and Ar are indicated. The primary beam consisted of 2 MeV He⁺ ions.
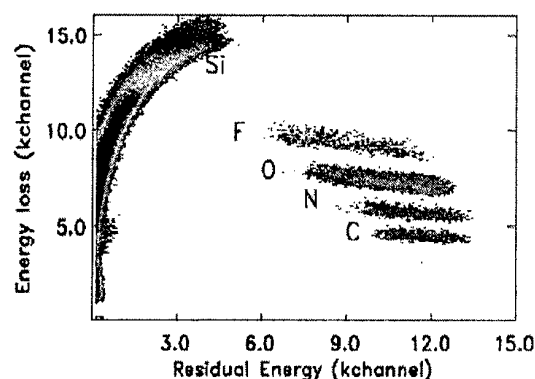
Fig 2. ERD spectra of a contaminated SiOₓ layer measured with a ΔE-E ionization chamber. The separation between elements and the depth for each element are revealed.

Elastic Recoil Detection (ERD) uses the information about the collision between the incident ion and the target atoms contained in recoiled ions. Because momentum is conserved, the detection necessarily occurs at forward angles. The advantages of RBS are preserved by ERD (good quantitative character, depth resolution, non-destructive technique) and more, the sensitivity for light elements is strongly enhanced. In ERD heavy ion (Si, Ag, Cu) beam of tens of MeV's are used. The ERD setup at Utrecht University is connected to a 6 MeV EN Tandem Van de Graaff Accelerator. A ΔE-E ionization chamber with Frisch grid is used as detector /6/. The entrance window of the detector is a 2 µm metalized Mylar foil which separates the 24 mbar iso-butane in the ionization chamber from the vacuum in the scattering chamber. The anode of the detector is composed of two segments: a 6 cm segment for ΔE signal and a 17 cm segment for the E signal. In this way a total energy spectrum for each light element is constructed from a two-dimensional ΔE-E spectrum. The depth resolution is comparable with the resolution obtained with RBS but the mass separation is enhanced. Figure 2 shows an example of ERD spectrum for a contaminated SiOₓ layer. Elements as C, N, O, F and Si are well separated. The number of atoms per cm² of the light elements in the film is obtained by comparing the yields in the different features with those of a reference thin film with a known abundance of one of the light elements. When no spectral overlap occurs, the minimum detectable amount of the considered elements is better than 10^{13} at.cm⁻².

High Resolution RBS (HR-RBS) spectra can be obtained using a magnetic spectrograph also installed at Utrecht University. It consists of a quadrupole lens, a Wien filter and a 90° dipole magnet with field corrections. The setup from Utrecht University was built in such a way that the spectrograph together with the main chamber (UHV chamber) can be rotated along a circular rail within 0° and 120°. The chamber is connected with a transfer system with a preparation chamber equipped with a load-lock facility. The fields in the components of the spectrograph can be set by a computer and can be tuned to select one ion species with given mass and charge to pass through the spectrograph. A two-dimensional position-sensitive detector (energy versus angle) images one charge state of a selected ion species scattered from the sample. An energy range of 10% of the nominal energy E is resolved with an energy resolution ΔE/E of 9 ×10⁻⁴ that can be translated into a depth resolution at the surface of 6Å /7/.

For comparison, we propose the spectra of the same multilayered sample (a-Si/SiO₂ with 8 nm/layer) obtained with conventional RBS (figure 3) and HR-RBS (figure 5). The first spectrum does no show any multilayered structure, the HR-RBS spectrum reveals the 8 nm of a-Si and SiO₂ respectively. The depth resolution of HR-RBS allows to determine the composition and the thickness of each layer from the structure.

To analyze our samples we used these three techniques in the following circumstances: i) The conventional RBS measurements were done with a 2.4 MeV He^+ beam. The angle between the incoming beam and the sample surface was $\alpha=65^0$. The detector was placed under an angle of $\theta=120^0$ with the beam direction. ii) ERD measurements were performed using a primary beam of 50 MeV Cu^{+9} incident at 20° with the surface of the sample and a recoil angle of 30°. iii) in HR-RBS a He^+ beam of 800 keV in a configuration with $\alpha=35^0$ and $\theta=140^0$ was used.

The structural study was completed with ESR measurements that were performed using a Bruker ESP 300 system. All samples were measured at room temperature and the microwave power was 1.68mW.

3. Results and discussions

3.1. Ion beam analyses

The conventional RBS spectra of multilayered a-Si/SiO_2 samples with 2, 4, 8 and 16 nm/layer are shown in Fig. 3. From this figure it is deduced that silicon, oxygen and argon are present in the layer structure. From previous experiments on single layers we know that the argon concentration is 1.6% for SiO_2 layers and 2.9% for a-Si. Its presence in the layer is explained by implantation of argon ions from the plasma during deposition. As can be seen, only the spectrum of the sample with layer thickness of 16 nm presents a multilayered structure. The simulation using the RUMP computer code confirms the composition of a-Si and SiO_2. Because of the limited depth resolution, all other samples with a layer thickness up to 8 nm have an unresolved RBS spectrum. All these spectra are similar with spectra of single a-SiO_x layers, i.e. x is averaged over all layers from the deposited stack. For sequences of a-Si/SiO_2 this average value of x should be the same indifferently on the individual layer thickness. As Fig 3 shows and the simulation confirms, <x> decreases with decreasing the layer thickness. This means that the SiO_2 composition changes into SiO_x and/or the interface layer has a dominant contribution. Similar results are obtained from ERD measurements as Fig. 4 shows. Because in ERD no interfering background signal is present, small changes of the oxygen contents can be determined. As we have seen in the previous chapter the ERD depth resolution for thin films is about 10 nm. Therefore, the multilayered structures with smaller layer thickness can not be seen, but the advantage of the method is a more accurate determination of the <x> value.
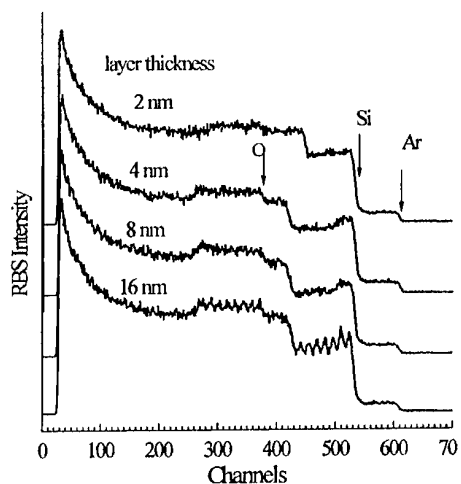

Fig. 3. Conventional RBS spectra of a-Si/SiO_2 multilayered structure. The total thickness of the stack is 256nm and the layer thickness is indicated on each spectrum.
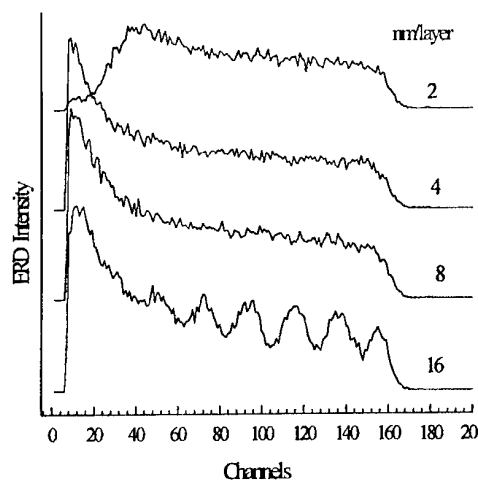
Fig. 4. Oxygen spectra obtained by ERD measurements for samples with RBS spectra in Fig. 3.

Using HR-RBS the composition of each layer from the multilayered stack can be determined. The results of these measurements are presented in figure 5 where the structure of the first 18 nm depth is resolved. The measurement conditions were chosen in such a way to have both the Si and the O signal in each spectrum. This is very helpful in the simulation process. The RUMP fit for each spectrum gives the composition and the thickness of the layers as they are presented in Table 1. We firstly note that the results of conventional RBS and ERD are confirmed: the composition of "SiO₂" layers is altered and SiO_x (with x<2) is obtained for layer with thickness up to 4 nm. Thus instead of 2 oxygen atoms per 1 silicon atom (which is normal for SiO_2) an average of 1.3 oxygen atoms for "SiO₂" 4 nm/layer and 0.8 oxygen atoms for 2 nm/layer was obtained. This means that the oxygen amount necessary to built SiO_2 was not reached in a "SiO₂" deposition time of 20 sec and 10 sec respectively (SiO_2 rate deposition is 12 nm/min). We have to note that these depositions were made with continuously silicon sputtering and the oxygen line was "opened" and "closed" at the right moment to grow SiO_2 layers of desired thicknesses. When the oxygen atoms reach the deposition surface the oxidation reaction is immediate, taking into account the reactivity of both the oxygen atoms and the new deposition surface. The Si spectrum of a-Si layer (see Fig. 5) is slightly asymmetric: the edge that corresponds to the moment of "close" the oxygen line is steeper than the edge of "open". The RUMP simulation reveals that this is a straggling effect.
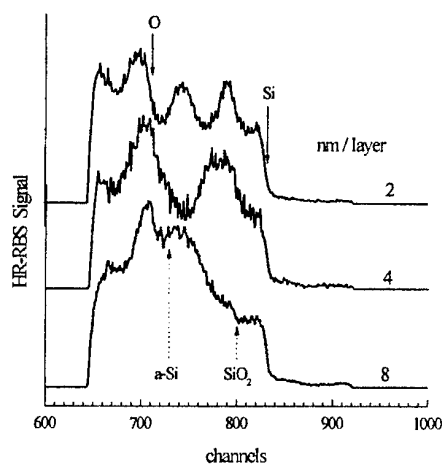

Fig. 5. HR-RBS spectra of samples with 2, 4 and 8 nm/layer. The multilayered structure is shown in the Si depth profile. On the top of the 3-rd a-Si layer (2nm) is the O profile from the 1-st SiO_2 layer .
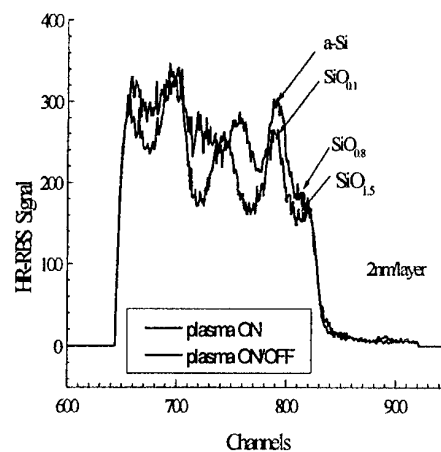
Fig. 6. A comparison of 2 nm/layer samples deposited by "plasma on" and "plasma on/off" procedures. With "plasma on/off" the O amount in "SiO₂" layer increases, but there is O in a-Si layers, too.

In order to obtain more information about the deposition process of SiO_2 films with a layer thickness up to 4 nm we have repeated the deposition of samples with 4 nm and 2 nm/layer but for each layer the deposition was separately started ("plasma on/off" procedure). A comparison of HR-RBS spectra of 2 nm/layer samples deposited by the two procedures described above is shown in figure 6. Large differences can be observed:

- in "plasma on/off" there is an oxygen contamination of the a-Si layers, and
- the "SiO₂" layers are richer in oxygen than the similar "plasma on" layers ($SiO_{1.4}$ instead of $SiO_{0.8}$).

Table 1. The composition and the areal thickness for each layer from the a-Si/SiO$_2$ stacks
obtained fitting HR-RBS spectra.

Layer nr	Si	Ar	8 nm/layer		4 nm/layer		2 nm/layer	
			Thickness (at. cm^{-2})	O	Thickness (at. cm^{-2})	O	Thickness (at. cm^{-2})	O
1	1	0.05	$30 \cdot 10^{15}$	2	$15 \cdot 10^{15}$	1.3	$13 \cdot 10^{15}$	1.2
2	1	0.03	$26 \cdot 10^{15}$	0	$14 \cdot 10^{15}$	0	$6 \cdot 10^{15}$	0
3	1	0.05			$14 \cdot 10^{15}$	1.3	$9 \cdot 10^{15}$	0.8
4	1	0.03			$14 \cdot 10^{15}$	0	$5.5 \cdot 10^{15}$	0
5	1	0.05			$12 \cdot 10^{15}$	1.2	$7 \cdot 10^{15}$	0.8
6	1	0.03					$6 \cdot 10^{15}$	0
7	1	0.05					$9 \cdot 10^{15}$	0.8
8	1	0.03					$7 \cdot 10^{15}$	0
9	1	0.05					$9 \cdot 10^{15}$	0.8

The amount of 10% oxygen in a-Si layers is the result of the oxidation of the Si surface after the oxygen line was opened while the plasma was switched off. An oxygen rich very thin layer is formed at the surface, during the pumping time. Oxygen molecules are also adsorbed on the vessel walls and sputter target during the growth of SiO$_2$ layers. When the deposition of the new a-Si layer starts, the sputtering process will begin with an oxidized surface of the target. These are the oxygen sources which could explain the oxygen content from the front edge of silicon spectrum. When the a-Si deposition is finished, the silicon surface is very reactive. Between the moment when the gases for the SiO$_2$ layer are introduced in vessel and the moment when plasma is in equilibrium conditions there is a period of time when high concentration oxygen is built on the surface. The ion bombardment and/or the oxidation process will determine silicon atoms to "diffuse" towards the new surface. In this way the a-Si layers deposited in "plasma on/off" procedure are thinner than that deposited in "plasma on".

3.2. Defects: ESR

An ESR experiment reveals the paramagnetic defects from the sample. Generally the derivative absorption of microwave power is measured as a function of the magnitude of an externally applied magnetic field. In Fig 8 the spectrum of the samples with 8 nm/layer is shown. As can be seen two types of defects are present and they are characterized by their g factor values /8/. The defect density and the g values associated with these defects are obtained by deconvolution of the spectra using two Lorentzian lineshapes. They are shown in table 2. We note that a g value of 2.0055 is assigned to a-Si dangling bond defects (DB) while 2.0012 is due to E' defects from SiO$_2$ /8/. As can be seen from the table2, the a-Si DB defects are identified. Their density of spins increases when the individual layer thickness decreases. The g values that we found for this type of defect are smaller (2.0048 instead of 2.0055) because of oxygen surroundings. Concerning the second type of defects, the g value associated slightly increases and its Lorentzian line becomes broader for thinner layer in the stack. This can be due to different surroundings of O$_3 \equiv$Si-- defect entity /9/. Very interesting is the evolution of the density of spins associated with this defect: it decreases for the sample with 4 nm/layer and can not be detected for that with 2 nm /layer. This is in good agreement with the results of HR-RBS where no SiO$_2$ was found for those samples. However it should be noted that using ESR only minority sites concerning defects are detected. The lack of O$_3 \equiv$Si-- defects could also indicate a more preferential existence of defects near Si clusters. As it is shown in /10/, by varying the microwave power we have reached the value where the E' defects were saturated. This experiment has allowed us a better separation between the two defects types.
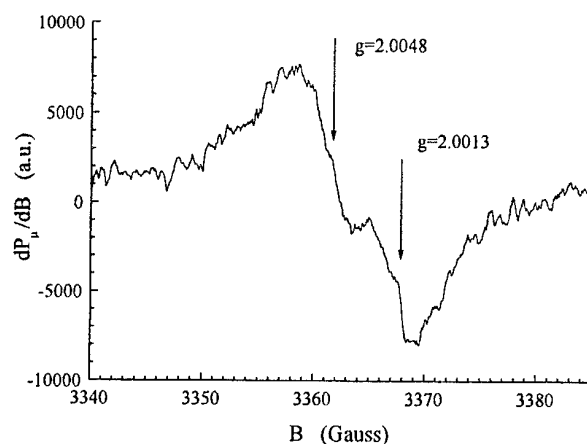
Fig. 7. ESR spectrum of multilayered samples with 8 nm/layer. With arrows are indicated the
a-Si DB and E' contributions at the spectrum

Tabel 2. The values of the g factor and the spin density as they result from the ESR spectra analysis.

Thickness (nm/layer)	g_1	g_2	n_{s1} (spins/cm^3)	n_{s2} (spins/cm^3)
8	2.00486	2.00138	$2.82 \cdot 10^{20}$	$8.74 \cdot 10^{19}$
4	2.00474	2.00158	$2.99 \cdot 10^{20}$	$4.54 \cdot 10^{19}$
2	2.00486	-	$5.73 \cdot 10^{20}$	-

4. Conclusions

From the results on our a-Si/SiO₂ multilayered samples we summarize:

i) The ion beam analysis techniques are competitive to determine the stoichiometry and the areal thickness of thin layers. Conventional RBS and ERD reveal layers with geometrical thickness larger than 16 nm. Best results are obtained using a combination of both RBS (for elements with larger atomic mass) and ERD (for elements with smaller mass) and to correlate their results in the region of the mass where the two techniques overlap.
High resolution RBS using a magnetic spectrograph has revealed layers with a thickness of 2 nm.

ii) With our sputtering deposition system we used two procedures in order to obtain layers as thin as possible of a-Si and SiO₂. The thinnest a-Si layer in a stack of a-Si/SiO₂ which is resolved by HR-RBS is 2nm while for SiO₂ we found 4 nm.

iii) The deposition procedure "plasma on/off" gives higher oxygen concentrations in "SiO₂" layer from the stack, but introduces also a small amount of oxygen in a-Si layers.

iv) ESR measurements show a convolution of two Lorentzian absorption lines. One of this can be identified as defects in silicon reach environment and the other one seems to be associated with defects in SiO₂ clusters.

References

[1] S. A. Fayek, A. F. Maged, M. R. Balboul, Vacuum 53, 447, (1999).
[2] D. R. Hamann, Phys. Rev B 122, 9899, (2000).
[3] L. C. Feldman, J. W. Mayer, Fundamentals of Surface and Thin Film Analyses, North-Holland, New York, 1986.

[4] J. F. Ziegler, J. P. Biersack, U. Littmark, The stopping and range of ions in solids Pergamon Press Inc., New York, 1985 (reviewed in 1990).

[5] L. R. Doolittle, Nucl. Instr. & Methods, **B9**, 344 (1985).

[6] G. F. Knoll, Radiation Detection and Measurements, 3-rd ed., John Wiley and sons, 152, 2000.

[7] W. M. Arnoldbik, W. Wolfswinkel, D. K. Inia, V. C. G. Verleun, S. Lobner, J. A. Reiders, F. Labohm, D. O. Boerma, Nucl. Instr. and Meth. in Phys. Research, **B118**, 566 (1996).

[8] M. Lannoo, P. Friedel, Atomic and Electronic Structure of Surfaces, Editor M. Cardona, Springer - Verlag, 196, 1991.

[9] W. L. Warren, E. H. Poindexter, M. Offenberg, W. Muller-Warmuth, J. Electrochem. Soc., 139, 872 (1992).

[10] N. Tomozeiu, E. E van Faassen, A. M. Vredenberg, F. H. P. M. Habraken, to be published in ICAMS 19-th Proceedings (J. Non-Cryst. Sol.).

CHARACTERIZATION OF THE Sb_2O_3 THIN FILMS BY X -RAY SCATTERING

C. Gheorghieş, L. Gheorghieş

University " Dunarea de Jos" of Galati, Romania

Thin films of Sb_2O_3 have been prepared by thermal sputtering on a substrate of SiO_2. The X-ray scattering experiment from the Sb_2O_3 films was accomplished using a reflectometer. It consists of an X-ray source, a curbed multilayer monochromator on the incident beam side, a slit in front of the sample mounted on the center of the circle of the goniometer and two slits preceding the detector on a circle of the diffracted beam side. Specular X-ray scattering is sensitive normal to the sample surface. It provides vertical structural structure parameters (the density and roughness of the substrate and the density, thickness and roughness of the Sb_2O_3 layers on top of the SiO_2 substrate). The scanning of the surface was done at an incidence angle of the X-ray is in the range of 0-8° and the reflected intensity was recorded. The specular and diffuse X-ray scattering obtained from the deposed thin films, having different thickness, represent a method that is sensitive to density contrasts and can therefore be applied to all sorts of unpatterned surfaces and layered structures. It is applicable to structures on the nanometer scale and roughnesses on the subnanometer scale. The obtained data have shown that at lest ultrathin Sb_2O_3 layers reveals a gradated layer structure. The results can be used in controlling of the thin layers fabrication, thickness determination that have to rely upon densities and optical constant of layers.

1. Introduction

The dielectric and semiconductor industry is increasing the wafer diameter for integrated circuit fabrication from 200 mm to 300 mm. According to Moore's law, the geometry of semiconductor devices is further reduced. The hystogram presented in Fig. 1 presents the progress of the "technology" in electronic industry [1, 2]. Frequently, the value of roughness is determined by atomic force microscopy. The value of roughness is important due to fact that in semiconductor technology, the gate length presents a decreasing tendency from 250nm to 180 nm. In consequence, the gate layer needs further perfection by reducing the interface and surface roughness.
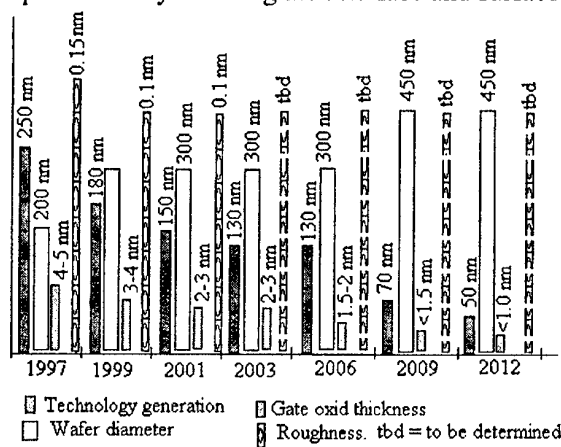

Fig. 1. The progress of technology and its consequences.

2. Sandwich structure

A sandwich structure is obtained by sputtering method and is typically in case of a transistor. The transistor performance is determined primarily by three parameters: gate length, gate dielectric

thickness and junction depth. Fig. 2 displays the schematic setup of a dielectric thin films deposited on a substrate having a typical microgeomety. For example, the thin gate oxides with oxide thickness < 10 nm, the Si /SiO$_2$ interface structure and the SiO$_2$ surface structure affect the insulating function of the SiO$_2$ layer [5]. More than, the channel mobility of electrical charge becomes smaller with increasing Si /SiO$_2$ interface roughness. Therefore, surfaces and interfaces have to be carefully monitored during wafer processing to keep them chemically clean and physically smooth [7].
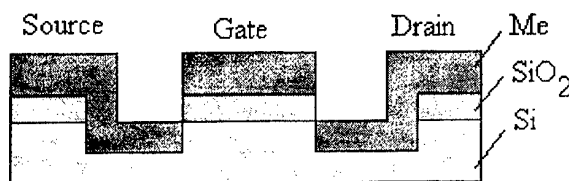
Fig. 2. Setup of a Si/SiO$_2$ used in a MOS transistor.

The physical structure of surfaces and ultrathin layers has emerged as a critical concern. For layer thickness < 5 nm and surface and interface roughness on the subnanometer scale, some standard methods of surface inspection and thickness control operate partly at their capability limits.

3. Investigation methods

A surface roughness value of 0.1 nm is not far from the noise level of atomic force microscopy [3]. Ellipsometry, a widely appreciated method to determine layer thickness, is not able to quantify thickness of changes of optical constants within thin layers [7, 8]. To avoid confusion, one has to keep in mind that the detection limit, which is frequently quoted to demonstrate the sensitivity of methods like atomic force microscopy, X-ray photoelectron spectroscopy or ellipssometry, refers to the lower limit of qualitative detection of thin layers and roughness under ideal conditions [5, 6]. X-ray scattering from surfaces and thin layers is a valuable tool to determine structure on the nanometer scale quantitatively and nondestructively. Its application to downsized semiconductor features of the near future is based on the weak interaction of subnanometer X-ray waves with matter. The sensitivity of X-ray to lateral and vertical density changes allows one to investigate surface as well as bulk properties of samples. In this way, the intensity and angular distribution of scattered X-ray allows one to calculate surface and interface roughness, densities as well as density profiles, thicknesses of layers and lateral properties such as the surface correlation length and the fractal dimension.

4. Surface parameters

For the Sb$_2$O$_3$/SiO$_2$ sample investigation, it is recommended to use the fractal description of surface. Fig. 3 provides a surface profile that changes its appearance because of changing fractal parameters. In figure, the mentioned parameters are: L is the correlation length, h is the hurst parameter and D is the fractal dimension. The surface roughness, σ, denotes the half-width of the distribution of height fluctuations (z-z$_0$) at the mean height (z$_0$) of the surface. For the Sb$_2$O$_3$/SiO$_2$ surface, the distribution can be described as a Gaussian. The parameters L and h provide information on the lateral structure of surfaces. As can be seen, the correlation length, l, is a measure for the length scale where σ does not change any more. The Hurst parameter, h, can be understood by comparing the three surface profiles in Fig. 3, where σ and L are kept constant. A decrease of h can be described by an increase of high-frequency, low-amplitude contributions to the surface profile.

The decrease of h does not affect σ, although the surface profile looks more jagged for lower h. For surfaces in general, D calculated to D = 3-h. D can be explained as a measure for the capacity of a fractal object to fill the space in which it is embedded.
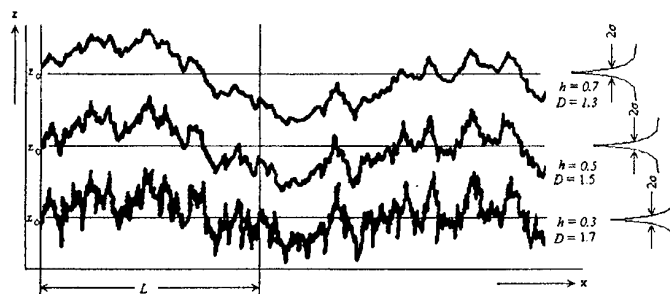
Fig. 3. Fractal parameters of a roughness surface.

5. Instrumentation

The X-ray scattering experiment from the Sb_2O_3/SiO_2 surface was accomplished at the reflectometer displayed in Fig. 4. It consists of an X-ray source; a curved, graded multilayer mirror on the incident beam side; a slit, S_1, in front of the sample mounted onto the Ω circle of the goniometer; and two slits S_2, S_3 preceding the detector on the 2Θ circle of the diffracted beam side.

The X-ray source was a sealed 1.0 kW Cu tube providing an 10 mm×0.05 mm line focus at a 6° take-off angle. The line focus was positioned in the focus of the parabolically curved, grade multilayer mirror acting as beam condenser. Additionally, the mirror plays role of monochromator and separates the $CuK\alpha_1$ and $CuK\alpha_2$ lines for the scattering experiments. For small scattering angles, no further energy resolution was necessary. The resulting wavelength was 0.154 nm. The purpose of S_1 was to cut out a 0.2 mm×10mm part of the incident beam for the scattering experiment. By reducing the beam width from 1 mm to 0.2 mm by S_1, the intensity decreased by a factor of five. This meant a loss for specular X-ray scattering, but it was necessary for the measurement and the interpretation of diffuse X-ray scattering. On the diffracted beam side, S_2 reduced the background scatter. S_2 was set to 0.4 mm×10 mm, and S_3 was set to 0.3 mm×10 mm. With this setup and an instrumental angular resolution of 0.06°, the primary beam intensity received at the scintillation counter detector was 10^6 cps. Eight orders of magnitude proved to be sufficient for the characterization of smooth Sb_2O_3/SiO_2 surfaces.

6. Experiments, results and discussion

Specular X-ray scattering is sensitive normal to the sample surface. It provides vertical structure parameters, i.e., the density and roughness of the Sb_2O_3 surface as well as the density, thickness and roughness of top of SiO_2. The Fig. 4 displays the scattering geometry. By increasing Ω, the scattering signal is recorded by the detector at the angular position $\Theta = \Omega$. The intensity distribution vs. θ, appears as a decreasing curve from $\Theta = 0°$ up to $\Theta = 8°$. The exact shape of the specular signal is determined by the vertical structure parameters. To get information about the lateral structure of the surface, the diffuse scattering has be measured. Hereby, the angle between incoming beam and outgoing beam (2Θ) remains fixed. The angle between incoming beam and sample surface (Ω) is changed from $\Omega = 0°$ to $\Omega = 1.5°$. The sharp peaks in the middle of the diffuse scattering curves ($\Omega = \Theta$) belong to the specular scattered intensity. The respective width of 0.03° is determined by the instrument angular resolution of the setup.
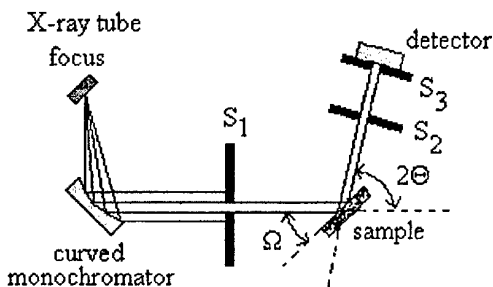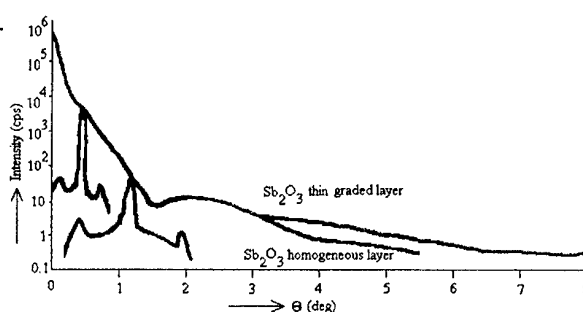

Fig. 4. The setup of the reflectometer.

Fig. 5. Specular and diffuse X-ray scattering curves.

The specular scattered signal has some distinct features: From $\Theta = 0°$ to $\Theta = 0,2°$ the intensity is nearly constant, with a count rate of 10^6 cps. The negative slope of the signal is affected by parameters

such as the Sb_2O_3 surface roughness, the Sb_2O_3/SiO_2 interface roughness, the density contrast between Sb_2O_3 and SiO_2 and the thickness of the Sb_2O_3 layer. The diffuse scattered signal originates solely in the imperfections of samples. With no surface or interface roughnesses, there would be no diffuse scattering. The small peaks on either side of the diffuse scattering curves in Fig. 5 originate from total external reflection; they are called Yoneda wings. With the exception of the shape specular peaks, the shape of the diffuse scattering curves is determined mainly by the Sb_2O_3 surface roughness, by the lateral correlation length of the surface and by its fractal dimension. The linear grading affects the roughness value of the Sb_2O_3/SiO_2 interface. With 0.02 nm, the interface roughness is below the determination limit of the X-ray scattering method. The thickness value of the Sb_2O_3 layer of 3.0nm demonstrates the sensitivity of the X-ray scattering method to ultrafin structures <10 nm. An intensity of 10^6 cps should be sufficient to quantify even thinner layers. The surface correlation length of 145 nm shows that the X-ray scattering model is wel suited to characterize dielectric structures on the nanometer scale, even laterally. The grading of the 3.0nm Sb_2O_3 layer is the most important result obtained from specular X-ray scattering. This finding is supported by the diffuse X-ray scattering measurements where the scattering signal turns out to be sensitive mainly to the Sb_2O_3 surface shape. The Sb_2O_3/SiO_2 interface looses its scattering contrast because of Sb_2O_3 layer grading, which starts at Sb_2O_3/SiO_2 and ends at the Sb_2O_3 surface. The layer grading reveals that oversimplified assumptions about the homogeneity of thin layers need to be reconsidered. The density values of the graded Sb_2O_3 are 4.88 g/cm^3 at the interface and 4.36 g/cm^3 at the surface. Compared to the oxide's theoretical density of 5.65 g/cm^3, the measured values are very small but quite common for natural oxides. The effect of the thickness and homogeneity on the deposed layer on the specular scattered X-ray curve is presented in the same Fig. 5. Up to $\theta = 3°$, and within an intensity range of seven orders of magnitude, both models yield appropriate fits to the experimental data. Between $\theta = 3°$ and $\theta = 8°$, the models differ.

7. Effects of surface parameters on device performance

As mentioned, real structure parameters affect the proper performance of downsized a sanwich structures. A bite further away from mainstream science, theorist have already shown the dependence of oxide growth on fractal dimension, which has been confirmed by experiment. The precise control of growth processes is crucial for the fabrication of ultrathin layered structures, and therefore, investigations of appropriate models to describe growth processes on atomic scales under nonequilibrium conditions continue. The homogeneity of the oxide density determines the dielectric constant of the oxide. In this way, undesigned density changes of the thin layer can degrade its insulating function.

8. Conclusions

1. In this paper, it is shown that for SiO_2 wafers with an ultrathin Sb_2O_3 layer on top, X-ray scattering is a method for future quality control in the front-end processes of dielectric production.. The method is sensitive to density contrasts and can therefore be applied to all sorts of unpatterned surfaces and layered structures. X-ray scattering is nondestructive and it is applied to structures on the nanometer scale and roughnesses on the subnanometer scale. Because of its sensitivity to density fluctuations, X-ray scattering reveals the inner density structure of ultrathin layers.

2. The results have shown that at least ultrathin Sb_2O_3 layers reveal a graded layer structure. The precise knowledge of the latter is critical for the fabrication of thin layers, and it is crucial for other method of thickness determination that have to rely upon densities and optical constants of layers.

3. X-ray scattering should can be considered as a standard methods for ultrathin layer and surface/interface characterization.

References

[1] P. Wagner, H. A. Gerber, D. Gräf, R. Velten, SPIE 2862, 152 (1996).
[2] R. K. Goodal, SPIE 2862, 2 (1996).
[3] G. Kamarinos, P. Felix, J. Phys. D: Appl. Phys. 29, 487 (1996).
[4] G. Jungk, Private communication.
[5] M. Dax, Semiconductor International, August 91 (1996).
[6] P. E. J. Flevit, R. K. Wild Physical methods for materials characterization, IOP, Bristol & Philadelphia, 1994.
[7] M. Schuster, H. Göbel J, Phys. D: Appl. Phys. A270, 28 (1995).
[8] R. A. Cowley, T. W. Ryan, J. Phys. D: Appl. Phys. 20, 61 (1987).
[9] Z. Z. Zinurova, M. A. Reveleva, Mikroelectronika 21, 24 (1992).

OPTICAL AND ELECTRICAL PROPERTIES OF AS-DEPOSITED LPCVD SiO$_x$N$_y$ THIN FILMS

M. Modreanu, Mariuca Gartner[a], N.Tomozeiu[b], A. Szekeres[c]

National Institute for R&D in Microtechnologies PO Box 38-160, Bucharest 72225 Romania
[a]Institute of Physical Chemistry, Spl.Independentei 202, Bucharest 77208, Romania
[b]Bucharest University, Faculty of Physics, PO Box 11 MG, Bucharest, Romania
[c]Institute of Solid State Physics, Tzarigradsko Chaussee 72, Sofia 1784, Bulgaria

The silicon oxynitride (SiO$_x$N$_y$) films have several applications in opto- and micro-electronics technology: thin gate dielectrics, optical wave guides and membranes for microelectromechanical systems (MEMS). In some applications it is necessary a controllable variable refractive index of the silicon oxynitride films. In others, the defect density at the Si/ a-SiO$_x$N$_y$ interface should be well controlled. This paper deals with these issues and an investigation of the relationship between deposition parameters and the physical properties of the a-SiO$_x$N$_y$ films is done. Amorphous silicon oxynitride films of various compositions were deposited by low-pressure chemical vapor deposition (LPCVD) at temperature around 800°C and 400 mTorr, using mixture of SiCl$_2$H$_2$-NH$_3$-N$_2$O. The investigations on optical and electrical properties of the samples were made using spectroellipsometry and capacitance-voltage measurements. Optical and microstructural parameters of the films were calculated from spectroellipsometry data using different approaches (Bruggeman-EMA, Cauchy, Sellmeier and Wemple-Di Domenico). The refractive index dispersion curves were well fitted with both the Cauchy and the Sellmeier theoretical models. The equivalence between the parameters that characterize the two models is established. As the Wemple and Di Domenico approximation applied to our samples has shown, the optical band gap values decrease with the increase of the nitrogen content in the SiO$_x$N$_y$ films.The analyses of 1 MHz capacitance-voltage characteristics revealed low densities of the interface traps. This is attributed to the nitrogen incorporation at the SiO$_x$N$_y$/Si interface, which leads to suppression of interface trap generation.

1. Introduction

The low pressure chemical vapour deposition (LPCVD) silicon oxynitride (SiO$_x$N$_y$) films have several applications in microelectronics and optoelectronics industry: passivating coatings [1-6], thin gate dielectrics [2] and, membranes and optical wave guides for microelectro-mechanical systems (MEMS) [3]. Controllable variable refractive index of the silicon oxynitride films, which are of growing interest in integrated opto-electronical devices, resistance to oxidation, low mechanical stress are some properties of these films.

This paper presents the correlation between deposition parameters, material properties and internal structure. The investigation on optical and electrical properties was made using spectroellipso-metry (SE) and the analyses of 1 MHz capacitance-voltage characteristics. In order to calculate the optical and microstructural properties of the films from SE data, we used three different approaches: Bruggeman-EMA [7] Cauchy and Sellmeier [8].

2. Experimental details

LPCVD silicon oxynitride thin films were deposited on 3-inch (100) p-type silicon wafers. The a-SiO$_x$N$_y$ films were formed by reacting dichlorosilane (SiH$_2$Cl$_2$) with nitrous oxide (N$_2$O) and ammonia (NH$_3$). The total deposition pressure was 400 mTorr. Relative gas flow ratio $r = Q_{N_2O}/Q_{NH_3}$, deposition temperature and pressure have a great influence on the film composition. Two of these

parameters were varied during our experiments: the relative gas flow ratio was between 0 and 8 for 860°C deposition temperature; keeping the r parameter constant (r=3.5) the deposition temperature was increased from 820°C to 880°C. We have also deposited the silicon nitride films from dichlorosilane and ammonia (NH_3) at 800°C using a relative gas flow ratio SiH_2Cl_2 / NH_3 = 0.25. Before deposition, the substrates were chemically cleaned using a 10 % HF solution in order to remove the native oxide.

The film thickness, the dispersion of the refractive index and optical gap were determined using spectroscopic ellipsometry in 320-800 nm wavelength range. All SE measurements were done at an incidence angle of 70°.

For electrical characterization of LPCVD-SiO_xN_y films, conventional, room temperature 1 MHz C-V technique was applied. For this purpose, metal-insulator-silicon (MIS) capacitors were formed by vacuum thermal evaporation of aluminum dots onto SiO_xN_y surface through a metal mask, while onto silicon backside continuous Al film was evaporated. The effective dielectric charge density (Q_{eff}) was calculated from the flat band voltage shift in the 1 MHz C-V curves. The interface traps density (D_{it}) was estimated from the comparison of the 1 MHz experimental with the corresponding ideal C-V characteristics.

3. Results and discussions

The most significant optical properties in amorphous materials, the optical gap (E_g) and the refractive index (n) are obtained using the SE measurements. Normally, both of them depend on the composition of the films.We have calculated the coefficients x and y in the SiO_xN_y formula using Temple-Boyer formula (error lower than 1%) [9]:

$$n=2-0.41x+0.07x^2=1.45+0.19y+0.16y^2 \qquad (1)$$

and the results are given in Table 1. The sample identification is made by its refractive index values (at λ=632.8 nm). In the last row of the table 1 there are the values for Si_3N_4 and we can observe that the normalization to the silicon label produces a good value for nitrogen.

Table 1. Results concerning the film composition, obtained using the Temple-Boyer formula.

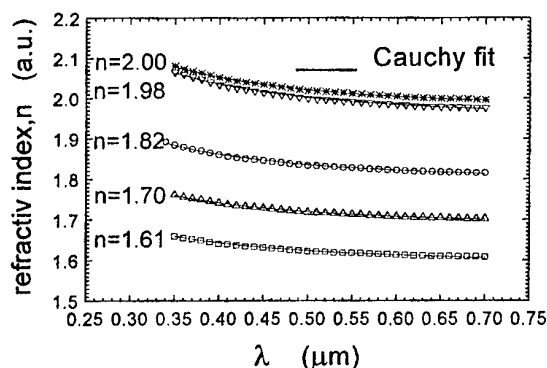| n	x	y
1.61	1.21	0.56
1.70	0.86	0.79
1.82	0.50	1.04
1.98	0.05	1.32
2.00	0	1.34

Fig. 1. The refractive index dispersion and the fit with Cauchy's formula.

We have studied the spectral dispersion of the refractive index for our five different a-SiO_xN_y samples (Fig.1). The dispersion spectra of the refractive index was fit using the Cauchy formula:

$$n = \alpha + \frac{\beta}{\lambda^2},$$ (2)

where α and β are the Cauchy's parameters and λ is the wavelength of light used at SE. For $\lambda \to \infty$, the significance of the α parameter appears immediately as n_∞. The values of the fit parameters and the fit quality parameter (x^2) are presented in Table 2.

Table 2. Cauchy parameters and the fit quality.

n	α	β (*10^{-2})	χ^2
1.61	1.59	0.87	$1.3 \ 10^{-6}$
1.70	1.68	0.90	$6.3 \ 10^{-7}$
1.82	1.78	0.11	$1.25 \ 10^{-6}$
1.98	1.94	1.5	$2.39 \ 10^{-6}$
2.00	1.97	1.3	$1.22 \ 10^{-6}$

Another model used in the refractive index dispersion study is the Sellmeier' model that gives:

$$n^2 = 1 + \frac{A\lambda^2}{\lambda^2 - B},$$ (3)

where A and B are the Sellmeier parameters. Under these conditions we can see that $n_\infty = \sqrt{1+A}$ and the calculated values are given in the fourth column of the Table 3. Comparing these values with the α values from table 2 we find a good agreement.

Table 3. Sellmeier constants for the studied SiO_xN_y thin films.

n	A	$B*10^{-2}$	n_∞	$B*10^{-2}$ (eqn (5))
1.61	1.826	1.579	1.59	1.512
1.7	1.847	1.565	1.68	1.564
1.82	2.221	1.614	1.79	1.610
1.98	2.792	1.787	1.85	1.784
2.00	2.882	1.646	1.97	1.644

Wemple and Di Domenico [10] have developed a model where the refractive index dispersion is studied in the region of transparency, bellow the gap, using the single-oscillator approximation. Defining two parameters, the oscillation energy, E_0, and the dispersion energy, E_d, the model concludes:

$$n^2(\omega) - 1 \cong \frac{E_d E_o}{E_o^2 - E^2}$$ (4)

Both Wemple parameters can be obtained from the slope and the intercept with the Y axis of the plot $(n^2-1)^{-1} = f(E^2)$. The energy oscillation and dispersion energy values are given in Table 4. The dispersion energy measures the average strength of interband optical transitions. Wemple and Di Domenico have related this parameter with the coordination number for anion and the valence electrons number per anion. In our case the E_d values increase with increasing the silicon nitride relative percentage in the films (the bonds' number per nitrogen atom is higher in comparison with that of oxygen atom). The oscillator energy is related by an empirical formula to optical gap value: $E_0=1.7E_g$ [11,12] The calculated values of the optical gap are also presented in table 4. We can see that, higher oxygen content in film means a higher optical gap value. This result is very important

because it shows that the refractive index and the optical gap of the material can be controlled by the deposition conditions.

Applying the Sellmeier's model and the Wemple's model on the same photon energy range, the A and B parameters can be expressed as:

$$A = \frac{E_d}{E_0} \quad \text{and} \quad B = \frac{h^2 c^2}{E_0^2} \tag{5}$$

where h is the Plank's constant and c is the light speed in vacuum.

We have calculated the B-parameter values using eqn (5) and the results are given in Table 3. A comparison between the third and the fifth columns shows the good agreement between the two optical models.

The influence of the relative percentage of oxygen on the optical gap values can be observed from the correlation of the results presented in Table 1 and 4. In such way, we have correlated the two optical films' parameters with each other and, an optical one with a structure parameter. As it is known, when the effective refractive index decreases, the value of the optical gap increases. One the other hand, higher silicon dioxide in the film means higher optical gap values. For silicon nitride film, we have obtained a good agreement with the literature, concerning the optical gap: 5.43eV in comparison with 5.35 eV [13].

Typical high-frequency capacitance curves for $SiO_{0.50}N_{1.04}$ and $SiO_{0.86}N_{0.79}$ samples are plotted in Fig. 2. The density of effective fixed charge Q_{eff} is estimated from the flatband voltage values and are presented in Table 5. For sample $SiO_{0.50}N_{1.04}$ no hysteresis in the C-V curve and lower Q_{eff} are observed. This can be related to higher amount of nitrogen present in the near- interface region, which attaches unsaturated Si bonds ($O_3\equiv Si\cdot$). As the oxygen content increases, the interface region approaches the standard Si/SiO_2 as can be seen in Fig.1. The small hysteresis is indicative for the presence of slow interface traps with a density of 4×10^{10} cm^{-2}.

The densities of the interface traps are given in Table 5. The dielectric permittivity, ε_i, is calculated from the dielectric capacitance, C_i, in the strong accumulation regime ($C_i=\varepsilon_i\varepsilon_0 s/t_i$). Its value is also given in Table 5. According to the refractive index behavior, as the oxide fraction becomes higher in the film structure the dielectric permittivity decreases.

Table 4. Optical gap and Wemple Di Domenico parameters for the studied films.

n	E_d (eV)	E_0 (eV)	E_g (eV)
1.61	15.48	10.09	5.93
1.73	18.25	9.96	5.86
1.82	21.66	9.78	5.75
1.98	25.94	9.28	5.46
2.00	27.87	9.23	5.43

Table 5. The dopant density, N_a, the effective dielectric charge density, Q_{eff}, and the dielectric permittivity, ε_i for $SiO_{0.50}N_{1.04}$ (1) and $SiO_{0.86}N_{0.79}$ (2) samples

Sample	N_a (cm^{-3})	Q_{eff} (cm^{-2})	ε_i
1	1.3×10^{15}	1.42×10^{11}	5.10
2	1.3×10^{15}	3.82×10^{11}	4.42

The distribution of the interface traps over the silicon energy gap is displayed in Fig. 3. Again, the higher nitrogen content leads to smaller density over most of the bandgap. Obviously, trivalent Si such as $Si_3\equiv Si\cdot$ forms rigid Si-N bonds reducing the intrinsic stress at the interface.

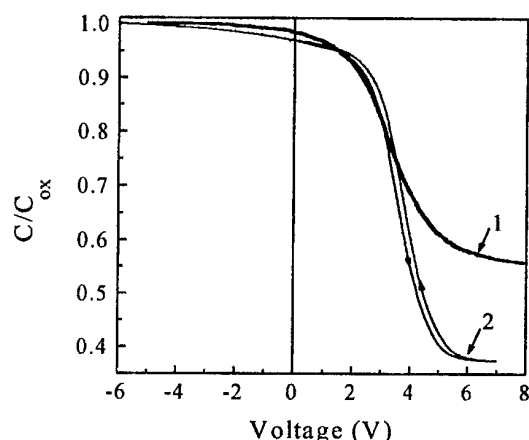Fig. 2. Normalized 1 MHz capacitance-voltage characteristics of MIS structures for $SiO_{0.5}N_{1.04}$ (1) and $SiO_{0.86}N_{0.79}$ (2).
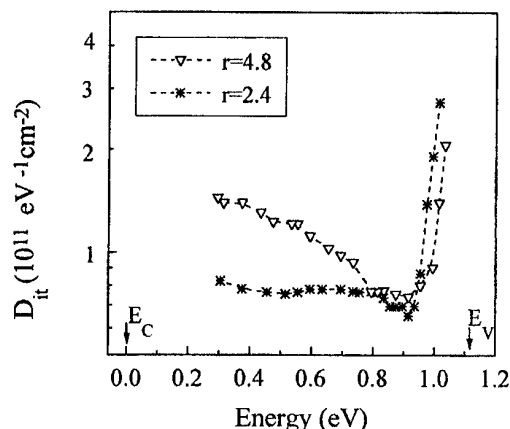
Fig. 3. Energy distribution of the interface traps, D_{it}, in the Si bandgap.

As a consequence, the density of interface traps related to deformed and/or dangling bonds becomes lower. The lower intrinsic stress at the interface is supported by the low trap density approaching the conduction band edges.

The higher density near midgap, in the sample with deficit in nitrogen, can be connected with large amount of trivalet Si defect centers.

4. Conclusion

The content of this paper can be synthesized as:

1. Deposition of LPCVD a-SiON films it's a good solution to obtain films with controlled refractive index;

2. The dispersion of the refractive index for samples with different silicon dioxide content was successfully fitted with Cauchy and Sellmeier formula;

3. The optical gap energy (E_g) and the oscillator energy (E_0) become higher, while the oscillator strength (E_d) lower, with increase of the silicon dioxide in the film. The latter is indicative for the stronger Si-N than Si-O bonds.

4. The optical gap and the dispersion energy values were determined using Wemple and Di Domenico approximation.

v) From the C-V data analysis we can conclude that the observed much lower total density of defects in SiO_xN_y in comparison with conventional thermal SiO_2/Si structures is due to the effect of nitrogen incorporation, which produces strong S-N bonds to replace the weak Si-O bonds and to saturate the $O_3\equiv Si^{\cdot}$ and $Si_3\equiv Si^{\cdot}$ dangling bonds.

References

[1] A. J. Lowe, M. J. Powell, S. R. Elliott, J. Appl. Phys. **59**, 1251 (1986).

[2] B. B. Ilic, Hewlett Packard J., **33**, 25 (1982).

[3] M. Modreanu, P. Cosmin, Procc. of Int. Conf. of Semic.-CAS'96, 323 (1996).

[4] H. Kurata, M. Hirose, Y. Osaka, Jap. J. of Appl. Phys., **20**, 11, L811, (1981).

[5] F. H. P. M. Habraken, R. H. G. Tijhaar, V. F van der Weg, A. E. T. Kuiper, M. F. C. Willemsen, J. Appl. Phys., **59**, 447 (1986).

[6] B. H. Augustine, E. A. Irene, Y. J. He, K. J. Price, L. E. McNeil, K. N. Christensen, D. M. Maher, J. Appl. Phys., **78**, 402 (1995).

[7] D. A. G. Bruggeman, Ann. Phys. **24**, 636 (1935).

[8] M. Born, E. Wolf, Principles of Optics, Pergamon Press, Oxford, Chapter II, (1975).
[9] P. Temple-Boyer, B. Hajji, J. L. Alay, J. R. Morante, A. Martinez, E'MRS'99, Book of abstracts.
[10] S. H. Wemple, M. DiDomenico, Phys. Rev., **B3**, 4, 1338 (1971).
[11] N. Tomozeiu, Ph. D. Thesis, Bucharest University, (1994).
[12] I. Solomon, M. P. Schmidt, C. Sénémaud, M. Driss Khodja, Phys.Rev., **B38**, 18, 13263 (1988).
[13] A. Borghesi, A. Sassela, S. Rojas, Thin Solid films, **233**, 227 (1993).

AUTHOR INDEX

A

Andriesh A. M., 443, 455
Arnoldbik W. M., 563
Azhniuk Yu. M., 509, 515

B

Balan V., 367
Balta P., 531
Botila T., 525
Boycheva S. V., 503
Bradaczek H., 249
Briois V., 553

C

Cerchez M., 559
Cernosek Z., 177, 459, 463
Černošková E., 459, 463
Churbanov M. F., 341, 351
Colomeyco E. P., 473
Cvejič N., 337

D

Dalgýç Serap, 537
Dalgýç Seyfettin, 537
Denisov D. V., 549
Dikova J., 395, 399

E

Elliott S.R., 361

F

Fadin I. E., 351
Fairushin A. R., 499
Filipecki J., 329
Frumar M., 177, 227, 459, 463
Frumarova B., 177
Furniss D., 443

G

Ganesan R., 467
Ganjoo A., 167, 221
Gartner M., 575
Gerasimenko V. V., 351
Gerzanich O. I., 515
Gheorghies C., 571
Gheorghies L., 571
Ghiordanescu V., 521
Golovchak R. Ya., 329
Gomonnai A. V., 509, 515
González-Hernández J., 333
González-Leal J. M., 287
Gopal E. S. R., 467
Grecu M. N., 521
Grigoras B., 559

H

Habraken F. H. P. M., 563
Halm Th., 255
Holubová J., 459, 463
Hosokawa S., 199
Hoyer W., 255, 303
Hyla M., 329

I

Indutnyy I. Z., 383
Ion L., 307
Ionescu L., 559
Iovu M. A., 473
Iovu M. S., 303, 443, 473
Ivanova Z. G., 481

J

Jedelsky J., 177
Jiménez-Garay R., 287

582

INSTRUCTIONS FOR AUTHORS

Journal Scope

The Journal of Optoelectronics and Advanced Materials appears quarterly and publishes review papers, research papers and short communications in the field of optoelectronics and new advanced materials: optoelecctronic devices, crystals of relevance in optoelectronics, amorphous and glassy materials, nanostructured materials, functional and smart materials. Theoretical papers are encouraged. Papers dealing with biomaterials and optoelectronic applications for medical purposes are accepted. An important aim of the Journal is to bring together the specialists from related fields: optoelectronics and materials.

Submission of papers

Authors are invited to send the manuscripts in British English, firstly by e-mail and then by regular mail. Two hard copies and an electronic record on a 3 ½ inches floppy disk are required.

Review papers are limited to 20 pages. Regular papers are limited to 10 pages. Short communications are limited to 4 pages. Excepting short communications, every paper must have an abstract with maximum 200 words. At least three keywords, which characterize the subject of the work, must be specified.

One full page of the Journal contains 54 rows with 95 characters/row (font size 11).

The following structure of a paper is recommended: 1. Introduction, 2. Experimental (Theory, Modeling, …), 3. Results, 4. Discussion, 5. Conclusions.

References will be consecutively numbered in the text and collected at the end of the paper in the following style for journals, proceedings and books, respectively:

[1] N. Rivier, Phil. Mag., **40**, 859 (1979).
[2] S. R. Ovshinsky, Proc. 7-th Intern. Conf. Liq. Amorph. Semic., Edinburgh, Ed. W. E. Spear, Institute of Physics, Bristol, UK, 1978, p. 519.
[3] N. F. Mott, E. A. Davis, Electron Processes in Non-Crystalline Materials, Clarendon Press, Oxford (1979).

Figures and tables are recommended to be introduced in the text with their legends.

The editor will send every manuscript to two referees for a critical examination. The comments of the referees and the decision of the Editorial Board regarding the publication will be sent to the corresponding authors.

The manuscripts accepted for publication will be published in maximum three months. The corresponding author will receive one free copy of the issue of the Journal where the paper was printed and 10 reprints without charge. The authors can order additional reprints.

All rights are reserved by "Journal of Optoelectronics and Advanced Materials". Any reproduction or dissemination of the information herein, even as excerpts of any extent, is permitted only by written consent of the Editor-in-Chief.

The manuscripts must be sent to the following address:

JOURNAL OF OPTOELECTRONICS AND ADVANCED MATERIALS

Subscriptions for *JOURNAL OF OPTOELECTRONICS AND ADVANCED MATERIALS* can be requested at the above address.
Subscription payment will be made to the following accounts:
2511.1-401.1/ROL (Romanian lei): 50699113623 - TREZORERIE Jud. ILFOV;
2511.1-401.19/USD (US dollars):Romanian Trade Bank, BCR UNIREA 55101
Subscription for 2001 (four issues):
500 000 ROL (for Romania); 100 USD (for other countries).

ISSN 1454-4164